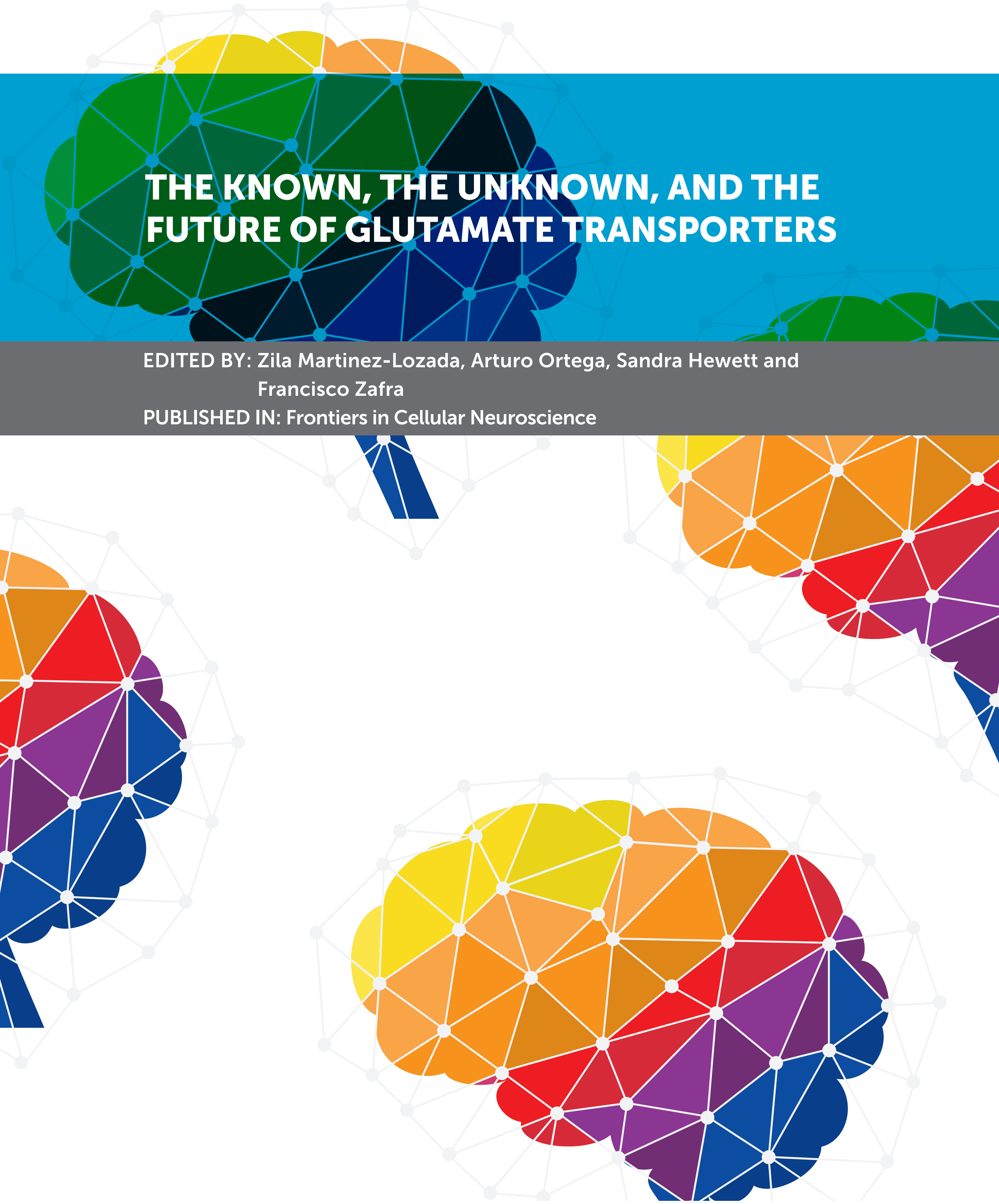

THE KNOWN, THE UNKNOWN, AND THE FUTURE OF GLUTAMATE TRANSPORTERS

EDITED BY: Zila Martinez-Lozada, Arturo Ortega, Sandra Hewett and
Francisco Zafra

PUBLISHED IN: Frontiers in Cellular Neuroscience

frontiers Research Topics

ISSN 1664-8714
ISBN 978-2-83250-090-3
DOI 10.3389/978-2-83250-090-3

About Frontiers

Frontiers is more than just an open-access publisher of scholarly articles: it is a pioneering approach to the world of academia, radically improving the way scholarly research is managed. The grand vision of Frontiers is a world where all people have an equal opportunity to seek, share and generate knowledge. Frontiers provides immediate and permanent online open access to all its publications, but this alone is not enough to realize our grand goals.

Frontiers Journal Series

The Frontiers Journal Series is a multi-tier and interdisciplinary set of open-access, online journals, promising a paradigm shift from the current review, selection and dissemination processes in academic publishing. All Frontiers journals are driven by researchers for researchers; therefore, they constitute a service to the scholarly community. At the same time, the Frontiers Journal Series operates on a revolutionary invention, the tiered publishing system, initially addressing specific communities of scholars, and gradually climbing up to broader public understanding, thus serving the interests of the lay society, too.

Dedication to Quality

Each Frontiers article is a landmark of the highest quality, thanks to genuinely collaborative interactions between authors and review editors, who include some of the world's best academicians. Research must be certified by peers before entering a stream of knowledge that may eventually reach the public - and shape society; therefore, Frontiers only applies the most rigorous and unbiased reviews.
Frontiers revolutionizes research publishing by freely delivering the most outstanding research, evaluated with no bias from both the academic and social point of view. By applying the most advanced information technologies, Frontiers is catapulting scholarly publishing into a new generation.

What are Frontiers Research Topics?

Frontiers Research Topics are very popular trademarks of the Frontiers Journals Series: they are collections of at least ten articles, all centered on a particular subject. With their unique mix of varied contributions from Original Research to Review Articles, Frontiers Research Topics unify the most influential researchers, the latest key findings and historical advances in a hot research area! Find out more on how to host your own Frontiers Research Topic or contribute to one as an author by contacting the Frontiers Editorial Office: frontiersin.org/about/contact

THE KNOWN, THE UNKNOWN, AND THE FUTURE OF GLUTAMATE TRANSPORTERS

Topic Editors:
Zila Martinez-Lozada, Children's Hospital of Philadelphia, United States
Arturo Ortega, Centro de Investigación y de Estudios Avanzados del Instituto Politécnico Nacional, Mexico
Sandra Hewett, Syracuse University, United States
Francisco Zafra, Autonomous University of Madrid, Spain

Citation: Martinez-Lozada, Z., Ortega, A., Hewett, S., Zafra, F., eds. (2022). The Known, the Unknown, and the Future of Glutamate Transporters. Lausanne: Frontiers Media SA. doi: 10.3389/978-2-83250-090-3

Table of Contents

04 ***Editorial: The Known, the Unknown, and the Future of Glutamate Transporters***
Zila Martinez-Lozada, Sandra J. Hewett, Francisco Zafra and Arturo Ortega

07 ***EAAT2 Expression in the Hippocampus, Subiculum, Entorhinal Cortex and Superior Temporal Gyrus in Alzheimer's Disease***
Jason H. Y. Yeung, Thulani H. Palpagama, Oliver W. G. Wood, Clinton Turner, Henry J. Waldvogel, Richard L. M. Faull and Andrea Kwakowsky

19 ***Aged xCT-Deficient Mice Are Less Susceptible for Lactacystin-, but Not 1-Methyl-4-Phenyl-1,2,3,6- Tetrahydropyridine-, Induced Degeneration of the Nigrostriatal Pathway***
Eduard Bentea, Laura De Pauw, Lise Verbruggen, Lila C. Winfrey, Lauren Deneyer, Cynthia Moore, Giulia Albertini, Hideyo Sato, Ann Van Eeckhaut, Charles K. Meshul and Ann Massie

34 ***Neuronal Loss of the Glutamate Transporter GLT-1 Promotes Excitotoxic Injury in the Hippocampus***
Theresa S. Rimmele, Shaomin Li, Jens Velde Andersen, Emil W. Westi, Alexander Rotenberg, Jianlin Wang, Blanca Irene Aldana, Dennis J. Selkoe, Chiye J. Aoki, Chris G. Dulla, Paul Allen Rosenberg

55 ***Cellular Physiology and Pathophysiology of EAAT Anion Channels***
Peter Kovermann, Miriam Engels, Frank Müller and Christoph Fahlke

69 ***Validation of a System x_c^- Functional Assay in Cultured Astrocytes and Nervous Tissue Samples***
Pauline Beckers, Olaya Lara, Ines Belo do Nascimento, Nathalie Desmet, Ann Massie and Emmanuel Hermans

80 ***Physiological Perspectives on Molecular Mechanisms and Regulation of Vesicular Glutamate Transport: Lessons From Calyx of Held Synapses***
Tetsuya Hori and Shigeo Takamori

95 ***Uncoupling the Excitatory Amino Acid Transporter 2 From Its C-Terminal Interactome Restores Synaptic Glutamate Clearance at Corticostriatal Synapses and Alleviates Mutant Huntingtin-Induced Hypokinesia***
Stefan Hirschberg, Anton Dvorzhak, Seyed M. A. Rasooli-Nejad, Svilen Angelov, Marieluise Kirchner, Philipp Mertins, Gilla Lättig-Tünnemann, Christoph Harms, Dietmar Schmitz and Rosemarie Grantyn

118 ***Activation of Glutamate Transport Increases Arteriole Diameter* in vivo*: Implications for Neurovascular Coupling***
Joshua G. Jackson, Elizabeth Krizman, Hajime Takano, Meredith Lee, Grace H. Choi, Mary E. Putt and Michael B. Robinson

140 ***The Cystine/Glutamate Antiporter, System x_c^-, Contributes to Cortical Infarction After Moderate but Not Severe Focal Cerebral Ischemia in Mice***
Yan He and Sandra J. Hewett

148 ***Deletion of the Sodium-Dependent Glutamate Transporter GLT-1 in Maturing Oligodendrocytes Attenuates Myelination of Callosal Axons During a Postnatal Phase of Central Nervous System Development***
Elizabeth J. Thomason, Edna Suárez-Pozos, Fatemah S. Afshari, Paul A. Rosenberg, Jeffrey L. Dupree and Babette Fuss

Frontiers in Cellular Neuroscience

TYPE Editorial
PUBLISHED 17 August 2022
DOI 10.3389/fncel.2022.1005834

OPEN ACCESS

EDITED AND REVIEWED BY
Enrico Cherubini,
European Brain Research Institute, Italy

*CORRESPONDENCE
Zila Martinez-Lozada
martinezlz@chop.edu

SPECIALTY SECTION
This article was submitted to
Cellular Neurophysiology,
a section of the journal
Frontiers in Cellular Neuroscience

RECEIVED 28 July 2022
ACCEPTED 04 August 2022
PUBLISHED 17 August 2022

CITATION
Martinez-Lozada Z, Hewett SJ, Zafra F and Ortega A (2022) Editorial: The known, the unknown, and the future of glutamate transporters.
Front. Cell. Neurosci. 16:1005834.
doi: 10.3389/fncel.2022.1005834

Editorial: The known, the unknown, and the future of glutamate transporters

Zila Martinez-Lozada[1]*, Sandra J. Hewett[2], Francisco Zafra[3,4] and Arturo Ortega[5]

[1]Department of Pediatrics, The Children's Hospital of Philadelphia, Philadelphia, PA, United States, [2]Program in Neuroscience, Department of Biology, Syracuse University, Syracuse, NY, United States, [3]Center of Molecular Biology Severo Ochoa, School of Science, Consejo Superior de Investigaciones Científicas, Universidad Autónoma de Madrid, Madrid, Spain, [4]Instituto de Investigación Sanitaria del Hospital Universitario La Paz — IdiPAZ, Madrid, Spain, [5]Department of Toxicology, Centro de Investigación y de Estudios Avanzados del Instituto Politécnico Nacional, Ciudad de México, Mexico

KEYWORDS

glutamate, glutamate transport, excitatory amino acid transporter (EAAT), vesicular glutamate transport proteins, system x_c^-

Editorial on the Research Topic
The known, the unknown, and the future of glutamate transporters

Glutamate is the main excitatory neurotransmitter in the central nervous system (Fonnum, 1984). It is required for essentially all cognitive functions, however, is also a neurotoxin. Therefore, maintenance of the glutamate extracellular concentration involves tight control of its release and uptake. Several glutamate transport proteins contribute to this regulation. Vesicular glutamate transporters (VGLUTs) package glutamate into synaptic vesicles (Omote et al., 2011). The excitatory amino acid transporters (EAATs), under physiological conditions, remove glutamate from the synaptic cleft (Danbolt et al., 2016). Lastly, the cystine/glutamate exchanger, also known as system x_c^-, exports glutamate in exchange for cystine (Jabaudon et al., 1999; Warr et al., 1999; Featherstone and Shippy, 2008). In this Research Topic, we assemble a review of current literature and new research on these transporters.

VGLUTs

Glutamate is packaged into synaptic vesicles *via* one of three VGLUTs. As part of our collection, Hori and Takamori describe a novel method to monitor glutamate transport *in living nerve terminals* using the rodent giant synapse, the calyx of Held. In addition, they discuss what is presently known about factors that alter the amount and rate of glutamate refilling of synaptic vesicles and the relevance of these findings to central nervous system disorders (Hori and Takamori).

EAATs

Termination of glutamate signaling is mediated *via* uptake by one of five EAATs (Hediger et al., 2013). Not surprisingly, impaired expression and/or activity of EAATs have negative repercussions on health. EAAT2 (GLT-1a,b) is predominately expressed by astrocytes, although a small portion of GLT-1a can be found on axon terminals (Chen et al., 2004; Furness et al., 2008; Melone et al., 2009; Zhou et al., 2018).

In this article collection, Yeung et al. examined the expression of EAAT2 in several brain regions from *postmortem* tissue of patients with Alzheimer's disease (AD) or control (Yeung et al.). The authors found no significant change in EAAT2 density but did observe spatial differences in EAAT2 expression in AD tissue with less immunoreactivity detected in main astrocyte branches, especially on those surrounding neuronal cell bodies (Yeung et al.). Whether this altered expression pattern has implications for glutamate recycling in AD remains to be determined. Direct evidence for pathological loss of function of EAAT2 in a mouse model of Huntington's disease (HD) comes from the paper of Hirschberg et al. Therein they report that abnormal protein-protein interactions of mutant huntingtin (mHTT) with EAAT2 binding partners reduce glutamate uptake in striatal astrocytes and mediate some of the HD-associated deficits studied. Abnormalities in uptake and motor function were alleviated *via* over-expression of a C-terminal truncated EAAT2 protein (Hirschberg et al.).

Because most of the glutamate clearance (80–90%) is mediated by astrocytic EAAT2/GLT-1, the function of GLT-1 in other cell types has remained largely unexplored. In this collection, two groups report interesting findings concerning the physiological function of GLT-1 in neurons and oligodendrocytes using cell-specific knockout mouse lines. The Rosenberg group found that hippocampal slices prepared from neuronal GLT-1 KO (synGLT-1 KO) mice are more vulnerable to excitotoxicity than slices from wild-type mice (Rimmele et al.). Whether this is due to metabolic compromise, or a disturbance of glutamate homeostasis is still unknown. Meanwhile, the Fuss group reports that deletion of GLT-1 ($GLT1^{Plp1}icKO$ mice) in maturing oligodendrocytes leads to hypomyelination in the *corpus callosum* of male, but not female, mice (Thomason et al.). The exact mechanism responsible for these abnormalities is at present unknown.

Finally, the Robinson group used pharmacological inhibition of EAAT function to demonstrate their importance to arteriole patency (Jackson et al.), highlighting another important function of EAATs, which is to act as a bridge between local neuronal activity and increases in blood flow. One can speculate that the dysfunction of EAATs observed in several neuropathologies could negatively affect neurovascular coupling.

It is worth nothing that EAATs not only transport glutamate but act as anion channels (Wadiche et al., 1995; Bergles et al., 2002; Jen et al., 2005). Herein, Kovermann et al. review what is known about this function of the EAATs in both health and disease (Kovermann et al.). For example, they discuss the relationship between EAAT mutations that alter anion channel activity (but not glutamate uptake) resulting in chloride dyshomeostasis and symptoms of neurological disease.

System x_c^-

System x_c^- (Sx_c^-) is a Na^+-independent, Cl^- -dependent heteromeric amino acid transporter — formed by two polypeptides, xCT, the subunit responsible for the transport function, and 4F2hc, the subunit required for membrane localization — that functions physiologically to export glutamate while importing cystine in a 1:1 ratio (Bannai and Kitamura, 1980; Bannai, 1986). Astrocytes appear to be the main cell type expressing Sxc- in the mature brain (Zhang et al., 2014; Ottestad-Hansen et al., 2018). Sx_c^- activity contributes to the maintenance of redox homeostasis (Banjac et al., 2008), is important for the synthesis of glutathione (Sato et al., 1998), and is a major source of ambient extracellular glutamate *in vivo* (Baker et al., 2002; De Bundel et al., 2011) However, under pathological conditions, glutamate release through Sx_c^- contributes to neurological diseases/disorders [for review see Lewerenz et al. (2013)].

In this article collection, the Hermans group describes and validates a method using tritiated glutamate as a substrate for reversed transport to evaluate the activity of system x_c^- (Beckers et al.) both in cultured cells and in synaptosomal preparations. Meanwhile, Bentea et al. investigated the effect of genetic deletion of xCT on two models of Parkinson's disease (PD) (Bentea et al.). They found protection against proteasome inhibition-induced nigrostriatal degeneration, — but not MPTP-induced striatal toxicity — in $xCT^{-/-}$ mice. Last but not least, He and Hewett evaluated the contribution of Sx_c^- to ischemic stroke (He and Hewett). Their results demonstrate that Sx_c^- contributes to cortical ischemic damage when blood flow is moderately but not severely reduced.

Altogether, in this Research Topic, the authors review current literature or provide original research centered on understanding more fully the physiological and/or pathophysiological function of glutamate transport. The work presented here highlights the need for further research on the myriad of roles glutamate transporters play in health and pathology. Therefore, we hope that this collection encourages additional research in this field.

Author contributions

ZM-L produced the initial draft. SH, FZ, and AO further edited and provided additional content and references. All authors approved the final version for publication.

Acknowledgments

We want to thank all the authors of this Research Topic for their contributions, and the reviewers for their insightful comments that helped maintain the articles at the highest standards.

Conflict of interest

The authors declare that the research was conducted in the absence of any commercial or financial relationships that could be construed as a potential conflict of interest.

Publisher's note

References

Baker, D. A., Xi, Z. X., Shen, H., Swanson, C. J., and Kalivas, P. W. (2002). The origin and neuronal function of in vivo nonsynaptic glutamate. *J. Neurosci.* 22, 9134–9141. doi: 10.1523/JNEUROSCI.22-20-09134.2002

Banjac, A., Perisic, T., Sato, H., Seiler, A., Bannai, S., Weiss, N., et al. (2008). The cystine/cysteine cycle: a redox cycle regulating susceptibility versus resistance to cell death. *Oncogene* 27, 1618–1628. doi: 10.1038/sj.onc.1210796

Bannai, S. (1986). Exchange of cystine and glutamate across plasma membrane of human fibroblasts. *J. Biol. Chem.* 261, 2256–2263. doi: 10.1016/S0021-9258(17)35926-4

Bannai, S., and Kitamura, E. (1980). Transport interaction of L-cystine and L-glutamate in human diploid fibroblasts in culture. *J. Biol. Chem.* 255, 2372–2376. doi: 10.1016/S0021-9258(19)85901-X

Bergles, D. E., Tzingounis, A. V., and Jahr, C. E. (2002). Comparison of coupled and uncoupled currents during glutamate uptake by GLT-1 transporters. *J. Neurosci.* 22, 10153–10162. doi: 10.1523/JNEUROSCI.22-23-10153.2002

Chen, W., Mahadomrongkul, V., Berger, U. V., Bassan, M., DeSilva, T., Tanaka, K., et al. (2004). The glutamate transporter GLT1a is expressed in excitatory axon terminals of mature hippocampal neurons. *J. Neurosci.* 24, 1136–1148. doi: 10.1523/JNEUROSCI.1586-03.2004

Danbolt, N., Furness, D., and Zhou, Y. (2016). Neuronal vs glial glutamate uptake: resolving the conundrum. *Neurochem. Int.* 98, 29–45. doi: 10.1016/j.neuint.2016.05.009

De Bundel, D., Schallier, A., Loyens, E., Fernando, R., Miyashita, H., Van Liefferinge, J., et al. (2011). Loss of system xc- does not induce oxidative stress but decreases extracellular glutamate in hippocampus and influences spatial working memory and limbic seizure susceptibility. *J. Neurosci.* 31, 5792–5803. doi: 10.1523/JNEUROSCI.5465-10.2011

Featherstone, D. E., and Shippy, S. A. (2008). Regulation of synaptic transmission by ambient extracellular glutamate. *Neuroscientist* 14, 171–181. doi: 10.1177/1073858407308518

Fonnum, F. (1984). Glutamate: a neurotransmitter in mammalian brain. *J. Neurochem.* 42, 1–11. doi: 10.1111/j.1471-4159.1984.tb09689.x

Furness, D., Dehnes, Y., Akhtar, A., Rossi, D., Hamann, M., Grutle, N., et al. (2008). A quantitative assessment of glutamate uptake into hippocampal synaptic terminals and astrocytes: new insights into a neuronal role for excitatory amino acid transporter 2 (EAAT2). *Neuroscience* 157, 80–94. doi: 10.1016/j.neuroscience.2008.08.043

Hediger, M. A., Clémençon, B., Burrier, R. E., and Bruford, E. A. (2013). The ABCs of membrane transporters in health and disease (SLC series): introduction. *Molec. Aspects Med.* 34, 95–107. doi: 10.1016/j.mam.2012.12.009

Jabaudon, D., Shimamoto, K., Yasuda-Kamatani, Y., Scanziani, M., Gahwiler, B. H., and Gerber, U. (1999). Inhibition of uptake unmasks rapid extracellular turnover of glutamate of nonvesicular origin. *Proc. Natl. Acad. Sci. U S A.* 96, 8733–8738. doi: 10.1073/pnas.96.15.8733

Jen, J. C., Wan, J., Palos, T. P., Howard, B. D., and Baloh, R. W. (2005). Mutation in the glutamate transporter EAAT1 causes episodic ataxia, hemiplegia, and seizures. *Neurology* 65, 529–534. doi: 10.1212/01.WNL.0000172638.58172.5a

Lewerenz, J., Hewett, S. J., Huang, Y., Lambros, M., Gout, P. W., Kalivas, P. W., et al. (2013). The cystine/glutamate antiporter system x(c)(-) in health and disease: from molecular mechanisms to novel therapeutic opportunities. *Antioxid Redox Signal* 18, 522–555. doi: 10.1089/ars.2011.4391

Melone, M., Bellesi, M., and Conti, F. (2009). Synaptic localization of GLT-1a in the rat somatic sensory cortex. *Glia* 57, 108–117. doi: 10.1002/glia.20744

Omote, H., Miyaji, T., Juge, N., and Moriyama, Y. (2011). Vesicular neurotransmitter transporter: bioenergetics and regulation of glutamate transport. *Biochemistry* 50, 5558–5565. doi: 10.1021/bi200567k

Ottestad-Hansen, S., Hu, Q. X., Follin-Arbelet, V. V., Bentea, E., Sato, H., Massie, A., et al. (2018). The cystine-glutamate exchanger (xCT, Slc7a11) is expressed in significant concentrations in a subpopulation of astrocytes in the mouse brain. *Glia* 66, 951–970. doi: 10.1002/glia.23294

Sato, Kuriyama-Matsumura, K., Siow, R., Ishii, T., Bannai, S., and Mann, G. E. (1998). Induction of cystine transport via system xc– and maintenance of intracellular glutathione levels in pancreatic acinar and islet cell lines. *Biochim. Biophys. Acta (BBA)-Biomembranes* 1414, 85–94. doi: 10.1016/S0005-2736(98)00159-X

Wadiche, J. I., Arriza, J. L., Amara, S. G., and Kavanaugh, M. P. (1995). Kinetics of a human glutamate transporter. *Neuron* 14, 1019–1027. doi: 10.1016/0896-6273(95)90340-2

Warr, O., Takahashi, M., and Attwell, D. (1999). Modulation of extracellular glutamate concentration in rat brain slices by cystine-glutamate exchange. *J. Physiol.* 514, 783–793. doi: 10.1111/j.1469-7793.1999.783ad.x

Zhang, Y., Chen, K., Sloan, S. A., Bennett, M. L., Scholze, A. R., O'Keeffe, S., et al. (2014). An RNA-sequencing transcriptome and splicing database of glia, neurons, and vascular cells of the cerebral cortex. *J. Neurosci.* 34, 11929–11947. doi: 10.1523/JNEUROSCI.1860-14.2014

Zhou, Y., Hassel, B., Eid, T., and Danbolt, N. C. (2018). Axon-terminals expressing EAAT2 (GLT-1; Slc1a2) are common in the forebrain and not limited to the hippocampus. *Neurochem. Int.* 123, 101–113. doi: 10.1016/j.neuint.2018.03.006

frontiers
in Cellular Neuroscience

ORIGINAL RESEARCH
published: 13 September 2021
doi: 10.3389/fncel.2021.702824

EAAT2 Expression in the Hippocampus, Subiculum, Entorhinal Cortex and Superior Temporal Gyrus in Alzheimer's Disease

Jason H. Y. Yeung[1]*, Thulani H. Palpagama*[1]*, Oliver W. G. Wood*[1]*, Clinton Turner*[2]*, Henry J. Waldvogel*[1]*, Richard L. M. Faull*[1] *and Andrea Kwakowsky*[1]*

[1]Centre for Brain Research, Department of Anatomy and Medical Imaging, Faculty of Medical and Health Sciences, University of Auckland, Auckland, New Zealand, [2]Department of Anatomical Pathology, LabPlus, Auckland City Hospital, Auckland, New Zealand

Alzheimer's disease (AD) is a neuropathological disorder characterized by the presence and accumulation of amyloid-beta plaques and neurofibrillary tangles. Glutamate dysregulation and the concept of glutamatergic excitotoxicity have been frequently described in the pathogenesis of a variety of neurodegenerative disorders and are postulated to play a major role in the progression of AD. In particular, alterations in homeostatic mechanisms, such as glutamate uptake, have been implicated in AD. An association with excitatory amino acid transporter 2 (EAAT2), the main glutamate uptake transporter, dysfunction has also been described. Several animal and few human studies examined EAAT2 expression in multiple brain regions in AD but studies of the hippocampus, the most severely affected brain region, are scarce. Therefore, this study aims to assess alterations in the expression of EAAT2 qualitatively and quantitatively through DAB immunohistochemistry (IHC) and immunofluorescence within the hippocampus, subiculum, entorhinal cortex, and superior temporal gyrus (STG) regions, between human AD and control cases. Although no significant EAAT2 density changes were observed between control and AD cases, there appeared to be increased transporter expression most likely localized to fine astrocytic branches in the neuropil as seen on both DAB IHC and immunofluorescence. Therefore, individual astrocytes are not outlined by EAAT2 staining and are not easily recognizable in the CA1–3 and dentate gyrus regions of AD cases, but the altered expression patterns observed between AD and control hippocampal cases could indicate alterations in glutamate recycling and potentially disturbed glutamatergic homeostasis. In conclusion, no significant EAAT2 density changes were found between control and AD cases, but the observed spatial differences in transporter expression and their functional significance will have to be further explored.

Keywords: glutamate transporter, EAAT2, hippocampus, subiculum, entorhinal cortex, superior temporal gyrus, Alzheimer's disease

Edited by:
Arturo Ortega,
Centro de Investigación y de Estudios Avanzados del Instituto Politécnico Nacional, Mexico

Reviewed by:
Alfredo Ribeiro-da-Silva,
McGill University, Canada
Amin Derouiche,
University of Frankfurt, Germany

***Correspondence:**
Andrea Kwakowsky
a.kwakowsky@auckland.ac.nz

Specialty section:
This article was submitted to Cellular Neurophysiology, a section of the journal Frontiers in Cellular Neuroscience

Received: *30 April 2021*
Accepted: *23 August 2021*
Published: *13 September 2021*

Citation:
Yeung JHY, Palpagama TH, Wood OWG, Turner C, Waldvogel HJ, Faull RLM and Kwakowsky A (2021) EAAT2 Expression in the Hippocampus, Subiculum, Entorhinal Cortex and Superior Temporal Gyrus in Alzheimer's Disease. Front. Cell. Neurosci. 15:702824. doi: 10.3389/fncel.2021.702824

Abbreviations: $A\beta_{1-42}$, Amyloid Beta; AD, Alzheimer's Disease; CA, Conus Ammonis; CNS, central nervous system; DG, Dentate Gyrus; EAAT2, Excitatory amino acid transporter 2; GABA, γ-aminobutyric acid; GFAP, Glial fibrillary acidic protein; NMDA, N-methyl-D-aspartate; PBS, phosphate-buffered saline; PMD, Post-mortem delay; RRID, Research Resource Identifier; RT, Room Temperature; STG, Superior temporal gyrus; Str, Stratum; TBS, Tris-Buffered Saline; TBST, Tris-Buffered Saline with Tween.

INTRODUCTION

Alzheimer's disease (AD) is the most common cause of dementia worldwide and is linked with a decline in cognitive function, behavior, and memory (McKhann et al., 1984). Alongside the predominant tau and beta-amyloid (Aβ) hypotheses, glutamatergic dysfunction has also been implicated in the pathogenesis of AD, with a significant effect on neuronal functioning and survival. Glutamatergic dysfunction is mediated through a range of mechanisms, including Aβ binding to glutamate receptors, tau tethering to intrinsic cytoskeletal proteins resulting in overactivation of receptors, and the internalization of glutamate transporters leading to glutamate accumulation in the synaptic and extrasynaptic space (Butterfield and Pocernich, 2003).

Glutamate is an endogenous amino acid with many physiological functions, including the synthesis of a variety of micro- and macro- compounds (Erecinska and Silver, 1990). In the central nervous system (CNS), glutamate serves three main functions: as an excitatory neurotransmitter, as the precursor molecule in the synthesis of γ-aminobutyric acid (GABA), the main inhibitory neurotransmitter in the CNS (Erecinska and Silver, 1990), and as a fuel for mitochondrial metabolism (Dienel, 2013; McKenna et al., 2016). It plays a central role in the regular functioning of cognition, memory, and learning, as well as overall normal brain performance (Fonnum, 1984). Homeostasis is maintained through efficient reuptake of glutamate by glial transporters, with most of the released neurotransmitters successfully contained within the local tripartite synaptic area (Vizi, 2000; Butterfield and Pocernich, 2003). Reuptake is predominantly astrocytic, resulting in a unidirectional glutamate shift from neurons to astrocytes, where glutamate is metabolized into glutamine *via* glutamine synthase. This flux of glutamate from neurons to astrocytes is restored through the transfer of glutamine from astrocytes back into neurons (Bak et al., 2006). The majority of glutamate uptake is through excitatory amino acid transporter 2 (EAAT2; rat GLT-1), which displays predominantly astrocytic expression patterns (Sheldon and Robinson, 2007; Rimmele and Rosenberg, 2016). Due to its tight regulation in normal physiology, the disruption of glutamate homeostasis as a mechanism for neuronal damage is one of the leading hypotheses implicating the glutamatergic system in AD pathogenesis.

The excitatory amino acid transporters (EAATs) are responsible for the uptake of glutamate from the extracellular space after its release from the presynaptic neuron (Purves, 2012). EAAT expression is highly brain-region specific. EAAT1 is highly expressed within the cerebellum (Storck et al., 1992) and plays an important role in neurodevelopment (Furuta et al., 1997b). EAAT2 is the primary glutamate transporter, responsible for ∼95% of glutamate uptake, and is widely expressed on astrocytes throughout the CNS (Rothstein et al., 1994; Vandenberg and Ryan, 2013). EAAT3 is present mainly in post-synaptic neurons throughout the brain and is highly expressed within the hippocampus, cerebellum, and basal ganglia (Rothstein et al., 1994). EAAT4 and 5 are chloride channels (Fairman and Amara, 1999) with weak glutamate transporter properties (Gameiro et al., 2011) and are present in the cerebellum (Furuta et al., 1997a) and retina respectively (Arriza et al., 1997). EAAT1–3 share similar mechanisms of glutamate transport. In each cycle, one glutamate molecule is cotransported with three Na^+ ions and one H^+ ion, with one K^+ ion transported in the opposite direction (Kanai et al., 1995; Wadiche et al., 1995).

Alterations in the regulation and expression of EAAT2 have been reported in both acute neurological conditions (Torp et al., 1995) and chronic neurodegenerative disorders (Rothstein et al., 1995; Li et al., 1997; Munch et al., 2002). Impairment of EAATs has been reported in AD, with studies observing a reduction in glutamate transporter capacity and selective loss of vesicular glutamate transporters with a concomitant rise in extracellular glutamate concentration (Li et al., 1997; Gu et al., 2004). This has been attributed partly to damage by reactive oxygen species and products of lipid peroxidation (Danysz and Parsons, 2012). Reversal of glutamate uptake has also been shown through the Aβ-mediated release of glutamate from microglia (Noda et al., 1999). This results in glutamate excitotoxicity, with glutamate diffusing into extrasynaptic areas and activating extrasynaptic receptors, notably N-methyl-D-aspartate (NMDA) receptors (Sheldon and Robinson, 2007). Overactivation of these receptors can result in excessive calcium influx, potentially disrupting the intracellular balance of calcium and other ions. In agreement with such observations, stimulation of EAATs appears to have neuroprotective effects against excitotoxicity through efficacious glutamate control (Masliah et al., 1998).

Currently, there are no effective therapeutic interventions for AD, with present FDA-approved drugs providing short-term efficacy at best. Further understanding of pathological changes to the glutamatergic system, in particular its homeostatic mechanisms and transporter alterations, can offer potential therapeutic targets in the future. Modulation of EAATs has also been shown to have possible therapeutic effects, with their ability to alter glutamate levels providing a logical link towards managing glutamate excitotoxicity. Upregulation of EAAT2 has been shown to reduce excitotoxic damage seen in a variety of acute and chronic neurological diseases (Sheldon and Robinson, 2007), with over-expression of EAAT3 appearing to be neuroprotective by decreasing the levels of extracellular glutamate (Lewerenz et al., 2006). Despite clear evidence of the glutamatergic system's role in neurodegeneration (Maragos et al., 1987; Greenamyre et al., 1988; Butterfield and Pocernich, 2003; Yeung et al., 2020a,b, 2021; Kwakowsky et al., 2021), the expression of EAAT2 is yet to be explored in AD. The results reported from the few human studies are inconclusive and controversial, with hippocampal studies that lack quantitative data (Li et al., 1997; Jacob et al., 2007) or information on the region and/or layer specificity of the transporter expression within hippocampal subfields of AD and control brains (Li et al., 1997; Abdul et al., 2009).

In this study, we examined the region- and layer-specific expression and pattern changes of EAAT2 within the hippocampus, subiculum, entorhinal cortex, and superior temporal gyrus (STG) in AD post-mortem samples compared to control, to gain a better understanding of how the glutamatergic system is altered in the disease.

TABLE 1 | Normal human brain case details used for immunohistochemistry.

Case	Age	Sex	PMD	Cause of death	Weight (g)
H122	72	F	9	Emphysema	1,230
H123	78	M	7.5	Aortic aneurysm	1,260
H169	81	M	24	Asphyxia	1,225
H180	73	M	33	Ischemic heart disease	1,318
H181	78	F	20	Aortic aneurysm	1,292
H202	83	M	14	Aortic aneurysm	1,245
H226[a]	73	F	48	Mesothelioma	1,279
H239[a]	64	M	15.5	Ischemeic Heart Disease	1,529
H245	63	M	20	Asphyxia	1,194

[a] Cases used for 3,3′-diaminobenzidine-peroxidase immunohistochemistry. Post-mortem delay (PMD).

MATERIALS AND METHODS

Human Brain Tissue Preparation and Neuropathological Analysis

The post-mortem human brain tissue was acquired through a donor program and was obtained from the Neurological Foundation Human Brain Bank. The procedures were approved by the University of Auckland Human Participant's Ethics Committee (Approval number: 011654). Processing of tissue was performed as described in Waldvogel et al. (2006). The right hemisphere of the brain was fixed by perfusion with 15% formalin, cut into anatomical blocks, cryoprotected with sucrose solutions, and frozen at −80°C. Hippocampal (also containing the subiculum and entorhinal cortex) and STG blocks were used for this study. Nine control (**Table 1**) and eight AD cases (**Table 2**), with an average age of 78.5 years and a maximum post-mortem time of 48 h were used for immunohistochemistry (IHC).

All Alzheimer's cases used in this study had clinical dementia. All control cases used had no history of any primary neurodegenerative, psychiatric disorder, and neurological disease abnormalities. Sections from the middle frontal gyrus, middle temporal gyrus, cingulate gyrus, hippocampus, caudate nucleus, substantia nigra, locus coeruleus, and cerebellum were examined from both control and AD groups by a neuropathologist. The distribution and density of tau and Aβ pathology were examined immunohistochemically. Based on neuritic plaque density AD cases were classified into sparse, moderate, or frequent according to the criteria from the Consortium to Establish a Registry for AD (Mirra et al., 1991), and cases that fit this criterion for definite or probable AD were included in this study.

Western Blotting

Specificity of the primary antibodies has been tested using Western blotting (**Supplementary Figure 1A**) and reported previously (Simpson et al., 2010; Yao et al., 2015; Wang et al., 2017; Germany et al., 2018; Bacci et al., 2019; Castaneda-Cabral et al., 2020; Li et al., 2020; Wilkie et al., 2020; Yoshino et al., 2020). Western blotting was performed as described by Kwakowsky et al. (2018). Protein concentrations of the human hippocampal tissue samples (20 μg) were measured by using the Bio-Rad Detergent Compatible Protein assay (Bio-Rad, California, USA). Twenty microgram of each protein extract and the Precision Plus molecular weight ladder (Bio-Rad, California, USA) were run on a gradient—polyacrylamide electrophoresis gel (NU PAGE 4–12% BT 1.5, NP0336BOX; Life Technologies, Carlsbad, CA, USA) and then blotted. Proteins were separated in XCell SureLock Mini-Cell system (Invitrogen, Scoresby, VIC, Australia) and transferred onto nitrocellulose membranes using a Mini Trans-Blot Electrophoretic Transfer system (Bio-Rad, California, USA). The membranes were washed in Tris-buffered saline pH 7.6, 0.1% Tween (TBST) for 5 min and then blocked with LiCor Odyssey Blocking Buffer (LI-COR Biosciences, Nebraska, USA) for 30 min at RT. Following another 5-min wash with TBST the membranes were overnight incubated at 4°C with the EAAT2 primary antibody diluted in 4% BSA-TBST (1:500). After three 5-min TBST washes the membrane was incubated with the secondary antibody (goat anti-mouse IRDye® 800CW, 926-32210, RRID:AB_621842) for 1 h at RT. Finally, the membrane was washed three times in TBST for 10 min each, followed by a wash in TBS for 10 min, and imaged on the Chemidoc MP Imaging System (BioRad).

Immunohistochemistry

Coronal sections of the hippocampus, subiculum, entorhinal cortex, and STG were cut on a freezing microtome at 60 μm and stored at 4°C in phosphate-buffered saline (PBS) containing 0.1% sodium azide. Two hippocampal and two STG sections were immunostained with an EAAT2 specific antibody. The hippocampal block starts from the midpoint of the anterior commissure at +21.2 mm (containing the hippocampus, subiculum, and entorhinal cortex, plate 38–41) and the STG block at +9.3 mm (plate 29–33 according to the Mai et al. brain atlas (Mai et al., 2008). Free-floating 3,3′-diaminobenzidine (DAB)-peroxidase and fluorescent IHC (Waldvogel et al., 2006; Kwakowsky et al., 2018) were utilized for the visualization of EAAT2. All antibody dilutions were optimized. Primary antibodies and dilutions are described in **Table 3**. The omission of the primary antibodies resulted in a complete absence of immunoreactivity (**Supplementary Figure 1B**). Primary antibodies were diluted in 1% normal goat serum, and 0.04% merthiolate in PBS (immunobuffer).

DAB-Peroxidase Immunohistochemistry

DAB-peroxidase IHC was performed as described by Kwakowsky et al. (2018). In brief, sections were washed in PBS with 0.2% Triton X-100 (PBST) before blocking for endogenous peroxidases (50% methanol and 1% H_2O_2) for 20 min, followed by three 10-min washes in PBST and incubated for 72 h in primary antibody in immunobuffer at 4°C (**Table 3**). Following three 10-min washes in PBST the sections were incubated for 24 h with the biotinylated secondary antibody (anti-mouse IgG-Biotin antibody produced in goat 1:1,000) in immunobuffer at room temperature (RT). The sections were then washed in PBST before incubation with ExtrAvidin (1:1,000, E2886; Sigma, St. Louis, MO, USA) in immunobuffer for 4 h at RT, followed by three 10-min washes in PBST before development in 0.05% DAB and

TABLE 2 | Alzheimer's disease human brain case details used for immunohistochemistry.

Case	Age	Sex	PM delay	Cause of death	CERAD Classification	Braak and Braak Score	Weight (g)
AZ45	82	M	4.5	Pneumonia	Probable AD	IV	1,230
AZ88[a]	83	M	21	Pneumonia	Definite AD	IV	1,121
AZ90	73	M	4	Gastrointestinal hemeorrhage	Definite AD	IV	1,260
AZ92	93	F	11.5	Bronchopneumonia	Probable AD	IV	1,225
AZ98	91	F	20.5	Alzheimer's dementia/atrial fibrillation	Definite AD	VI	1,318
AZ102	84	F	14.5	Lower respiratory tract infection and hyaline arteriosclerosis	Definite AD	VI	1,292
AZ103	87	M	<24	Cerebrovascular accident	Definite AD	VI	1,245
AZ113[a]	77	M	3.5	Alzheimer's dementia/pneumonia	Definite AD	IV	1,261

[a] *Cases used for 3,3′-diaminobenzidine-peroxidase immunohistochemistry.*

TABLE 3 | Primary antibodies used in this study.

Antigen	Immunogen	Source, Host, Species, Catalogue Number	Dilutions
EAAT2	Amino acids 1–85 mapping near the N terminus of EAAT2 of human origin.	Santa Cruz Biotech, Mouse, sc-365634 (E-1), RRID:AB_10844832.	1:2,000
GFAP	Full-length native protein of cow glial fibrillary acidic protein.	Abcam, Chicken, ab4674, RRID:AB_304558.	1:10,000
Anti-Neuronal Nuclei (NeuN)	Purified cell nuclei from mouse brain.	Millipore, Rabbit, ABN78, RRID:AB_10807945.	1:1,000
Anti-Neuronal Nuclei (NeuN)	GST-tagged recombinant protein corresponding to the N-terminus of mouse NeuN.	Millipore, Guinea pig, ABN90P, RRID:AB_2341095.	1:1,000

0.01% H_2O_2 in 0.1 M phosphate buffer. Sections were washed in PBST, mounted onto glass slides, dried, dehydrated through a graded series of ethanol, and cleared in xylene. The slides were coverslipped with DPX mountant (1019790500; Merck, Whitehouse Station, NJ, USA). The sections were imaged on either a Leica DMRB light microscope or a Leica MZ6 dissecting microscope (Wetzlar, Germany).

Fluorescent Immunohistochemistry

A total of 13 cases, seven control, and six AD were used in this experiment. Two hippocampal and two STG tissue sections from each case were randomized following standard simple randomization procedures in a blinded fashion. Free-floating fluorescent IHC was performed as described previously by Kwakowsky et al. (2018). In brief, sections were incubated in PBST overnight at 4°C followed by three 10-min washes with PBST and incubation for 72 h in the primary antibodies EAAT2 and NeuN and/or GFAP diluted in immunobuffer at 4°C (**Table 3**). Sections were washed three times for 10 min in PBST before the addition of secondary antibodies goat anti-mouse Alexa Fluor 647 (1:500, A21236, RRID:AB_141725; Invitrogen), goat anti-rabbit Alexa Fluor 488 (1:500, A11034, RRID:AB_2576217; Invitrogen), goat anti-guinea pig Alexa Fluor 594 (1:500, A11076, RRID:AB_141930; Invitrogen), goat anti-chicken Alexa Fluor 488 (1:500, ab150173, RRID:AB_2827653; Abcam), and incubated for a further 24 h at RT. Sections were then washed for 10 min in PBST before incubation for 35 min at RT with Hoechst nuclei counterstain (1:10,000, 33342, RRID:AB_10626776, Invitrogen) diluted in PBS. After three subsequent 10-min washes in PBS, sections were mounted onto glass slides, coverslipped with Mowiol mounting medium, and sealed with nail varnish.

Imaging and Analysis

Imaging was conducted using a Zeiss 710 inverted confocal laser-scanning microscope (Carl Zeiss, Jena, Germany). Brain regions and layers were differentiated based on cell type and relative location, utilizing NeuN and Hoechst staining. An argon laser was used to excite NeuN-positive neurons at a 488-nm wavelength, a helium-neon laser with a 633 nm wavelength was used for Alexa 647 immunolabeled antigens of interest, and a blue diode laser with a 405 nm wavelength was used for Alexa 405 for Hoechst counterstained nuclei with a 20x objective. After background subtraction and grayscale threshold determination, EAAT2 density measurements were performed from a 31,000 μm^2 area in each analyzed layer in the dentate gyrus (DG; str. granulosum, str. moleculare and hilus), CA1, CA2, and CA3 subregions (str. oriens, str. pyramidale, str. radiatum) using ImageJ software (U. S. National Institutes of Health, Bethesda, Maryland, USA). Density measurements for the subsequent regions were obtained from a 432,000 μm^2 region in the subiculum, a 605,000 μm^2 region in the entorhinal cortex, and a 692,000 μm^2 region in the STG through all cortical layers. Both the threshold and the size of the region of interest were constant across all sections for each region in each experiment. The image acquisition and analysis were performed blinded to eliminate bias during the experiment.

Statistical Analysis

The data did not meet the assumptions of parametric tests assessed by the D'Agostino–Pearson omnibus and Brown–Forsythe tests. Therefore, to examine differences between groups, an unpaired Mann–Whitney test was used. No data points were identified and excluded as outliers using the ROUT method. All statistical analyses were conducted using Graph-Pad Prism software version 8 (GraphPad software;

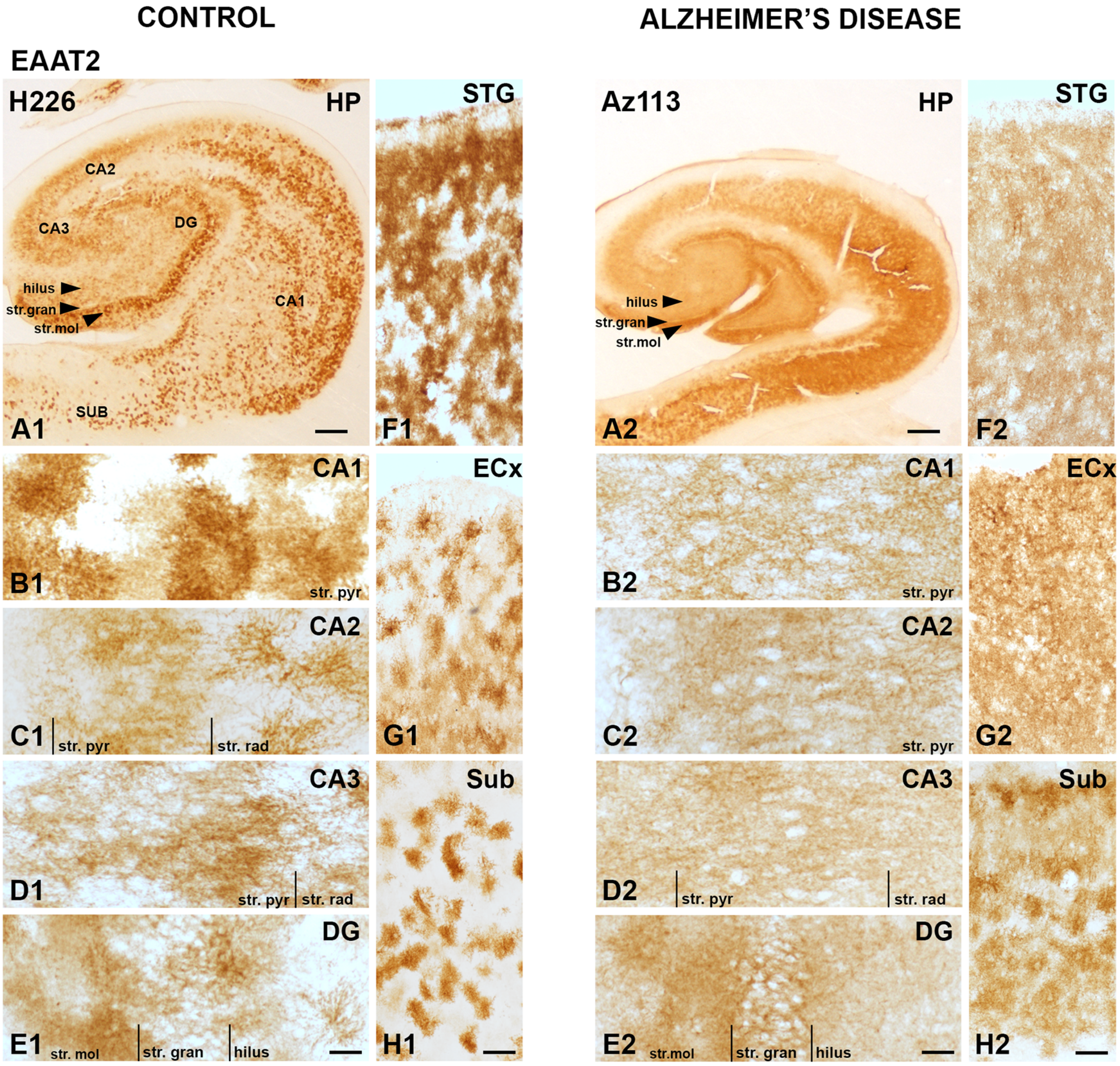

FIGURE 1 | EAAT2 expression in the hippocampus, subiculum, entorhinal cortex, and superior temporal gyrus in human control and Alzheimer's disease (AD) cases visualized by 3,3′-diaminobenzidine-peroxidase immunohistochemistry. The EAAT2 staining is localized to astrocytes and appears relatively strong within the str. pyramidale of the CA1 subregion **(A1,B1)**, the stratum (str.) moleculare of the dentate gyrus **(A1,E1)** with more diffuse labeling in AD cases **(A2–H2)**. CA, cornu ammonis; DG, dentate gyrus; ECx, entorhinal cortex; HP, hippocampus; STG, superior temporal gyrus; str. pyr, stratum pyramidale; str. rad, stratum radiatum; str. gran, stratum granulosum; Sub, subiculum. Scale bars: **(A1–A2)** = 1,000 μm; **(B1–E1, B2–E2)** = 100 μm; **(F1–H1, F2–H2)** = 400 μm.

RRID:SCR_002798) with a value of $p \leq 0.05$ considered significant. Adobe Photoshop CC 2018 (Adobe Systems Software, San Jose, CA, USA) was used to prepare the figures. All experimental data are expressed as the mean ± Standard Error of Mean (SEM).

RESULTS

Expression of EAAT2 in the Human Hippocampus, Subiculum, Entorhinal Cortex, and Superior Temporal Gyrus

EAAT2 DAB IHC revealed strong astrocytic staining across all brain regions examined, with particularly strong staining in the CA1 subfield (**Figures 1A1,B1**), the str. moleculare of the DG (**Figures 1A1,E1**), and the STG (**Figure 1F**). Both control and AD cases display strong immunoreactivity in astrocytes, which confirms literature indicating its expression in astrocytes, but the AD cases show more labeling in the neuropil that makes individual astrocytes less recognizable (**Figure 1**). This is better visualized with fluorescence IHC (**Figures 2–5**).

Astrocytic staining was patchy in some regions, but much more intense and condensed in others. Within the CA1 subfield, immunoreactivity was localized to astrocytic processes and appeared diffuse throughout the str. pyramidale, str. oriens, and str. radiatum (**Figure 2A**). There appears to be a lack of staining surrounding and within neuronal bodies stained with NeuN,

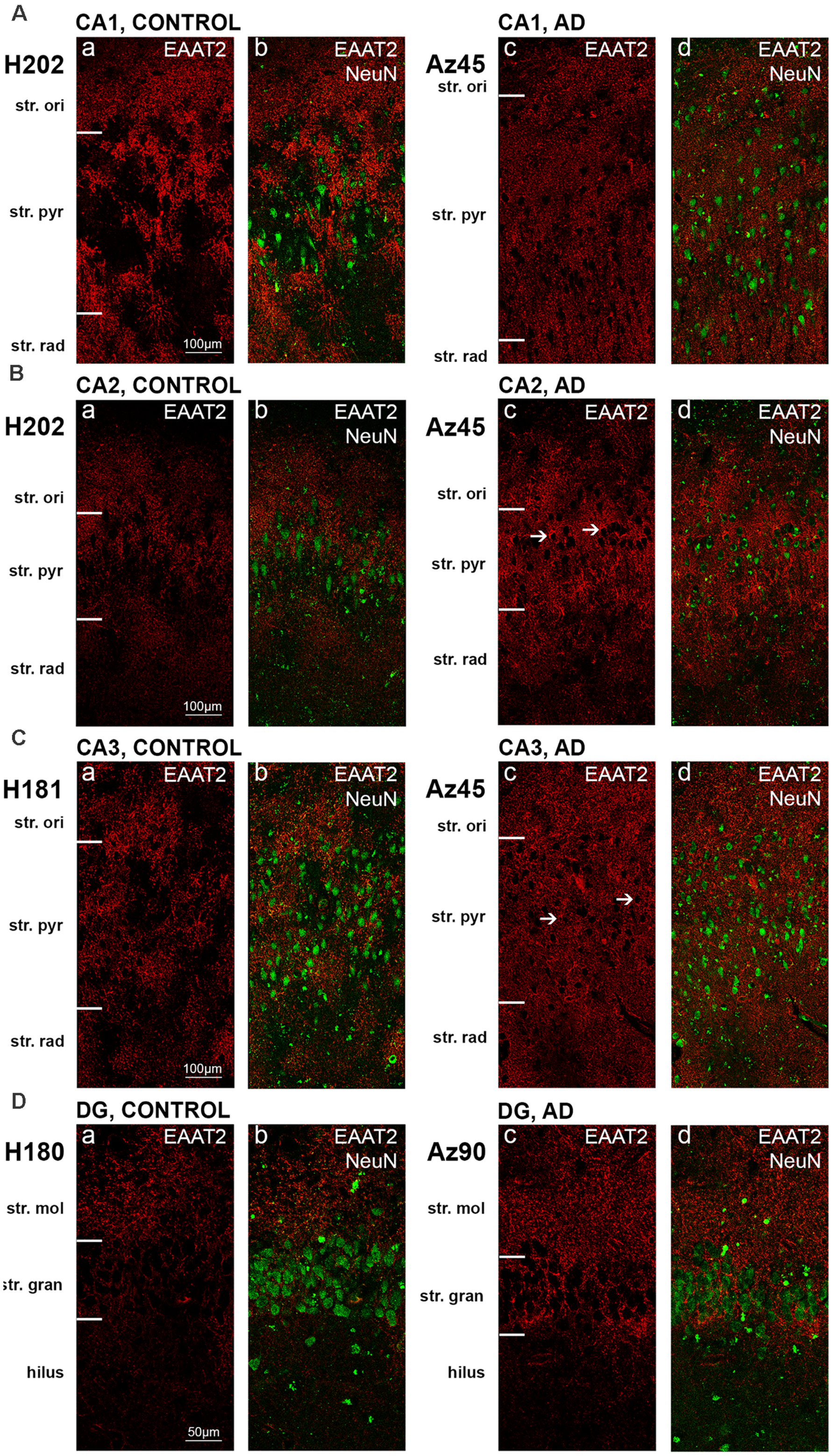

FIGURE 2 | EAAT2 expression in the hippocampus in human control and Alzheimer's disease (AD) cases visualized by fluorescent immunohistochemistry. Photomicrographs of representative regions of the CA1 **(A)**, CA2 **(B)**, CA3 **(C)**, and dentate gyrus **(D)** showing EAAT2 (red) and EAAT2 overlaid with NeuN (green) immunoreactivity for representative AD and control cases. AD, Alzheimer's disease; CA, cornu ammonis; DG, dentate gyrus; str. ori, straum oriens; str. pyr, stratum pyramidale; str. rad, stratum radiatum; str. mol, stratum moleculare; str. gran, stratum granulosum. Scale bars **(A–C)** = 100 μm; **(D)** = 50 μm.

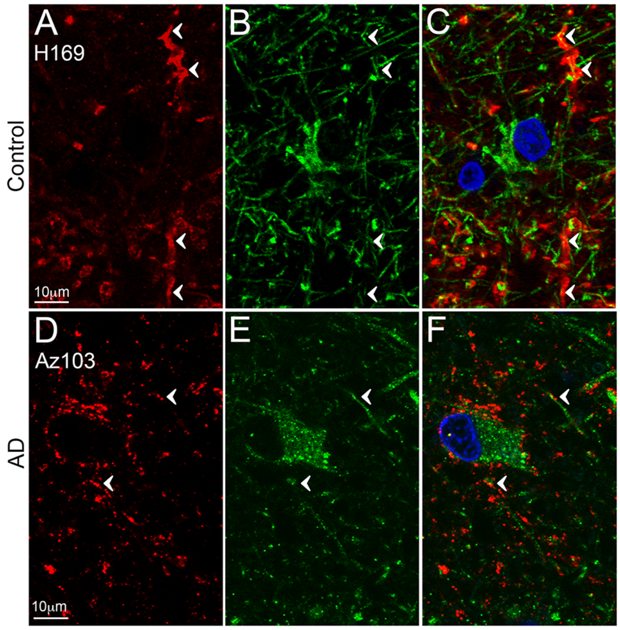

FIGURE 3 | EAAT2 expression in the dentate gyrus. Photomicrographs of the stratum moleculare of the denate gyrus showing EAAT2 (**A,D**, red), GFAP (**B,E**, green) and EAAT2 overlaid with GFAP **(C,F)** immunoreactivity for a representative control (**A,B**, H169) and Alzheimer's disease (AD) (**D–F**, Az103) case. EAAT2 labeling is mainly localized to membranes of astrocytic stem and fine branches, and soma, while GFAP staining is observed in the cytoplasm of the branches and soma (**A–F**, arrowheads). Cell nuclei are labeled with Hoechst nuclei counterstain (**C,F**, blue). Scale bar **(A–C)** = 10 μm.

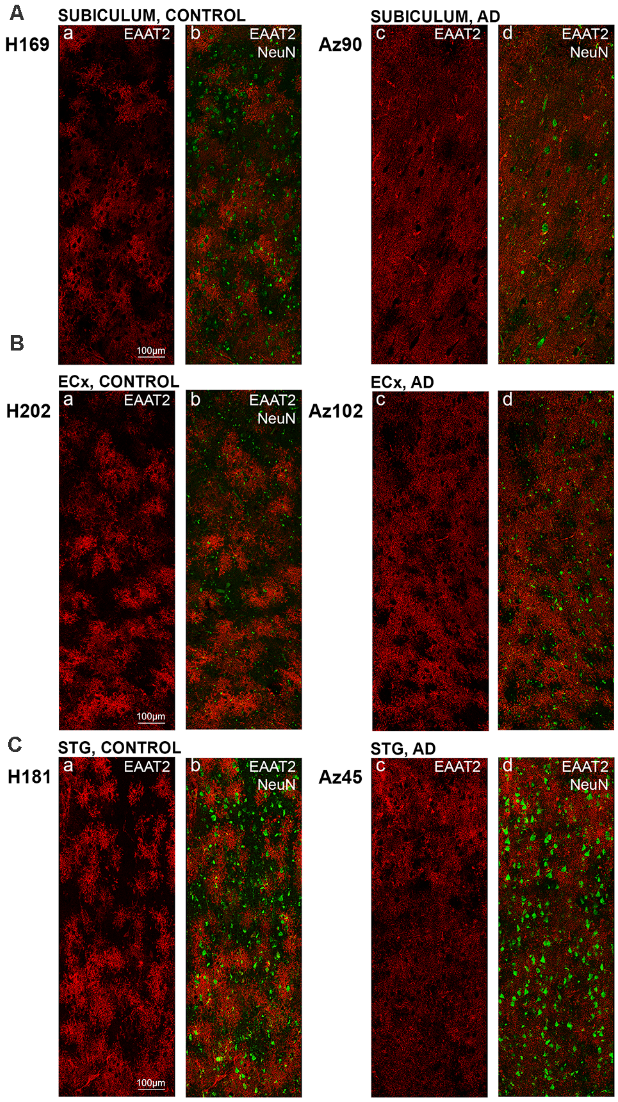

FIGURE 4 | EAAT2 expression in the subiculum, entorhinal cortex, and superior temporal gyrus in human control and Alzheimer's disease (AD) cases. Photomicrographs of representative regions of the subiculum **(A)**, entorhinal cortex **(B)**, and STG **(C)** showing EAAT2 (red) and EAAT2 overlaid with NeuN (green) immunoreactivity for representative AD and control cases. AD, Alzheimer's disease; CA, cornu ammonis; DG, dentate gyrus; ECx, entorhinal cortex: STG, superior temporal gyrus. Scale bars **(A–C)** = 100 μm.

with the majority of labeling observed on astrocytic processes (**Figure 2A**). Within the CA2 subfield, EAAT2 immunolabeling was relatively uniform between the three layers, with slightly higher expression levels within the str. pyramidale (**Figure 2B**). Staining appears to be localized only to astrocytes and not neurons. In comparison to control sections, the CA2 region of AD sections exhibited much stronger immunoreactivity in astrocytic main branches surrounding some of the NeuN positive cell bodies within the str. pyramidale (**Figure 2B**, arrows), and this difference was also observed within the CA3 (**Figure 2C**, arrows) and the str. granulosum of the DG (**Figure 2D**). The CA3 subfield and DG exhibited a similar staining pattern to the CA1 and CA2 (**Figures 2C,D**). Within the DG, there was greater immunoreactivity in the str. moleculare compared to the hilus and the str. granulosum (**Figure 2D**). The subiculum (**Figure 4A**), entorhinal cortex (**Figure 4B**), and STG (**Figure 4C**) regions exhibited similar staining patterns, with immunolabeling on astrocytes and on their processes, and AD cases displaying much more diffuse staining (**Figures 4A–C, 5A–F**). Protoplasmic astrocytes between layers II-VI of the entorhinal cortex and STG (Oberheim et al., 2009) are strongly stained for EAAT2 and this results in patchy staining. Interlaminar astrocytes in cortical layer I and polarized astrocytes in cortical layers V to VI also express EAAT2. Protoplasmic astrocytes often overlap with one another and also show overlap with polarized astrocytes (**Figure 4**; Oberheim et al., 2009).

Quantification of EAAT2 labeling density performed based on fluorescence IHC experiments (**Figures 2, 4**) did not reveal any statistically significant differences between AD and control brains in any of the brain regions investigated (**Figures 6A–G**). While the labeling can be stronger on some individual astrocytes in controls, this does not result in overall transporter density differences between control and AD due to the increased expression in neuropil in AD cases.

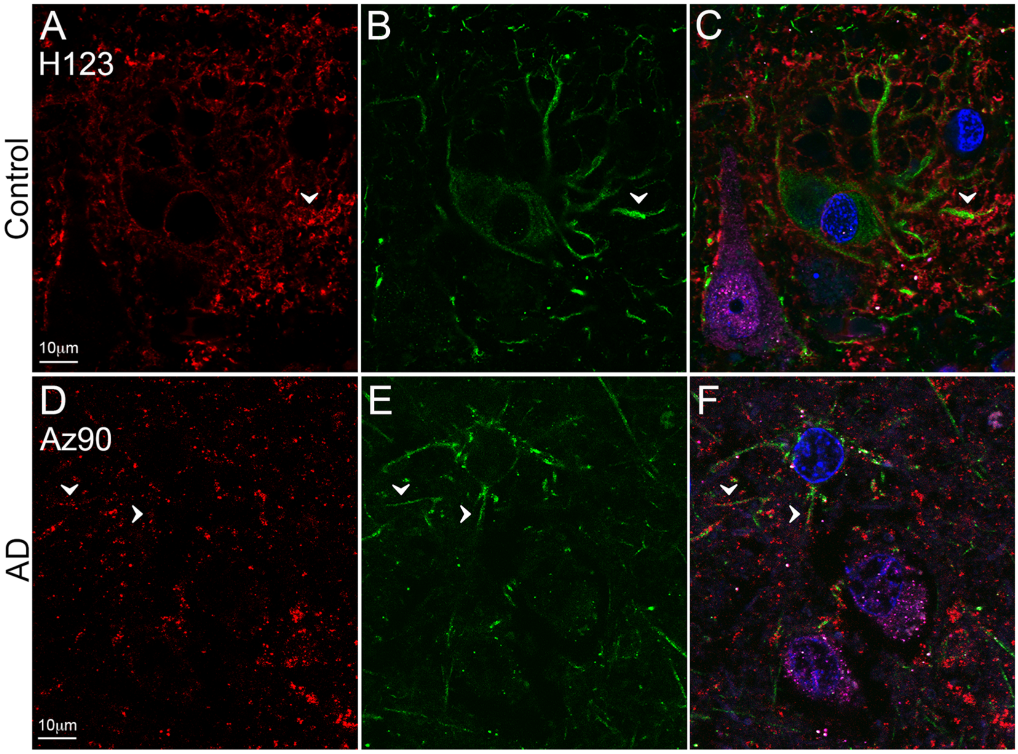

FIGURE 5 | EAAT2 expression in the superior temporal gyrus (STG). Photomicrographs of layer III of the STG showing EAAT2 (**A,D**, red), GFAP (**B,E**, green), and EAAT2 overlaid with GFAP and NeuN (magenta; **C,F**) immunoreactivity for a representative control (**A–C**, H123) and Alzheimer's disease (AD) (**D–F**, Az90) case. In controls, EAAT2 labeling is more localized to membranes of astrocytic stem processes, while in AD the staining is weaker on astrocytic main branches (**A–F**, arrowheads), but more labeling is likely localized to fine astrocytic branches in the neuropil. Cell nuclei are labeled with Hoechst nuclei counterstain (**C,F**, blue). Scale bar **(A–F)** = 10 μm.

DISCUSSION

The present study is the first to provide a comprehensive examination of expression levels and patterns of glutamate EAAT2 in the human hippocampus, subiculum, entorhinal cortex, and STG, and how this expression is altered in AD. EAAT2 shows strong labeling of astrocytic cell bodies and processes in all these brain regions. We report a significantly altered staining pattern of EAAT2 in AD cases, with a more diffuse staining in the neuropil, particularly within the CA1–3 and DG regions. Our findings indicate no significant region- and layer-specific density changes of this glutamate transporter in the human hippocampus, subiculum, entorhinal cortex, and STG in comparison to healthy controls.

EAAT2 is mainly expressed in astrocytes and is responsible for ∼95% of all L-glutamate uptake in the CNS from the synaptic cleft (Vandenberg and Ryan, 2013). EAAT2 is also an important element of the glutamate-glutamine cycle (Beart and O'Shea, 2007). During the past few decades, mouse models have provided important but conflicting data regarding the role and regulation of glutamate transporters in AD pathology. However, AD is a human disease, and studies involving human tissue remain the most reliable and representative mode of investigating pathological changes. Human studies involving EAAT2 expression changes have however been scarce. An early radiolabeling study found a ∼30% decrease in [^{3}H]aspartate binding in the midfrontal cortex of AD brains, suggesting decreased glutamate transporter activity associated with increased excitotoxicity and neurodegeneration (Masliah et al., 1996). EAAT2 IHC revealed strong glial labeling in the frontal cortex and hippocampus with reduced astrocytic localization in AD cases, but no quantitative data was provided regarding the hippocampal expression (Li et al., 1997). Interestingly, the pattern of the staining in the hippocampus (the hippocampal subfield is not identified) seems to be similar to our findings, with an increased labeling in the neuropil (Li et al., 1997). Jacob et al. (2007) reported impairment in the expression of EAAT1 and EAAT2 at both gene and protein levels in the hippocampus and gyrus frontalis medialis of AD patients, but up-regulation in the cerebellum. These findings confirm that EAAT2 expression alterations are brain region-specific in AD. However, the semi-quantitative examination by Jacob et al. (2007) does not show a clear decrease in EAAT2 expression in the hippocampus. The low case number (n = 4, controls), and high variability in staining pattern and intensity make it difficult to draw any significant conclusions. Furthermore, the immunohistochemical labeling of EAAT2 is relatively weak and the differences between control and AD cases are not shown.

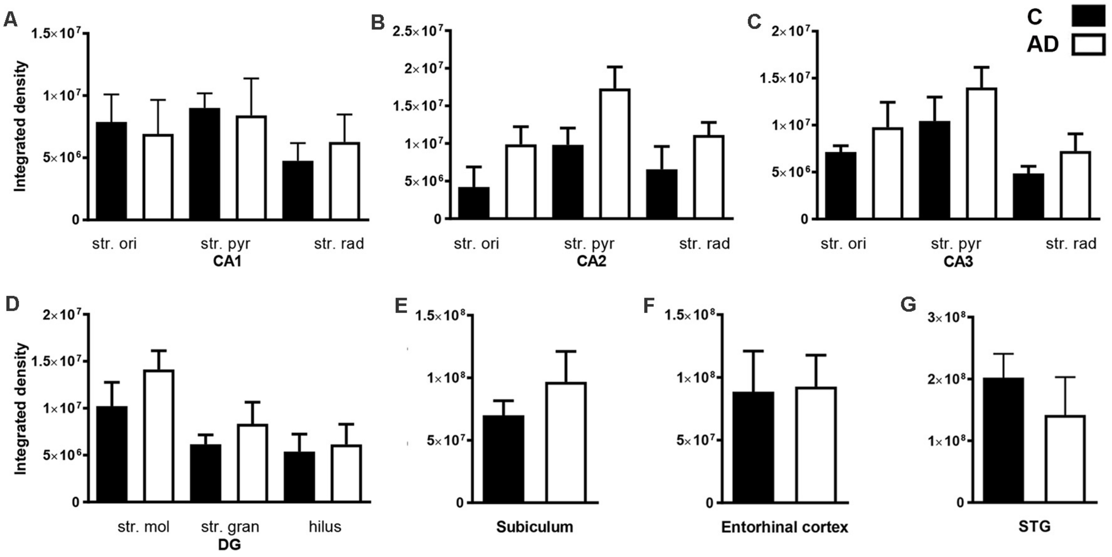

FIGURE 6 | Quantification of EAAT2 immunoreactivity within the CA1, CA2, CA3, dentate gyrus hippocampal subfields, subiculum, entorhinal cortex, and STG in control and AD groups. In the hippocampal CA1 **(A)**, CA2 **(B)**, CA3 **(C)**, DG **(D)**, subiculum **(E)**, entorhinal cortex **(F)** and STG **(G)** EAAT2 density shows no statistically significant change in AD (white bars; *n* = 6) compared to control (black bars; *n* = 7) cases (Unpaired Mann–Whitney test). Data are expressed as mean with error bars representing standard error of mean (SEM). AD, Alzheimer's disease; C, control; CA, cornu ammonis; DG, dentate gyrus; STG, superior temporal gyrus, str. ori, stratum oriens; str. pyr, stratum pyramidale; str. rad, stratum radiatum; str. mol, stratum moleculare; str. gran, stratum granulosum.

EAAT2 is the major glutamate transporter and represents 1% of total brain protein, therefore EAAT2 labeling would be expected to be strong and widespread in the hippocampus (Lehre and Danbolt, 1998). In contrast, other studies have demonstrated no decrease in the expression of EAAT2 in AD. In the cingulate and inferior temporal gyri, EAAT2 protein levels are well preserved in AD subjects, with normal transporter levels found in a high percentage of AD cases (Beckstrom et al., 1999). EAAT2 expression was also preserved in the frontal cortex in the advanced stages of AD (Garcia-Esparcia et al., 2018). Our study, the first comprehensive examination of EAAT2 expression in the AD hippocampus, subiculum, entorhinal cortex, and STG, does not show EAAT2 density change in AD either.

EAAT2 is predominantly expressed in astrocytes, although they are also expressed in other types of glial cells, including microglia, macrophages, and oligodendrocytes (Kondo et al., 1995; Gras et al., 2012; Parkin et al., 2018; Pajarillo et al., 2019). Whilst astrocytic EAAT2 staining is well established, the presence of EAAT2 in neurons is controversial. Neuronal EAAT2 mRNA expression has been demonstrated in multiple rat studies (Torp et al., 1994; Schmitt et al., 1996; Berger et al., 2005) but its presence at the protein level is still controversial. Multiple animal and few human studies suggest that EAAT2 protein is exclusively expressed in astrocytes (Rothstein et al., 1994; Lehre et al., 1995; Li et al., 1997; Simpson et al., 2010) while others provide evidence of neuronal expression (Rimmele and Rosenberg, 2016). However, several technical issues could lead to false-positive findings, such as weak antibody labeling that might represent nonspecific background staining; labeling that is localized to astrocytic processes wrapping around the neurons rather than the expression on neuronal membranes; and astrocytic contamination of synaptosomes (Rimmele and Rosenberg, 2016). Differences in tissue processing methodology can also contribute to variable findings regarding EAAT2 protein localization and expression levels. Interestingly, one study reported a large variability in astrocytic EAAT2 expression in AD human tissue within the lateral temporal cortex, and categorized the cases into three groups with minimal, moderate, or extensive immunoreactivity (Simpson et al., 2010). However, while the number of astrocytes and their morphology were variable between cases, we did not observe the "minimal and extensive" type of staining that might represent the lack of staining or high non-specific background labeling. While the authors ruled out that neither pH nor post-mortem delay (PMD) significantly correlates with either GFAP or EAAT2 immunoreactivity, they were not able to exclude the effect of fixation on the detection of these proteins. Long–term storage in formalin can significantly influence antibody binding, therefore our protocol involves a standardized fixation protocol followed by cryoprotection with sucrose solutions, freeze down, and storage at −80°C. However, staining variability is one of the main challenges of using human tissue, which can be the result of many other factors related to post-mortem conditions that cannot be controlled or correlated with transporter expression patterns. In this study, we did not observe neuronal EAAT2 expression, but strong labeling is localized to astrocytic processes wrapping around the neurons.

Reactive astrocytes are easily identified by their GFAP immunoreactivity, but GFAP expression in non-reactive (resting) astrocytes is often below the detection level of IHC, that can make co-localization experiments challenging. The up-regulation of GFAP in reactive astrocytes can impair physiological protein degradation and restrict migration and process motion (Orre et al., 2013; Perez-Nievas and Serrano-Pozo, 2018). With significant neuronal loss, the reorientation of astrocyte processes towards amyloid plaques, and increased astrocytosis, the cellular architecture of the hippocampus and cortex seems to be disorganized in AD compared to healthy controls (Buldyrev et al., 2000; Colombo et al., 2000, 2002), which might contribute to the diffuse EAAT2 staining that remains localized to astrocytic processes. Furthermore, in AD, more EAAT2 staining seems to localize to neuropil; this could be the result of labeling on fine astrocytic branches that are usually not stained with GFAP (Derouiche and Frotscher, 2001). However, it is also possible that the staining is localized to fragmented astrocyte processes and this can result in staining that appears as homogenous labeling of the neuropil.

In conclusion, no significant EAAT2 density changes were found between control and AD cases, however, the observed spatial differences in transporter expression could underly alterations in glutamate recycling and potentially disturbed glutamatergic homeostasis. Further studies will be required to explore how EAAT2 function is affected in AD and its potential as a therapeutic target.

DATA AVAILABILITY STATEMENT

The original contributions presented in the study are included in the article, further inquiries can be directed to the corresponding author.

ETHICS STATEMENT

The studies involving human participants were reviewed and approved by University of Auckland Human Participant's Ethics Committee. The patients/participants provided their written informed consent to participate in this study.

AUTHOR CONTRIBUTIONS

JY, TP, OW, HW, and AK performed the research. CT carried out the pathology for all human brain tissue. AK, RF, and HW designed the research. JY and AK wrote the manuscript. AK was responsible for project administration. HW, RF, and AK supervised the study. All authors contributed to the article and approved the submitted version.

FUNDING

This work was supported by Alzheimers New Zealand Charitable Trust (AK; 370836), Alzheimers New Zealand (AK; 3718869), Freemasons New Zealand (AK; 3719321), Aotearoa Foundation, Centre for Brain Research and University of Auckland (AK; 3705579), Health Research Council of New Zealand (RF and HW; 3627373), Neurological Foundation of New Zealand (TP and AK; 3715525), and Brain Research New Zealand.

ACKNOWLEDGMENTS

We acknowledge the excellent work and assistance of Kristina Hubbard, Marika Eszes, and Jacqueline Ross.

SUPPLEMENTARY MATERIAL

The Supplementary Material for this article can be found online at: https://www.frontiersin.org/articles/10.3389/fncel.2021.702824/full#supplementary-material.

SUPPLEMENTARY FIGURE 1 | Western blot against human hippocampus homogenates probed with EAAT2 antibody **(A)**. The omission of the primary antibodies **(B)** resulted in a complete absence of immunoreactivity except for a small amount of background lipofuscin staining **(B,c)**. The section was stained with goat anti-mouse Alexa Fluor 647 **(B,b)** and goat anti-rabbit Alexa Fluor 488 **(B,c)**. Nuclei were counterstained with Hoechst dye (blue; **B,a**). Scale bar B = 25 μm.

REFERENCES

Abdul, H. M., Sama, M. A., Furman, J. L., Mathis, D. M., Beckett, T. L., Weidner, A. M., et al. (2009). Cognitive decline in Alzheimer's disease is associated with selective changes in calcineurin/NFAT signaling. *J. Neurosci.* 29, 12957–12969. doi: 10.1523/JNEUROSCI.1064-09.2009

Arriza, J. L., Eliasof, S., Kavanaugh, M. P., and Amara, S. G. (1997). Excitatory amino acid transporter 5, a retinal glutamate transporter coupled to a chloride conductance. *Proc. Natl. Acad. Sci. U S A* 94, 4155–4160. doi: 10.1073/pnas.94.8.4155

Bacci, M., Lorito, N., Ippolito, L., Ramazzotti, M., Luti, S., Romagnoli, S., et al (2019). Reprogramming of amino acid transporters to support aspartate and glutamate dependency sustains endocrine resistance in breast cancer. *Cell Rep.* 28, P104–118.E8. doi: 10.1016/j.celrep.2019.06.010

Bak, L. K., Schousboe, A., and Waagepetersen, H. S. (2006). The glutamate/GABA-glutamine cycle: aspects of transport, neurotransmitter homeostasis and ammonia transfer. *J. Neurochem.* 98, 641–653. doi: 10.1111/j.1471-4159.2006.03913.x

Beart, P. M., and O'Shea, R. D. (2007). Transporters for L-glutamate: an update on their molecular pharmacology and pathological involvement. *Br. J. Pharmacol.* 150, 5–17. doi: 10.1038/sj.bjp.0706949

Beckstrom, H., Julsrud, L., Haugeto, O., Dewar, D., Graham, D. I., Lehre, K. P., et al. (1999). Interindividual differences in the levels of the glutamate transporters GLAST and GLT, but no clear correlation with Alzheimer's disease. *J. Neurosci. Res.* 55, 218–229. doi: 10.1002/(SICI)1097-4547(19990115)55:2<218::AID-JNR9>3.0.CO;2-L

Berger, U. V., DeSilva, T. M., Chen, W., and Rosenberg, P. A. (2005). Cellular and subcellular mRNA localization of glutamate transporter isoforms GLT1a and GLT1b in rat brain by *in situ* hybridization. *J. Comp. Neurol.* 492, 78–89. doi: 10.1002/cne.20737

Buldyrev, S. V., Cruz, L., Gomez-Isla, T., Gomez-Tortosa, E., Havlin, S., Le, R., et al. (2000). Description of microcolumnar ensembles in association cortex and their disruption in Alzheimer and lewy body dementias. *Proc. Natl. Acad. Sci. U S A* 97, 5039–5043. doi: 10.1073/pnas.060009897

Butterfield, D. A., and Pocernich, C. B. (2003). The glutamatergic system and Alzheimer's disease: therapeutic implications. *CNS Drugs* 17, 641–652. doi: 10.2165/00023210-200317090-00004

Castaneda-Cabral, J. L., Lopez-Ortega, J. G., Fajardo-Fregoso, B. F., Beas-Zarate, C., and Urena-Guerrero, M. E. (2020). Glutamate induced neonatal excitotoxicity modifies the expression level of EAAT1 (GLAST) and EAAT2 (GLT-1) proteins in various brain regions of the adult rat. *Neurosci. Lett.* 735:135237. doi: 10.1016/j.neulet.2020.135237

Colombo, J. A., Fuchs, E., Hartig, W., Marotte, L. R., and Puissant, V. (2000). "Rodent-like" and "primate-like" types of astroglial architecture in the adult cerebral cortex of mammals: a comparative study. *Anat. Embryol. (Berl)* 201, 111–120. doi: 10.1007/pl00008231

Colombo, J. A., Quinn, B., and Puissant, V. (2002). Disruption of astroglial interlaminar processes in Alzheimer's disease. *Brain Res. Bull.* 58, 235–242. doi: 10.1016/s0361-9230(02)00785-2

Danysz, W., and Parsons, C. G. (2012). Alzheimer's disease, β-amyloid, glutamate, NMDA receptors and memantine - searching for the connections. *Br. J. Pharmacol.* 167, 324–352. doi: 10.1111/j.1476-5381.2012.02057.x

Derouiche, A., and Frotscher, M. (2001). Peripheral astrocyte processes: monitoring by selective immunostaining for the actin-binding ERM proteins. *Glia* 36, 330–341. doi: 10.1002/glia.1120

Dienel, G. A. (2013). Astrocytic energetics during excitatory neurotransmission: what are contributions of glutamate oxidation and glycolysis. *Neurochem. Int.* 63, 244–258. doi: 10.1016/j.neuint.2013.06.015

Erecinska, M., and Silver, I. A. (1990). Metabolism and role of glutamate in mammalian brain. *Prog. Neurobiol.* 35, 245–296. doi: 10.1016/0301-0082(90)90013-7

Fairman, W. A., and Amara, S. G. (1999). Functional diversity of excitatory amino acid transporters: ion channel and transport modes. *Am. J. Physiol.* 277, F481–F486. doi: 10.1152/ajprenal.1999.277.4.F481

Fonnum, F. (1984). Glutamate: a neurotransmitter in mammalian brain. *J. Neurochem.* 42, 1–11. doi: 10.1111/j.1471-4159.1984.tb09689.x

Furuta, A., Martin, L. J., Lin, C. L., Dykes-Hoberg, M., and Rothstein, J. D. (1997a). Cellular and synaptic localization of the neuronal glutamate transporters excitatory amino acid transporter 3 and 4. *Neuroscience* 81, 1031–1042. doi: 10.1016/s0306-4522(97)00252-2

Furuta, A., Rothstein, J. D., and Martin, L. J. (1997b). Glutamate transporter protein subtypes are expressed differentially during rat CNS development. *J. Neurosci.* 17, 8363–8375. doi: 10.1523/JNEUROSCI.17-21-08363.1997

Gameiro, A., Braams, S., Rauen, T., and Grewer, C. (2011). The discovery of slowness: low-capacity transport and slow anion channel gating by the glutamate transporter EAAT5. *Biophys. J.* 100, 2623–2632. doi: 10.1016/j.bpj.2011.04.034

Garcia-Esparcia, P., Diaz-Lucena, D., Ainciburu, M., Torrejon-Escribano, B., Carmona, M., Llorens, F., et al. (2018). Glutamate transporter GLT1 expression in Alzheimer disease and dementia with lewy bodies. *Front. Aging Neurosci.* 10:122. doi: 10.3389/fnagi.2018.00122

Germany, C. E., Reker, A. N., Hinton, D. J., Oliveros, A., Shen, X., Andres-Beck, L. G., et al. (2018). Pharmacoproteomics profile in response to acamprosate treatment of an alcoholism animal model. *Proteomics* 18:e1700417. doi: 10.1002/pmic.201700417

Gras, G., Samah, B., Hubert, A., Leone, C., Porcheray, F., and Rimaniol, A. C. (2012). EAAT expression by macrophages and microglia: still more questions than answers. *Amino. Acids* 42, 221–229. doi: 10.1007/s00726-011-0866-6

Greenamyre, J. T., Maragos, W. F., Albin, R. L., Penney, J. B., and Young, A. B. (1988). Glutamate transmission and toxicity in Alzheimer's disease. *Prog. Neuropsychopharmacol. Biol. Psychiatry* 12, 421–430. doi: 10.1007/s00726-011-0866-6

Gu, Q. B., Zhao, J. X., Fei, J., and Schwarz, W. (2004). Modulation of Na(+),K(+) pumping and neurotransmitter uptake by beta-amyloid. *Neuroscience* 126, 61–67. doi: 10.1016/j.neuroscience.2004.03.022

Jacob, C., Koutsilieri, E., Bartl, J., Neuen-Jacob, E., Arzberger, T., Zander, N., et al. (2007). Alterations in expression of glutamatergic transporters and receptors in sporadic Alzheimer's disease. *J. Alzheimers Dis.* 11, 97–116. doi: 10.3233/jad-2007-11113

Kanai, Y., Nussberger, S., Romero, M. F., Boron, W. F., Hebert, S. C., and Hediger, M. A. (1995). Electrogenic properties of the epithelial and neuronal high affinity glutamate transporter. *J. Biol. Chem.* 270, 16561–16568. doi: 10.1074/jbc.270.28.16561

Kondo, K., Hashimoto, H., Kitanaka, J., Sawada, M., Suzumura, A., Marunouchi, T., et al. (1995). Expression of glutamate transporters in cultured glial cells. *Neurosci. Lett.* 188, 140–142. doi: 10.1016/0304-3940(95)11408-o

Kwakowsky, A., Calvo-Flores Guzman, B., Pandya, M., Turner, C., Waldvogel, H. J., and Faull, R. L. (2018). GABAA receptor subunit expression changes in the human Alzheimer's disease hippocampus, subiculum, entorhinal cortex and superior temporal gyrus. *J. Neurochem.* 145, 374–392. doi: 10.1111/jnc.14325

Kwakowsky, A., Waldvogel, H. J., and Faull, R. L. (2021). The effects of amyloid-beta on hippocampal glutamatergic receptor and transporter expression. *Neural. Regen. Res.* 16, 1399–1401. doi: 10.4103/1673-5374.301009

Lehre, K. P., and Danbolt, N. C. (1998). The number of glutamate transporter subtype molecules at glutamatergic synapses: chemical and stereological quantification in young adult rat brain. *J. Neurosci.* 18, 8751–8757. doi: 10.1523/JNEUROSCI.18-21-08751.1998

Lehre, K. P., Levy, L. M., Ottersen, O. P., Storm-Mathisen, J., and Danbolt, N. C. (1995). Differential expression of two glial glutamate transporters in the rat brain: quantitative and immunocytochemical observations. *J. Neurosci.* 15, 1835–1853. doi: 10.1523/JNEUROSCI.15-03-01835.1995

Lewerenz, J., Klein, M., and Methner, A. (2006). Cooperative action of glutamate transporters and cystine/glutamate antiporter system Xc- protects from oxidative glutamate toxicity. *J. Neurochem.* 98, 916–925. doi: 10.1111/j.1471-4159.2006.03921.x

Li, S., Mallory, M., Alford, M., Tanaka, S., and Masliah, E. (1997). Glutamate transporter alterations in Alzheimer disease are possibly associated with abnormal APP expression. *J. Neuropathol. Exp. Neurol.* 56, 901–911. doi: 10.1097/00005072-199708000-00008

Li, W., Gao, H., and Li, W. (2020). Effects of combined bushen zhichan recipe and levodopa in a rodent model of Parkinson disease: potential mechanisms. *Med. Sci. Monit.* 26:e922345. doi: 10.12659/MSM.922345

Mai, J., Paxinos, A., and Voss, T. (2008). *Atlas of the Human Brain*, 3rd Edn. San Diego, CA: Elsevier. Available online at: https://www.elsevier.com/books/atlas-of-the-human-brain/mai/978-0-12-802800-1

Maragos, W. F., Greenamyre, J. T., Penney Jr, J. B., and Young, A. B. (1987). Glutamate dysfunction in Alzheimer's disease: an hypothesis. *Trends Neurosci.* 10, 65–68. doi: 10.1016/0166-2236(87)90025-7

Masliah, E., Alford, M., DeTeresa, R., Mallory, M., and Hansen, L. (1996). Deficient glutamate transport is associated with neurodegeneration in Alzheimer's disease. *Ann. Neurol.* 40, 759–766. doi: 10.1002/ana.410400512

Masliah, E., Raber, J., Alford, M., Mallory, M., Mattson, M. P., Yang, D., et al. (1998). Amyloid protein precursor stimulates excitatory amino acid transport. implications for roles in neuroprotection and pathogenesis. *J. Biol. Chem.* 273, 12548–12554. doi: 10.1074/jbc.273.20.12548

McKenna, M. C., Stridh, M. H., McNair, L. F., Sonnewald, U., Waagepetersen, H. S., and Schousboe, A. (2016). Glutamate oxidation in astrocytes: roles of glutamate dehydrogenase and aminotransferases. *J. Neurosci. Res.* 94, 1561–1571. doi: 10.1002/jnr.23908

McKhann, G., Drachman, D., Folstein, M., Katzman, R., Price, D., and Stadlan, E. M. (1984). Clinical diagnosis of Alzheimer's disease: report of the NINCDS-ADRDA Work Group under the auspices of department of health and human services task force on Alzheimer's disease. *Neurology* 34, 939–944. doi: 10.1212/wnl.34.7.939

Mirra, S. S., Heyman, A., McKeel, D., Sumi, S. M., Crain, B. J., Brownlee, L. M., et al. (1991). The consortium to establish a registry for Alzheimer's disease (CERAD). part II. standardization of the neuropathologic assessment of Alzheimer's disease. *Neurology* 41, 479–486. doi: 10.1212/wnl.41.4.479

Munch, C., Ebstein, M., Seefried, U., Zhu, B., Stamm, S., Landwehrmeyer, G. B., et al. (2002). Alternative splicing of the 5'-sequences of the mouse EAAT2 glutamate transporter and expression in a transgenic model for amyotrophic lateral sclerosis. *J. Neurochem.* 82, 594–603. doi: 10.1046/j.1471-4159.2002.01012.x

Noda, M., Nakanishi, H., and Akaike, N. (1999). Glutamate release from microglia *via* glutamate transporter is enhanced by amyloid-beta peptide. *Neuroscience* 92, 1465–1474. doi: 10.1016/s0306-4522(99)00036-6

Oberheim, N. A., Takano, T., Han, X., He, W., Lin, J. H. C., Wang, F., et al. (2009). Uniquely hominid features of adult human astrocytes. *J. Neurosci.* 29, 3276–3287. doi: 10.1523/JNEUROSCI.4707-08.2009

Orre, M., Kamphuis, W., Dooves, S., He, W., Lin, J. H. C., Wang, F., et al. (2013). Reactive glia show increased immunoproteasome activity in Alzheimer's disease. *Brain* 136, 1415–1431. doi: 10.1093/brain/awt083

Pajarillo, E., Rizor, A., Lee, J., Aschner, M., and Lee, E. (2019). The role of astrocytic glutamate transporters GLT-1 and GLAST in neurological disorders: potential targets for neurotherapeutics. *Neuropharmacology* 161:107559. doi: 10.1016/j.neuropharm.2019.03.002

Parkin, G. M., Udawela, M., Gibbons, A., and Dean, B. (2018). Glutamate transporters, EAAT1 and EAAT2, are potentially important in the pathophysiology and treatment of schizophrenia and affective disorders. *World J. Psychiatry* 8, 51–63. doi: 10.5498/wjp.v8.i2.51

Perez-Nievas, B. G., and Serrano-Pozo, A. (2018). Deciphering the astrocyte reaction in Alzheimer's disease. *Front. Aging Neurosci.* 10:114. doi: 10.3389/fnagi.2018.00114

Purves, D. (2012). *Neuroscience*. Oxford, United Kingdom: Oxford University Press.

Rimmele, T. S., and Rosenberg, P. A. (2016). GLT-1: The elusive presynaptic glutamate transporter. *Neurochem. Int.* 98, 19–28. doi: 10.1016/j.neuint.2016.04.010

Rothstein, J. D., Martin, L., Levey, A. I., Dykes-Hoberg, M., Jin, L., Wu, D., et al. (1994). Localization of neuronal and glial glutamate transporters. *Neuron* 13, 713–725. doi: 10.1016/0896-6273(94)90038-8

Rothstein, J. D., Van Kammen, M., Levey, A. I., Martin, L. J., and Kuncl, R. W. (1995). Selective loss of glial glutamate transporter GLT-1 in amyotrophic lateral sclerosis. *Ann. Neurol.* 38, 73–84. doi: 10.1002/ana.410380114

Schmitt, A., Asan, E., Puschel, B., Jons, T., and Kugler, P. (1996). Expression of the glutamate transporter GLT1 in neural cells of the rat central nervous system: non-radioactive *in situ* hybridization and comparative immunocytochemistry. *Neuroscience* 71, 989–1004. doi: 10.1016/0306-4522(95)00477-7

Sheldon, A. L., and Robinson, M. B. (2007). The role of glutamate transporters in neurodegenerative diseases and potential opportunities for intervention. *Neurochem. Int.* 51, 333–355. doi: 10.1016/j.neuint.2007.03.012

Simpson, J. E., Ince, P. G., Lace, G., Forster, G., Shaw, P. J., Matthews, F., et al. (2010). Astrocyte phenotype in relation to Alzheimer-type pathology in the ageing brain. *Neurobiol. Aging* 31, 578–590. doi: 10.1016/j.neurobiolaging.2008.05.015

Storck, T., Schulte, S., Hofmann, K., and Stoffel, W. (1992). Structure, expression and functional analysis of a Na(+)-dependent glutamate/aspartate transporter from rat brain. *Proc. Natl. Acad. Sci. U S A* 89, 10955–10959. doi: 10.1073/pnas.89.22.10955

Torp, R., Danbolt, N. C., Babaie, E., Bjoras, M., Seeberg, E., Storm-Mathisen, J., et al. (1994). Differential expression of two glial glutamate transporters in the rat brain: an *in situ* hybridization study. *Eur. J. Neurosci.* 6, 936–942. doi: 10.1111/j.1460-9568.1994.tb00587.x

Torp, R., Lekieffre, D., Levy, L. M., Haug, F. M., Danbolt, N. C., Meldrum, B. S., et al. (1995). Reduced postischemic expression of a glial glutamate transporter, GLT1, in the rat hippocampus. *Exp. Brain Res.* 103, 51–58. doi: 10.1007/BF00241964

Vandenberg, R. J., and Ryan, R. M. (2013). Mechanisms of glutamate transport. *Physiol. Rev.* 93, 1621–1657. doi: 10.1152/physrev.00007.2013

Vizi, E. S. (2000). Role of high-affinity receptors and membrane transporters in nonsynaptic communication and drug action in the central nervous system. *Pharmacol. Rev.* 52, 63–89.

Wadiche, J. I., Arriza, J. L., Amara, S. G., and Kavanaugh, M. P. (1995). Kinetics of a human glutamate transporter. *Neuron* 14, 1019–1027. doi: 10.1016/0896-6273(95)90340-2

Waldvogel, H. J., Curtis, M. A., Baer, K., Rees, M. I., and Faull, R. L. (2006). Immunohistochemical staining of post-mortem adult human brain sections. *Nat. Protoc.* 1, 2719–2732. doi: 10.1038/nprot.2006.354

Wang, Y., Lu, S., Qu, Z., Wu, L., and Wang, Y. (2017). Sonic hedgehog induces GLT-1 degradation *via* PKC delta to suppress its transporter activities. *Neuroscience* 365, 217–225. doi: 10.1016/j.neuroscience.2017.09.051

Wilkie, C. M., Barnes, J. R., Benson, C. M., Brymer, K. J., Nafar, F., and Parsons, M. P. (2020). Hippocampal synaptic dysfunction in a mouse model of huntington disease is not alleviated by ceftriaxone treatment. *eNeuro* 7:ENEURO.0440-19.2020. doi: 10.1523/ENEURO.0440-19.2020

Yao, J., Zheng, K., and Zhang, X. (2015). Rosiglitazone exerts neuroprotective effects *via* the suppression of neuronal autophagy and apoptosis in the cortex following traumatic brain injury. *Mol. Med. Rep.* 12, 6591–6597. doi: 10.3892/mmr.2015.4292

Yeung, J. H. Y., Calvo-Flores Guzman, B., Palpagama, T. H., Ethiraj, J., Zhai, Y., Tate, W. P., et al. (2020a). Amyloid-beta1–42 induced glutamatergic receptor and transporter expression changes in the mouse hippocampus. *J. Neurochem.* 155, 62–80. doi: 10.1111/jnc.15099

Yeung, J. H., Palpagama, T. H., Tate, W. P., Peppercorn, K., Waldvogel, H. J., Faull, R. L., et al. (2020b). The acute effects of amyloid-beta1–42 on glutamatergic receptor and transporter expression in the mouse hippocampus. *Front. Neurosci.* 13:1427. doi: 10.3389/fnins.2019.01427

Yeung, J. H. Y., Walby, J. L., Palpagama, T. H., Turner, C., Waldvogel, H. J., Faull, R. L. M., et al. (2021). Glutamatergic receptor expression changes in the Alzheimer's disease hippocampus and entorhinal cortex. *Brain Pathol.* e13005. doi: 10.1111/bpa.13005

Yoshino, K., Oda, Y., Kimura, M., Kimura, H., Nangaku, M., Shirayama, Y., et al. (2020). The alterations of glutamate transporter 1 and glutamine synthetase in the rat brain of a learned helplessness model of depression. *Psychopharmacology (Berl)* 237, 2547–2553. doi: 10.1007/s00213-020-05555-3

Conflict of Interest: The authors declare that the research was conducted in the absence of any commercial or financial relationships that could be construed as a potential conflict of interest.

frontiers
in Cellular Neuroscience

ORIGINAL RESEARCH
published: 17 December 2021
doi: 10.3389/fncel.2021.796635

Aged xCT-Deficient Mice Are Less Susceptible for Lactacystin-, but Not 1-Methyl-4-Phenyl-1,2,3,6-Tetrahydropyridine-, Induced Degeneration of the Nigrostriatal Pathway

Eduard Bentea[1†], Laura De Pauw[1†], Lise Verbruggen[1], Lila C. Winfrey[2], Lauren Deneyer[1], Cynthia Moore[2], Giulia Albertini[1], Hideyo Sato[3], Ann Van Eeckhaut[4], Charles K. Meshul[2,5‡] and Ann Massie[1*‡]

[1] Laboratory of Neuro-Aging and Viro-Immunotherapy, Vrije Universiteit Brussel, Brussels, Belgium, [2] Neurocytology Laboratory, Veterans Affairs Medical Center, Research Services, Portland, OR, United States, [3] Department of Medical Technology, Niigata University, Niigata, Japan, [4] Research Group Experimental Pharmacology, Department of Pharmaceutical Chemistry, Drug Analysis and Drug Information, Vrije Universiteit Brussel, Brussels, Belgium, [5] Department of Behavioral Neuroscience and Pathology, Oregon Health and Science University, Portland, OR, United States

Edited by:
Francisco Zafra,
Autonomous University of Madrid,
Spain

Reviewed by:
Laura Civiero,
University of Padua, Italy
Eduardo Luiz Gasnhar Moreira,
Federal University of Santa Catarina,
Brazil

***Correspondence:**
Ann Massie
Ann.Massie@vub.be

†These authors have contributed equally to this work and share first authorship

‡These authors have contributed equally to this work and share last authorship

Specialty section:
This article was submitted to Cellular Neurophysiology, a section of the journal Frontiers in Cellular Neuroscience

Received: *17 October 2021*
Accepted: *24 November 2021*
Published: *17 December 2021*

Citation:
Bentea E, De Pauw L, Verbruggen L, Winfrey LC, Deneyer L, Moore C, Albertini G, Sato H, Van Eeckhaut A, Meshul CK and Massie A (2021) Aged xCT-Deficient Mice Are Less Susceptible for Lactacystin-, but Not 1-Methyl-4-Phenyl-1,2,3,6-Tetrahydropyridine-, Induced Degeneration of the Nigrostriatal Pathway. Front. Cell. Neurosci. 15:796635. doi: 10.3389/fncel.2021.796635

The astrocytic cystine/glutamate antiporter system x_c^- (with xCT as the specific subunit) imports cystine in exchange for glutamate and has been shown to interact with multiple pathways in the brain that are dysregulated in age-related neurological disorders, including glutamate homeostasis, redox balance, and neuroinflammation. In the current study, we investigated the effect of genetic xCT deletion on lactacystin (LAC)- and 1-methyl-4-phenyl-1,2,3,6-tetrahydropyridine (MPTP)-induced degeneration of the nigrostriatal pathway, as models for Parkinson's disease (PD). Dopaminergic neurons of adult xCT knock-out mice ($xCT^{-/-}$) demonstrated an equal susceptibility to intranigral injection of the proteasome inhibitor LAC, as their wild-type ($xCT^{+/+}$) littermates. Contrary to adult mice, aged $xCT^{-/-}$ mice showed a significant decrease in LAC-induced degeneration of nigral dopaminergic neurons, depletion of striatal dopamine (DA) and neuroinflammatory reaction, compared to age-matched $xCT^{+/+}$ littermates. Given this age-related protection, we further investigated the sensitivity of aged $xCT^{-/-}$ mice to chronic and progressive MPTP treatment. However, in accordance with our previous observations in adult mice (Bentea et al., 2015a), xCT deletion did not confer protection against MPTP-induced nigrostriatal degeneration in aged mice. We observed an increased loss of nigral dopaminergic neurons, but equal striatal DA denervation, in MPTP-treated aged $xCT^{-/-}$ mice when compared to age-matched $xCT^{+/+}$ littermates. To conclude, we reveal age-related protection against proteasome inhibition-induced nigrostriatal degeneration in $xCT^{-/-}$ mice, while xCT deletion failed to protect nigral dopaminergic neurons of aged mice against MPTP-induced toxicity. Our findings thereby provide new insights into the role of system x_c^- in mechanisms of dopaminergic cell loss and its interaction with aging.

Keywords: glutamate, neuroprotection, aging, proteasome inhibition, Parkinson's disease

INTRODUCTION

The cystine/glutamate antiporter system x_c^- is an astrocytic plasma membrane antiporter (Ottestad-Hansen et al., 2018) that couples the export of glutamate to the import of cystine in an equimolar ratio (Sato et al., 2005). System x_c^- functions as a heterodimer, in which the specific subunit xCT (encoded by the gene *Slc7a11*) mediates the transport function of the antiporter, while 4F2hc functions as a molecular chaperone anchoring xCT to the plasma membrane (Massie et al., 2015).

After reaching the cytosol, cystine imported by system x_c^- is rapidly reduced to cysteine, an essential substrate in the synthesis of glutathione. Furthermore, cystine delivered *via* system x_c^- can modulate the extracellular cysteine/cystine redox couple after being shuttled *via* system Alanine-Serine-Cysteine (ASC) or system L (Lewerenz et al., 2013). Importantly, while *in vitro* cells are dependent on system x_c^- for intracellular glutathione homeostasis and survival (Sato et al., 2005), no change in glutathione levels or signs of oxidative stress have been reported in the brain of xCT-deficient mice (De Bundel et al., 2011; Massie et al., 2011; Dang et al., 2017), indicating that cells may be less dependent on system x_c^- for basal glutathione production *in vivo*.

In addition to its role in regulating redox function, system x_c^- provides up to 70% of the extracellular glutamate levels in areas of the brain such as the hippocampus (De Bundel et al., 2011) and striatum (Massie et al., 2011). Accumulating evidence supports the extrasynaptic location of system x_c^- and glutamate released by system x_c^- will thus act on extrasynaptic ionotropic and metabotropic glutamate receptors to fine-tune excitatory neurotransmission at the neuron-glia interface (Baker et al., 2002; Bridges et al., 2012; Soria et al., 2014). Consistent with this, pharmacological or genetic modulation of the antiporter has been shown to modulate various synaptic circuits in the brain, including cortico-striatal (Bentea et al., 2021), cortico-accumbens (Moran et al., 2005), and hippocampal CA3-CA1 synapses (Williams and Featherstone, 2014). At the same time, excessive extrasynaptic glutamate levels can be toxic *via* overstimulation of ionotropic glutamate receptors (Hardingham and Bading, 2010), a pathway of neuronal stress and toxicity -i.e., excitotoxicity- involved in various neurodegenerative disorders including Parkinson's disease (PD) (Ambrosi et al., 2014).

Previous findings suggest an involvement of system x_c^- in pathogenic pathways leading to degeneration of nigral dopaminergic neurons. Expression of xCT is affected in PD models, although findings have been inconsistent, depending on the brain region investigated, model employed, and time point post-lesion evaluated (Massie et al., 2008; Bentea et al., 2015a, 2017a; El Arfani et al., 2015). Moreover, genetic deletion of xCT was neuroprotective in the 6-hydroxydopamine (6-OHDA) mouse model of PD, as evidenced by decreased nigral cell loss following intra-striatal administration of the dopaminergic toxin in adult and aged xCT knock-out ($xCT^{-/-}$) mice vs. age-matched wild-type ($xCT^{+/+}$) littermates (Massie et al., 2011). Similarly, genetic deletion of xCT or pharmacological inhibition of system x_c^- was found to be protective against metamphetamine-induced dopaminergic neurotoxicity and microglial activation (Dang et al., 2017). On the other hand, xCT deletion did not affect nigrostriatal degeneration induced by systemic administration of MPTP in adult mice, suggesting that the neuroprotective effects may be dependent on the mechanisms of toxicity (Bentea et al., 2015a).

To further obtain insight into the neuroprotective potential of targeting system x_c^- in PD, we here investigated the link between system x_c^- and proteasome inhibition-induced neurodegeneration. Recent studies revealed structural and functional deficits in the ubiquitin-proteasome pathway in PD, suggesting that impaired proteostasis plays an important role in the pathogenesis (Lehtonen et al., 2019). In line with this, administration of proteasome inhibitors, such as lactacystin (LAC), to the nigrostriatal pathway in rodents replicates features characteristic of PD, including nigrostriatal degeneration and deficits in motor function (Bentea et al., 2017b). While this mechanism has been acknowledged to play an important role in the pathogenesis, targets affecting this pathway may be unique in their profile when compared to other classical PD toxin-based models (Konieczny et al., 2014; Harrison et al., 2019), allowing for a better understanding of the mechanisms of cell loss in PD. Previously, expression of xCT was found to be increased following proteasome inhibition in T24 bladder carcinoma cells, indicating that its levels may be controlled *via* proteasomal degradation of its upstream transcription factors Nrf2 and ATF4 (Ye et al., 2014). In addition, a toxic synergistic interplay has been reported between glutamate excitotoxicity and proteasome inhibition, with extrasynaptic NMDA receptors preferentially coupled to the downregulation of the proteasome system (Caldeira et al., 2013). All together, these findings suggest that modulation of extrasynaptic glutamate may influence proteasome inhibition-induced toxicity and prompted us to study the susceptibility of xCT-deficient mice to LAC-induced neurodegeneration. As aging represents the main risk factor for PD (Abdullah et al., 2015) and to improve translatability of our findings, both adult and aged mice were studied.

Next, we investigating whether aged xCT-deficient mice are protected in the chronic and progressive MPTP model. As for the interplay with proteasome inhibition, an interaction between glutamate excitotoxicity/extrasynaptic NMDA activation and mitochondrial dysfunction has been identified (Gouix et al., 2009; Stanika et al., 2009), whereas mitochondrial dysfunction elicited by the active metabolite of MPTP, MPP+, upregulates the expression of xCT in LUHMES neurons (Tong et al., 2020). Although we did not reveal a differential effect of xCT deletion in the MPTP model in adult mice (Bentea et al., 2015a), aging sensitizes neurons to the toxicity of glutamate (Brewer, 1998; Brewer et al., 2005), possibly due to age-related depolarization of the mitochondrial membrane potential and increased production of mitochondrial reactive oxygen species (Parihar and Brewer, 2007), prompting us to investigate a possible link between xCT and MPTP-induced neurotoxicity in aged animals.

In the current study we reveal age-dependent protection of $xCT^{-/-}$ mice against LAC-induced nigrostriatal degeneration. However, in accordance to our previous observations in adult mice, xCT deletion did not confer any protection against MPTP-induced toxicity.

MATERIALS AND METHODS

xCT-Deficient Mouse Model

$xCT^{-/-}$ and $xCT^{+/+}$ littermates were obtained from a colony of heterozygous high-generation descendants of the strain described previously by Sato et al. (2005). The xCT null mutants were generated by targeted disruption of the START codon in exon 1 of the *Slc7a11* gene and were backcrossed for more than 12 generations on a C57BL/6J background. Genotyping of xCT mutant mice was performed by PCR amplification of ear punch DNA using the REDExtract-N-Amp Tissue PCR Kit (Sigma-Aldrich), and the following primers: 5′-GATGCCCTTCAGCTCGATGCGGTTCACCAG-3′ (GFPR3); 5′-CAGAGCAGCCCTAAGGCACTTTCC-3′ (mxCT5′flankF6); 5′-CCGATGACGCTGCCGATGATGATGG-3′ [mxCT(Dr4)R8].

For investigating the susceptibility of xCT-deficient mice in the LAC model, adult (3–4 months old) and aged (19–23 months old) male $xCT^{-/-}$ and $xCT^{+/+}$ littermates were used. Mice were bred and group-housed under standardized conditions (25°C, 10/14 h dark/light cycle), with free access to food and water, in the animal facilities of the Vrije Universiteit Brussel. Studies were performed according to national guidelines on animal experimentation and were approved by the Ethical Committee for Animal Experimentation of the Vrije Universiteit Brussel.

For investigating the susceptibility of xCT-deficient mice in the MPTP model, aged (17 months old) male $xCT^{-/-}$ and $xCT^{+/+}$ littermates were used. Mice originating from the colony of the Vrije Universiteit Brussel were bred at Janvier Laboratories (France) and shipped to the animal facility of the Veterans Affairs Medical Center (Portland, Oregon) to age. Mice were housed under standardized conditions, on a 12/12 h light/dark cycle, with food and water available *ad libitum*. All procedures were carried out in accordance with the National Institutes of Health (NIH) Guide for the Care and Use of Laboratory Animals and were approved by the Portland VA Medical Center Institutional Animal Care and Use Committee.

Stereotaxic Administration of Lactacystin

Mice were anesthetized with a mixture of ketamine (100 mg/kg i.p.; Ketamine 1000 Ceva, Ceva Sante Animale) and xylazine (10 mg/kg i.p.; Rompun 2%, Bayer N.V.), and positioned in a Kopf Model 963 Ultra Precise Small Animal Stereotaxic Frame, with a mouse adaptor (David Kopf Instruments). The skull was exposed, and a small hole was made through the skull above the left substantia nigra (SN) pars compacta (SNc). A volume of 1.5 μL of 2 μg/μL LAC was injected into the left SNc at the following coordinates: anterior-posterior (AP) −3.0, medial-lateral (ML) −1.0, dorsal-ventral (DV) −4.5 from bregma (Paxinos and Franklin, 2004). To minimize lesion variability due to *ex vivo* degradation of the toxin which can yield an inactive LAC analog (Dick et al., 1996), fresh LAC solutions were prepared for every four mice by dissolving 50 μg LAC (Cayman Chemicals) in 25 μL NaCl 0.9%, and immediately stored on ice. The same batch of LAC was used to lesion all animals within each age group. Control sham-operated mice received the same volume of vehicle (NaCl 0.9%), at the same coordinates. To minimize unspecific tissue damage, microinjections were performed using a 10 μL Model 1701 RN Neuros Syringe (Hamilton Company), at a flow rate of 0.5 μL/min. After injection, the syringe was left in place for an additional 5 min, and then slowly removed. At the end of the surgery, the skin was sutured, and mice received 4 mg/kg ketoprofen i.p. (Ketofen, Merial) for post-operative analgesia.

Motor function of adult mice was investigated (rotarod test) at 1–3 weeks post-stereotaxic surgery. All mice were sacrificed at 3 weeks post-surgery by cervical dislocation. The caudal part of the brains was fixed in 4% paraformaldehyde for immunohistochemistry (IHC), while striata were dissected from the rostral part of the brain for analysis of dopamine (DA) and 3,4-dihydroxyphenylacetic acid (DOPAC) content.

1-Methyl-4-Phenyl-1,2,3,6-Tetrahydropyridine Treatment Paradigm

Aged mice were administered progressively increasing doses of MPTP (dissolved in saline; 0.9% NaCl) at a frequency of one i.p. injection daily for 5 days/week, according to a previously designed protocol (Hood et al., 2016). The first week, mice received a dose of 10 mg/kg, followed by 20 mg/kg and eventually 24 mg/kg during the final week of injections. Due to the high mortality of the mice during the third week of injections, partly induced by their frailty because of their age, the MPTP treatment paradigm was stopped after the third week, and the mice received five injections less compared to our previous protocol (Hood et al., 2016). Vehicle groups received daily saline injections (1 mL/kg).

One week after the final MPTP injection, mice were tested behaviorally using the DigiGait apparatus to analyze gait differences. Next, half of the animals of each group were transcardially perfused for IHC and the brains of the other half of the mice were dissected and snap frozen for DA analysis and immunoblotting.

Behavioral Assessment

For detecting LAC-induced motor deficits, we used an accelerating rotarod system (TSE RotaRod Advanced, TSE Systems), as described previously (Bentea et al., 2015b). Prior to surgery, mice were trained for 5 min at a constant speed of 5 rpm. During this initial training phase, mice were placed immediately back on the rod after falling, allowing them to get familiarized to the test. In the second phase of training, mice underwent three repeated trials of 1 min at a fixed speed of 5 rpm, with 3 min of rest between trials. For testing the rotarod performance at baseline and after lesion, mice underwent five repeated trials that started at constant speed of 5 rpm for 30 s and continued with a 5–25 rpm accelerating protocol during 200 s, leading to a maximum total rod time of 230 s. Mice were allowed 3 min of rest between trials. The mean of the five test trials underwent statistical analysis.

MPTP-induced motor impairment was assessed using the DigiGait apparatus (Mouse Specifics, Inc.), starting 7 days following the last injection, as previously described (Goldberg et al., 2011; Hood et al., 2016; Churchill et al., 2019; Massaquoi et al., 2020). The gait of each mouse was captured by ventral plane videography through a transparent, motor-driven treadmill belt. Digital images of the paws of each mouse were taken at 150 frames/s while the mice ran at a velocity of 24 cm/s. The area of the underside of each paw relative to the area of the treadmill belt at each frame was used for spatial and temporal measurements. Data were analyzed using DigiGait Analysis 15 software. Animals that ran less than 5 s on the treadmill were excluded from the analysis.

Immunohistochemistry

Immunodetection and Quantification of Nigral Dopaminergic Neurons and Microglial Cells Following Lactacystin

Forty micrometer vibratome sections were cut from the post-fixed caudal part of the brain (Leica Microsystems) and stored in serial order in 10 mM phosphate buffer saline (PBS) supplemented with 1.5 mM sodium azide at 4°C. Sections of the SN were selected to quantify the presence of dopaminergic neurons and microglial cells, using rabbit anti-TH antibody (AB152, Millipore; 1/2,000 in Tris-buffered saline, incubation overnight at room temperature) and rabbit anti-mouse Iba-1 antibody (019-19741, Wako Pure Chemicals; 1/1,000 in 20% pre-immune goat serum, incubation overnight at 4°C), respectively, and employing the ABC peroxidase technique as described previously (Bentea et al., 2015b). Immunoreactivity was visualized using 3,3'-diaminobenzidine as chromogen. Photomicrographs were taken of the stained sections, and cell counts were performed using ImageJ software (NIH). The total number of TH + profiles in the ipsi- and contralateral SNc was counted by an investigator blinded to treatment in six serial sections throughout the entire rostro-caudal extent of this brain region (AP – 2.92 to – 3.64 from bregma). The cell number and morphology of Iba-1 + cells were evaluated blindly in three representative 150 × 150 μm squares covering the entire width of the SN of three serial sections spanning the whole SN. Morphological analysis of Iba-1 + cells was performed as described previously (Albertini et al., 2018) by measuring the cell area and Feret's diameter (the longest distance between any two points of the selected region of interest) using ImageJ.

Immunodetection and Quantification of Nigral Dopaminergic Neurons and Striatal Dopaminergic Terminals Following 1-Methyl-4-Phenyl-1,2,3,6-Tetrahydropyridine

Immunohistochemistry following MPTP injection was performed as described previously (Bentea et al., 2015a). MPTP-treated mice were euthanized using a solution of 1% ketamine/0.1% xylazine (20 mL/kg, i.p.) after which they were transcardially perfused with 2.5% glutaraldehyde/0.5% paraformaldehyde/0.1% picric acid. Brains were removed and cut in half coronally at the level of the hypothalamus. Both halves were placed in the same fixative and further fixed in a microwave tissue processor (Pelco BioWave, Ted Pella, Inc.), containing a temperature controlled fixation bath using a thermoelectric recirculating chiller (Pelco Steady Temp Pro, Ted Pella, Inc.) for a total of 30 min [20 min, 150 watts (W) at 28°C/10 min, 650 W at 25°C], as previously described (Xu et al., 2019; Moore et al., 2021). Brain halves were then rinsed and left in 0.1 M PBS at 4°C until being serially sectioned through the striatum (starting at bregma + 1.2 mm and ending at the level of the anterior commissure, + 0.25 mm) at 60 μm thickness, and through the entire rostral-caudal extent of the SN (AP from bregma, −2.50 to −4.24 mm) at 40 μm thickness, using a vibratome (Leica vibratome, Leica Microsystems). Every third slice of the SN or striatum was collected, resulting in a total of six slices per region per mouse. Slices were immuno-labeled using the Pelco BioWave®Pro (Ted Pella Inc.) as described previously (Goldberg et al., 2011; Xu et al., 2019; Moore et al., 2021), using a primary mouse monoclonal antibody for TH (1/250 dilution, Immunostar), a secondary biotinylated goat anti-mouse antibody (1/400 dilution, Jackson ImmunoResearch), and the ABC peroxidase technique. Mounted slices at the level of the SN were counterstained with Cresyl Violet (0.2% in H_2O) and imaged at a magnification of 5× using a Zeiss Axioplan (Carl Zeiss) and a Microbrightfield (MBF) camera and software setup (MBF Bioscience). TH + cells were counted using the ImagePro Software (ImagePro 6.3, Media Cybernetics, Inc.). Cell numbers for each side were added together and the average number of TH + cells/slice was calculated across the six slices, as previously described (Churchill et al., 2019; Massaquoi et al., 2020). Slices containing the striatum were imaged for optical density measurement at 1.25× magnification (numerical aperture of 0.035) and analyzed using ImagePro software. Both the left and right side of the brain was analyzed by subtracting the background (optical density of overlying cortex) for each side, averaging the optical density per slice, then taking the mean from all slices per mouse and eventually by making an overall mean for each group of mice.

Western Blotting

Striatal and nigral tissue of MPTP-treated mice was homogenized in 300 μL extraction buffer [2% sodium dodecyl sulfate (SDS), 60 mM Tris, 100 mM DTT, with phosphatase and protease inhibitor cocktails (Sigma–Aldrich), pH 7.5]. Samples were incubated for 30 min at 37°C and centrifuged for 10 min at 9,500 g at 4°C. Supernatants were stored at –20°C. Protein concentrations were assessed using a fluorometric method (Qubit, Invitrogen). Equal concentrations of protein were loaded on a 4–12% gel (Criterion XT Bis-Tris Precast Gels, Bio-Rad Laboratories) and separated by SDS-polyacrylamide gel electrophoresis (PAGE) under reducing conditions (200 V, 200 mA, 25 W, 45 min). Next, proteins were transferred to a polyvinylidene fluoride membrane using the Trans-Blot Turbo Transfer System (Bio-Rad Laboratories). Non-specific binding was blocked by incubating the membranes for 1 h at room temperature in 5% enhanced chemiluminescence (ECL) Advance Membrane Blocking Agent (Cytiva Life Sciences, Amersham) before overnight incubation with rabbit polyclonal anti-TH (AB152, 1/2,000, diluted in blocking agent at room temperature), or anti-Iba-1 (019-19741, 1/1,000, diluted in blocking agent at 4°C). The following day, membranes were incubated at room temperature for 30 min with horse-radish-peroxidase conjugated anti-rabbit Immunoglobulin G antiserum (1/4,000 for TH; 1/25,000 for Iba-1; DakoCytomation). Immunoreactive proteins were visualized using ECL Prime (Cytiva Life Sciences). After immunodetection, membranes were washed overnight. The next day, membranes were incubated in stripping buffer (0.78% beta-mercaptoethanol, 2% SDS, 62.5 mM Tris, pH 6.7), after which a ServaPurple total protein stain was performed following the manufacturer's instructions (SERVA Electrophoresis GmbH). Densitometric analysis of the immunoreactive bands was performed using the ImageQuant LAS4000 software (Cytiva Life Sciences Amersham). Densities of immunoreactive bands were normalized to the densities of the total protein stain detected on the same membrane. All immunoblots were repeated at least once, resulting in identical results.

Neurochemical Analysis

For the analysis of DA and DOPAC content, dissected striata were weighed and homogenized in 400 μL antioxidant solution (0.05 M HCl, 0.5% $Na_2S_2O_5$, and 0.05% Na_2EDTA) containing 100 ng/mL 3,4-dihydroxybenzylamine as internal standard. Homogenates were centrifuged for 20 min at 10,000 × g at 4°C. Supernatants were diluted 1:5 in 0.5 M acetic acid and 20 μL of this sample dilution was analyzed for DA and DOPAC content on a narrow-bore (XBridge C18, 3.5 μm, 2.1 × 150 mm; Waters) liquid chromatography system with an electrochemical detector (Antec), as described previously (Massie et al., 2011).

Statistical Analysis

Data are expressed as mean ± s.e.m. Statistical analyses were performed using GraphPad Prism 9.0.1 software, using two-way ANOVA followed by Tukey *post hoc* tests. The α-value was set at 0.05.

RESULTS

xCT Deletion Has No Effect on Lactacystin-Induced Nigrostriatal Degeneration in Adult Mice

To evaluate whether genetic deletion of xCT influences proteasome inhibition-induced nigrostriatal degeneration in adult mice, 3–4 months old $xCT^{-/-}$ and $xCT^{+/+}$ littermates were stereotaxically injected with LAC in the left SNc. After behavioral analysis, various markers of the nigrostriatal pathway were comparatively assessed at the ipsi- and contralateral sides.

Behavioral evaluation of the adult mice revealed a LAC-induced acute loss of motor function as assessed using the rotarod test, that could be observed already at 1 week post-surgery in both genotypes [lesion factor: $F_{(1,\ 40)} = 9.74$, $p = 0.003$], and did not progress until 3 weeks post-surgery [lesion factor: $F_{(1,\ 40)} = 8.38$, $p = 0.006$] (**Figure 1A**). This acute and non-progressive time-course of LAC-induced behavioral deficit is in line with previous reported data (Bentea et al., 2015b), and indicates an acute effect of the toxin on nigral dopaminergic neurons. As we initially planned to perform rotarod analysis on aged mice as well, we decided to continue our experiments 3 weeks post-lesion to ensure these mice would be sufficiently recovered after surgery.

Intranigral administration of LAC led to an overall reduction in the ratio of TH + profiles in the ipsilateral vs. contralateral SNc of both genotypes [lesion factor: $F_{(1,\ 26)} = 36.07$, $p < 0.0001$], with a significant decrease in both $xCT^{+/+}$ ($p = 0.003$) and $xCT^{-/-}$ mice ($p = 0.0005$), when compared with their corresponding sham-injected mice (**Figure 1B**). Similarly, LAC administration induced an overall reduction of DA content in the ipsilateral vs. contralateral striatum of lesioned mice, that could be observed to a similar extent in both genotypes [lesion factor: $F_{(1,\ 40)} = 98.76$, $p < 0.0001$] (**Figure 1C**). The loss of DA was mirrored by a general decrease in the content of DOPAC in the lesioned mice of both genotypes [lesion factor: $F_{(1,\ 40)} = 65.74$, $p < 0.0001$] (**Figure 1D**). The resulting increased DOPAC/DA ratio [lesion factor: $F_{(1,\ 40)} = 6.09$, $p = 0.018$] (**Figure 1E**) indicates a compensatory reaction following the lesion.

Aged Mice Lacking xCT Show Reduced Susceptibility to Lactacystin-Induced Nigral Dopaminergic Neurodegeneration

To evaluate the impact of aging in the LAC model, aged (19–23 months old) $xCT^{-/-}$ and $xCT^{+/+}$ mice were intranigrally injected with LAC and characterized in terms of nigrostriatal degeneration at 3 weeks post-surgery.

Similar to the adult mice, we have attempted to evaluate motor function of the aged mice using the rotarod test. However, using the current protocol, we were unable to obtain a consistent baseline performance prior to the surgery and were not able to pursue this test as a lesion-induced outcome.

Statistical analysis revealed a global effect of both LAC lesion and genotype on the number of TH + profiles in the ipsi-/contralateral SNc [lesion factor: $F_{(1,\ 23)} = 16.91$, $p = 0.0004$; genotype factor: $F_{(1,\ 23)} = 5.62$, $p = 0.026$]. *Post hoc* analyses revealed that this effect could be attributed to a significant decrease in the ratio of TH + profiles in $xCT^{+/+}$ mice ($p = 0.005$), with no change in $xCT^{-/-}$ mice relative to their corresponding sham (**Figure 2A**), resulting in a higher ratio of TH + profiles in the ipsi-/contralateral SNc of LAC-injected $xCT^{-/-}$ mice compared to $xCT^{+/+}$ mice ($p = 0.036$). This difference in the degree of nigral neurodegeneration translated to changes in striatal DA loss following the lesion. LAC administration led to a general decrease in DA content in the ipsi- vs. contralateral striatum that was significantly influenced by genotype [lesion × genotype factor: $F_{(1,\ 22)} = 7.62$, $p = 0.011$], and driven by a significant loss of DA in $xCT^{+/+}$ mice ($p < 0.0001$), with no difference in $xCT^{-/-}$ mice, when compared to their corresponding sham groups (**Figure 2B**). Similarly, LAC lesion resulted in an overall decrease of striatal DOPAC content [lesion factor: $F_{(1,\ 22)} = 12.94$, $p = 0.0016$], attributed to a significant decrease in $xCT^{+/+}$ mice ($p = 0.021$), with no change in $xCT^{-/-}$ mice compared to their corresponding sham controls (**Figure 2C**). No changes could be observed in the striatal DOPAC/DA ratio following the lesion [lesion factor: $F_{(1,\ 22)} = 1.17$, $p > 0.05$] (**Figure 2D**).

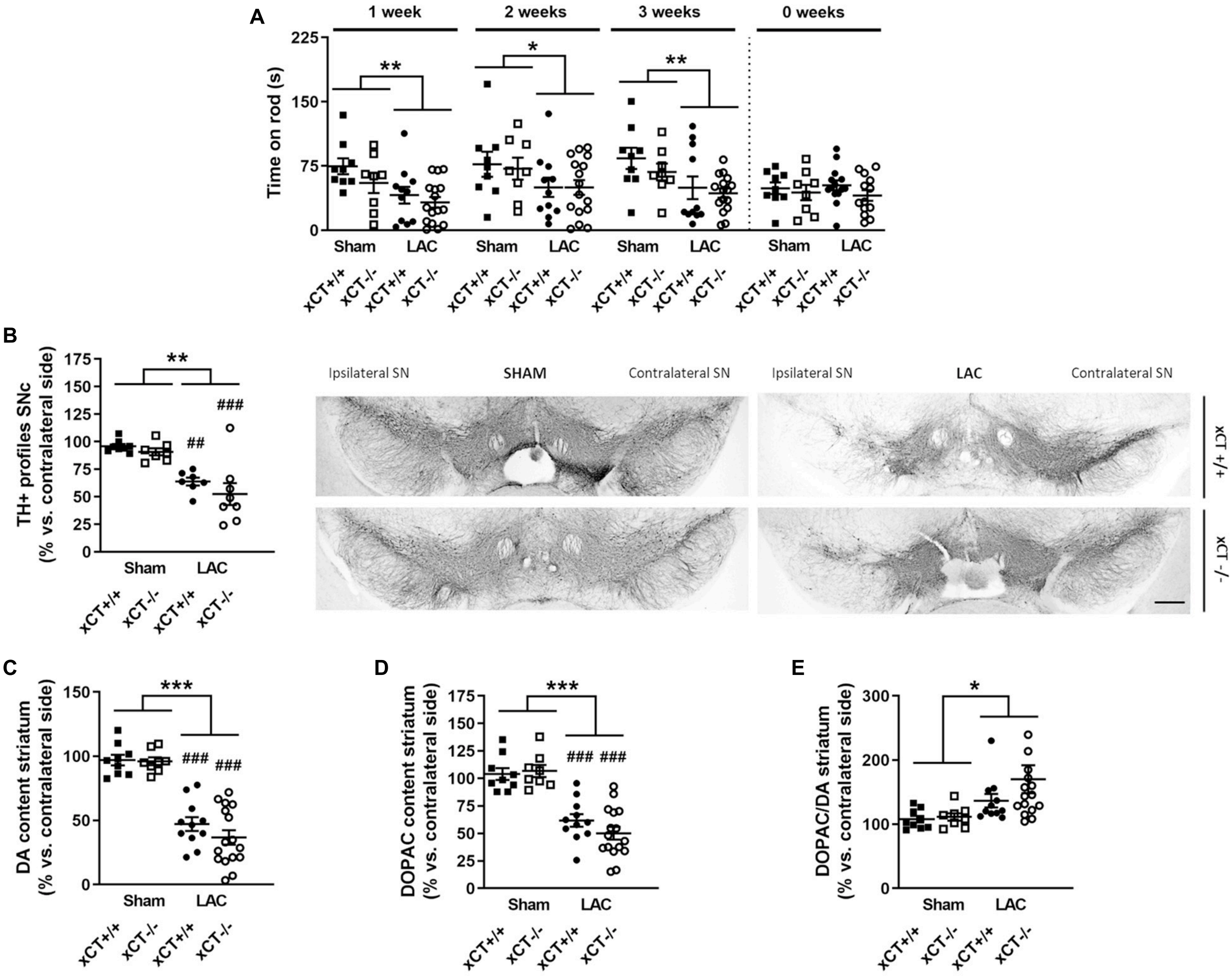

F

	Adult mice	LAC	Rotarod	Snap-freeze striatum (HPLC)	Post-fix SN (IHC)
Sham	n = 10 +/+ n = 10 -/-	† – 1 +/+ – 2 -/-	n = 9 +/+ n = 8 -/-	n = 9 +/+ n = 8 -/-	n = 8 +/+ n = 7 -/-
LAC	n = 12 +/+ n = 17 -/-	– 1 +/+ – 1 -/-	n = 11 +/+ n = 16 -/-	n = 11 +/+ n = 16 -/-	n = 7 +/+ n = 8 -/-

FIGURE 1 | xCT deletion does not influence nigrostriatal dopaminergic degeneration or motor impairment, at 3 weeks after LAC administration in adult mice. **(A)** The rotarod test indicated a decrease in motor coordination and balance induced by LAC lesion in both xCT$^{-/-}$ and xCT$^{+/+}$ mice. **(B)** TH immunohistochemistry revealed a global reduction in the ipsilateral vs. contralateral ratio in the number of nigral dopaminergic neurons following LAC, to a similar extent in xCT$^{-/-}$ and xCT$^{+/+}$ mice. **(C)** Likewise, the loss of DA content in the ipsilateral vs. contralateral striatum following LAC was comparable between xCT$^{-/-}$ and xCT$^{+/+}$ mice. **(D,E)** LAC injection led to an equivalent loss of striatal DOPAC content between the genotypes **(D)** and an increase in the striatal DOPAC/DA ratio **(E)**. Data are presented as mean + s.e.m. $^{*}p < 0.05$, $^{**}p < 0.01$, $^{***}p < 0.001$ (two-way ANOVA, lesion effect), $^{\#\#}p < 0.01$, $^{\#\#\#}p < 0.001$ (Tukey *post hoc* vs. corresponding sham group). **(F)** Experimental design and sample size allocation (also applies to **Figure 3**); †indicates mortality post-surgery; *n* = 8–16 mice/group in **(A)**, *n* = 7–8 mice/group in **(B)**, *n* = 8–16 mice/group in **(C–E)**. DA, dopamine; DOPAC, 3,4-dihydroxyphenylacetic acid; HPLC, high-performance liquid chromatography; IHC, immunohistochemistry; LAC, lactacystin; SN, substantia nigra; SNc, substantia nigra pars compacta; TH, tyrosine hydroxylase. Scale bar 400 μm.

Decreased Microglial Proliferation in Aged xCT-Deficient Mice Following Intranigral Administration of Lactacystin

Administration of LAC has been found to lead to widespread nigral microglial activation, observed to a higher degree in aged animals (Xiao et al., 2015; Savolainen et al., 2017). Given the role of system x_c^- in mediating the neuroinflammatory reaction (Albertini et al., 2018), we tested its involvement in the microglial activation following LAC, and its interplay with aging, by staining SN sections of adult and aged mice for the microglial marker Iba-1.

In adult mice, LAC administration led to an overall increase in the density of microglial cells in the ipsilateral SN that

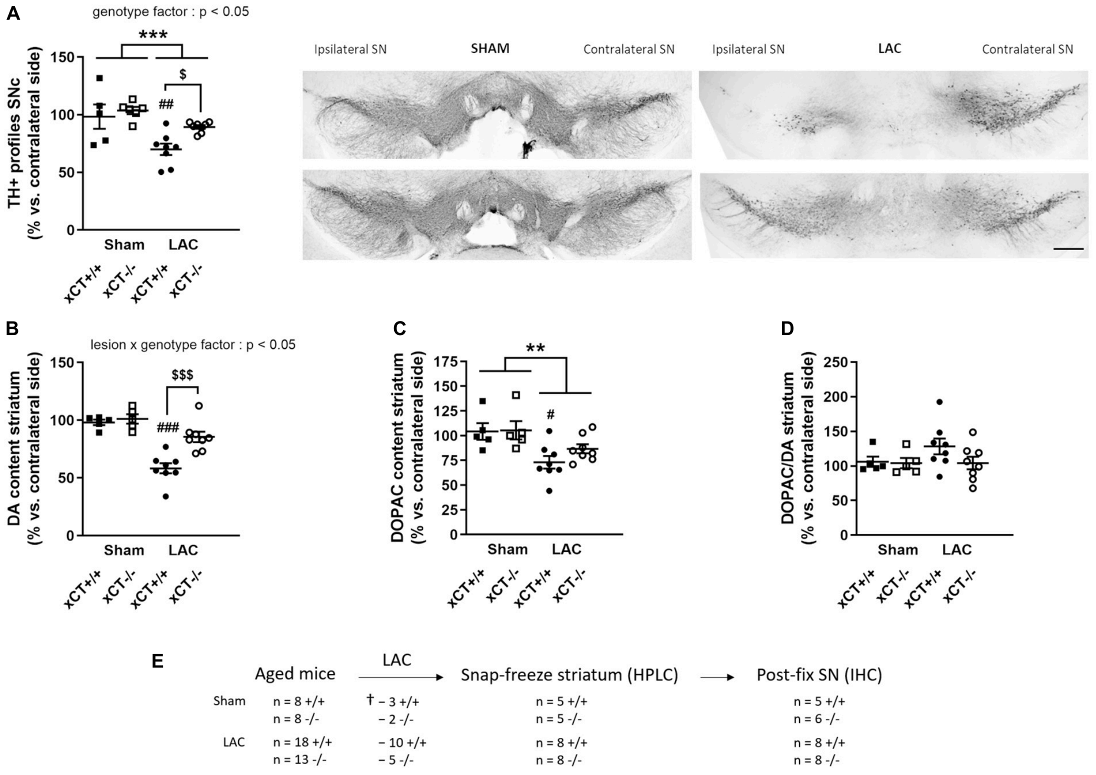

FIGURE 2 | xCT deletion protects the nigrostriatal dopaminergic pathway of aged mice against LAC-induced degeneration. **(A)** TH immunohistochemistry revealed a global loss of nigral TH + profiles following LAC that was driven by a significant decrease of dopaminergic neurons in xCT$^{+/+}$, but not xCT$^{-/-}$ mice, as well as a significant increase in the number of TH + profiles in LAC-lesioned xCT$^{-/-}$ vs. xCT$^{+/+}$ mice. **(B)** LAC significantly decreased DA content in xCT$^{+/+}$, but not xCT$^{-/-}$, mice, with a significant difference in the % DA loss between the two genotypes. **(C)** Similarly, LAC injection led to a loss of striatal DOPAC levels in xCT$^{+/+}$, an effect that was absent in xCT$^{-/-}$ mice. **(D)** No change could be observed in the striatal DOPAC/DA ratio following lesion. Data are presented as mean + s.e.m. $^{**}p < 0.01$, $^{***}p < 0.001$ (two-way ANOVA, lesion effect), $^{\#}p < 0.05$, $^{\#\#}p < 0.01$, $^{\#\#\#}p < 0.001$ (Tukey *post hoc* vs. corresponding sham group), $^{\$}p < 0.05$, $^{\$\$\$}p < 0.001$ (Tukey *post hoc* comparing LAC xCT$^{+/+}$ vs. LAC xCT$^{-/-}$). **(E)** Experimental design and sample size allocation (also applies to **Figure 4**); †indicates mortality post-surgery; n = 5–8 mice/group. DA, dopamine; DOPAC, 3,4-dihydroxyphenylacetic acid; HPLC, high-performance liquid chromatography; IHC, immunohistochemistry; LAC, lactacystin; SN, substantia nigra; SNc, substantia nigra pars compacta; TH, tyrosine hydroxylase. Scale bar 400 μm.

could be observed to a similar extent in both genotypes [lesion factor: $F_{(1,\ 23)} = 55.66$, $p < 0.0001$], when compared to their corresponding sham groups (**Figure 3A**). Evaluating the morphology of the microglial cells, we failed to distinguish any difference in the Iba-1 + cell area [lesion factor: $F_{(1,\ 23)} = 2.57$, $p > 0.05$] (**Figure 3B**) or diameter [lesion factor: $F_{(1,\ 23)} = 0.72$, $p > 0.05$] (**Figure 3C**), following lesion in either genotype.

In aged mice, intranigral LAC resulted in an increase in Iba-1 + microglial cell density in xCT$^{+/+}$ mice, in presence of a significant lesion x genotype interaction factor [$F_{(1,\ 17)} = 6.34$, $p = 0.022$]. Our analyses revealed a ∼ 35% increase in the density of microglial profiles in the ipsilateral SN of xCT$^{+/+}$ mice ($p = 0.027$), with no change in microglial density in xCT$^{-/-}$ mice when compared to their corresponding sham mice (**Figure 4A**). LAC lesion did not significantly influence the area of microglial cells [lesion factor: $F_{(1,\ 17)} = 4.10$, $p > 0.05$] (**Figure 4B**), but did cause a slight global reduction in cell diameter in both genotypes [lesion factor: $F_{(1,\ 17)} = 4.89$, $p < 0.05$] (**Figure 4C**).

Genetic Loss of xCT Increases the Susceptibility of Nigral Dopaminergic Neurons to 1-Methyl-4-Phenyl-1,2,3,6-Tetrahydropyridine-Induced Degeneration but Does Not Influence Striatal Dopamine Denervation in Aged Mice

To evaluate whether xCT deletion in aged mice confers protection against toxins with a distinct mechanism of action, we tested the susceptibility of aged xCT$^{-/-}$ mice in the mitochondrial inhibition-based MPTP model.

Behavioral evaluation of the treated mice using the DigiGait apparatus revealed MPTP-induced changes that could be observed preferentially either in xCT$^{+/+}$ or xCT$^{-/-}$ mice. MPTP administration led to an overall increase in stride duration, an effect observed in presence of a significant lesion x genotype effect [$F_{(1,\ 52)} = 6.86$, $p = 0.011$]. In particular, MPTP was found to increase the duration of the stride by ∼15% in xCT$^{+/+}$ mice ($p = 0.0028$), with no apparent change in xCT$^{-/-}$

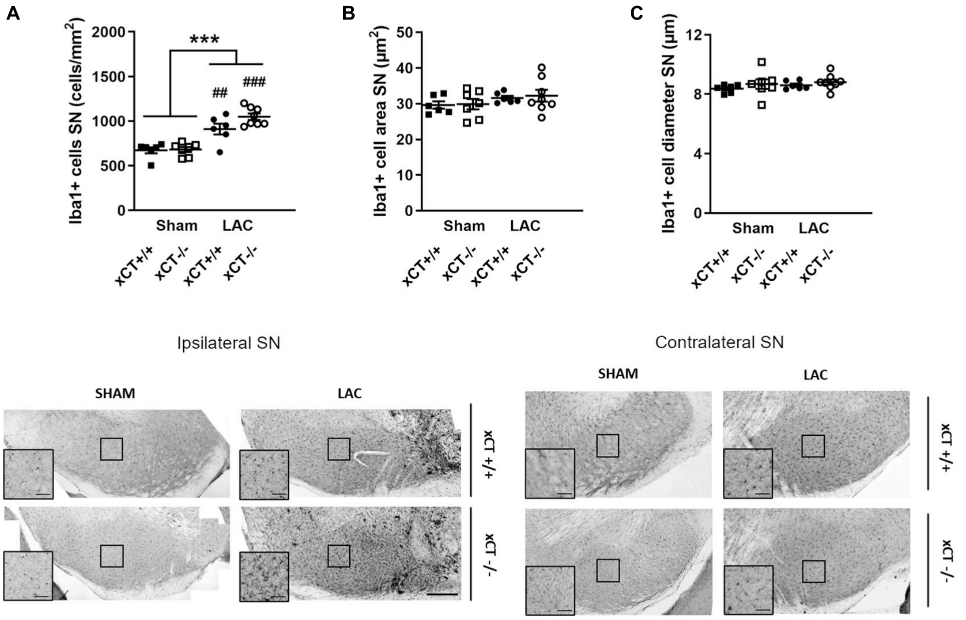

FIGURE 3 | Similar neuroinflammatory reaction in the SN at 3 weeks after LAC administration in adult xCT$^{+/+}$ and xCT$^{-/-}$ mice. **(A)** Iba-1 immunohistochemistry revealed an increase in microglial density in the ipsilateral SN following LAC lesion, in both xCT$^{+/+}$ and xCT$^{-/-}$ mice. **(B,C)** No lesion-induced changes could be observed in Iba-1 + cell area **(B)** or Iba-1 + cell diameter **(C)** in xCT$^{+/+}$ or xCT$^{-/-}$ mice. Data are presented as mean + s.e.m. ***$p < 0.001$ (two-way ANOVA, lesion effect), $^{\#\#}p < 0.01$, $^{\#\#\#}p < 0.001$ (Tukey *post hoc* vs. corresponding sham group). *n* = 6–8 mice/group. LAC, lactacystin; SN, substantia nigra. Scale bar 200 µm (inset scale bar 50 µm).

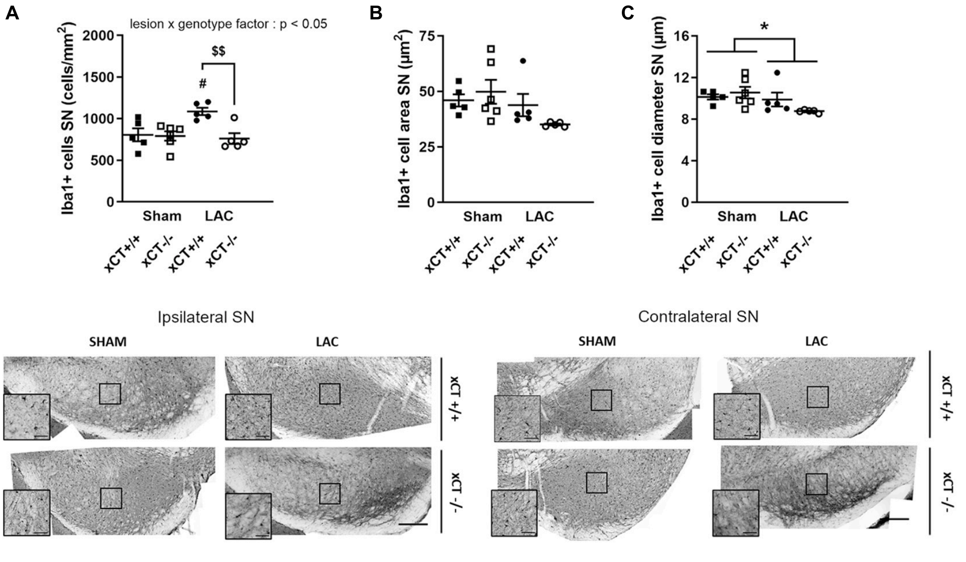

FIGURE 4 | Decreased microglial reaction in the SN at 3 weeks after LAC administration in aged xCT$^{-/-}$ mice. **(A)** Iba-1 immunohistochemistry revealed an increase in microglial density in the ipsilateral SN following LAC lesion in aged xCT$^{+/+}$, but not xCT$^{-/-}$ mice, when compared to their corresponding sham-injected groups. **(B,C)** No changes could be observed in Iba-1 + cell area **(B)**, while a modest general decrease of Iba-1 + cell diameter was present following lesion **(C)**. Data are presented as mean + s.e.m. *$p < 0.05$ (two-way ANOVA, lesion effect), $^{\#}p < 0.05$ (Tukey *post hoc* vs. corresponding sham group), $^{\$\$}p < 0.01$ (Tukey *post hoc* comparing LAC xCT$^{+/+}$ vs. LAC xCT$^{-/-}$). *n* = 5–6 mice/group. LAC, lactacystin; SN, substantia nigra. Scale bar 200 µm (inset scare bar 50 µm).

mice, when compared to their corresponding vehicle-injected mice (**Figure 5A**). Similarly, MPTP led to an increased stance duration, defined as the duration in which the paws are in contact with the treadmill, in xCT$^{+/+}$, but not xCT$^{-/-}$ mice, compared to the corresponding vehicle-treated mice [lesion × genotype factor: $F_{(1,\ 51)} = 6.13$, $p = 0.017$] (**Figure 5B**). MPTP-treated xCT$^{+/+}$ mice also showed an increase in stride length, contrary to xCT$^{-/-}$ mice [lesion × genotype factor:

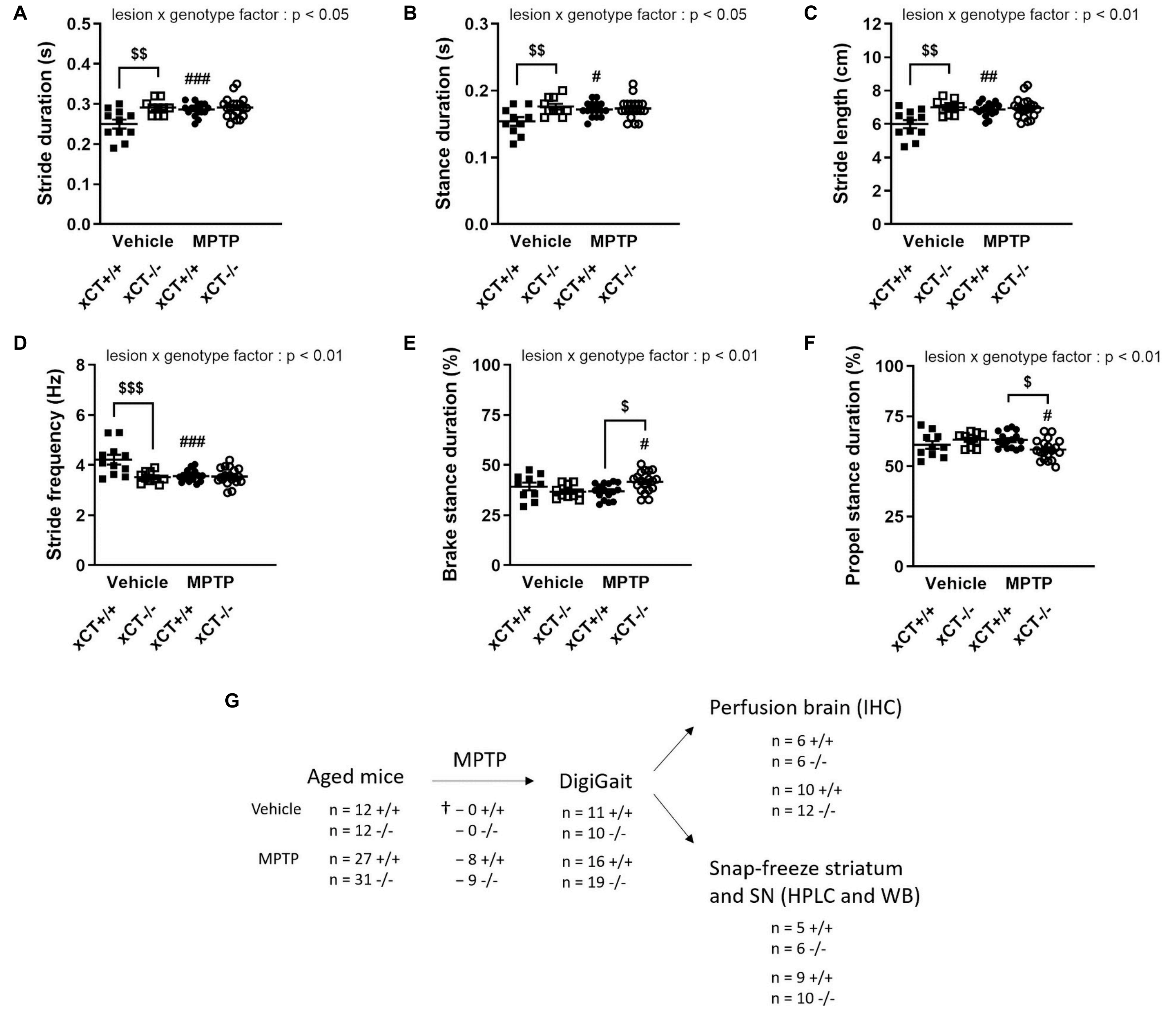

FIGURE 5 | Behavioral changes following MPTP administration in aged xCT$^{+/+}$ and xCT$^{-/-}$ mice. **(A–D)** Administration of MPTP led to an increase in stride duration **(A)**, stance duration **(B)**, stride length **(C)**, and a decrease in stride frequency **(D)**, in aged xCT$^{+/+}$ mice, an effect that was absent in aged xCT$^{-/-}$ mice. **(E,F)** On the other hand, MPTP treatment led to a different composition of the stance phase in aged xCT$^{-/-}$ mice, with an increase in the brake stance duration **(E)**, and a corresponding decrease in the propel stance duration **(F)**, an effect that could not be observed in aged xCT$^{+/+}$ mice. Data are presented as mean + s.e.m. $^{\#}p < 0.05$, $^{\#\#}p < 0.01$, $^{\#\#\#}p < 0.001$ (Tukey *post hoc* vs. corresponding vehicle group), $^{\$}p < 0.05$, $^{\$\$}p < 0.01$, $^{\$\$\$}p < 0.001$ (Tukey *post hoc* comparing MPTP xCT$^{+/+}$ vs. MPTP xCT$^{-/-}$). **(G)** Experimental design and sample size allocation (also applies to **Figure 6**); † indicates mortality post MPTP injection; $n = 10$–19 mice/group. HPLC, high-performance liquid chromatography; IHC, immunohistochemistry; MPTP, 1-methyl-4-phenyl-1,2,3,6-tetrahydropyridine; WB, Western blot.

$F_{(1,\ 52)} = 8.02$, $p = 0.0066$] (**Figure 5C**), with a corresponding decrease in the stride frequency [lesion × genotype factor: $F_{(1,\ 52)} = 10.81$, $p = 0.0018$], that was not observed in MPTP-treated xCT$^{-/-}$ mice (**Figure 5D**). For all aforementioned parameters, while MPTP had no added effect in xCT$^{-/-}$ mice, we could measure significant differences in vehicle-injected xCT$^{-/-}$ vs. xCT$^{+/+}$ mice (**Figures 5A–D**), that mirrored changes observed in MPTP-treated xCT$^{+/+}$ mice. This increase in stride length and duration, with the corresponding decrease in stride frequency, indicates that MPTP-treated xCT$^{+/+}$ mice and vehicle-treated xCT$^{-/-}$ mice demonstrated gait deficits, taking longer steps, in a longer period of time, and with a corresponding decrease in the frequency of steps, compared to vehicle-treated xCT$^{+/+}$ mice. On the other hand, qualitative assessment of the stance revealed differences specifically in the MPTP-treated xCT$^{-/-}$ mice. MPTP treatment led to an increase in the brake stance duration [lesion × genotype factor: $F_{(1,\ 51)} = 7.56$, $p = 0.0082$; ~13% increase in xCT$^{-/-}$, $p = 0.048$ vs. corresponding vehicle; no change in xCT$^{+/+}$ vs. corresponding vehicle] (**Figure 5E**), with a corresponding decrease in the propel stance duration [lesion × genotype factor: $F_{(1,\ 51)} = 7.56$, $p = 0.0082$; ∼8% decrease in xCT$^{-/-}$, $p = 0.048$ vs. corresponding vehicle; no change in xCT$^{+/+}$ vs. corresponding vehicle] (**Figure 5F**), an effect that could not be observed in MPTP-treated xCT$^{+/+}$ mice. This indicates that the MPTP-lesioned xCT$^{-/-}$ mice spent more time in the braking portion of the stance, and less time in the propelling portion of the stance, reflecting qualitative changes in their gait during the test. As such, MPTP administration led to motor deficits in both xCT$^{-/-}$ and xCT$^{+/+}$ mice, with particular aspects of gait affected in each genotype.

Administration of MPTP in aged mice led to an overall reduction of nigral TH + profiles in presence of a significant lesion × genotype effect [$F_{(1,\ 27)} = 11.48$, $p = 0.0022$]. MPTP treatment induced a ∼15% loss of TH + profiles in xCT$^{+/+}$ mice ($p = 0.011$), and a comparatively higher loss of ∼34% TH + profiles in xCT$^{-/-}$ mice ($p < 0.0001$), when compared to their corresponding vehicle-injected groups (**Figure 6A**). In contrast, the loss of DA-ergic fibers, as evaluated by measuring the optical density of TH immunoreactivity at the level of the striatum, was observed to a similar degree in both genotypes following administration of the toxin [lesion factor: $F_{(1,\ 30)} = 41.72$, $p < 0.0001$] (**Figure 6B**). In a second group of mice, lesion degree was analyzed using Western blotting. Nigral/midbrain TH expression was shown to be reduced following MPTP in both genotypes [lesion factor: $F_{(1,\ 19)} = 4.85$, $p = 0.04$] (**Figures 6C,E**). Similarly, MPTP treatment led to a reduction of TH expression in striatal homogenates, that could be observed to a similar extent in both genotypes [lesion factor: $F_{(1,\ 26)} = 56.94$, $p < 0.0001$] (**Figures 6D,E**). This was mirrored by a similar genotype-independent loss of striatal DA content following MPTP [lesion factor: $F_{(1,\ 26)} = 170.4$, $p < 0.0001$], compared to the corresponding vehicle groups (**Figure 6F**). A loss of striatal DOPAC content could be observed to a similar extent in both genotypes [lesion factor: $F_{(1,\ 26)} = 28.98$, $p < 0.0001$] (**Figure 6G**), and MPTP administration led to an increased DOPAC/DA ratio in both xCT$^{+/+}$ and xCT$^{-/-}$ mice [lesion factor: $F_{(1,\ 26)} = 31.33$, $p < 0.0001$] (**Figure 6H**).

Western blotting was used to evaluate Iba-1 expression as a measure for microglial reaction to MPTP treatment, and failed to reveal any significant lesion-induced changes in either the SN/midbrain [lesion factor: $F_{(1,\ 19)} = 0.02$, $p > 0.05$] (**Figures 6I,K**), or striatal extracts [lesion factor: $F_{(1,\ 19)} = 0.85$, $p > 0.05$] (**Figures 6J,K**).

DISCUSSION

Despite a surge of ongoing efforts to find and validate novel neuroprotective targets in PD, the greatest pitfall remains the translation of pre-clinical findings to the clinic. The most promising therapeutic targets identified in pre-clinical research, eventually fail to fulfill their purpose in clinical trials. Multiple reasons have been proposed that might cause these problems, such as the lack of external validity of the used model or the lack of heterogeneity in pre-clinical studies, including reliance on animal models with a limited number of mechanisms of action (van der Worp et al., 2010; Athauda and Foltynie, 2015). Moreover, since PD is an age-related disease, the importance of the use of an aged animal model is highly underestimated (Reeve et al., 2014). Therefore, applying various PD mouse models to aged mice might increase the chances of successful clinical translation.

We previously reported that adult and aged mice lacking xCT were protected against 6-OHDA-induced nigral dopaminergic neurodegeneration (Massie et al., 2011), whereas adult xCT-deficient mice were equally susceptible in the systemic MPTP model (Bentea et al., 2015a). In the present study, we investigated whether loss of xCT can mitigate nigrostriatal degeneration induced by intranigral injection of the proteasome inhibitor LAC in adult and aged mice, and following systemic administration of MPTP in aged animals.

Contrary to adult mice, aged mice lacking xCT are remarkably resistant to LAC-induced nigral dopaminergic cell loss. When subjecting aged male xCT$^{-/-}$ mice to nigral proteasome inhibition, we failed to observe any significant loss of nigral TH + neurons or striatal DA levels in the ipsilateral hemisphere. The finding that neuroprotection conferred by loss of xCT is age-dependent is intriguing and suggests that different pathways might be activated by proteasome inhibition in the aged vs. young brain. Previously, Gavilan et al. (2009) identified deficits in the activation of the unfolded protein response in the aged brain that might account for an increased sensitivity toward proteasome inhibition-induced neurodegeneration. In our study we did not observe a potentiation of the degree of lesioning following LAC with aging, however, caution must be drawn as adult and aged mice were lesioned with different batches of LAC, that may have an impact on the severity of the extent of the lesion (personal observation).

Previous findings also support the notion that administration of neuroprotective agents can lead to differential effects when evaluated in aged vs. young animals. For instance, adenovirus-mediated delivery of GDNF to the SN has decreased neuroprotective properties against intrastriatal 6-OHDA in aged vs. young rats (Choi-Lundberg et al., 1997; Connor et al., 1999). While the reason for such age-related effects is not always clear, it might be linked with a differential expression of the target (or the environment in which the target is expressed) in the aging brain. However, we failed to detect any age-related change in xCT expression in different regions of the brain, including cortex and striatum (unpublished observations). In addition, aging affects a multitude of pathways [e.g., neuroinflammation, oxidative stress, mitochondrial dysfunction, protein degradation systems (Collier et al., 2011)], which form a complex environment in which the therapeutic target should act. One of the intricate outcomes of such a complex interaction is that aged neurons become more sensitive to the toxicity of glutamate (Brewer, 1998; Brewer et al., 2005), possibly as a result of age-related depolarization of the mitochondrial membrane potential and increased production of mitochondrial reactive oxygen species (Parihar and Brewer, 2007), as well as migration of glutamate receptors to extrasynaptic sites (Avila et al., 2017). Noteworthy, system x_c^- has been identified to play a major role in controlling extracellular glutamate levels in distinct brain regions

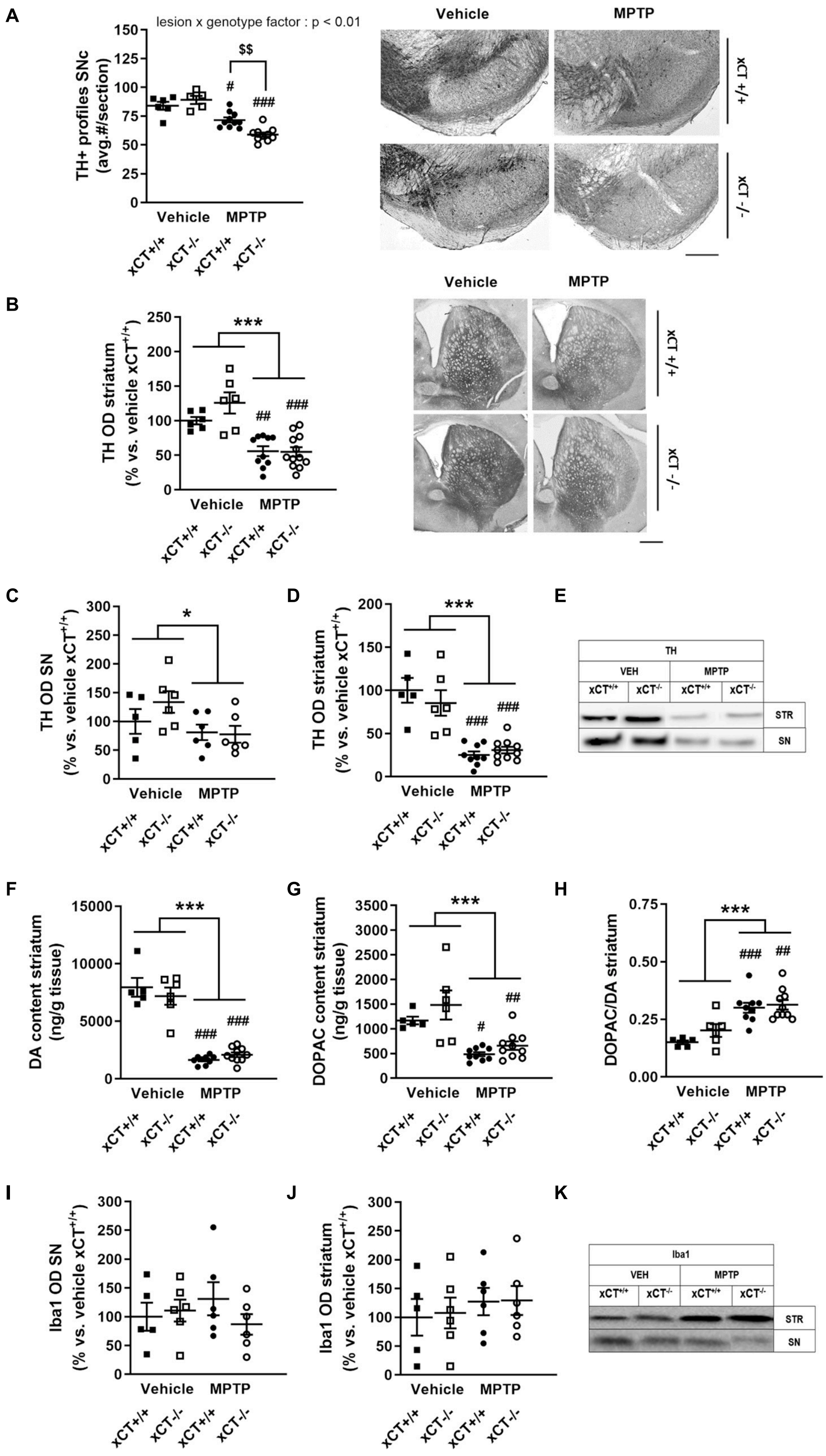

FIGURE 6 | xCT deletion increases the susceptibility of nigral dopaminergic neurons for MPTP-induced degeneration in aged mice, without affecting striatal DA denervation or microglial reaction. **(A,B)** TH immunohistochemistry revealed a greater loss of nigral TH/dopaminergic neurons in xCT$^{-/-}$ mice following chronic administration of MPTP **(A)**, but an equivalent decrease of TH + striatal innervation between genotypes **(B)**. **(C–E)** Evaluation of TH expression in SN **(C)** and striatal **(D)** extracts revealed a comparable loss of TH protein following MPTP of both genotypes. **(F)** This was reflected in a similar MPTP-induced loss of striatal DA content in xCT$^{-/-}$ and xCT$^{+/+}$ mice. **(G,H)** MPTP administration led to an equivalent reduction of striatal DOPAC content in both genotypes **(G)**, and an increase in striatal

(Continued)

FIGURE 6 | DOPAC/DA ratio **(H)**. **(I–K)** No significant MPTP-induced changes in expression of Iba-1 in SN **(I)** or striatum **(J)** could be revealed in either $xCT^{-/-}$ or $xCT^{+/+}$ mice. Data are presented as mean + s.e.m. $^{*}p < 0.05$, $^{***}p < 0.001$ (two-way ANOVA, lesion effect), $^{\#}p < 0.05$, $^{\#\#}p < 0.01$, $^{\#\#\#}p < 0.001$ (Tukey *post hoc* vs. corresponding vehicle group), $^{\$\$}p < 0.01$ (Tukey *post hoc* comparing MPTP $xCT^{+/+}$ vs. MPTP $xCT^{-/-}$). *n* = 5–10 mice/group in **(A)**, *n* = 6–12 mice/group in **(B)**, *n* = 5–6 mice/group in **(C)**, *n* = 5–10 mice/group in **(D–H)**, *n* = 5–6 mice/group in **(I–J)**. DA, dopamine; DOPAC, 3,4-dihydroxyphenylacetic acid; MPTP, 1-methyl-4-phenyl-1,2,3,6-tetrahydropyridine; OD, optical density; SN, substantia nigra; SNc, substantia nigra pars compacta; TH, tyrosine hydroxylase. Scale bar 400 μm.

(De Bundel et al., 2011; Massie et al., 2011). It is likely that system x_c^-—mediated glutamate release in the SN can represent a direct source of toxicity to nigral dopaminergic cell bodies causing excitotoxic cell damage in the model, especially in the context of an age-dependent decrease in the expression of glutamate reuptake transporters (Farrand et al., 2015), and redistribution of N2B-containing NMDA receptors to extrasynaptic sites with aging (Avila et al., 2017). In line with this hypothesis, intranigral administration of NMDA or the NMDA agonist quinolinic acid was found to lead to excitotoxic damage of nigral dopaminergic neurons (Connop et al., 1995), while inhibition of glutamate reuptake transporters in the SNc using L-trans-pyrrolidine-2,4-dicarboxylate similarly triggers death of nigral dopaminergic neurons *via* excitotoxic pathways, in the presence of microglial activation (Assous et al., 2014). As such, xCT deletion in the aged brain may reduce excitotoxic stress on nigral dopamine neurons leading to their increased resilience.

Qualitative differences might also exist in the reaction of the aged brain to environmental stimuli. For instance, microglial cells become primed with aging, and exhibit an exaggerated inflammatory response to secondary (even sub-threshold) challenges (Norden et al., 2015). Furthermore, chronic persistent neuroinflammation, as occurring during aging (Lynch, 2010), can synergize with proteasome inhibition and exacerbate the ensuing pathology. For instance, intra-hippocampal administration of lipopolysaccharide (LPS) 24 h prior to intra-hippocampal LAC leads to increased accumulation of ubiquitinated proteins and neurodegeneration, compared to each toxin alone (Pintado et al., 2012). Similarly, prior systemic administration of LPS to trigger brain inflammation in adult mice increases the susceptibility of the nigrostriatal pathway for LAC-induced neurodegeneration (Deneyer et al., 2019).

Interestingly, system x_c^- has recently emerged as a novel regulator of the microglial phenotype. Cultured $xCT^{-/-}$ primary microglial cells exposed to LPS showed reduced production of nitric oxide and release of pro-inflammatory cytokines such as TNF-α and IL-6 (Mesci et al., 2015). Furthermore, $xCT^{-/-}$ mice demonstrate reduced peripheral and central inflammatory reaction and sickness behavior following systemic LPS administration, indicating a primary role of system x_c^- in regulating the inflammatory response (Albertini et al., 2018). Our findings reveal decreased microglial activation in the SN of aged $xCT^{-/-}$ mice that paralleled the neuroprotection observed in these conditions. While in this study it is difficult to temporally connect these findings, one possibility is that loss of xCT might maintain the brain in a decreased primed state during aging, lowering the subsequent reaction to toxic stimuli. Alternatively, the reduced neuroinflammatory reaction observed following LAC in aged $xCT^{-/-}$ mice might also be the result of reduced neurodegeneration. In light of the age-dependent neuroprotection observed in $xCT^{-/-}$ mice, it remains of interest to further investigate the impact of xCT deficiency on aging and age-related microglial priming.

In contrast with the age-dependent neuroprotection observed in the LAC model, aged $xCT^{-/-}$ mice demonstrated an enhanced susceptibility for nigral dopaminergic neuron loss following progressive MPTP administration. Despite this increased susceptibility at the level of the cell bodies, markers of striatal dopaminergic innervation, including TH expression and DA content, decreased to a similar extent in $xCT^{-/-}$ and $xCT^{+/+}$ mice following MPTP treatment, potentially indicating the capacity of the remaining dopaminergic neurons to compensate for the loss of striatal innervation. Our previous findings revealed equivalent susceptibility of adult $xCT^{-/-}$ mice to nigral dopaminergic neurodegeneration and striatal denervation following progressive administration of MPTP (Bentea et al., 2015a). Together with the present results, this indicates that nigral dopaminergic neurons of aged, but not adult, $xCT^{-/-}$ mice show an increase in the susceptibility to the toxic effects of MPTP, which contrasts with our current observations in the LAC model and the 6-OHDA model (Massie et al., 2011). It is interesting to speculate on these dissimilar findings, and they may be related with age-related changes in mitochondrial metabolism and generation of reactive oxygen species, the distinct mechanism of action of MPTP in aged animals (Ali et al., 1994; Kuhn et al., 2003), and the nature of the induced cell loss (chronic and progressive for MPTP vs. acute for LAC and 6-OHDA). The different mechanism of action (proteasomal vs. mitochondrial inhibition) might also play a factor in the dissimilar findings in the two models, in line with the observation that targets, such as the ghrelin receptor, may differentially influence LAC- or MPTP-induced death of nigral dopaminergic neurons (Andrews et al., 2009; Coppens et al., 2017). Finally, the site of delivery (intracerebral vs. systemic) may also trigger different neuroinflammatory reactions in primed mice, that may subsequently contribute to the mechanisms of neurodegeneration. In addition, it is noteworthy that MPTP requires metabolism by monoamine oxidase B to form the active metabolite 1-methyl-4-phenylpyridinium (MPP +) in astrocytes, and further studies would be required to evaluate possible age-related changes in this enzyme in $xCT^{-/-}$ mice.

In conclusion, we demonstrate age-dependent neuroprotection of nigral dopaminergic neurons in $xCT^{-/-}$ mice injected with the proteasome inhibitor LAC. These results indicate that system x_c^- is an important mediator of proteasome inhibition-induced dopaminergic neurodegeneration in aged animals and underline the need for further studies to investigate its interplay with aging, proteasomal dysfunction and mechanisms of neurotoxicity. Given the contrasting findings obtained in the progressive MPTP model, our study highlights the importance of using animal models with distinct mechanisms of action and applying them to both adult and aged animals, for profiling pre-clinical targets in PD. Future studies are required to obtain further insight into the extent to which system x_c^- can modulate nigral cell loss in PD. In addition, exploring the therapeutic efficiency in female animals, as well as confirming the effects of the genetic knock-out using system x_c^- inhibitors as described recently (Dang et al., 2017), will further shed light on the translatability of this approach in PD patients.

DATA AVAILABILITY STATEMENT

The raw data supporting the conclusions of this article will be made available by the authors, without undue reservation.

ETHICS STATEMENT

The animal study was reviewed and approved by the Ethical Committee for Animal Experimentation Vrije Universiteit Brussel, and Portland VA Medical Center Institutional Animal Care and Use Committee.

AUTHOR CONTRIBUTIONS

EB, HS, AV, CM, and AM designed the experiments. EB, LDP, LV, LW, LD, CM, and GA performed the experiments. EB, LDP, LV, AV, CM, and AM analyzed and interpreted data. EB, LDP, CM, and AM wrote the manuscript. All authors discussed the results, edited and commented on the article.

FUNDING

This work was supported by grants of the Vrije Universiteit Brussel (SRP40/49) and the "Wetenschappelijk Fonds Willy Gepts" of the UZ Brussel to AM, Research Foundation-Flanders (FWO) #1510218N to EB. FWO Aspirant fellowship (116582ON) to LDP, and was partially supported by Merit Review #BX001643 to CM from the United States (U.S.) and Department of Veterans Affairs Biomedical Laboratory Research and Development. The contents do not represent the views of the U.S. Department of Veterans Affairs or the United States Government.

ACKNOWLEDGMENTS

We kindly thank Frank Van Der Kelen and Carina De Rijck (Vrije Universiteit Brussel, Belgium) for their technical assistance.

REFERENCES

Abdullah, R., Basak, I., Patil, K. S., Alves, G., Larsen, J. P., and Moller, S. G. (2015). Parkinson's disease and age: the obvious but largely unexplored link. *Exp. Gerontol.* 68, 33–38. doi: 10.1016/j.exger.2014.09.014

Albertini, G., Deneyer, L., Ottestad-Hansen, S., Zhou, Y., Ates, G., Walrave, L., et al. (2018). Genetic deletion of xCT attenuates peripheral and central inflammation and mitigates LPS-induced sickness and depressive-like behavior in mice. *Glia* 66, 1845–1861. doi: 10.1002/glia.23343

Ali, S. F., David, S. N., Newport, G. D., Cadet, J. L., and Slikker, W. Jr. (1994). MPTP-induced oxidative stress and neurotoxicity are age-dependent: evidence from measures of reactive oxygen species and striatal dopamine levels. *Synapse* 18, 27–34. doi: 10.1002/syn.890180105

Ambrosi, G., Cerri, S., and Blandini, F. (2014). A further update on the role of excitotoxicity in the pathogenesis of Parkinson's disease. *J. Neural Transm.* 121, 849–859. doi: 10.1007/s00702-013-1149-z

Andrews, Z. B., Erion, D., Beiler, R., Liu, Z. W., Abizaid, A., Zigman, J., et al. (2009). Ghrelin promotes and protects nigrostriatal dopamine function *via* a UCP2-dependent mitochondrial mechanism. *J. Neurosci.* 29, 14057–14065. doi: 10.1523/JNEUROSCI.3890-09.2009

Assous, M., Had-Aissouni, L., Gubellini, P., Melon, C., Nafia, I., Salin, P., et al. (2014). Progressive Parkinsonism by acute dysfunction of excitatory amino acid transporters in the rat substantia nigra. *Neurobiol. Dis.* 65, 69–81. doi: 10.1016/j.nbd.2014.01.011

Athauda, D., and Foltynie, T. (2015). The ongoing pursuit of neuroprotective therapies in Parkinson disease. *Nat. Rev. Neurol.* 11, 25–40. doi: 10.1038/nrneurol.2014.226

Avila, J., Llorens-Martin, M., Pallas-Bazarra, N., Bolos, M., Perea, J. R., Rodriguez-Matellan, A., et al. (2017). Cognitive decline in neuronal aging and Alzheimer's disease: role of NMDA receptors and associated proteins. *Front. Neurosci.* 11:626. doi: 10.3389/fnins.2017.00626

Baker, D. A., Xi, Z. X., Shen, H., Swanson, C. J., and Kalivas, P. W. (2002). The origin and neuronal function of *in vivo* nonsynaptic glutamate. *J. Neurosci.* 22, 9134–9141.

Bentea, E., Sconce, M. D., Churchill, M. J., Van Liefferinge, J., Sato, H., Meshul, C. K., et al. (2015a). MPTP-induced parkinsonism in mice alters striatal and nigral xCT expression but is unaffected by the genetic loss of xCT. *Neurosci. Lett.* 593, 1–6. doi: 10.1016/j.neulet.2015.03.013

Bentea, E., Van der Perren, A., Van Liefferinge, J., El Arfani, A., Albertini, G., Demuyser, T., et al. (2015b). Nigral proteasome inhibition in mice leads to motor and non-motor deficits and increased expression of Ser129 phosphorylated alpha-synuclein. *Front. Behav. Neurosci.* 9:68. doi: 10.3389/fnbeh.2015.00068

Bentea, E., Van Liefferinge, J., Verbruggen, L., Martens, K., Kobayashi, S., Deneyer, L., et al. (2017a). Zonisamide attenuates lactacystin-induced parkinsonism in mice without affecting system xc<up>. *Exp. Neurol.* 290, 15–28. doi: 10.1016/j.expneurol.2016.12.009

Bentea, E., Verbruggen, L., and Massie, A. (2017b). The proteasome inhibition model of Parkinson's disease. *J. Parkinsons Dis.* 7, 31–63. doi: 10.3233/JPD-160921

Bentea, E., Villers, A., Moore, C., Funk, A. J., O'Donovan, S. M., Verbruggen, L., et al. (2021). Corticostriatal dysfunction and social interaction deficits in mice lacking the cystine/glutamate antiporter. *Mol. Psychiatry* 26, 4754–4769. doi: 10.1038/s41380-020-0751-3

Brewer, G. J. (1998). Age-related toxicity to lactate, glutamate, and beta-amyloid in cultured adult neurons. *Neurobiol. Aging* 19, 561–568. doi: 10.1016/s0197-4580(98)00091-8

Brewer, G. J., Lim, A., Capps, N. G., and Torricelli, J. R. (2005). Age-related calcium changes, oxyradical damage, caspase activation and nuclear condensation in hippocampal neurons in response to glutamate and beta-amyloid. *Exp. Gerontol.* 40, 426–437. doi: 10.1016/j.exger.2005.03.007

Bridges, R., Lutgen, V., Lobner, D., and Baker, D. A. (2012). Thinking outside the cleft to understand synaptic activity: contribution of the cystine-glutamate antiporter (System xc-) to normal and pathological glutamatergic signaling. *Pharmacol. Rev.* 64, 780–802. doi: 10.1124/pr.110.003889

Caldeira, M. V., Curcio, M., Leal, G., Salazar, I. L., Mele, M., Santos, A. R., et al. (2013). Excitotoxic stimulation downregulates the ubiquitin-proteasome system through activation of NMDA receptors in cultured hippocampal neurons. *Biochim. Biophys. Acta* 1832, 263–274. doi: 10.1016/j.bbadis.2012.10.009

Choi-Lundberg, D. L., Lin, Q., Chang, Y. N., Chiang, Y. L., Hay, C. M., Mohajeri, H., et al. (1997). Dopaminergic neurons protected from degeneration by GDNF gene therapy. *Science* 275, 838–841. doi: 10.1126/science.275.5301.838

Churchill, M. J., Cantu, M. A., Kasanga, E. A., Moore, C., Salvatore, M. F., and Meshul, C. K. (2019). Glatiramer acetate reverses motor dysfunction and the decrease in tyrosine hydroxylase levels in a mouse model of Parkinson's disease. *Neuroscience* 414, 8–27. doi: 10.1016/j.neuroscience.2019.06.006

Collier, T. J., Kanaan, N. M., and Kordower, J. H. (2011). Ageing as a primary risk factor for Parkinson's disease: evidence from studies of non-human primates. *Nat. Rev. Neurosci.* 12, 359–366. doi: 10.1038/nrn3039

Connop, B. P., Boegman, R. J., Jhamandas, K., and Beninger, R. J. (1995). Excitotoxic action of NMDA agonists on nigrostriatal dopaminergic neurons: modulation by inhibition of nitric oxide synthesis. *Brain Res.* 676, 124–132. doi: 10.1016/0006-8993(95)00103-w

Connor, B., Kozlowski, D. A., Schallert, T., Tillerson, J. L., Davidson, B. L., and Bohn, M. C. (1999). Differential effects of glial cell line-derived neurotrophic factor (GDNF) in the striatum and substantia nigra of the aged Parkinsonian rat. *Gene Ther.* 6, 1936–1951. doi: 10.1038/sj.gt.3301033

Coppens, J., Bentea, E., Bayliss, J. A., Demuyser, T., Walrave, L., Albertini, G., et al. (2017). Caloric restriction protects against lactacystin-induced degeneration of dopamine neurons independent of the ghrelin receptor. *Int. J. Mol. Sci.* 18:558. doi: 10.3390/ijms18030558

Dang, D. K., Shin, E. J., Tran, H. Q., Kim, D. J., Jeong, J. H., Jang, C. G., et al. (2017). The role of system Xc(-) in methamphetamine-induced dopaminergic neurotoxicity in mice. *Neurochem. Int.* 108, 254–265. doi: 10.1016/j.neuint.2017.04.013

De Bundel, D., Schallier, A., Loyens, E., Fernando, R., Miyashita, H., Van Liefferinge, J., et al. (2011). Loss of system x(c)- does not induce oxidative stress but decreases extracellular glutamate in hippocampus and influences spatial working memory and limbic seizure susceptibility. *J. Neurosci.* 31, 5792–5803. doi: 10.1523/JNEUROSCI.5465-10.2011

Deneyer, L., Albertini, G., Bentea, E., and Massie, A. (2019). Systemic LPS-induced neuroinflammation increases the susceptibility for proteasome inhibition-induced degeneration of the nigrostriatal pathway. *Parkinsonism Relat. Disord.* 68, 26–32. doi: 10.1016/j.parkreldis.2019.09.025

Dick, L. R., Cruikshank, A. A., Grenier, L., Melandri, F. D., Nunes, S. L., and Stein, R. L. (1996). Mechanistic studies on the inactivation of the proteasome by lactacystin: a central role for clasto-lactacystin beta-lactone. *J. Biol. Chem.* 271, 7273–7276. doi: 10.1074/jbc.271.13.7273

El Arfani, A., Albertini, G., Bentea, E., Demuyser, T., Van Eeckhaut, A., Smolders, I., et al. (2015). Alterations in the motor cortical and striatal glutamatergic system and D-serine levels in the bilateral 6-hydroxydopamine rat model for Parkinson's disease. *Neurochem. Int.* 88, 88–96. doi: 10.1016/j.neuint.2015.07.005

Farrand, A. Q., Gregory, R. A., Scofield, M. D., Helke, K. L., and Boger, H. A. (2015). Effects of aging on glutamate neurotransmission in the substantia nigra of Gdnf heterozygous mice. *Neurobiol. Aging* 36, 1569–1576. doi: 10.1016/j.neurobiolaging.2014.11.017

Gavilan, M. P., Pintado, C., Gavilan, E., Jimenez, S., Rios, R. M., Vitorica, J., et al. (2009). Dysfunction of the unfolded protein response increases neurodegeneration in aged rat hippocampus following proteasome inhibition. *Aging Cell* 8, 654–665. doi: 10.1111/j.1474-9726.2009.00519.x

Goldberg, N. R., Haack, A. K., Lim, N. S., Janson, O. K., and Meshul, C. K. (2011). Dopaminergic and behavioral correlates of progressive lesioning of the nigrostriatal pathway with 1-methyl-4-phenyl-1,2,3,6-tetrahydropyridine. *Neuroscience* 180, 256–271. doi: 10.1016/j.neuroscience.2011.02.027

Gouix, E., Leveille, F., Nicole, O., Melon, C., Had-Aissouni, L., and Buisson, A. (2009). Reverse glial glutamate uptake triggers neuronal cell death through extrasynaptic NMDA receptor activation. *Mol. Cell. Neurosci.* 40, 463–473. doi: 10.1016/j.mcn.2009.01.002

Hardingham, G. E., and Bading, H. (2010). Synaptic versus extrasynaptic NMDA receptor signalling: implications for neurodegenerative disorders. *Nat. Rev. Neurosci.* 11, 682–696. doi: 10.1038/nrn2911

Harrison, I. F., Powell, N. M., and Dexter, D. T. (2019). The histone deacetylase inhibitor nicotinamide exacerbates neurodegeneration in the lactacystin rat model of Parkinson's disease. *J. Neurochem.* 148, 136–156. doi: 10.1111/jnc.14599

Hood, R. L., Liguore, W. A., Moore, C., Pflibsen, L., and Meshul, C. K. (2016). Exercise intervention increases spontaneous locomotion but fails to attenuate dopaminergic system loss in a progressive MPTP model in aged mice. *Brain Res.* 1646, 535–542. doi: 10.1016/j.brainres.2016.06.032

Konieczny, J., Jantas, D., Lenda, T., Domin, H., Czarnecka, A., Kuter, K., et al. (2014). Lack of neuroprotective effect of celastrol under conditions of proteasome inhibition by lactacystin in *in vitro* and *in vivo* studies: implications for Parkinson's disease. *Neurotox. Res.* 26, 255–273. doi: 10.1007/s12640-014-9477-9

Kuhn, K., Wellen, J., Link, N., Maskri, L., Lubbert, H., and Stichel, C. C. (2003). The mouse MPTP model: gene expression changes in dopaminergic neurons. *Eur. J. Neurosci.* 17, 1–12. doi: 10.1046/j.1460-9568.2003.02408.x

Lehtonen, S., Sonninen, T. M., Wojciechowski, S., Goldsteins, G., and Koistinaho, J. (2019). Dysfunction of cellular proteostasis in Parkinson's disease. *Front. Neurosci.* 13:457. doi: 10.3389/fnins.2019.00457

Lewerenz, J., Hewett, S. J., Huang, Y., Lambros, M., Gout, P. W., Kalivas, P. W., et al. (2013). The cystine/glutamate antiporter system x(c)(-) in health and disease: from molecular mechanisms to novel therapeutic opportunities. *Antioxid. Redox Signal.* 18, 522–555. doi: 10.1089/ars.2011.4391

Lynch, M. A. (2010). Age-related neuroinflammatory changes negatively impact on neuronal function. *Front. Aging Neurosci.* 1:6. doi: 10.3389/neuro.24.006.2009

Massaquoi, M. S., Liguore, W. A., Churchill, M. J., Moore, C., Melrose, H. L., and Meshul, C. K. (2020). Gait deficits and loss of striatal tyrosine Hydroxlase/Trk-B are restored following 7,8-dihydroxyflavone treatment in a progressive MPTP mouse model of Parkinson's disease. *Neuroscience* 433, 53–71. doi: 10.1016/j.neuroscience.2020.02.046

Massie, A., Boillee, S., Hewett, S., Knackstedt, L., and Lewerenz, J. (2015). Main path and byways: non-vesicular glutamate release by system xc(-) as an important modifier of glutamatergic neurotransmission. *J. Neurochem.* 135, 1062–1079. doi: 10.1111/jnc.13348

Massie, A., Schallier, A., Kim, S. W., Fernando, R., Kobayashi, S., Beck, H., et al. (2011). Dopaminergic neurons of system x(c)(-)-deficient mice are highly protected against 6-hydroxydopamine-induced toxicity. *FASEB J.* 25, 1359–1369.

Massie, A., Schallier, A., Mertens, B., Vermoesen, K., Bannai, S., Sato, H., et al. (2008). Time-dependent changes in striatal xCT protein expression in hemi-Parkinson rats. *Neuroreport* 19, 1589–1592. doi: 10.1097/WNR.0b013e328312181c

Mesci, P., Zaidi, S., Lobsiger, C. S., Millecamps, S., Escartin, C., Seilhean, D., et al. (2015). System xC- is a mediator of microglial function and its deletion slows symptoms in amyotrophic lateral sclerosis mice. *Brain* 138, 53–68. doi: 10.1093/brain/awu312

Moore, C., Xu, M., Bohlen, J. K., and Meshul, C. K. (2021). Differential ultrastructural alterations in the Vglut2 glutamatergic input to the substantia nigra pars compacta/pars reticulata following nigrostriatal dopamine loss in a progressive mouse model of Parkinson's disease. *Eur. J. Neurosci.* 53, 2061–2077. doi: 10.1111/ejn.14894

Moran, M. M., McFarland, K., Melendez, R. I., Kalivas, P. W., and Seamans, J. K. (2005). Cystine/glutamate exchange regulates metabotropic glutamate receptor presynaptic inhibition of excitatory transmission and vulnerability to cocaine seeking. *J. Neurosci.* 25, 6389–6393. doi: 10.1523/JNEUROSCI.1007-05.2005

Norden, D. M., Muccigrosso, M. M., and Godbout, J. P. (2015). Microglial priming and enhanced reactivity to secondary insult in aging, and traumatic CNS injury, and neurodegenerative disease. *Neuropharmacology* 96, 29–41. doi: 10.1016/j.neuropharm.2014.10.028

Ottestad-Hansen, S., Hu, Q. X., Follin-Arbelet, V. V., Bentea, E., Sato, H., Massie, A., et al. (2018). The cystine-glutamate exchanger (xCT, Slc7a11) is expressed in significant concentrations in a subpopulation of astrocytes in the mouse brain. *Glia* 66, 951–970. doi: 10.1002/glia.23294

Parihar, M. S., and Brewer, G. J. (2007). Simultaneous age-related depolarization of mitochondrial membrane potential and increased mitochondrial reactive oxygen species production correlate with age-related glutamate excitotoxicity in rat hippocampal neurons. *J. Neurosci. Res.* 85, 1018–1032. doi: 10.1002/jnr.21218

Paxinos, G., and Franklin, K. B. J. (2004). *The Mouse Brain in Stereotaxic Coordinates*. San Diego, CA: Academic Press.

Pintado, C., Gavilan, M. P., Gavilan, E., Garcia-Cuervo, L., Gutierrez, A., Vitorica, J., et al. (2012). Lipopolysaccharide-induced neuroinflammation leads to the accumulation of ubiquitinated proteins and increases susceptibility to neurodegeneration induced by proteasome inhibition in rat hippocampus. *J. Neuroinflammation* 9:87. doi: 10.1186/1742-2094-9-87

Reeve, A., Simcox, E., and Turnbull, D. (2014). Ageing and Parkinson's disease: Why is advancing age the biggest risk factor? *Ageing Res. Rev.* 14, 19–30. doi: 10.1016/j.arr.2014.01.004

Sato, H., Shiiya, A., Kimata, M., Maebara, K., Tamba, M., Sakakura, Y., et al. (2005). Redox imbalance in cystine/glutamate transporter-deficient mice. *J. Biol. Chem.* 280, 37423–37429. doi: 10.1074/jbc.M506439200

Savolainen, M. H., Albert, K., Airavaara, M., and Myohanen, T. T. (2017). Nigral injection of a proteasomal inhibitor, lactacystin, induces widespread glial cell activation and shows various phenotypes of Parkinson's disease in young and adult mouse. *Exp. Brain Res.* 235, 2189–2202. doi: 10.1007/s00221-017-4962-z

Soria, F. N., Perez-Samartin, A., Martin, A., Gona, K. B., Llop, J., Szczupak, B., et al. (2014). Extrasynaptic glutamate release through cystine/glutamate antiporter contributes to ischemic damage. *J. Clin. Invest.* 124, 3645–3655. doi: 10.1172/JCI71886

Stanika, R. I., Pivovarova, N. B., Brantner, C. A., Watts, C. A., Winters, C. A., and Andrews, S. B. (2009). Coupling diverse routes of calcium entry to mitochondrial dysfunction and glutamate excitotoxicity. *Proc. Natl. Acad. Sci. U.S.A.* 106, 9854–9859. doi: 10.1073/pnas.0903546106

Tong, Z. B., Braisted, J., Chu, P. H., and Gerhold, D. (2020). The MT1G gene in LUHMES neurons is a sensitive biomarker of neurotoxicity. *Neurotox. Res.* 38, 967–978. doi: 10.1007/s12640-020-00272-3

van der Worp, H. B., Howells, D. W., Sena, E. S., Porritt, M. J., Rewell, S., O'Collins, V., et al. (2010). Can animal models of disease reliably inform human studies? *PLoS Med.* 7:e1000245. doi: 10.1371/journal.pmed.1000245

Williams, L. E., and Featherstone, D. E. (2014). Regulation of hippocampal synaptic strength by glial xCT. *J. Neurosci.* 34, 16093–16102. doi: 10.1523/JNEUROSCI.1267-14.2014

Xiao, Q., Yang, S., and Le, W. (2015). G2019S LRRK2 and aging confer susceptibility to proteasome inhibitor-induced neurotoxicity in nigrostriatal dopaminergic system. *J. Neural Transm.* 122, 1645–1657. doi: 10.1007/s00702-015-1438-9

Xu, M., Bohlen, J. K., Moore, C., Nipper, M. A., Finn, D. A., Jones, C. E., et al. (2019). Effects of sleep disruption on stress, nigrostriatal markers, and behavior in a chronic/progressive MPTP male mouse model of parkinsonism. *J. Neurosci. Res.* 97, 1706–1719. doi: 10.1002/jnr.24520

Ye, P., Mimura, J., Okada, T., Sato, H., Liu, T., Maruyama, A., et al. (2014). Nrf2- and ATF4-dependent upregulation of xCT modulates the sensitivity of T24 bladder carcinoma cells to proteasome inhibition. *Mol. Cell. Biol.* 34, 3421–3434. doi: 10.1128/MCB.00221-14

Conflict of Interest: The authors declare that the research was conducted in the absence of any commercial or financial relationships that could be construed as a potential conflict of interest.

ORIGINAL RESEARCH
published: 29 December 2021
doi: 10.3389/fncel.2021.788262

Neuronal Loss of the Glutamate Transporter GLT-1 Promotes Excitotoxic Injury in the Hippocampus

Theresa S. Rimmele[1†], Shaomin Li[2†], Jens Velde Andersen[3], Emil W. Westi[3], Alexander Rotenberg[1,4], Jianlin Wang[1], Blanca Irene Aldana[3], Dennis J. Selkoe[2], Chiye J. Aoki[5,6], Chris G. Dulla[7‡], Paul Allen Rosenberg[1,4]*‡

[1]Department of Neurology and the F. M. Kirby Neurobiology Center, Boston Children's Hospital, Boston, MA, United States, [2]Ann Romney Center for Neurologic Diseases, Department of Neurology, Brigham and Women's Hospital and Harvard Medical School, Boston, MA, United States, [3]Department of Drug Design and Pharmacology, University of Copenhagen, Copenhagen, Denmark, [4]Program in Neuroscience, Harvard Medical School, Boston, MA, United States, [5]Center for Neural Science, New York University, NY, United States, [6]Neuroscience Institute NYU Langone Medical Center, NY, United States, [7]Department of Neuroscience, Tufts University School of Medicine, Boston, MA, United States

Edited by:
*Arturo Ortega,
Centro de Investigación y de Estudios Avanzados del Instituto Politécnico Nacional, Mexico*

Reviewed by:
*Matthew Philip Parsons,
Memorial University of Newfoundland, Canada
Magdalena Zielińska,
Mossakowski Medical Research Centre, Polish Academy of Sciences, Poland*

***Correspondence:**
*Paul Allen Rosenberg
paul.rosenberg@childrens.harvard.edu*

†These authors share first authorship

‡These authors share senior authorship

Specialty section:
This article was submitted to Cellular Neurophysiology, a section of the journal Frontiers in Cellular Neuroscience

Received: *01 October 2021*
Accepted: *08 December 2021*
Published: *29 December 2021*

Citation:
Rimmele TS, Li S, Andersen JV, Westi EW, Rotenberg A, Wang J, Aldana BI, Selkoe DJ, Aoki CJ, Dulla CG and Rosenberg PA (2021) Neuronal Loss of the Glutamate Transporter GLT-1 Promotes Excitotoxic Injury in the Hippocampus. Front. Cell. Neurosci. 15:788262. doi: 10.3389/fncel.2021.788262

GLT-1, the major glutamate transporter in the mammalian central nervous system, is expressed in presynaptic terminals that use glutamate as a neurotransmitter, in addition to astrocytes. It is widely assumed that glutamate homeostasis is regulated primarily by glutamate transporters expressed in astrocytes, leaving the function of GLT-1 in neurons relatively unexplored. We generated conditional GLT-1 knockout (KO) mouse lines to understand the cell-specific functions of GLT-1. We found that stimulus-evoked field extracellular postsynaptic potentials (fEPSPs) recorded in the CA1 region of the hippocampus were normal in the astrocytic GLT-1 KO but were reduced and often absent in the neuronal GLT-1 KO at 40 weeks. The failure of fEPSP generation in the neuronal GLT-1 KO was also observed in slices from 20 weeks old mice but not consistently from 10 weeks old mice. Using an extracellular FRET-based glutamate sensor, we found no difference in stimulus-evoked glutamate accumulation in the neuronal GLT-1 KO, suggesting a postsynaptic cause of the transmission failure. We hypothesized that excitotoxicity underlies the failure of functional recovery of slices from the neuronal GLT-1 KO. Consistent with this hypothesis, the non-competitive NMDA receptor antagonist MK801, when present in the ACSF during the recovery period following cutting of slices, promoted full restoration of fEPSP generation. The inclusion of an enzymatic glutamate scavenging system in the ACSF conferred partial protection. Excitotoxicity might be due to excess release or accumulation of excitatory amino acids, or to metabolic perturbation resulting in increased vulnerability to NMDA receptor activation. Previous studies have demonstrated a defect in the utilization of glutamate by synaptic mitochondria and aspartate production in the synGLT-1 KO *in vivo*, and we found evidence for similar metabolic perturbations in the slice preparation. In addition, mitochondrial cristae density was higher in synaptic mitochondria in the CA1 region in 20–25 weeks old synGLT-1 KO mice in the CA1 region, suggesting compensation for loss of axon terminal GLT-1 by increased mitochondrial efficiency. These data suggest that GLT-1 expressed in presynaptic terminals serves an important role in the regulation of vulnerability to excitotoxicity, and this regulation may be related to the metabolic role of GLT-1 expressed in glutamatergic axon terminals.

Keywords: homeostasis, excitotoxicity glutamatergic, aging, neurodegeneration, mitochondria, Alzheimer's disease, repair

INTRODUCTION

Most synapses have a mechanism for neurotransmitter reuptake in the presynaptic terminal, and the demonstration of a high-affinity specific uptake system for glutamate in purified synaptosomes provided important biochemical evidence that this amino acid is a neurotransmitter (Logan and Snyder, 1971; Bennett et al., 1972; Rimmele and Rosenberg, 2016). In excitatory presynaptic terminals, the high-affinity glutamate transporter GLT-1 is expressed in many but not all synapses (Chen et al., 2004; Berger et al., 2005; Furness et al., 2008). In the hippocampus, 80–90% of GLT-1 is found in glial cells and 5–10% in axon terminals (Furness et al., 2008), and a consensus has arisen that glutamate clearance is primarily if not exclusively accomplished by astrocytic GLT-1 (Bergles et al., 1999; Danbolt, 2001; Tzingounis and Wadiche, 2007). Glutamate homeostasis (Schousboe and Hertz, 1981; Ottersen et al., 1996; Schousboe et al., 1997; Takahashi et al., 1997; Bezzi et al., 1999; Kalivas, 2009) is important for the survival of neurons in the CNS in the face of the constant threat of excitotoxicity due to excess or abnormal activation of glutamate receptors (Lipton and Rosenberg, 1994). In addition, glutamate homeostasis has emerged as a critical determinant of important neurobiological phenomena, including pain (Inquimbert et al., 2012, 2018), addiction (Fischer et al., 2020), mental illness (Hu et al., 2015; O'Donovan et al., 2015; Parkin et al., 2018, 2020) plasticity (Levenson et al., 2000a,b, 2002; Collado et al., 2007, 2009), and chronic neurodegeneration, in particular, in Alzheimer's disease (Li et al., 2009; Zott et al., 2019). In general, it has been assumed that these multiple roles for GLT-1 are implemented by GLT-1 expressed in astrocytes, whereas the functions of the small amount of GLT-1 expressed in axon terminals remain largely unknown.

Recent studies have shown that GLT-1 expressed in axon terminals may serve an important metabolic role (McNair et al., 2019, 2020; Andersen et al., 2021a), although the functional importance of this metabolic involvement of GLT-1 and the consequences of its perturbation or disruption have not been explored. To pursue the cell-type specific functions of GLT-1, we generated a conditional GLT-1 knockout and mouse lines using Cre/lox technology to: *(i)* inactivate the GLT-1 gene in astrocytes, by a tamoxifen-inducible glial fibrillary acidic protein (GFAP) driver (Casper et al., 2007) of Cre-recombinase expression (gfapGLT-1 KO), and *(ii)* using a synapsin 1 driver of Cre-recombinase expression (Zhu et al., 2001) to inactivate GLT-1 specifically in neurons (synGLT-1 KO; Petr et al., 2015). Like the pan GLT-1 KO (Tanaka et al., 1997), gfapGLT-1 KO mice have intractable seizures and a shortened life span (Petr et al., 2015). The synGLT-1 KO, in contrast, is behaviorally normal up to 12 months of age (Petr et al., 2015; Sharma et al., 2019) but has been found to have a defect in the performance of the Morris Water Maze at 18 months of age suggesting impaired hippocampal memory formation (Vorhees and Williams, 2006; Sharma et al., 2019).

Neurons in the CA3 region of the hippocampus express GLT-1 mRNA at the highest levels found in neurons anywhere in the brain (Torp et al., 1994, 1997; Schmitt et al., 1996; Berger and Hediger, 1998; Berger et al., 2005). If GLT-1 expressed in axon terminals has a role in synaptic transmission it should be manifest at the CA3 to CA1 synapse that can be conveniently studied using the hippocampal slice preparation. The hippocampal slice preparation is also considered to be a model for brain injury and repair, in that during the preparation of slices the brain is subjected to both ischemic and traumatic injury and after an initial period of electrical silence undergoes repair processes that restore synaptic transmission (Kirov et al., 1999; Fiala et al., 2003; Buskila et al., 2014; Rae and Balcar, 2014; Frenguelli, 2019). Accordingly, the slice preparation has been used as a model in which it is possible to study how genetic and other manipulations affect processes associated with repair and recovery from injury (Hossmann, 2008; Hall and Frenguelli, 2018; Frenguelli, 2019; Frenguelli and Dale, 2020). In this study, we took advantage of the hippocampal slice preparation to test whether the inactivation of GLT-1 in neurons affects synaptic function and synaptic health. In fact, we found that the generation of field excitatory postsynaptic potentials was compromised in slices from synGLT-1 KO animals 20 weeks and older, and this compromise appeared to be due to excitotoxic injury. Remarkably, fEPSP generation in gfapGLT-1 KO animals was normal at least through 40 weeks of age. These findings suggest that, despite its low level of expression, GLT-1 expressed in axon terminals serves an important role in regulating vulnerability to excitotoxicity.

MATERIALS AND METHODS

Mice

Male conditional GLT-1 knock-out mice were obtained from the founding colony at Boston Children's Hospital (Slc1A2$^{tm1.1Pros}$; MGI: 5752263; Petr et al., 2015). Neuronal GLT-1 knockout mice were generated in which the GLT-1 gene was inactivated in neurons by expression of synapsin-Cre as described previously (GLT-1$^{flox/flox}$; synapsin-Cre; Petr et al., 2015; Fischer et al., 2018), and littermate controls with normal GLT-1 function (GLT-1$^{flox/flox}$). These are referred to in the current article as synGLT-1 KO and wild-type littermate controls, respectively.

In order to determine that our observations were not due to Cre-recombinase expression, *per se* (Harno et al., 2013), we generated and used synapsin-Cre control mice. Male mice with a tamoxifen-inducible astrocyte-specific knock-out of GLT-1 (GLT-$1^{\Delta/\Delta}$;GFAP-Cre ERT2) are referred to as gfapGLT-1 KO and were generated using the hGFAP-CreER^{T2} driver (Casper et al., 2007) as described previously (Petr et al., 2015). Pups from an entire litter were treated daily with tamoxifen (T5648, Sigma-Aldrich; 33 mg/kg, i.p. or oral gavage in sunflower oil) starting from P5 and for 4–5 consecutive days (Ganat et al., 2006). Tamoxifen solutions were made fresh for a given litter and never frozen. Experiments were conducted on adult male mice, synGLT-1 KO experiments were performed with three age groups, 10–12 weeks (referred to as 10 weeks throughout the manuscript), 18–21 weeks (referred to as 20 weeks throughout the manuscript), and 30–40 weeks of age, using age-matched littermates as controls; gfapGLT-1 KO experiments were performed with 24–40 weeks old mice and littermate controls. For the electron microscopic study, a single age group of 22–24 weeks was used. Animals were housed in a temperature-controlled room on a 12-h light/12-h dark cycle and had ad libitum access to food and water.

Mice were maintained on a 129S4/SvJaeJ (JAX Stock No. 009104) × C57BL/6J (JAX Stock No. 000664) genetic background as a mixed background is most likely to produce the widest range of phenotypes (Doetschman, 2009). The composition of the hybrid background was periodically evaluated using the Jackson Labs Genome Screening Service, and the colony was refreshed either with C57BL/6J or 129S4/SvJaeJ to approximate a 50:50 mix. In all experiments, littermate controls were used.

All animal experiments were performed in accordance with NIH guidelines and were approved by the Children's Hospital Boston Institutional Animal Care and Use Committee.

Hippocampal Slice Preparation

Mice (synGLT-1 KO and wild-type littermates; gfapGLT-1 KO and wild-type littermates) were euthanized with Isoflurane. The brain was quickly removed and placed in chilled (4°C) low-Ca, high-Mg, low-Na slicing solution consisting of (in mM): 234 sucrose, 11 D-glucose, 24 $NaHCO_3$, 2.5 KCl, 1.25 NaH_2PO_4, 10 $MgSO_4$, and 0.5 $CaCl_2$, equilibrated with a mixture of 95% O_2:5% CO_2, pH 7.4 (**Figures 2–5**, **6C**). For some experiments, a slightly altered composition for the low-Na slicing solution was used: (in mM) 206 sucrose, 10 D-glucose, 26 $NaHCO_3$, 2.8 KCl, 1.0 NaH_2PO_4, 2 $MgSO_4$, 1 $CaCl_2$, 5 $MgCl_2$, pH 7.4 (**Figures 1A–D**, **6A,B**). The brain was glued to the slicing stage of a Leica VT1200S Vibratome sectioning system and slices were cut at 350 μm in a coronal orientation. The slices were then incubated in 32°C oxygenated artificial cerebrospinal fluid (ACSF: in mM: 126 NaCl, 2.5 KCl, 1.25 NaH_2PO_4, 1 $MgSO_4$, 2 $CaCl_2$, 10 D-glucose, 26 $NaHCO_2$, pH 7.4) for at least 60 min (**Figures 2–5**, **6C**). In some experiments, slices were incubated in ACSF that contained the following (in mM): 124 NaCl, 2.8 KCl, 1.25 NaH_2PO_4, 2 $MgSO_4$, 2.5 $CaCl_2$, 10 D-glucose, 26 $NaHCO_3$, 0.4 sodium ascorbate, pH 7.4 (**Figures 1A–D**, **6A,B**). The volume used for the recovery incubation was 300–500 ml (**Figures 1A–D**, **2A–E**, **3**, **4**) except when drugs were being tested (**Figures 5**, **6A,B**) when the reduced volume (25–100) was used to conserve the drug.

Electrophysiological Recordings

A single slice was transferred to the recording chamber and continuously perfused with ACSF at ∼34°C that had been saturated with 95% O_2 and 5% CO_2 after recovery at the same temperature. In some experiments, recording (and recovery incubation) was performed at 26°C (**Figures 1A–D**, **6A,B**). For field recording and glutamate imaging, this was done in an interface chamber; in some experiments, submerged slices were used (**Figures 1A–D**, **6A,B**). Whole cell recording was performed using submerged slices.

A bipolar stimulating electrode (FHC Inc., Bowdoin, ME) was placed in the Schaeffer collaterals to deliver stimuli. A borosilicate glass recording electrode filled with ACSF was positioned in the stratum radiatum of CA1, 200–300 μm from the stimulating electrode. The input/output relationship was determined with a series of increasing stimulation intensities. Paired pulse facilitation of fEPSP was tested by two stimuli 50 ms apart with an intensity of 300 μA. Electrophysiological data were recorded with an Axon Multiclamp 700A amplifier or with an Axon Instruments 200 B amplifier and Digidata 1322A digitizer (sampling rate = 10 or 20 kHz; filtered at 2 kHz) with pClamp software (Molecular Devices).

Recovery times were similar between genotypes, and the minimum time for recovery was 60 min. Slices were taken as needed from the recovery ACSF for recording after the 60-min recovery period. Although the first slices were recorded following 60 min recovery period, the last to be recorded on a given day may have been in the recovery ACSF for up to 4 h. No effect was observed of time in recovery ACSF on the phenotype observed in the synGLT-1 KO. In all cases comparing wild-type and KO slices, slices from wild-type and KO littermates were compared on the same experimental day. Therefore, slices from both mutant and control genotypes were always subjected to the same experimental conditions.

Glutamate Biosensor Imaging

Production, loading of glutamate biosensor, and collection of biosensor data were performed as previously described (Dulla et al., 2008). A 35 mm tissue culture dish was filled with ∼2 ml ACSF and a 0.4 μm Millicell (Millipore) culture plate was inserted. Care was taken to ensure that no bubbles were present under the plate insert and that no ACSF spilled onto its top surface. A single brain slice was transferred from the incubation chamber onto the plate insert and excess ACSF was removed. The dish containing the slice was then placed in a humidified and warmed (32°C) chamber equilibrated with 95% O_2:5% CO_2. Fifty microliter of concentrated glutamate FRET sensor protein (≈ 50 ng/μl) was then carefully applied to the top surface of the slice. After 5–10 min of incubation, slices were removed from the loading chamber and placed into the recording chamber.

Slices were placed into the recording chamber of an Olympus Bx51WI microscope with continual superfusion of ACSF for simultaneous imaging with an Olympus 4× objective. Excitation

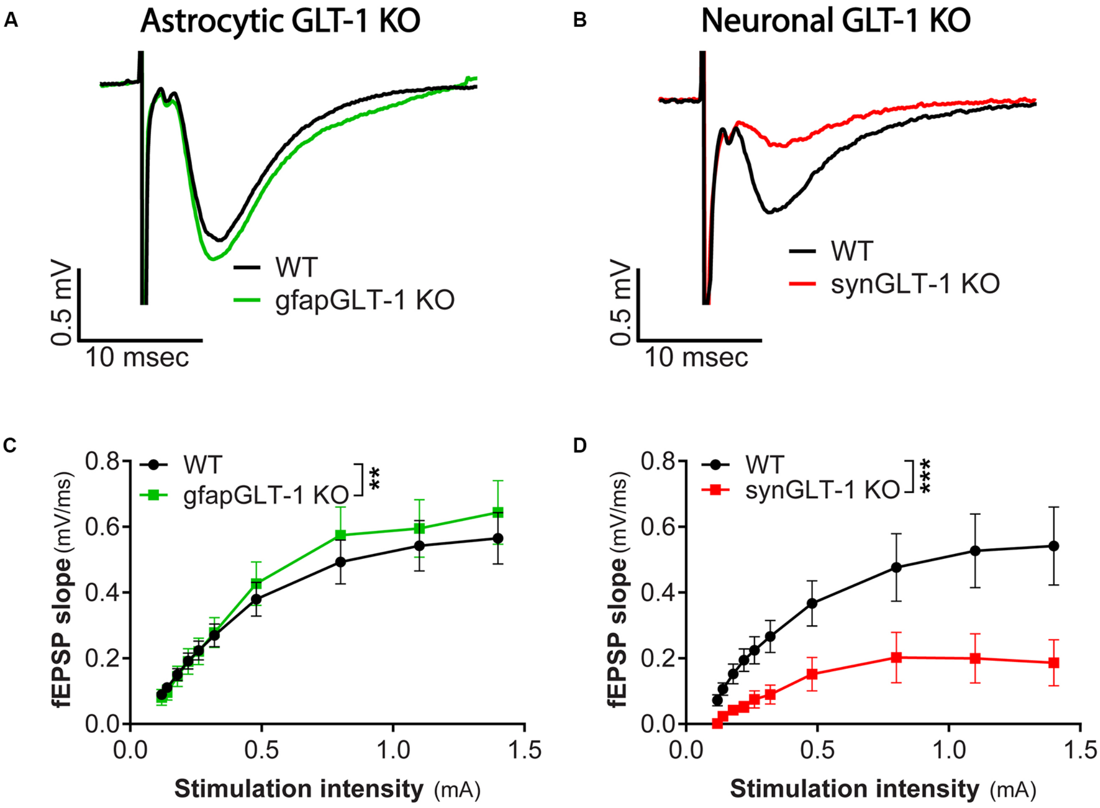

FIGURE 1 | Decreased field potentials in CA1 region of hippocampal slices from synGLT-1 KO but not gfapGLT-1 KO mice. Field excitatory post-synaptic potentials (fEPSPs) were recorded in the stratum radiatum in the CA1 region of hippocampal slices in response to a single electrical stimulus applied to the Schaeffer collateral/commissural fibers in 30–40 weeks old gfapGLT-1 KO ("Astrocytic GLT-1 KO"; **A,C**) and 30–40 weeks old synGLT-1 KO ("Neuronal GLT-1 KO"; **B,D**) mice and wild-type (WT) littermate controls. **(A)** Representative traces from WT (black trace) and gfapGLT-1 KO (green trace) littermates (0.3 mA stimulus). **(B)** Representative traces from WT (black trace) and synGLT-1 KO (red trace) littermates (0.3 mA stimulus). **(C,D)** Input-output relationship of fEPSP slope produced by stimuli between 0 and 1 mA in gfapGLT-1 and WT littermates **(C)** and in synGLT-1 KO and WT littermates **(D)**. ** = $p < 0.01$, *** = $p < 0.001$ in panels **(C,D)** indicate effect of genotype in a linear mixed model.

with 440 nm wavelength light was used. Imaging was performed using a Zyla (Andor) camera imaging at 200 Hz, illuminated by a 480 nm LED (Thorlabs), using the Endow-GFP filter cube (Chroma) and controlled by MicroManager (Edelstein et al., 2014). Each imaging experiment consisted of collecting 500 images at 5 ms acquisition time. A direct trigger sent from the camera triggered evoked stimuli delivery by stimulation isolator after the acquisition of 20 images. Emission signals first passed through a 455 nm DCLP dichroic mirror to eliminate excitation fluorescence and were then separated into two channels using a Photometrics Dual-View or Optosplit two channel imaging system to isolate cyan fluorescent protein (CFP) and Venus, a variant of yellow fluorescent protein (YFP), signals.

Regions of interest (ROIs) were manually drawn within the CA1 stratum radiatum symmetrically around the stimulation electrode to include regions from both the CA1 and CA3 sides of the electrode. Raw imaging data was first split into CFP and Venus and the ratio of the two fluorophores was computed. An average pre-stimulation ratio image was then made by averaging the first three images. The pre-stimulation image was then subtracted from all images resulting in a ΔFRET image. Processed ΔFRET images were then converted into ΔFRETsignal/ΔFRETnoise data, pixel-by-pixel, by dividing all time-points by the standard deviation of ΔFRET during the pre-stimulus time period. Bleaching of the biosensor was corrected by calculating an exponential function fit. Imaging data were then analyzed to determine the peak amplitude of the signal.

Assay of Extracellular Amino Acids

Extracellular Amino Acids

Medium ($V = 3$ ml) incubating single slices during the recovery period of 60 min was collected and assayed for amino acids. Slices from a single animal were used for each experiment and wild-type and synGLT-1 KO animals were used on sequential days. The medium was kept frozen at −20°C after collection and until assay. At the time of assay, 0.9 ml medium was added to 0.1 ml 35% sulfosalicylic acid to remove proteins. The acidified medium was kept on ice for 20 min, after which it was centrifuged, and the supernatant was decanted and assayed. Amino acid content was determined by the Biochemical Genetics Laboratory at the Kennedy Krieger Institute using a Biochrom 30 amino acid analyzer (Pei et al., 2010). In these

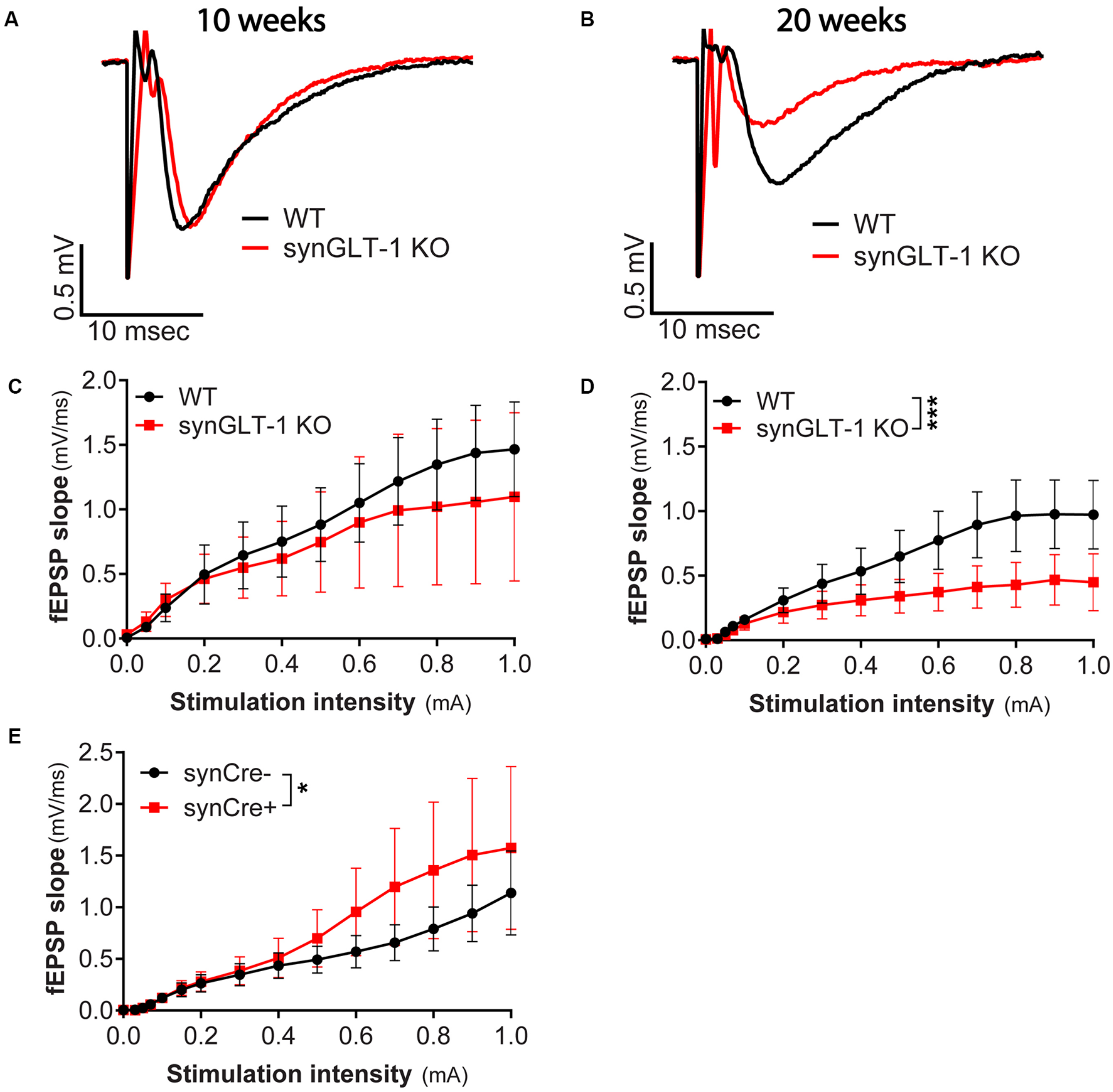

FIGURE 2 | Age-dependent impairment in excitatory synaptic transmission in synGLT-1 KO mice. **(A,B)** Representative fEPSPs recorded in the stratum radiatum of the CA1 region in hippocampal slices in response to a single electrical stimulus applied to the Schaeffer collateral/commissural fibers in 10 weeks **(A)** and 20 weeks old **(B)** WT littermate controls (black traces) and in synGLT-1 KO (red traces). fEPSP slope in 10 weeks old **(C)** and 20 weeks old **(D)** synGLT-1 KO produced by stimuli between 0 and 1 mA. **(E)** Cre-recombinase expression on a true wild-type background (GLT-1$^{+/+}$; 20 weeks) does not impair fEPSP generation. * = $p < 0.05$, *** = $p < 0.001$ in panels **(D,E)** indicate effect of genotype in a linear mixed model.

experiments, slices from single animals were incubated for selected times in ACSF, incubated at 34°C. Wild-type and KO animals were run on sequential days. Three pairs were assayed, four slices per animal on a given experimental day, for a total of 12 slices/genotype.

Glutamate Uptake and Metabolism in Hippocampal Brain Slices

Glutamate uptake and metabolism were investigated by incubation of acutely isolated hippocampal mouse brain slices as previously described (Andersen et al., 2021b). The mouse was euthanized by cervical dislocation and the brain transferred to ice-cold artificial cerebrospinal fluid (ACSF) containing in mM: 128 NaCl, 25 $NaHCO_3$, 10 D-glucose, 3 KCl, 2 $CaCl_2$, 1.2 $MgSO_4$, 0.4 KH_2PO_4, pH 7.4. The hippocampi were dissected and sliced (350 μm) using a McIlwain tissue chopper (The Vibratome Company, O'Fallon, MO, USA). The hippocampal slices were kept just below the surface of 10 ml 37°C oxygenated (5% CO_2/95% O_2) ACSF and pre-incubated for 60 min. Subsequently, the media were exchanged for ACSF (with an adjusted D-glucose concentration of 5 mM) containing 200 μM [U-^{13}C]glutamate and incubated for additional 60 min. Incubations were terminated by transferring the slices into ice-cold 70% ethanol. Slices were subsequently sonicated and centrifuged (4,000 *g* × 20 min) and the supernatant was removed and lyophilized before further analysis. The protein content of

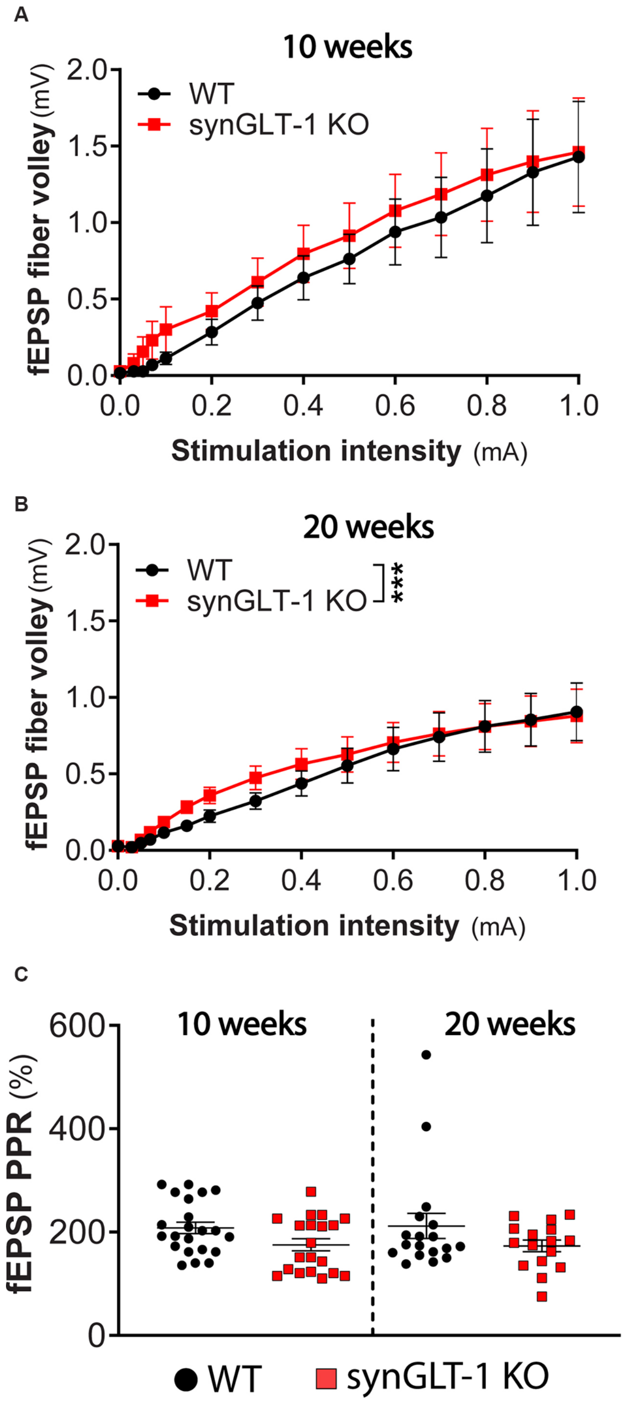

FIGURE 3 | Presynaptic fiber recruitment and paired-pulse facilitation were largely unchanged in synGLT-1 KO compared to wild-type littermates. The fEPSP fiber volley component of field potential recording in the stratum pyramidale of CA1 hippocampal slices in 10 **(A)** and 20 weeks old **(B)** synGLT-1 KO (red traces) and WT littermate controls (black traces) is shown. **(C)** Pair pulse facilitation ratio (PPR) of two paired electrical stimuli at 20 Hz applied to the Schaeffer collateral/commissural fibers in 10 weeks (left) and 20 weeks (right) old WT littermate controls (black symbols) and synGLT-1 KO (red symbols). *** = $p < 0.001$ in panel **(B)** indicates the effect of genotype in a linear mixed model.

the pellets was determined by Pierce protein assay. The ^{13}C enrichment of tricarboxylic acid (TCA) cycle intermediates and amino acids from [U-^{13}C]glutamate metabolism was determined by gas chromatography-mass spectrometry (GC-MS) analysis. Slice extracts were reconstituted in water, acidified, extracted with ethanol and the metabolites were derivatized using *N*-tert-butyldimethylsilyl-*N*-methyltrifluoroacetamide. Samples were analyzed by GC (Agilent Technologies, 7820A, J&W GC column HP-5 MS) coupled to MS (Agilent Technologies, 5977E). The isotopic enrichment was corrected for the natural abundance of ^{13}C by analyzing the standards of the unlabeled metabolites of interest. The expected labeling pattern of [U-^{13}C]glutamate metabolism is described in Andersen et al. (2017a) and data is presented as M + X, where M is the molecular ion and X is the number of ^{13}C atoms in the molecule. Aqueous slice extracts were further analyzed by reverse-phase high-performance liquid chromatography (HPLC, Agilent Technologies, 1260 Infinity, Agilent ZORBAX Eclipse Plus C18 column) to quantitatively determine the amounts of amino acids (Andersen et al., 2017b). Ten male mice of each genotype, 20 mice in total, were used for the metabolic slice experiments.

One mouse was used at a time for experiments. For each incubation (20 in total, 10 WT and 10 KO), 5–6 hippocampal slices were tested/condition i.e., incubated together exposed to [U-^{13}C]glutamate. All of the 5–6 slices were then homogenized and analyzed together to provide one data point.

Electron Microscopic Immunocytochemical (EM-ICC) Detection of GLT-1 and Analysis of Hippocampal Mitochondria

The procedures used were exactly as reported previously (Petr et al., 2015) and are described only briefly here. Animals, all male, were transcardially perfused under anesthesia at 22–24 weeks of age, in one session, using a mixture of 0.1% glutaraldehyde/4% paraformaldehyde in 0.1 M phosphate buffer (PB, pH 7.4) to fix their brains. All subsequent steps for tissue preparation were conducted strictly in parallel, so as to minimize inter-animal differences in ultrastructural preservation due to unintended differences in tissue handling or of chemical reagents.

Brains were cut at a coronal plane using a vibrating microtome, with thickness of sections set to 50 µm. Brain sections spanning the dorsal hippocampus were collected, treated with sodium borohydride (1%, in PB, pH 7.4) for 30 min, then rinsed in PB and stored for a month in a 4°C cold room, free-floating in PBS (phosphate buffered saline, pH 7.6) that contained 0.05% sodium azide. EM-ICC was achieved by using a monoclonal anti-GLT-1a antibody at a dilution of 1:10,000 (generous gift of Dr. Jeff Rothstein, Johns Hopkins U) and detected using HRP-DAB/osmium.

Ultrastructural analysis was performed strictly from the stratum radiatum of CA1 of the dorsal hippocampus, after capturing electron microscopic images at a magnification of 40,000× from portions of the vibratome section that were most superficial and thus optimal for immunodetection. Synaptic neuropil that fulfilled these two criteria were captured

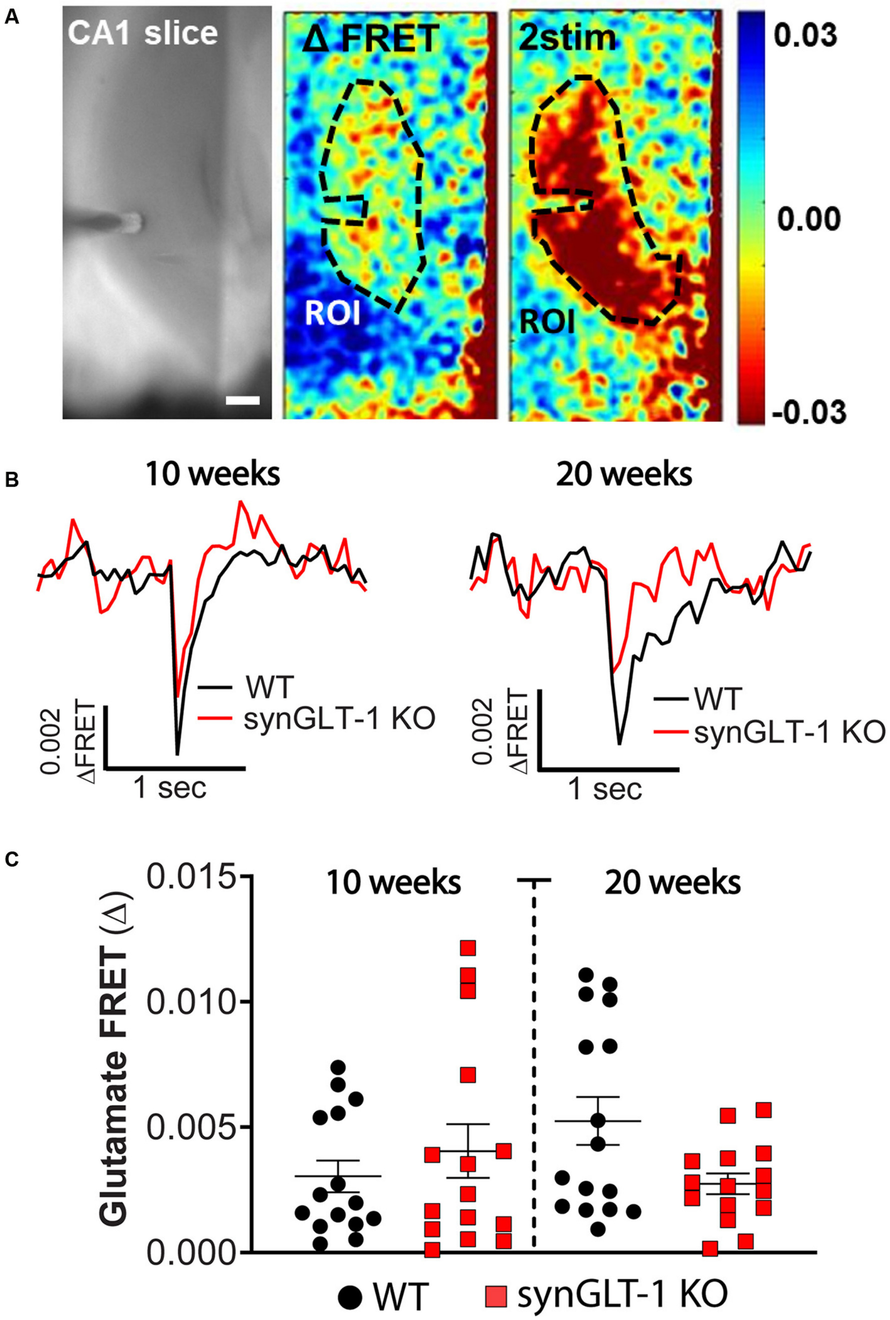

FIGURE 4 | Comparison of stimulus-evoked glutamate release in synGLT-1 KO and wild-type slices. Acute hippocampal slices were prepared from synGLT-1 KO and WT mice and loaded with a glutamate FRET sensor. A recording electrode was placed in the stratum radiatum of CA1 and a bipolar stimulating electrode was placed in the Schaeffer collateral/commissural fibers. **(A)** An example of images from a WT hippocampal slice. Left: phase contrast. Center: pseudo-colored glutamate response after one stimulus (center) and two stimuli at 20 Hz (right) and 0.3 mA intensity. The dashed line in the center and right images indicates the region of interest used in **(B,C)**. **(B)** Single trace of evoked extracellular glutamate FRET biosensor response in 10 weeks (left) and 20 weeks (right) old synGLT-1 KO (red) and WT littermate (black) mice. **(C)** Population of responses obtained at 10 (left) and 20 (right) weeks old synGLT-1 KO and WT mice. The responses in **(B)** and **(C)** were evoked by a single stimulus. There were no significant differences between responses in WT and synGLT-1 KO mice at 10 [Mann-Whitney U 106; $p = 0.806$ $n = 15$ (WT), 15 (KO)] or 20 weeks [(Mann-Whitney U 87; $p = 0.202$ $n = 15$ (WT), 16 (KO)]. Scale bar = 250 micrometers.

systematically, strictly in the order of encounter, while kept blind to the genotype of the animal. Encounter with asymmetric (presumably excitatory) synapses was recorded, together with the presence vs. absence of GLT-1 immunoreactivity and presence vs. absence of mitochondria within the presynaptic axon terminal. The rate of encounter with GLT-1 immunoreactivity

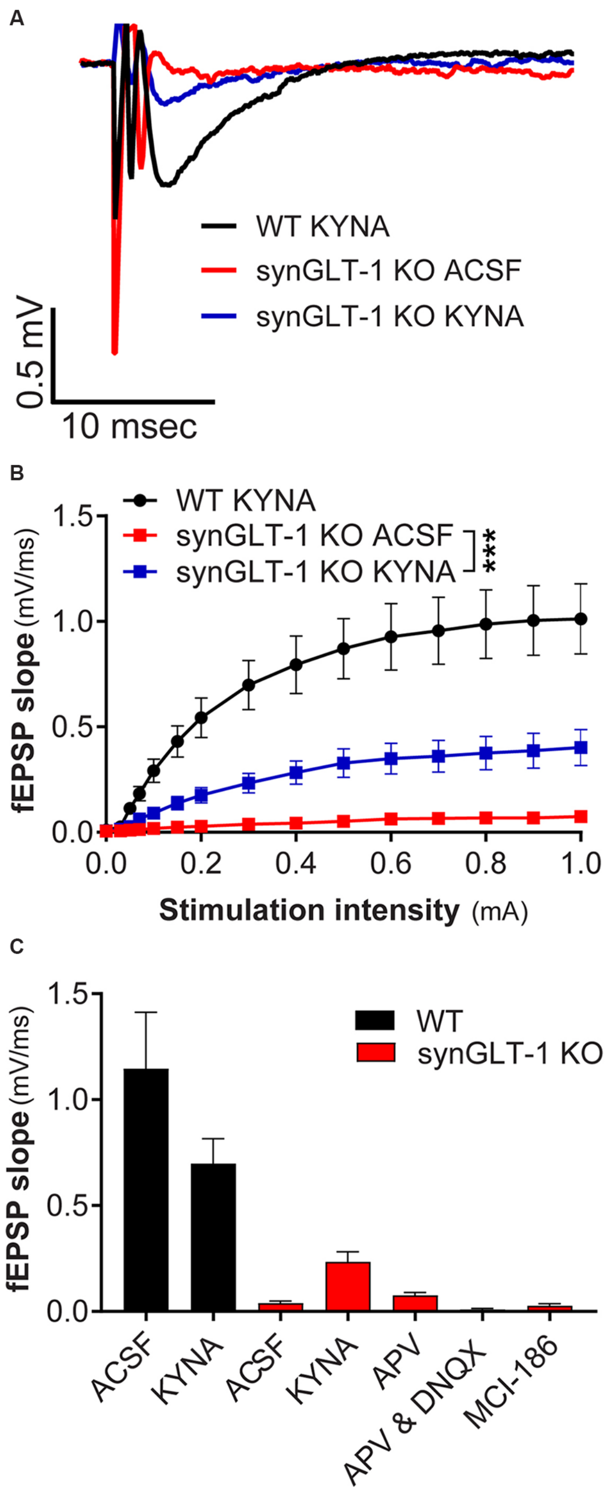

FIGURE 5 | Kynurenic acid partially restored excitatory synaptic transmission in synGLT-1 KO mice. **(A)** Representative field potentials recorded in the stratum radiatum of CA1 hippocampal slices in response to a single electrical stimulus of 0.3 mA applied to the Schaeffer collateral/commissural fibers in 20 weeks old WT littermate controls with 3 mM kynurenic acid treatment (black trace), synGLT-1 KO (red trace) and *(Continued)*

FIGURE 5 | Continued
synGLT-1 KO with kynurenic acid treatment (blue trace). **(B)** Input-output relationship of fEPSP slope between 0 and 1 mA in 20 weeks old synGLT-1 KO with kynurenic acid treatment (blue squares) or without treatment (red squares) and WT littermates (black circles). **(C)** Summary of data obtained with kynurenic acid and related treatments in ACSF during the recovery period at 0.3 mA stimulus intensity: ACSF, kynurenic acid, 50 μM D-APV, 50 μm D-APV in combination with 20 μM DNQX; MCI-186. *** = $p < 0.001$ in panel **(B)** indicates drug effect in a linear mixed model.

was measured for every group of 10 excitatory synapses, and this assessment of the rate of the encounter was repeated approximately 20 times, thereby assessing the rate of encounter of a neuropil region spanning 200 or more excitatory synapses. Within the mitochondria encountered, the average distances between cristae were calculated as described below, under "Statistical Analyses".

Statistical Analyses

Electrophysiology and Biochemistry

For comparison between two experimental groups other than electron microscopy, Student's unpaired t-test was used. Values of $p < 0.05$ or less were considered statistically significant. For cases in which the same brain slice was stimulated multiple times, and other repeated measures, linear mixed modeling (LMM) was used to examine the effects of genotype or drug treatment. This approach estimates the effect size of each factor while accounting for intra- and inter-animal variability (Aarts et al., 2014; Boisgontier and Cheval, 2016; Yu et al., 2021) and is gaining wide acceptance (Lau et al., 2017; Huang et al., 2018; Hanson et al., 2019; Koenig et al., 2019; Grieco et al., 2020; Kurucu et al., 2021). LMMs were fitted with random intercepts to assess for the correlation between repeated measurements on the same mouse, and experiment-specific effects were analyzed for statistical significance. LMM was performed in R-Studio using the lme4 and lmreTest libraries. Slices were considered nested within animals when considering intra- vs. inter-animal variability. For each test examining the effect of genotype, R code similar to the following was used "output ∼ (Amp + Amp: Genotype) + (1 | Animal) + (1 | Animal: Slice)" where "output" is the measure of interest, "Amp" is the stimulation intensity and "genotype" is the animal genotype. For each test examining the effect of drug treatment, an R code similar to the following was used "output" ∼ (Amp * Genotype * drug) + +(1 | Animal) + (1 | Animal:Slice) where "drug" was the dose of drug used. For no drug controls, "drug" equaled zero, values >1.96 and < -1.96 were considered to be statistically significant and corresponded to 95% confidence intervals that did not cross zero. Each LMM examined both main fixed effects (genotype, drug treatment, stimulation intensity, etc.) and interactions between the effects.

Electron Microscopy

GLT-1 immunoreactivity revealed the genotype of the animal to be wild-type or synGLT-1 KO. After this identification, and genotype validation from tail DNA that was collected prior to euthanasia, the values of the rate of encounter with GLT-1 immunoreactive presynaptic terminals were pooled

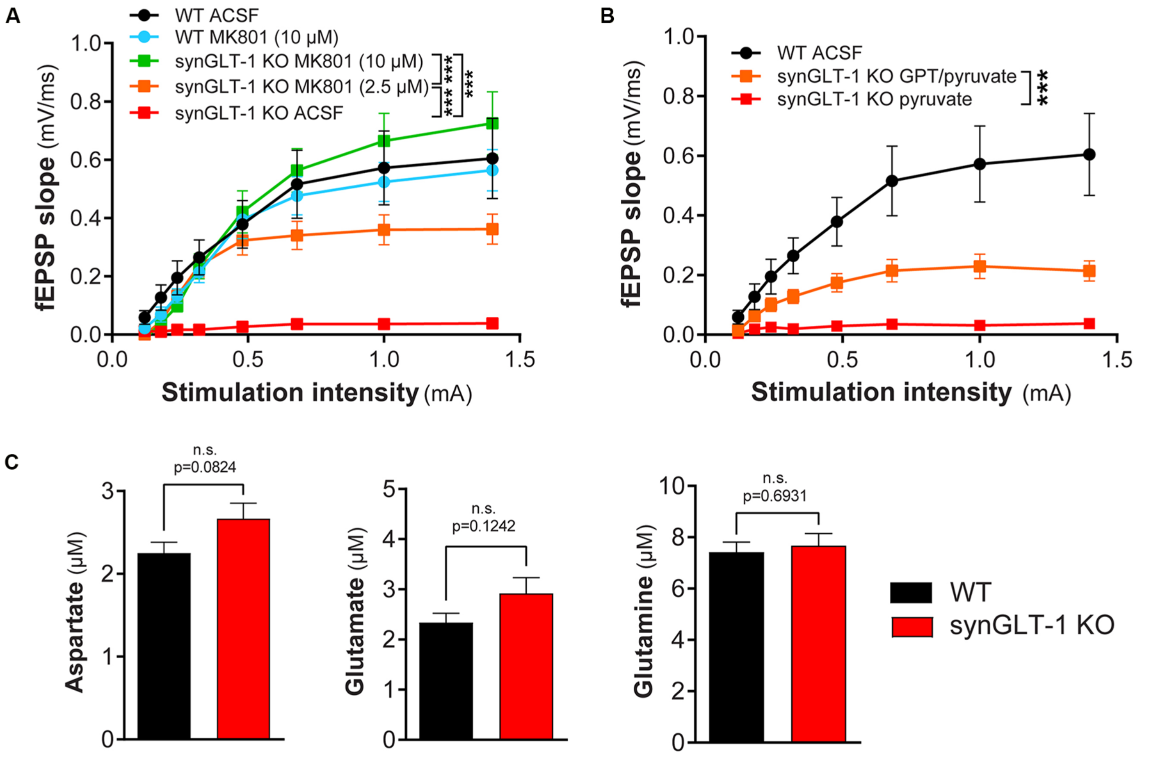

FIGURE 6 | Functional impairment of hippocampal slices was blocked by MK801 or by glutamate-pyruvate transaminase (GPT) in recovery ACSF. **(A)** The non-competitive NMDA receptor blocker MK801 prevented synaptic transmission compromise in synGLT-1 KO slices. Brain slices were allowed to recover in ACSF or ACSF containing MK801 (10 μM or 2.5 μM). Incubation with either 2.5 and 10 μM MK801 significantly increased the fEPSP slope in synGLT1-KO slices. SynGLT-1 KO slices in the presence of 10 μM MK801 (green, 11 slices from four mice) showed a normal input-output relationship compared with WT-ACSF slices (black, nine slices from five mice). A low dose of MK801 (2.5 μM, orange, nine slices from three mice) partially restored fEPSP generation. In ACSF without drug, synGLT-1 KO (red, seven slices from three mice) showed very abnormal I/O. Slices from littermate controls exposed to 10 μM MK801 during the recovery period (WT-MK801, blue, eight slices from two mice) showed responses similar to slices from littermate controls that recovered in ACSF alone (WT-ACSF, black). *** = $p < 0.001$ indicates the effect of drug dose in a linear mixed model. **(B)** The glutamate scavenger system GPT/pyruvate partially prevented synaptic transmission deficits in synGLT-1 KO slices. SynGLT-1 KO slices in the presence of GPT/pyruvate (GPT 10 unit/ml, 10 mM pyruvate, orange, 12 slices from three mice) showed a partially restored input-output relationship compared with slices treated only with pyruvate (red, nine slices from three mice). *** = $p < 0.001$ in panel **(B)** indicates effect of GPT in a linear mixed model. **(C)** Extracellular amino acids following 60 min incubation. Extracellular medium bathing single slices for the recovery incubation period of 60 min was collected and assayed for amino acids. The medium volume was 3 ml. No reliable differences were noted in extracellular glutamate, aspartate, or glutamine concentrations between synGLT-1 KO and wild-type littermate slices.

across animals of the same genotype. The number of pooled values was equalized across animals (∼20). Normality test indicated failure by the Anderson-Darling, D'Agostino and Pearson, Shapiro-Wilke, and Kolmogorov-Smirnov tests. Thus, the Mann-Whitney test was used to determine the significance of the difference between the median values from wild-type vs. synGLT-1 KO tissue. Graphpad Prism (version 9 for MacOS) was used to perform these tests and to plot the graphs.

The frequency of encounters with mitochondria within presynaptic terminals of excitatory synapses was assessed as described above for assessing the frequency of encounters with GLT-1 immunoreactivity.

Mitochondrial Cristae Density

Mitochondria occurred in both GLT-1 labeled and unlabeled axon terminals forming excitatory synapses. The average distance between cristae was calculated to assess cristae density. The distance, d, spanning from one crista to another or two neighboring cristae within a single mitochondrion was measured, using ImageJ's tool for measuring the lengths of line segments (version 2.1.0/1.53c). The average distance between neighboring cristae of a mitochondrion was calculated based on the following formula: Average distance = d/(number of cristae-1). The average distance values of mitochondria were pooled across animals of the same genotype (∼30 mitochondria per animal), then compared across genotype groups using the Mann-Whitney test, as described above. The pooled samples were equalized in sample size across animals.

Error bars used in the data presentation in the figures represent the standard error of the mean (SEM) throughout.

Drugs and Reagents

All salts and glucose for buffers and other reagents were obtained from Sigma-Aldrich, except as noted. MCI-186 was obtained from Cayman Chemical. MK801 was obtained from

Tocris. D-APV was from Tocris and Abcam. DNQX was from Tocris.

RESULTS

Hippocampal Field Excitatory Postsynaptic Potentials in Neuron- and Astrocyte-Specific GLT-1 KO

We first recorded field excitatory postsynaptic potentials (fEPSPs) in the CA1 region of gfapGLT-1 KO and synGLT-1 KO mice, and compared responses with wild-type littermate controls (WT). Schaeffer collaterals were stimulated and fEPSPs from pyramidal neurons in the CA1 region of the hippocampus of 30–40 weeks old gfapGLT-1 KO (**Figure 1A**) and WT mice were recorded. fEPSP slope [**Figure 1C**; LMM, t = 3.15, p = 0.0017, interaction of stimulation intensity and genotype, n = 18 slices from seven animals (WT), 18 slices from five animals (KO)] was slightly, but significantly increased, compared to WT mice. We next measured field responses in 25–40 weeks old synGLT-1 KO (**Figure 1B**) and WT mice and found that the fEPSP slope [**Figure 1D**; LMM, t = 5.393, p = 2.28e-07, n = 10 slices from four animals (WT), nine slices from seven animals (KO)] of the neuronal GLT-1 KO was significantly decreased compared to WT mice. As such, the loss of GLT-1 from presynaptic terminals but not from astrocytes appeared to negatively affect synaptic transmission in the CA1 region of hippocampal slices.

Age-Dependent Decrease of fEPSP in the Neuronal GLT-1 KO

Since we observed abnormal field responses in the synGLT-1 KO but not gfapGLT-1 KO mice, we next focused on characterizing this defect in the synGLT-1 KO further. We recorded fEPSPs of synGLT-1 KO and WT mice at 10 (**Figures 2A,C**) and 20 weeks of age (**Figures 2B,D**). At 10 weeks of age, we found that fEPSP slope [LMM, interaction of stimulation and genotype, $t = -1.93$, $p = 0.053$; $n = 15$ slices from five animals (WT), $n = 15$ slices from four animals (KO)] was not significantly decreased in synGLT-1 KO, as compared to WT mice (**Figures 2A,C**). In contrast, at 20 weeks, fEPSP slope ($t = -5.34$, p = 1.45e-7) was significantly reduced (53% reduction) in the synGLT-1 KO compared with the WT [n = 18 slices from six animals (WT), 17 slices from five animals (KO); **Figures 2B,D**]. These results suggest an age-dependent defect in fEPSP generation in synGLT-1 KO hippocampal slices.

The Expression of Cre Does Not Decrease fEPSPs

To exclude the possibility that the decrease in fEPSPs in synGLT-1 KO that we observed was due to expression of Cre-recombinase, *per se*, we used synapsin-Cre control mice, i.e., animals that express Cre, but on a WT genetic background, and their WT littermates (synCre+ and synCre-). Expression of Cre caused a small, but significant, increase in fEPSP slope [**Figure 2E**; LMM, interaction of stimulation and genotype, t = 2.48, p = 0.02; n = 10 slices from three animals (WT), n = 11 slices from four animals (KO)] in slices from animals at 20 weeks of age. These data indicate that the decrease in fEPSPs in synGLT-1 KO is not the result of Cre-recombinase expression, but rather, from a loss of GLT-1 from the presynaptic terminal.

Presynaptic Fiber Recruitment of Schaeffer Collaterals and Paired Pulse Facilitation Are Largely Unaffected in synGLT-1 KO

The fiber volley reflects the excitation of axons projecting into the dendritic field recording site and produces a small peak that occurs prior to the fEPSP (Otmakhova and Lisman, 1999; Kim et al., 2012; Tani et al., 2014). The amplitude of this phenomenon did not significantly differ in 10 weeks old synGLT-1 KO mice, as compared to WT [**Figure 3A**; LMM, interaction of stimulation and genotype, t = -0.12, p = 0.91, n = 15 slices from five animals (WT), n = 15 slices from four animals (KO)]. At 20 weeks of age, the fiber volley was slightly but significantly increased in synGLT1-KO mice compared to WT [**Figure 3B**; LMM, interaction of stimulation and genotype, t = 6.865 p = 7.15e-11, n = 18 slices from six animals (WT), n = 17 slices from five animals (KO)], indicating that the presynaptic fiber recruitment of Schaeffer collaterals is, at most, mildly affected by the loss of presynaptic neuronal GLT-1. Paired pulse ratio (PPR) is an important measure of presynaptic function, sensitively reflecting changes in calcium dynamics in the presynaptic terminal (Schulz et al., 1994, 1995; Wu and Saggau, 1994; Mukhamedyarov et al., 2006; Krall et al., 2020), and may be influenced by fast inhibitory transmission as well (Nathan et al., 1990; Nathan and Lambert, 1991; Stuart and Redman, 1991). We found no significant difference in PPR in 10 weeks [p = 0.0928, n = 22 slices from six animals (WT), n = 17 slices from five animals (KO)] and 20 weeks old synGLT-1 KO mice compared to WT [p = 0.6455, n = 18 slices from six animals (WT), n = 16 slices from five animals (KO); **Figure 3C**]. The lack of a change in PPR suggests that the impairment of fEPSP generation observed in the synGLT-1 KO hippocampal slices is not due to a compromise of presynaptic function, for example, by impaired calcium dynamics (Wu and Saggau, 1994; Dittman et al., 2000; Mukhamedyarov et al., 2006).

Glutamate Imaging in Hippocampal Slices of Neuronal GLT-1 KO

Expression of GLT-1 in axon terminals might be required to maintain stores of the neurotransmitter glutamate, and also might participate in the clearance of glutamate from the extracellular space after release. We tested whether stimulus-evoked extracellular glutamate accumulation was affected by neuronal GLT-1 KO by measuring stimulus-evoked changes in extracellular glutamate using a FRET-based glutamate sensor (**Figure 4**). These glutamate imaging studies revealed that evoked glutamate release was only marginally, but not significantly, reduced in 20 weeks old synGLT-1 KO compared to WT mice [Mann-Whitney U 87; p = 0.202 n = 17 slices from five animals (WT), n = 16 slices from (KO); **Figure 4C**], and there was no difference in evoked glutamate release in synGLT-1 KO mice compared to WT mice at 10 weeks [Mann-Whitney U 106; $p = 0.806$ $n = 15$ slices from five animals (WT), $n = 15$ slices from four animals (KO)]. These results provide additional evidence that the impairment of fEPSP generation in the synGLT-1 KO slices is not due to a presynaptic deficit of neurotransmitter glutamate, and also argue against a significant role for neuronal GLT-1 in glutamate clearance.

MK801 in the Recovery ACSF Restores fEPSP Generation

We intended to use patch clamp recordings to further pursue the cellular basis of the age-dependent deficit in synaptic transmission observed in the synGLT-1 KO. Upon optical assessment after slice preparation and a 1 h resting period, pyramidal cells in the stratum radiatum of the CA1 region in acute brain slices of 20 weeks old synGLT-1 KO were found to be significantly swollen compared to WT littermates, and it was not possible to obtain stable patch-clamp recordings from them. Impaired glutamate uptake can lead to excessive activation of excitatory amino acid receptors and cell death, a process known as excitotoxicity (Rothman and Olney, 1986; Choi, 1988; Meldrum and Garthwaite, 1990; Lipton and Rosenberg, 1994). Excitotoxicity produces an initial phase of cell swelling of neurons that precedes cell death (Choi, 1985; Choi et al., 1987; Ramnath et al., 1992; Churchwell et al., 1996). Kynurenic acid is an antagonist of all ionotropic glutamate receptors and is known to prevent excitotoxicity (Ganong et al., 1983; Foster et al., 1984; Espanol et al., 1994; Pozzo Miller et al., 1994; Urenjak and Obrenovitch, 2000; Feher et al., 2019; Toth et al., 2021). We added kynurenic acid (3 mM) to the recovery ACSF after slicing to attempt to prevent possible excitotoxicity in the synGLT-1 KO acute hippocampal slices. We then compared fEPSPs of 20 weeks old synGLT-1 KO and WT mice with or without kynurenic acid treatment (**Figures 5A–C**). In synGLT-1 KO animals kynurenic acid significantly increased fEPSP slope from 0.039 ± 0.0106 mV/ms (synGLT1 ACSF) to 0.235 ± 0.047 mV/ms (synGLT1 KYNA) [LMM, interaction of stimulation and dose effect, $t = 12.20$, $p = 2e\text{-}16$; $n = 16$ slices from four animals (KO ACSF), $n = 16$ slices from four animals (KO KYNA)], $n = 15$ slices from four animals (WT KYNA; **Figure 5B**) representing 34% of the WT KYNA fEPSP slope (0.699 ± 0.117mV/ms) at 0.3 mA stimulation. The partial recovery of function produced by kynurenic acid in the recovery ACSF was consistent with the possibility that excitotoxic injury might be occurring in the synGLT-1 KO slices.

To ascertain whether the effect of kynurenic acid was due to blocking glutamate receptors we tested the effects of the competitive NMDA receptor antagonist 2-amino-5-phosphonovalerate (D-APV; 50 μM; Davies et al., 1981; Kass et al., 1989) alone or in combination with DNQX (20 μM), which is a competitive inhibitor of non-NMDA receptors (Honore et al., 1988; Sheardown et al., 1990). Surprisingly, APV, alone [Mann-Whitney U = 8, $p = 0.0719$, $n = 17$, 3; 0.3 mA; $n = 3$ slices from one animal (KO plus APV)] or in combination with DNQX [Mann-Whitney U = 29, $p = 0.0553$, $n = 17$, 7; 0.3 mA; $n = 7$ slices from two animals (KO plus APV/DNQX, $n = 17$ slices from four animals (KO no drugs)], did not produce a significant recovery of the fEPSP slope in synGLT-1 KO mice (**Figure 5C**). Kynurenic acid itself did not have a significant effect on the fEPSP in slices from WT animals [$n = 14$ slices from five animals WT), $n = 16$ slices from five animals (WT plus KYNA)]. Since kynurenic acid was used here at 3 mM, well above its affinity for glutamate receptors (Albuquerque and Schwarcz, 2013), we considered the possibility that other actions of kynurenic acid might be involved, for example, oxygen-free radical scavenging properties (Lugo-Huitron et al., 2011; Gonzalez Esquivel et al., 2017). Therefore, we tested a membrane-permeable reactive oxygen species (ROS) scavenger (MCI-186, 33 μM; Wu et al., 2006; Schurr and Gozal, 2012). Addition of this compound to the recovery ACSF (Mann-Whitney U = 23, $p = 0.8421$, $n = 17$, 3; 0.3 mA; $n = 3$ slices from one animal) did not improve neurotransmission in synGLT-1 (**Figure 5C**). We found that kynurenic acid at 500 μM had no effect (data not shown), making it unlikely that it could be acting at nicotinic receptors, to which kynurenic acid binds with high affinity (Albuquerque and Schwarcz, 2013).

Since excitotoxicity in acute slices is primarily due to excessive activation of NMDA receptors (Feig and Lipton, 1990), we tested MK801, a non-competitive NMDA receptor antagonist. We found that 10 μM MK801 in the recovery medium promoted full recovery of fEPSP generation (WT-ACSF, $n = 9$ slices from five animals, WT-MK801, $n = 8$ slices from two animals, synGLT-1 KO MK801 10 μM, $n = 11$ slices from four animals; **Figure 6A**), and 2.5 μM was also effective (synGLT-1 KO MK801 2.5 μM, 9 slices from three animals), producing 65% recovery of the fEPSP slope [LMM, interaction of stimulation and dose effect, $t = -10.43$, $p = 2e\text{-}16$ compared with WT MK801]. These data suggested that excitotoxic injury prevented functional recovery of acute slices derived from the synGLT-1 KO. Excitotoxicity might be due to excess accumulation of excitatory amino acids in the extracellular medium or increased sensitivity to normal extracellular glutamate concentrations due to metabolic compromise (Novelli et al., 1988; Henneberry et al., 1989a,b). To test the possibility that excitotoxic injury in the synGLT-1 slices might be due to extracellular glutamate, we used a glutamate scavenging system (O'Brien and Fischbach, 1986; Blitzblau et al., 1996) to remove glutamate from the extracellular medium (**Figure 6B**). We found that glutamate pyruvate transaminase (GPT) in combination with pyruvate added to the recovery medium provided partial protection and recovery of fEPSP generation [34%; LMM, interaction of stimulation and drug, $t = -5.66$, $p = 7.86e\text{-}8$; $n = 9$ slices from three animals (KO pyruvate); $n = 12$ slices from three animals (KO GPT/pyruvate); **Figure 6B**]. Pyruvate alone had no effect (**Figure 6B**), nor did α-ketoglutarate, one of the products of the reaction driven by GPT (data not shown). We assayed excitatory amino acids in the medium bathing the slices during the recovery period. Both glutamate and aspartate were detectable, but there was no significant difference in either in the media bathing the synGLT-1 KO and WT control slices following a 60-min incubation (**Figure 6C**; pooled data from three separate experiments for each genotype, medium incubated with each of four slices assayed individually/genotype/experiment × 3 experiments = 12 slices/genotype; 30–47 weeks old animals), consistent with the normal expression of astrocytic GLT-1 in both the synGLT-1 KO and WT control slices.

Ultrastructural Changes in Mitochondria in the CA1 Region in synGLT-1 KO Mice

We have previously reported that synGLT-1 KO mice at 8–10 weeks of age had increased density of mitochondria in synaptic terminals in the cortex and hippocampus, and increased cristae packing density in these two regions as well as in the striatum, possibly an adaptive response to decreased access to glutamate as a substrate for synaptic mitochondrial metabolism (McNair et al., 2019, 2020). Since the electrophysiological phenotype we observed occurred in slices from 20 weeks old mice, we wanted to determine whether similar ultrastructural changes were present in this older cohort of mice (**Figure 7**).

Electron microscopic analysis verified the genotype of the animals to be WT vs. synGLT-1 KO (**Figures 7A–C**). Astrocytic immunocytochemical labeling for GLT-1a was intense for both genotypes within WT and synGLT-1 tissue of the stratum radiatum of dorsal CA1 of the hippocampus (**Figures 7A,B**). The HRP-DAB reaction product was associated with the astrocytic plasma membrane and had diffused intracellularly, but leaving the lumen of intracellular organelles, such as vesicles and mitochondria unlabeled. In comparison, GLT-1 immunoreactivity within axon terminals was less intense but still identifiable, and distinctly more electron-dense than the neighboring mitochondria. Most axon terminals in the vicinity exhibited equal electron density across pre- and post-synaptic sides and no greater electron density than mitochondria or postsynaptic densities (PSDs). Such axon terminals were categorized as unlabeled (UL). Using these criteria to judge immunoreactivity in a blinded analysis, the frequency of encounter with GLT-1 immunoreactive axon terminals forming excitatory synapses was significantly higher for tissue from WT animals (median value of 3 per 10 synapses) than for tissue from synGLT-1 KO animals (median value of 0 per 10 synapses) [$p < 0.0001$, Mann-Whitney U 168.5; $n = 3$ animals per genotype, $n = 67$ sections (WT), $n = 60$ sections (KO)]. As further validation of the genotype, tissue of the WT animals, but not of the synGLT-1 KO animals exhibited axons of passage, without synaptic contacts but with GLT-1 immunoreactivity.

The same electron micrograph sets were used to assess the frequency of mitochondria within axon terminals forming excitatory synapses (**Figure 7D**). This analysis revealed a remarkable similarity across the genotypes ($p > 0.9999$, the median value of 1.500 per 10 synapses for both genotypes; Mann-Whitney U 1800; $n = 60$ for both genotypes). This result indicates that at 20 weeks of age altered excitatory synaptic transmission within the hippocampus of synGLT-1 KO brains did not perturb the size or rate of autophagy of mitochondria (Eskelinen et al., 2011) to culminate in altered mitochondrial presence within synaptic terminals forming excitatory synapses.

The same electron micrograph sets were used to assess the average distances between cristae of mitochondria within axon terminals forming excitatory synapses (**Figure 7E**). This analysis revealed a significant difference in the average distance between neighboring cristae within single mitochondria. The average distance was lower for the synGLT-1 KO tissue (median 40.42 nm, $n = 90$ mitochondria), compared to WT (46.25 nm, $n = 87$ mitochondria). This 17% difference was statistically significant ($p = 0.0008$, Mann-Whitney U 2784). These data show that the changes in cristae density previously reported in 8–10 weeks old mice persist in 20–25 weeks old mice.

Impaired Glutamate Metabolism in Hippocampal Slices of Neuronal GLT-1 KO

To characterize the metabolic compromise present in the synGLT-1 KO slices that might contribute to excitotoxic injury, we performed metabolic labeling studies with ^{13}C enriched glutamate ([U-^{13}C]glutamate). By exposing slices to [U-^{13}C]glutamate and then using mass spectrometry, we were able to measure the ^{13}C label in intracellular glutamate as well as TCA cycle intermediates and derived amino acids (**Figure 8A**). We found a significant decrease in the ^{13}C-labeling of intracellular glutamate [$t = 4.212$, $p = 0.000524$, $n = 10$ WT animals, $n = 10$ KO animals], consistent with the synapsin 1-Cre driven deletion of GLT-1 in neurons and previous studies of the impact of knockout of GLT-1 in neurons on uptake radiolabeled glutamate into synaptosomes (Petr et al., 2015; Rimmele and Rosenberg, 2016; Zhou et al., 2019; McNair et al., 2020). These studies establish that even though neuronal GLT-1 is a small fraction of total brain GLT-1, it is capable of actual transport of glutamate across the plasma membrane of axon terminals, and, in fact, mediates a disproportionately large fraction of uptake of glutamate into synaptosomes when assayed using radiolabeled substrate. A similar conclusion was reached in studies of D-aspartate uptake into hippocampal slices (Furness et al., 2008). As expected from a decrease in glutamate uptake in the synGLT-1 KO slices, ^{13}C-labeling of malate [$t = 2.287$, $p = 0.0345$, $n = 10$ (WT), 10 (KO)], aspartate [$i = 4.212$, $p = 0.000524$, $n = 10$ (WT), 10 (KO)], citrate [$t = 3.253$, $p = 0.00441$, $n = 10$ (WT), 10 (KO)], α-ketoglutarate [$t = 2.185$, $p = 0.0423$, $n = 10$ (WT), 10 (KO)] and GABA [$t = 2.231$, $p = 0.0386$, $n = 10$ (WT), 10 (KO)] were likewise significantly decreased. Quantification of intracellular amino acids amounts in the slices (**Figure 8B**) showed decrease in glutamate [$t = 2.547$, $p = 0.0202$, $n = 10$ (WT), 10 (KO)] and aspartate concentrations [$t = 2.833$, $p = 0.0110$, $n = 10$ (WT), 10 (KO)] in the synGLT-1 KO slices, which is in line with previous observations. Taken together, the ultrastructural and metabolic labeling studies confirm that hippocampal slices of synGLT-1 KO mice display the same metabolic phenotype as observed *in vivo* (McNair et al., 2019) and are consistent with the hypothesis that metabolic perturbation caused by the deletion of GLT-1 from axon terminals could drive excitotoxicity in the synGLT-1 KO slices.

DISCUSSION

In this study, we found impairment of synaptic responses in the CA1 region of hippocampal slices from animals with a conditional knockout of GLT-1 in neurons. Field EPSPs were

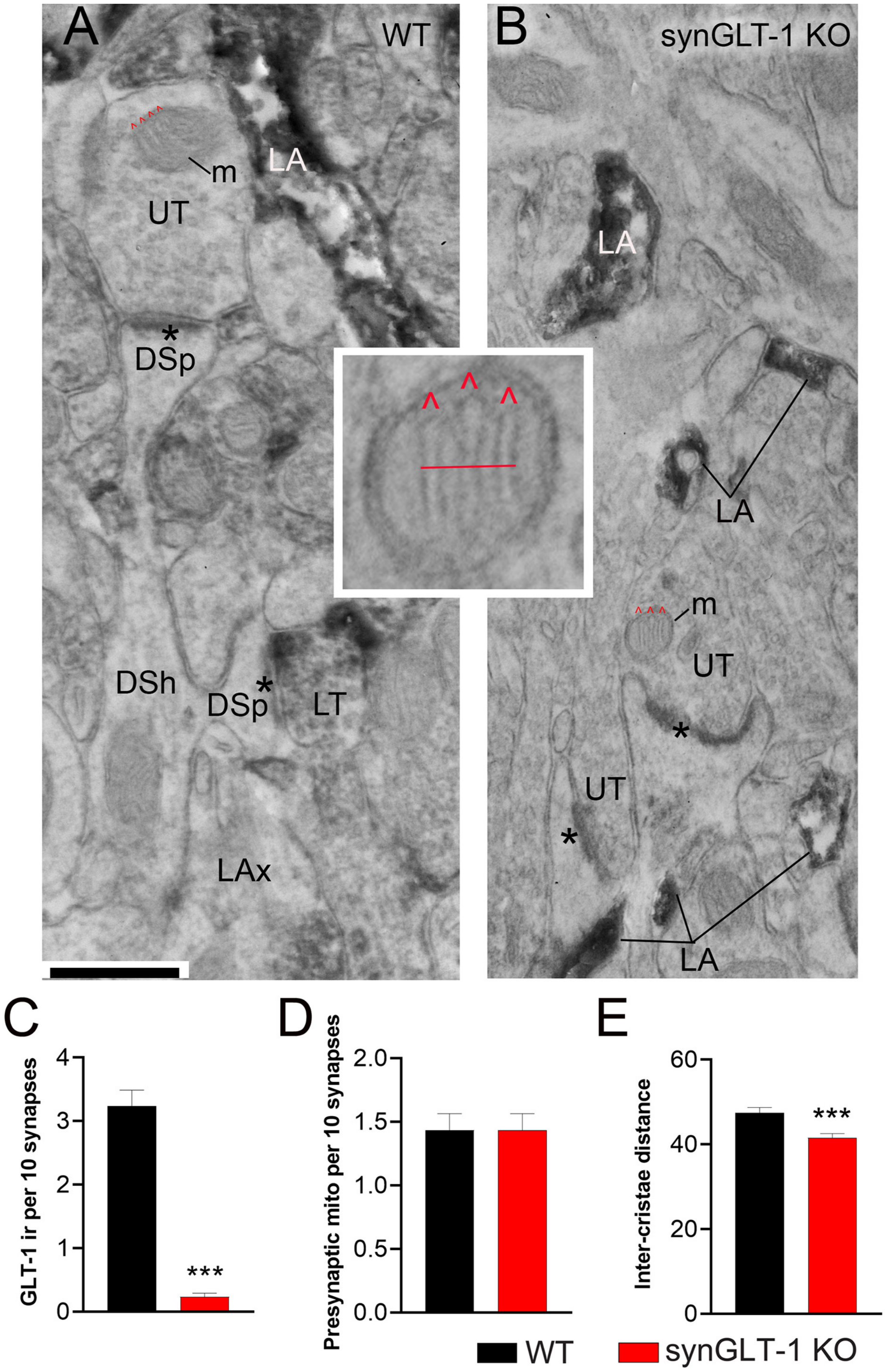

FIGURE 7 | Neuronal GLT-1 knockout decreased inter-cristae distance of presynaptic mitochondria. Panels **(A,B)** show examples of electron micrographs taken from the WT **(A)** vs. synGLT-1 KO **(B)** hippocampus at 22–24 weeks of age. Within the synaptic neuropil of WT animals, only a fraction of axon terminals forming asymmetric synapses with thick PSDs (asterisks; presumably excitatory) upon dendritic spines (DSp) are GLT-1 immunolabeled (LT, abbreviation for "labeled terminal"). Immunolabeling within the axon terminal is evident, based on the diffuse distribution of electron-dense material reflecting the HRP-DAB reaction product. Immunolabeling extends beyond the terminal portion of axons (LAx, abbreviation for "labeled axons"). Axon terminals lacking immunolabeling are labeled as UT (unlabeled terminals). As expected, LT is scarce within KO tissue but both synGLT-1 KO and WT tissue exhibit intense GLT-1 immunolabeling of astrocytic processes (LA, abbreviation for "labeled astrocyte"). DSh = dendritic shaft. Each panel shows examples of mitochondria (m) within axon terminals, with cristae indicated

(*Continued*)

FIGURE 7 | Continued
using the symbol ^ in red. The small panel in the center highlights the presynaptic mitochondrion from panel **(B)**, magnified 4x beyond the magnification *via* the electron microscope, to depict the distance (red line) measured spanning the three cristae. Inter-crista distance was calculated as this distance, divided by the number of cristae minus 1 (3–1 = 2 for this example). Calibration bar = 500 nm. Graphs **(C–E)** show group mean averages of GLT-1 immunoreactivity **(C)**, frequency of occurrence of mitochondria within presynaptic axon terminals forming excitatory synapses **(D)**, and average inter-crista distance of mitochondria within presynaptic axon terminals. For all graph panels, the repeated measure of occurrence of the ultrastructural element per every 10 synapses was pooled across three animals of the same genotype (for **C**, $n = 67$ repeated measures for 670 synapses within WT tissue and $n = 60$ repeated measures for 600 synapses within synGLT-1 KO tissue; for **D**, $n = 60$ repeated measures for 600 synapses each from WT and synGLT-1 KO tissue). For **(C)**, the Mann Whitney t-test revealed significant genotype difference ($p < 0.0001$, Mann Whitney U 168.5). For **(E)**, the inter-crista distance values were pooled across animals of the same genotype ($n = 87$ mitochondria for WT, $n = 90$ mitochondria for synGLT-1 KO). Mann-Whitney test revealed significant genotype difference ($p = 0.0008$, Mann Whitney U 2784) *** = $p < 0.001$.

either absent or decreased in slices from 30 to 50 weeks as well as 20 weeks old animals but were not consistently diminished in slices from 10 weeks old animals. We compared the effect of conditional inactivation of GLT-1 in neurons with conditional inactivation of GLT-1 in astrocytes, and, remarkably, fEPSPs in slices from the astrocytic GLT-1 knockout at 40 weeks were not decreased, compared to wild-type littermates, suggesting an important role of neuronal GLT-1 in the recovery of synaptic function in the CA1 region of hippocampal slices.

CA3 neurons express GLT-1 mRNA at very high levels, perhaps the highest in the brain, whereas CA1 neurons express very low if any GLT-1 mRNA (Berger et al., 2005). Because of the high expression of GLT-1 in CA3 neurons, we expected that the CA3-CA1 synapse would be particularly relevant for studying the effects of deletion of GLT-1 in neurons on synaptic function and synaptic health. In other regions, the expression of GLT-1 in axon terminals might be significantly lower or non-existent, and in these regions, it might be expected that the phenotype we observed by recording in the stratum radiatum might not be present.

Previous studies have shown that GLT-1 is not significantly reduced in the synGLT-1 KO by immunoblot analysis of forebrain lysates (Petr et al., 2015) consistent with the small fraction (5–10%) of total GLT-1 expressed in axon terminals (Furness et al., 2008). Light microscopic (LM) and electron microscopic (EM) immunocytochemical studies focused on the hippocampus showed that at the LM level, there was no obvious loss of GLT-1 immunoreactivity in the hippocampus in the synGLT-1 KO in any region (Petr et al., 2015). At the ultrastructural (EM) level, in the same report, it was shown that there is a ca. 90% reduction in GLT-1 labeling of excitatory axon terminals in the stratum radiatum of synGLT-1 KO animals (Petr et al., 2015). In a subsequent study, it was shown that ^{3}H-L-glutamate uptake is decreased 84% in crude synaptosomes prepared from the hippocampus of synGLT-1 KO animals compared with littermate controls (McNair et al., 2020), consistent with the expression of GLT-1 in axon terminals in the hippocampus (Chen et al., 2004; Furness et al., 2008) and the efficacious deletion of GLT-1 from axon terminals in this region by the use of synapse-Cre mediated recombination (Petr et al., 2015; Zhou et al., 2019). Zhou et al. (2019) also reported that GLT-1 immunoreactivity is not detectably altered at the LM level in the hippocampus in the synGLT-1 KO, but ^{3}H-L-glutamate uptake into crude hippocampal synaptosomes is diminished.

We considered the possibility that persistent tissue damage produced by excitotoxic injury might be contributing to the impairment of functional recovery in the synGLT-1 KO slices. Kynurenic acid, which has been previously used in millimolar concentrations to prevent excitotoxic injury to brain slices during preparation (Mitra and Brownstone, 2012), provided partial functional restoration of function when present at 3 mM during the recovery period. Although the NMDA receptor antagonist D-APV (Paoletti and Neyton, 2007), either alone or together with the non-NMDA glutamate receptor antagonist DNQX (Honore et al., 1988; Sheardown et al., 1990), had no effect, MK801, a non-competitive antagonist (Huettner and Bean, 1988; Chen and Lipton, 1997) was completely protective. Extracellular glutamate scavenging, in the form of GPT plus pyruvate during the recovery period, promoted partial recovery of physiological function in the synGLT-1 KO slices, providing additional evidence that excitotoxic injury blocks recovery of function in the synGLT-1 KO slices. The lack of complete protection might be due to the absence of the scavenging system in the recording medium, or incomplete penetration of GPT and/or pyruvate into the depths of the slice. MK801, which is a non-competitive channel blocker whose washout is at least partially dependent on channel opening (McKay et al., 2013), might provide greater protection than APV because of incomplete washout during the recording period. Other examples of protection of hippocampal slices against excitotoxicity by MK801 but not APV have been reported (Schurr et al., 1995a,b; Schilp et al., 1999; Pringle et al., 2000), as well as a recent observation that MK801, but not APV, downregulates the expression of misfolded isoforms (PrP^{Sc}) of cellular prior protein (PrP^{C}; Zattoni et al., 2021).

Excitotoxicity as a cause of injury in acute slices was reported initially by Feig and Lipton (Feig and Lipton, 1990), and it has been invoked in many subsequent studies as a reason for using glutamate receptor antagonists during slice preparation to block injury and promote recovery (Buskila et al., 2020). Feig and Lipton showed that morphological evidence of injury in guinea pig slices, in particular swelling of neuronal cell bodies, was alleviated by inclusion of ketamine, an NMDA receptor blocker in the recovery medium, or using a medium lacking calcium but with high magnesium (10 mM). Interestingly, they found that the decline in ATP content in acute slices, which had been documented previously (Whittingham et al., 1984), was not affected by either ketamine or low calcium/high magnesium, and suggested that the energy collapse in acute slices might underlie increased vulnerability to excitotoxicity (Novelli et al., 1988; Henneberry et al., 1989a,b). The novelty of the present observations is in finding that heightened vulnerability to excitotoxicity distinguishes synGLT-1 KO slices from slices of *both* WT littermates and of gfapGLT-1 KO slices. This heightened vulnerability might be due to metabolic compromise,

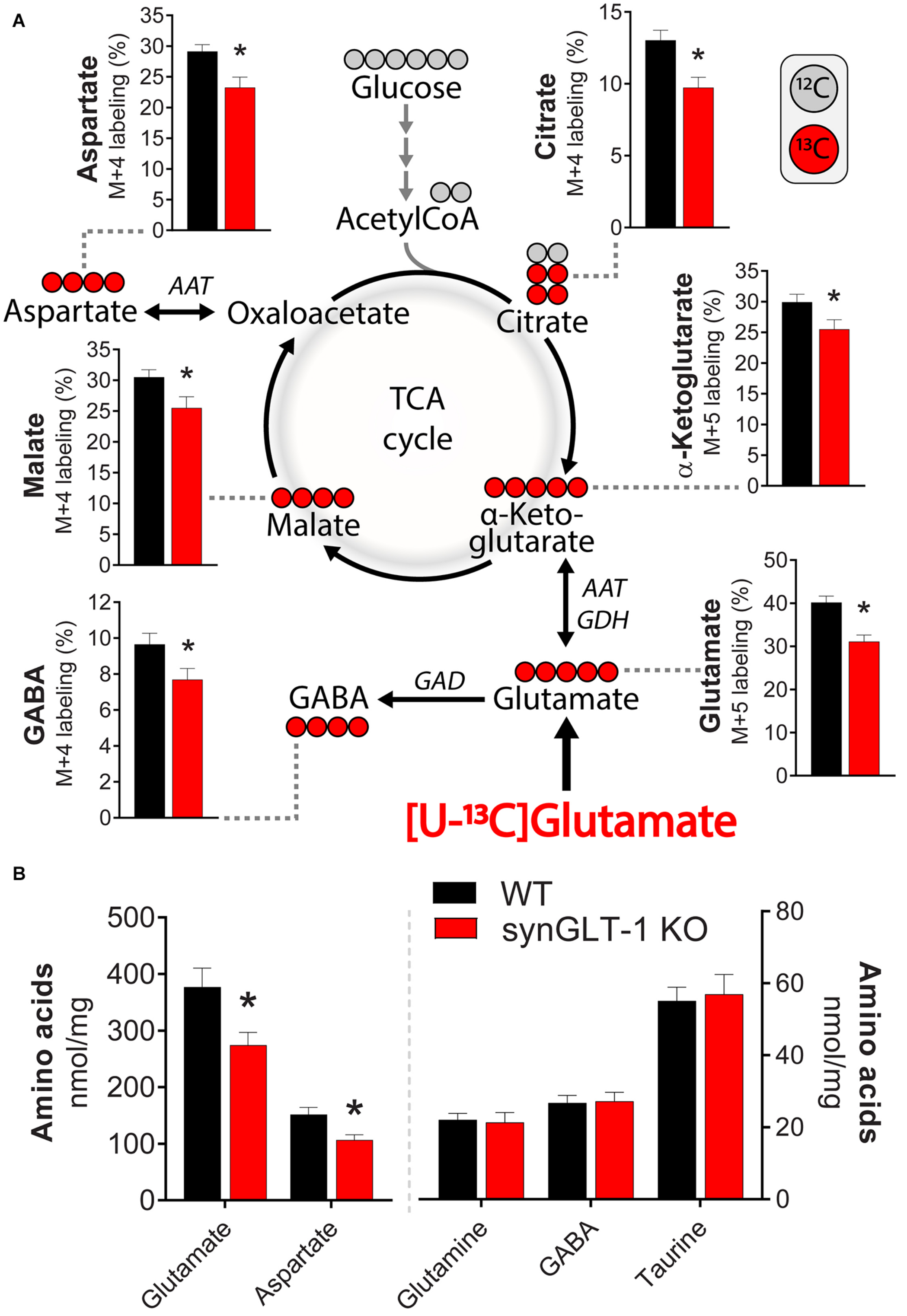

FIGURE 8 | Deletion of neuronal GLT-1 impaired glutamate uptake and glutamate utilization in hippocampal slices. **(A)** Metabolic mapping of [U-^{13}C]glutamate in hippocampal slices of WT mice (black bars) and synGLT-1 KO mice (red bars). The slices were incubated in the presence of 200 μM [U-^{13}C]glutamate in addition to 5 mM D-glucose (^{12}C). Metabolism of ^{13}C enriched substrates will lead to ^{13}C incorporation in TCA cycle metabolites and derived amino acids, visualized by red circles (^{13}C) and gray circles (^{12}C). **(B)** Amino acid content in hippocampal slices of WT mice (black bars) and synGLT-1 KO mice (red bars) incubated with 200 μM [U-^{13}C]glutamate in addition to 5 mM D-glucose. AAT, aspartate aminotransferase; GAD, glutamate decarboxylase; GDH, glutamate dehydrogenase. Mean ± SEM, *n* = 10, each point derived from individual animals, Student's *t*-test with Benjamini-Hochberg correction, *$p < 0.05$. See text for exact p values.

making CA1 neurons more vulnerable to the levels of glutamate normally encountered in acute slices, or to a disturbance of glutamate homeostasis in proximity to post-synaptic NMDA receptors, or to a change in NMDA receptor signaling, or a combination of these abnormalities.

Previous studies have examined the impact of constitutive deletion of GLT-1 in all cells, including both astrocytes and neurons, on synaptic transmission in the CA1 region of hippocampal slices (Tanaka et al., 1997). Of necessity, these studies were performed on animals significantly younger than those used in the present study (5–7 weeks) because GLT-1 pan KO mice have a 50% survival at 6 weeks on the original mixed background (Tanaka et al., 1997). Tanaka et al. (1997) found that the peak concentration of synaptically released glutamate was increased in the pan KO, consistent with an important role for GLT-1 in glutamate clearance from the synaptic cleft. In a subsequent study, NMDA receptor-dependent LTP was found to be impaired in GLT-1 pan KO mice due to excess basal activation of NMDA receptors, which could be rescued by a low concentration of D-APV (Katagiri et al., 2001). More recently, electrophysiological studies have been performed in slices from an astrocytic GLT-1 knockout (Aida et al., 2015) using animals at 12–16 weeks and showed normal synaptic transmission at corticostriate synapses in response to single stimuli, consistent with our observations related to the astrocytic GLT-1 KO reported here in the CA1 region of the hippocampus.

The observation in the present study that slices from synGLT-1 KO animals are functionally impaired due to excitotoxicity, whereas slices from gfapGLT-1 KO animals recover similarly to WT animals is surprising since the defect in clearance of glutamate is expected to be much greater in the astrocytic KO. It may be argued that glutamate transporters located in presynaptic terminals, because of their special localization, make an outsize contribution to glutamate clearance "where it counts" because they are close to the sites of the release of glutamate. However, this view is not consistent with our observations that stimulus-evoked glutamate accumulation was similar between genotypes. An alternative explanation is that the cause of the excitotoxic injury in the synGLT-1 KO slices is not a deficit in glutamate clearance *per se* but rather a metabolic defect related to the absence of GLT-1 in synaptic terminals resulting in increased vulnerability to excitotoxicity in postsynaptic cellular elements (spines, dendrites, cell bodies). Importantly, the impairment of synaptic utilization of glutamate reported previously in synaptosomal preparations from the synGLT-1 (McNair et al., 2019, 2020) was also observed in acute hippocampal slices of the synGLT-1 KO mice in the present studies.

One explanation to consider for the "normal" behavior of slices from gfapGLT-1 KO animals is that the astrocyte-specific knockout is not complete. In a previous publication characterizing the astrocyte-specific and neuron-specific GLT-1 knockouts, it was found that the astrocyte-specific knockout reduced GLT-1 expression by 75–95% (Petr et al., 2015). It is possible that the remainder of GLT-1 in the astrocyte KO is sufficient to provide protection. An observation that might be relevant to this question is that in the light microscopic immunocytochemistry for GLT-1 performed in the astrocytic GLT-1 KO in that study, there were certain cells in the neuropil that stained strongly for GLT-1, despite the KO (Petr et al., 2015). It is possible that these cells make a large contribution to the clearance of glutamate necessary for slice recovery.

The astrocytic GLT-1 KO was induced postnatally using an inducible driver of Cre-recombinase expression, whereas the neuronal GLT-1 KO was driven constitutively by a synapsin-Cre driver, suggesting the possibility that compensatory pathways activated in response to the two types of knockout might be different. However, no evidence was found for upregulation of GLAST, the other major glutamate transporter, in the astrocyte- or neuron-specific knockouts by immunoblot analysis (Petr et al., 2015). Even if residual glutamate clearance activity mediated by persistent expression of GLT-1 or other transporters contributes to slice recovery in the astrocytic GLT-1 KO, that would not explain why the neuronal knockout, which by immunoblot analysis does not delete enough GLT-1 to be readily detectable on immunoblot analysis (Petr et al., 2015), produces the impairment of recovery that it does, given that astrocytic glutamate clearance is still intact. The issue may not be glutamate clearance *per se* but some other factor, perhaps related to a metabolic or signaling function of GLT-1 expressed in axon terminals.

It is conceivable that the postnatal exposure to tamoxifen in some way provides the slices from adult astrocytic GLT-1 KO protection against the excitotoxic injury observed in the neuronal GLT-1 KO. However, such long-term protection has never been demonstrated. Instead, there is literature demonstrating an acute beneficial effect of tamoxifen in OGD in a brain slice model (Wakade et al., 2008), focal ischemia in the CNS (Zhang et al., 2005, 2007, 2009), and manganese toxicity (Lee et al., 2009a,b; Pajarillo et al., 2018). In our studies, the tamoxifen is administered to gfapGLT-1 KO pups at least 9–10 weeks prior to the age when slices are taken for experiments. It is unlikely that the normal recovery of gfapGLT-1 KO slices is due to an enduring effect of tamoxifen exposure. In any case, even if that were true, the unexpected, heightened vulnerability of synGLT-1 KO slices to excitotoxicity would not be explained.

The "WT controls" used in most experiments in this study are flox controls (GLT-$1^{flox/flox}$) from the same litter. Conceivably insertion of loxP cassettes has an effect on gene expression and function. Breeding to produce Cre negative and flox negative (GLT-$1^{+/+}$) littermates of animals to serve as controls for test animals that are homozygous floxed and expressing Cre (GLT-$1^{flox/flox}$; Cre-recombinase+) is very inefficient, because of low yields. The breeding scheme we have chosen produces 50% test animals and 50% animals used as littermate controls and allows for the testing of the effects of Cre-mediated excision on a constant genetic background (GLT-$1^{flox/flox}$). This approach requires additional experiments to test the effects of Cre recombinase expression itself, which we have done testing slices from wild-type animals (GLT-$1^{+/+}$) compared with synapsin-Cre expressing animals on a wild-type background (GLT-$1^{+/+}$;Syn-Cre; SynCre+ vs. SynCre- in **Figure 2E**). Of note, there is not a significant difference between the fEPSP generation in slices from GLT-$1^{flox/flox}$

animals (**Figures 1**, **2**, **5**, **6**) and GLT-1$^{+/+}$ animals (Syn-Cre- in **Figure 2**).

GLT-1 has been shown to physically interact with multiple mitochondrial proteins as well as enzymes involved in glycolysis, presumably by one or more scaffolding proteins that have yet to be identified (Genda et al., 2011). It has been suggested that this association between GLT-1 and proteins involved in energy production serves the function of localizing energy production close to sites of GLT-1 mediated transport, which is highly energy consuming, and possibly to provide glutamate as a fuel for mitochondrial metabolism (Robinson et al., 2020). The assumption has been that this association takes place in astrocytes, but recent data (McNair et al., 2019, 2020) and the present studies raise the question of whether these associations are taking place in neurons. This question has, as yet, not been directly addressed.

In two previous studies (McNair et al., 2019, 2020), we analyzed the prevalence and cristae density of mitochondria in axon terminals, because morphological differences such as cristae density are reflective of the efficiency of mitochondrial metabolism, including ATP production (Leveille et al., 2017). As was observed for the hippocampus at 8–10 weeks of age (McNair et al., 2019), the hippocampus of animals at 22–24 weeks of age in the present study revealed a decrease in the inter-cristae distance within presynaptic mitochondria for the synGLT-1 KO animals, relative to WT littermates (**Figure 7E**). The inter-cristae distance may have been influenced not only by the genotype but also by the age: the measured values were less for both genotypes at 22–24 weeks of age, compared to the distances observed at 8–10 weeks of age. However, since the tissues of the two age groups were not processed jointly for electron microscopic analysis, we cannot rule out the possibility that the age difference was due to unintentional differences in tissue preparation for electron microscopy. The results suggest that the loss of GLT-1 within axon terminals may be compensated by increased efficiency of the mitochondrial TCA cycle and ATP production (Gomes et al., 2011; Cogliati et al., 2013; Leveille et al., 2017; McNair et al., 2019).

In contrast to the previous study in which we analyzed the impact of neuronal GLT-1 KO upon the dorsal hippocampus at 8–10 weeks of age (McNair et al., 2020), neuronal GLT-1 KO at 22–24 weeks of age (this study) no longer resulted in an increase of the presynaptic mitochondrial frequency, relative to the frequency measured in the CA1 region of the hippocampus of WT littermates (**Figure 7D**). The difference observed in mitochondrial frequency in axon terminals in the synGLT-1 KO at 20 weeks and 10 weeks in comparison with control littermates is unlikely to have resulted from subtle unintentional differences in tissue processing because differences in tissue handling could not have caused differential disappearance or appearance of axons or of mitochondria postmortem or during transcardial perfusion of animals to fix brain tissue. The difference across the ages could reflect developing compensation for the metabolic defect known to occur in the synGLT-1 KO mice. Early on, before compensation for this defect is fully developed, more mitochondria might be trafficked to the terminals, whereas at older ages, some form of metabolic compensation may have occurred, so that the mitochondria traffic into the terminals does not have to be increased. One could explain, potentially, the age dependence of the phenomenon of increased vulnerability to excitotoxicity of slices from the synGLT-1 KO at 20 weeks of age compared with 8–10 weeks of age by the relative decrease in mitochondria in the terminals at 20 weeks of age compared with 10 weeks of age. The increased density of mitochondria in terminals at 10 weeks may allow the slices to cope with the insult of slice preparation more readily than they are able to at 20 weeks of age.

The present study implicates neuronal GLT-1 in regulating the vulnerability of neurons in the CNS to excitotoxicity, which has long been thought to play an important role in acute and chronic neurodegenerative disorders (Lewerenz and Maher, 2015; Choi, 2020). The work presented here suggests that the hippocampal slice preparation provides a useful model system for the study of the metabolic role of GLT-1 expressed in neurons and the consequences of interfering with it. The importance of neuronal GLT-1 in regulating the vulnerability of CA1 neurons to excitotoxicity in hippocampal slices raises the possibility that there are pathways that have been little explored that may play a determinative role in devastating neurodegenerative disorders and that need to be better understood.

DATA AVAILABILITY STATEMENT

The raw data supporting the conclusions of this article will be made available by the authors, without undue reservation.

ETHICS STATEMENT

The animal study was reviewed and approved by Children's Hospital Boston Institutional Animal Care and Use Committee.

AUTHOR CONTRIBUTIONS

TR, SL, JA, AR, BA, DS, CA, CD, and PR contributed to the design of experiments and analysis and interpretation of data. PR, TR, CD, JA, BA, and CA wrote the manuscript. PR, TR, CD, JA, BA, CA, and DS edited and revised the manuscript. TR, SL, CA, JA, EW, and JW performed experiments.

FUNDING

This work was supported, in part, by National Institute of Health grants P30 HD018655, RO1 NS066019, R21 MH104318, R01 EY027881, R01 NS113499, R01 AG006173, and the Vulnerable Brain Project. The Deutsche Forschungsgemeinschaft provided a research fellowship to TR to support this work.

ACKNOWLEDGMENTS

Special thanks to Drs. Elias Aizenman and Moritz Armbruster for constructive feedback on the manuscript. TR acknowledges the Deutsche Forschungsgemeinschaft for granting a research fellowship to support this work. CA acknowledges the help of Morgan Pierce Lange and Ikponmwosa Pat-Osagie. We are grateful to Dr. Jeff Rothstein for the generous gift of the monoclonal anti-GLT-1a antibody.

REFERENCES

Aarts, E., Verhage, M., Veenvliet, J. V., Dolan, C. V., and van der Sluis, S. (2014). A solution to dependency: using multilevel analysis to accommodate nested data. *Nat. Neurosci.* 17, 491–496. doi: 10.1038/nn.3648

Aida, T., Yoshida, J., Nomura, M., Tanimura, A., Iino, Y., Soma, M., et al. (2015). Astroglial glutamate transporter deficiency increases synaptic excitability and leads to pathological repetitive behaviors in mice. *Neuropsychopharmacology* 40, 1569–1579. doi: 10.1038/npp.2015.26

Albuquerque, E. X., and Schwarcz, R. (2013). Kynurenic acid as an antagonist of alpha7 nicotinic acetylcholine receptors in the brain: facts and challenges. *Biochem. Pharmacol.* 85, 1027–1032. doi: 10.1016/j.bcp.2012.12.014

Andersen, J. V., Markussen, K. H., Jakobsen, E., Schousboe, A., Waagepetersen, H. S., Rosenberg, P. A., et al. (2021a). Glutamate metabolism and recycling at the excitatory synapse in health and neurodegeneration. *Neuropharmacology* 196:108719. doi: 10.1016/j.neuropharm.2021.108719

Andersen, J. V., Christensen, S. K., Westi, E. W., Diaz-delCastillo, M., Tanila, H., Schousboe, A., et al. (2021b). Deficient astrocyte metabolism impairs glutamine synthesis and neurotransmitter homeostasis in a mouse model of Alzheimer's disease. *Neurobiol. Dis.* 148:105198. doi: 10.1016/j.nbd.2020.105198

Andersen, J. V., Nissen, J. D., Christensen, S. K., Markussen, K. H., and Waagepetersen, H. S. (2017a). Impaired hippocampal glutamate and glutamine metabolism in the db/db mouse model of type 2 diabetes mellitus. *Neural Plasticity* 2017:2107084. doi: 10.1155/2017/2107084

Andersen, J. V., Christensen, S. K., Aldana, B. I., Nissen, J. D., Tanila, H., and Waagepetersen, H. S. (2017b). Alterations in cerebral cortical glucose and glutamine metabolism precedes amyloid plaques in the APPswe/PSEN1dE9 mouse model of Alzheimer's disease. *Neurochem. Res.* 42, 1589–1598. doi: 10.1007/s11064-016-2070-2

Bennett, J. P., Jr., Logan, W. J., and Snyder, S. H. (1972). Amino acid neurotransmitter candidates: sodium-dependent high-affinity uptake by unique synaptosomal fractions. *Science* 178, 997–999. doi: 10.1126/science.178.4064.997

Berger, U. V., DeSilva, T. M., Chen, W., and Rosenberg, P. A. (2005). Cellular and subcellular mRNA localization of glutamate transporter isoforms GLT1a and GLT1b in rat brain by *in situ* hybridization. *J. Comp. Neurol.* 492, 78–89. doi: 10.1002/cne.20737

Berger, U. V., and Hediger, M. A. (1998). Comparative analysis of glutamate transporter expression in rat brain using differential double *in situ* hybridization. *Anat. Embryol. (Berl)* 198, 13–30. doi: 10.1007/s004290050161

Bergles, D. E., Diamond, J. S., and Jahr, C. E. (1999). Clearance of glutamate inside the synapse and beyond. *Curr. Opin. Neurobiol.* 9, 293–298. doi: 10.1016/s0959-4388(99)80043-9

Bezzi, P., Vesce, S., Panzarasa, P., and Volterra, A. (1999). Astrocytes as active participants of glutamatergic function and regulators of its homeostasis. *Adv. Exp. Med. Biol.* 468, 69–80. doi: 10.1007/978-1-4615-4685-6_6

Blitzblau, R., Gupta, S., Djali, S., Robinson, M. B., and Rosenberg, P. A. (1996). The glutamate transport inhibitor L- trans-pyrrolidine-2,4-dicarboxylate indirectly evokes NMDA receptor mediated neurotoxicity in rat cortical cultures. *Eur. J. Neurosci.* 8, 1840–1852. doi: 10.1111/j.1460-9568.1996.tb01328.x

Boisgontier, M. P., and Cheval, B. (2016). The anova to mixed model transition. *Neurosci. Biobehav. Rev.* 68, 1004–1005. doi: 10.1016/j.neubiorev.2016.05.034

Buskila, Y., Bellot-Saez, A., Kekesi, O., Cameron, M. A., and Morley, J. W. (2020). "Extending the life span of acute neuronal tissue for imaging and electrophysiological studies," in *Basic Neurobiology Techniques*, ed N. J. D. Wright (USA: Humana Press), 235–259. doi: 10.1007/978-1-4939-9944-6_10

Buskila, Y., Breen, P. P., Tapson, J., van Schaik, A., Barton, M., and Morley, J. W. (2014). Extending the viability of acute brain slices. *Sci. Rep.* 4:5309. doi: 10.1038/srep05309

Casper, K. B., Jones, K., and McCarthy, K. D. (2007). Characterization of astrocyte-specific conditional knockouts. *Genesis* 45, 292–299. doi: 10.1002/dvg.20287

Chen, H. S., and Lipton, S. A. (1997). Mechanism of memantine block of NMDA-activated channels in rat retinal ganglion cells: uncompetitive antagonism. *J. Physiol.* 499, 27–46. doi: 10.1113/jphysiol.1997.sp021909

Chen, W., Mahadomrongkul, V., Berger, U. V., Bassan, M., DeSilva, T., Tanaka, K., et al. (2004). The glutamate transporter GLT1a is expressed in excitatory axon terminals of mature hippocampal neurons. *J. Neurosci.* 24, 1136–1148. doi: 10.1523/JNEUROSCI.1586-03.2004

Choi, D. W. (1985). Glutamate neurotoxicity in cortical cell culture is calcium dependent. *Neurosci. Lett.* 58, 293–297. doi: 10.1016/0304-3940(85)90069-2

Choi, D. W. (1988). Glutamate neurotoxicity and diseases of the nervous system. *Neuron* 1, 623–634. doi: 10.1016/0896-6273(88)90162-6

Choi, D. W. (2020). Excitotoxicity: still hammering the ischemic brain in 2020. *Front. Neurosci.* 14:579953. doi: 10.3389/fnins.2020.579953

Choi, D. W., Maulucci-Gedde, M., and Kriegstein, A. R. (1987). Glutamate neurotoxicity in cortical cell culture. *J. Neurosci.* 7, 357–368. doi: 10.1523/JNEUROSCI.07-02-00357.1987

Churchwell, K. B., Wright, S. H., Emma, F., Rosenberg, P. A., and Strange, K. (1996). NMDA receptor activation inhibits neuronal volume regulation after swelling induced by veratridine-stimulated Na+ influx in rat cortical cultures. *J. Neurosci.* 16, 7447–7457. doi: 10.1523/JNEUROSCI.16-23-07447.1996

Cogliati, S., Frezza, C., Soriano, M. E., Varanita, T., Quintana-Cabrera, R., Corrado, M., et al. (2013). Mitochondrial cristae shape determines respiratory chain supercomplexes assembly and respiratory efficiency. *Cell* 155, 160–171. doi: 10.1016/j.cell.2013.08.032

Collado, M. S., Khabour, O., Fioravante, D., Byrne, J. H., and Eskin, A. (2009). Post-translational regulation of an Aplysia glutamate transporter during long-term facilitation. *J. Neurochem.* 108, 176–189. doi: 10.1111/j.1471-4159.2008.05757.x

Collado, M. S., Lyons, L. C., Levenson, J. M., Khabour, O., Pita-Almenar, J. D., Schrader, L., et al. (2007). *in vivo* regulation of an Aplysia glutamate transporter, ApGT1, during long-term memory formation. *J. Neurochem.* 100, 1315–1328. doi: 10.1111/j.1471-4159.2006.04298.x

Danbolt, N. C. (2001). Glutamate uptake. *Prog. Neurobiol.* 65, 1–105. doi: 10.1016/s0301-0082(00)00067-8

Davies, J., Francis, A. A., Jones, A. W., and Watkins, J. C. (1981). 2-amino-5-phosphonovalerate (2-APV)., a potent and selective antagonist of amino acid-induced and synaptic excitation. *Neurosci. Lett.* 21, 77–81. doi: 10.1016/0304-3940(81)90061-6

Dittman, J. S., Kreitzer, A. C., and Regehr, W. G. (2000). Interplay between facilitation, depression and residual calcium at three presynaptic terminals. *J. Neurosci.* 20, 1374–1385. doi: 10.1523/jneurosci.20-04-01374.2000

Doetschman, T. (2009). Influence of genetic background on genetically engineered mouse phenotypes. *Methods Mol. Biol.* 530, 423–433. doi: 10.1007/978-1-59745-471-1_23

Dulla, C., Tani, H., Okumoto, S., Frommer, W. B., Reimer, R. J., and Huguenard, J. R. (2008). Imaging of glutamate in brain slices using FRET sensors. *J. Neurosci. Methods* 168, 306–319. doi: 10.1016/j.jneumeth.2007.10.017

Eskelinen, E. L., Reggiori, F., Baba, M., Kovacs, A. L., and Seglen, P. O. (2011). Seeing is believing: the impact of electron microscopy on autophagy research. *Autophagy* 7, 935–956. doi: 10.4161/auto.7.9.15760

Espanol, M. T., Xu, Y., Litt, L., Chang, L. H., James, T. L., Weinstein, P. R., et al. (1994). Modulation of edema by dizocilpine, kynurenate and NBQX in respiring brain slices after exposure to glutamate. *Acta Neurochir. Suppl. (Wien).* 60, 58–61. doi: 10.1007/978-3-7091-9334-1_15

Feher, E., Szatmari, I., Dudas, T., Zalatnai, A., Farkas, T., Lorinczi, B., et al. (2019). Structural evaluation and electrophysiological effects of some kynurenic acid analogs. *Molecules* 24:3502. doi: 10.3390/molecules24193502

Feig, S., and Lipton, P. (1990). N-methyl-D-aspartate receptor activation and Ca2+ account for poor pyramidal cell structure in hippocampal slices. *J. Neurochem.* 55, 473–483. doi: 10.1111/j.1471-4159.1990.tb04160.x

Fiala, J. C., Kirov, S. A., Feinberg, M. D., Petrak, L. J., George, P., Goddard, C. A., et al. (2003). Timing of neuronal and glial ultrastructure disruption during brain slice preparation and recovery *in vitro*. *J. Comp. Neurol.* 465, 90–103. doi: 10.1002/cne.10825

Fischer, K. D., Houston, A. C. W., Desai, R. I., Doyle, M. R., Bergman, J., Mian, M., et al. (2018). Behavioral phenotyping and dopamine dynamics in mice with conditional deletion of the glutamate transporter GLT-1 in neurons: resistance to the acute locomotor effects of amphetamine. *Psychopharmacology (Berl).* 235, 1371–1387. doi: 10.1007/s00213-018-4848-1

Fischer, K. D., Knackstedt, L. A., and Rosenberg, P. A. (2020). Glutamate homeostasis and dopamine signaling: implications for psychostimulant addiction behavior. *Neurochem. Int.* 144:104896. doi: 10.1016/j.neuint.2020.104896

Foster, A. C., Vezzani, A., French, E. D., and Schwarcz, R. (1984). Kynurenic acid blocks neurotoxicity and seizures induced in rats by the related brain metabolite quinolinic acid. *Neurosci. Lett.* 48, 273–278. doi: 10.1016/0304-3940(84)90050-8

Frenguelli, B. G. (2019). The purine salvage pathway and the restoration of cerebral ATP: implications for brain slice physiology and brain injury. *Neurochem. Res.* 44, 661–675. doi: 10.1007/s11064-017-2386-6

Frenguelli, B. G., and Dale, N. (2020). Purines: from diagnostic biomarkers to therapeutic agents in brain injury. *Neurosci. Bull.* 36, 1315–1326. doi: 10.1007/s12264-020-00529-z

Furness, D. N., Dehnes, Y., Akhtar, A. Q., Rossi, D. J., Hamann, M., Grutle, N. J., et al. (2008). A quantitative assessment of glutamate uptake into hippocampal synaptic terminals and astrocytes: new insights into a neuronal role for excitatory amino acid transporter 2 (EAAT2).. *Neuroscience* 157, 80–94. doi: 10.1016/j.neuroscience.2008.08.043

Ganat, Y. M., Silbereis, J., Cave, C., Ngu, H., Anderson, G. M., Ohkubo, Y., et al. (2006). Early postnatal astroglial cells produce multilineage precursors and neural stem cells *in vivo*. *J. Neurosci.* 26, 8609–8621. doi: 10.1523/JNEUROSCI.2532-06.2006

Ganong, A. H., Lanthorn, T. H., and Cotman, C. W. (1983). Kynurenic acid inhibits synaptic and acidic amino acid-induced responses in the rat hippocampus and spinal cord. *Brain Res.* 273, 170–174. doi: 10.1016/0006-8993(83)91108-3

Genda, E. N., Jackson, J. G., Sheldon, A. L., Locke, S. F., Greco, T. M., O'Donnell, J. C., et al. (2011). Co-compartmentalization of the astroglial glutamate transporter, GLT-1, with glycolytic enzymes and mitochondria. *J. Neurosci.* 31, 18275–18288. doi: 10.1523/JNEUROSCI.3305-11.2011

Gomes, L. C., Di Benedetto, G., and Scorrano, L. (2011). Essential amino acids and glutamine regulate induction of mitochondrial elongation during autophagy. *Cell Cycle* 10, 2635–2639. doi: 10.4161/cc.10.16.17002

Gonzalez Esquivel, D., Ramirez-Ortega, D., Pineda, B., Castro, N., Rios, C., and Perez de la Cruz, V. (2017). Kynurenine pathway metabolites and enzymes involved in redox reactions. *Neuropharmacology* 112, 331–345. doi: 10.1016/j.neuropharm.2016.03.013

Grieco, S. F., Qiao, X., Zheng, X., Liu, Y., Chen, L., Zhang, H., et al. (2020). Subanesthetic ketamine reactivates adult cortical plasticity to restore vision from amblyopia. *Curr. Biol.* 30, 3591–3603.e8. doi: 10.1016/j.cub.2020.07.008

Hall, J., and Frenguelli, B. G. (2018). The combination of ribose and adenine promotes adenosine release and attenuates the intensity and frequency of epileptiform activity in hippocampal slices: evidence for the rapid depletion of cellular ATP during electrographic seizures. *J. Neurochem.* 147, 178–189. doi: 10.1111/jnc.14543

Hanson, E., Armbruster, M., Lau, L. A., Sommer, M. E., Klaft, Z. J., Swanger, S. A., et al. (2019). Tonic activation of GluN2C/GluN2D-containing NMDA receptors by ambient glutamate facilitates cortical interneuron maturation. *J. Neurosci.* 39, 3611–3626. doi: 10.1523/JNEUROSCI.1392-18.2019

Harno, E., Cottrell, E. C., and White, A. (2013). Metabolic pitfalls of CNS Cre-based technology. *Cell Metab.* 18, 21–28. doi: 10.1016/j.cmet.2013.05.019

Henneberry, R. C., Novelli, A., Cox, J. A., and Lysko, P. G. (1989a). Neurotoxicity at the N-methyl-D-aspartate receptor in energy-compromised neurons. An hypothesis for cell death in aging and disease. *Ann. N Y Acad. Sci.* 568, 225–233. doi: 10.1111/j.1749-6632.1989.tb12512.x

Henneberry, R. C., Novelli, A., Vigano, M. A., Reilly, J. A., Cox, J. A., and Lysko, P. G. (1989b). Energy-related neurotoxicity at the NMDA receptor: a possible role in Alzheimer's disease and related disorders. *Prog. Clin. Biol. Res.* 317, 143–156.

Honore, T., Davies, N., Drejer, J., Fletcher, E. J., Jacobsen, P., Lodge, D., et al. (1988). Quinoxalinediones: potent competitive non-NMDA glutamate receptor antagonists. *Science* 241, 701–703. doi: 10.1126/science.2899909

Hossmann, K. A. (2008). Cerebral ischemia: models, methods and outcomes. *Neuropharmacology* 55, 257–270. doi: 10.1016/j.neuropharm.2007.12.004

Hu, W., MacDonald, M. L., Elswick, D. E., and Sweet, R. A. (2015). The glutamate hypothesis of schizophrenia: evidence from human brain tissue studies. *Ann. N Y Acad. Sci.* 1338, 38–57. doi: 10.1111/nyas.12547

Huang, Z., Khaled, H. G., Kirschmann, M., Gobes, S. M., and Hahnloser, R. H. (2018). Excitatory and inhibitory synapse reorganization immediately after critical sensory experience in a vocal learner. *eLife* 7:e37571. doi: 10.7554/eLife.37571

Huettner, J. E., and Bean, B. P. (1988). Block of N-methyl-D-aspartate-activated current by the anticonvulsant MK-801: selective binding to open channels. *Proc. Natl. Acad. Sci. U S A* 85, 1307–1311. doi: 10.1073/pnas.85.4.1307

Inquimbert, P., Bartels, K., Babaniyi, O. B., Barrett, L. B., Tegeder, I., and Scholz, J. (2012). Peripheral nerve injury produces a sustained shift in the balance between glutamate release and uptake in the dorsal horn of the spinal cord. *Pain* 153, 2422–2431. doi: 10.1016/j.pain.2012.08.011

Inquimbert, P., Moll, M., Latremoliere, A., Tong, C. K., Whang, J., Sheehan, G. F., et al. (2018). NMDA receptor activation underlies the loss of spinal dorsal horn neurons and the transition to persistent pain after peripheral nerve injury. *Cell Rep.* 23, 2678–2689. doi: 10.1016/j.celrep.2018.04.107

Kalivas, P. W. (2009). The glutamate homeostasis hypothesis of addiction. *Nat. Rev. Neurosci.* 10, 561–572. doi: 10.1038/nrn2515

Kass, I. S., Chambers, G., and Cottrell, J. E. (1989). The N-methyl-D-aspartate antagonists aminophosphonovaleric acid and MK-801 reduce anoxic damage to dentate granule and CA1 pyramidal cells in the rat hippocampal slice. *Exp. Neurol.* 103, 116–122. doi: 10.1016/0014-4886(89)90072-1

Katagiri, H., Tanaka, K., and Manabe, T. (2001). Requirement of appropriate glutamate concentrations in the synaptic cleft for hippocampal LTP induction. *Eur. J. Neurosci.* 14, 547–553. doi: 10.1046/j.0953-816x.2001.01664.x

Kim, E., Owen, B., Holmes, W. R., and Grover, L. M. (2012). Decreased afferent excitability contributes to synaptic depression during high-frequency stimulation in hippocampal area CA1. *J. Neurophysiol.* 108, 1965–1976. doi: 10.1152/jn.00276.2011

Kirov, S. A., Sorra, K. E., and Harris, K. M. (1999). Slices have more synapses than perfusion-fixed hippocampus from both young and mature rats. *J. Neurosci.* 19, 2876–2886. doi: 10.1523/JNEUROSCI.19-08-02876.1999

Koenig, J. B., Cantu, D., Low, C., Sommer, M., Noubary, F., Croker, D., et al. (2019). Glycolytic inhibitor 2-deoxyglucose prevents cortical hyperexcitability after traumatic brain injury. *JCI Insight* 5:e126506. doi: 10.1172/jci.insight.126506

Krall, R. F., Moutal, A., Phillips, M. B., Asraf, H., Johnson, J. W., Khanna, R., et al. (2020). Synaptic zinc inhibition of NMDA receptors depends on the association of GluN2A with the zinc transporter ZnT1. *Sci. Adv.* 6:eabb1515. doi: 10.1126/sciadv.abb1515

Kurucu, H., Colom-Cadena, M., Davies, C., Wilkins, L., King, D., Rose, J., et al. (2021). Inhibitory synapse loss and accumulation of amyloid beta in inhibitory presynaptic terminals in Alzheimer's disease. *Eur. J. Neurol.* doi: 10.1111/ene.15043. [Online ahead of print].

Lau, L. A., Noubary, F., Wang, D., and Dulla, C. G. (2017). alpha2delta-1 signaling drives cell death, synaptogenesis, circuit reorganization and gabapentin-mediated neuroprotection in a model of insult-induced cortical malformation. *eNeuro* 4:ENEURO.0316-17.2017. doi: 10.1523/ENEURO.0316-17.2017

Lee, E. S., Yin, Z., Milatovic, D., Jiang, H., and Aschner, M. (2009a). Estrogen and tamoxifen protect against Mn-induced toxicity in rat cortical primary cultures of neurons and astrocytes. *Toxicol. Sci.* 110, 156–167. doi: 10.1093/toxsci/kfp081

Lee, E. S., Sidoryk, M., Jiang, H., Yin, Z., and Aschner, M. (2009b). Estrogen and tamoxifen reverse manganese-induced glutamate transporter impairment in astrocytes. *J. Neurochem.* 110, 530–544. doi: 10.1111/j.1471-4159.2009.06105.x

Leveille, C. F., Mikhaeil, J. S., Turner, K. D., Silvera, S., Wilkinson, J., and Fajardo, V. A. (2017). Mitochondrial cristae density: a dynamic entity that is critical for energy production and metabolic power in skeletal muscle. *J. Physiol.* 595, 2779–2780. doi: 10.1113/JP274158

Levenson, J., Sherry, D. M., Dryer, L., Chin, J., Byrne, J. H., and Eskin, A. (2000a). Localization of glutamate and glutamate transporters in the sensory neurons of Aplysia. *J. Comp. Neurol.* 423, 121–131. doi: 10.1002/1096-9861(20000717)423:1<121::aid-cne10>3.0.co;2-e

Levenson, J., Endo, S., Kategaya, L. S., Fernandex, R. I., Brabham, D. G., Chin, J., et al. (2000b). Long-term regulation of neuronal high-affinity glutamate and glutamine uptake in Aplysia. *Proc. Natl. Acad. Sci. U S A* 97, 12858–12863. doi: 10.1073/pnas.220256497

Levenson, J. M., Weeber, E. J., Sweatt, J. D., and Eskin, A. (2002). Glutamate uptake in synaptic plasticity: from mollusc to mammal. *Curr. Mol. Med.* 2, 593–603. doi: 10.2174/1566524023362069

Lewerenz, J., and Maher, P. (2015). Chronic glutamate toxicity in neurodegenerative diseases-what is the evidence?. *Front. Neurosci.* 9:469. doi: 10.3389/fnins.2015.00469

Li, S., Hong, S., Shepardson, N. E., Walsh, D. M., Shankar, G. M., and Selkoe, D. (2009). Soluble oligomers of amyloid beta protein facilitate hippocampal long-term depression by disrupting neuronal glutamate uptake. *Neuron* 62, 788–801. doi: 10.1016/j.neuron.2009.05.012

Lipton, S. A., and Rosenberg, P. A. (1994). Excitatory amino acids as a final common pathway for neurologic disorders. *N. Engl. J. Med.* 330, 613–622. doi: 10.1056/NEJM199403033300907

Logan, W. J., and Snyder, S. H. (1971). Unique high affinity system for glycine, glutamic and aspartic acids in central nervous tissue in the rat. *Nature* 234, 297–299. doi: 10.1038/234297b0

Lugo-Huitron, R., Blanco-Ayala, T., Ugalde-Muniz, P., Carrillo-Mora, P., Pedraza-Chaverri, J., Silva-Adaya, D., et al. (2011). On the antioxidant properties of kynurenic acid: free radical scavenging activity and inhibition of oxidative stress. *Neurotoxicol. Teratol.* 33, 538–547. doi: 10.1016/j.ntt.2011.07.002

McKay, S., Bengtson, C. P., Bading, H., Wyllie, D. J., and Hardingham, G. E. (2013). Recovery of NMDA receptor currents from MK-801 blockade is accelerated by Mg2+ and memantine under conditions of agonist exposure. *Neuropharmacology* 74, 119–125. doi: 10.1016/j.neuropharm.2013.01.024

McNair, L. F., Andersen, J. V., Aldana, B. I., Hohnholt, M. C., Nissen, J. D., Sun, Y., et al. (2019). Deletion of neuronal GLT-1 in mice reveals its role in synaptic glutamate homeostasis and mitochondrial function. *J. Neurosci.* 39, 4847–4863. doi: 10.1523/JNEUROSCI.0894-18.2019

McNair, L. F., Andersen, J. V., Nissen, J. D., Sun, Y., Fischer, K. D., Hodgson, N. W., et al. (2020). Conditional knockout of GLT-1 in neurons leads to alterations in aspartate homeostasis and synaptic mitochondrial metabolism in striatum and hippocampus. *Neurochem. Res.* 45, 1420–1437. doi: 10.1007/s11064-020-03000-7

Meldrum, B., and Garthwaite, J. (1990). Excitatory amino acid neurotoxicity and neurodegenerative disease. *Trends Pharmacol. Sci.* 11, 379–387. doi: 10.1016/0165-6147(90)90184-a

Mitra, P., and Brownstone, R. M. (2012). An *in vitro* spinal cord slice preparation for recording from lumbar motoneurons of the adult mouse. *J. Neurophysiol.* 107, 728–741. doi: 10.1152/jn.00558.2011

Mukhamedyarov, M. A., Zefirov, A. L., and Palotas, A. (2006). Paired-pulse facilitation of transmitter release at different levels of extracellular calcium concentration. *Neurochem. Res.* 31, 1055–1058. doi: 10.1007/s11064-006-9115-x

Nathan, T., Jensen, M. S., and Lambert, J. D. (1990). GABAB receptors play a major role in paired-pulse facilitation in area CA1 of the rat hippocampus. *Brain Res.* 531, 55–65. doi: 10.1016/0006-8993(90)90757-3

Nathan, T., and Lambert, J. D. (1991). Depression of the fast IPSP underlies paired-pulse facilitation in area CA1 of the rat hippocampus. *J. Neurophysiol.* 66, 1704–1715. doi: 10.1152/jn.1991.66.5.1704

Novelli, A., Reilly, J. A., Lysko, P. G., and Henneberry, R. C. (1988). Glutamate becomes neurotoxic *via* the N-methyl-D-aspartate receptor when intracellular energy levels are reduced. *Brain Res.* 451, 205–212. doi: 10.1016/0006-8993(88)90765-2

O'Brien, R. J., and Fischbach, G. D. (1986). Modulation of embryonic chick motoneuron glutamate sensitivity by interneurons and agonists. *J. Neurosci.* 6, 3290–3296. doi: 10.1523/JNEUROSCI.06-11-03290.1986

O'Donovan, S. M., Hasselfeld, K., Bauer, D., Simmons, M., Roussos, P., Haroutunian, V., et al. (2015). Glutamate transporter splice variant expression in an enriched pyramidal cell population in schizophrenia. *Transl. Psychiatry* 5:e579. doi: 10.1038/tp.2015.74

Otmakhova, N. A., and Lisman, J. E. (1999). Dopamine selectively inhibits the direct cortical pathway to the CA1 hippocampal region. *J. Neurosci.* 19, 1437–1445. doi: 10.1523/JNEUROSCI.19-04-01437.1999

Ottersen, O. P., Laake, J. H., Reichelt, W., Haug, F. M., and Torp, R. (1996). Ischemic disruption of glutamate homeostasis in brain: quantitative immunocytochemical analyses. *J. Chem. Neuroanat.* 12, 1–14. doi: 10.1016/s0891-0618(96)00178-0

Pajarillo, E., Johnson, J., Jr., Kim, J., Karki, P., Son, D. S., Aschner, M., et al. (2018). 17beta-estradiol and tamoxifen protect mice from manganese-induced dopaminergic neurotoxicity. *Neurotoxicology* 65, 280–288. doi: 10.1016/j.neuro.2017.11.008

Paoletti, P., and Neyton, J. (2007). NMDA receptor subunits: function and pharmacology. *Curr. Opin. Pharmacol.* 7, 39–47. doi: 10.1016/j.coph.2006.08.011

Parkin, G. M., Gibbons, A., Udawela, M., and Dean, B. (2020). Excitatory amino acid transporter (EAAT).1 and EAAT2 mRNA levels are altered in the prefrontal cortex of subjects with schizophrenia. *J. Psychiatr. Res.* 123, 151–158. doi: 10.1016/j.jpsychires.2020.02.004

Parkin, G. M., Udawela, M., Gibbons, A., and Dean, B. (2018). Glutamate transporters, EAAT1 and EAAT2, are potentially important in the pathophysiology and treatment of schizophrenia and affective disorders. *World J. Psychiatry* 8, 51–63. doi: 10.5498/wjp.v8.i2.51

Pei, W., Kratz, L. E., Bernardini, I., Sood, R., Yokogawa, T., Dorward, H., et al. (2010). A model of costeff syndrome reveals metabolic and protective functions of mitochondrial OPA3. *Development* 137, 2587–2596. doi: 10.1242/dev.043745

Petr, G. T., Sun, Y., Frederick, N. M., Zhou, Y., Dhamne, S. C., Hameed, M. Q., et al. (2015). Conditional deletion of the glutamate transporter GLT-1 reveals that astrocytic GLT-1 protects against fatal epilepsy while neuronal GLT-1 contributes significantly to glutamate uptake into synaptosomes. *J. Neurosci.* 35, 5187–5201. doi: 10.1523/JNEUROSCI.4255-14.2015

Pozzo Miller, L. D., Mahanty, N. K., Connor, J. A., and Landis, D. M. (1994). Spontaneous pyramidal cell death in organotypic slice cultures from rat hippocampus is prevented by glutamate receptor antagonists. *Neuroscience* 63, 471–487. doi: 10.1016/0306-4522(94)90544-4

Pringle, A. K., Self, J., and Iannotti, F. (2000). Reducing conditions produce a loss of neuroprotective efficacy of competitive but not non-competitive antagonists in a model of NMDA-mediated excitotoxicity in organotypic hippocampal slice cultures. *Acta Neurochir. Suppl.* 76, 79–80. doi: 10.1007/978-3-7091-6346-7_16

Rae, C., and Balcar, V. J. (2014). "A chip off the old block: the brain slice as a model for metabolic studies of brain compartmentation and neuropharmacology," in *Brain Enrgy Metabolism*, eds J. Hirrlinger, and H. Waagepetersen (New York: Springer), 217–241.

Ramnath, R. R., Strange, K., and Rosenberg, P. A. (1992). Neuronal injury evoked by depolarizing agents in rat cortical cultures. *Neuroscience* 51, 931–939. doi: 10.1016/0306-4522(92)90530-f

Rimmele, T. S., and Rosenberg, P. A. (2016). GLT-1: the elusive presynaptic glutamate transporter. *Neurochem. Int.* 98, 19–28. doi: 10.1016/j.neuint.2016.04.010

Robinson, M. B., Lee, M. L., and DaSilva, S. (2020). Glutamate transporters and mitochondria: signaling, co-compartmentalization, functional coupling and future directions. *Neurochem. Res.* 45, 526–540. doi: 10.1007/s11064-020-02974-8

Rothman, S. M., and Olney, J. W. (1986). Glutamate and the pathophysiology of hypoxic-ischemic brain damage. *Ann. Neurol.* 19, 105–111. doi: 10.1002/ana.410190202

Schilp, D. E., Sorensen, S. M., Wettstein, J. G., and Black, M. D. (1999). Effects of glycine antagonists in an acute *in vitro* electrophysiological model of ischemia. *Drug Dev. Res.* 46, 134–138. doi: 10.1002/(SICI)1098-2299(199902)46:2<134::AID-DDR6>3E3.0.CO;2-9

Schmitt, A., Asan, E., Puschel, B., Jons, T., and Kugler, P. (1996). Expression of the glutamate transporter GLT1 in neural cells of the rat central nervous system: non-radioactive *in situ* hybridization and comparative immunocytochemistry. *Neuroscience* 71, 989–1004. doi: 10.1016/0306-4522(95)00477-7

Schousboe, A., and Hertz, L. (1981). Role of astroglial cells in glutamate homeostasis. *Adv. Biochem. Psychopharmacol.* 27, 103–113.

Schousboe, A., Sonnewald, U., Civenni, G., and Gegelashvili, G. (1997). Role of astrocytes in glutamate homeostasis - Implications for excitotoxicity. *Adv. Exp. Med. Biol.* 429, 195–206. doi: 10.1007/978-1-4757-9551-6_14

Schulz, P. E., Cook, E. P., and Johnston, D. (1994). Changes in paired-pulse facilitation suggest presynaptic involvement in long-term potentiation. *J. Neurosci.* 14, 5325–5337. doi: 10.1523/JNEUROSCI.14-09-05325.1994

Schulz, P. E., Cook, E. P., and Johnston, D. (1995). Using paired-pulse facilitation to probe the mechanisms for long-term potentiation (LTP). *J. Physiol. Paris* 89, 3–9. doi: 10.1016/0928-4257(96)80546-8

Schurr, A., and Gozal, E. (2012). Aerobic production and utilization of lactate satisfy increased energy demands upon neuronal activation in hippocampal slices and provide neuroprotection against oxidative stress. *Front. Pharmacol.* 2:96. doi: 10.3389/fphar.2011.00096

Schurr, A., Payne, R. S., and Rigor, B. M. (1995a). Synergism between diltiazem and MK-801 but not APV in protecting hippocampal slices against hypoxic damage. *Brain Res.* 684, 233–236. doi: 10.1016/0006-8993(95)00466-4

Schurr, A., Payne, R. S., and Rigor, B. M. (1995b). Protection by MK-801 against hypoxia-, excitotoxin- and depolarization-induced neuronal damage *in vitro*. *Neurochem. Int.* 26, 519–525. doi: 10.1016/0197-0186(94)00148-n

Sharma, A., Kazim, S. F., Larson, C. S., Ramakrishnan, A., Gray, J. D., McEwen, B. S., et al. (2019). Divergent roles of astrocytic versus neuronal EAAT2 deficiency on cognition and overlap with aging and Alzheimer's molecular signatures. *Proc. Natl. Acad. Sci. U S A* 116, 21800–21811. doi: 10.1073/pnas.1903566116

Sheardown, M. J., Nielsen, E. O., Hansen, A. J., Jacobsen, P., and Honore, T. (1990). 2,3-Dihydroxy-6-nitro-7-sulfamoyl-benzo-(F).quinoxaline: a neuroprotectant for cerebral ischemia. *Science* 247, 571–574. doi: 10.1126/science.2154034

Stuart, G. J., and Redman, S. J. (1991). Mechanisms of presynaptic inhibition studied using paired-pulse facilitation. *Neurosci. Lett.* 126, 179–183. doi: 10.1016/0304-3940(91)90548-8

Takahashi, M., Billups, B., Rossi, D., Sarantis, M., Hamann, M., and Attwell, D. (1997). The role of glutamate transporters in glutamate homeostasis in the brain. *J. Exp. Biol.* 200, 401–409. doi: 10.1242/jeb.200.2.401

Tanaka, K., Watase, K., Manabe, T., Yamada, K., Watanabe, M., Takahashi, K., et al. (1997). Epilepsy and exacerbation of brain injury in mice lacking the glutamate transporter GLT-1. *Science* 276, 1699–1702. doi: 10.1126/science.276.5319.1699

Tani, H., Dulla, C. G., Farzampour, Z., Taylor-Weiner, A., Huguenard, J. R., and Reimer, R. J. (2014). A local glutamate-glutamine cycle sustains synaptic excitatory transmitter release. *Neuron* 81, 888–900. doi: 10.1016/j.neuron.2013.12.026

Torp, R., Danbolt, N. C., Babaie, E., Bjoras, M., Seeberg, E., Storm-Mathisen, J., et al. (1994). Differential expression of two glial glutamate transporters in the rat brain: an *in situ* hybridization study. *Eur. J. Neurosci.* 6, 936–942. doi: 10.1111/j.1460-9568.1994.tb00587.x

Torp, R., Hoover, F., Danbolt, N. C., Storm-Mathisen, J., and Ottersen, O. P. (1997). Differential distribution of the glutamate transporters GLT1 and rEAAC1 in rat cerebral cortex and thalamus: an *in situ* hybridization analysis. *Anat. Embryol. (Berl).* 195, 317–326. doi: 10.1007/s004290050051

Toth, F., Cseh, E. K., and Vecsei, L. (2021). Natural molecules and neuroprotection: kynurenic acid, pantethine and alpha-lipoic acid. *Int. J. Mol. Sci.* 22:403. doi: 10.3390/ijms22010403

Tzingounis, A. V., and Wadiche, J. I. (2007). Glutamate transporters: confining runaway excitation by shaping synaptic transmission. *Nat. Rev. Neurosci.* 8, 935–947. doi: 10.1038/nrn2274

Urenjak, J., and Obrenovitch, T. P. (2000). Neuroprotective potency of kynurenic acid against excitotoxicity. *Neuroreport* 11, 1341–1344. doi: 10.1097/00001756-200004270-00038

Vorhees, C. V., and Williams, M. T. (2006). Morris water maze: procedures for assessing spatial and related forms of learning and memory. *Nat. Protoc.* 1, 848–858. doi: 10.1038/nprot.2006.116

Wakade, C., Khan, M. M., De Sevilla, L. M., Zhang, Q. G., Mahesh, V. B., and Brann, D. W. (2008). Tamoxifen neuroprotection in cerebral ischemia involves attenuation of kinase activation and superoxide production and potentiation of mitochondrial superoxide dismutase. *Endocrinology* 149, 367–379. doi: 10.1210/en.2007-0899

Whittingham, T. S., Lust, W. D., Christakis, D. A., and Passonneau, J. V. (1984). Metabolic stability of hippocampal slice preparations during prolonged incubation. *J. Neurochem.* 43, 689–696. doi: 10.1111/j.1471-4159.1984.tb12788.x

Wu, T., Ding, X. S., Wang, W., and Wu, J. (2006). MCI-186 (3-methyl-1-phenyl-2-pyrazolin-5-one). attenuated simulated ischemia/reperfusion injury in cultured rat hippocampal cells. *Biol. Pharm. Bull.* 29, 1613–1617. doi: 10.1248/bpb.29.1613

Wu, L. G., and Saggau, P. (1994). Presynaptic calcium is increased during normal synaptic transmission and paired-pulse facilitation, but not in long-term potentiation in area CA1 of hippocampus. *J. Neurosci.* 14, 645–654. doi: 10.1523/jneurosci.14-02-00645.1994

Yu, Z., Guindani, M., Grieco, S. F., Chen, L., Holmes, T. C., and Xu, X. (2021). Beyond t test and ANOVA: applications of mixed-effects models for more rigorous statistical analysis in neuroscience research. *Neuron* doi: 10.1016/j.neuron.2021.10.030.[Online ahead of print].

Zattoni, M., Garrovo, C., Xerxa, E., Spigolon, G., Fisone, G., Kristensson, K., et al. (2021). NMDA receptor and L-type calcium channel modulate prion formation. *Cell Mol. Neurobiol.* 41, 191–198. doi: 10.1007/s10571-020-00834-1

Zhang, Y., Jin, Y., Behr, M. J., Feustel, P. J., Morrison, J. P., and Kimelberg, H. K. (2005). Behavioral and histological neuroprotection by tamoxifen after reversible focal cerebral ischemia. *Exp. Neurol.* 196, 41–46. doi: 10.1016/j.expneurol.2005.07.002

Zhang, Y., Milatovic, D., Aschner, M., Feustel, P. J., and Kimelberg, H. K. (2007). Neuroprotection by tamoxifen in focal cerebral ischemia is not mediated by an agonist action at estrogen receptors but is associated with antioxidant activity. *Exp. Neurol.* 204, 819–827. doi: 10.1016/j.expneurol.2007.01.015

Zhang, H., Xie, M., Schools, G. P., Feustel, P. F., Wang, W., Lei, T., et al. (2009). Tamoxifen mediated estrogen receptor activation protects against early impairment of hippocampal neuron excitability in an oxygen/glucose deprivation brain slice ischemia model. *Brain Res.* 1247, 196–211. doi: 10.1016/j.brainres.2008.10.015

Zhou, Y., Hassel, B., Eid, T., and Danbolt, N. C. (2019). Axon-terminals expressing EAAT2 (GLT-1; Slc1a2). are common in the forebrain and not limited to the hippocampus. *Neurochem. Int.* 123, 101–113. doi: 10.1016/j.neuint.2018.03.006

Zhu, Y., Romero, M. I., Ghosh, P., Ye, Z., Charnay, P., Rushing, E. J., et al. (2001). Ablation of NF1 function in neurons induces abnormal development of cerebral cortex and reactive gliosis in the brain. *Genes Dev.* 15, 859–876. doi: 10.1101/gad.862101

Zott, B., Simon, M. M., Hong, W., Unger, F., Chen-Engerer, H. J., Frosch, M. P., et al. (2019). A vicious cycle of beta amyloid-dependent neuronal hyperactivation. *Science* 365, 559–565. doi: 10.1126/science.aay0198

Conflict of Interest: DS is a director and consultant of Prothena Biosciences.

The remaining authors declare that the research was conducted in the absence of any commercial or financial relationships that could be construed as a potential conflict of interest.

frontiers in Cellular Neuroscience

REVIEW
published: 06 January 2022
doi: 10.3389/fncel.2021.815279

Cellular Physiology and Pathophysiology of EAAT Anion Channels

Peter Kovermann, Miriam Engels, Frank Müller and Christoph Fahlke*

Institute of Biological Information Processing, Molekular- und Zellphysiologie (IBI-1), Forschungszentrum Jülich, Jülich, Germany

Excitatory amino acid transporters (EAATs) optimize the temporal resolution and energy demand of mammalian excitatory synapses by quickly removing glutamate from the synaptic cleft into surrounding neuronal and glial cells and ensuring low resting glutamate concentrations. In addition to secondary active glutamate transport, EAATs also function as anion channels. The channel function of these transporters is conserved in all homologs ranging from archaebacteria to mammals; however, its physiological roles are insufficiently understood. There are five human EAATs, which differ in their glutamate transport rates. Until recently the high-capacity transporters EAAT1, EAAT2, and EAAT3 were believed to conduct only negligible anion currents, with no obvious function in cell physiology. In contrast, the low-capacity glutamate transporters EAAT4 and EAAT5 are thought to regulate neuronal signaling as glutamate-gated channels. In recent years, new experimental approaches and novel animal models, together with the discovery of a human genetic disease caused by gain-of-function mutations in EAAT anion channels have enabled identification of the first physiological and pathophysiological roles of EAAT anion channels.

Keywords: excitatory amino acid transporter, glutamate transporter, anion channels, chloride homeostasis, retina, channelopathies

Edited by:
Sandra Hewett,
Syracuse University, United States

Reviewed by:
Baruch Kanner,
Hebrew University of Jerusalem, Israel
Suzanne Underhill,
National Institutes of Health (NIH), United States

****Correspondence:***
Peter Kovermann
p.kovermann@fz-juelich.de

Specialty section:
This article was submitted to Cellular Neurophysiology, a section of the journal Frontiers in Cellular Neuroscience

Received: *15 November 2021*
Accepted: *13 December 2021*
Published: *06 January 2022*

Citation:
Kovermann P, Engels M, Müller F and Fahlke C (2022) Cellular Physiology and Pathophysiology of EAAT Anion Channels.
Front. Cell. Neurosci. 15:815279.
doi: 10.3389/fncel.2021.815279

INTRODUCTION

Glial and neuronal excitatory amino acid transporters (EAATs) ensure low resting neurotransmitter concentrations in the synaptic cleft and prevent glutamate excitotoxicity by transporting glutamate from the synaptic cleft into neuronal and glial cells (Danbolt, 2001; Kanner, 2006). EAATs are prototypical dual function proteins that act as both secondary active glutamate transporters and anion channels (Fairman et al., 1995; Wadiche et al., 1995; Larsson et al., 1996). Whereas, the molecular basis of these two transport functions is now well-understood (Fahlke et al., 2016), we are just starting to appreciate the cellular functions of these glutamate-gated chloride channels in the human body.

About 30 years ago, EAAT anion channel behavior was discovered almost simultaneously in two different experimental systems: cloned transporters in heterologous expression systems and native transporters in retinal preparations. Heterologous expression of EAAT1, EAAT2, and EAAT3 in *Xenopus* oocytes and electrophysiological analysis revealed the existence of a current component carried by anions that is not coupled to electrogenic glutamate transport (Wadiche et al., 1995). Moreover, after identification and characterization of the first three isoforms (Kanai and Hediger, 1992; Pines et al., 1992; Storck et al., 1992), homology cloning of EAAT4 (Fairman et al., 1995) and

EAAT5 (Arriza et al., 1997) revealed the existence of family members that predominantly function as anion channels.

A glutamate-gated anion channel with many of the functional features of EAAT glutamate transporters was first observed on cone photoreceptors of salamander retina (Picaud et al., 1995b; Larsson et al., 1996) and on dendrites of ON-bipolar cells in white perch retina (Grant and Dowling, 1995; Picaud et al., 1995b; Larsson et al., 1996). On cone photoreceptors, this channel allows cells to respond to glutamate that they themselves have released and provides a feedback signal about the concentration of glutamate released into the synaptic cleft (Picaud et al., 1995a). In ON-bipolar cells of white perch retina, chloride conductance mediates an inhibitory input that keeps the cells hyperpolarized in the dark, when photoreceptors release glutamate. The retina-specific mammalian EAAT5 (Arriza et al., 1997; Gameiro et al., 2011; Schneider et al., 2014) closely resembles salamander *s*EAAT5A (Eliasof et al., 1998) and is, thus, assumed to fulfill similar functions in the mammalian retina. However, until recently, the lack of EAAT5-specific blockers and an EAAT5-knockout animal model have prevented the experimental verification of this hypothesis.

Here we review recent progress in the cellular physiology and pathophysiology of EAAT anion channels.

EAAT ANION CHANNELS EXHIBIT LOW UNITARY CURRENT AMPLITUDES AND ABSOLUTE OPEN PROBABILITIES

Initially, EAAT anion channels were mainly studied in *Xenopus* oocytes. In this system, EAAT anion currents are small compared with endogenous current components and subtraction procedures are usually needed to identify the EAAT anion channel-specific current (Fairman et al., 1995; Wadiche et al., 1995; Wadiche and Kavanaugh, 1998; Ryan et al., 2004; Cater et al., 2014, 2016). The use of a mammalian cell expression system and more permeable anions permit the direct recording of EAAT anion currents under various conditions. **Figure 1** shows representative EAAT4 anion current recordings from HEK293T cells expressing rat EAAT4. Because of the current convention, inward currents at negative potentials correspond to anion efflux. The currents are small in the absence of Na^+ and glutamate, and the application of Na^+ alone or of Na^+ plus glutamate increases current amplitudes in a dose-dependent manner. EAAT4 anion currents exhibit time- and voltage-dependent changes in current amplitudes that resemble voltage-dependent gating (**Figures 1A–C**) (Kovermann et al., 2010). This "gating" is affected by transporter substrates (Machtens et al., 2011), but also by permeant anion concentrations (**Figures 1D,E**) (Kovermann et al., 2010). Such experiments support the notion that EAAT anion channels need Na^+ ions to be active (Mim et al., 2005; Tao et al., 2006; Grewer et al., 2008). However, glial EAAT anion channels are Na^+ independent in the absence of glutamate (Leinenweber et al., 2011; Divito et al., 2017) and can also be active when K^+ is the only monovalent cation present (Kortzak et al., 2019).

Since EAAT anion currents are large compared with uptake currents and are not coupled to glutamate transport, they were always assumed to be channel mediated. Definitive proof was provided by measurements of unitary current amplitudes *via* noise analysis. Larsson et al. (1996) studied glutamate transporter-associated anion channels on tiger salamander cones using whole-cell patch-clamp recordings. They demonstrated that glutamate transporter-associated current fluctuations are Lorentzian, i.e., generated by the random opening and closing of individual channels. Stationary noise analysis involving the adjustment of anion channel open probabilities by modifying external glutamate provided a single-channel conductance of 0.7 pS at symmetric chloride concentration $[Cl^-]$ (Picaud et al., 1995b; Larsson et al., 1996). These single-channel amplitudes are too high to be accounted for by carrier-mediated transport. Thus, these data establish channel-like anion conduction by EAAT glutamate transporters.

Noise analysis of mammalian EAAT1–EAAT5 proteins in transfected HEK293T cells provided a unitary conductance of around 1 pS: EAAT5 had the highest single-channel amplitude (Schneider et al., 2014), EAAT4 (Torres-Salazar and Fahlke, 2007) had the lowest, and the high-capacity transporters EAAT1 (Winter et al., 2012), EAAT2 (Schneider et al., 2014), and EAAT3 (Torres-Salazar and Fahlke, 2007) displayed intermediate values. Noise analysis of the EAAT-associated anion channel amplitudes demonstrated identical unitary current amplitudes for various external [glutamate], indicating the existence of a single anion pore that is either open or closed (Kovermann et al., 2010). Absolute open probabilities (determined by comparing EAAT anion and transport currents) turned out to be extremely low, i.e., 0.06 ± 0.01% for EAAT2 (Kolen et al., 2020).

MOLECULAR DETERMINANTS OF EAAT-ASSOCIATED ANION CHANNEL FUNCTION

EAATs assemble as homo- or heterotrimers (Gendreau et al., 2004; Yernool et al., 2004; Nothmann et al., 2011), with each subunit mediating both transport functions independently of its neighboring subunits (Grewer et al., 2005; Koch et al., 2007; Leary et al., 2007). They are prototypical elevator transporters: each subunit contains a trimerization domain that provides a scaffold for transmembrane movements of the transport domain and has binding sites for all substrates (Yernool et al., 2003; Boudker et al., 2007; Reyes et al., 2009; Verdon and Boudker, 2012; Jensen et al., 2013; Verdon et al., 2014; Guskov et al., 2016; Arkhipova et al., 2019). Substrate transport is based on large-scale (∼18 Å) rotational translational movement of the transport domain relative to the static trimerization domain (Crisman et al., 2009; Reyes et al., 2009). For many years, none of the reported structures exhibited a hydrophilic pore-like structure that could be structurally correlated to the EAAT anion pore.

A convincing molecular model of the EAAT anion pore was obtained *via* molecular dynamics simulation of Glt_{Ph}

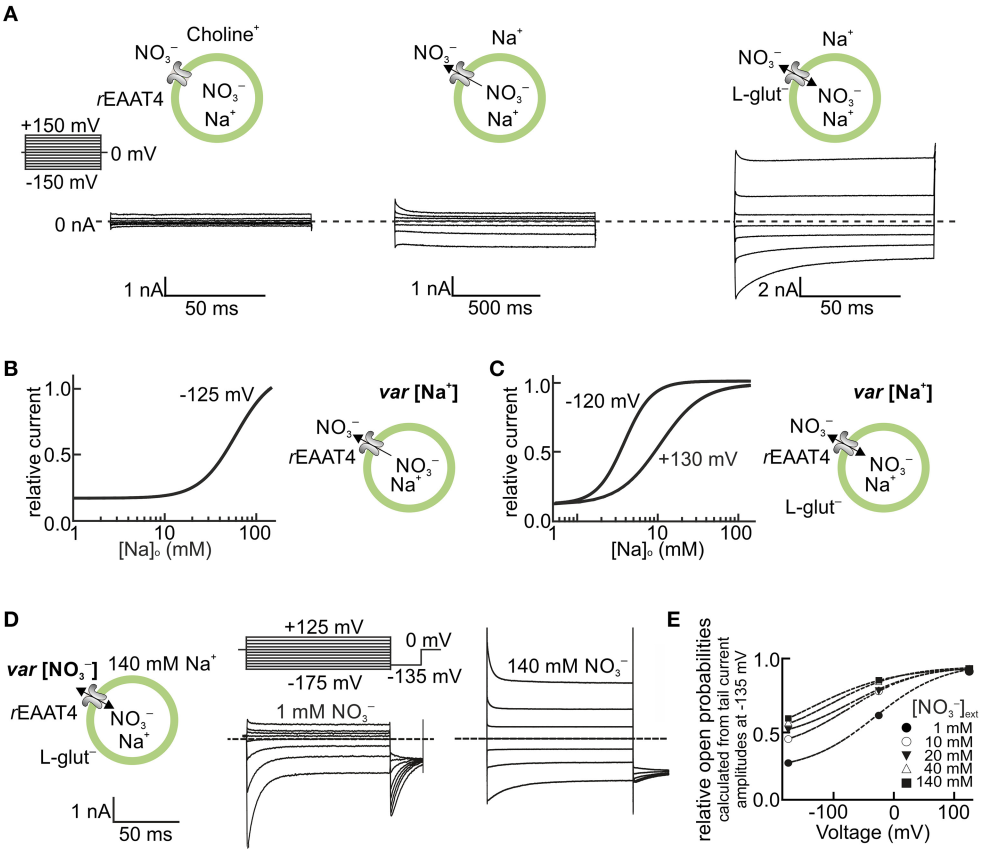

FIGURE 1 | EAAT anion channels are modulated by transport substrates and permeant anions. **(A–C)** Na$^+$ dependence of EAAT4 anion channels heterologously expressed in HEK293T cells. **(A)** Representative whole-cell current recordings of rat EAAT4 with symmetric NO$_3^+$ as the permeable anion, in the absence of external Na$^+$ and L-glutamate (Glu$^-$) (left), in the presence of external Na$^+$ (middle), and in the presence of external Na$^+$ and 5 mM L-glutamate (right, see insets). The Na$^+$ concentration dependence of EAAT4 anion channel currents is shown in the absence **(B)** and presence **(C)** of external L-glutamate for high positive and negative voltages (internal Na$^+$ concentration in **A,B** was set to ∼114 mM). **(D,E)** Dependence of EAAT4 anion channel gating on permeant anions. **(D)** Representative whole-cell recordings from rat EAAT4 whole-cell currents with different external concentrations of NO$_3^+$ (1–140 mM) (see insets, the internal NO$_3^+$ concentration in **C,D** was set to 110 mM). **(E)** Relative open probabilities of rat EAAT4 anion channels at different external concentrations of the permeant anion NO$_3^+$. In the depicted experiments, Na$^+$ was replaced by equimolar amounts of choline **(A–C)**, and NO$_3^+$ by the impermeant anion D-gluconate$^-$ **(D,E)**. Relative open probabilities in E were calculated from instantaneous tail current amplitudes at −135 mV, as shown in the voltage protocol in D. rEAAT4: rat EAAT4. var, varying. This figure is modified and reprinted from Kovermann et al. (2010), with permission.

(Machtens et al., 2015). At the time, Glt$_{Ph}$ structures were available for the inward- (Reyes et al., 2009) and outward-facing conformations (Yernool et al., 2004; Boudker et al., 2007; Verdon et al., 2014), as well as for one intermediate state (Verdon and Boudker, 2012). Each of these conformations was tested for possible anion permeation using a computational electrophysiology approach that permitted the observation of ion permeation events under constant voltages (Kutzner et al., 2011). At a [NaCl] of 1 M and voltages of around 800 mV, no Cl$^-$ permeation event was observed for any of these conformations. However, in simulations starting from various intermediate conformations—either using a published structure (Verdon and Boudker, 2012) or obtained using an essential dynamics approach—lateral movement of the transport domain opened the interface between the trimerization and transport domains. Subsequent wetting caused the formation of an anion-selective pore with functional properties resembling experimental results for EAAT anion channels.

This novel conformation (named ChC) was experimentally verified using tryptophan-scanning mutagenesis and by combined *in silico* and *in vitro* mutagenesis. Tryptophan fluorescence is collisionally quenched by anions; thus, fluorescence spectroscopy at various anion concentrations permits tryptophan side chains protruding onto the anion permeation pathway to be distinguished from those in other localizations. Predictions of side-chain accessibility to the aqueous medium in different conformations, including the ChC conformation, perfectly matched with iodide (I$^-$) accessibility for Glt$_{Ph}$ mutants with a single tryptophan substitution (Machtens et al., 2015). Computational electrophysiology is well-suited to estimate the effects of amino acid exchange on unitary current amplitudes and anion-to-cation selectivity. An extensive mutational scan revealed perfect agreement between simulated permeation properties and experimental values, which included unitary current amplitudes determined by noise analysis and anion-cation selectivities obtained from whole-cell recordings under varying anion/cation gradients. These results demonstrate that the ChC conformation is indeed formed and is responsible for anion conduction in EAATs (Machtens et al., 2015).

Recently, an intermediate conformation of Glt_{Ph}, captured *via* crosslinking of an inserted cysteine pair was obtained by cryo-electron microscopy (Chen et al., 2021). The authors used

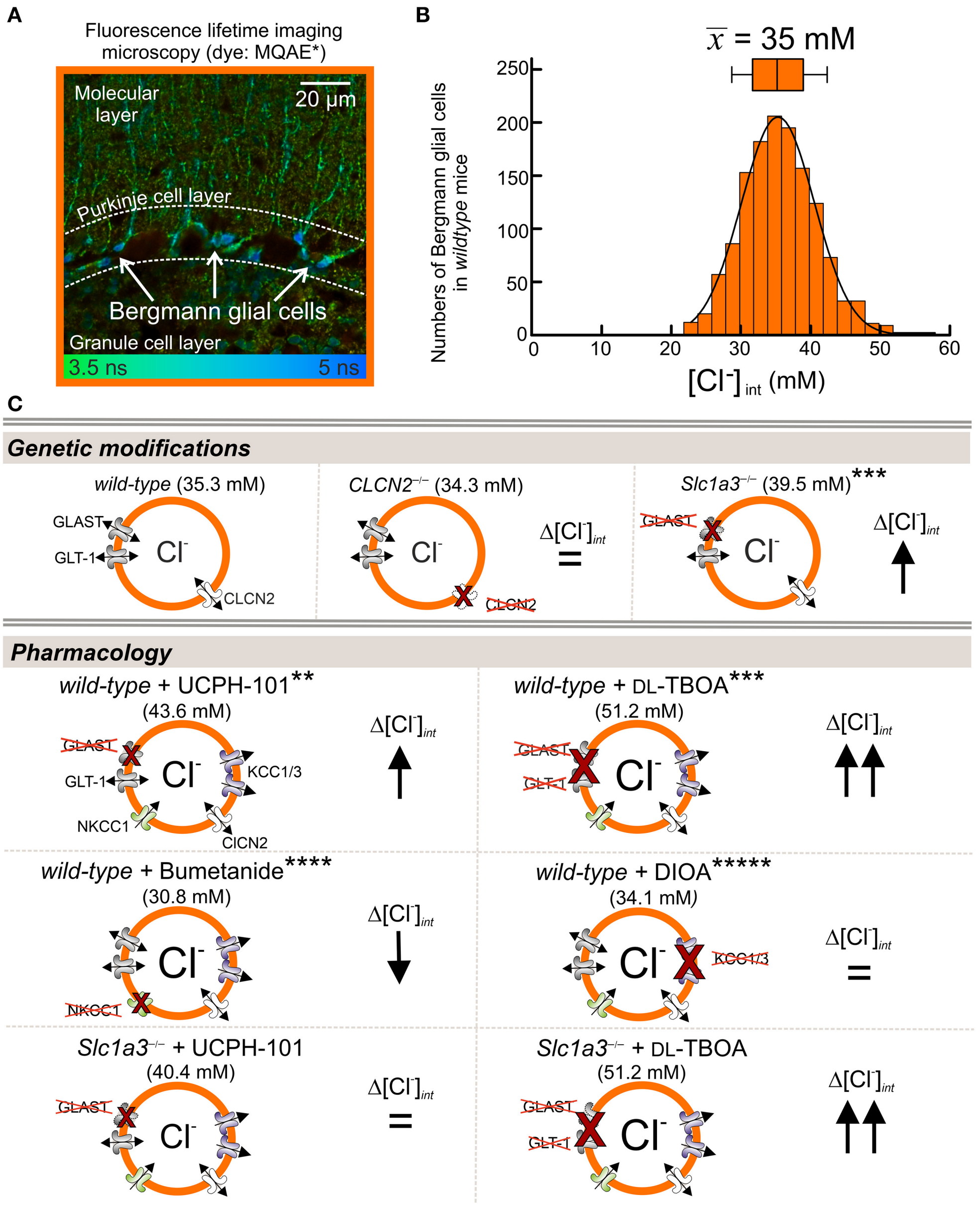

FIGURE 2 | EAAT1/GLAST contributes to $[\text{Cl}^-]_{\text{int}}$ in Bergmann glial cells. **(A,B)** Fluorescence lifetime imaging with the Cl^--sensitive dye MQAE. **(A)** Representative FLIM images from acute sagittal slices of the cerebellar cortex show MQAE-stained Bergmann glial cells (BGLs, arrows) in the Purkinje cell layer. **(B)** Distribution of $[\text{Cl}^-]_{\text{int}}$ from BGLs, with a mean (± SD) of 35.3 ± 6.3 mM. **(C)** $[\text{Cl}^-]_{\text{int}}$ is higher in GLAST-knockout (*Slc1a3*$^{-/-}$) than in wild-type (WT) BGLs, but is not affected by genetic ablation of CLCN2 (chloride voltage-gated channel 2). $[\text{Cl}^-]_{\text{int}}$ increases upon pharmacological blockage by the EAAT1-specific inhibitor UCPH-101 and the EAAT-specific blocker DL-TBOA. Reduction of Cl^- import by the NKCC1-specific inhibitor bumetanide decreases $[\text{Cl}^-]_{\text{int}}$, whereas inhibition of glial Cl^--exporters KCC1 and KCC3 by DIOA has no effect on $[\text{Cl}^-]_{\text{int}}$. Control experiments with *Slc1a3*$^{-/-}$ mice showed, that GLT-1 also contributes to chloride homeostasis (lower panel). Modified and reprinted from Untiet et al. (2017), with permission. *MQAE: 6-(Methoxychinolinio)acetic acid ethyl ester bromide ($C_{14}H_{16}BrNO_3$). **UCPH-101: 2-Amino-4-(4-methoxyphenyl)-7-(1-naphthyl)-5-oxo-5,6,7,8-tetrahydro-4H-chromene-3-carbonitrile ($C_{27}H_{22}N_2O_3$). ***DL-TBOA: DL-Threo-β-benzyloxyaspartate ($C_{11}H_{13}NO_5$). ****Bumetanide: 3-Butylamino-4-phenoxy-5-sulfamoyl benzoic acid ($C_{17}H_{20}N_2O_5S$). *****DIOA: R(+)-Butylindazone ($C_{20}H_{24}Cl_2O_4$).

molecular dynamics simulation to show the formation of a continuous hydration pathway at the interface of transport and trimerization domain. Subsequently, umbrella sampling simulations were used to determine free-energy profiles for pulling Cl^- through this aqueous pore. However, no spontaneous permeations were reported, and it is therefore not clear whether this intermediate conformation can conduct anions under physiological chemical/electrical gradients without application of external force. Neither unitary currents nor selectivities between anions or between anions and cation were computed. To experimentally support the role of the novel intermediate conformation in EAAT anion permeation, EAAT1 was mutated at seven position (Chen et al., 2021; #4525). Most of these mutations were already tested by Machtens et al. (2015). Each of the mutation modified reversal potentials of combined EAAT1 transport/anion currents. This analysis does not permit to separate effects of the mutations on glutamate transport, on the likelihood of anion channel opening or on the unitary current amplitude. All tested mutations will also affect the ChC anion conduction pathway, and the used crosslink does not prevent formation of the ChC conformation. Thus, neither experiments nor simulations demonstrate that the novel intermediate conformation is anion-conducting.

At present, it is therefore not possible to assess the functional role of this intermediate conformation. It may represent an additional anion-conductive state under physiological conditions or a translocation intermediate, from which anion channel opening may occur. In contrast, the ChC conformation has been shown to account for EAAT anion conduction with permeation rates and selectivity in full agreement with experimental results and to explain all available mutagenesis results (Machtens et al., 2015).

EAAT ANION CHANNELS CONTRIBUTE TO CHLORIDE HOMEOSTASIS IN GLIAL CELLS

The association of a missense mutation in *SLC1A3* (encoding the glial glutamate transporter EAAT1) with a case of a human genetic disease (Jen et al., 2005; Winter et al., 2012) was the basis to evaluate the role of EAAT anion channels in glial chloride homeostasis. Glial cells display predominant K^+ conductance that allows the buffering of $[K^+]$ in the extracellular space and ensures a stable negative resting potential (Lothman and Somjen, 1975; Futamachi and Pedley, 1976). The K^+ conductance prevents glial depolarization upon electrogenic glutamate uptake. However, internal Cl^- concentrations ($[Cl^-]_{int}$) in glial cells are larger than expected from passive distribution (Kimelberg, 1981; Kettenmann et al., 1987; Bevensee et al., 1997; Walz, 2002), and EAAT anion channels might reduce the resting $[Cl^-]_{int}$ *via* mediating a chloride efflux pathway in parallel to K^+ efflux through glial K^+ channels.

Untiet et al. (2017) measured $[Cl^-]_{int}$ in Bergmann glial cells in acute cerebellar slices using fluorescence lifetime imaging (FLIM) with the Cl^--sensitive dye MQAE. The experiments revealed a mean resting concentration of 35 mM in juvenile animals (postnatal days P20–P30; **Figures 2A,B**). Blocking the cation–chloride cotransporter NKCC1 decreased $[Cl^-]_{int}$ in Bergmann glial cells, whereas DIOA inhibition of two glial K^+-Cl^- cotransporters, KCC1 and KCC3 (**Figure 2C**), had only minor effects on $[Cl^-]_{int}$. In *Slc1a3*$^{-/-}$ mice lacking the glutamate transporter EAAT1/GLAST, but not in *Clc2*$^{-/-}$ mice, $[Cl^-]_{int}$ was increased to 40 mM (**Figure 2C**). Inhibition of EAAT1/GLAST by the highly specific EAAT1 blocker UCPH-101 (Abrahamsen et al., 2013) raised $[Cl^-]_{int}$ to 44 mM in wild-type Bergmann glia, and TBOA blockage of both glial glutamate transporters, EAAT1 and EAAT2, raised $[Cl^-]_{int}$ to around 50 mM. The expression of EAATs is developmentally controlled, and such changes in EAAT expression results in a developmental chloride switch. At P8, $[Cl^-]_{int}$ were comparable to those of juvenile animals after blocking EAAT1 and EAAT2 with TBOA, with $[Cl^-]_{int}$ decreasing to adult levels between P9 and P12. These results demonstrate that EAAT anion channels are major determinants of $[Cl^-]_{int}$ in Bergmann glial cells (Untiet et al., 2017).

Subsequent work on hippocampal and cortical glia revealed that resting $[Cl^-]_{int}$ differs even in highly similar glia types and that the contribution of EAAT anion channels in setting the glial $[Cl^-]_{int}$ is quite variable (**Figure 3**) (Engels et al., 2021). $[Cl^-]_{int}$ varied from 14 mM in cortical astrocytes (**Figure 3A**) to >20 mM in CA1 astrocytes (**Figure 3B**) and radial-glia-like cells (**Figure 3C**), and to 28 mM in dentate gyrus astrocytes (**Figure 3D**). The use of anion transport blockers identified differences in anion transport protein expression as the mechanistic basis of this variability. Whereas, blockage of NKCC1 by bumetanide reduced $[Cl^-]_{int}$ in hippocampal astrocytes (**Figures 3B,C**), no significant change was observed in cortical astrocytes (**Figure 3A**), or radial-glia-like cells (**Figure 3D**). Blockage of KCC1 and KCC3 or of EAAT anion channels substantially increased $[Cl^-]_{int}$ in cortical and CA1 astrocytes and in radial-glia-like cells (**Figures 3A,B,D**), but not in dentate gyrus astrocytes (**Figure 3C**). The experiments showed that EAAT anion channels are involved in the regulation of internal chloride concentrations of certain, but not in all glial cells.

GLIAL CHLORIDE HOMEOSTASIS IN *SLC1A3*-ASSOCIATED NEUROLOGICAL DISEASE

Episodic ataxias are a group of six genetic syndromes characterized by paroxysmal cerebellar incoordination and other neurological symptoms, but differing in their clinical symptoms. Episodic ataxia 6 was first reported in a 10-year-old boy with long ataxia attacks, epilepsy and cerebellar degeneration (Jen et al., 2005), but without myokymia, nystagmus, or tinnitus. The patient was heterozygous for a *SLC1A3* mutation that predicts the substitution of proline by arginine at position 290 in EAAT1. The functional consequences of P290R substitution were evaluated after heterologous expression of the mutant protein in mammalian cells and demonstrated that P290R substitution has opposing effects on the two transport functions of EAAT1:

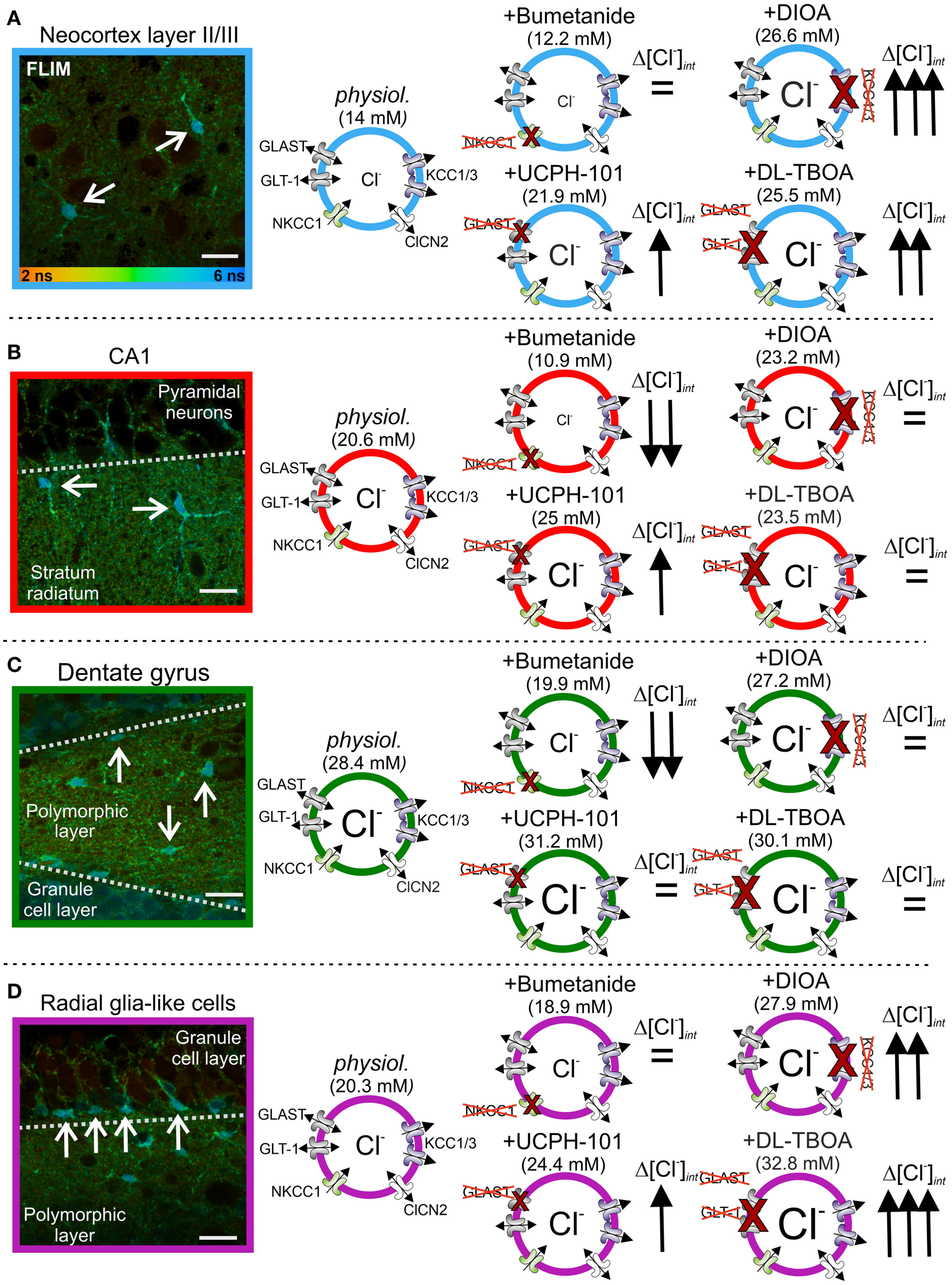

FIGURE 3 | Glial $[Cl^-]_{int}$ varies between brain regions. **(A–D)** Fluorescence lifetime microscopy (FLIM) images of neocortical **(A)** and hippocampal **(B)** CA1 and **(C)** dentate gyrus astrocytes, as well as **(D)** radial-glia-like cells (arrows). The $[Cl^-]_{int}$ varies between 14 mM in cortical astrocytes and 28 mM in dentate gyrus astrocytes. Modification of $[Cl^-]_{int}$ by anion transport blockers illustrate that differences in anion transport protein expression cause this variability. Scale bars: 20 μm. Modified and reprinted from Engels et al. (2021), with permission.

it reduces glutamate uptake (Jen et al., 2005; Winter et al., 2012) and enhances EAAT1 anion channel activity (Winter et al., 2012) (**Figure 4**). The neurological symptoms of the heterozygous patient were much more pronounced than the neurological phenotype of EAAT1/GLAST (the rodent EAAT1 homolog)-knockout animals (Watase et al., 1998; Stoffel et al., 2004; Miyazaki et al., 2017), suggesting that the disease is not caused by loss of function of the EAAT1 glutamate transport.

A heterozygous knock-in mouse (*Slc1a3*$^{P290R/+}$) carrying the disease-causing P290R mutation (Jen et al., 2005) showed ataxia and epilepsy, thus closely resembling the neurological symptoms of the human patient (Kovermann et al., 2020). In

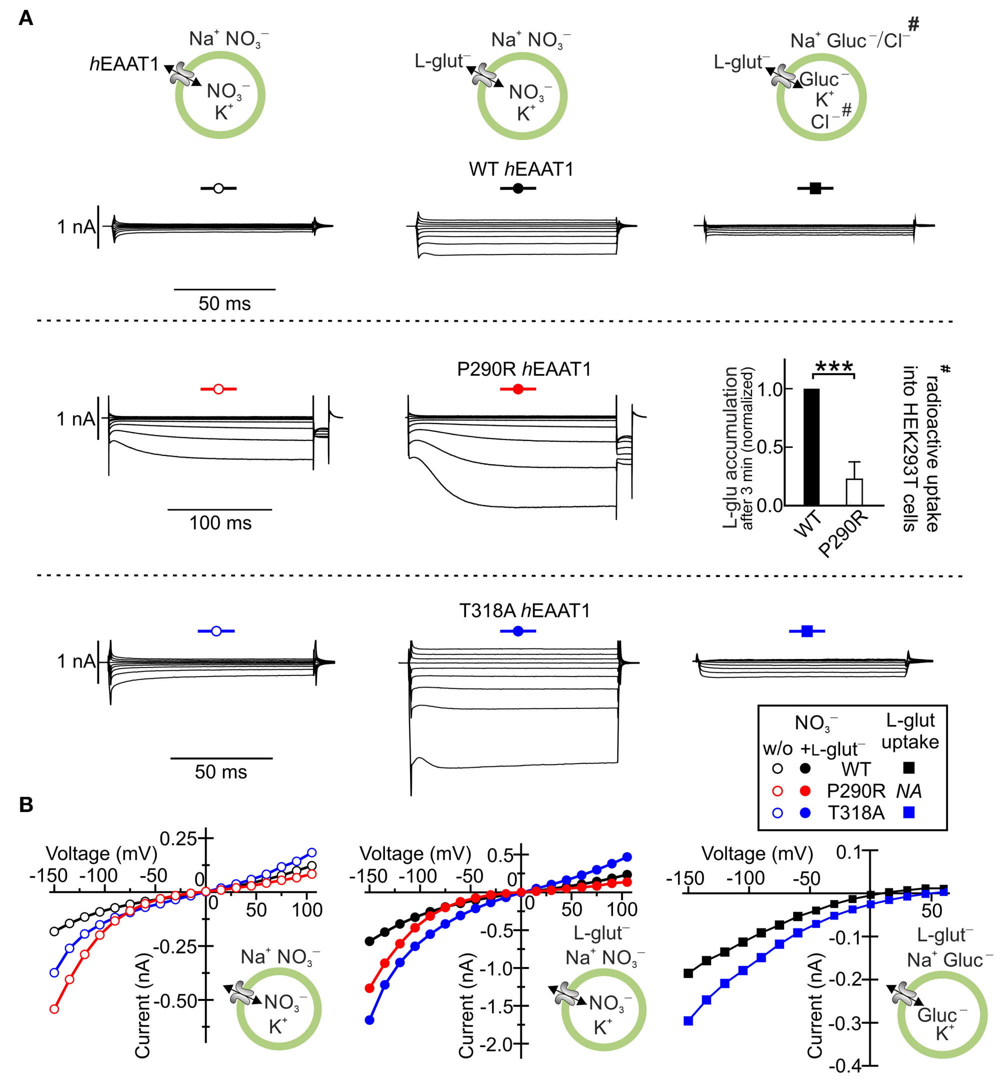

FIGURE 4 | *SLC1A3* mutations associated with episodic ataxia 6 modify EAAT1 anion channels. **(A)** Representative whole-cell current recordings of human wild-type (WT) EAAT1 and episodic ataxia 6-associated EAAT1 variants P290R and T318A heterologously expressed in HEK293T cells in the absence (left) and presence (middle) of external L-glutamate. Representative L-glutamate uptake currents are shown for WT EAAT1 and the variant T318A EAAT1 (right) and the results from radioactive uptake of L-^{3}[H]-glutamate$^{\#}$ into HEK293T cell lines stably expressing WT EAAT1 and the P290R EAAT1 variant (right). **(B)** Mean current–voltage relationships from whole-cell recordings of WT and variant EAAT1 proteins, as shown in **(A)**. *h*EAAT1: human EAAT1. Level of significance: ****p* ≤ 0.001. Reprinted in part from Winter et al. (2012) and Chivukula et al. (2020), with permissions.

Slc1a3$^{P290R/+}$animals, Bergmann glial cells almost completely disappeared between P10 and P20 due to apoptosis. Unaltered numbers of these cells in *Slc1a3*$^{-/-}$ animals showed that gain of function of the EAAT1/GLAST anion channel (rather than impaired glutamate transport) causes glial apoptosis (Watase et al., 1998; Stoffel et al., 2004; Miyazaki et al., 2017; Kovermann et al., 2020) (**Figures 5A,B**).

Glutamate-activated Cl^{-} currents were increased in electrophysiological recordings from *Slc1a3*$^{P290R/+}$ Bergmann glial cells (**Figure 5C**). Since EAAT1 contributes to chloride homeostasis in these cells, $[Cl^{-}]_{int}$ between P10 and P20 was compared in *Slc1a3*$^{P290R/+}$ and wild-type Bergmann glia (Kovermann et al., 2020). FLIM revealed a reduction in $[Cl^{-}]_{int}$ by ∼20% in *Slc1a3*$^{P290R/+}$ Bergmann glia (**Figures 5D,E**), indicating an increased outward Cl^{-} flux. Apoptotic events in Bergmann glial cells were significantly increased in mutant animals over the experimental time course (**Figure 5F**), suggesting that increased Cl^{-} efflux through P290R EAAT1/GLAST triggers Bergmann glial cell shrinking and apoptosis (Kovermann et al., 2020). Thus, impaired glial chloride homeostasis appears to be a major pathomechanism in episodic ataxia 6.

Functional analysis of other disease-associated *SLC1A3* mutations in heterologous expression systems revealed a variety of alterations in EAAT1 function (Chivukula et al., 2020), indicating that episodic ataxia 6 is not always caused by changes

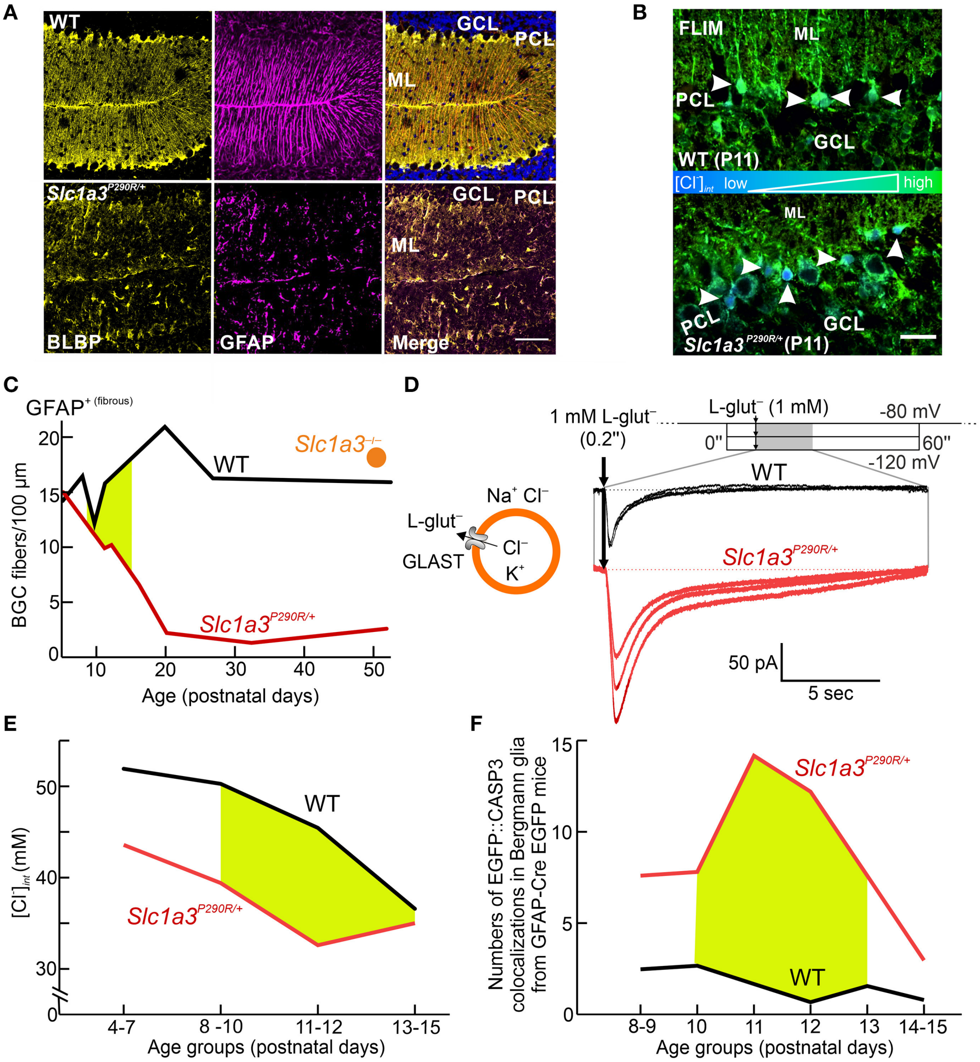

FIGURE 5 | Cellular Cl$^-$ depletion causes apoptosis in *Slc1a3*$^{P290R/+}$ Bergmann glial cells. **(A)** Confocal images show the disappearance of Bergmann glial cells (BGCs) in young mice (P20) heterozygous for the P290R mutation in EAAT1/GLAST by immunostaining BGCs for brain lipid-binding protein (BLBP, yellow) and glial fibrillary acidic protein (GFAP, magenta). **(B)** FLIM imaging of cerebellar cortices from wild-type (WT) and *Slc1a3*$^{P290R/+}$ mice indicates that P290R decreases [Cl$^-$]$_{\text{int}}$. Arrowheads depict MQAE-filled Bergmann glial cells. GCL, granule cell layer; ML, molecular layer; PCL, Purkinje cell layer. **(C)** Time course of BGC numbers in the cerebella of WT (black), *Slc1a3*$^{P290R/+}$ (red), and *Slc1a3*$^{-/-}$ (orange) mice shows that loss of BGCs occurs only in P290R mice—not in knockout animals. **(D)** Whole-cell patch-clamp recordings of acute brain slices from WT and *Slc1a3*$^{P290R/+}$ animals show gain of function of *Slc1a3*$^{P290R/+}$ anion channels in BGCs from mutant animals upon brief pulses of L-glutamate (L-glut). **(E)** [Cl$^-$]$_{\text{int}}$ is decreased in BGCs from *Slc1a3*$^{P290R/+}$ mice at all stages of early postnatal development. The age period for BGC loss is shown in yellow. **(F)** Number of cerebellar CASP3 signals in GFAP-EGFP-expressing mice during the second week of life. Reprinted in part and modified from Kovermann et al. (2020), with permission.

in the EAAT1 anion channel function but instead involves a range of functional defects in this transporter. The mutations C186S (RefSeq: NM_004172.4: c.556T>A), A329T (NM_004172.4: c.985G>A), V393I (NM_004172.4: c.1177G>A), and R499Q (alias R454Q, XM_024446182.1: c.1361G>A) (De Vries et al., 2009; Choi et al., 2017a,b; Iwama et al., 2018) increased protein expression but decreased glutamate uptake and anion channel function in *h*EAAT1. One mutation (M128R: NM_004172.4: c.383T>G) led to complete loss of transport and channel function, accompanied by decreased protein expression. Only one of the tested mutations, threonine to alanine substitution at position 318 in *h*EAAT1 (T318A: RefSeq NM_004172.4: c.952A>G), increased anion conductance and L-glutamate uptake through increased membrane insertion by factors of 2.4 and 1.6, respectively (Chivukula et al., 2020) (**Figure 4**). To understand how these subtle changes in function result in cerebellar incoordination, additional disease models need to be generated and analyzed.

SLC1A3 variants are not only associated with episodic ataxia 6. We reported a *SLC1A3* mutation in a young man with migraine with aura including hemiplegia (T387P); this mutation prevents glutamate transport by impairing K$^+$ binding

(Kovermann et al., 2017). A sequence variant predicting E219D in EAAT1 (RefSeq: NM_004172.4: c.657G>C) was recently associated with Tourette syndrome and hemiplegic migraine (Adamczyk et al., 2011); the variant shown to increase the surface expression of EAAT1 (Adamczyk et al., 2011). However, the E219D variant is also found in healthy individuals (gnomAD v2.1.1)—both heterozygous and homozygous—(Karczewski et al., 2020); therefore, this variant alone is unlikely to be responsible for Tourette syndrome. Gene duplication of *SLC1A3* was reported in patients with autism and attention deficit hyperactivity disorder (van Amen-Hellebrekers et al., 2016). Both *SLC1A3* duplication and the E219D variant might increase glutamate-activated anion channel currents in glial cells, and subsequent changes in anion currents or anion concentration in radial-glia-like cells might modify network formation during development, thus contributing to complex neuropsychiatric diseases. The EAAT3 variant R445W was found in a patient with symptoms of obsessive compulsive disorder who was also diagnosed with dicarboxyluria. R445 is highly conserved within vertebrate EAATs, and The R445W variant of EAAT3 has changed glutamate affinity (Bailey et al., 2011). Since this residue is critical for the anion selectivity of EAAT anion channels (Machtens et al., 2015; Cater et al., 2016), it is tempting to speculate that this variant might also affect the ion channel function of EAAT3.

GLIAL CHLORIDE HOMEOSTASIS UNDER ISCHEMIC STRESS

Reduced intracellular [ATP] is expected to inhibit primary active Na^+-K^+-ATPase and, thus, increase intracellular $[Na^+]$ and extracellular $[K^+]$. Since such alterations stimulate NKCC and KCC transport, and also enhance EAAT anion currents *via* impaired neurotransmitter uptake, energy restrictions are likely to interfere with glial chloride homeostasis. Engels et al. recently studied glial $[Cl^-]_{int}$ under transient ischemic stress in acute brain slices by FLIM. Whereas, $[Cl^-]_{int}$ and cell volumes stayed constant during 10 min of chemical ischemia, energy depletion during blockage of NKCC1 and KCCs significantly changed $[Cl^-]_{int}$. Thus, metabolic stress upregulates Cl^- inward and outward transport; increases in Cl^- flux in both directions compensate for each other and keep glial $[Cl^-]_{int}$ constant during transient moderate ischemia (Engels et al., 2021).

Glial $[Cl^-]_{int}$ under both control conditions and transient energy restriction can be quantitatively described with mathematical models, in which ion transport in pre- and post-synaptic neurons and astrocytes are described with a set of differential equations (Engels et al., 2021; Kalia et al., 2021). Differences in $[Cl^-]_{int}$ between cortical and hippocampal astrocytes under both control conditions and energy restriction could be modeled by varying NKCC and KCC densities. The role of EAAT anion channels during ischemic chloride homeostasis was tested by modifying the TBOA-sensitive leak conductance in such simulations. This did not affect the modeling results, indicating that EAAT anion channels contribute only slightly to energy restriction-induced changes in glial $[Cl^-]_{int}$. Taken together, these results support the notion that glial $[Cl^-]_{int}$ is in dynamic equilibrium between chloride inward transport and outward flux/transport by cation-coupled transporters and EAAT anion channels and that changes in transport rates are compensated during the initial phases of transient ischemia.

EAAT5 IMPROVES TEMPORAL RESOLUTION IN THE RETINA

The retina is a well-layered neuronal network (**Figure 6A**). Glutamate is released by photoreceptors (gray) in the outer plexiform layer (OPL) and bipolar cells (red and blue) in the inner plexiform layer (IPL). Photoreceptor synapses are complex structures with invaginations that harbor several post-synaptic processes and a pre-synaptic ribbon decorated with synaptic vesicles marking the glutamate release site at each invagination (**Figure 6B**, rod terminal, ribbon in blue). Each bipolar cell terminal makes several output synapses with ribbons and with two postsynaptic processes per ribbon (**Figure 6C**, shown for a rod bipolar terminal (RBT, blue, an interneuron relaying information from rod photoreceptors), ribbons in green, AC, amacrine cell process). EAAT1 is expressed at high levels in Müller cells (**Figure 6D**, left) and is assumed to mediate most of the retinal glutamate uptake (Derouiche and Rauen, 1995; Rauen et al., 1996, 1998; Lehre et al., 1997; Pow and Barnett, 1999; Izumi et al., 2002; Sarthy et al., 2005). EAAT2 is expressed in photoreceptors and bipolar cells (Rauen et al., 1996, 1998; Harada et al., 1998; Rauen and Wiessner, 2000), suggesting that it has a role in glutamate reuptake and recycling in glutamatergic cells. EAAT5 expression has been described in both synaptic layers and the somata of some bipolar, amacrine, and ganglion cells, as well as in photoreceptors, including their inner segments (Pow and Barnett, 2000; Wersinger et al., 2006). However, a recent study (Gehlen et al., 2021) found that *m*EAAT5 is strongly expressed in a punctate manner (**Figure 6D**, right) and is closely associated with glutamate release sites (indicated by the presence of synaptic ribbons) on both rod and cone photoreceptors in the outer plexiform layer (**Figures 6E–G**) and rod bipolar cells in the inner plexiform layer of the mouse retina (**Figure 6H**). While rod bipolar cell terminals were decorated with numerous *m*EAAT5-positive puncta (**Figure 6H**, colors correspond to scheme in **Figure 6C**), the label in cone bipolar cells was less clear. Evidence for EAAT5 expression in photoreceptors and rod bipolar cells also comes from electrophysiological studies (Eliasof and Werblin, 1993; Picaud et al., 1995b; Hasegawa et al., 2006; Veruki et al., 2006; Wersinger et al., 2006; Bligard et al., 2020). The striking difference in the expression patterns of EAAT1 and EAAT5 suggests that they have different functions. Owing to its close association with the glutamate-release site, EAAT5 is perfectly located to mediate glutamate-driven negative feedback.

Recordings from isolated retinae *in vitro* revealed that *m*EAAT5 is important to achieve high temporal resolution of retinal light responses when both rods and cones are active (Gehlen et al., 2021). When recording local field potentials in response to flicker stimuli of different frequencies (**Figure 6I**), temporal resolution was significantly compromised in *m*EAAT5$^{-/-}$ compared with wild-type retina (**Figure 6J**). A

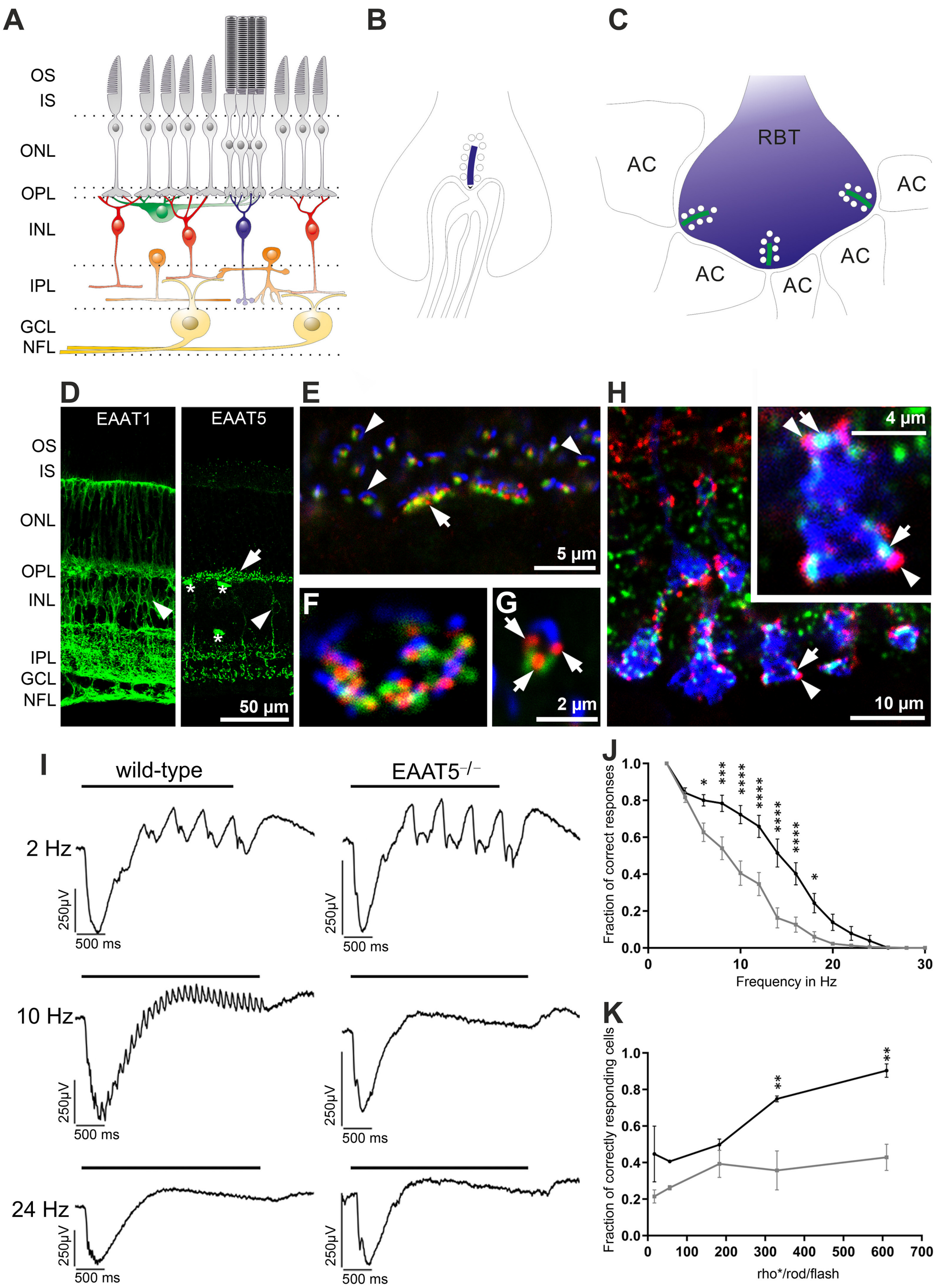

FIGURE 6 | Expression and role of EAAT5 in the retina. **(A)** Schematic diagram of the retinal network (photoreceptors in gray, horizontal cells in green, cone bipolar cells in red, rod bipolar cell in blue, amacrine cells in orange, ganglion cells in yellow) with synapses formed in the outer plexiform layer (OPL) and inner plexiform layer (IPL). GCL, ganglion cell layer; INL, inner nuclear layer; IPL, inner plexiform layer; IS, inner segments; NFL, nerve fiber layer; ONL, outer nuclear layer; OPL, outer plexiform layer; OS, outer segments. **(B)** Synapse at a rod terminal with presynaptic ribbon (blue) and invaginating post-synaptic processes of bipolar and horizontal cells. **(C)** Synapses at a rod bipolar terminal (RBT) with two post-synaptic amacrine processes (AC) per ribbon (green). **(D)** Comparison of EAAT1 (left) and EAAT5 (right) expression. EAAT1 is widely expressed in retinal Müller cells (arrowhead), whose processes span the entire retina. EAAT5 is mostly found in bright puncta (arrow) in both OPL and IPL and is expressed weakly in some bipolar cell bodies (arrowhead). Asterisks mark blood vessels stained unspecifically by the secondary antibody. **(E–G)** Triple staining with antibodies against mGluR6 (green, on ON-bipolar cell dendrites), EAAT5 (red), and piccolo (blue, synaptic ribbon, glutamate-release site) in the OPL of a wild-type retina. **(E)** EAAT5 puncta are always highly associated with the glutamate-release site. Arrow: cone terminal; arrowheads: rod terminals. **(F)** Higher magnification image showing the terminal of a cone in horizontal view. **(G)** Rod terminal in side view (three EAAT5 puncta are seen at the rod terminal, arrows). **(H)** Triple staining in the IPL, showing close association of EAAT5 puncta (red, arrowheads) with the synaptic ribbons (green, arrows) on rod bipolar cell terminals (blue, colors correspond to scheme in **C**). **(I)** Recordings of local field potentials in response to flicker stimuli of different frequencies. In contrast to the wild-type retina (left), EAAT5$^{-/-}$ retina (right) did not resolve the 10-Hz flicker stimulus. Bar represents duration of the flicker stimulus (total stimulus duration: 3 s; individual flash

(Continued)

FIGURE 6 | duration: 20 ms; 610 activated rhodopsin molecules (rho*) per rod and flash (rho*/rod/flash); mesopic conditions). **(J)** The fraction of correct responses was significantly reduced in EAAT5$^{-/-}$ (gray curve) compared with wild-type (black curve) retina. Stimulus parameters were the same as in **(I)**. **(K)** The impact of EAAT5 on temporal resolution in ON-ganglion cells increases with stimulus intensity [indicated as activated rhodopsin molecules (rho*) per rod and flash (rho*/rod/flash)]; flicker stimulus: 12 Hz, total stimulus duration: 3 s; individual flash duration: 20 ms. Black: wild type; gray: EAAT5$^{-/-}$. Levels of significance are: *$p \le 0.05$; **$p \le 0.01$; ***$p \le 0.001$; ****$p \le 0.0001$. Figure is modified and reprinted from Gehlen et al. (2021), with permission.

similar pattern was observed upon comparing the light responses of individual ganglion cells in the form of action potential trains. Moreover, the effect of *m*EAAT5 on temporal resolution grew stronger with increasing stimulus intensity (**Figure 6K**), consistent with the fact that the light-evoked modulation of glutamate release—and, hence, the impact of EAAT5—depends on the brightness of the stimulus. The effect of *m*EAAT5 deletion is in perfect agreement with the postulated role for EAAT5 at rod bipolar cell terminals, where it was shown to act as a glutamate-gated chloride channel (Veruki et al., 2006; Wersinger et al., 2006) and may be important for gain control (Bligard et al., 2020). Upon depolarization of the rod bipolar cell, glutamate release at the output synapse would activate not only the glutamate receptors on postsynaptic cells but also presynaptic EAAT5, leading to chloride influx, hyperpolarization of the cell, and consequently, reduced bipolar cell output. This negative feedback would curtail the bipolar cell response to individual flashes during repetitive stimulation and, therefore, increase temporal resolution. However, the effect of EAAT5 on glutamate buffering and reuptake in the synaptic cleft might also help to fine-tune the action of glutamate at post-synaptic cells. The synergistic action of both mechanisms might account for the increased temporal resolution in wild-type retina.

Obviously, the role of EAAT5 in photoreceptor terminals needs to be addressed in future studies. Hasegawa et al. (2006) reported that EAAT5-mediated glutamate clearance at the photoreceptor synapse is important for shaping light responses at rod–rod bipolar cell synapses in mice. However, the photoreceptor synapse is highly complex and a number of feedback mechanisms have been described. EAAT5 knockout in photoreceptors might lead to elevated levels of glutamate in the synaptic cleft, thus triggering a variety of possible mechanisms. For example, a metabotropic glutamate receptor was reported on cone terminals, and this might become activated and could affect the rate of glutamate release (Van Hook et al., 2017). EAAT5 might also affect photoreceptor output *via* its function as chloride channel by regulating $[\mathrm{Cl}^-]_{\mathrm{int}}$ at the terminal. In salamander photoreceptors, chloride dynamics in the photoreceptor terminal affect the activation properties of voltage-activated calcium channels (Thoreson et al., 2000, 2003; Thoreson and Bryson, 2004; Li et al., 2008) and, hence, synaptic transmission.

In white perch retina, a glutamate-gated chloride conductance (probably mediated by EAAT5) was also found postsynaptic to photoreceptors on dendrites of certain ON-bipolar cell types that receive a mixed input from rods and cones (Grant and Dowling, 1995). As photoreceptors are depolarized in the dark, their glutamate must hyperpolarize ON-bipolar cells. Typically, glutamate binding to mGluR6 closes TRPM1 channels in ON-bipolar cells (Koike et al., 2010; Morgans et al., 2010), leading to hyperpolarization. The ON-bipolar cells recorded by Grant and Dowling (1995) also contain a mGluR6 cascade that relays information by rod input, while cone input activates the EAAT anion conductance. Thus, in this particular ON-bipolar cell type, hyperpolarization is achieved by two functionally distinct mechanisms.

Interestingly, EAAT5 was also reported at the ribbon synapses of vestibular hair cells (Dalet et al., 2012) but not at the calyx of Held (Palmer et al., 2003), a well-studied conventional glutamatergic synapse. Compared with conventional synapses, ribbon synapses are characterized by much higher and sustained vesicular release based on graded potentials. It is, therefore, tempting to speculate that EAAT5-mediated feedback triggered by glutamate release might be a common mechanism to regulate synaptic output at ribbon synapses.

CONCLUSIONS

Glutamate transport seems to be inseparably linked to anion channel function. Even archaebacterial EAAT homologs exhibit this curious dual function (Ryan and Mindell, 2007; Machtens et al., 2015), and not only EAAT glutamate transporters but also vesicular glutamate transporters can function as anion channels (Schenck et al., 2009; Eriksen et al., 2016). In recent years, considerable progress has been made in assigning cellular processes to EAAT anion channels in selected cell types. In glial cells, EAAT1 and EAAT2 anion channels have been shown to contribute to glial chloride homeostasis (Untiet et al., 2017; Engels et al., 2021) under normal conditions. In a human genetic disease, gain of function in EAAT anion currents causes severe neurological symptoms by impairing glial chloride homeostasis (Winter et al., 2012; Kovermann et al., 2020). In non-retinal neurons, the role of EAAT anion channels has not yet been addressed. We postulate that presynaptic EAAT2 transporters (Petr et al., 2015) may contribute to cytoplasmic $[\mathrm{Cl}^-]_{\mathrm{int}}$ in nerve terminals. As the anion channel function of vesicular glutamate transporters likely also affects glutamate accumulation in synaptic vesicles (Martineau et al., 2017), EAAT2 anion channels might contribute to setting vesicular glutamate concentrations. Additionally, presynaptic EAAT2 might fulfill similar roles to EAAT5 in the retina and mediate negative feedback in glutamate release; however, presynaptic $[\mathrm{Cl}^-]_{\mathrm{int}}$ is not currently known. The potential roles of anion channels associated with epithelial EAAT isoforms (Kanai and Hediger, 1992; Bailey et al., 2011) have not yet been investigated.

The cellular physiology and pathophysiology of EAAT anion channels are insufficiently understood, but recent progress leaves little doubt that this transport function, which was initially thought to represent transporter slippage (i.e., ion flux through accidental pore opening due to imperfect coordination of transporters during coupled transport), serves important cellular functions.

AUTHOR CONTRIBUTIONS

PK, ME, FM, and CF wrote the manuscript. PK and FM generated the figures. All authors approved the submitted version.

FUNDING

This work was supported by the Deutsche Forschungsgemeinschaft (DFG, German Research Foundation) to CF (FA 301/13-1) as part of the Research Unit FOR 2795 (Synapses under stress) and by the German Ministry of Education and Research (E-RARE network Treat-ION, BMBF 01GM1907C to CF).

ACKNOWLEDGMENTS

The authors gratefully acknowledge the computing time granted through JARA on the supercomputer JURECA at the Forschungszentrum Jülich.

REFERENCES

Abrahamsen, B., Schneider, N., Erichsen, M. N., Huynh, T. H., Fahlke, C., Bunch, L., et al. (2013). Allosteric modulation of an excitatory amino acid transporter: the subtype-selective inhibitor UCPH-101 exerts sustained inhibition of EAAT1 through an intramonomeric site in the trimerization domain. *J. Neurosci.* 33, 1068–1087. doi: 10.1523/JNEUROSCI.3396-12.2013

Adamczyk, A., Gause, C. D., Sattler, R., Vidensky, S., Rothstein, J. D., Singer, H., et al. (2011). Genetic and functional studies of a missense variant in a glutamate transporter, SLC1A3, in Tourette syndrome. *Psychiatr. Genet.* 21, 90–97. doi: 10.1097/YPG.0b013e328341a307

Arkhipova, V., Trinco, G., Ettema, T. W., Jensen, S., Slotboom, D. J., and Guskov, A. (2019). Binding and transport of D-aspartate by the glutamate transporter homolog GltTk. *Elife* 8:e45286. doi: 10.7554/eLife.45286.015

Arriza, J. L., Eliasof, S., Kavanaugh, M. P., and Amara, S. G. (1997). Excitatory amino acid transporter 5, a retinal glutamate transporter coupled to a chloride conductance. *Proc. Natl. Acad. Sci. U.S.A.* 94, 4155–4160. doi: 10.1073/pnas.94.8.4155

Bailey, C. G., Ryan, R. M., Thoeng, A. D., Ng, C., King, K., Vanslambrouck, J. M., et al. (2011). Loss-of-function mutations in the glutamate transporter SLC1A1 cause human dicarboxylic aminoaciduria. *J. Clin. Invest.* 121, 446–453. doi: 10.1172/JCI44474

Bevensee, M. O., Weed, R. A., and Boron, W. F. (1997). Intracellular pH regulation in cultured astrocytes from rat hippocampus. I. Role Of HCO_3?. *J. Gen. Physiol.* 110, 453–465. doi: 10.1085/jgp.110.4.453

Bligard, G. W., DeBrecht, J., Smith, R. G., and Lukasiewicz, P. D. (2020). Light-evoked glutamate transporter EAAT5 activation coordinates with conventional feedback inhibition to control rod bipolar cell output. *J. Neurophysiol.* 123, 1828–1837. doi: 10.1152/jn.00527.2019

Boudker, O., Ryan, R. M., Yernool, D., Shimamoto, K., and Gouaux, E. (2007). Coupling substrate and ion binding to extracellular gate of a sodium-dependent aspartate transporter. *Nature* 445, 387–393. doi: 10.1038/nature05455

Cater, R. J., Vandenberg, R. J., and Ryan, R. M. (2014). The domain interface of the human glutamate transporter EAAT1 mediates chloride permeation. *Biophys. J.* 107, 621–629. doi: 10.1016/j.bpj.2014.05.046

Cater, R. J., Vandenberg, R. J., and Ryan, R. M. (2016). Tuning the ion selectivity of glutamate transporter-associated uncoupled conductances. *J. Gen. Physiol.* 148, 13–24. doi: 10.1085/jgp.201511556

Chen, I., Pant, S., Wu, Q., Cater, R. J., Sobti, M., Vandenberg, R. J., et al. (2021). Glutamate transporters have a chloride channel with two hydrophobic gates. *Nature* 591, 327–331. doi: 10.1038/s41586-021-03240-9

Chivukula, A. S., Suslova, M., Kortzak, D., Kovermann, P., and Fahlke, C. (2020). Functional consequences of *SLC1A3* mutations associated with episodic ataxia 6. *Hum. Mutat.* 41, 1892–1905. doi: 10.1002/humu.24089

Choi, K. D., Jen, J. C., Choi, S. Y., Shin, J., Kim, H., Kim, H., et al. (2017b). Late-onset episodic ataxia associated with *SLC1A3* mutation. *J. Hum. Genet.* 62, 443–446. doi: 10.1038/jhg.2016.137

Choi, K. D., Kim, J. S., Kim, H. J., Jung, I., Jeong, S. H., Lee, S. H., et al. (2017a). Genetic variants associated with episodic ataxia in Korea. *Sci. Rep.* 7:13855. doi: 10.1038/s41598-017-14254-7

Crisman, T. J., Qu, S., Kanner, B. I., and Forrest, L. R. (2009). Inward-facing conformation of glutamate transporters as revealed by their inverted-topology structural repeats. *Proc. Natl. Acad. Sci. U.S.A.* 106, 20752–20757. doi: 10.1073/pnas.0908570106

Dalet, A., Bonsacquet, J., Gaboyard-Niay, S., Calin-Jageman, I., Chidavaenzi, R. L., Venteo, S., et al. (2012). Glutamate transporters EAAT4 and EAAT5 are expressed in vestibular hair cells and calyx endings. *PLoS ONE* 7:e46261. doi: 10.1371/journal.pone.0046261

Danbolt, N. C. (2001). Glutamate uptake. *Prog. Neurobiol.* 65, 1–105. doi: 10.1016/S0301-0082(00)00067-8

De Vries, B., Mamasa, H., Stam, A. H., Wan, J., Bakker, S. L., Vanmolkot, K. R., et al. (2009). Episodic ataxia associated with EAAT1 mutation C186S affecting glutamate reuptake. *Arch. Neurol.* 66, 97–101. doi: 10.1001/archneurol.2008.535

Derouiche, A., and Rauen, T. (1995). Coincidence of L-glutamate/L-aspartate transporter (GLAST) and glutamine synthetase (GS) immunoreactions in retinal glia: evidence for coupling of GLAST and GS in transmitter clearance. *J. Neurosci. Res.* 42, 131–143. doi: 10.1002/jnr.490420115

Divito, C. B., Borowski, J. E., Glasgow, N. G., Gonzalez-Suarez, A. D., Torres-Salazar, D., Johnson, J. W., et al. (2017). Glial and neuronal glutamate transporters differ in the Na^+ requirements for activation of the substrate-independent anion conductance. *Front. Mol. Neurosci.* 10:150. doi: 10.3389/fnmol.2017.00150

Eliasof, S., Arriza, J. L., Leighton, B. H., Kavanaugh, M. P., and Amara, and, S. G. (1998). Excitatory amino acid transporters of the salamander retina: identification, localization, and function. *J. Neurosci.* 18, 698–712. doi: 10.1523/JNEUROSCI.18-02-00698.1998

Eliasof, S., and Werblin, F. (1993). Characterization of the glutamate transporter in retinal cones of the tiger salamander. *J. Neurosci.* 13, 402–411. doi: 10.1523/JNEUROSCI.13-01-00402.1993

Engels, M., Kalia, M., Rahmati, S., Petersilie, L., Kovermann, P., van Putten, M. J. A. M., et al. (2021). Glial Chloride Homeostasis Under Transient Ischemic Stress. *Front. Cell. Neurosci.* 15:735300. doi: 10.3389/fncel.2021.735300

Eriksen, J., Chang, R., McGregor, M., Silm, K., Suzuki, T., and Edwards, R. H. (2016). Protons regulate vesicular glutamate transporters through an allosteric mechanism. *Neuron* 90, 768–780. doi: 10.1016/j.neuron.2016.03.026

Fahlke, C., Kortzak, D., and Machtens, J. P. (2016). Molecular physiology of EAAT anion channels. *Pflugers Arch.* 468, 491–502. doi: 10.1007/s00424-015-1768-3

Fairman, W. A., Vandenberg, R. J., Arriza, J. L., Kavanaugh, M. P., and Amara, S. G. (1995). An excitatory amino-acid transporter with properties of a ligand-gated chloride channel. *Nature* 375, 599–603. doi: 10.1038/375599a0

Futamachi, K. J., and Pedley, T. A. (1976). Glial cells and extracellular potassium: their relationship in mammalian cortex. *Brain Res.* 109, 311–322. doi: 10.1016/0006-8993(76)90532-1

Gameiro, A., Braams, S., Rauen, T., and Grewer, C. (2011). The discovery of slowness: Low-capacity transport and slow anion channel gating by the glutamate transporter EAAT5. *Biophys. J.* 100, 2623–2632. doi: 10.1016/j.bpj.2011.04.034

Gehlen, J., Aretzweiler, C., Mataruga, A., Fahlke, C., and Müller, F. (2021). Excitatory amino acid transporter EAAT5 improves temporal resolution in the retina. *eNeuro* 8, 1–15. doi: 10.1523/ENEURO.0406-21.2021

Gendreau, S., Voswinkel, S., Torres-Salazar, D., Lang, N., Heidtmann, H., Detro-Dassen, S., et al. (2004). A trimeric quaternary structure is conserved in bacterial and human glutamate transporters. *J. Biol. Chem.* 279, 39505–39512. doi: 10.1074/jbc.M408038200

Grant, G. B., and Dowling, J. E. (1995). A glutamate-activated chloride current in cone-driven ON bipolar cells of the white perch retina. *J. Neurosci.* 15(5 Pt 2), 3852–3862. doi: 10.1523/JNEUROSCI.15-05-03852.1995

Grewer, C., Balani, P., Weidenfeller, C., Bartusel, T., Tao, Z., and Rauen, T. (2005). Individual subunits of the glutamate transporter EAAC1 homotrimer function independently of each other. *Biochemistry* 44, 11913–11923. doi: 10.1021/bi050987n

Grewer, C., Gameiro, A., Zhang, Z., Tao, Z., Braams, S., and Rauen, T. (2008). Glutamate forward and reverse transport: from molecular mechanism to transporter-mediated release after ischemia. *IUBMB Life* 60, 609–619. doi: 10.1002/iub.98

Guskov, A., Jensen, S., Faustino, I., Marrink, S. J., and Slotboom, D. J. (2016). Coupled binding mechanism of three sodium ions and aspartate in the glutamate transporter homologue GltTk. *Nat. Commun.* 7:13420. doi: 10.1038/ncomms13420

Harada, T., Harada, C., Watanabe, M., Inoue, Y., Sakagawa, T., Nakayama, N., et al. (1998). Functions of the two glutamate transporters GLAST and GLT-1 in the retina. *Proc. Natl. Acad. Sci. U.S.A.* 95, 4663–4666. doi: 10.1073/pnas.95.8.4663

Hasegawa, J., Obara, T., Tanaka, K., and Tachibana, M. (2006). High-density presynaptic transporters are required for glutamate removal from the first visual synapse. *Neuron* 50, 63–74. doi: 10.1016/j.neuron.2006.02.022

Iwama, K., Iwata, A., Shiina, M., Mitsuhashi, S., Miyatake, S., Takata, A., et al. (2018). A novel mutation in *SLC1A3* causes episodic ataxia. *J. Hum. Genet*. 63, 207–211. doi: 10.1038/s10038-017-0365-z

Izumi, Y., Shimamoto, K., Benz, A. M., Hammerman, S. B., Olney, J. W., and Zorumski, C. F. (2002). Glutamate transporters and retinal excitotoxicity. *Glia* 39, 58–68. doi: 10.1002/glia.10082

Jen, J. C., Wan, J., Palos, T. P., Howard, B. D., and Baloh, R. W. (2005). Mutation in the glutamate transporter EAAT1 causes episodic ataxia, hemiplegia, and seizures. *Neurology* 65, 529–534. doi: 10.1212/01.WNL.0000172638.58172.5a

Jensen, S., Guskov, A., Rempel, S., Hanelt, I., and Slotboom, D. J. (2013). Crystal structure of a substrate-free aspartate transporter. *Nat. Struct. Mol. Biol.* 20, 1224–1226. doi: 10.1038/nsmb.2663

Kalia, M., Meijer, H. G. E., Van Gils, S. A., van Putten, M. J., and Rose, C. R. (2021). Ion dynamics at the tripartite synapse. *PLoS Comput. Biol.* 17:e1009019. doi: 10.1371/journal.pcbi.1009019

Kanai, Y., and Hediger, M. A. (1992). Primary structure and functional characterization of a high-affinity glutamate transporter. *Nature* 360, 467–471. doi: 10.1038/360467a0

Kanner, B. I. (2006). Structure and function of sodium-coupled GABA and glutamate transporters. *J. Membr. Biol.* 213, 89–100. doi: 10.1007/s00232-006-0877-5

Karczewski, K. J., Francioli, L. C., Tiao, G., Cummings, B. B., Alfoldi, J., Wang, Q., et al. (2020). The mutational constraint spectrum quantified from variation in 141,456 humans. *Nature* 581, 434–443. doi: 10.1038/s41586-020-2308-7

Kettenmann, H., Backus, K. H., and Schachner, M. (1987). γ-Aminobutyric acid opens Cl-channels in cultured astrocytes. *Brain Res.* 404, 1–9. doi: 10.1016/0006-8993(87)91349-7

Kimelberg, H. K. (1981). Active accumulation and exchange transport of chloride in astroglial cells in culture. *Biochim. Biophys. Acta* 646, 179–184. doi: 10.1016/0005-2736(81)90285-6

Koch, H. P., Brown, R. L., and Larsson, H. P. (2007). The glutamate-activated anion conductance in excitatory amino acid transporters is gated independently by the individual subunits. *J. Neurosci.* 27, 2943–2947. doi: 10.1523/JNEUROSCI.0118-07.2007

Koike, C., Obara, T., Uriu, Y., Numata, T., Sanuki, R., Miyata, K., et al. (2010). TRPM1 is a component of the retinal ON bipolar cell transduction channel in the mGluR6 cascade. *Proc. Natl. Acad. Sci. U.S.A.* 107, 332–337. doi: 10.1073/pnas.0912730107

Kolen, B., Kortzak, D., Franzen, A., and Fahlke, C. (2020). An amino-terminal point mutation increases EAAT2 anion currents without affecting glutamate transport rates. *J. Biol. Chem*. 295, 14936–14947. doi: 10.1074/jbc.RA120.013704

Kortzak, D., Alleva, C., Weyand, I., Ewers, D., Zimmermann, M. I., Franzen, A., et al. (2019). Allosteric gate modulation confers K^+ coupling in glutamate transporters. *EMBO J.* 38:e101468. doi: 10.15252/embj.2019101468

Kovermann, P., Hessel, M., Kortzak, D., Jen, J. C., Koch, J., Fahlke, C., et al. (2017). Impaired K^+ binding to glial glutamate transporter EAAT1 in migraine. *Sci. Rep.* 7:13913. doi: 10.1038/s41598-017-14176-4

Kovermann, P., Machtens, J. P., Ewers, D., and Fahlke, C. (2010). A conserved aspartate determines pore properties of anion channels associated with excitatory amino acid transporter 4 (EAAT4). *J. Biol. Chem.* 285, 23676–23686. doi: 10.1074/jbc.M110.126557

Kovermann, P., Untiet, V., Kolobkova, Y., Engels, M., Baader, S., Schilling, K., et al. (2020). Increased glutamate transporter-associated anion currents cause glial apoptosis in episodic ataxia 6. *Brain Commun.* 2:fcaa022. doi: 10.1093/braincomms/fcaa022

Kutzner, C., Grubmuller, H., de Groot, B. L., and Zachariae, U. (2011). Computational electrophysiology: the molecular dynamics of ion channel permeation and selectivity in atomistic detail. *Biophys. J.* 101, 809–817. doi: 10.1016/j.bpj.2011.06.010

Larsson, H. P., Picaud, S. A., Werblin, F. S., and Lecar, H. (1996). Noise analysis of the glutamate-activated current in photoreceptors. *Biophys. J.* 70, 733–742. doi: 10.1016/S0006-3495(96)79613-3

Leary, G. P., Stone, E. F., Holley, D. C., and Kavanaugh, M. P. (2007). The glutamate and chloride permeation pathways are colocalized in individual neuronal glutamate transporter subunits. *J. Neurosci.* 27, 2938–2942. doi: 10.1523/JNEUROSCI.4851-06.2007

Lehre, K. P., Davanger, S., and Danbolt, N. C. (1997). Localization of the glutamate transporter protein GLAST in rat retina. *Brain Res.* 744, 129–137. doi: 10.1016/S0006-8993(96)01022-0

Leinenweber, A., Machtens, J. P., Begemann, B., and Fahlke, C. (2011). Regulation of glial glutamate transporters by C-terminal domains. *J. Biol. Chem.* 286, 1927–1937. doi: 10.1074/jbc.M110.153486

Li, B., McKernan, K., and Shen, W. (2008). Spatial and temporal distribution patterns of Na-K-2Cl cotransporter in adult and developing mouse retinas. *Vis. Neurosci.* 25, 109–123. doi: 10.1017/S0952523808080164

Lothman, E. W., and Somjen, G. G. (1975). Extracellular potassium activity, intracellular and extracellular potential responses in the spinal cord. *J. Physiol.* 252, 115–136. doi: 10.1113/jphysiol.1975.sp011137

Machtens, J. P., Kortzak, D., Lansche, C., Leinenweber, A., Kilian, P., Begemann, B., et al. (2015). Mechanisms of anion conduction by coupled glutamate transporters. *Cell* 160, 542–553. doi: 10.1016/j.cell.2014.12.035

Machtens, J. P., Kovermann, P., and Fahlke, C. (2011). Substrate-dependent gating of anion channels associated with excitatory amino acid transporter 4. *J. Biol. Chem.* 286, 23780–23788. doi: 10.1074/jbc.M110.207514

Martineau, M., Guzman, R. E., Fahlke, C., and Klingauf, J. (2017). VGLUT1 functions as a glutamate/proton exchanger with chloride channel activity in hippocampal glutamatergic synapses. *Nat. Commun.* 8:2279. doi: 10.1038/s41467-017-02367-6

Mim, C., Balani, P., Rauen, T., and Grewer, C. (2005). The glutamate transporter subtypes EAAT4 and EAATs 1-3 transport glutamate with dramatically different kinetics and voltage dependence but share a common uptake mechanism. *J. Gen. Physiol.* 126, 571–589. doi: 10.1085/jgp.200509365

Miyazaki, T., Yamasaki, M., Hashimoto, K., Kohda, K., Yuzaki, M., Shimamoto, K., et al. (2017). Glutamate transporter GLAST controls synaptic wrapping by Bergmann glia and ensures proper wiring of Purkinje cells. *Proc. Natl. Acad. Sci. U.S.A.* 114, 7438–7443. doi: 10.1073/pnas.1617330114

Morgans, C. W., Brown, R. L., and Duvoisin, R. M. (2010). TRPM1: the endpoint of the mGluR6 signal transduction cascade in retinal ON-bipolar cells. *Bioessays* 32, 609–614. doi: 10.1002/bies.200900198

Nothmann, D., Leinenweber, A., Torres-Salazar, D., Kovermann, P., Hotzy, J., Gameiro, A., et al. (2011). Hetero-oligomerization of neuronal glutamate transporters. *J. Biol. Chem.* 286, 3935–3943. doi: 10.1074/jbc.M110.187492

Palmer, M. J., Taschenberger, H., Hull, C., Tremere, L., and von Gersdorff, H. (2003). Synaptic activation of presynaptic glutamate transporter currents in nerve terminals. *J. Neurosci.* 23, 4831–4841. doi: 10.1523/JNEUROSCI.23-12-04831.2003

Petr, G. T., Sun, Y., Frederick, N. M., Zhou, Y., Dhamne, S. C., Hameed, M. Q., et al. (2015). Conditional deletion of the glutamate transporter GLT-1 reveals that astrocytic GLT-1 protects against fatal epilepsy while neuronal GLT-1 contributes significantly to glutamate uptake into synaptosomes. *J. Neurosci.* 35, 5187–5201. doi: 10.1523/JNEUROSCI.4255-14.2015

Picaud, S. A., Larsson, H. P., Grant, G. B., Lecar, H., and Werblin, F. S. (1995b). Glutamate-gated chloride channel with glutamate-transporter-like properties in cone photoreceptors of the tiger salamander. *J. Neurophysiol.* 74, 1760–1771. doi: 10.1152/jn.1995.74.4.1760

Picaud, S. A., Larsson, H. P., Wellis, D. P., Lecar, H., and Werblin, F. (1995a). Cone photoreceptors respond to their own glutamate release in the tiger salamander. *Proc. Natl. Acad. Sci. U.S.A.* 92, 9417–9421. doi: 10.1073/pnas.92.20.9417

Pines, G., Danbolt, N. C., Bjoras, M., Zhang, Y., Bendahan, A., Eide, L., et al. (1992). Cloning and expression of a rat brain L-glutamate transporter. *Nature* 360, 464–467. doi: 10.1038/360464a0

Pow, D. V., and Barnett, N. L. (1999). Changing patterns of spatial buffering of glutamate in developing rat retinae are mediated by the Muller cell glutamate transporter GLAST. *Cell Tissue Res.* 297, 57–66. doi: 10.1007/s004410051333

Pow, D. V., and Barnett, N. L. (2000). Developmental expression of excitatory amino acid transporter 5: a photoreceptor and bipolar cell glutamate transporter in rat retina. *Neurosci. Lett.* 280, 21–24. doi: 10.1016/S0304-3940(99)00988-X

Rauen, T., Rothstein, J. D., and Wassle, H. (1996). Differential expression of three glutamate transporter subtypes in the rat retina. *Cell Tissue Res.* 286, 325–336. doi: 10.1007/s004410050702

Rauen, T., Taylor, W. R., Kuhlbrodt, K., and Wiessner, M. (1998). High-affinity glutamate transporters in the rat retina: a major role of the glial glutamate transporter GLAST-1 in transmitter clearance. *Cell Tissue Res.* 291, 19–31. doi: 10.1007/s004410050976

Rauen, T., and Wiessner, M. (2000). Fine tuning of glutamate uptake and degradation in glial cells: common transcriptional regulation of GLAST1 and GS. *Neurochem. Int.* 37, 179–189. doi: 10.1016/S0197-0186(00)00021-8

Reyes, N., Ginter, C., and Boudker, O. (2009). Transport mechanism of a bacterial homologue of glutamate transporters. *Nature* 462, 880–885. doi: 10.1038/nature08616

Ryan, R. M., and Mindell, J. A. (2007). The uncoupled chloride conductance of a bacterial glutamate transporter homolog. *Nat. Struct. Mol. Biol.* 14, 365–371. doi: 10.1038/nsmb1230

Ryan, R. M., Mitrovic, A. D., and Vandenberg, R. J. (2004). The chloride permeation pathway of a glutamate transporter and its proximity to the glutamate translocation pathway. *J. Biol. Chem.* 279, 20742–20751. doi: 10.1074/jbc.M304433200

Sarthy, V. P., Pignataro, L., Pannicke, T., Weick, M., Reichenbach, A., Harada, T., et al. (2005). Glutamate transport by retinal Muller cells in glutamate/aspartate transporter-knockout mice. *Glia* 49, 184–196. doi: 10.1002/glia.20097

Schenck, S., Wojcik, S. M., Brose, N., and Takamori, S. (2009). A chloride conductance in VGLUT1 underlies maximal glutamate loading into synaptic vesicles. *Nat. Neurosci.* 12, 156–162. doi: 10.1038/nn.2248

Schneider, N., Cordeiro, S., Machtens, J. P., Braams, S., Rauen, T., and Fahlke, C. (2014). Functional properties of the retinal glutamate transporters GLT-1c and EAAT5. *J. Biol. Chem.* 289:1815. doi: 10.1074/jbc.M113.517177

Stoffel, W., Korner, R., Wachtmann, D., and Keller, B. U. (2004). Functional analysis of glutamate transporters in excitatory synaptic transmission of GLAST1 and GLAST1/EAAC1 deficient mice. *Brain Res. Mol. Brain Res.* 128, 170–181. doi: 10.1016/j.molbrainres.2004.06.026

Storck, T., Schulte, S., Hofmann, K., and Stoffel, W. (1992). Structure, expression, and functional analysis of a Na^+-dependent glutamate/aspartate transporter from rat brain. *Proc. Natl. Acad. Sci. U.S.A.* 89, 10955–10959. doi: 10.1073/pnas.89.22.10955

Tao, Z., Zhang, Z., and Grewer, C. (2006). Neutralization of the aspartic acid residue Asp-367, but not Asp-454, inhibits binding of Na^+ to the glutamate-free form and cycling of the glutamate transporter EAAC1. *J. Biol. Chem.* 281, 10263–10272. doi: 10.1074/jbc.M510739200

Thoreson, W. B., and Bryson, E. J. (2004). Chloride equilibrium potential in salamander cones. *BMC Neurosci.* 5:53. doi: 10.1186/1471-2202-5-53

Thoreson, W. B., Bryson, E. J., and Rabl, K. (2003). Reciprocal interactions between calcium and chloride in rod photoreceptors. *J. Neurophysiol.* 90, 1747–1753. doi: 10.1152/jn.00932.2002

Thoreson, W. B., Nitzan, R., and Miller, R. F. (2000). Chloride efflux inhibits single calcium channel open probability in vertebrate photoreceptors: chloride imaging and cell-attached patch-clamp recordings. *Vis. Neurosci.* 17, 197–206. doi: 10.1017/S0952523800172025

Torres-Salazar, D., and Fahlke, C. (2007). Neuronal glutamate transporters vary in substrate transport rate but not in unitary anion channel conductance. *J. Biol. Chem.* 282, 34719–34726. doi: 10.1074/jbc.M704118200

Untiet, V., Kovermann, P., Gerkau, N. J., Gensch, T., Rose, C. R., and Fahlke, C. (2017). Glutamate transporter-associated anion channels adjust intracellular chloride concentrations during glial maturation. *Glia* 65, 388–400. doi: 10.1002/glia.23098

van Amen-Hellebrekers, C. J., Jansen, S., Pfundt, R., Schuurs-Hoeijmakers, J. H., Koolen, D. A., Marcelis, C. L., et al. (2016). Duplications of *SLC1A3*: Associated with ADHD and autism. *Eur. J. Med. Genet.* 59, 373–376. doi: 10.1016/j.ejmg.2016.06.003

Van Hook, M. J., Babai, N., Zurawski, Z., Yim, Y. Y., Hamm, H. E., and Thoreson, W. B. (2017). A presynaptic group III mGluR recruits Gβγ/SNARE interactions to inhibit synaptic transmission by cone photoreceptors in the vertebrate retina. *J. Neurosci.* 37, 4618–4634. doi: 10.1523/JNEUROSCI.2948-16.2017

Verdon, G., and Boudker, O. (2012). Crystal structure of an asymmetric trimer of a bacterial glutamate transporter homolog. *Nat. Struct. Mol. Biol.* 19, 355–357. doi: 10.1038/nsmb.2233

Verdon, G., Oh, S., Serio, R. N., and Boudker, O. (2014). Coupled ion binding and structural transitions along the transport cycle of glutamate transporters. *Elife* 3:e02283. doi: 10.7554/eLife.02283.029

Veruki, M. L., Morkve, S. H., and Hartveit, E. (2006). Activation of a presynaptic glutamate transporter regulates synaptic transmission through electrical signaling. *Nat. Neurosci.* 9, 1388–1396. doi: 10.1038/nn1793

Wadiche, J. I., Amara, S. G., and Kavanaugh, M. P. (1995). Ion fluxes associated with excitatory amino acid transport. *Neuron* 15, 721–728. doi: 10.1016/0896-6273(95)90159-0

Wadiche, J. I., and Kavanaugh, M. P. (1998). Macroscopic and microscopic properties of a cloned glutamate transporter/chloride channel. *J. Neurosci.* 18, 7650–7661. doi: 10.1523/JNEUROSCI.18-19-07650.1998

Walz, W. (2002). Chloride/anion channels in glial cell membranes. *Glia* 40, 1–10. doi: 10.1002/glia.10125

Watase, K., Hashimoto, K., Kano, M., Yamada, K., Watanabe, M., Inoue, Y., et al. (1998). Motor discoordination and increased susceptibility to cerebellar injury in GLAST mutant mice. *Eur. J. Neurosci.* 10, 976–988. doi: 10.1046/j.1460-9568.1998.00108.x

Wersinger, E., Schwab, Y., Sahel, J. A., Rendon, A., Pow, D. V., Picaud, S., et al. (2006). The glutamate transporter EAAT5 works as a presynaptic receptor in mouse rod bipolar cells. *J. Physiol.* 577(Pt 1), 221–234. doi: 10.1113/jphysiol.2006.118281

Winter, N., Kovermann, P., and Fahlke, C. (2012). A point mutation associated with episodic ataxia 6 increases glutamate transporter anion currents. *Brain* 135(Pt 11), 3416–3425. doi: 10.1093/brain/aws255

Yernool, D., Boudker, O., Folta-Stogniew, E., and Gouaux, E. (2003). Trimeric subunit stoichiometry of the glutamate transporters from *Bacillus caldotenax* and *Bacillus stearothermophilus*. *Biochemistry* 42, 12981–12988. doi: 10.1021/bi030161q

Yernool, D., Boudker, O., Jin, Y., and Gouaux, E. (2004). Structure of a glutamate transporter homologue from *Pyrococcus horikoshii*. *Nature* 431, 811–818. doi: 10.1038/nature03018

Conflict of Interest: The authors declare that the research was conducted in the absence of any commercial or financial relationships that could be construed as a potential conflict of interest.

frontiers
in Cellular Neuroscience

ORIGINAL RESEARCH
published: 13 January 2022
doi: 10.3389/fncel.2021.815771

Validation of a System x_c^- Functional Assay in Cultured Astrocytes and Nervous Tissue Samples

Pauline Beckers[1], Olaya Lara[2], Ines Belo do Nascimento[1], Nathalie Desmet[1], Ann Massie[2] and Emmanuel Hermans[1]*

[1] Group of Neuropharmacology, Institute of Neuroscience, Université catholique de Louvain, Brussels, Belgium,
[2] Neuro-Aging & Viro-Immunotherapy, Center for Neurosciences, Vrije Universiteit Brussel, Brussels, Belgium

OPEN ACCESS

Edited by:
Arturo Ortega,
Centro de Investigación y de Estudios Avanzados del Instituto Politécnico Nacional, Mexico

Reviewed by:
Gilberto L. Pardo Andreu,
University of Havana, Cuba
Donají Chi-Castañeda,
Universidad Veracruzana, Mexico

****Correspondence:***
Emmanuel Hermans
emmanuel.hermans@uclouvain.be

Specialty section:
This article was submitted to Cellular Neurophysiology, a section of the journal Frontiers in Cellular Neuroscience

Received: *15 November 2021*
Accepted: *24 December 2021*
Published: *13 January 2022*

Citation:
Beckers P, Lara O, Belo do Nascimento I, Desmet N, Massie A and Hermans E (2022) Validation of a System x_c^- Functional Assay in Cultured Astrocytes and Nervous Tissue Samples. Front. Cell. Neurosci. 15:815771. doi: 10.3389/fncel.2021.815771

Disruption of the glutamatergic homeostasis is commonly observed in neurological diseases and has been frequently correlated with the altered expression and/or function of astrocytic high-affinity glutamate transporters. There is, however, a growing interest for the role of the cystine-glutamate exchanger system x_c^- in controlling glutamate transmission. This exchanger is predominantly expressed in glial cells, especially in microglia and astrocytes, and its dysregulation has been documented in diverse neurological conditions. While most studies have focused on measuring the expression of its specific subunit xCT by RT-qPCR or by Western blotting, the activity of this exchanger in tissue samples remains poorly examined. Indeed, the reported use of sulfur- and carbon-radiolabeled cystine in uptake assays shows several drawbacks related to its short radioactive half-life and its relatively high cost. We here report on the elaborate validation of a method using tritiated glutamate as a substrate for the reversed transport mediated by system x_c^-. The uptake assay was validated in primary cultured astrocytes, in transfected cells as well as in crude synaptosomes obtained from fresh nervous tissue samples. Working in buffers containing defined concentrations of Na^+, allowed us to differentiate the glutamate uptake supported by system x_c^- or by high-affinity glutamate transporters, as confirmed by using selective pharmacological inhibitors. The specificity was further demonstrated in primary astrocyte cultures from transgenic mice lacking xCT or in cell lines where xCT expression was genetically induced or reduced. As such, this assay appears to be a robust and cost-efficient solution to investigate the activity of this exchanger in physiological and pathological conditions. It also provides a reliable tool for the screening and characterization of new system x_c^- inhibitors which have been frequently cited as valuable drugs for nervous disorders and cancer.

Keywords: xCT, synaptosomes, glutamate uptake, primary astrocyte culture, xCT knock out mice, cystine glutamate exchanger, SLC7A11 (xCT)

INTRODUCTION

Initially proposed in the early fifties, the role of glutamate as a neurotransmitter was demonstrated 20 years later. Since then, this rather simple amino acid has been unveiled as one of the most essential bioactive chemicals in the central nervous system (CNS) of mammalians. In most excitatory synapses, glutamate is released from presynaptic nerve terminals to activate a large diversity of ionotropic (iGluRs) and metabotropic (mGluRs) glutamate receptors. As major excitatory neurotransmitter, glutamate plays a crucial role in complex physiological processes including synaptic plasticity, learning and memory (Malenka and Nicoll, 1999). Glutamate also participates in the formation of glutathione (GSH), the most abundant antioxidant in the CNS (Had-Aissouni, 2012) and may serve as an alternative source of energy for diverse cells of the nervous system (McKenna, 2013). Besides these roles in physiological activities in the CNS, glutamate is also known for its implication in a large variety of nervous disorders (Lewerenz and Maher, 2015). High concentrations of this excitatory transmitter can cause damage to neuronal cells, a process known as excitotoxicity (Dong et al., 2009).

The control of glutamate transmission in the CNS does not solely depend on the interplay between neuronal cells, but also on closely associated glial cells in what is known as the tripartite synapse (Perea et al., 2009). Indeed, astrocytes play multiple roles in the control of glutamate homeostasis, in particular because they express excitatory amino acid transporters (EAATs), that ensure the clearance of extracellular glutamate and thereby protect neurons against excitotoxic insults (Anderson and Swanson, 2000; Oliet et al., 2001). Hence, impaired glial function and the associated excitotoxicity is frequently proposed as an important mechanism involved in several neurological disorders (Beart and O'Shea, 2007) and this has been validated in animal models of human diseases. Besides, astrocytes contribute to synaptic activity through the non-vesicular release of substantial amounts of glutamate by the cystine-glutamate exchanger, also known as system x_c^- (De Bundel et al., 2011; Massie et al., 2011). Its widespread distribution throughout the CNS and the critical roles played by this exchanger suggest that it could be an important determinant of brain functions under physiological and pathological conditions (Lewerenz et al., 2013; Lutgen et al., 2014). There is a growing interest in the study of its physiological regulation in glial cells and in the possibility to develop specific drugs to pharmacologically manipulate its activity.

The cystine-glutamate exchanger is a Na^+-independent transporter that is constituted of a heavy chain subunit common to several amino acid transporters, 4F2hc (encoded by the Slc3a2 gene), and a specific light chain subunit, xCT (encoded by the Slc7a11 gene). While the 4F2hc subunit ensures the trafficking and the cell surface expression of the heterodimer, xCT confers transport function and substrate specificity (Sato et al., 1999). Under physiological conditions, system x_c^- supports the exchange of intracellular L-glutamate for extracellular L-cystine at a 1:1 molecular ratio, driven by their concentration gradients across the plasma membrane (Bannai, 1986). Once taken up by the cell, cystine is intracellularly reduced into cysteine, a building block for GSH synthesis which is essential to face oxidative stress (Bannai and Kitamura, 1980). Astrocytic GSH can be transferred to neurons and therefore, system x_c^- contributes to the antioxidant protection throughout the CNS. Furthermore, through its glutamate release activity, the exchanger constitutes a substantial source of extracellular glutamate in several brain regions, likely impacting on the glutamatergic neurotransmission across the CNS (Barger and Basile, 2001; Massie et al., 2015).

The implication of system x_c^- in essential functions of astrocytes has encouraged the study of its modulation in diverse conditions both *in vivo* and *in vitro*. Exposing cultured astrocytes to the pituitary adenylate cyclase-activating polypeptide (Kong et al., 2016), interleukin 1β (Jackman et al., 2010; Shi et al., 2016) or substance P (Johnson and Johnson, 1993) has been shown to regulate the exchanger. Besides, impaired expression or activity of system x_c^- was documented in several animal models of neurological disorders such as Parkinson's disease, amyotrophic lateral sclerosis and in glioblastoma (Lewerenz et al., 2013). So far, most of these studies have examined the regulation of system x_c^- by RT-qPCR to quantify xCT mRNA. For a while, the lack of reliable anti-xCT antibodies has limited the study of its protein expression, yielding rather inconsistent published data (Van Liefferinge et al., 2016). Functional characterization of the cystine-glutamate exchanger is limited and frequently poorly described. In these studies, $[^{14}C]$ and $[^{35}S]$ radiolabeled-cystine is used as substrate in uptake assays (Bridges et al., 2001; Lewerenz et al., 2006; Liu et al., 2009; Massie et al., 2011; Merckx et al., 2015), but its high cost and relatively limited shelf-life constitute experimental drawbacks.

These issues have prompted us to validate a robust and cost-effective uptake assay for the functional study of system x_c^- in physiological and pathological conditions. We here report the use of tritiated L-glutamate as a substrate for system x_c^- (Bridges et al., 2001). Monitoring the reverse uptake of glutamate was already reported for measuring the activity of system x_c^- on models of cell cultures (Gochenauer and Robinson, 2001; Shih and Murphy, 2001; Shih et al., 2003; Patel et al., 2004; Webster et al., 2014). In the current study, the specificity of this assay was strongly consolidated by using cell lines with induced or repressed xCT expression as well as crude synaptosome preparations and primary cultures of astrocytes derived from transgenic mice lacking xCT. Furthermore, the use of selective pharmacological inhibitors allowed us to distinguish the uptake supported by system x_c^- or by EAATs.

MATERIALS AND METHODS

Animals and Ethics Statement

All experiments were conducted in strict accordance with the recommendation of the European commission and with the agreement of the Belgian Ministry of Agriculture (code number LA 1230618). The Ethical Committee of the Université catholique de Louvain (UCLouvain) for animal experiments specifically approved this study (code number 2019/UCL/MD/033). $xCT^{+/+}$, $xCT^{+/-}$, and $xCT^{-/-}$ mice used in this study were high-generation descendants of the strain previously described by Sato et al. (2005).

One to three days old pups and adult female mice [wild-type or xCT transgenic with a C57BL/6 background (Sato et al., 2005)] and rats (Sprague Dawley) aged between 10 and 12 weeks were used and kept in groups of maximum six per cage. All animals were accommodated under standard laboratory conditions, receiving food and water *ad libitum*, and were housed in the animal facility at the UCLouvain (Brussels), in controlled light/dark cycle, temperature and humidity conditions. xCT transgenic mice were genotyped by PCR on genomic DNA extracted from a tail biopsy using specific primers for Slc7a11 gene in order to identify bands corresponding to wild-type ($xCT^{+/+}$), homozygous ($xCT^{-/-}$), or heterozygous ($xCT^{\pm}$) genotypes (Sato et al., 2005; De Bundel et al., 2011).

Primary Cultures of Cortical Astrocytes

Cortices from rats or mouse pups were collected at postnatal day 2 and mechanically dissociated. Meninges were carefully removed, and astrocytes were separated from other cell types using 30 and 60% Percoll gradient (GE Healthcare) and seeded into coated flasks. Cells were left to proliferate at 37°C in a humidified atmosphere containing 5% CO_2 in Dulbecco's Modified Eagle's Medium (DMEM-GlutaMAX, Thermo Fisher Scientific) supplemented with 10% fetal bovine serum (FBS) (VWR), 100 μg/mL penicillin-streptomycin (Thermo Fisher Scientific), 2.5 μg/mL fungizone (Thermo Fisher Scientific), 50 μg/mL L-proline (Thermo Fisher Scientific), and 50 μM of b-mercaptoethanol (Gibco). The medium was renewed on day 7, and on day 14, astrocytes were collected by trypsinization (Trypsin-EDTA, Thermo Fisher Scientific) and seeded at 70,000 cells per well in six-well plates for Western blotting and into poly-L-lysine coated 24-well plates at 35,000 cells per well for uptake measurement. On day 16, serum concentration was reduced to 3% as culture medium was renewed. When indicated, a supplement of 250 μM N^6,2′-O-dibutyryladenosine 3′,5′-cyclic monophosphate (dBcAMP) (Sigma-Aldrich) was added on day 16. For all the experiments, the astrocytes were used after 23 days in culture.

CRISPR/Cas9-Induced xCT Deletion in C6 Astrocytoma Cells

Guide RNA targeting the mouse xCT sequence (5′CACCGTCATTACACATACATTCTGG3′) was cloned into the lentiCRISPRv2-PURO vector (Backx et al., 2021). Lentiviral transduction and clone selection were performed as previously described by Backx et al. (2021) with little modifications. Briefly, cells were seeded in a six-well plate at a density of 100,000 cells per well. After 4 h, cells were transduced with lentivirus-containing supernatant supplemented with protamine sulfate (10 μg/mL, Sigma-Aldrich) and 50 μM b-mercaptoethanol for 24 h. Before renewing the medium (DMEM medium supplemented with 10% FBS, 100 μg/mL penicillin-streptomycin, 2.5 μg/mL fungizone, and 50 μM b-mercaptoethanol), cells were washed with PBS. After expanding the cells to T25 flasks and proliferation for 1 week, cells were selected with 5 μg/mL puromycin (InvivoGen) for at least 1 more week before any experiments were performed.

Overexpression of xCT in Transfected Cells

The cDNA sequence encoding xCT (Slc7a11) was amplified from primary cultures of rat astrocytes and cloned into pcDNA3.1 (Invitrogen). Chinese hamster ovary (CHO) cells were cultivated at 37°C in a humidified environment (5% CO_2) with Ham's F-12 medium supplemented with 10% FBS and 100 μg/mL penicillin-streptomycin (Thermo Fisher Scientific). 2×10^6 cells were seeded in a six-well plate a few hours before transfection with a mix consisting of 200 μL Ham's F-12 medium, xCT DNA and X-tremeGENE^{TM} HP DNA transfection reagent according to the manufacturer's instructions. Selection with geneticin (G418) (1000 μg/mL, Gibco) was initiated 72 h after transfection, resulting in a stable transfected cell line, herein referred to as CHO-xCT. These cells were routinely passaged and grown in the presence of geneticin (250 μg/mL), except when plated for dedicated experiments.

Crude Synaptosome Preparation

Mice were euthanized with CO_2 and the spinal cord was immediately flushed out with phosphate-buffered saline (PBS; Meikle and Martin, 1981). Freshly isolated tissues were used for synaptosome preparation as previously described by Berger et al. (2011), with little modifications. Briefly, the samples were homogenized in an ice-cold solution of 320 mM sucrose by up-and-down movements with a pre-chilled Teflon/glass potter followed by up-and-down movements with a tight Downs. The homogenates were centrifuged at 1,000 *g* for 10 min at 4°C and the supernatants were carefully collected and stored on ice. The pellets were resuspended in ice-cold 320 mM sucrose solution and centrifuged again at 4°C at 1,000 *g* for 10 min. The two supernatants were combined and finally centrifuged at 4°C for 30 min at 17,500 *g*. The final pellet containing the crude synaptosomes was suspended in 1 mL of ice-cold appropriate buffer (see below). Protein concentration was determined by the Bradford method with the Bio-Rad protein assay (Bio-Rad Laboratories) and samples were diluted to 33.33 μg/mL for uptake assay.

[^{3}H]-L-Glutamate and [^{3}H]-D-Aspartate Uptake Assays

On crude synaptosome preparations: To assess the uptake, [^{3}H]-L-glutamate and [^{3}H]-D-aspartate (with specific activity of 48.6 Ci/mmol and 12.2 Ci/mmol, respectively, PerkinElmer) were used as substrates at tracing concentrations of 20 and 50 nM, respectively. In a total volume of 500 μL, 10 μg of protein from the synaptosome preparation was incubated with the substrate at 37°C in a 96-well Masterblock (Greiner Bio-one). The assay was performed in a Na^+-free buffer containing 140 mM *N*-methyl-D-glucamine (NMDG, as a substitute for NaCl), 5.4 mM KCl, 2.5 mM $CaCl_2$, 1 mM $MgCl_2$, 0.4 mM KH_2PO_4, 10 mM HEPES and 5 mM D-glucose, pH 7.4 adjusted with HCl, or with a Na^+-containing buffer composed of 120 mM NaCl, 4.8 mM KCl, 1.2 mM KH_2PO_4, 1.2 mM $MgSO_4$, 120 mM NaCl, 1.3 mM $CaCl_2$, 25 mM HEPES pH 7.4, and 6 mM D-glucose. When indicated, homocysteic acid (HCA, Sigma-Aldrich) and L-threo-3-hydroxyaspartic acid (LTHA, Tocris) were included in the assay. After 20 min incubation at 37°C, the suspension was filtered through a GF/B glass fiber filter adapted to a 96-well plate (UniFilter GF/B, PerkinElmer), and washed three times with the ice-cold Na^+-free buffer. After drying overnight at room temperature, MicroScint 20 (PerkinElmer) was added to each well of the filter plate. Plates were shaken for 2 h and then counted with a TopCount® NXT Microplate scintillation and luminescence counter (PerkinElmer). Results are expressed as cpm per μg of protein.

On cell cultures: Primary cultured astrocytes or CHO cells were grown on poly-L-lysine coated 24-well plates. Culture medium was removed and immediately replaced with preheated Na^+-free or Na^+-containing buffers. After a brief incubation of 10 min, the plate was placed on the surface of a 37°C water bath and the buffer was removed and replaced with the same buffer supplemented with either [^{3}H]-L-glutamate or [^{3}H]-D-aspartate at a final concentration of 20 and 50 nM, respectively. When indicated, specific inhibitors (see above) were added to the assay. After 20 min ([^{3}H]-L-glutamate) or 10 min ([^{3}H]-D-aspartate), the uptake was stopped by three rinses with ice-cold buffer and cells were lysed with 0.1 M NaOH. A fraction of the lysate was collected and the radioactivity content was measured using the liquid scintillation solution MicroScint 40 and the TopCount® NXT Microplate scintillation and luminescence counter. Another fraction of the lysate was used for protein quantification using the Bradford method with the Bio-Rad protein assay. Results are expressed as pmol of radiolabeled substrate transported per min per mg of protein.

Western Blotting

Cells seeded in six-well plates were rinsed with PBS and scraped in ice-cold lysis buffer (100 mM Tris, 150 mM NaCl, 1 mM ethylene diamine tetra acetic acid, 1% Triton-X100, 0.1% SDS, 1% deoxycholic acid sodium salt, 99% pH 7.4) while synaptosome samples where directly resuspended in 1 mL of the same lysis buffer after the last centrifugation. Protein concentration was determined by the Pierce™ BCA method (Thermo Fisher Scientific) and samples were diluted to a concentration of 1 μg/μL. After adding Western blot loading buffer to the samples (final concentrations: Tris–HCl 60 mM pH 6.8, glycerol 10%, sodium dodecyl sulfate 2%,β-mercaptoethanol 5%, and bromophenol blue 0.01%), proteins were separated through a 10% SDS-PAGE and transferred to nitrocellulose membrane by electroblotting. Membranes were then incubated for 1 h in Tris-buffered saline (50 mM Tris pH 7.4, 150 mM NaCl) containing 0.05% Tween-20 and 5% bovine serum albumin (BSA, Carl Roth) to reduce non-specific labeling. Immunoprobing was carried out by incubating membranes overnight at 4°C with primary antibodies recognizing xCT [rabbit polyclonal antibody, 1:1000, (Massie et al., 2008; Van Liefferinge et al., 2016)] or EEF2 (rabbit monoclonal antibody, 1:1000, Thermo Fisher Scientific). Membranes were rinsed in TBS-Tween 0.05% and then incubated for 1 h with a peroxidase-conjugated secondary antibody (goat anti-rabbit IgG, 1:5000, Jackson ImmunoResearch Laboratories, Inc.). Immunoreactive proteins were detected with enhanced chemiluminescence reagent (Clarity, Bio-Rad Laboratories). Densitometric analysis of the signal was performed using ImageJ (Broken Symmetry Software).

Statistical Analysis

Data were presented as means of three different experiments with the standard error of the mean (SEM). All statistical analyses were performed using GraphPad Prism version 5.01 (GraphPad Software, CA, United States). For multiple comparisons, data from distinct experimental conditions were analyzed using a one-way ANOVA followed by a Dunnett's or a Bonferroni test. A p-value < 0.05 was considered significant for all statistical analyses.

RESULTS

System x_c^- and Excitatory Amino Acid Transporter-Dependent Uptake in Cultured Astrocytes and C6 Astrocytoma Cells

Primary cultures of astrocytes derived from the cortices of rat and mouse pups were used to measure the uptake of [^{3}H]-L-glutamate and [^{3}H]-D-aspartate. Indeed, astrocytes are best known for their capacity to take up excitatory amino acids through diverse EAATs which recognize both glutamate and aspartate whereas system x_c^- only achieves the transport of glutamate. Another noticeable feature of EAATs is their dependency on the Na^+ gradient across the cell membrane that provides the driving force for the uptake. Thus, in contrast to system x_c^- of which activity is Na^+-independent, EAAT activity requires the presence of a high concentration of Na^+ in the buffer. To distinguish the [^{3}H]-L-glutamate uptake supported by EAATs or by system x_c^-, the assays were therefore performed both in Na^+-containing or Na^+-free buffers.

As shown in **Figures 1A,C**, both substrates were taken up by rat derived astrocytes in the buffer containing Na^+. On the other hand, only [^{3}H]-L-glutamate was taken up in the Na^+-free buffer (**Figures 1B,D**). The implication of EAATs and system x_c^- in the uptake of the two substrates was further examined using specific inhibitors of these transporters. The system x_c^- inhibitor HCA did not affect the uptake of [^{3}H]-D-aspartate whereas a large proportion of this uptake was inhibited by LTHA (**Figure 1A**), an EAATs inhibitor. Regarding the influence of these inhibitors on the transport of [^{3}H]-L-glutamate, data presented in **Figure 1C** showed that LTHA considerably reduced the uptake in the Na^+-containing buffer whereas only HCA was inhibiting the uptake in the Na^+-free buffer (**Figure 1D**). Together, these data confirm that astrocytes achieve glutamate uptake through both system x_c^- and EAATs. Comparing the absolute uptake values in the different conditions indicates that in the Na^+-containing buffer, EAATs predominantly contribute to the uptake of [^{3}H]-L-glutamate that reaches up to 40 pmol/min/mg of protein. Conducting the assay with [^{3}H]-L-glutamate in a Na^+-free buffer appears as the optimal experimental condition to characterize the

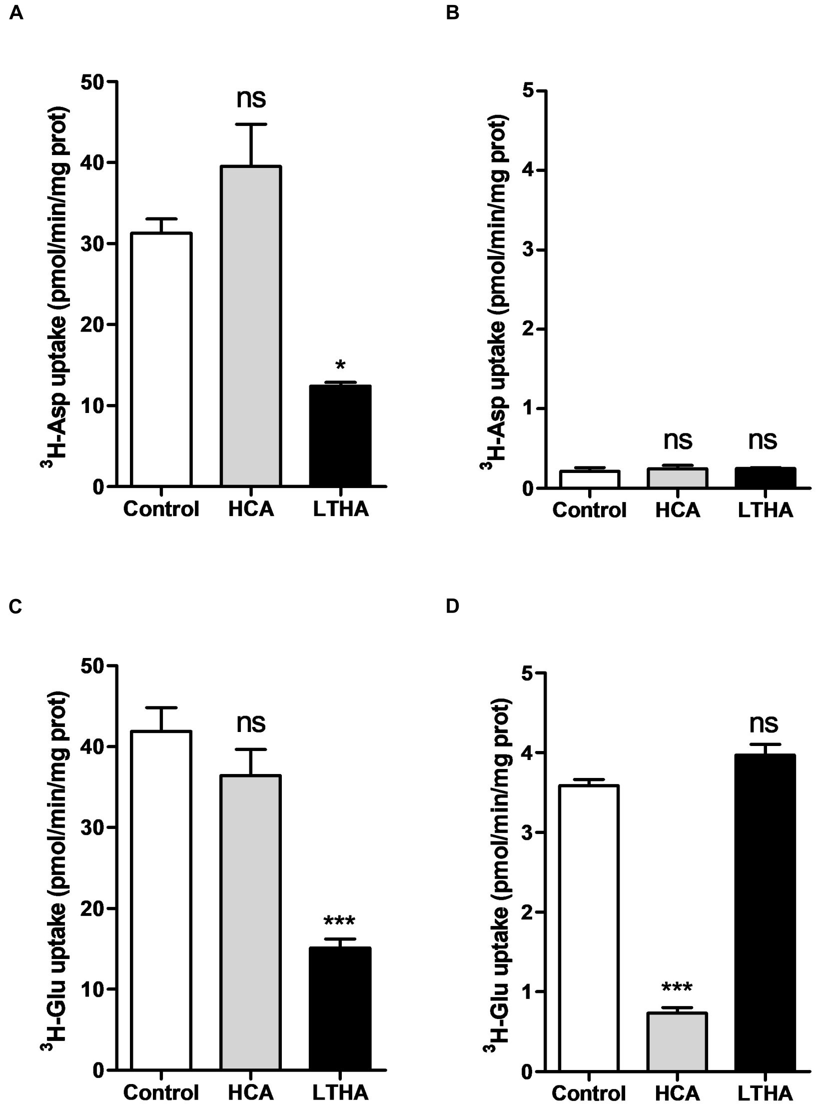

FIGURE 1 | Influence of extracellular Na^+ on [^{3}H]-D-aspartate and [^{3}H]-L-glutamate uptake in primary cultured rat astrocytes. The [^{3}H]-D-aspartate **(A,B)** or [^{3}H]-L-glutamate **(C,D)** uptake assays were performed in Na^+-containing **(A,C)** or Na^+-free **(B,D)** buffers. HCA (10^{-4} M) and LTHA (10^{-4} M) were used to discriminate the involvement of EAATs or system x_c^- in the uptake. Data shown are the mean with SEM of the uptake capacity from three independent experiments performed in quadruplicate. Statistical analyses were performed using a one-way ANOVA followed by a Dunnett's test for multiple comparisons (ns $p > 0.05$, *$p < 0.05$, ***$p < 0.001$ when compared to control).

activity of system x_c^- without any interference of EAATs. The uptake through system x_c^- represents approximately one tenth of the total uptake in rat astrocytes (approx. 3.5 pmol/min/mg of protein).

The [^{3}H]-L-glutamate uptake assay evaluating system x_c^- activity was also performed in primary cultures of astrocytes derived from the cortices of xCT$^{+/+}$ and xCT$^{-/-}$ mouse pups. In astrocytes derived from xCT$^{+/+}$ mice, the uptake of [^{3}H]-L-glutamate measured in the Na^+-free buffer was particularly low (**Figure 2A**). Exposing the cells during the period of maturation (7 days in a 3% FBS medium) to dBcAMP (250 μM) significantly increased the uptake values by 10-fold, reaching up to 2 pmol/min/mg of protein. Confirming the sole involvement of system x_c^-, this uptake was almost completely inhibited in the presence of HCA whereas LTHA was without effect. As shown in **Figure 2B**, the uptake of [^{3}H]-L-glutamate was barely detectable in astrocytes derived from the transgenic mice lacking xCT, even when the culture was exposed to dBcAMP. Similarly, [^{3}H]-L-glutamate uptake measured in the Na^+-free buffer in the C6 astrocytoma cells was considerably reduced in the presence of HCA whereas LTHA was without such influence on the uptake capacity (**Figure 2C**). In the C6 cell line where xCT expression was specifically targeted using CRISPR-Cas9, the uptake of [^{3}H]-L-glutamate was hardly detectable and was insensitive to HCA (**Figure 2C**). Together, these data validate the measure of [^{3}H]-L-glutamate uptake in the

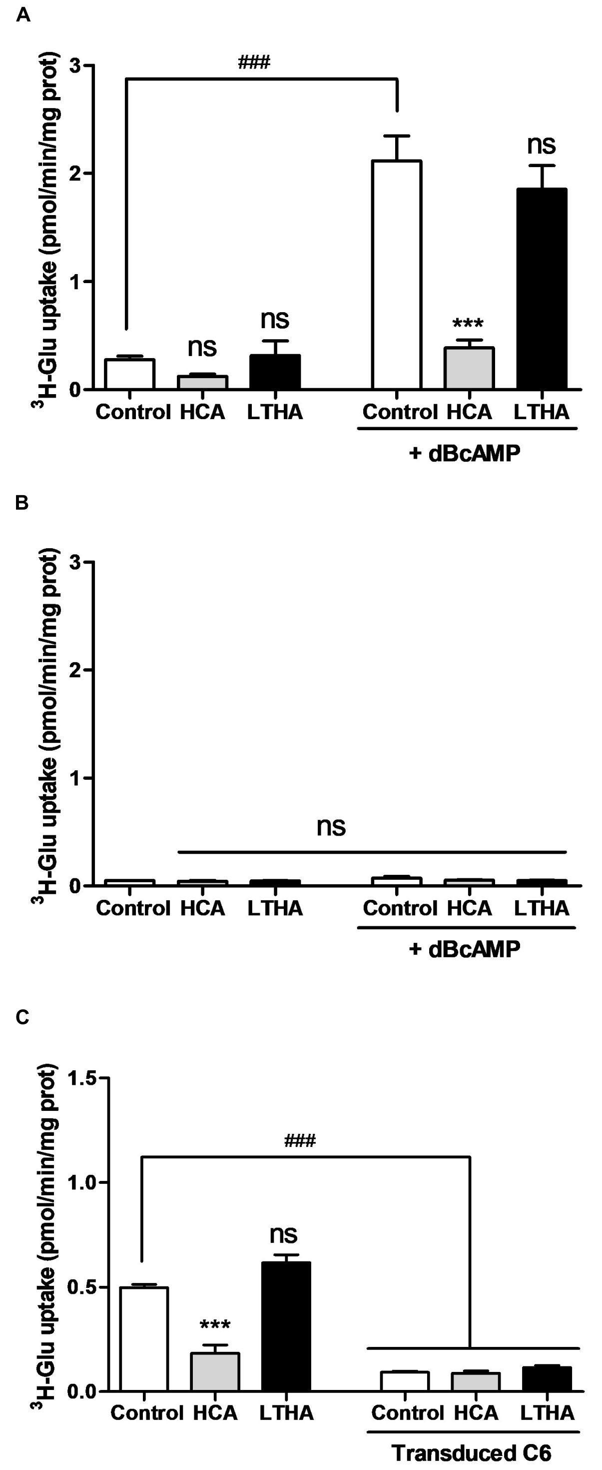

FIGURE 2 | Influence of genetic xCT deletion on [^{3}H]-L-glutamate uptake supported by system x_c^- in cultured astrocytes and C6 astrocytoma cells. [^{3}H]-L-glutamate uptake was quantified in primary cultured astrocytes derived from wild-type **(A)** or xCT$^{-/-}$ mice **(B)** maturated for 7 days in the presence or the absence of dBcAMP, as well as on C6 astrocytoma cells with and without CRISPR/Cas9-mediated xCT deletion **(C)**. Specific pharmacological inhibitors were used (10^{-4} M) and added to the radioactive preparation when indicated. *(Continued)*

FIGURE 2 | Histograms represent the mean with SEM of the uptake capacity from three independent experiments performed in quadruplicate. Statistical analyses were performed with a one-way ANOVA followed by a Dunnett's test for multiple comparisons [ns $p > 0.05$, $^{***}p < 0.001$ refer to the comparison within the same cellular population (vs. control). $^{\#\#\#}p < 0.001$ in **(A,B)** refers to the comparison between dBcAMP-maturated and non-maturated astrocytes or in **(C)** between C6 cells with and without xCT deletion].

Na$^+$-free buffer as a selective functional monitoring of system x_c^- activity.

xCT Expression in Chinese Hamster Ovary Cell Increases Glutamate Transport Supported by System x_c^-

Chinese hamster ovary cells were stably transfected with the eukaryotic expression vector pcDNA3.1 carrying the rat xCT coding sequence. While some expression of xCT was detected by immunoblotting in samples from non-transfected cells, geneticin selected transfectants showed a higher expression level of the immunoreactive signal (**Figure 3A**). Accordingly, [^{3}H]-L-glutamate uptake measured in the transfected cells was significantly higher as compared to non-transfected cells (**Figure 3B**). The specificity of this [^{3}H]-L-glutamate uptake was confirmed using the system x_c^- inhibitor HCA which causes a significant decrease in the uptake in both transfected and non-transfected cells. Non-linear analysis of the concentration-dependent uptake inhibition curves allowed to determine a half-maximal inhibitory concentration (IC_{50}) of HCA in control and CHO-xCT cells in the 10 μM range (pIC_{50} values of 5.01 ± 0.12 and 5.24 ± 0.11, respectively) (**Figure 3C**). In contrast, LTHA did not influence the [^{3}H]-L-glutamate uptake in these experimental conditions (**Figure 3B**).

System x_c^--Dependent Glutamate Uptake and xCT Expression in Crude Spinal Cord Synaptosomes

As previously described by Berger et al. (2011), crude synaptosomes from spinal cord samples were obtained after several steps of homogenization and centrifugation in ice-cold isotonic conditions. For the functional characterization of system x_c^-, crude synaptosomes from xCT$^{+/+}$, xCT$^{+/-}$, and xCT$^{-/-}$ mice were prepared and resuspended in Na$^+$-free buffer before the uptake experiment. The respective decreased expression or suppression of xCT in the heterozygous and xCT knockout animals was first validated by Western blotting on synaptosome samples submitted to detergent lysis (**Figure 4A**). In synaptosomes from xCT$^{+/+}$ animals, a substantial [^{3}H]-L-glutamate uptake was measured in the Na$^+$-free buffer, which was almost completely inhibited in the presence of HCA (100 μM) but entirely preserved in the presence of LTHA (100 μM) (**Figure 4B**). Synaptosome samples prepared from the spinal cord of xCT$^{-/-}$ mice presented a minimal glutamate uptake capacity as compared to xCT$^{+/+}$ mice. This modest uptake was not affected by the pharmacological inhibitor HCA. In samples prepared from xCT$^{+/-}$ mice, the substrate uptake value was

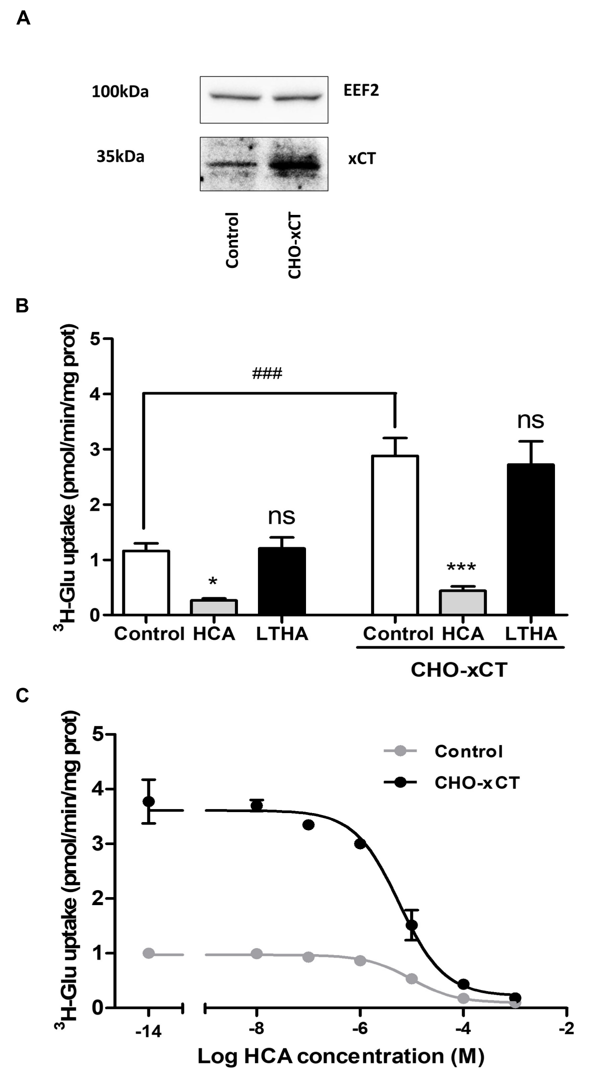

FIGURE 3 | Influence of xCT overexpression on [^{3}H]-L-glutamate uptake capacity of CHO cells. The increased expression of xCT was validated by Western blotting comparing protein samples from control and CHO-xCT cells using a specific rodent xCT antibody. Detection of the EEF2 was used as a control for sample loading and protein blotting. The blot shown is representative of three independent experiments **(A)**. [^{3}H]-L-glutamate uptake capacity was measured on control and CHO-xCT cells. Pharmacological inhibitors (10^{-4} M) were added to the preparation to further confirm the nature of the transporter involved **(B)**. The potency of HCA at inhibiting system x_c^--dependent [^{3}H]-L-glutamate uptake capacity was examined by performing the assay in the presence of increasing concentrations of HCA **(C)**. Data represent the mean of the uptake capacity with SEM from three independent experiments performed in quadruplicate. Statistical analyses were performed using a one-way ANOVA followed by a Dunnett's test for multiple comparisons [ns $p > 0.05$, $^*p < 0.05$, $^{***}p < 0.001$ refer to the comparison within the same cellular population (vs. control). $^{\#\#\#}p < 0.001$ refers to the comparison between CHO and CHO-xCT cells].

estimated at 60% of the uptake measured in samples from the wild-type animals. In the conditions tested (Na^+-free buffer), this uptake was completely inhibited in the presence of HCA and not influenced by LTHA.

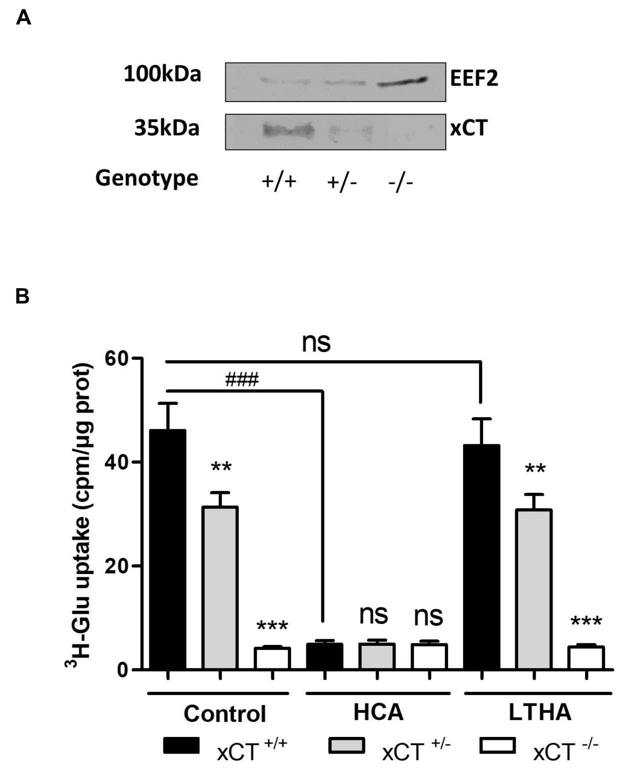

FIGURE 4 | xCT expression and system x_c^--dependent [^{3}H]-L-glutamate uptake using spinal cord synaptosome preparations. xCT expression **(A)** and [^{3}H]-L-glutamate uptake **(B)** in crude synaptosomes prepared from freshly isolated spinal cord samples. Tissues were obtained from transgenic xCT$^{+/-}$ and xCT$^{-/-}$ C57BL/6 mice and from wild-type littermates (xCT$^{+/+}$). The genetic deletion of xCT was validated by Western blot using a specific antibody against rodent xCT. EEF2 detection was used as a control for sample loading and protein blotting. The blot shown is representative of three independent experiments. Histograms represent the mean with SEM of the uptake capacity from three independent experiments performed in quadruplicate. Statistical analyses were conducted using a one-way ANOVA followed by a Dunnett's test for multiple comparisons [ns $p > 0.05$, $^{**}p < 0.01$, $^{***}p < 0.001$ refer to the comparison between genotypes (vs. xCT$^{+/+}$). ns $p > 0.05$, $^{\#\#\#}p < 0.001$ refers to the comparison within the same genotype].

DISCUSSION

While the implication of astrocytic EAATs in the control of glutamate homeostasis and the protection against excitotoxicity is well characterized (Kanai et al., 1993), accumulating reports identify system x_c^- as another essential actor in the regulation of excitatory glutamate transmission in the CNS (Lewerenz et al., 2013; Williams and Featherstone, 2014; Bentea et al., 2020). By ensuring the uptake of cystine in exchange for glutamate, the activity of system x_c^- provides astrocytes with cysteine that is incorporated into glutathione which serves as an antioxidant in the nervous tissues. This, however, concurs with the release of glutamate in the synapse.

While several studies have repeatedly documented the importance of EAATs dysfunction in the alteration of glutamate homeostasis (Rodríguez-Campuzano and Ortega, 2021), the impact of physiological and pathological changes affecting system x_c^- should not be overlooked. So far, most studies have focused on assessing the expression of its specific subunit xCT by RT-qPCR or by Western blotting. Importantly, different studies have revealed an upregulation of xCT expression in animal models of several nervous system disorders, including Parkinson's disease (Massie et al., 2008), epilepsy (Lewerenz et al., 2014), or amyotrophic lateral sclerosis (Mesci et al., 2015). This increased expression promotes the release of glutamate and it is indeed noteworthy that alteration in the glutamate homeostasis is commonly cited amongst the pathogenic mechanisms of these disorders [for review, see Massie et al. (2015)]. Beside these reports focusing on the regulation of xCT expression, only few studies have considered changes in the activity of the exchanger in neurological disease models. Functional studies are, however, essential in order to appreciate the consequences of the altered expression of the exchanger on the glutamate/cystine handling. Some laboratories have reported on *in vitro* and *ex vivo* experiments evaluating system x_c^- activity using radiolabeled cystine ([^{35}S]-cystine or [^{14}C]-cystine) as substrate (Murphy et al., 1989; Fogal et al., 2007; Massie et al., 2011; Resch et al., 2014; Merckx et al., 2015). Previously validated on cell cultures, cystine uptake has been conducted on spinal cord and brain slices to monitor the activity of system x_c^- (Kato et al., 1993; Melendez et al., 2005; Albano et al., 2013; Huang et al., 2018). This approach is, however, not routinely exploited as it presents several drawbacks including the high cost of these cystine radiochemicals and the limited radioactive half-life ([^{35}S]-cystine). Siska et al. (2016) have recently reported on the use of a fluorescent derivative of cystine (fluorescein isothiocyanate – FITC) as a non-radioactive alternative to characterize system x_c^- activity. The use of the cystine-FITC probe was validated on T-cells in flow cytometry, but its use for large scale pharmacological screening or functional studies on tissue samples requires further optimization. Moreover, the use of radiolabeled substrate in biochemical assays offers a higher sensitivity that is essential for quantitative studies on small biological samples.

For *in vitro* experiments, functional studies have been conducted using tritiated glutamate as substrate for a reverse transport supported by the exchanger (Gochenauer and Robinson, 2001; Shih and Murphy, 2001; Shih et al., 2003; Patel et al., 2004; Webster et al., 2014). Several transporters and ions channels, including system x_c^- operate according to the concentration gradient of the transported chemicals across the cell membrane. For numerous transporters, a reversed activity has been documented in pathological conditions [GABA and glutamate transporters in epilepsy and ischemia (Szatkowski et al., 1990; Rossi et al., 2000; Wu et al., 2003)], in response to drugs [influence of psychostimulants on the dopamine transporter (Sulzer et al., 1995)] or at some stages of the development {chloride channel in the GABA$_A$ ionotropic receptor [for review, see Peerboom and Wierenga (2021)]}. In biochemical assays, the transport direction can be manipulated by changing the extracellular concentrations of the transported chemicals and this is the case for system x_c^- for which a reverse transport activity can be exploited. In the absence of extracellular cystine, the exchanger operates in a reverse direction and takes up glutamate (Bannai, 1986), which allows the use of radiolabeled glutamate to monitor system x_c^- activity.

The use of glutamate as substrate for functional studies of system x_c^-, inevitably leads to difficult data interpretation related to the implication of other glutamate carriers. In particular, GLT-1 (EAAT2), which represents up to 1% of total proteins in the nervous system of mammals (Lehre and Danbolt, 1998). This transporter, commonly detected in maturated primary cultures of astrocytes, is recognized as the major contributor to glutamate uptake in most of the experimental models. The evaluation of the glutamate uptake specifically achieved by other mechanisms, including system x_c^-, necessitates to develop and validate experimental conditions that exclude the activity of GLT-1 and other EAATs. The strict Na$^+$ dependency of EAAT, which is not shared by system x_c^-, offers the possibility to focus on the latter by removing Na$^+$ from the assay buffers.

Even though a few publications have already exploited this approach (Bridges et al., 2001; Shih and Murphy, 2001; Shih et al., 2003; Patel et al., 2004; Melendez et al., 2005, 2016; Mysona et al., 2009), we here report on the validation of the assay and its selectivity using pharmacological inhibitors and genetically modified models, and its adaptation to samples of the nervous tissues where both glutamate transporters and the exchanger are expressed. Thus, in the absence of Na$^+$, the uptake of radiolabeled glutamate was almost completely inhibited by HCA with an IC$_{50}$ value consistent with a previous report on the inhibition of cystine uptake by system x_c^- (Patel et al., 2004). In these conditions, the pan-EAAT inhibitor LTHA was without any significant impact on the glutamate uptake. Also, in the absence of Na$^+$, the glutamate uptake measured in primary cultures of astrocytes derived from transgenic mice lacking xCT was barely detectable and unchanged in the presence of HCA. Together, these experimental observations validate the robustness and selectivity of the functional assay used for the evaluation of system x_c^- activity.

Excitatory amino acid transporters and system x_c^- also differ in their specificity for amino acid substrates. While EAATs equivalently transport the L- and D- enantiomers of both glutamate and aspartate, system x_c^- only recognizes L-glutamate as substrate (Bridges et al., 2001; Patel et al., 2004). As a result, only EAAT-associated activity is assessed when examining the uptake of radiolabeled D-aspartate, as indicated here by the lack of its uptake in the absence of Na$^+$. Quantitative analysis of the uptake values in these different experimental conditions allowed to clearly confirm that in primary cultured astrocytes, the glutamate uptake is predominantly assured by EAATs whereas system x_c^- only partially contributes to the uptake (10%). Several protocols for the maturation/differentiation of cultured astrocytes derived from new-born rodent brain have been proposed (decrease in serum concentration, supplementation with a cocktail of growth factors or addition of dBcAMP) (Moonen et al., 1976; Sensenbrenner et al., 1980; Vermeiren et al., 2005; Prah et al., 2019). These procedures commonly increase the expression and activity of EAATs (Eng et al., 1997; Schlag et al., 1998; Vermeiren et al., 2005). Similarly, exposing the primary cultured astrocytes to dBcAMP during the differentiation step considerably increased the system x_c^--dependent glutamate uptake, in accordance with the documented increased expression of the exchanger in the same conditions (Gochenauer and Robinson, 2001). The absence of dBcAMP-induced increase in Na^+-independent glutamate uptake in astrocyte cultures derived from transgenic mice lacking xCT further consolidates the specificity of the assay.

The growing interest for the study of system x_c^- as a major actor in the control of glutamate transmission is largely supported by reports highlighting the regulation of this exchanger in models of diseases both in peripheral tissues and in the CNS. While the characterization of system x_c^- function in cell cultures may contribute to study some molecular mechanisms of its regulation, the possibility to examine the function of this exchanger in tissue samples is essential. We here successfully applied the reverse transport of radiolabeled glutamate to monitor the activity of system x_c^- in crude synaptosomes prepared from the mouse spinal cord. These subcellular fractions are prepared from nervous tissues by homogenization and centrifugation in an isotonic buffer, yielding a suspension of large resealed cell vesicles with preserved membrane integrity and functional properties. The assay was adapted to a 96-well plate format allowing the harvesting of several samples simultaneously and limiting the amount of tissue needed to less than 10 μg of protein per sample. Initially performed on crude synaptosomes prepared from freshly dissected spinal cord, the experiment was successfully reproduced on hippocampal tissue as well as on frozen samples without loss of uptake activity (data not shown). Considering the heterogeneity of CNS samples and the large diversity of transporter systems in these tissues, the specificity of the assay appears essential. Our data evidence a substantial Na^+-independent glutamate uptake in synaptosomes that was inhibited by HCA and totally absent in synaptosomes prepared from tissues of transgenic mice lacking xCT. Obviously, performing functional studies on synaptosomes appears far less quantitatively restrictive than on freshly prepared tissue slices, as frequently used for diverse transmitter uptake assays in the literature (Melendez et al., 2005; Albano et al., 2013). While an elaborated fractionation procedure can be used to enrich synaptosome preparations with nervous terminals, crude synaptosome samples are known to contain a large proportion of glial contaminants (Henn et al., 1976). As demonstrated for EAATs (Petr et al., 2015), system x_c^- is predominantly expressed in glial cells but also detected in neurons (Jackman et al., 2010) and the possibility to discriminate the activity of the exchanger and other glutamate transporters is essential to study their specific regulation.

The documented increase in the expression of system x_c^- in several neurological and non-neurological disorders, in particular, in contexts of inflammatory insults should encourage to consider this exchanger as a valuable pharmacological target. The protocol that we here describe and validate, appears as a robust, cost-effective, and reliable biochemical method for the screening and characterization of new system x_c^- inhibitors both in cell culture models and in tissue samples. Combined with protein/mRNA expression studies it offers access to a comprehensive toolbox for the study of this exchanger in models of diseases.

DATA AVAILABILITY STATEMENT

The raw data supporting the conclusions of this article will be made available by the authors, without undue reservation.

ETHICS STATEMENT

The animal study was reviewed and approved by the Ethical Committee of the Université catholique de Louvain (UCLouvain) for animal experiments. Written informed consent was obtained from the owners for the participation of their animals in this study.

AUTHOR CONTRIBUTIONS

EH and PB designed all the experiments and wrote the manuscript. PB and ND performed the experiments and analysis. AM helped for the experimental design and essential scientific feedback. AM and OL provided us with reagents and animals. IB assisted with the critical reviewing of the manuscript. All authors have read the manuscript and approved the submitted version.

FUNDING

This work was supported by the Fonds Spéciaux de Recherche from the Université catholique de Louvain (UCLouvain) and Association Belge contre les Maladies neuro-Musculaires (ABMM).

ACKNOWLEDGMENTS

Transgenic mice lacking xCT were generously provided by H. Sato (Department of Medical Technology, Niigata University, Japan). We thank R. Carvajal for the excellent assistance for animal care.

REFERENCES

Albano, R., Liu, X., and Lobner, D. (2013). Regulation of system x(c)- in the SOD1-G93A mouse model of ALS. *Exp. Neurol.* 250, 69–73. doi: 10.1016/j.expneurol.2013.09.008

Anderson, C. M., and Swanson, R. A. (2000). Astrocyte glutamate transport: review of properties, regulation, and physiological functions. *Glia* 32, 1–14. doi: 10.1002/1098-1136(200010)32:1<1::aid-glia10>3.0.co;2-w

Backx, E., Wauters, E., Baldan, J., Van Bulck, M., Michiels, E., Heremans, Y., et al. (2021). MECOM permits pancreatic acinar cell dedifferentiation avoiding cell death under stress conditions. *Cell Death Differ.* 28, 2601–2615. doi: 10.1038/s41418-021-00771-6

Bannai, S. (1986). Exchange of cystine and glutamate across plasma membrane of human fibroblasts. *J. Biol. Chem.* 261, 2256–2263.

Bannai, S., and Kitamura, E. (1980). Transport interaction of L-cystine and L-glutamate in human diploid fibroblasts in culture. *J. Biol. Chem.* 255, 2372–2376. doi: 10.1016/s0021-9258(19)85901-x

Barger, S. W., and Basile, A. S. (2001). Activation of microglia by secreted amyloid precursor protein evokes release of glutamate by cystine exchange and attenuates synaptic function. *J. Neurochem.* 76, 846–854. doi: 10.1046/j.1471-4159.2001.00075.x

Beart, P. M., and O'Shea, R. D. (2007). Transporters for L-glutamate: an update on their molecular pharmacology and pathological involvement. *Br. J. Pharmacol.* 150, 5–17. doi: 10.1038/sj.bjp.0706949

Bentea, E., Villers, A., Moore, C., Funk, A. J., ODonovan, S. M., Verbruggen, L., et al. (2020). Corticostriatal dysfunction and social interaction deficits in mice lacking the cystine/glutamate antiporter. *Mol. Psychiatry* 26, 1–16. doi: 10.1038/s41380-020-0751-3

Berger, J. V., Deumens, R., Goursaud, S., Schäfer, S., Lavandhomme, P., Joosten, E. A., et al. (2011). Enhanced neuroinflammation and pain hypersensitivity after peripheral nerve injury in rats expressing mutated superoxide dismutase 1. *J. Neuroinflammation* 8:33. doi: 10.1186/1742-2094-8-33

Bridges, C. C., Kekuda, R., Wang, H., Prasad, P. D., Mehta, P., Huang, W., et al. (2001). Structure, function, and regulation of human cystine/glutamate transporter in retinal pigment epithelial cells. *Invest. Ophthalmol. Vis. Sci.* 42, 47–54.

De Bundel, D., Schallier, A., Loyens, E., Fernando, R., Miyashita, H., Van Liefferinge, J., et al. (2011). Loss of system x(c)- does not induce oxidative stress but decreases extracellular glutamate in hippocampus and influences spatial working memory and limbic seizure susceptibility. *J. Neurosci.* 31, 5792–5803. doi: 10.1523/JNEUROSCI.5465-10.2011

Dong, X. X., Wang, Y., and Qin, Z. H. (2009). Molecular mechanisms of excitotoxicity and their relevance to pathogenesis of neurodegenerative diseases. *Acta Pharmacol. Sin.* 30, 379–387. doi: 10.1038/aps.2009.24

Eng, D. L., Lee, Y. L., and Lal, P. G. (1997). Expression of glutamate uptake transporters after dibutyryl cyclic AMP differentiation and traumatic injury in cultured astrocytes. *Brain Res.* 778, 215–221. doi: 10.1016/s0006-8993(97)01093-7

Fogal, B., Li, J., Lobner, D., McCullough, L. D., and Hewett, S. J. (2007). System x(c)- activity and astrocytes are necessary for interleukin-1 beta-mediated hypoxic neuronal injury. *J. Neurosci.* 27, 10094–10105. doi: 10.1523/JNEUROSCI.2459-07.2007

Gochenauer, G. E., and Robinson, M. B. (2001). Dibutyryl-cAMP (dbcAMP) up-regulates astrocytic chloride-dependent L-[3H]glutamate transport and expression of both system xc(-) subunits. *J. Neurochem.* 78, 276–286. doi: 10.1046/j.1471-4159.2001.00385.x

Had-Aissouni, L. (2012). Toward a new role for plasma membrane sodium-dependent glutamate transporters of astrocytes: maintenance of antioxidant defenses beyond extracellular glutamate clearance. *Amino Acids* 42, 181–197. doi: 10.1007/s00726-011-0863-9

Henn, F. A., Anderson, D. J., and Rustad, D. G. (1976). Glial contamination of synaptosomal fractions. *Brain Res.* 101, 341–344. doi: 10.1016/0006-8993(76)90274-2

Huang, M. W., Lin, Y. J., Chang, C. W., Lei, F. J., Ho, E. P., Liu, R. S., et al. (2018). RGS4 deficit in prefrontal cortex contributes to the behaviors related to schizophrenia via system x(c)(-)-mediated glutamatergic dysfunction in mice. *Theranostics* 8, 4781–4794. doi: 10.7150/thno.25189

Jackman, N. A., Uliasz, T. F., Hewett, J. A., and Hewett, S. J. (2010). Regulation of system x(c)(-)activity and expression in astrocytes by interleukin-1β: implications for hypoxic neuronal injury. *Glia* 58, 1806–1815. doi: 10.1002/glia.21050

Johnson, C. L., and Johnson, C. G. (1993). Substance P regulation of glutamate and cystine transport in human astrocytoma cells. *Recept. Channels* 1, 53–59.

Kanai, Y., Smith, C. P., and Hediger, M. A. (1993). A new family of neurotransmitter transporters: the high-affinity glutamate transporters. *FASEB J.* 7, 1450–1459. doi: 10.1096/fasebj.7.15.7903261

Kato, S., Ishita, S., Sugawara, K., and Mawatari, K. (1993). Cystine/glutamate antiporter expression in retinal müller glial cells: implications for DL-alpha-aminoadipate toxicity. *Neuroscience* 57, 473–482. doi: 10.1016/0306-4522(93)90080-y

Kong, L., Albano, R., Madayag, A., Raddatz, N., Mantsch, J. R., Choi, S., et al. (2016). Pituitary Adenylate cyclase-activating polypeptide orchestrates neuronal regulation of the astrocytic glutamate-releasing mechanism system xc (.). *J. Neurochem.* 137, 384–393. doi: 10.1111/jnc.13566

Lehre, K. P., and Danbolt, N. C. (1998). The number of glutamate transporter subtype molecules at glutamatergic synapses: chemical and stereological quantification in young adult rat brain. *J. Neurosci.* 18, 8751–8757. doi: 10.1523/JNEUROSCI.18-21-08751.1998

Lewerenz, J., and Maher, P. (2015). Chronic glutamate toxicity in neurodegenerative diseases-what is the evidence?. *Front. Neurosci.* 9:469. doi: 10.3389/fnins.2015.00469

Lewerenz, J., Baxter, P., Kassubek, R., Albrecht, P., Van Liefferinge, J., Westhoff, M. A., et al. (2014). Phosphoinositide 3-kinases upregulate system xc(-) via eukaryotic initiation factor 2α and activating transcription factor 4 - A pathway active in glioblastomas and epilepsy. *Antioxid. Redox Signal.* 20, 2907–2922. doi: 10.1089/ars.2013.5455

Lewerenz, J., Hewett, S. J., Huang, Y., Lambros, M., Gout, P. W., Kalivas, P. W., et al. (2013). The cystine/glutamate antiporter system x(c)(-) in health and disease: from molecular mechanisms to novel therapeutic opportunities. *Antioxid Redox Signal.* 18, 522–555. doi: 10.1089/ars.2011.4391

Lewerenz, J., Klein, M., and Methner, A. (2006). Cooperative action of glutamate transporters and cystine/glutamate antiporter system Xc- protects from oxidative glutamate toxicity. *J. Neurochem.* 98, 916–925. doi: 10.1111/j.1471-4159.2006.03921.x

Liu, X., Rush, T., Zapata, J., and Lobner, D. (2009). Beta-N-methylamino-l-alanine induces oxidative stress and glutamate release through action on system Xc(-). *Exp. Neurol.* 217, 429–433. doi: 10.1016/j.expneurol.2009.04.002

Lutgen, V., Resch, J., Qualmann, K., Raddatz, N. J., Panhans, C., Olander, E. M., et al. (2014). Behavioral assessment of acute inhibition of system xc (-) in rats. *Psychopharmacology (Berl)* 231, 4637–4647. doi: 10.1007/s00213-014-3612-4

Malenka, R. C., and Nicoll, R. A. (1999). Long-term potentiation–a decade of progress?. *Science* 285, 1870–1874. doi: 10.1126/science.285.5435.1870

Massie, A., Boillée, S., Hewett, S., Knackstedt, L., and Lewerenz, J. (2015). Main path and byways: non-vesicular glutamate release by system xc(-) as an important modifier of glutamatergic neurotransmission. *J. Neurochem.* 135, 1062–1079. doi: 10.1111/jnc.13348

Massie, A., Schallier, A., Kim, S. W., Fernando, R., Kobayashi, S., Beck, H., et al. (2011). Dopaminergic neurons of system $x(c)^-$-deficient mice are highly protected against 6-hydroxydopamine-induced toxicity. *FASEB J.* 25, 1359–1369. doi: 10.1096/fj.10-177212

Massie, A., Schallier, A., Mertens, B., Vermoesen, K., Bannai, S., Sato, H., et al. (2008). Time-dependent changes in striatal xCT protein expression in hemi-Parkinson rats. *Neuroreport* 19, 1589–1592. doi: 10.1097/WNR.0b013e328312181c

McKenna, M. C. (2013). Glutamate pays its own way in astrocytes. *Front. Endocrinol. (Lausanne)* 4:191. doi: 10.3389/fendo.2013.00191

Meikle, A. D., and Martin, A. H. (1981). A rapid method for removal of the spinal cord. *Stain Technol.* 56, 235–237. doi: 10.3109/10520298109067317

Melendez, R. I., Roman, C., Capo-Velez, C. M., and Lasalde-Dominicci, J. A. (2016). Decreased glial and synaptic glutamate uptake in the striatum of HIV-1 gp120 transgenic mice. *J. Neurovirol.* 22, 358–365. doi: 10.1007/s13365-015-0403-6

Melendez, R. I., Vuthiganon, J., and Kalivas, P. W. (2005). Regulation of extracellular glutamate in the prefrontal cortex: focus on the cystine glutamate exchanger and group I metabotropic glutamate receptors. *J. Pharmacol. Exp. Ther.* 314, 139–147. doi: 10.1124/jpet.104.081521

Merckx, E., Demuyser, T., Bentea, E., Van Liefferinge, J., Albertini, G., Deneyer, L., et al. (2015). Lack of effect of Theilers murine encephalomyelitis virus infection on system xc^-. *Neurosci. Lett.* 593, 124–128. doi: 10.1016/j.neulet.2015.03.026

Mesci, P., Zaïdi, S., Lobsiger, C. S., Millecamps, S., Escartin, C., Seilhean, D., et al. (2015). System xC- is a mediator of microglial function and its deletion slows symptoms in amyotrophic lateral sclerosis mice. *Brain* 138, 53–68. doi: 10.1093/brain/awu312

Moonen, G., Heinen, E., and Goessens, G. (1976). Comparative ultrastructural study of the effects of serum-free medium and dibutyryl-cyclic AMP on newborn rat astroblasts. *Cell Tissue Res.* 167, 221–227. doi: 10.1007/BF00224329

Murphy, T. H., Miyamoto, M., Sastre, A., Schnaar, R. L., and Coyle, J. T. (1989). Glutamate toxicity in a neuronal cell line involves inhibition of cystine transport leading to oxidative stress. *Neuron* 2, 1547–1558. doi: 10.1016/0896-6273(89)90043-3

Mysona, B., Dun, Y., Duplantier, J., Ganapathy, V., and Smith, S. B. (2009). Effects of hyperglycemia and oxidative stress on the glutamate transporters GLAST and system xc- in mouse retinal Müller glial cells. *Cell Tissue Res.* 335, 477–488. doi: 10.1007/s00441-008-0742-1

Oliet, S. H., Piet, R., and Poulain, D. A. (2001). Control of glutamate clearance and synaptic efficacy by glial coverage of neurons. *Science* 292, 923–926. doi: 10.1126/science.1059162

Patel, S. A., Warren, B. A., Rhoderick, J. F., and Bridges, R. J. (2004). Differentiation of substrate and non-substrate inhibitors of transport system xc(-): an obligate exchanger of L-glutamate and L-cystine. *Neuropharmacology* 46, 273–284. doi: 10.1016/j.neuropharm.2003.08.006

Peerboom, C., and Wierenga, C. J. (2021). The postnatal GABA shift: a developmental perspective. *Neurosci. Biobehav. Rev.* 124, 179–192. doi: 10.1016/j.neubiorev.2021.01.024

Perea, G., Navarrete, M., and Araque, A. (2009). Tripartite synapses: astrocytes process and control synaptic information. *Trends Neurosci.* 32, 421–431. doi: 10.1016/j.tins.2009.05.001

Petr, G. T., Sun, Y., Frederick, N. M., Zhou, Y., Dhamne, S. C., Hameed, M. Q., et al. (2015). Conditional deletion of the glutamate transporter GLT-1 reveals that astrocytic GLT-1 protects against fatal epilepsy while neuronal GLT-1 contributes significantly to glutamate uptake into synaptosomes. *J. Neurosci.* 35, 5187–5201. doi: 10.1523/JNEUROSCI.4255-14.2015

Prah, J., Winters, A., Chaudhari, K., Hersh, J., Liu, R., and Yang, S. H. (2019). A novel serum free primary astrocyte culture method that mimic quiescent astrocyte phenotype. *J. Neurosci. Methods* 320, 50–63. doi: 10.1016/j.jneumeth.2019.03.013

Resch, J. M., Albano, R., Liu, X., Hjelmhaug, J., Lobner, D., Baker, D. A., et al. (2014). Augmented cystine-glutamate exchange by pituitary adenylate cyclase-activating polypeptide signaling via the VPAC1 receptor. *Synapse* 68, 604–612. doi: 10.1002/syn.21772

Rodríguez-Campuzano, A. G., and Ortega, A. (2021). Glutamate transporters: critical components of glutamatergic transmission. *Neuropharmacology* 192:108602. doi: 10.1016/j.neuropharm.2021.108602

Rossi, D. J., Oshima, T., and Attwell, D. (2000). Glutamate release in severe brain ischaemia is mainly by reversed uptake. *Nature* 403, 316–321. doi: 10.1038/35002090

Sato, H., Shiiya, A., Kimata, M., Maebara, K., Tamba, M., Sakakura, Y., et al. (2005). Redox imbalance in cystine/glutamate transporter-deficient mice. *J. Biol. Chem.* 280, 37423–37429. doi: 10.1074/jbc.M506439200

Sato, H., Tamba, M., Ishii, T., and Bannai, S. (1999). Cloning and expression of a plasma membrane cystine/glutamate exchange transporter composed of two distinct proteins. *J. Biol. Chem.* 274, 11455–11458. doi: 10.1074/jbc.274.17.11455

Schlag, B. D., Vondrasek, J. R., Munir, M., Kalandadze, A., Zelenaia, O. A., Rothstein, J. D., et al. (1998). Regulation of the glial Na+-dependent glutamate transporters by cyclic AMP analogs and neurons. *Mol. Pharmacol.* 53, 355–369. doi: 10.1124/mol.53.3.355

Sensenbrenner, M., Devilliers, G., Bock, E., and Porte, A. (1980). Biochemical and ultrastructural studies of cultured rat astroglial cells: effect of brain extract and dibutyryl cyclic AMP on glial fibrillary acidic protein and glial filaments. *Differentiation* 17, 51–61. doi: 10.1111/j.1432-0436.1980.tb01081.x

Shi, J., He, Y., Hewett, S. J., and Hewett, J. A. (2016). Interleukin 1β Regulation of the System xc- Substrate-specific Subunit, xCT, in primary mouse astrocytes involves the RNA-binding Protein HuR. *J. Biol. Chem.* 291, 1643–1651. doi: 10.1074/jbc.M115.697821

Shih, A. Y., and Murphy, T. H. (2001). XCt cystine transporter expression in HEK293 cells: pharmacology and localization. *Biochem. Biophys. Res. Commun.* 282, 1132–1137. doi: 10.1006/bbrc.2001.4703

Shih, A. Y., Johnson, D. A., Wong, G., Kraft, A. D., Jiang, L., Erb, H., et al. (2003). Coordinate regulation of glutathione biosynthesis and release by Nrf2-expressing glia potently protects neurons from oxidative stress. *J. Neurosci.* 23, 3394–3406. doi: 10.1523/JNEUROSCI.23-08-03394.2003

Siska, P. J., Kim, B., Ji, X., Hoeksema, M. D., Massion, P. P., Beckermann, K. E., et al. (2016). Fluorescence-based measurement of cystine uptake through xCT shows requirement for ROS detoxification in activated lymphocytes. *J. Immunol. Methods* 438, 51–58. doi: 10.1016/j.jim.2016.08.013

Sulzer, D., Chen, T. K., Lau, Y. Y., Kristensen, H., Rayport, S., and Ewing, A. (1995). Amphetamine redistributes dopamine from synaptic vesicles to the cytosol and promotes reverse transport. *J. Neurosci.* 15, 4102–4108. doi: 10.1523/JNEUROSCI.15-05-04102.1995

Szatkowski, M., Barbour, B., and Attwell, D. (1990). Non-vesicular release of glutamate from glial cells by reversed electrogenic glutamate uptake. *Nature* 348, 443–446. doi: 10.1038/348443a0

Van Liefferinge, J., Bentea, E., Demuyser, T., Albertini, G., Follin-Arbelet, V., Holmseth, S., et al. (2016). Comparative analysis of antibodies to xCT (Slc7a11): forewarned is forearmed. *J. Comp. Neurol.* 524, 1015–1032. doi: 10.1002/cne.23889

Vermeiren, C., Najimi, M., Maloteaux, J. M., and Hermans, E. (2005). Molecular and functional characterisation of glutamate transporters in rat cortical astrocytes exposed to a defined combination of growth factors during in vitro differentiation. *Neurochem. Int.* 46, 137–147. doi: 10.1016/j.neuint.2004.08.004

Webster, J. M., Morton, C. A., Johnson, B. F., Yang, H., Rishel, M. J., Lee, B. D., et al. (2014). Functional imaging of oxidative stress with a novel PET imaging agent, 18F-5-fluoro-L-aminosuberic acid. *J. Nucl. Med.* 55, 657–664. doi: 10.2967/jnumed.113.126664

Williams, L. E., and Featherstone, D. E. (2014). Regulation of hippocampal synaptic strength by glial xCT. *J. Neurosci.* 34, 16093–16102. doi: 10.1523/JNEUROSCI.1267-14.2014

Wu, Y., Wang, W., and Richerson, G. B. (2003). Vigabatrin induces tonic inhibition via GABA transporter reversal without increasing vesicular GABA release. *J. Neurophysiol.* 89, 2021–2034.s doi: 10.1152/jn.00856.2002

Conflict of Interest: The authors declare that the research was conducted in the absence of any commercial or financial relationships that could be construed as a potential conflict of interest.

frontiers
in Cellular Neuroscience

REVIEW
published: 13 January 2022
doi: 10.3389/fncel.2021.811892

Physiological Perspectives on Molecular Mechanisms and Regulation of Vesicular Glutamate Transport: Lessons From Calyx of Held Synapses

Tetsuya Hori[1]* *and Shigeo Takamori*[2]*

[1]Cellular and Molecular Synaptic Function Unit, Okinawa Institute of Science and Technology Graduate University, Okinawa, Japan, [2]Laboratory of Neural Membrane Biology, Graduate School of Brain Science, Doshisha University, Kyoto, Japan

Accumulation of glutamate, the primary excitatory neurotransmitter in the mammalian central nervous system, into presynaptic synaptic vesicles (SVs) depends upon three vesicular glutamate transporters (VGLUTs). Since VGLUTs are driven by a proton electrochemical gradient across the SV membrane generated by vacuolar-type H^+-ATPases (V-ATPases), the rate of glutamate transport into SVs, as well as the amount of glutamate in SVs at equilibrium, are influenced by activities of both VGLUTs and V-ATPase. Despite emerging evidence that suggests various factors influencing glutamate transport by VGLUTs *in vitro*, little has been reported in physiological or pathological contexts to date. Historically, this was partially due to a lack of appropriate methods to monitor glutamate loading into SVs in living synapses. Furthermore, whether or not glutamate refilling of SVs can be rate-limiting for synaptic transmission is not well understood, primarily due to a lack of knowledge concerning the time required for vesicle reuse and refilling during repetitive stimulation. In this review, we first introduce a unique electrophysiological method to monitor glutamate refilling by VGLUTs in a giant model synapse from the calyx of Held in rodent brainstem slices, and we discuss the advantages and limitations of the method. We then introduce the current understanding of factors that potentially alter the amount and rate of glutamate refilling of SVs in this synapse, and discuss open questions from physiological viewpoints.

Keywords: calyx of Held, glutamate, VGLUT, synaptic transmission, V-ATPase

Edited by:
Sandra Hewett,
Syracuse University, United States

Reviewed by:
Christoph Fahlke,
Helmholtz Association of German Research Centres (HZ), Germany
Jeffrey Erickson,
Louisiana State University, United States
Salah El Mestikawy,
McGill University, Canada

****Correspondence:***
Tetsuya Hori
tetsuya.hori@oist.jp
Shigeo Takamori
stakamor@mail.doshisha.ac.jp

Specialty section:
This article was submitted to Cellular Neurophysiology, a section of the journal Frontiers in Cellular Neuroscience

Received: *09 November 2021*
Accepted: *07 December 2021*
Published: *13 January 2022*

Citation:
Hori T and Takamori S (2022) Physiological Perspectives on Molecular Mechanisms and Regulation of Vesicular Glutamate Transport: Lessons From Calyx of Held Synapses. Front. Cell. Neurosci. 15:811892. doi: 10.3389/fncel.2021.811892

INTRODUCTION

Upon the arrival of action potentials at presynaptic sites, synaptic vesicles (SVs) that store neurotransmitters in the lumen undergo exocytic fusion with the presynaptic plasma membrane, thereby releasing their contents to neighboring neurons. The main excitatory neurotransmitter in the mammalian brain is the acidic amino acid, glutamate. Three vesicular glutamate transporters (VGLUT1–3) are responsible for packaging it into SVs (Takamori, 2006). Deletion of each VGLUT gene in mice, as well as other model organisms such as *Drosophila*, largely silenced glutamatergic transmission, indicating that VGLUTs are essential for brain functions (Fremeau et al., 2004; Wojcik et al., 2004; Daniels et al., 2006).

Furthermore, alterations of VGLUT expression, in addition to the expression of plasma membrane glutamate transporters (O'Donovan et al., 2017), are associated with a wide range of neurological disorders, such as epilepsy, anxiety and mood disorders, Alzheimer's disease, Parkinson's disease, and schizophrenia (summarized in a recent review by Pietrancosta et al., 2020). Therefore, mechanisms and regulators of vesicular glutamate transport mediated by VGLUTs offer potential treatment targets for these disorders.

Like other neurotransmitters, glutamate transport into SVs is driven by a proton electrochemical gradient ($\Delta\mu H^+$) across SV membranes (**Figure 1**). The $\Delta\mu H^+$ is composed of both electrical ($\Delta\Psi$) and chemical (ΔpH) gradients, the balance of which is influenced by the presence of permeable ions (Takamori, 2016; Farsi et al., 2017). Biochemical analysis indicates that $\Delta\Psi$ constitutes the dominant driver of glutamate transport (Maycox et al., 1988), although contributions of ΔpH or luminal pH have been a matter of intensive debate (Tabb et al., 1992; Schenck et al., 2009; Juge et al., 2010; Eriksen et al., 2016). Proportions of the two components of $\Delta\mu H^+$, as well as the net $\Delta\mu H^+$, are largely affected by permeant Cl^- ions. For instance, extravesicular (cytoplasmic) Cl^- can serve as a shunt for H^+ movement, facilitating net H^+ movement. As a result, external Cl^- ions increase ΔpH, while decreasing $\Delta\Psi$, as evidenced by *in vitro* experiments using isolated vesicles (Cidon and Sihra, 1989; Xie et al., 1989). Additionally, in living synapses, SVs are regenerated either directly from the plasma membrane or from endosome-like vacuoles derived from the plasma membrane (Gan and Watanabe, 2018). As a plausible consequence, newly regenerated SVs must contain an extracellular solution with high Cl^- concentrations (e.g., 130 mM), and Cl^- efflux will thus contribute to increase $\Delta\Psi$ until the Cl^- gradient across the SV membrane reaches equilibrium. Such changes in the driving force by Cl^- would significantly modulate glutamate transport. Intriguingly, some observations indicate that Cl^- ions bind directly to VGLUT and allosterically modulate its activity (Hartinger and Jahn, 1993; Juge et al., 2010). Furthermore, accumulating evidence suggests that VGLUT itself exhibits Cl^- conductance (Bellocchio et al., 2000; Schenck et al., 2009), which is activated by H^+ and eventually inhibits glutamate transport by a competing transport pathway (Eriksen et al., 2016) or increases it by compensating charge imbalance through an exchange mechanism (Schenck et al., 2009).

In addition to Cl^- conductance, recent *in vitro* experiments indicate that VGLUTs transport surprisingly diverse substances. One of these is inorganic phosphate. In fact, before the recognition of glutamate transport activities, VGLUT1 and VGLUT2 were originally cloned as plasma membrane Na^+-dependent inorganic phosphate transporters, given that their heterologous expression stimulates Na^+/Pi co-transport into *Xenopus* oocytes (Ni et al., 1994; Aihara et al., 2000; Bellocchio et al., 2000; Takamori et al., 2000). Recent results from VGLUT reconstitution not only support Na^+-dependent phosphate transport (Juge et al., 2006), but indicate that VGLUTs also promote H^+-dependent Pi transport into SVs, which competes with glutamate transport (Preobraschenski et al., 2018), indicating that VGLUTs transport Pi by utilizing two discrete driving forces, depending on their locations (Preobraschenski et al., 2018; Cheret et al., 2021). More surprisingly, VGLUTs also seem to mediate cation/H^+ exchange in SVs, which would convert ΔpH to $\Delta\Psi$, thereby facilitating the $\Delta\Psi$-driven glutamate transport (Preobraschenski et al., 2014).

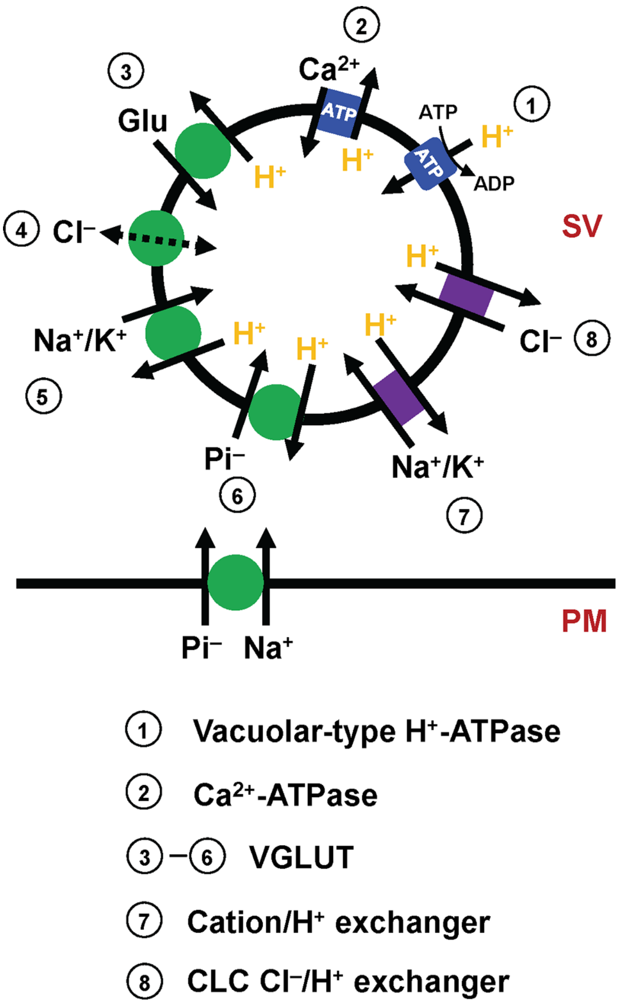

FIGURE 1 | Molecular elements that affect glutamate transport into SVs. Mammalian SVs contain two primary pumps (blue square), vacuolar-type H^+-ATPases (V-ATPases, 1) and plasma membrane Ca^{2+}-ATPases (PMCAs, 2). V-ATPases create a proton electrochemical gradient $\Delta\mu H^+$, which is essential for glutamate transport by VGLUTs. PMCAs attenuate ΔpH, and conversely potentiate $\Delta\Psi$, thereby affecting VGLUT activity. The primary function of VGLUTs (3–6, green circle) is to transport glutamate into SVs, although how VGLUTs utilize $\Delta\mu H^+$ during the transport cycle has long been debated (3). In addition to glutamate transport, biochemical studies indicate that VGLUTs mediate various transport processes, such as proton-dependent Cl^- conductance (4), cation/proton exchange (5), and inorganic Pi transport (6). Importantly, VGLUTs are thought to mediate both Na^+/Pi transport and H^+/Pi, depending on locations. Although molecular identities are uncertain, SVs contain cation/H^+ exchangers (7) and CLC-family members that mediate Cl^-/H^+ exchange (8), activities of which modulate the driving force for glutamate transport.

Despite accumulating *in vitro* evidence from mechanistic insights into glutamate transport modulation by various ions, the physiological relevance of the foregoing biochemical observations in living synapses is largely unexplored, mainly due to technical constraints in manipulating and quantitatively measuring glutamate and various ion concentrations in the cytoplasm and in vesicle lumens. Recent years have witnessed some important observations concerning vesicular glutamate transport mechanisms by utilizing a giant synapse—the calyx of Held synapse—as a model. Furthermore, a recent analysis of VGLUT1-deficient calyces has invoked several regulatory mechanisms regarding how VGLUT expression level, as well as expression of individual VGLUT isoforms, would impact synaptic transmission (Nakakubo et al., 2020). In this review, we will summarize key observations using the calyx of Held synapses that have shed further light on mechanisms and regulation of glutamate transport into SVs and will highlight some of the unknowns underlying the process.

THE CALYX OF HELD SYNAPSE: A MODEL SYNAPSE SUITABLE FOR INVESTIGATING PRESYNAPTIC MECHANISMS

The calyx of Held is the largest nerve terminal in the mammalian central nervous system, occupying 25–50% of the postsynaptic cell body, located in the medial nucleus of the trapezoid body (MNTB) within the superior olivary complex (**Figure 2A**). The origin of the calyx nerve terminal comes from the globular bushy cell, located in the ventral cochlear nucleus (VCN). Globular bushy cells are contacted by multiple large endings of auditory nerve fibers. The ability of bushy cells to encode temporal fine structure in the incident acoustic wave and their involvement in brainstem auditory circuits that mediate sound localization implicates the calyx of Held synapses in localizing sound in space.

During embryogenesis, multiple axons form synaptic contacts on neurons in the MNTB at around embryonic day 17, when synapses already have the ability to induce action potentials on the postsynaptic cell (Hoffpauir et al., 2010). Characteristic calyx presynaptic terminals emerge between postnatal days 2 and 4. During this period, only one major projection input remains, while other input fibers are eliminated, establishing a 1:1 correspondence between a calyx presynaptic terminal and the postsynaptic cell (Hoffpauir et al., 2006). Ear canals generally open at around postnatal day 10 in rodents. At this time, robust morphological and molecular changes occur in the calyx of Held synapses. Morphologically, the shape of the calyx of Held presynaptic termini changes from spoon-shaped to finger-shaped (Kandler and Friauf, 1993; Ford et al., 2009). In addition, the expression of various proteins related to synaptic transmission, including voltage-gated channels, SV proteins, and postsynaptic receptors drastically changes during hearing onset (Iwasaki and Takahashi, 1998; Futai et al., 2001; Blaesse et al., 2005). These expression changes underlie developmental changes in synaptic functions in this synapse (Iwasaki and Takahashi, 2001; Schneggenburger and Forsythe, 2006; Borst and Soria van Hoeve, 2012).

Structural analysis using electron microscopy revealed that calyx terminals are filled with spherical synaptic vesicles, an indication of excitatory connections, and they contain multiple active zones, a hallmark of presynaptic release sites. The number of synaptic sites ranges from 300 in mice to 600 in rats. Later studies showed that calyces contain ∼180,000 synaptic vesicles per terminal (Satzler et al., 2002; de Lange et al., 2003; Neher, 2010). In accordance with the contemporary three-vesicle pool model (Rizzoli and Betz, 2005), the calyx of Held synapses contains ∼3,000 vesicles in the readily releasable pool (RRP), which can be released immediately upon AP arrival (Sakaba and Neher, 2001). They also contain ∼40,000 vesicles in the recycling pool, which replenish the RRP during sustained stimulation (de Lange et al., 2003; Yamashita et al., 2005), and ∼180,000 vesicles in the reserve pool, which are used only during intense stimulation (Satzler et al., 2002; de Lange et al., 2003; **Figure 2D**). In spite of this extraordinary large number of total SVs, the sizes of each SV pool per release site are comparable to those of conventional synapses, e.g., small hippocampal synapses, making it a suitable model for glutamatergic presynaptic terminals (Rizzoli and Betz, 2005). Like other conventional synapses, efficient endocytic retrieval of SV membranes after exocytosis is essential to sustain transmission in this synapse (Yamashita et al., 2005), although modes of endocytosis, as well as the fate of endocytosed vesicles, i.e., which routes endocytosed materials travel until they are reused for exocytosis, and how long it takes, are not fully understood (Neher, 2010).

Because of its extraordinarily large size, the calyx of Held synapses in acutely prepared brain slices are amenable to patch clamp techniques (**Figure 2B**). Since the pioneering work by Forsythe (1994) showed that direct patch-clamp recording from the presynaptic plasma membrane is possible, calyx of Held synapses have been one of the most powerful preparations to investigate biophysical properties and underlying presynaptic molecular mechanisms of synaptic transmission in the mammalian brain. There are several reasons, to mention a few, that make the calyx of Held a suitable model for analysis. (1) It is a unique "one calyx–one MNTB" synapse. Although an MNTB neuron receives other inputs, mainly from surrounding interneurons, one bushy cell makes synaptic contact exclusively with one MNTB neuron. This simple connection ensures the identity of the origin of the postsynaptic response. It also ensures that spontaneous responses elicited by single-vesicle exocytosis and evoked responses elicited either by depolarization of the presynaptic membrane or by electrical stimulation of an afferent fiber are of the same origin. (2) It is a pure glutamatergic neuron, so that knowledge from the calyx of Held may be applicable to most other excitatory synapses throughout the brain. It should be noted, however, that unlike other glutamatergic synapses that predominantly express one of the two VGLUT isoforms (VGLUT1 and VGLUT2) in adulthood (Fremeau et al., 2001; Fujiyama et al., 2001), the calyx of Held synapse expresses both VGLUT1 and VGLUT2 at relatively high levels (Billups, 2005; Blaesse et al., 2005). Unlike hippocampus and neocortex in which VGLUT2 is weakly expressed in early development and is replaced by VGLUT1 during the 2nd or 3rd postnatal week (Fremeau et al., 2004; De Gois et al., 2005), VGLUT2 expression is constant until the 4th week while VGLUT1 expression gradually increases

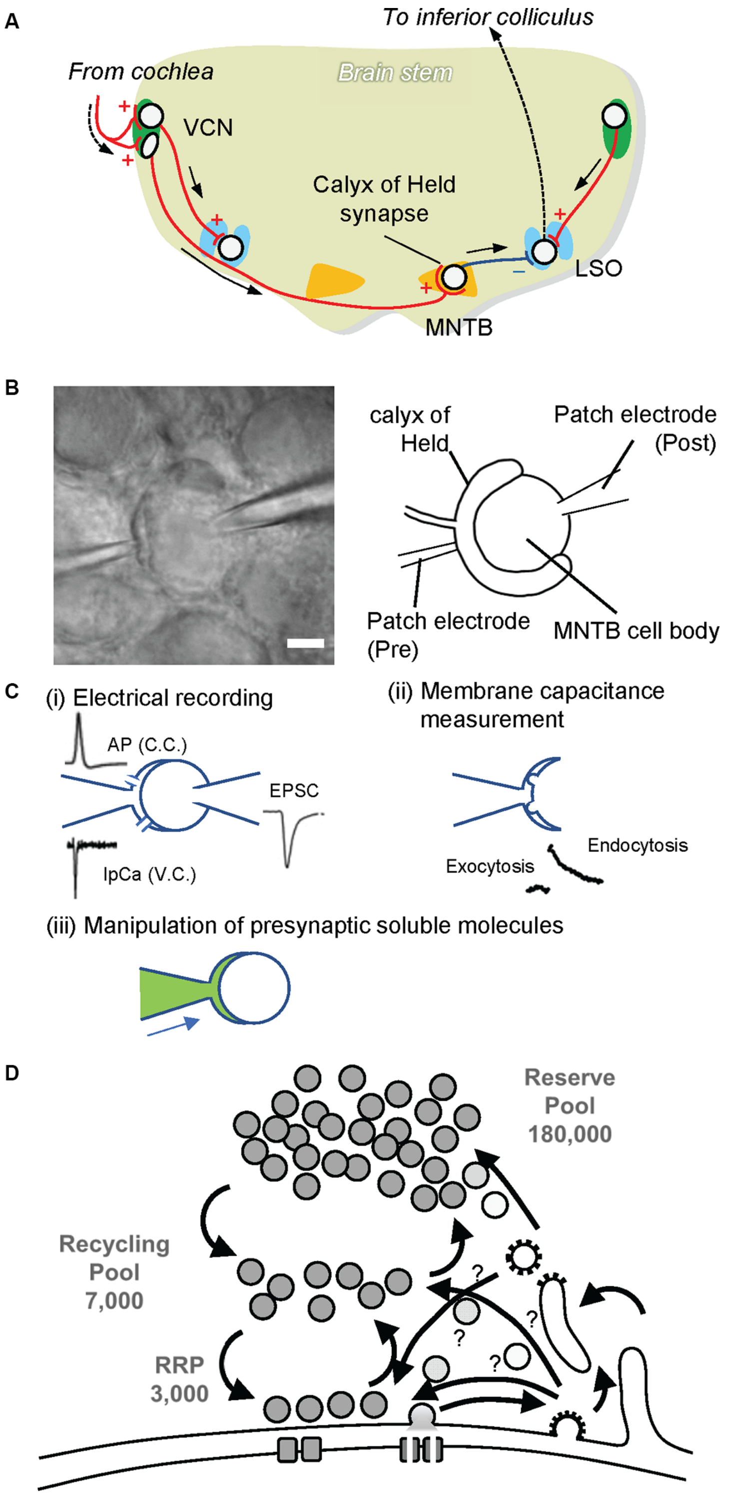

FIGURE 2 | The calyx of Held synapse. **(A)** The auditory circuit in rodent brainstem. Globular and spherical bushy cells in the ventral cochlear nucleus (VCN) receive excitatory synaptic input from the cochlea. Spherical bushy cells send their axons to the ipsilateral lateral superior olive (LSO), whereas globular bushy cells project to the contralateral medial nucleus of the trapezoid body (MNTB). Excitatory synapses on MNTB principal cells, called the calyx of Held. MNTB principal cells form inhibitory synapses to the ipsilateral LSO. The LSO projects to the inferior colliculus, where sound information is integrated. Red lines with + and a blue line with — indicate excitatory and inhibitory inputs, respectively. **(B)** Paired whole-cell patch clamp recording at the calyx of Held. A patch electrode on the left is set to perform whole-cell patch clamp recording from the calyx of Held presynaptic terminal (Pre), while a patch electrode on the right is placed for electrical recordings

(*Continued*)

FIGURE 2 | Continued
whole-cellfrom MNTB principal cells (Post). The scale bar indicates 5 μm. **(C)** Various advantages of the presynaptic terminal patch clamp method. (i) By establishing paired patch clamping at the calyx of Held synapse, one can record action potentials (APs) under current clamp mode (C.C.) from presynaptic terminals, and Ca^{2+} currents (IpCa) under voltage clamp mode (V.C.). Simultaneously, excitatory postsynaptic currents (EPSCs) can be recorded from postsynaptic cells. In addition, through the electrode at the presynaptic terminal, one can trigger neurotransmitter release by applying depolarization pulses as well as local Ca^{2+} uncaging. (ii) SV exocytosis and subsequent membrane retrieval (endocytosis) can be monitored by membrane capacitance measurements. (iii) Through the presynaptic electrode, one can manipulate the composition of presynaptic cytoplasm by dialyzing it with an intra-pipet solution of the desired composition (green). This in turn enables the application of membrane-impermeable drugs directly into presynaptic terminals, washout of intrinsic glutamate from the cytoplasm, and the subsequent glutamate uncaging experiment to monitor glutamate refilling into emptied SVs. **(D)** A schematic drawing depicting three pools of SVs. A calyx terminal contains ∼200,000 SVs, consisting of only ∼3,000 synapses in the readily releasable pool (RRP) that swiftly responds upon AP arrival, ∼7,000 synapses in the recycling pool that replenishes the RRP during sustained stimulation, and a reserve pool that participates only during intensive repetitive stimulation (Rizzoli and Betz, 2005).

during this developmental stage (Billups, 2005). (3) Thanks to its extraordinarily large size, whole-cell patch clamping can easily be established at the presynaptic site. By doing so, one can directly record the presynaptic membrane potential in current clamp mode and activities of ion channels present on the presynaptic membrane in the form of currents in membranes under a voltage clamp configuration with extremely high spatio-temporal precision (**Figure 2C**). In particular, the Na^+ current upon generation of an action potential (AP), the K^+ current related to AP termination, and the Ca^{2+} current that is coupled to trigger SV exocytosis can be measured from the presynaptic plasma membrane. In addition, with membrane capacitance measurements, one can monitor activity-dependent SV dynamics, consisting of exocytic increases of membrane capacitance and subsequent decay due to compensatory endocytosis of exocytosed SV membranes (Sun and Wu, 2001). (4) Whole-cell presynaptic patch clamping enables experimental manipulations of presynaptic cytoplasmic composition, which cannot be achieved in conventional smaller synapses, i.e., dialysis of presynaptic cytoplasm with an intra-pipet solution, application of membrane-impermeable drugs into presynaptic cytoplasm through a pipet with defined concentrations, and so on. The inevitable downside of this manipulation is, however, that whole-cell patch clamping definitely leads to the loss of endogenous soluble molecules from presynaptic terminals, which may change the properties of presynaptic terminals in a physiological environment.

In addition to electrophysiologically amenable preparations of the calyx of Held synapses in acute brainstem slices, these giant presynaptic terminals were successfully reconstituted by culturing two types of dissociated cells derived from cochlear nuclei and from medial nuclei of the trapezoid body in the same dish (Dimitrov et al., 2016). This novel preparation allows genetic manipulation and enables them to be adapted for optical measurements of SV dynamics with simultaneous presynaptic electrical recordings, which cannot be readily achieved with acute slice preparations. However, the current protocol seems to hamper feasible applications due to a relatively low success rate, the necessity of long-term culture, e.g., DIV20–22, to establish single input-output pairs, and relatively small postsynaptic currents seen in this preparation (<1 nA), necessitating further optimization.

MANIPULATION OF VESICULAR GLUTAMATE CONTENT BY DIALYZING PRESYNAPTIC TERMINALS WITH SOLUTIONS CONTAINING VARIOUS GLUTAMATE CONCENTRATIONS

Direct access to the giant presynaptic terminal of the calyx of Held using glass pipets allows us to clamp the presynaptic cytoplasm with a solution of the desired composition. In particular, one can clamp presynaptic glutamate concentrations and monitor vesicular glutamate contents through excitatory postsynaptic current (EPSC) recordings in a voltage-clamp configuration at postsynaptic MNTB cells. An additional *tour-de-force* technique to "micro-inject' a desired solution through a thinner tube installed in a presynaptic patch pipet and connected to a syringe enables the consecutive exchange of presynaptic solutions. Switching a solution containing 10 mM glutamate to a glutamate-free solution results in a gradual decrease in both evoked EPSCs amplitudes and miniature EPSC amplitudes, albeit to a lesser extent, over 30 min, indicating that vesicular glutamate content can be depleted by the exocytic release of pre-filled glutamate and subsequent blockade of glutamate refilling of endocytosed vesicles (Ishikawa et al., 2002). The leakage of glutamate from pre-filled SVs does not seem to be a source of rundown (Ikeda and Bekkers, 2009; Takami et al., 2017). In turn, switching a solution with 1 mM glutamate to that with 100 mM glutamate increases both evoked and miniature EPSC amplitudes by ∼100% and by ∼50% respectively, indicating that vesicular glutamate content is critically determined by cytoplasmic glutamate concentrations, as previously indicated by a number of biochemical transport studies using isolated vesicles (Naito and Ueda, 1985; Wolosker et al., 1996; Wilson et al., 2005). Detailed assessment of cytoplasmic glutamate concentrations that are needed to maintain mEPSC amplitudes in an invasive situation (without presynaptic whole-cell recordings) revealed that the presynaptic glutamate concentration at the calyx of Held is ∼1 mM (Ishikawa et al., 2002), which is within the rage of Kms of glutamate transport measured in isolated SVs. However, the seemingly non-saturable nature of glutamate contents in the presence of up to 100 mM is surprising and incompatible with biochemical transport assays *in vitro* (Naito and Ueda, 1985; Wolosker et al., 1996; Wilson et al., 2005). Thus, different mechanisms to regulate glutamate content at equilibrium *in vivo* must exist, e.g., changes in vesicle volume and in glutamate leakage that are associated with the exceeded glutamate refilling under these conditions that may be non-physiological.

In addition to the increase in quantal size in the presence of 100 mM $[Glu]_{cyto}$, quantal content was concomitantly increased

(Ishikawa et al., 2002), suggesting an increase either in the number of releasable vesicles or in the release probability of those vesicles, or a combination of both. Interestingly, experiments conducted later using hippocampal autaptic cultures support the concept that the degree of filling of SVs with glutamate affects their release probability, i.e., more glutamate in the vesicle increases the release probability (Herman et al., 2014). However, how the filling status of SVs with glutamate influences the release properties of SVs is unknown. It has been proposed that physical changes of the vesicle membrane due to the hyper-osmotic condition conferred by glutamate may be responsible. Likewise, the absence of glutamate is thought to cause the distorted morphology of empty SVs observed in VGLUT1-KO neurons under certain fixation conditions (Siksou et al., 2013; Herman et al., 2014). Interestingly, glutamate loading into isolated SVs induces an expansion of vesicle volume by ∼100% *in vitro*, in which multi-transmembrane protein, Synaptic Vesicle-associated Glycoprotein 2 (SV2), performs a critical function (Budzinski et al., 2009). These results collectively indicate that the amount of glutamate in the lumen indirectly regulates the vesicle release probability *via* changes in the biophysical properties of SV membranes. Other potential molecular mechanisms controlling release probability conferred by distinct VGLUT-isoforms will be discussed below.

KINETICS OF GLUTAMATE TRANSPORT INTO SVs AT CALYX OF HELD SYNAPSES

Micro-perfusion of presynaptic terminals with solutions containing fixed glutamate concentrations described above, shed light on various essential points concerning vesicular glutamate content and its regulation in physiological contexts. However, since it is intrinsically difficult to measure the time required to replace presynaptic solutions using microinjection, the source of changes in EPSCs upon solution exchange cannot be identified with certainty, either due to the slow changes in steady-state glutamate content of pre-filled vesicles, or to changes in glutamate refilling into endocytosed SVs during measurements. To directly monitor dynamics of glutamate refilling into endocytosed “empty” SVs, Hori and Takahashi developed an efficient method to swiftly increase cytoplasmic glutamate concentrations using glutamate uncaging after vesicular glutamate was largely washed out by dialyzing the terminals with a glutamate-free solution (Hori and Takahashi, 2012). When simultaneous presynaptic and postsynaptic whole-cell recordings were made with a presynaptic pipet containing 0 mM glutamate and 10 mM 4-methoxy-7-nitroindolinyl (MNI)-glutamate, EPSCs elicited at 1 Hz declined gradually over ∼15 min, due to depletion of the recycling pool (**Figure 3**). When the EPSC amplitude reached a low level, a UV flash (1 s) was applied to photorelease glutamate from MNI-glutamate in the presynaptic terminals (The presynaptic pipet was “detached’ from the terminals to avoid a rapid diffusion of released glutamate back into the pipet, and an afferent fiber was continuously stimulated to monitor EPSCs throughout measurement). Unlike replacement of solutions by microperfusion (from 1 mM to 100 mM glutamate), EPSCs recovered with much faster kinetics upon glutamate uncaging with a time constant of ∼15 s, which is 10–100 times faster than those estimated in isolated vesicles (Naito and Ueda, 1985; Maycox et al., 1988; Carlson et al., 1989). Furthermore, titration of glutamate concentrations achieved by glutamate uncaging revealed that the Km of glutamate refilling measured in the calyces was 0.91 mM, which is in the range of those measured biochemically using isolated vesicles (Maycox et al., 1988; Carlson et al., 1989) as well as heterologous preparations expressing VGLUTs (Kaneko and Fujiyama, 2002). The large discrepancy in refilling kinetics between isolated vesicles and intact vesicles in the living nerve terminals is enigmatic but may arise from a loss of original luminal ionic composition, or from inevitable damage or loss of the VGLUT transport system during fractionation of vesicle membranes. Notably, SVs isolated from native brains by standard cell fractionation protocols lose glutamate completely during purification (Burger et al., 1989). Thus, it is conceivable that they also lose luminal ions that might influence glutamate transport.

Despite this first success toward estimating the rate of glutamate transport in living synapses, there remain several critical concerns regarding the protocol. First, as noted, uncaging MNI-caged glutamate produced unexpected cytotoxicity, which impede the recovery of EPSCs (Hori and Takahashi, 2012). Although the inclusion of 20 mM glutathione seemed to effectively prevent toxicity (on Ca^{2+} influx and exocytosis), the possibility of toxicity affecting VGLUT, V-ATPase, and other vesicular components inhibiting the glutamate transport rate cannot be fully excluded. Second, this protocol allows the measurement of glutamate transport into SVs that are already acidified by V-ATPase. If acidification of SVs is rate-limiting, glutamate refilling would take much longer as a whole. In fact, clathrin-coats by which newly-regenerated SVs are surrounded, severely inhibit ATP-dependent acidification of SVs (Farsi et al., 2018). Finally, cytoplasmic factors may have been removed after dialysis of presynaptic terminals, which potentially modulate the rate of glutamate transport into SVs (Ozkan et al., 1997; Winter et al., 2005).

UNIQUE CHLORIDE DEPENDENCE OF VESICULAR GLUTAMATE TRANSPORT

As summarized in the “Introduction” section, both external and luminal Cl^- concentrations have a profound influence on glutamate transport measured *in vitro*. In particular, external (cytoplasmic) Cl^- concentrations exhibit a biphasic effect on glutamate transport with maximal activity in the presence of 4–30 mM Cl^-, depending on glutamate concentrations used for the transport assay (40 μM and 5 mM glutamate, respectively; Naito and Ueda, 1985; Wolosker et al., 1996). At calyx of Held synapses, Cl^- concentration at presynaptic terminals was ∼21 mM (Price and Trussell, 2006), which seems to be optimal for glutamate transport measured *in vitro*. However, dialyzing presynaptic terminals with a solution containing various Cl^- concentrations from 5 to 100 mM did not cause any changes in mEPSC amplitudes (Price and Trussell, 2006), indicating that Cl^- concentrations do not affect

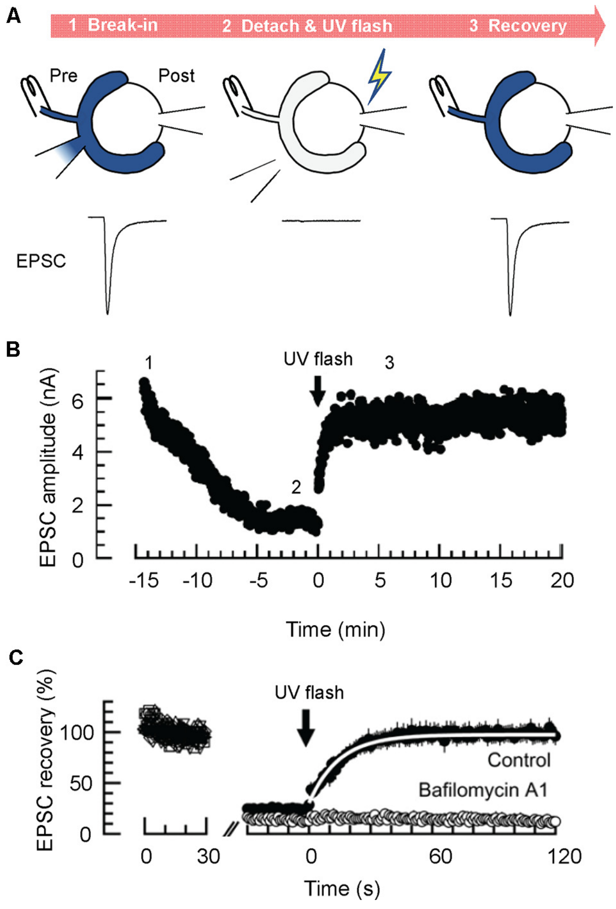

FIGURE 3 | Glutamate uncaging experiments enable estimation of the rate of glutamate refilling into SVs in calyx of Held synapses. **(A)** Glutamate uncaging experiments. Dialysis of the presynaptic terminal with a glutamate-free solution containing 4-methoxy-7-nitroindolinyl (MNI)-caged glutamate is established, while an afferent fiber is continuously stimulated with a bipolar stimulation electrode (at 1 Hz; STEP1). After EPSCs decline substantially, the presynaptic patch pipet is detached, and a UV flash (1 s) is applied to induce a rapid increase of cytosolic glutamate by uncaging MNI-caged glutamate (STEP 2). This results in the recovery of EPSCs, which may reflect the rate of glutamate transport into pre-acidified, but empty SVs (STEP 3). **(B)** A representative time course of EPSCs monitored during glutamate uncaging experiments. **(C)** Representative magnified EPSC traces during glutamate uncaging experiments. Note that EPSCs recover nearly completely after glutamate uncaging under control conditions, whereas they do not recover in the presence of the V-ATPase blocker, bafilomycin A1. A white line indicates an exponential fit to the EPSCs to deduce the glutamate refilling rate. Panels in **(B,C)** are reproduced and slightly modified from Hori and Takahashi (2012).

steady-state glutamate content in SVs. This is compatible with biochemical observations using isolated SVs, in which external Cl$^-$ concentrations affect steady-state glutamate content only when ΔpH is dissipated pharmacologically (Wolosker et al., 1996). On the contrary, the glutamate refilling rate monitored by glutamate uncaging experiments clearly shows similar biphasic dependence on cytosolic Cl$^-$ concentrations with maximum glutamate transport at 30 mM (Hori and Takahashi, 2012). Further, effects of cytosolic Cl$^-$ concentrations on the kinetics of glutamate transport and the magnitude of steady-state glutamate content, at least within the measured time frame, differ among Cl$^-$ concentrations (Hori and Takahashi, 2012), indicating complex regulation mechanisms by Cl$^-$, as suggested by biochemical analysis (Hartinger and Jahn, 1993; Wolosker et al., 1996). Importantly, synaptic fidelity during high-frequency stimulation, assessed by postsynaptic action potential generation, was retarded when presynaptic terminals were dialyzed with a solution having non-optimal presynaptic Cl$^-$ concentrations (either 0.02 mM or 120 mM; Nakakubo et al., 2020). These observations at the calyx of Held synapses strengthen the contribution of cytosolic Cl$^-$ in the regulation of glutamate transport. Since cytoplasmic Cl$^-$ concentrations can be altered by activity of plasma membrane transporters, such as the K$^+$-Cl$^-$ cotransporter, KCC2, and a Na$^+$-K$^+$-2Cl$^-$ cotransporter, NKCC1, during development, in general (Kaila et al., 2014) as well as upon synaptic inhibition that involves a transient Cl$^-$ influx through GABA$_A$ or glycine receptors expressed in calyx terminals (Turecek and Trussell, 2001, 2002; Trojanova et al., 2014), regulation of glutamate transport into SVs by Cl$^-$ is likely to be physiologically relevant. Furthermore, changes in cytosolic [Cl$^-$] are associated with various diseases such as epilepsy and chronic pain (Kaila et al., 2014), indicating its pathological implications.

In contrast to the effect of cytosolic [Cl$^-$], contributions of luminal Cl$^-$ on glutamate refilling in a physiological context remain to be determined. Although simple replacement of luminal Cl$^-$ at living synapses can be achieved, in principle, by turnover of vesicle pools in the presence of external solution with desired Cl$^-$ concentrations, the large size of vesicle pools in the calyx of Held may impede the feasibility of assessment by postsynaptic recordings. In cultured hippocampal neurons, however, it seems that glutamate loading is associated with Cl$^-$ efflux, and luminal Cl$^-$ is critical for efficient vesicle acidification, indicating pivotal roles of luminal Cl$^-$ on glutamate refilling in living synapses (Martineau et al., 2017).

REGULATION OF VESICULAR GLUTAMATE CONTENT BY CYTOPLASMIC CATIONS THROUGH CATION/H$^+$ EXCHANGE MECHANISMS ON SVs

Biochemical analysis of isolated SVs revealed that SVs exhibit an electro-neutral cation/H$^+$ exchange activity, which converts ΔpH to $\Delta\Psi$, thereby facilitating glutamate transport into SVs (Goh et al., 2011). Furthermore, reconstitution of VGLUTs suggested that VGLUT itself mediates the cation/H$^+$ exchange activity (Preobraschenski et al., 2014). These observations raise the possibility that changes in presynaptic cation concentrations may regulate vesicular glutamate transport and have the potential to influence synaptic transmission.

Cytosolic Na$^+$ concentration is maintained at relatively low levels (~15 mM) by the activity of Na$^+$/K$^+$-ATPases on the plasma membrane. At calyx of Held terminals, hyperpolarization-activated cyclin nucleotide-gated (HCN) channels, which allow Na^+ to pass through the membrane, also contribute to the resting cytosolic Na^+ concentration. Activation of HCN channels increases resting Na^+ concentrations by ∼5 mM (Huang and Trussell, 2014). Further, the Na^+ influx through voltage-gated Na^+ channels during repetitive AP firing also contributes to increased cytosolic $[Na^+]$. In fact, $[Na^+]$ reaches ∼80 mM when 100-Hz stimulation is applied for 10 s (Huang and Trussell, 2014). As such, presynaptic $[Na^+]$ is subjected to control at physiologically relevant conditions.

Dialysis of calyces with a buffer containing high Na^+ (40 mM) significantly increases both amplitude and frequency of mEPSCs, whereas that with a buffer lacking Na^+ (0 mM) decreases them (Huang and Trussell, 2014; **Figure 4A**). Furthermore, pharmacological activation of HCN channels through cAMP activation increases mEPSC amplitudes, while inhibition of HCN channels decreases mEPSC amplitudes (Huang and Trussell, 2014). All these observations are compatible with a proposal from biochemical transport assays, that activation of Na^+/H^+ exchange potentiates $\Delta\Psi$, which would optimally drive glutamate transport.

Although regulation of presynaptic $[K^+]$ is less understood, manipulations of cytoplasmic $[K^+]$ at the calyx of Held synapses exerted similar effects on miniature EPSC amplitudes, i.e., complete replacement of presynaptic K^+ with $NMDG^+$ resulted in a gradual decline of mEPSC amplitudes by ∼30%, while no decrease was observed in the presence of 130 mM K^+ (**Figure 4B**; Goh et al., 2011). Interestingly, the inclusion of 10 mM Na^+ in a pipet solution, which mimics physiological conditions to some extent, did not reverse the reduction of mEPSC amplitudes in the absence of K^+, supporting the importance of K^+ rather than Na^+ in maintaining vesicular glutamate content under resting conditions. Finally, EIPA, an inhibitor of the Na^+/H^+ exchanger, also resulted in the reduction of mEPSC amplitudes to an extent similar to that in the absence of K^+, indicating that the Na^+/H^+ exchanger is involved in this regulation, consistent with biochemical results.

Despite clear indications that cation/H^+ exchange activity on SVs regulates vesicular glutamate contents under physiological conditions, the molecular identity of the Na^+/H^+ exchanger on SVs, as well as its contribution to the intrinsic cation/H^+ exchange activity in VGLUTs are still uncertain. Among the SLC9/sodium proton exchanger (NHE) family, some members of which are suggested to be responsible for regulating organellar acidity in various cell types and tissues (Donowitz et al., 2013), NHE-1, -6, and -7 were identified in isolated SV membranes by a recent proteomic study (Taoufiq et al., 2020), and NHE6 is enriched in SVs (Preobraschenski et al., 2014). Of note, recent evidence from hippocampal neurons suggests that NHE6 may be central because knock-down of NHE6 alone results in a reduction of mEPSC amplitudes (Lee et al., 2021a,b). Furthermore, secretory carrier membrane protein 5 (SCAMP5), one of the genuine SV residents (Takamori et al., 2006), is responsible for proper sorting of NHE6 to fusion-competent SVs, and SCAMP5 knock-down also results in a similar reduction in mEPSCs. Since both NHE6 and SCAMP5 are associated with autism spectrum disorder (ASDs; Morrow et al., 2008; Castermans et al., 2010; Kondapalli et al., 2014; Schwede et al., 2014), regulation of vesicular glutamate content by NHE6 and SCAMP5 may be implicated in the pathogenesis of ASDs. Whether the same mechanisms are implemented in the calyx of Held synapses needs further investigation.

IS VESICULAR REFILLING A RATE-LIMITING STEP FOR NEUROTRANSMISSION?

Given the rate of glutamate transport into SVs, an important question remains as to whether the refilling speed can be rate-limiting for glutamatergic transmission. This can happen if the reuse of vesicles that have undergone exocytosis is faster than the time required for complete vesicle refilling (<20 s). Although we currently do not know the time required for vesicle reuse, recent studies using hippocampal synapses as well as cerebellar mossy fiber terminals in slices (Watanabe et al., 2013, 2014; Delvendahl et al., 2016), indicate that at physiological temperature, clathrin-independent rapid endocytosis occurs much more rapidly than previously believed (<100 ms), leaving room for exocytosis of incompletely filled vesicles upon vesicle reuse.

A suggestion of rapid reuse of incompletely filled vesicles comes from experiments in which vesicular glutamate transport was abolished by dialyzing presynaptic terminals with a glutamate-free pipet solution, while EPSCs were continuously monitored (Hori and Takahashi, 2012). Immediately after whole-cell voltage clamp was established at a presynaptic terminal, EPSCs evoked by afferent fiber stimulation at 1 Hz tend to decline when the pipet contained glutamate-free solution, although systematic analysis has not been done to determine how long it takes to detect a significant decrease from the initial EPSCs. This rapid decline was not observed when the pipet solution contained 3 mM glutamate, strongly indicating that SVs that had experienced exocytosis and had lost glutamate were reused multiple times during this short time. Consistent with this observation, blockade of glutamate refilling either by the V-ATPase inhibitor, folimycin, or by attenuating $\Delta\mu H^+$ buildup of endocytosed vesicles with strong buffers, results in rapid synaptic depression in hippocampal preparations (Ertunc et al., 2007). Oddly, rundown observed in the presence of another membrane-permeable V-ATPase inhibitor, bafilomycin, did not seem to cause immediate depression with the same onset (Hori and Takahashi, 2012). This is probably due to a side effect of bafilomycin, by which the release probability of SVs dramatically increases, which would mask the initial synaptic rundown due to the blockade of glutamate transport (Ikeda and Bekkers, 2009).

A second indication comes from an experiment in which the input-output relationship of presynaptic and postsynaptic AP firings is monitored, while vesicular glutamate transport is slowed by changing the presynaptic Cl^- concentrations (Nakakubo et al., 2020). Essentially, the calyx of Held synapses 16–19 days after birth endure a train of 1,000 stimuli at 100 Hz (for 10 s) without large failures (**Figure 5A**). However,

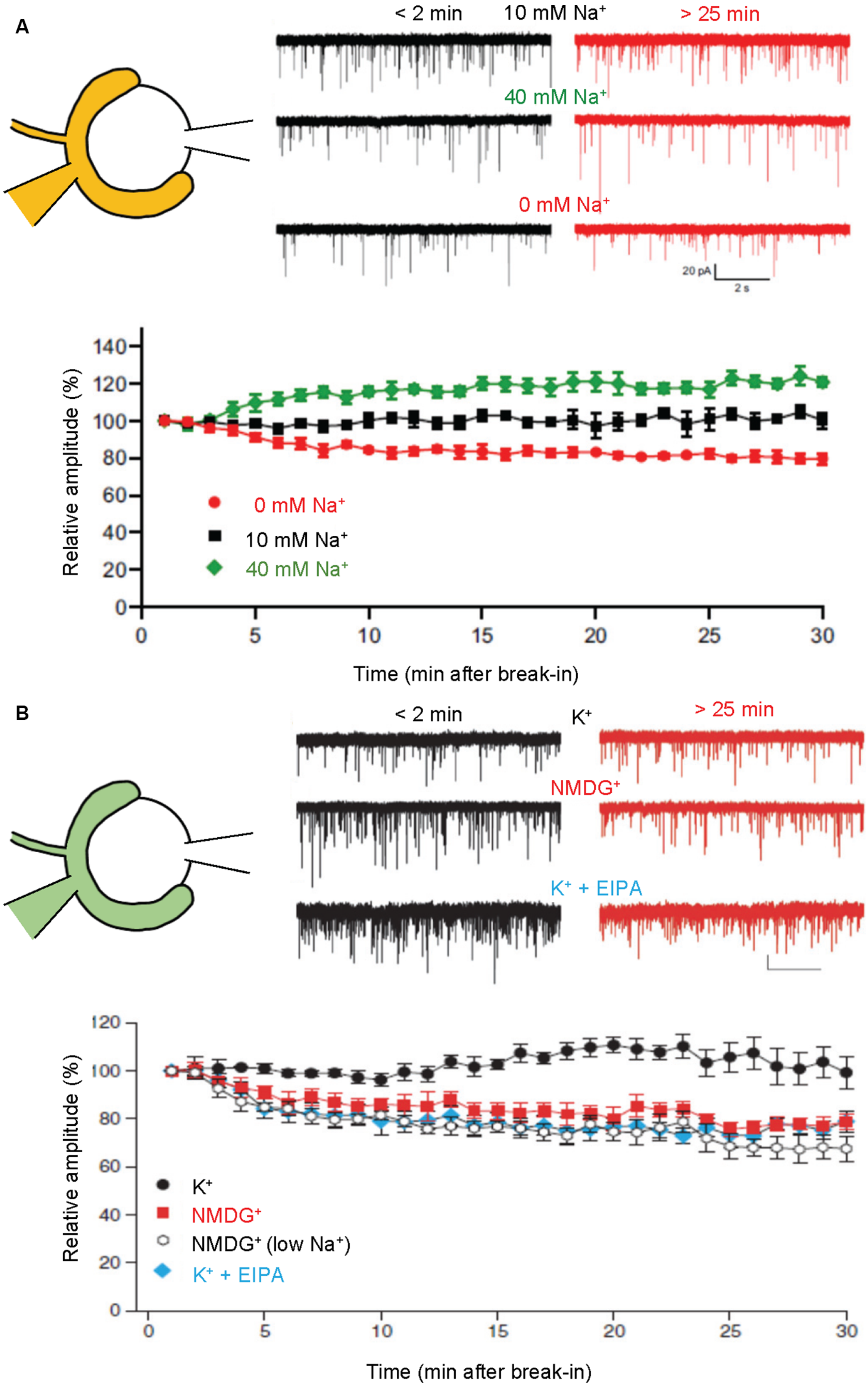

FIGURE 4 | Presynaptic cations regulate mEPSC amplitudes through cation/H⁺ exchange in SVs. Paired recordings were performed from both pre- and postsynaptic compartments in a calyx of Held-MNTB neuron. mEPSCs were recorded postsynaptically immediately (within 2 min) and 25–30 min after a break-in to the presynaptic terminal with a pipet containing indicated buffers. Relative mEPSC amplitudes of initial mEPSCs were plotted as a function of time after a break-in. **(A)** Traces indicate mEPSCs measured under control (10 mM Na⁺; top), high Na⁺ (40 mM Na⁺, middle), and Na⁺-free (0 mM, bottom) immediately after break-in (<2 min, black) and after 25–30 min (>25 min, red). The bottom plot indicates mEPSC amplitudes relative to initial mEPSC amplitudes in the presence of 0 mM Na⁺ (red), 10 mM Na⁺ (black), and 40 mM Na⁺. Figures were modified from Huang and Trussell (2014). **(B)** Traces indicate mEPSCs measured under control (130 mM K⁺; top), K⁺-free (130 mM NMDG⁺; middle), and 130 mM K⁺ with EIPA (bottom) immediately after break-in (<2 min, black) and after 25–30 min (>25 min, red). The bottom plot indicates mEPSC amplitudes relative to initial mEPSCs in the presence of 130 mM K⁺ (K⁺; black circle), 130 mM NMDG⁺ (NMDG⁺; red), 10 mM NaCl, K⁺-free solution [NMDG⁺ (low Na⁺); open], and 130 mM K⁺ with 50–100 μM EIPA (K⁺ + EIPA; blue). Figures were modified from Goh et al. (2011).

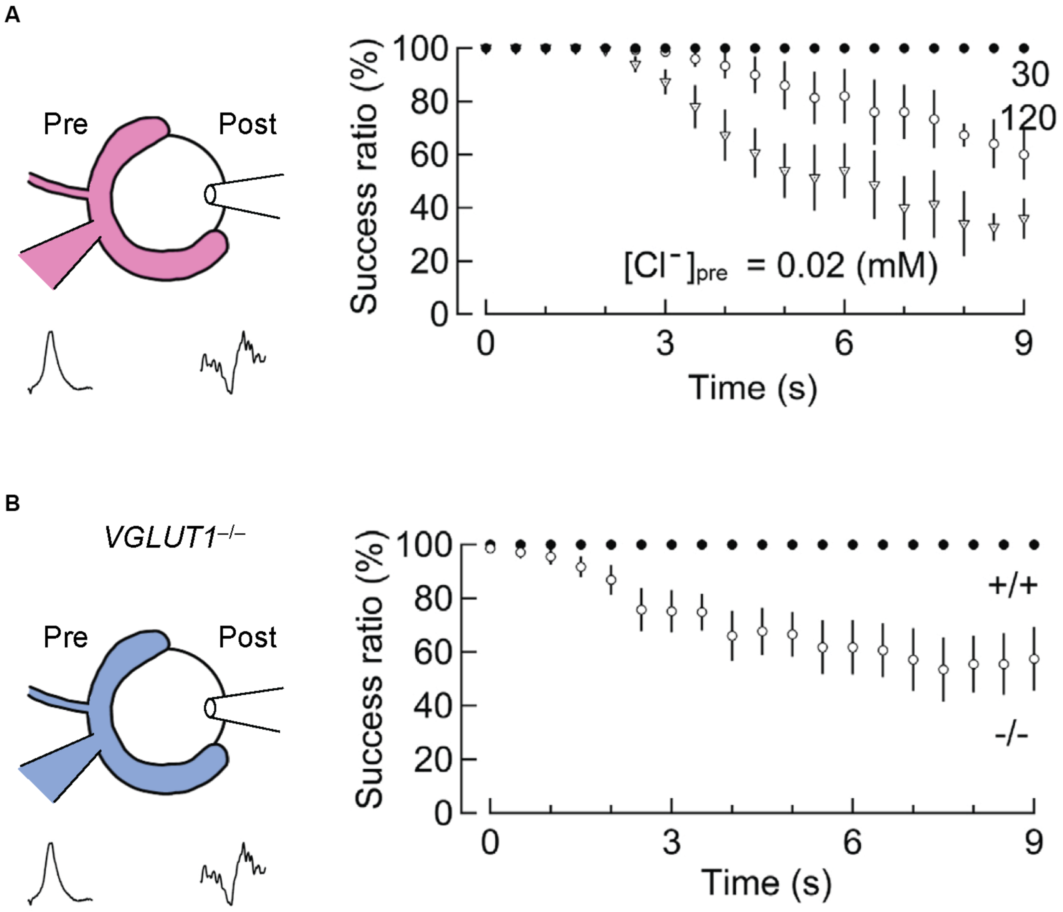

FIGURE 5 | Slowed vesicular glutamate refilling impairs synaptic fidelity during high-frequency firing. **(A)** The impairment of synaptic fidelity when presynaptic Cl^- concentrations are not optimal for efficient glutamate refilling. In the presence of very low $[Cl^-]_{pre}$ (0.02 mM) or high $[Cl^-]_{pre}$ (120 mM), at which rates of glutamate refilling are dramatically slowed, synaptic fidelity upon long high-frequency stimulation (100 Hz) causes apparent synaptic failure within several seconds. This synaptic failure does not occur in the presence of 30 mM $[Cl^-]_{pre}$ within these time frames (modified from Nakakubo et al., 2020). **(B)** Impairment of synaptic fidelity in the calyx of Held synapses of *VGLUT1*$^{-/-}$ mice. Despite considerable differences in basic synaptic parameters of the calyx of Held synapses between wild-type and *VGLUT1*$^{-/-}$ mice, the rate of glutamate refilling in SVs is slowed in VGLUT1-decifient synapses by ∼4-fold compared to wild-type. Presumably, as a consequence, synaptic fidelity during high-frequency firing is impaired within several seconds in VGLUT1-deficient synapses. Figures are modified from Nakakubo et al. (2020).

when presynaptic Cl^- concentrations are clamped either at very low (0.02 mM) or at very high (120 mM) concentrations, both of which significantly retard glutamate refilling in this synapse (Hori and Takahashi, 2012), synaptic failures occur within 3–5 s (Nakakubo et al., 2020). This was also observed when VGLUT1 was genetically deleted (see below for details; Nakakubo et al., 2020; **Figure 5B**), supporting the notion that efficient vesicle refilling with glutamate can be rate-limiting for synaptic transmission during high-firing. Knowing that the rate of glutamate refilling measured under relatively milder conditions is much longer ($\tau \sim 15$ s), this, in turn, suggests that mechanism(s) to accelerate vesicular refilling must exist during intensive stimulation. Whether Na^+ or Ca^{2+}, the latter of which also converts ΔpH to $\Delta\Psi$ to facilitate glutamate uptake *in vitro* (Goncalves et al., 1999a,b; Ono et al., 2019), enhances glutamate refilling in these situations remains to be explored.

WHICH MATTERS MOST, VGLUT ISOFORMS OR TOTAL VGLUT EXPRESSION AT THE CALYX OF HELD?

Expression of both VGLUT1 and VGLUT2 at the calyx of Held synapses (Billups, 2005) offers a unique opportunity to address possible functional differences between them using VGLUT1 knockout mice. While the transmembrane domains of the three VGLUTs are almost identical, N-termini and C-termini of VGLUTs, both of which face the cytoplasm, are quite different (Reimer, 2013). In fact, transport properties, i.e., the transport rate, the biphasic dependence on extra-vesicular $[Cl^-]$, the predominant utilization of $\Delta\Psi$, are quite similar among the three isoforms, despite some diversity in the requirement of ΔpH for transport (Bai et al., 2001; Kaneko and Fujiyama, 2002; Eriksen et al., 2016). In turn, distribution of these transporters in a heterologous system, as well as recycling properties and dynamics within presynaptic terminals, seem to differ among the isoforms in several respects (Voglmaier et al., 2006; Guillaud et al., 2017; Li et al., 2017), indicating differences in trafficking and sorting. Furthermore, in previous experiments using hippocampal autapses, as well as hippocampal slices, in which VGLUT1 expression predominates over other isoforms, it was reported that VGLUT1 confers low release probability, whereas VGLUT2 bestows high release probability (Weston et al., 2011; He et al., 2012). It is also unclear, in a subpopulation of hippocampal neurons as well as cortical neurons that express both VGLUT1 and VGLUT2, whether they are expressed at the same boutons (or even on the same vesicles) or whether they are segregated into distinct release sites (or distinct boutons; Fremeau et al., 2004; Schuske and Jorgensen, 2004; Wojcik et al., 2004; De Gois et al., 2005; Herzog et al., 2006). These studies also reached different conclusions as to how net VGLUT expression on an SV affects the quantal size of glutamate (Fremeau et al., 2004; Wojcik et al., 2004; Wilson et al., 2005; Herman et al., 2014). These complex issues have recently been addressed by analyzing the calyx of Held synapses derived from VGLUT1-KO mice (Nakakubo et al., 2020). It should be noted that since VGLUT1-KO mice die at around ∼20 days after birth, most experiments were performed during postnatal days 16–19.

The first question is whether VGLUT1 and VGLUT2 are segregated into distinct vesicle populations. An immunohistochemical approach by triple staining of VGLUT1, VGLUT2, and an SV marker synaptophysin (Syp) revealed that although substantial populations of vesicle clusters are dominated by one of the two VGLUT isoforms, the majority of Syp-positive presynaptic structures contain both isoforms at different levels, consistent with other studies (Billups, 2005; Blaesse et al., 2005). Interestingly, unlike hippocampal preparations where VGLUT1 expression clearly predominates (Fremeau et al., 2004; Wojcik et al., 2004), there are no alterations in evoked EPSC amplitudes, or in the frequency and amplitude of miniature EPSCs in VGLUT1-deficient calyx of Held synapses (Nakakubo et al., 2020). Although exact copy numbers of both VGLUT isoforms in wild-type calyces and in VGLUT1-deficient calyces are difficult to measure, these data suggest that all "releasable" SVs in the calyx of Held synapses may contain at least a single copy of both VGLUT isoforms, and that VGLUT1-loss results in a decrease of net VGLUT expression of unknown extent (note that the average copy number of VGLUTs in an SV was estimated to be ∼10; Takamori et al., 2006). This interpretation is compatible with studies of *Drosophila* neuromuscular junctions in which gradual reduction of the ortholog, DVGLUT, results in a reduction of mini frequencies, but not mini amplitudes, arguing that a single copy of VGLUT on an SV suffices to fill up SVs completely (Daniels et al., 2006). It also supports observations in rodent neurons that decreasing VGLUT3 expression in various mutants by as much as ∼80% only minimally affects VGLUT3 function (Ramet et al., 2017). It seems, however, incompatible with observations that decreased VGLUT expression (VGLUT heterogyzous) resulted in decreased mEPSC amplitudes or increased mEPSC amplitudes when VGLUT is overexpressed (Wojcik et al., 2004; Wilson et al., 2005; Moechars et al., 2006, but see Fremeau et al., 2004). As it stands, with these contradictory observations, whether and how glutamate content in SVs is controlled by VGLUT levels remains controversial.

It seems conceivable, however, that VGLUT levels affect refilling speed until SVs are fully refilled with glutamate. When glutamate refilling after presynaptic glutamate washout is measured by glutamate uncaging, glutamate refilling was substantially slowed in VGLUT1-deficient synapses (τ ∼80 s at room temperature), i.e., four times slower than observed in wild-type synapses (Nakakubo et al., 2020). In addition, recovery of EPSCs after glutamate uncaging was hardly observed when synapses were continuously stimulated at 1 Hz, necessitating lower stimulation at 0.1 Hz to observe the recovery of EPSCs in VGLUT1-deficient synapses. This was probably due to the involvement of exocytosis of partially re-filled SVs that could never reach a fully refilled state at continuous 1-Hz stimulation. The notion that VGLUT levels dictate the speed of refilling, but not the steady-state levels of glutamate content observed in the calyx of Held synapses is somewhat contradictory to earlier biochemical transport assays using pharmacological manipulations, arguing that the number of available VGLUTs on SVs influences the magnitude and to a lesser extent, the rate of glutamate uptake (Wilson et al., 2005), although the reason remains enigmatic.

Studies using hippocampal preparations revealed that EPSCs persisting in VGLUT1-KO neurons, apparently mediated by VGLUT2, exhibited higher release probability and rapid recovery after synaptic depression (Fremeau et al., 2004; Weston et al., 2011). Although these features seen in VGLUT1-deficient synapses have typically been attributed to VGLUT2, it is also possible that other components of respective synapses contribute to these different features. By taking advantage of the calyx of Held synapses in which both VGLUT1 and VGLUT2 are normally expressed on the same vesicles, albeit to different extents, analysis of the remaining EPSCs in VGLUT1-deficient calyces may provide deeper insights into differences in synaptic properties conferred by VGLUT isoforms. Estimation of RRP sizes and release probabilities deduced from short-term depression (STD) reveal that VGLUT2-laden vesicles exhibit a higher release probability than wild-type vesicles, while RRP sizes were not altered. Furthermore, recovery from STD was faster in VGLUT1-deficient synapses than in wild-type synapses, which was ablated in the presence of EGTA, indicating that faster replenishment of RRP by VGLUT2-laden vesicles is mediated by a Ca^{2+}-dependent process. These observations are largely compatible with reports using hippocampal preparations from VGLUT1-KO mice (Fremeau et al., 2004), and strengthen the notion that expression of VGLUT isoforms regulates vesicle dynamics. The best-studied molecular difference among VGLUTs is the presence of a proline-rich domain at the carboxyl-terminal tail of VGLUT1, which offers a binding site for an endocytosis-related protein, endophilin (De Gois et al., 2006; Vinatier et al., 2006; Voglmaier et al., 2006). Although endophilin binding to VGLUT1 reportedly facilitates endocytosis of VGLUT1 during mild prolonged repetitive stimulation (Voglmaier et al., 2006) and reduces SV-release probability (Weston et al., 2011), a recent study using hippocampal neurons suggests that it also reduces SV mobility mediated by an additional endocytic protein, intersectin (Zhang et al., 2019), presumably representing a molecular mechanism underlying faster recovery after STD in the absence of VGLUT1. It should be noted, however, that vesicle tracking experiments on heterologous expression of fluorescently-labeled VGLUT1 and VGLUT2 in unique culture preparations of the calyx of Held terminals revealed that VGLUT1-laden vesicles move faster and travel longer distances than VGLUT2-laden vesicles (Guillaud et al., 2017), incompatible with facilitation of EPSC recovery from STD observed in VGLUT1-deficient synapses. How the binding ability of VGLUT1 to endophilin, which has been implicated in endocytosis, confers low release probability is difficult to explain. It was proposed that the number of available endophilin molecules influences vesicle release probability, and that VGLUT1 acts as an intrinsic "buffer" to inactivate endophilin by reducing its cytoplasmic concentrations (Weston et al., 2011). Intriguingly, more recent studies indicate that endophilin is involved directly in vesicle priming and fusion of neurosecretory granules in chromaffin cells and in modulation of presynaptic Ca^{2+} channel function in rodent cochlear inner hair cells (Kroll et al., 2019; Gowrisankaran et al., 2020), presumably relating to endophilin-dependent distinct release probabilities between VGLUT1- and VGLUT2-encoding synapses. Currently, precise actions of endophilin on the regulation of release probability and the presence of other key partners involved in these VGLUT isoform-specific properties in SV mobility and physiological consequences remain largely unknown.

CONCLUDING REMARKS

In this review, we introduced recent key findings concerning mechanisms of vesicular glutamate transport processes in the calyx of Held and discussed their physiological relevance. Although mechanistic insights obtained from *in vitro* studies also suggest the importance of luminal ions that are engulfed by vesicles during endocytosis, e.g., facilitation of glutamate refilling by luminal Cl^{-} during the initial phase of glutamate loading, it is still uncertain how much this proposed mechanism contributes in physiological contexts. As for the refilling speed, studies using presynaptic glutamate uncaging indicate that it is much faster than rates observed biochemically using isolated SVs. Yet, with some experimental concerns and possible rapid use of filled vesicles during highly repetitive stimulation described above, it may be even faster than measured values. In addition to multiple modes of SV endocytosis with distinct time scales depending on stimulation strength, the time required for reuse of endocytosed vesicles may be an important key to fully understanding whether refilling speed can be rate-limiting for neurotransmission. A future innovation that enables direct observations of glutamate refilling of individual SVs at presynaptic terminals, in addition to indirect measures of synaptic outputs from postsynaptic cells, under precise manipulations and stimulation will likely give us the answer.

AUTHOR CONTRIBUTIONS

TH and ST: conceptualization, manuscript initial draft, manuscript critical correction, and approval of final version. All authors contributed to the article and approved the submitted version.

FUNDING

This work was supported in part by grants from JSPS KAKENHI (19H03330), the JSPS core-to-core program A. Advanced Research Networks (Grant No: JPJSCCA20170008), and a grant from the Takeda Science Foundation to ST.

ACKNOWLEDGMENTS

We thank Dr. Steven D. Aird (www.sda-technical-editor.org) for English editing.

REFERENCES

Aihara, Y., Mashima, H., Onda, H., Hisano, S., Kasuya, H., Hori, T., et al. (2000). Molecular cloning of a novel brain-type Na(+)-dependent inorganic phosphate cotransporter. *J. Neurochem.* 74, 2622–2625. doi: 10.1046/j.1471-4159.2000.0742622.x

Bai, L., Xu, H., Collins, J. F., and Ghishan, F. K. (2001). Molecular and functional analysis of a novel neuronal vesicular glutamate transporter. *J. Biol. Chem.* 276, 36764–36769. doi: 10.1074/jbc.M104578200

Bellocchio, E. E., Reimer, R. J., Fremeau, R. T., Jr., and Edwards, R. H. (2000). Uptake of glutamate into synaptic vesicles by an inorganic phosphate transporter. *Science* 289, 957–960. doi: 10.1126/science.289.5481.957

Billups, B. (2005). Colocalization of vesicular glutamate transporters in the rat superior olivary complex. *Neurosci. Lett.* 382, 66–70. doi: 10.1016/j.neulet.2005.02.071

Blaesse, P., Ehrhardt, S., Friauf, E., and Nothwang, H. G. (2005). Developmental pattern of three vesicular glutamate transporters in the rat superior olivary complex. *Cell Tissue Res.* 320, 33–50. doi: 10.1007/s00441-004-1054-8

Borst, J. G., and Soria van Hoeve, J. (2012). The calyx of held synapse: from model synapse to auditory relay. *Annu. Rev. Physiol.* 74, 199–224. doi: 10.1146/annurev-physiol-020911-153236

Budzinski, K. L., Allen, R. W., Fujimoto, B. S., Kensel-Hammes, P., Belnap, D. M., and Bajjalieh, S. M. (2009). Large structural change in isolated synaptic vesicles upon loading with neurotransmitter. *Biophys J.* 97, 2577–2584. doi: 10.1016/j.bpj.2009.08.032

Burger, P. M., Mehl, E., Cameron, P. L., Maycox, P. R., Baumert, M., Lottspeich, F., et al. (1989). Synaptic vesicles immunoisolated from rat cerebral cortex contain high levels of glutamate. *Neuron* 3, 715–720. doi: 10.1016/0896-6273(89)90240-7

Carlson, M. D., Kish, P. E., and Ueda, T. (1989). Glutamate uptake into synaptic vesicles: competitive inhibition by bromocriptine. *J. Neurochem.* 53, 1889–1894. doi: 10.1111/j.1471-4159.1989.tb09258.x

Castermans, D., Volders, K., Crepel, A., Backx, L., De Vos, R., Freson, K., et al. (2010). SCAMP5, NBEA and AMISYN: three candidate genes for autism involved in secretion of large dense-core vesicles. *Hum. Mol. Genet.* 19, 1368–1378. doi: 10.1093/hmg/ddq013

Cheret, C., Ganzella, M., Preobraschenski, J., Jahn, R., and Ahnert-Hilger, G. (2021). Vesicular glutamate transporters (SLCA17 A6, 7, 8) control synaptic phosphate levels. *Cell Rep.* 34:108623. doi: 10.1016/j.celrep.2020.108623

Cidon, S., and Sihra, T. S. (1989). Characterization of a H+-ATPase in rat brain synaptic vesicles. coupling to L-glutamate transport. *J. Biol. Chem.* 264, 8281–8288.

Daniels, R. W., Collins, C. A., Chen, K., Gelfand, M. V., Featherstone, D. E., and DiAntonio, A. (2006). A single vesicular glutamate transporter is sufficient to fill a synaptic vesicle. *Neuron* 49, 11–16. doi: 10.1016/j.neuron.2005.11.032

De Gois, S., Jeanclos, E., Morris, M., Grewal, S., Varoqui, H., and Erickson, J. D. (2006). Identification of endophilins 1 and 3 as selective binding partners for VGLUT1 and their co-localization in neocortical glutamatergic synapses: implications for vesicular glutamate transporter trafficking and excitatory vesicle formation. *Cell Mol. Neurobiol.* 26, 679–693. doi: 10.1007/s10571-006-9054-8

De Gois, S., Schafer, M. K., Defamie, N., Chen, C., Ricci, A., Weihe, E., et al. (2005). Homeostatic scaling of vesicular glutamate and GABA transporter expression in rat neocortical circuits. *J. Neurosci.* 25, 7121–7133. doi: 10.1523/JNEUROSCI.5221-04.2005

de Lange, R. P., de Roos, A. D., and Borst, J. G. (2003). Two modes of vesicle recycling in the rat calyx of Held. *J. Neurosci.* 23, 10164–10173. doi: 10.1523/JNEUROSCI.23-31-10164.2003

Delvendahl, I., Vyleta, N. P., von Gersdorff, H., and Hallermann, S. (2016). Fast, temperature-sensitive and clathrin-independent endocytosis at central synapses. *Neuron* 90, 492–498. doi: 10.1016/j.neuron.2016.03.013

Dimitrov, D., Takagi, H., Guillaud, L., Saitoh, N., Eguchi, K., and Takahashi, T. (2016). Reconstitution of giant mammalian synapses in culture for molecular functional and imaging studies. *J. Neurosci.* 36, 3600–3610. doi: 10.1523/JNEUROSCI.3869-15.2016

Donowitz, M., Ming Tse, C., and Fuster, D. (2013). SLC9/NHE gene family, a plasma membrane and organellar family of Na(+)/H(+) exchangers. *Mol. Aspects Med.* 34, 236–251. doi: 10.1016/j.mam.2012.05.001

Eriksen, J., Chang, R., McGregor, M., Silm, K., Suzuki, T., and Edwards, R. H. (2016). Protons regulate vesicular glutamate transporters through an allosteric mechanism. *Neuron* 90, 768–780. doi: 10.1016/j.neuron.2016.03.026

Ertunc, M., Sara, Y., Chung, C., Atasoy, D., Virmani, T., and Kavalali, E. T. (2007). Fast synaptic vesicle reuse slows the rate of synaptic depression in the CA1 region of hippocampus. *J. Neurosci.* 27, 341–354. doi: 10.1523/JNEUROSCI.4051-06.2007

Farsi, Z., Gowrisankaran, S., Krunic, M., Rammner, B., Woehler, A., Lafer, E. M., et al. (2018). Clathrin coat controls synaptic vesicle acidification by blocking vacuolar ATPase activity. *eLife* 7:e32569. doi: 10.7554/eLife.32569

Farsi, Z., Jahn, R., and Woehler, A. (2017). Proton electrochemical gradient: driving and regulating neurotransmitter uptake. *Bioessays* 39:1600240. doi: 10.1002/bies.201600240

Ford, M. C., Grothe, B., and Klug, A. (2009). Fenestration of the calyx of Held occurs sequentially along the tonotopic axis, is influenced by afferent activity and facilitates glutamate clearance. *J. Comp. Neurol.* 514, 92–106. doi: 10.1002/cne.21998

Forsythe, I. D. (1994). Direct patch recording from identified presynaptic terminals mediating glutamatergic EPSCs in the rat CNS, *in vitro*. *J. Physiol.* 479, 381–387. doi: 10.1113/jphysiol.1994.sp020303

Fremeau, R. T., Jr., Kam, K., Qureshi, T., Johnson, J., Copenhagen, D. R., Storm-Mathisen, J., et al. (2004). Vesicular glutamate transporters 1 and 2 target to functionally distinct synaptic release sites. *Science* 304, 1815–1819. doi: 10.1126/science.1097468

Fremeau, R. T., Jr., Troyer, M. D., Pahner, I., Nygaard, G. O., Tran, C. H., Reimer, R. J., et al. (2001). The expression of vesicular glutamate transporters defines two classes of excitatory synapse. *Neuron* 31, 247–260. doi: 10.1016/s0896-6273(01)00344-0

Fujiyama, F., Furuta, T., and Kaneko, T. (2001). Immunocytochemical localization of candidates for vesicular glutamate transporters in the rat cerebral cortex. *J. Comp. Neurol.* 435, 379–387. doi: 10.1002/cne.1037

Futai, K., Okada, M., Matsuyama, K., and Takahashi, T. (2001). High-fidelity transmission acquired via a developmental decrease in NMDA receptor expression at an auditory synapse. *J. Neurosci.* 21, 3342–3349. doi: 10.1523/JNEUROSCI.21-10-03342.2001

Gan, Q., and Watanabe, S. (2018). Synaptic vesicle endocytosis in different model systems. *Front. Cell Neurosci.* 12:171. doi: 10.3389/fncel.2018.00171

Goh, G. Y., Huang, H., Ullman, J., Borre, L., Hnasko, T. S., Trussell, L. O., et al. (2011). Presynaptic regulation of quantal size: K+/H+ exchange stimulates vesicular glutamate transport. *Nat. Neurosci.* 14, 1285–1292. doi: 10.1038/nn.2898

Goncalves, P. P., Meireles, S. M., Neves, P., and Vale, M. G. (1999a). Ionic selectivity of the Ca2+/H+ antiport in synaptic vesicles of sheep brain cortex. *Brain Res. Mol. Brain Res.* 67, 283–291. doi: 10.1016/s0169-328x(99)00081-9

Goncalves, P. P., Meireles, S. M., Neves, P., and Vale, M. G. (1999b). Synaptic vesicle Ca2+/H+ antiport: dependence on the proton electrochemical gradient. *Brain Res. Mol. Brain Res.* 71, 178–184. doi: 10.1016/s0169-328x(99)00183-7

Gowrisankaran, S., Houy, S., Del Castillo, J. G. P., Steubler, V., Gelker, M., Kroll, J., et al. (2020). Endophilin-A coordinates priming and fusion of neurosecretory vesicles via intersectin. *Nat. Commun.* 11:1266. doi: 10.1038/s41467-020-14993-8

Guillaud, L., Dimitrov, D., and Takahashi, T. (2017). Presynaptic morphology and vesicular composition determine vesicle dynamics in mouse central synapses. *eLife* 6:e24845. doi: 10.7554/eLife.24845

Hartinger, J., and Jahn, R. (1993). An anion binding site that regulates the glutamate transporter of synaptic vesicles. *J. Biol. Chem.* 268, 23122–23127.

He, H., Mahnke, A. H., Doyle, S., Fan, N., Wang, C. C., Hall, B. J., et al. (2012). Neurodevelopmental role for VGLUT2 in pyramidal neuron plasticity, dendritic refinement and in spatial learning. *J. Neurosci.* 32, 15886–15901. doi: 10.1523/JNEUROSCI.4505-11.2012

Herman, M. A., Ackermann, F., Trimbuch, T., and Rosenmund, C. (2014). Vesicular glutamate transporter expression level affects synaptic vesicle release probability at hippocampal synapses in culture. *J. Neurosci.* 34, 11781–11791. doi: 10.1523/JNEUROSCI.1444-14.2014

Herzog, E., Takamori, S., Jahn, R., Brose, N., and Wojcik, S. M. (2006). Synaptic and vesicular co-localization of the glutamate transporters VGLUT1 and VGLUT2 in the mouse hippocampus. *J. Neurochem.* 99, 1011–1018. doi: 10.1111/j.1471-4159.2006.04144.x

Hoffpauir, B. K., Grimes, J. L., Mathers, P. H., and Spirou, G. A. (2006). Synaptogenesis of the calyx of Held: rapid onset of function and one-to-one morphological innervation. *J. Neurosci.* 26, 5511–5523. doi: 10.1523/JNEUROSCI.5525-05.2006

Hoffpauir, B. K., Kolson, D. R., Mathers, P. H., and Spirou, G. A. (2010). Maturation of synaptic partners: functional phenotype and synaptic organization tuned in synchrony. *J. Physiol.* 588, 4365–4385. doi: 10.1113/jphysiol.2010.198564

Hori, T., and Takahashi, T. (2012). Kinetics of synaptic vesicle refilling with neurotransmitter glutamate. *Neuron* 76, 511–517. doi: 10.1016/j.neuron.2012.08.013

Huang, H., and Trussell, L. O. (2014). Presynaptic HCN channels regulate vesicular glutamate transport. *Neuron* 84, 340–346. doi: 10.1016/j.neuron.2014.08.046

Ikeda, K., and Bekkers, J. M. (2009). Counting the number of releasable synaptic vesicles in a presynaptic terminal. *Proc. Natl. Acad. Sci. U S A* 106, 2945–2950. doi: 10.1073/pnas.0811017106

Ishikawa, T., Sahara, Y., and Takahashi, T. (2002). A single packet of transmitter does not saturate postsynaptic glutamate receptors. *Neuron* 34, 613–621. doi: 10.1016/s0896-6273(02)00692-x

Iwasaki, S., and Takahashi, T. (1998). Developmental changes in calcium channel types mediating synaptic transmission in rat auditory brainstem. *J. Physiol.* 509, 419–423. doi: 10.1111/j.1469-7793.1998.419bn.x

Iwasaki, S., and Takahashi, T. (2001). Developmental regulation of transmitter release at the calyx of held in rat auditory brainstem. *J. Physiol.* 534, 861–871. doi: 10.1111/j.1469-7793.2001.00861.x

Juge, N., Gray, J. A., Omote, H., Miyaji, T., Inoue, T., Hara, C., et al. (2010). Metabolic control of vesicular glutamate transport and release. *Neuron* 68, 99–112. doi: 10.1016/j.neuron.2010.09.002

Juge, N., Yoshida, Y., Yatsushiro, S., Omote, H., and Moriyama, Y. (2006). Vesicular glutamate transporter contains two independent transport machineries. *J. Biol. Chem.* 281, 39499–39506. doi: 10.1074/jbc.M607670200

Kaila, K., Price, T. J., Payne, J. A., Puskarjov, M., and Voipio, J. (2014). Cation-chloride cotransporters in neuronal development, plasticity and disease. *Nat. Rev. Neurosci.* 15, 637–654. doi: 10.1038/nrn3819

Kandler, K., and Friauf, E. (1993). Pre- and postnatal development of efferent connections of the cochlear nucleus in the rat. *J. Comp. Neurol.* 328, 161–184. doi: 10.1002/cne.903280202

Kaneko, T., and Fujiyama, F. (2002). Complementary distribution of vesicular glutamate transporters in the central nervous system. *Neurosci. Res.* 42, 243–250. doi: 10.1016/s0168-0102(02)00009-3

Kondapalli, K. C., Prasad, H., and Rao, R. (2014). An inside job: how endosomal Na(+)/H(+) exchangers link to autism and neurological disease. *Front. Cell Neurosci.* 8:172. doi: 10.3389/fncel.2014.00172

Kroll, J., Jaime Tobon, L. M., Vogl, C., Neef, J., Kondratiuk, I., Konig, M., et al. (2019). Endophilin-A regulates presynaptic Ca(2+) influx and synaptic vesicle recycling in auditory hair cells. *EMBO J.* 38:e100116. doi: 10.15252/embj.2018100116

Lee, U., Choi, C., Ryu, S. H., Park, D., Lee, S. E., Kim, K., et al. (2021a). SCAMP5 plays a critical role in axonal trafficking and synaptic localization of NHE6 to adjust quantal size at glutamatergic synapses. *Proc. Natl. Acad. Sci. U S A* 118:e2011371118. doi: 10.1073/pnas.2011371118

Lee, U., Ryu, S. H., and Chang, S. (2021b). SCAMP5 mediates activity-dependent enhancement of NHE6 recruitment to synaptic vesicles during synaptic plasticity. *Mol. Brain* 14:47. doi: 10.1186/s13041-021-00763-0

Li, H., Santos, M.S., Park, C.K., Dobry, Y., and Voglmaier, S.M. (2017). VGLUT2 trafficking is differentially regulated by adaptor proteins AP-1 and AP-3. *Front. Cell Neurosci.* 11:324. doi: 10.3389/fncel.2017.00324

Martineau, M., Guzman, R. E., Fahlke, C., and Klingauf, J. (2017). VGLUT1 functions as a glutamate/proton exchanger with chloride channel activity in hippocampal glutamatergic synapses. *Nat. Commun.* 8:2279. doi: 10.1038/s41467-017-02367-6

Maycox, P. R., Deckwerth, T., Hell, J. W., and Jahn, R. (1988). Glutamate uptake by brain synaptic vesicles. energy dependence of transport and functional reconstitution in proteoliposomes. *J. Biol. Chem.* 263, 15423–15428.

Moechars, D., Weston, M. C., Leo, S., Callaerts-Vegh, Z., Goris, I., Daneels, G., et al. (2006). Vesicular glutamate transporter VGLUT2 expression levels control quantal size and neuropathic pain. *J. Neurosci.* 26, 12055–12066. doi: 10.1523/JNEUROSCI.2556-06.2006

Morrow, E. M., Yoo, S. Y., Flavell, S. W., Kim, T. K., Lin, Y., Hill, R. S., et al. (2008). Identifying autism loci and genes by tracing recent shared ancestry. *Science* 321, 218–223. doi: 10.1126/science.1157657

Naito, S., and Ueda, T. (1985). Characterization of glutamate uptake into synaptic vesicles. *J. Neurochem.* 44, 99–109. doi: 10.1111/j.1471-4159.1985.tb07118.x

Nakakubo, Y., Abe, S., Yoshida, T., Takami, C., Isa, M., Wojcik, S. M., et al. (2020). Vesicular glutamate transporter expression ensures high-fidelity synaptic transmission at the calyx of held synapses. *Cell Rep.* 32:108040. doi: 10.1016/j.celrep.2020.108040

Neher, E. (2010). What is rate-limiting during sustained synaptic activity: vesicle supply or the availability of release sites. *Front. Synaptic. Neurosci.* 2:144. doi: 10.3389/fnsyn.2010.00144

Ni, B., Rosteck, P. R., Jr., Nadi, N. S., and Paul, S. M. (1994). Cloning and expression of a cDNA encoding a brain-specific Na(+)-dependent inorganic phosphate cotransporter. *Proc. Natl. Acad. Sci. U S A* 91, 5607–5611. doi: 10.1073/pnas.91.12.5607

O'Donovan, S.M., Sullivan, C.R., and McCullumsmith, R.E. (2017). The role of glutamate transporters in the pathophysiology of neuropsychiatric disorders. *NPJ Schizophr.* 3:32. doi: 10.1038/s41537-017-0037-1

Ono, Y., Mori, Y., Egashira, Y., Sumiyama, K., and Takamori, S. (2019). Expression of plasma membrane calcium ATPases confers Ca(2+)/H(+) exchange in rodent synaptic vesicles. *Sci. Rep.* 9:4289. doi: 10.1038/s41598-019-40557-y

Ozkan, E. D., Lee, F. S., and Ueda, T. (1997). A protein factor that inhibits ATP-dependent glutamate and gamma-aminobutyric acid accumulation into synaptic vesicles: purification and initial characterization. *Proc. Natl. Acad. Sci. U S A* 94, 4137–4142. doi: 10.1073/pnas.94.8.4137

Pietrancosta, N., Djibo, M., Daumas, S., El Mestikawy, S., and Erickson, J. D. (2020). Molecular, structural, functional and pharmacological sites for vesicular glutamate transporter regulation. *Mol. Neurobiol.* 57, 3118–3142. doi: 10.1007/s12035-020-01912-7

Preobraschenski, J., Cheret, C., Ganzella, M., Zander, J. F., Richter, K., Schenck, S., et al. (2018). Dual and direction-selective mechanisms of phosphate transport by the vesicular glutamate transporter. *Cell Rep.* 23, 535–545. doi: 10.1016/j.celrep.2018.03.055

Preobraschenski, J., Zander, J. F., Suzuki, T., Ahnert-Hilger, G., and Jahn, R. (2014). Vesicular glutamate transporters use flexible anion and cation binding sites for efficient accumulation of neurotransmitter. *Neuron* 84, 1287–1301. doi: 10.1016/j.neuron.2014.11.008

Price, G. D., and Trussell, L. O. (2006). Estimate of the chloride concentration in a central glutamatergic terminal: a gramicidin perforated-patch study on the calyx of Held. *J. Neurosci.* 26, 11432–11436. doi: 10.1523/JNEUROSCI.1660-06.2006

Ramet, L., Zimmermann, J., Bersot, T., Poirel, O., De Gois, S., Silm, K., et al. (2017). Characterization of a human point mutation of VGLUT3 (p.A211V) in the rodent brain suggests a nonuniform distribution of the transporter in synaptic vesicles. *J. Neurosci.* 37, 4181–4199. doi: 10.1523/JNEUROSCI.0282-16.2017

Reimer, R. J. (2013). SLC17: a functionally diverse family of organic anion transporters. *Mol. Aspects Med.* 34, 350–359. doi: 10.1016/j.mam.2012.05.004

Rizzoli, S. O., and Betz, W. J. (2005). Synaptic vesicle pools. *Nat. Rev. Neurosci.* 6, 57–69. doi: 10.1038/nrn1583

Sakaba, T., and Neher, E. (2001). Calmodulin mediates rapid recruitment of fast-releasing synaptic vesicles at a calyx-type synapse. *Neuron* 32, 1119–1131. doi: 10.1016/s0896-6273(01)00543-8

Satzler, K., Sohl, L. F., Bollmann, J. H., Borst, J. G., Frotscher, M., Sakmann, B., et al. (2002). Three-dimensional reconstruction of a calyx of Held and its postsynaptic principal neuron in the medial nucleus of the trapezoid body. *J. Neurosci.* 22, 10567–10579. doi: 10.1523/JNEUROSCI.22-24-10567.2002

Schenck, S., Wojcik, S. M., Brose, N., and Takamori, S. (2009). A chloride conductance in VGLUT1 underlies maximal glutamate loading into synaptic vesicles. *Nat. Neurosci.* 12, 156–162. doi: 10.1038/nn.2248

Schneggenburger, R., and Forsythe, I. D. (2006). The calyx of Held. *Cell Tissue Res.* 326, 311–337. doi: 10.1007/s00441-006-0272-7

Schuske, K., and Jorgensen, E. M. (2004). Neuroscience. vesicular glutamate transporter—shooting blanks. *Science* 304, 1750–1752. doi: 10.1126/science.1100475

Schwede, M., Garbett, K., Mirnics, K., Geschwind, D. H., and Morrow, E. M. (2014). Genes for endosomal NHE6 and NHE9 are misregulated in autism brains. *Mol. Psychiatry* 19, 277–279. doi: 10.1038/mp.2013.28

Siksou, L., Silm, K., Biesemann, C., Nehring, R. B., Wojcik, S. M., Triller, A., et al. (2013). A role for vesicular glutamate transporter 1 in synaptic vesicle clustering and mobility. *Eur. J. Neurosci.* 37, 1631–1642. doi: 10.1111/ejn.12199

Sun, J. Y., and Wu, L. G. (2001). Fast kinetics of exocytosis revealed by simultaneous measurements of presynaptic capacitance and postsynaptic currents at a central synapse. *Neuron* 30, 171–182. doi: 10.1016/s0896-6273(01)00271-9

Tabb, J. S., Kish, P. E., Van Dyke, R., and Ueda, T. (1992). Glutamate transport into synaptic vesicles. roles of membrane potential, pH gradient and intravesicular pH. *J. Biol. Chem.* 267, 15412–15418.

Takami, C., Eguchi, K., Hori, T., and Takahashi, T. (2017). Impact of vesicular glutamate leakage on synaptic transmission at the calyx of Held. *J. Physiol.* 595, 1263–1271. doi: 10.1113/JP273467

Takamori, S. (2006). VGLUTs: "exciting" times for glutamatergic research. *Neurosci. Res.* 55, 343–351. doi: 10.1016/j.neures.2006.04.016

Takamori, S. (2016). Presynaptic molecular determinants of quantal size. *Front. Synaptic Neurosci.* 8:2. doi: 10.3389/fnsyn.2016.00002

Takamori, S., Holt, M., Stenius, K., Lemke, E. A., Gronborg, M., Riedel, D., et al. (2006). Molecular anatomy of a trafficking organelle. *Cell* 127, 831–846. doi: 10.1016/j.cell.2006.10.030

Takamori, S., Rhee, J. S., Rosenmund, C., and Jahn, R. (2000). Identification of a vesicular glutamate transporter that defines a glutamatergic phenotype in neurons. *Nature* 407, 189–194. doi: 10.1038/35025070

Taoufiq, Z., Ninov, M., Villar-Briones, A., Wang, H. Y., Sasaki, T., Roy, M. C., et al. (2020). Hidden proteome of synaptic vesicles in the mammalian brain. *Proc. Natl. Acad. Sci. U S A* 117, 33586–33596. doi: 10.1073/pnas.2011870117

Trojanova, J., Kulik, A., Janacek, J., Kralikova, M., Syka, J., and Turecek, R. (2014). Distribution of glycine receptors on the surface of the mature calyx of Held nerve terminal. *Front. Neural Circuits* 8:120. doi: 10.3389/fncir.2014.00120

Turecek, R., and Trussell, L. O. (2001). Presynaptic glycine receptors enhance transmitter release at a mammalian central synapse. *Nature* 411, 587–590. doi: 10.1038/35079084

Turecek, R., and Trussell, L. O. (2002). Reciprocal developmental regulation of presynaptic ionotropic receptors. *Proc. Natl. Acad. Sci. U S A* 99, 13884–13889. doi: 10.1073/pnas.212419699

Vinatier, J., Herzog, E., Plamont, M. A., Wojcik, S. M., Schmidt, A., Brose, N., et al. (2006). Interaction between the vesicular glutamate transporter type 1 and endophilin A1, a protein essential for endocytosis. *J. Neurochem.* 97, 1111–1125. doi: 10.1111/j.1471-4159.2006.03821.x

Voglmaier, S. M., Kam, K., Yang, H., Fortin, D. L., Hua, Z., Nicoll, R. A., et al. (2006). Distinct endocytic pathways control the rate and extent of synaptic vesicle protein recycling. *Neuron* 51, 71–84. doi: 10.1016/j.neuron.2006.05.027

Watanabe, S., Rost, B. R., Camacho-Perez, M., Davis, M. W., Sohl-Kielczynski, B., Rosenmund, C., et al. (2013). Ultrafast endocytosis at mouse hippocampal synapses. *Nature* 504, 242–247. doi: 10.1038/nature12809

Watanabe, S., Trimbuch, T., Camacho-Perez, M., Rost, B. R., Brokowski, B., Sohl-Kielczynski, B., et al. (2014). Clathrin regenerates synaptic vesicles from endosomes. *Nature* 515, 228–233. doi: 10.1038/nature13846

Weston, M. C., Nehring, R. B., Wojcik, S. M., and Rosenmund, C. (2011). Interplay between VGLUT isoforms and endophilin A1 regulates neurotransmitter release and short-term plasticity. *Neuron* 69, 1147–1159. doi: 10.1016/j.neuron.2011.02.002

Wilson, N. R., Kang, J., Hueske, E. V., Leung, T., Varoqui, H., Murnick, J. G., et al. (2005). Presynaptic regulation of quantal size by the vesicular glutamate transporter VGLUT1. *J. Neurosci.* 25, 6221–6234. doi: 10.1523/JNEUROSCI.3003-04.2005

Winter, S., Brunk, I., Walther, D. J., Holtje, M., Jiang, M., Peter, J. U., et al. (2005). Galphao2 regulates vesicular glutamate transporter activity by changing its chloride dependence. *J. Neurosci.* 25, 4672–4680. doi: 10.1523/JNEUROSCI.0549-05.2005

Wojcik, S. M., Rhee, J. S., Herzog, E., Sigler, A., Jahn, R., Takamori, S., et al. (2004). An essential role for vesicular glutamate transporter 1 (VGLUT1) in postnatal development and control of quantal size. *Proc. Natl. Acad. Sci. U S A* 101, 7158–7163. doi: 10.1073/pnas.0401764101

Wolosker, H., de Souza, D. O., and de Meis, L. (1996). Regulation of glutamate transport into synaptic vesicles by chloride and proton gradient. *J. Biol. Chem.* 271, 11726–11731. doi: 10.1074/jbc.271.20.11726

Xie, X. S., Crider, B. P., and Stone, D. K. (1989). Isolation and reconstitution of the chloride transporter of clathrin-coated vesicles. *J. Biol. Chem.* 264, 18870–18873.

Yamashita, T., Hige, T., and Takahashi, T. (2005). Vesicle endocytosis requires dynamin-dependent GTP hydrolysis at a fast CNS synapse. *Science* 307, 124–127. doi: 10.1126/science.1103631

Zhang, X. M., Francois, U., Silm, K., Angelo, M. F., Fernandez-Busch, M. V., Maged, M., et al. (2019). A proline-rich motif on VGLUT1 reduces synaptic vesicle super-pool and spontaneous release frequency. *eLife* 8:e50401. doi: 10.7554/eLife.50401

Conflict of Interest: The authors declare that the research was conducted in the absence of any commercial or financial relationships that could be construed as a potential conflict of interest.

frontiers
in Cellular Neuroscience

ORIGINAL RESEARCH
published: 31 January 2022
doi: 10.3389/fncel.2021.792652

Uncoupling the Excitatory Amino Acid Transporter 2 From Its C-Terminal Interactome Restores Synaptic Glutamate Clearance at Corticostriatal Synapses and Alleviates Mutant Huntingtin-Induced Hypokinesia

Stefan Hirschberg[1†], Anton Dvorzhak[1†], Seyed M. A. Rasooli-Nejad[1], Svilen Angelov[1], Marieluise Kirchner[2,3], Philipp Mertins[2,3], Gilla Lättig-Tünnemann[4,5], Christoph Harms[4,5], Dietmar Schmitz[6,7,8] and Rosemarie Grantyn[1,4,7,8]*

[1] Synaptic Dysfunction Lab, Neuroscience Research Center, Charité – Universitätsmedizin Berlin, Corporate Member of Freie Universität Berlin, Humboldt-Universität zu Berlin, Berlin Institute of Health, Berlin, Germany, [2] Proteomics Platform, Max Delbrück Center for Molecular Medicine in the Helmholtz Association, Berlin, Germany, [3] Berlin Institute of Health (BIH), Berlin, Germany, [4] Department of Experimental Neurology, Charité – Universitätsmedizin Berlin, Berlin, Germany, [5] Center for Stroke Research Berlin, Charité – Universitätsmedizin Berlin, Berlin, Germany, [6] German Center for Neurodegenerative Diseases (DZNE), Berlin, Germany, [7] Cluster of Excellence NeuroCure, Berlin, Germany, [8] Einstein Center for Neurosciences Berlin, Berlin, Germany

Edited by:
Arturo Ortega,
Centro de Investigación y de Estudios Avanzados del Instituto Politécnico Nacional, Mexico

Reviewed by:
Suzanne Underhill,
National Institutes of Health (NIH), United States
Annalisa Scimemi,
University at Albany, United States

***Correspondence:**
Rosemarie Grantyn
rosemarie.grantyn@charite.de

† These authors have contributed equally to this work

Specialty section:
This article was submitted to Cellular Neurophysiology, a section of the journal Frontiers in Cellular Neuroscience

***Received:** 10 October 2021*
***Accepted:** 21 December 2021*
***Published:** 31 January 2022*

Citation:
Hirschberg S, Dvorzhak A, Rasooli-Nejad SMA, Angelov S, Kirchner M, Mertins P, Lättig-Tünnemann G, Harms C, Schmitz D and Grantyn R (2022) Uncoupling the Excitatory Amino Acid Transporter 2 From Its C-Terminal Interactome Restores Synaptic Glutamate Clearance at Corticostriatal Synapses and Alleviates Mutant Huntingtin-Induced Hypokinesia. Front. Cell. Neurosci. 15:792652. doi: 10.3389/fncel.2021.792652

Rapid removal of glutamate from the sites of glutamate release is an essential step in excitatory synaptic transmission. However, despite many years of research, the molecular mechanisms underlying the intracellular regulation of glutamate transport at tripartite synapses have not been fully uncovered. This limits the options for pharmacological treatment of glutamate-related motor disorders, including Huntington's disease (HD). We therefore investigated the possible binding partners of transgenic EAAT2 and their alterations under the influence of mutant huntingtin (mHTT). Mass spectrometry analysis after pull-down of striatal YFP-EAAT2 from wild-type (WT) mice and heterozygote (HET) Q175 mHTT-knock-in mice identified a total of 148 significant (FDR < 0.05) binders to full-length EAAT2. Of them 58 proteins exhibited mHTT-related differences. Most important, in 26 of the 58 mHTT-sensitive cases, protein abundance changed back toward WT levels when the mice expressed a C-terminal-truncated instead of full-length variant of EAAT2. These findings motivated new attempts to clarify the role of astrocytic EAAT2 regulation in cortico-basal movement control. Striatal astrocytes of Q175 HET mice were targeted by a PHP.B vector encoding EAAT2 with different degree of C-terminal modification, i.e., EAAT2-S506X (truncation at S506), EAAT2-4KR (4 lysine to arginine substitutions) or EAAT2 (full-length). The results were compared to HET and WT injected with a tag-only vector (CTRL). It was found that the presence of a C-terminal-modified EAAT2 transgene (i) increased the level of native EAAT2 protein in striatal lysates and perisynaptic astrocyte processes, (ii) enhanced the glutamate uptake of transduced astrocytes, (iii) stimulated glutamate clearance at individual corticostriatal synapses, (iv) increased the glutamate uptake of striatal astrocytes and (iv) alleviated the mHTT-related hypokinesia (open field indicators of movement initiation). In contrast, over-expression of full-length EAAT2 neither facilitated glutamate uptake nor locomotion. Together, our results support the new hypothesis that preventing abnormal protein-protein interactions at the C-terminal of EAAT2 could eliminate the mHTT-related deficits in corticostriatal synaptic glutamate clearance and movement initiation.

Keywords: astrocyte activation, Huntington's disease (HD), EAAT2 interaction proteomics, synaptic glutamate clearance, corticostriatal pathology, hypokinesia

INTRODUCTION

In the adult rodent striatum most of the glutamate transport is carried out by EAAT2 (gene name *Slc1a2*) (Danbolt, 2001; Beart and O'Shea, 2007; Vandenberg and Ryan, 2013). Clustering of the EAAT2 protein at the sites of synaptic glutamate release ensures the rapid return of the extracellular glutamate concentration to very low resting levels (Bergles and Jahr, 1998). In comparison with other synaptic proteins, including the postsynaptic glutamate receptors, EAAT2 is present in larger amounts (Danbolt, 2001). It has been a matter of much debate whether or not synaptic glutamate uptake can ever become insufficient in the healthy brain. Under pathological conditions, a relative deficiency of glutamate uptake could result from the following distinct mechanisms: (i) insufficient *Slc1a2* transcription, (ii) impaired membrane targeting of EAAT2, (iii) exaggerated intracellular degradation of EAAT2 and/or iv) altered transporter-substrate interactions. Heterologous expression studies with recombinant chimeric EAAT2 variants illuminated the possible significance of particular EAAT2 domains. It turned out that a region close to the distal end of the last transmembrane domain is relevant for the interaction with the transport substrate (Leinenweber et al., 2011), but it also affects the balance between cytoplasmic retention and membrane insertion (Kalandadze et al., 2002; Underhill et al., 2015). Due to detailed studies from the Zafra lab, it is known that ubiquitination of 4 C-terminal lysine sites (Gonzalez-Gonzalez et al., 2008) substantially contributes to the internalization of the transporter from the plasma membrane. Finally, it was reported that sumoylated toxic C-terminal fragments may inhibit the *Slc1a2* transcription in the astrocyte nucleus (Gibb et al., 2007; Foran et al., 2011; Rosenblum et al., 2017). All these studies imply that EAAT2 binding partners at the C-terminal end can participate in the regulation of glutamate uptake, but detailed information on the spectrum of EAAT2 interactors in health and disease is not yet available. This limits further understanding of EAAT2-related disease mechanisms.

Impairment of glutamate homeostasis due to insufficient EAAT2 expression or function has already been implicated in neurodegenerative disease. This also includes HD – an autosomal dominant neurodegenerative disease of monogenic origin. A trinucleotide (CAG) expansion of exon 1 in the mutant huntingtin gene (*mHTT*) on chromosome 4 causes abnormally long polyglutamine (polyQ) stretches in the already large huntingtin protein. *mHTT* is expressed not only in neurons but also in astrocytes (Faideau et al., 2010) where the loss of normal huntingtin function and additional effects of misfolded polyQ fragments can produce a variety of alterations (Mrzljak and Munoz-Sanjuan, 2015; Tabrizi et al., 2019; Zeitler et al., 2019), including the modification of other proteins (Wanker et al., 2019). The clinical picture of HD is characterized by progressive motor, cognitive and emotional disturbances (Tabrizi et al., 2013). A motor symptom of advanced HD in humans and most rodents with *mHTT* expression is hypo-/bradykinesia (Berardelli et al., 1999; Hart et al., 2013; Horton et al., 2019), whereas jerky uncontrolled spontaneous movements (chorea) are mostly observed at earlier stages of HD (Rosenblatt et al., 2003; Tabrizi et al., 2013). Thorough quantification of the hypo- vs. hyperkinetic aspects of motor performance is important for the pharmacological management of the disease (Hart et al., 2013). In general, phenotype progression is less faithfully predicted by the scores of chorea as compared to those of hypo-/bradykinesia (Rosenblatt et al., 2003; Tabrizi et al., 2013).

The origin of mHTT-related hypokinesia is not well understood. According to the information available from extracellular recordings or imaging of neuronal activity in a mouse model of HD, motor symptoms may evolve as a consequence of disinhibition and abnormal synchronicity in the corticostriatal pathway (Miller et al., 2012; Burgold et al., 2019). However, most studies point to functional uncoupling rather than enhanced glutamatergic input to the striatum (Plotkin and Surmeier, 2015; Reiner and Deng, 2018; Veldman and Yang, 2018). On the presynaptic side, there is a tendency for down-regulation of vGlut1 immunofluorescence (Rothe et al., 2015), decrease in vGluT1+ terminal numbers (Deng et al., 2013) and impairment of synaptic glutamate release at individual corticostriatal terminals (Dvorzhak et al., 2019). On the postsynaptic side, corticostriatal synaptic transmission might be affected by insufficient supply with brain-derived neurotrophic factor (Plotkin et al., 2014) or reduced signal transfer from distal dendrites (Carrillo-Reid et al., 2019). The duration of the NMDAR component of corticostriatal EPSCs could be prolonged (Dvorzhak et al., 2019), which might be due to a reduced glutamate uptake capacity of striatal astrocytes (Tong et al., 2014; Dvorzhak et al., 2016). Indeed, targeted expression of *mHTT* in astrocytes consistently impeded their glutamate uptake function

(Shin et al., 2005; Bradford et al., 2009; Faideau et al., 2010; Meunier et al., 2016) and induced or exacerbated the motor symptoms of HD (Bradford et al., 2009; Meunier et al., 2016).

The present study pursued 2 major aims: (1) to identify the protein binding partners of full-length and C-terminal-modified EAAT2 in normal and mHTT-expressing mice and (2) to explore the functional consequences of modified EAAT2 expression. The underlying hypothesis would be that, in the abnormal environment of a polyQ astrocyte, EAAT2 can establish pathological protein-protein interactions. Bypassing the latter by removal of selected EAAT2 binding sites may increase the availability of glutamate transporter, restore the compromised glutamate clearance function of the corticostriatal pathway and improve locomotion.

MATERIALS AND METHODS

Adeno-Associated Virus Plasmid Design and Vector Production

Supplementary Table 1 presents an overview of the used vectors, the sites of injections and the purpose of a chosen indicator. Plasmid pRcCMV-mYFP-EAAT2 and pRcCMV-mYFP-EAAT2-S506X were gifts from Christoph Fahlke and Arnd Baumann (Forschungszentrum Jülich). pRcCMV-mYFP-EAAT2 contains the expression cassette for the human *Slc1a2* fused to N-terminal mYFP. In pRcCMV-mYFP-EAAT2-S506X a serine at position 506 is point-mutated to generate a stop codon that causes the truncation of the last 68 amino acids of the C-terminus. This truncation does not interfere with the membrane insertion of the protein or glutamate transport (Leinenweber et al., 2011). In contrast, the mutation of four C-terminal lysine (Lys, K) residues to arginine (Arg, R) in the full-length EAAT2 has been shown to be critical for transporter internalization (Gonzalez-Gonzalez et al., 2008). All EAAT2 plasmids were derived from human EAAT2, with the understanding that there is a close similarity between the human and mouse *Slc1a2* homologs (Kirschner et al., 1994).

Four consecutive cycles of site-directed mutagenesis were applied to generate EAAT2-4KR. In brief, pRcCMV-mYFP-EAAT2 was amplified by PCR using the mutagenesis primers listed in **Supplementary Table 1**, and the template was subsequently destroyed by DpnI digest. For high-efficiency transformation, NEB C2987H alpha-competent *Escherichia coli* were incubated with the DpnI-digested PCR mix. Successful mutants were screened by Sanger sequencing (Eurofins Genomics, Köln). The expression cassettes for mYFP-EAAT2, mYFP-EAAT2-4KR, and mYFP-EAAT2-S506X were subcloned by restriction digest with BamHI and EcoRI and ligation into a preexisting adeno-associated virus (AAV) backbone [pAAV-gfaABC1D-ChR2(LCTC)-p2a-FP635-WPRE] to produce pAAV-gfaABC1D-mYFP-EAAT2-WPRE, pAAV-gfaABC1D -mYFP-EAAT2-4KR-WPRE, and pAAV-gfaABC1D -mYFP-EAAT2-S506X-WPRE. Monomeric mRuby was subcloned from pKanCMV-mRuby-10aa-H2B into the three AAV vectors with AgeI and BsrGI to facilitate detection of the transduced astrocytes and the EGFP-based iGlu$_u$ in the corticostriatal terminals of the same preparation. Control vectors were constructed by amplifying mRuby or mYFP by PCR adding a 3′ stop codon and a SalI restriction site and were then cloned into an AAV backbone to generate pAAV-gfaABC1D-mYFP-WPRE or pAAV-gfaABC1D-mRuby-WPRE. The plasmids used or modified for further use are listed in **Supplementary Table 1**. The AAV vectors were produced at the Vector Core Facility of the Charité - University Medicine or at UPenn Vector Core. We acknowledge the contribution of Viviana Gradinaru and Benjamin Devermann for generating the PHP.eB adeno-associated virus (AAV) serotype (Chan et al., 2017).

Antibodies

The primary and secondary antibodies used for the quantification of WB or IR are also listed in **Supplementary Table 1**. For concentrations see the "Materials and Methods" sections "Quantitative Immunofluorescence (IF)" and "Western Blot Analysis of Striatal Lysates." The EAAT2-Ab (Abcam, Cambridge, United Kingdom) was raised against a synthetic peptide within rat EAAT2 aa 550 to the C-terminus (C terminal) conjugated to keyhole limpet haemocyanin. The exact sequence is proprietary. Apart from several other C-terminus-directed Abs, we also tried Ab77039 and Ab203130 from Abcam were peptide fragments between aa143 and 239 were used as antigen but did not achieve the quality of immunostaining seen with Ab41621.

Animals

All data was obtained from aged (14–18 mo) Z-Q175-KI mice, a widely used mouse model of HD (Menalled et al., 2012). The mice were obtained from CHDI ("Cure Huntington's Disease Initiative," see stock # 027410 of the Jackson Laboratory, Bar Harbor, United States). The applicable international, national and institutional guidelines for the care and use of the animals were followed. Study design, performance of experiments and statistical evaluation have been approved by the Berlin Office of Health Protection and Technical Safety (G0218/17), with a yearly update of the experimental guidelines by the local authorities according to the 10 essential rules of ARRIVE [see latest update from July 14, 2020 and (Percie du et al., 2020)]. The experiments were performed in animals of either sex at an age of 51–76 weeks. The number of CAG repeats ranged from 182 to 201 and were determined by Laragen (Culver City, CA, United States). Care was taken that all experimental groups contained an equal number of males and females (±1). Apart from the body weight, no systematic differences could be detected in any of the evaluated indicators. Blinding was not applied, since the animals were used at a stage of HD when the experimenters could recognize the respective genotype and select the appropriate mice among a usually very small number of available animals. The necessary sample size was kept to a minimum and was calculated beforehand to achieve hypothesis testing at a significance level of 5%.

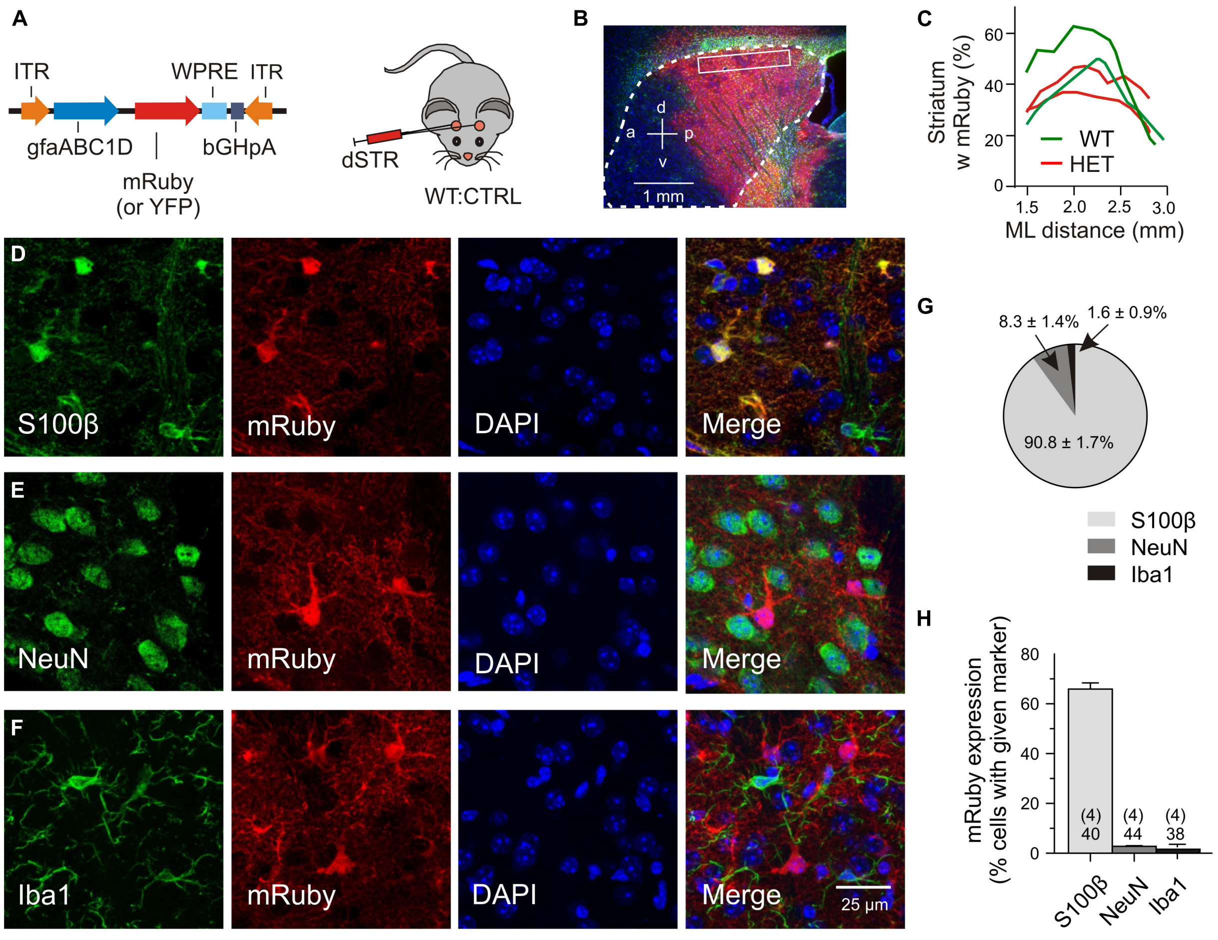

FIGURE 1 | Validation of transgene expression. **(A)** Injected vector. **(B)** Transduced area (red) visualized with mRuby on the background of DAPI (blue) and GFAP immunofluorescence (green). The putative margin of the striatum is marked with a dotted line. **(C)** The mRuby+ area at the indicated mediolateral distance. **(D–F)** Immunostained sections for evaluation of viral expression patterns. Triple labeling with representative astrocytic **(D)**, neuronal **(E)**, or microglial **(F)** markers, together with an antibody against mRuby and nuclear counterstaining with DAPI. **(G)** Fraction of the astrocytic, neuronal or microglial phenotype among the mRuby+ population in the dorsal striatum. **(H)** Incidence of transduced cells within the S100β-, NeuN-, or Iba1-expressing cell populations. Numbers on columns: evaluated sections and animals (in brackets). bGHpA, bovine growth hormone polyadenylation sequence; DAPI, 4′,6-diamidino-2-phenylindol; dSTR, dorsal striatum; GFAP, glial fibrillar acidic protein; gfapABC1D, modified promoter sequence of GFAP; Iba1, ionized calcium-binding adapter molecule 1; ITR, inverted terminal repeat; mRuby, monometric Ruby; NeuN, neuron-specific protein, equivalent to Fox-3, S100β, S100 calcium-binding protein B; WPRE, woodchuck hepatitis virus post-transcriptional regulatory element; YFP, yellow fluorescent protein.

Stereotaxic and Intravenous Injections of Viral Expression Vectors for Treatment and Diagnostic Purposes

Q175 WT and HET were anesthetized by intraperitoneal injection of a mixture containing 87.5 mg/kg ketamine and 12.5 mg/kg xylazine (both from Sigma-Aldrich, Taufkirchen) before receiving bilateral intrastriatal injections of PHP.eB-mRuby-gfaABS1D-EAAT2 (or respective isoforms/controls) as part of the treatment. The therapeutic vectors or controls were given at a concentration of $1.0^{*}10^{12}$ gc/ml and an amount of 1 μl per site ($1.0^{*}10^{9}$ gc/striatum) at the following coordinates with respect to bregma (mm): anterior 0.75, lateral 2.0, ventral 2.5. The intravenous injections (100 μl) were performed under slight isoflurane anesthesia and adjusted to an injected amount of $2.0^{*}10^{11}$–$3.5^{*}10^{11}$ gc/animal. The expression vector for the glutamate sensor AAV9-CamKII.iGlu$_{u}$.WPRE-hGH ($7.34^{*}10^{13}$ gc/ml–0.3 μl) was applied at four sites at: anterior 1.5, lateral 1.56, 1.8, 2.04, 2.28, and ventral 1.7. The expression time between injection and sacrifice was 3–5 weeks.

Validation of Transgene Expression

For the transfer of recombinant DNA the adeno-associated viral vectors were injected into the dorsal striatum, the region most affected by mHTT-related neurodegeneration (Vonsattel and DiFiglia, 1998). For detection of the transgene, mRuby or, in some experiments, mYFP was fused to the N-terminus of the *Slc1a2* sequence. Expression of the transgene was limited by the chosen experimental conditions, including (i) the amount of injected particles (a single injection of $1.0^{*}10^{9}$ gc/striatum), (ii) the expression time (3–5 weeks, if not mentioned otherwise), (iii) the type of the viral serotype (PHP.eB) and (iv) the promoter sequence (gfaABC1D). To examine the abundance and specificity of transduction we have analyzed immunostained parasagittal sections of fixed brains after intrastriatal injection of mRuby CTRL or YFP CTRL vectors (**Figure 1A**). The outcome was similar (2 WT:CTRL and 2 HET:CTRL). In both cases cell counts were performed at a mediolateral distance of 2–2.5 mm within the boxed area of the dorsal striatum, each contributing 10 view fields of 100 μm × 100 μm. **Figure 1B** illustrates that the area of evaluation was well within the extensively labeled zone. The latter covered about 40% of the striatal volume (**Figure 1C**). There also was some labeling in the overlaying cortex and a small degree of unintended transgene expression in neurons and microglial cells. To examine the specificity of viral targeting to striatal astrocytes, the entire cell population in the dorsal striatum (boxed area in **Figure 1B**) was visualized with DAPI and tested for co-localization of mRuby with three cell-specific markers (**Figures 1D–F**). It was found that 90.8% of the transduced cells were S100β+ cells (astrocytes), 8.3% – NeuN+ cells (neurons) and 1.6% – Iba1+ cells (microglial cells) (**Figure 1G**). Considering the proposed astrocyte/neuron ratio of about 6:1 in the murine striatum (Chai et al., 2017), one can classify this transduction pattern as astrocyte-specific. We also determined the effective transduction rate of astrocytes. It amounted to 65.9 ± 2.47% (**Figure 1H**). In contrast, neurons and microglial cells were only transduced in 2.76 ± 0.44% and 1.64 ± 0.85% of the respective cell population. Together, these cell counts indicate that the viral transduction was local (dorsal striatum), specific (astrocytes) and effective (two thirds of the entire astrocyte population in the labeled area).

Preparation of Acute Brain Slices

The animals were anesthetized with isoflurane, transcardially perfused with cooled aerated saline containing (in mM): NMDG – 92, KCl – 2.5, NaH_2PO_4 – 1.25, $NaHCO_3$ – 25, glucose – 20, $CaCl_2$ – 0.5, $MgCl_2$ – 10, sodium pyruvate – 3, and sodium ascorbate – 5 (pH 7.35, 303 mosmol/l). After decapitation and removal of the brains, parasagittal (10 deg off) sections (300 μm) containing the striatum were prepared as previously described (Dvorzhak et al., 2016). The slices were kept in artificial cerebrospinal fluid (ACSF) containing (in mM): NaCl – 125, KCl – 3, NaH_2PO_4 – 1.25, $NaHCO_3$ – 25, $CaCl_2$ – 2, $MgCl_2$ – 1, glucose – 10 (pH 7.3, 303 mosmol/l), supplemented with (in mM) sodium pyruvate – 0.5, sodium ascorbate – 2.8 and glutathione – 0.005. These perfusion and recovery solutions preserved the astrocytes better than physiological ACSF, sucrose- or choline-containing solutions, the criterion being the astrocyte resting membrane potential at break-in WT (≤ -75 mV).

Preparation of Striatal Lysates

The animals were anesthetized with isoflurane, transcardially perfused with cooled aerated saline containing (in mM): *N*-methyl-D-glucamine chloride (NMDG) – 92, KCl – 2.5, NaH_2PO_4 – 1.25, $NaHCO_3$ – 25, glucose – 20, $CaCl_2$ – 0.5, $MgCl_2$ – 10, Na pyruvate – 3, and Na ascorbate – 5 (pH 7.35, 303 mosmol/l). If not mentioned otherwise, all chemicals and drugs mentioned here and in the following were obtained from Sigma-Aldrich (Taufkirchen). Brains were quickly removed, placed into a custom-made slicing mold and immersed into ice-cold oxygenated NMDG preparation solution. 2 mm thick sagittal slices where cut at a distance of 1–3 mm from midline. The striata were dissected and snap-frozen in liquid nitrogen. The tissue was pulverized under cryogenic conditions using a cryo-grinder set (CG 08-02, OPS Diagnostics, Lebanon, NJ, United States). The samples were solubilized in 200 μl lysis buffer containing (in mM) NaCl 150, Tris pH 7.5 50, *n*-ethylmaleimide 20, dithiothreitol (DTT) 1 supplemented with glycerol 5%, igepal ca-630 1% and Roche cOmplete protease inhibitor cocktail -1x (all from Sigma-Aldrich), kept on ice for 30 min and homogenized at 5,000 rpm using a Polytron PT1300D homogenizer. Cell debris was removed by centrifugation at 14.000 × *g* for 10 min at 4°C.

The cleared lysates were either directly submitted to WB analysis or used for the immunoprecipitation of YFP-tagged EAAT2 variants with magnetic beads for subsequent WB analysis or mass spectrometry.

Western Blot Analysis of Striatal Lysates

Samples were prepared according to the NuPAGE Technical Guide of Invitrogen. Briefly, after denaturation in NuPAGE LDS sample buffer with DTT 50 mM for 10 min at 70°C the samples and markers were run on a Novex bis-tris gradient gel (4–12%, Thermo Fischer Scientific) using NuPAGE MOPS SDS running buffer and subsequently blotted on a Novex 0.45 μm nitrocellulose membrane (LC2001, Thermo Fischer Scientific). The membranes were washed and blocked in ReadyTector solution A (CANDOR Bioscience GmbH, Wangen im Allgäu), and the primary antibodies rabbit anti-EAAT2 1:2000 (Abcam, Cambridge, United Kingdom) and mouse anti-GAPDH 1:1000 (Sigma-Aldrich) were directly applied for 1 h at room temperature in solution B that also contained horseradish peroxidase (HRP) coupled to the secondary antibodies against rabbit or mouse, respectively. To detect mYFP, membranes were blocked for 30 min in 1× Roti-block solution (Carl Roth GmbH, Karlsruhe) before applying rabbit anti-GFP 1:1000 (ChromoTek GmbH, Martinsried) over night at 4°C in the same solution. Then the HRP-coupled secondary antibodies (Dianova GmbH, Hamburg) were applied at 1:2500 for 3 h at 4°C. Proteins were detected using respective kits from Biozym Scientific GmbH (Hessisch Oldendorf). Proteins were detected by chemiluminescence and submitted to image analysis with ImageJ.

Immunoprecipitation of YFP-Tagged Excitatory Amino Acid Transporter 2 for Western Blotting or Mass Spectrometry

Striatal lysates were diluted with 300 μl wash buffer (in mM) NaCl 150, Tris pH 7.5 50, DTT 1, glycerol 5% and incubated for 2 h with 30 μl of pre-washed GFP-Trap magnetic agarose beads (gtma-20, ChromoTek, Planegg-Martinsried) using gentle rotation at 4°C. The beads-protein complexes were isolated using a DynaMag-2 magnet (Thermo Fisher Scientific), applying 3 wash-resuspension cycles before short-term storage of the immunoprecipitate at −18°C. The first wash solution contained igepal ca-630 0.05%. For WB analysis the beads were for 10 min incubated in the NuPAGE LDS sample buffer and treated as described in the previous chapter. For liquid chromatography tandem mass spectrometry (LC-MS), the beads were first incubated in digestion buffer (sodium deoxycholate – 1%, dithiothreitol – 10 mM, ammonium bicarbonate – 50 mM, 45 min, r. t.). The proteins were then submitted to alkylation with 55 mM chloroacetamide (30 min, r. t. complete darkness) and over-night digestion with 500 ng endopeptidase LysC (Wako, Neuss) and 500 ng sequence grade trypsin (Promega, Mannheim, GER) at 37°C. The samples were then acidified with formic acid (final concentration 1%).

Excitatory Amino Acid Transporter 2 Interaction Proteomics

The peptides were extracted and desalted using the StageTips protocol. Separation was carried out using in-house-manufactured 20 cm fritless silica microcolumns with an inner diameter of 75 μm, packed with ReproSil-Pur C18-AQ 1.9 μm resin (Dr. Maisch GmbH, Ammerbuch), a 98 min gradient with a 250 nl/min flow rate of increasing Buffer B concentration (from 2 to 60%, Buffer B: 90% acetonitrile) on an High Performance Liquid Chromatography (HPLC) system from Thermo Fischer Scientific. The eluting peptides were directly ionized by electrospray ionization and transferred into a Thermo Orbitrap Fusion mass spectrometer. The instrument was operated in the data-dependent mode with performing full scans in Orbitrap (60K resolution; 4×10^5 ion count target; maximum injection time 50 ms), followed by top 20 MS2 scans using higher-energy collision dissociation (NCE of 32; 15K resolution, 5×10^4 ion count target; 0.7 m/z isolation window; maximum injection time: 250 ms). Only precursor with charge states between 2 and 7 were fragmented. Dynamic exclusion was set to 30 s. Raw data were analyzed using the MaxQuant software (v1.6.0.1). The internal Andromeda search engine was used to search MS2 spectra against a decoy UniProt database for mouse (MOUSE.2018-05), as well as the sequences of the mYFP fusion constructs, containing forward and reverse sequences. The search included variable modifications of oxidation (M) and N-terminal acetylation, deamidation (N and Q) and fixed modification of carbamidomethyl cysteine. Minimal peptide length was set to 7 amino acids and a maximum of two missed cleavages was allowed. The false discovery rate (FDR) was set to 0.05 for peptide and protein identifications. The integrated label-free quantification (LFQ) and the intensity-based absolute quantification (IBAQ) calculation algorithm were activated. Unique and razor peptides were considered for quantification. Retention times were recalibrated based on the built-in non-linear time-rescaling algorithm and MS/MS identifications were transferred between LC-MS/MS runs with the "Match between runs" option, in which the maximal retention time window was set to 0.7 min. The resulting text files were used for further analyses using the Perseus software package (omicX, v. 1.6.2.1). LFQ intensity values were used for quantification. Reverse hits, contaminants and proteins only identified by site were filtered out. Technical and biological replicates for each condition were defined as groups and intensity values were filtered for "minimum value of 3" per group. After log2 transformation missing values were imputed with random noise simulating the detection limit of the mass spectrometer. Imputed values are taken from a log normal distribution with 0.25× the standard deviation of the measured, logarithmized values, down-shifted by 1.8 standard deviations. The data was obtained from 4 test groups, each comprising at least 4 animals per group. The signals obtained from any given animal (pooling the tissue from both striata) were normalized to the mYFP signal median intensity calculated from all samples. Only proteins with >3 peptide detection and abundance of log2 intensities ≥ 23 in all 4 samples were included in the list of significant binders. Differential protein abundance was calculated using two-sample Student's *t*-tests. Abundance differences between the samples with a *p*-value of ≤ 0.05 in a two-tailed *t*-test were considered significant. Please note that the present assay only included 3.790 from a total of 13.000 proteins so far identified in the mouse brain (Sharma et al., 2015).

The original mass spectrometry proteomics data has been deposited to the ProteomeXchange Consortium via the PRIDE partner repository with the dataset identifier PXD029194.

Quantitative Immunofluorescence at Glutamatergic Synapses

Using deep isoflurane anesthesia, mice were transcardially perfused with 60 ml ice-cold phosphate-buffered saline (PBS) containing 4% (w/v) paraformaldehyde in PBS. Sagittal sections (30 μm) were prepared as previously described (Rothe et al., 2015). For the quantification of the transduction rate and transduction specificity freely floating sections were triple-stained with goat anti-td-Tomato (also detects RFP variants like mRuby) 1:6000 (Sicgen-Acris, Carcavelos), mouse anti S100β 1:2000 (Novus, Abingdon) and rabbit anti-Iba1 1:1000 (Wako Chemicals GmbH, Neuss) or double-stained with goat anti-td-Tomato and mouse anti-NeuN 1:500 (Merck Millipore, Darmstadt). Counter-staining for nuclei with 4′,6-diamidin-2-phenylindol (DAPI) 1:10000 was performed in both experiments. For the quantification of synaptic EAAT2 fluorescence, the sections were triple-stained with goat anti-tdTomato- 1:6000 (Sicgen-Acris), guinea pig anti-vGluT1 1:1600 (Synaptic Systems, Göttingen) and rabbit anti-EAAT2 1:2000 (Abcam), followed by respective secondary antibodies, as listed in **Supplementary Table 1**. All sections from the different test groups were stained together for reliable comparison of EAAT2 IF levels.

RGB 24 bit images (1,024 pixels × 1,024 pixels, no binning) were acquired from the dorsal striatum using a Leica TCS SP8 or DMI 6000 confocal microscope with an HCX PL Apo 63× oil objective (NA1.4) and stored in the tiff file format. Areas of interest (AOIs, 400 pixels × 400 pixels) were cropped from the larger view fields, selecting neuropil areas with a minimum of cell somata or vessels. Quantification of EAAT2 IF was performed using Image-Pro Plus (Media Cybernetics, Inc., Roper, Sarasota). For comparison purposes, the same staining conditions and acquisition settings were applied to achieve reliable EAAT2 quantification in 4–5 groups with at least 4 animals per group. Within the selected AOIs, smaller rectangular ROIs (40 pixels × 40 pixels, pixel size 90.19 nm) were centered to individual vGluT1+ spots to determine the level of synaptic EAAT2 IF. A threshold algorithm was used to define the boundaries of the EAAT2+ area excluding pixels with $F <$ ROI mean + 0.5 SD. The data is expressed as integral intensity of suprathreshold pixels. The term "Synaptic integral EAAT2 IF" refers to the mean value from 30 individually assessed ROIs within the boundaries of one transduced (i.e., mRuby+) astrocyte.

Sodium Imaging of Astrocytes in Striatal Slices

Our methods for sodium imaging in striatal astrocytes largely followed the techniques already described (Dvorzhak et al., 2016). Briefly, the slices were incubated for 20–30 min in oxygenated ACSF containing 222 μM of the membrane-permeable form of SBFI (#S-1264, Thermo Fisher Scientific), and 2.5% dimethyl sulfoxide (DMSO) and 0.5% Pluronic F-127 at 36°C. For recording of the L-aspartate-induced sodium transients, the gap junction blocker CBX (100 μM, Abcam) was added to the superfusion solution, along with blockers of ionotropic glutamate receptor blockers (DNQX 10 μM and MK801 1 μM, Tocris, Bristol, United Kingdom). Wide-field fluorescence imaging of SBFI-AM-stained slices was performed using a digital live acquisition imaging system (Andor Solis version 4.30.30034.0, Acal GmbH, Gröbenzell) and a sCMOS camera (Andor Zyla 4.2 plus) attached to an upright Zeiss microscope (Axio Examiner A1, Göttingen). Images were collected with a Zeiss 63× NA 1.0 water immersion plan apochromat objective. Cells were selected based on the resting levels of SBFI and mRuby fluorescence excited by a UVICO ultraviolet or visible light source (Rapp OptoElectronic, Hamburg), combined with suitable filter sets from Omega Optical (Brattleboro, VT, United States) attached to a FW 1,000 filter wheel (Applied Scientific Instrumentation, Eugene, OR, United States). Single wavelength sodium imaging was performed by excitation of SBFI at 380 nm (sodium-sensitive wavelength). SBFI emission was collected at >510 nm (dichroic mirror XF2002, emission filter XF3086, Omega Optical). Regions of interest (ROIs) with a size of 3.2 μm × 3.2 μm were defined on the cell body. Binning was 8 × 8. The spatial resolution was then 0.8 μm/pixel. The exposure times was set to 150 ms in all experiments. Images were acquired every 3 s. Custom-written software was used to control image acquisition and the valves operating the superfusion system. After 1 min of baseline recordings (20 images), L-aspartate (1 mM) was applied for 1 min followed by a 3 min washout period. Subsequently, the same routine was repeated in the presence of the glutamate transport blocker TFB-TBOA 2 μM (Tocris). For both traces the fluorescence change was calculated from the average of the baseline fluorescence intensities for each ROI as $\Delta F/F = (F_{SBFI} - F_{SBFI(baseline)}/F_{SBFI(baseline)}]$. The difference between the two traces represents the L-aspartate-induced sodium transient that is mediated by all available glutamate transporters. The response to L-aspartate was verified by student's t-test comparison between response peak and baseline.

Glutamate Imaging at Single Corticostriatal Synapses

The methods established to image glutamate release from single corticostriatal presynaptic terminals and to identify synapses exhibiting an HD phenotype have already been described in some detail (Dvorzhak et al., 2019). Briefly, a vector for CaMKII-driven expression of the ultrafast glutamate sensor iGlu$_u$ was injected in the motor cortex (unilateral triple injections). Six weeks were allowed before sacrificing the animals. With this expression time the membrane-bound iGlu$_u$ sensor of corticostriatal terminals can even be detected at rest which helps the positioning of a stimulating micropipette for single bouton activation in the presence of action potential block. Acute slices were submerged into a perfusion chamber with a constant flow of oxygenated ACSF at a rate of 1–2 ml/min. The temperature during the recordings was maintained at 26–27°C. Single varicosities expressing the ultrafast glutamate sensor iGlu$_u$ (Helassa et al., 2018) were visualized using a Zeiss wide field microscope (Axioscope 2, FS Plus) with a 63×/NA 1.0 water immersion objective and brief (180 ms) discontinuous exposure to a 473 nm laser beam focused to a circular area of ∼4.5 μm in diameter. For evaluation of evoked responses, the iGlu$_u$ fluorescence was acquired at a frequency of 2.5 kHz from a rectangular ROI of 4 μm × 4 μm (20 pixels × 20 pixels, binning 2) using a sCMOS camera (Andor Zyla4.2 plus). Laser, camera and electrical stimulation of the axon/bouton were controlled by in-house written software routines. Each pixel of the ROI was evaluated separately. The iGlu$_u$ pixel signal was expressed as change of fluorescence intensity ΔF in % of baseline fluorescence of the given pixel. The baseline is the mean of the intensity values obtained during the 50 ms period prior to stimulation. For the construction of time- and space-dependent [Glu] profiles after evoked release, suprathreshold pixels were determined, the threshold being defined as 3 SD of the $\Delta F/F$ baseline. The stimulus-induced changes of suprathreshold $\Delta F/F$ in time or space will be referred to as "iGlu$_u$ transients" or simply "transients." The term "Peak amplitude" refers to the peak $\Delta F/F$ value of an averaged intensity transient derived from all suprathreshold pixels. "Tau decay" or "TauD" is the time constant of decay derived by fitting a monoexponential function to the decay from the peak of the averaged transients. The spatial extension of the iGlu$_u$ signal is described on the basis of a virtual diameter derived from the area of all suprathreshold pixels combined to form a virtual circle. The area of suprathreshold pixels and the resulting virtual diameter were used as indicators of "Bouton size" (at rest, before stimulation) or "Spread" (after stimulation and glutamate release). The term "Peak spread" refers to the peak value of the averaged spread transient. Dysfunctional synapses could best be detected by analysis of single-pixel iGlu$_u$, using the pixel with the highest iGlu$_u$ elevation at any given terminal. The highest iGlu$_u$ elevations were always found within or next to the bouton at rest. The peak amplitude of the single pixel transient with the highest iGlu$_u$ elevation are referred to as "Maximal amplitude." The respective TauD values are referred to as "TauDmax."

Identification of Dysfunctional Synapses

To induce the glutamate release from individual synaptic boutons under physiological conditions, a depolarizing current pulse was applied through an ACSF-filled glass pipette (tip diameter <1 μM, resistance 10 MΩ) placed next to an axon in close proximity with a fluorescent varicosity. Responses were elicited at minimal intensity at a repetition frequency of 0.1 Hz. To challenge the glutamate uptake mechanisms at the site of release, individual synapses were stimulated under condition of blocked action potential generation (in the presence of tetrodotoxin, TTX, 1 μM and in elevated (5 mM) $[Ca^{2+}]_{ec}$. This standardized activation mode bypassed eventually existing disease-related differences in the myelination and excitability of corticostriatal axons. The identification of an HD phenotype in corticostriatal synapses is based on the TauD value of the glutamate transient (Dvorzhak et al., 2019).

Behavioral Tests in Wild-Type and Q175 Heterozygote

On the day of sacrifice, the animals were submitted to a classical open field test (53 cm × 33 cm), as described in a previous study with Q175 homozygotes (Rothe et al., 2015). The mice were individually tested between 9 a.m. and 2 p.m. using an open-field box made of gray plastic with 53 cm × 33 cm surface and 19 cm walls, illuminated by a spot of 25 W placed 1 m above the shadow-free box. Monitoring of 5-min sessions was done by a video camera (Logitech C525 Webcam, 15 frames/s). A customary software was designed to quantify not only running activity but also the motor activity at rest. This required the calculation of the centroid of all pixels derived from the black mouse body. To this end, the background frame without mouse was subtracted from frames with mouse using an intensity threshold of mean + 3SD. A virtual mouse radius (v.m.r.) was derived from the area of suprathreshold mouse pixels approximated as a circle. The identification of the resting state is based on the time needed to cross 2 v.m.r. For more details and definitions see **Supplementary Table 2**.

For the "step-over test" the animal was placed into the center of a Petri dish (diameter 18.5 cm and wall height 2.8 cm). The movements were recorded with a video camera. Using offline analysis, a software routine determined the time between the take-off of the experimenter's hand (in a black glove) and the moment when the animal has reached the outside of the dish with all 4 feet. This parameter was called "step-over latency" and correlated with the open field total path in 5 min.

Data Evaluation and Statistical Analysis

The comparison of the means could be influenced by inter-animal variance. Therefore, in the case that individual sections, cells or synapses were obtained from different animals, multi-level ("nested data") analysis was performed with Prism 8 (GraphPad, San Diego, CA, United States). *P*-values of <0.05 were considered statistically significant. Differences between the groups were tested with ANOVA or respective non-parametric methods (Kruskal–Wallis-test), followed by multiple comparison (Dunnet's or Dunn's tests). Significance levels were marked by asterisks, where * corresponds to $P < 0.05$, ** – $P < 0.01$ and *** – $P < 0.001$. The HET-CTRL data served as reference for comparison with WT-CTRL or HET-TEST. Effect strength was described according to Cohen's *D* or Hedges' *G*. *D*- or *G*-values larger 0.8 suggest that the respective effect was strong.

RESULTS

Mutant Huntingtin-Induced Changes in the Striatal Excitatory Amino Acid Transporter 2 Interactome and Effects of C-Terminal Truncation

Failing glutamate uptake in mHTT-expressing mice could be derived from deficient EAAT2 expression and alterations in EAAT2 regulation. The latter should be reflected in the composition of the EAAT2 interactor spectrum. Previous studies have identified some of the EAAT2 binding proteins, see for instance (Bassan et al., 2008; Piniella et al., 2018). However, a complete overview of the EAAT2 interactors from native (whole animal) striatal tissue as well as information on their sensitivity to mHTT were still missing. To fill this important gap of knowledge we performed a mass spectroscopy analysis of immunoprecipitated transgenic EAAT2 and its C-terminal-truncated version EAAT2-S506X. This variant lacked the last 68 amino acids, i.e., it was devoid of almost the entire C-terminal domain. An YFP vector without the EAAT2 sequence served as CONTROL.

Wild-Type and HET mice received bilateral striatal injections with one of 3 YFP-tagged expression vectors (**Figure 2A**) and were sacrificed 3 weeks later. **Figure 2B** lists the resulting animal groups. Nanobody-coated magnetic beads were used to isolate the YFP-tagged EAAT2 protein and its interactors (**Figure 2C**). The quality of the immunoprecipitate was verified by YFP- and EAAT2-immunostained Western blots (WBs, see **Figure 2D** for identification and properties of the WB bands). Note the shift of the truncated YFP-EAAT2-S506X (boxed in red) in the respective WB bands (**Figures 2E,F**). The total amount of YFP pulled down by the beads was very similar in the 3 tested groups (**Figure 2G**), as should be the case if the amounts of "bait" were equal in the 3 groups, and the amount of "prey" (YFP-EAAT2) sufficed to saturate the binding sites.

The immunoprecipitate was further submitted to liquid chromatography tandem mass spectrometry (LC-MS). Statistical analysis revealed a total of 148 significant EAAT2 interactors in WT or HET. Our **Supplementary Table 3**: "Significant EAAT2-binders-in-WT-and-Q175HET.xlsx" lists these interactors along with some additional information on the binding characteristics. About 40% (58/148) were sensitive to mHTT, i.e., they exhibited a significant LFQ intensity difference between the EAAT2-expressing HET and WT (**Table 1**). But only few of them (*Tfam*, *Rbm39*, *Dmd, PDE10a,* and *Uba2*) were so far mentioned in connection with corticobasal pathologies. A differential effect of EAAT2 truncation ("X-effect") was found in a total

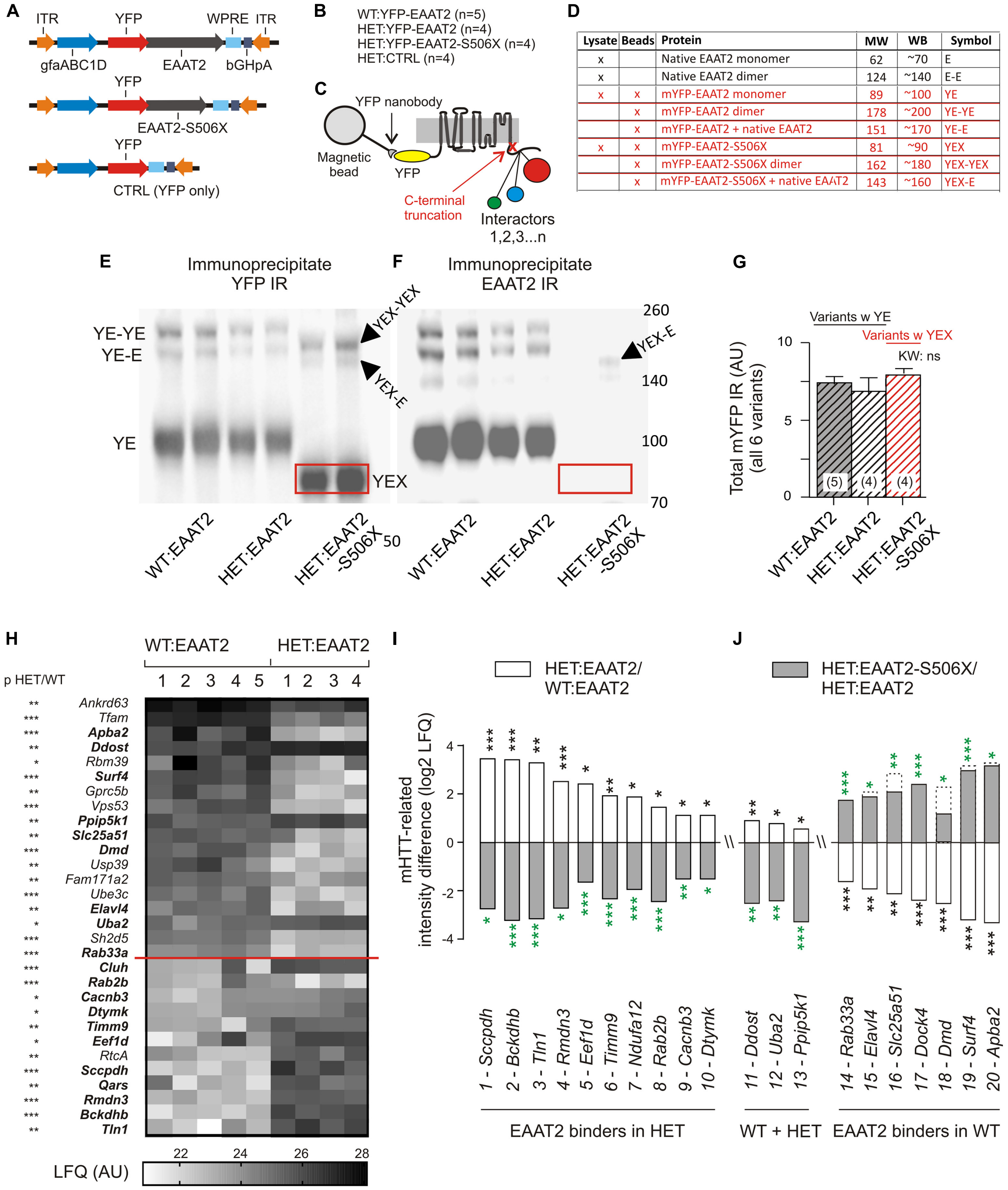

Lysate	Beads	Protein	MW	WB	Symbol
x		Native EAAT2 monomer	62	~70	E
x		Native EAAT2 dimer	124	~140	E-E
x	x	mYFP-EAAT2 monomer	89	~100	YE
	x	mYFP-EAAT2 dimer	178	~200	YE-YE
	x	mYFP-EAAT2 + native EAAT2	151	~170	YE-E
x	x	mYFP-EAAT2-S506X	81	~90	YEX
	x	mYFP-EAAT2-S506X dimer	162	~180	YEX-YEX
	x	mYFP-EAAT2-S506X + native EAAT2	143	~160	YEX-E

FIGURE 2 | mHTT- and S506X-related changes in the abundance of YFP-EAAT2 binders. **(A)** Injected vectors. **(B)** Animal groups. **(C)** Scheme of immunoprecipitation experiment. **(D)** List of EAAT2 bands to be detected in the Western blots (WB) from the beads preparation (this figure) or lysates (**Figure 3**). **(E,F)** Western blot samples prepared from the beads YFP-immunoprecipitate. Note dimer bands and shift of the EAAT2-S506X band (YEX, boxed). **(G)** Similar amounts of mYFP immunoreactivity (YE or YEX bands) pulled down in the three animal test groups. **(H)** Heat-map plot illustrating the mHTT-related differences between WT:EAAT2 and HET:EAAT2. The signal from each animal was normalized to the mYFP median intensity value in a histogram constructed from all samples. The inter-group intensities were compared by a two-tailed *t*-test. The asterisks next to the listed genes denote the significance level of the difference. The proteins are listed with their gene names and sorted according to their abundance in WT:EAAT2. **(I,J)** Plot illustrating the recovery potential of significant EAAT2 binders. The LFQ intensity difference denotes the log2 difference between the compared groups. Compared were WT:EAAT2 vs. HET:EAAT2 (empty bars with black asterisks) and HET:EAAT2-S506X vs. HET:EAAT2 (filled bars with green asterisks). The dashed bars indicate the corresponding WT levels. An up-regulation is shown as upward bar, a down-regulation as downward bar. *$p < 0.05$, **$p < 0.01$, ***$p < 0.001$.

TABLE 1 | Summary binders with mHTT-related difference and effect of EAAT2 C-terminal truncation.

EAAT2 binders*				With mHTT effect**		With mHHT and X effect**	
Total	**WT + HET**	**WT only**	**HET only**	**In HET down**	**In HET up**	**X effect up**	**X effect down**
148	42	40	66	28	30	8 (31%)	18 (69%)

*FDR5, **t-test $p < 0.05$.*

of 26 binders. Eighteen of them (69%) showed a protein down-regulation when HET mice expressed EAAT2-S506 instead of EAAT2.

Figure 2H displays the individual LFQ intensity values of 30 EAAT2 binders with significant mHTT-related down- or up-regulation. They were sorted according to their mean LFQ intensity values in WT. The proteins of **Figures 2I,J** were selected to illustrate the X-effect in EAAT2 binders with FDR5 and listed according to their log2 LFQ intensity difference between the groups of HET:EAAT2 and WT:EAAT2 (empty bars/black asterisks). The log2 LFQ intensity difference for HET:EAAT2-S506X and HET:EAAT2 is shown as gray bars/green asterisks. Among the proteins up-regulated by mHTT (**Figure 2I**) were saccharopine dehydrogenase-like oxidoreductase (gene name *Sccpdh*), 2-oxoisovalerate dehydrogenase subunit beta (*Bckdhb*) and talin1 (*Tln1*) and NEDD8-activating enzyme E1 catalytic subunit (*Uba2*), also known as SUMO-activating enzyme subunit 2. A down-regulating X-effect is typically observed in HET with mHHT-related upregulation, whereas up-regulating X-effects were seen in WT with mHTT-related reduction of the protein abundance. Among the proteins most downregulated by mHTT were amyloid beta A4 precursor protein-binding family A member 2 (*Apba2*), surfeit locus protein 4 (*Surf4*) and dystrophin (*Dmd*). All 3 exhibited a recovery under the influence of EAAT2-S506x. Other proteins with mHTT-related down-regulation (e.g., phosphodiesterase 10A, *Pde10a*) remained unchanged after expression of EAAT2-S506X.

These proteomics results are consistent with the hypothesis that: (i) the EAAT2 interactome is influenced by the presence of mHTT, (ii) some of the mHTT-related changes are reversible and (iii) expression of C-terminal-truncated EAAT2 can block abnormal binders in favor of a more physiological protein interaction pattern. Together, these results both justify and motivate a more detailed investigation of the capacity of C-terminal-modified EAAT2 transgene expression to restore mHTT-impaired function.

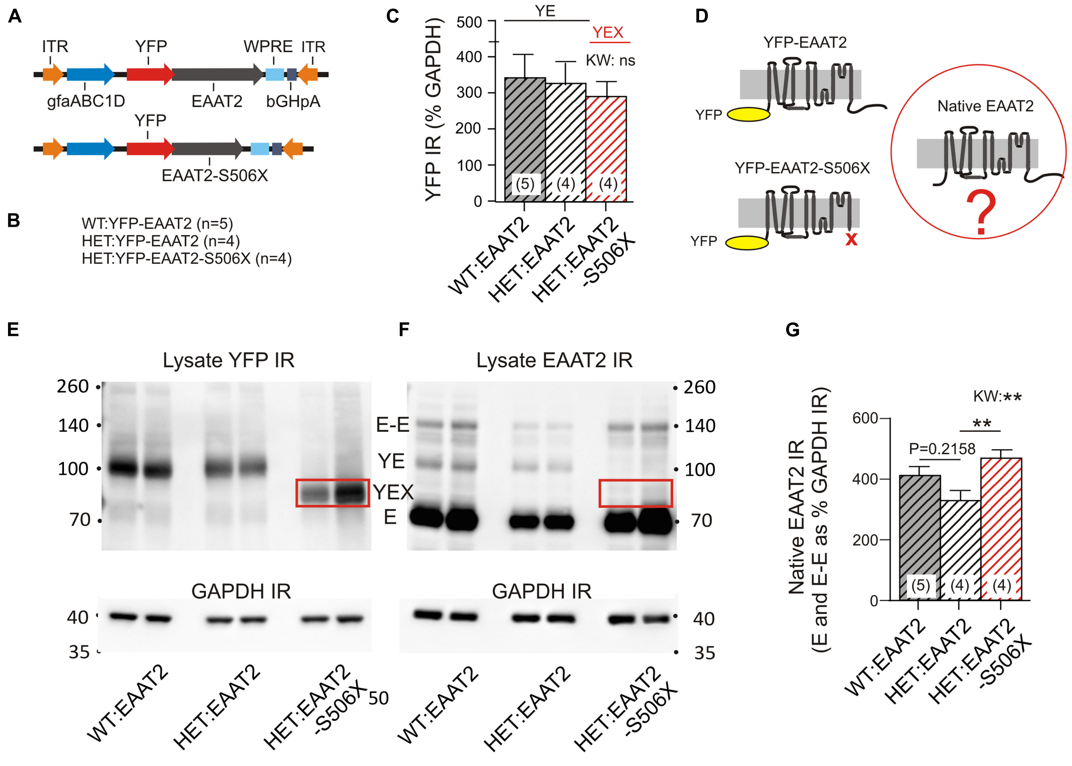

FIGURE 3 | Effects of mHTT and S506X on the native murine EAAT2. **(A)** Injected vectors. **(B)** Animal groups. **(C)** Same amounts of YFP IR in the 3 samples. **(D)** Three principal variants of EAAT2 to be detected by in the lysates. **(E,F)** WB samples for quantification of YFP and EAAT2 IR in striatal lysates. At least four animals per group (shown are two). The boxed band YEX is not detected in **(F)** since the preferred antibody against EAAT2 binds to a region located on the deleted C-terminal. For the abbreviations see **Figure 2D**. **(G)** Mean intensity of native EAAT2 IR (mono- and dimers). Note increase of native EAAT2 level in HET:EAAT2-S506Xs. Non-parametric Kruskal–Wallis test (KW) and Dunn's *post hoc* comparison. **$p < 0.01$.

Mutant Huntingtin-Induced Changes in Native Excitatory Amino Acid Transporter 2 Levels and Effects of Excitatory Amino Acid Transporter 2-S506X

Mass spectroscopy allowed a first glimpse at the normal and pathological binding partners of the EAAT2 transgene but it does not show what actually happened to the native murine EAAT2 protein. To provide the missing information, we analyzed the WBs of striatal lysates. WT and HET were injected with one of two EAAT2 vectors (**Figure 3A**) which resulted in the animal groups listed in **Figure 3B**. Quantification of the YFP immunoreactivity (IR) indicates that the YFP-tagged transgenes were equally expressed in the three animal groups (**Figure 3C**). However, the native

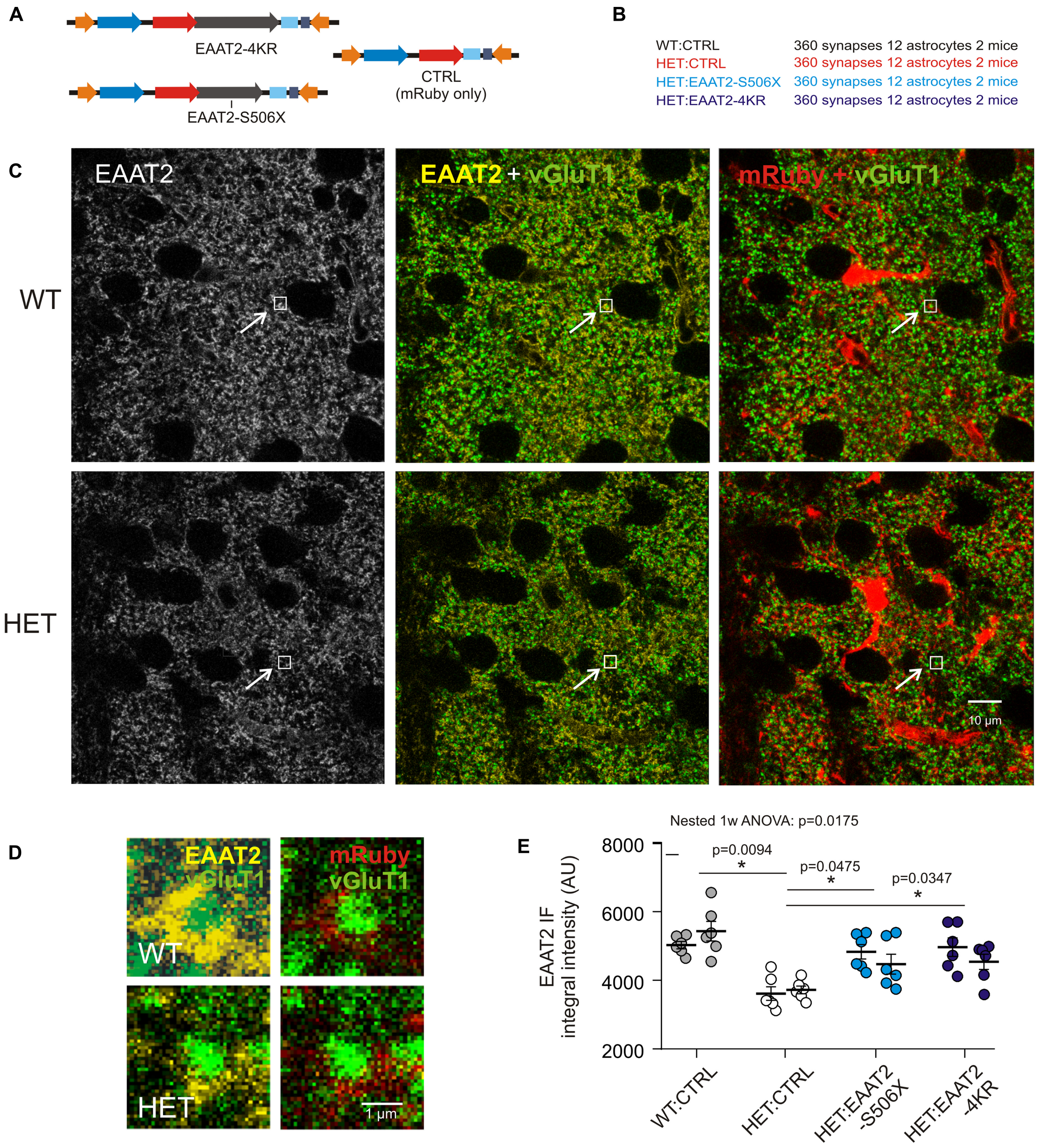

FIGURE 4 | Evaluation of synaptic EAAT2 immunofluorescence in fixed sections. **(A)** Injected vectors. **(B)** Animal groups. **(C)** Confocal images from WT:CTRL and HET:CTRL to illustrate the mHTT-related decrease in the overall EAAT2 IF. In the illustrated samples the mean intensity values were 3078 ± 38.4 (WT:CTRL) and 2673 ± 31.7 (HET:CTRL). **(D)** Regions of interest (ROIs) comprising just one synapse. The ROIs correspond to the small boxed areas in **(C)**. The EAAT2-immunopositive area corresponds to an astrocyte perisynaptic process (PAP), as it is labeled with mRuby. **(E)** Quantification of integral EAAT2 IF from ROIs comprising only one vGluT1-immunopositive terminal. Numbers in brackets: evaluated synapses per group. Each data point is the mean value from 30 synapses on 1 mRuby-labeled astrocyte. Separate plot of data from the 2 animals per group. *$p < 0.05$ or 0.01.

murine EAAT2 devoid of YFP might be sensitive to transgene expression (**Figure 3D**).

The YFP-containing EAAT2 transgene has a higher molecular weight than the native EAAT2 (see **Figure 2D** for identification and properties of the WB bands). It should also be noted that the selected EAAT2 antibody recognizes only full-length EAAT2. Therefore the YFP-EAAT2-S506X band is missing in the EAAT2 WB (compare boxed in **Figures 3E,F**). Quantification of native EAAT2 IR revealed a significant increase in HET:EAAT2-S506X as compared to HET:EAAT2 (**Figure 3G**). As WT and HET differed in the occurrence of EAAT2 dimers, it was conceivable that the EAAT2-S506X-induced increase of native EAAT2 IR resulted from enhanced multimer formation. However, under the given experimental conditions, i.e., Western blotting, only a small percentage of EAAT2 (less than 15%) retained or re-established a dimeric form. The dimer-promoting effect of EAAT2-S506X, if at all present, remained below significance level.

These experiments lead to the interesting conclusion that the presence of an EAAT2 transgene may not be indifferent to native EAAT2. EAAT2-S506X expression in striatal astrocytes resulted in a higher abundance of native EAAT2.

Mutant Huntingtin-Related Excitatory Amino Acid Transporter 2 Deficit at Immunostained Corticostriatal Synapses and Recovery in Heterozygote Treated With Excitatory Amino Acid Transporter 2-S506X or Excitatory Amino Acid Transporter 2-4KR

Examination of immunostained fixed brain sections could verify the above impression and answer the question of whether C-terminal-modified EAAT2 transgene can affect EAAT2 IR at sites where it really matters – the corticostriatal synapses. It

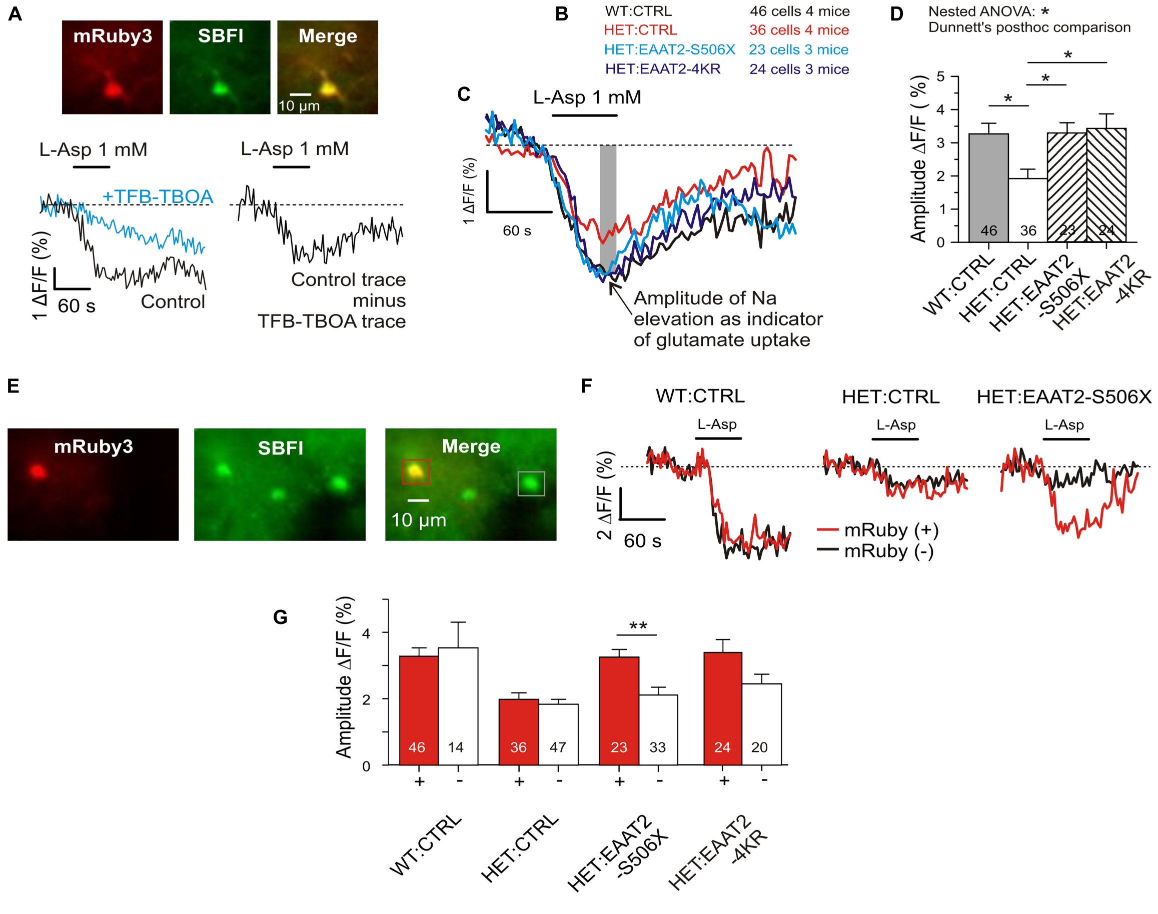

FIGURE 5 | Recovery of glutamate uptake in striatal astrocytes. **(A)** Measurement of glutamate uptake by sodium imaging with SBFI, in the presence of CBX (100 µM), DNQX (10 µM), and MK801 (1 µM). Traces recorded in the absence and presence of TFB-TBOA (2 µM). The amplitude of this differential response was expressed as Δ*F*/*F* during the last 15 s of L-Asp application. *F* is the mean fluorescence at rest, before drug application. **(B)** Tested animal groups. **(C)** Averaged traces of SBFI fluorescence. Results from mRuby-positive astrocytes only. **(D)** Quantification of the L-aspartate-induced sodium elevation. Two-level ("nested") statistics (animal level, cell level, and *post hoc* comparison between groups). **(E)** The applied SBFI loading protocol was selective for astrocytes. View field with 3 astrocytes, where one is transduced and two are not. **(F)** Traces from mRuby+ as opposed to mRuby– in three test groups. Averaged traces from one animal per group. **(G)** Comparison of results obtained in the different groups from mRuby+ vs. mRuby– astrocytes. *$p < 0.05$, **$p < 0.01$.

should again be mentioned that the selected antibody only reacts against EAAT2 with intact C-terminal. **Figures 4A,B** lists the injected vectors and animal groups. Here (**Figure 4**) and in some of the following experimental series (**Figure 5**) HET mice were available in larger numbers. This provided us with an opportunity for the testing of more selective C-terminal modifications. In the case of HET:EAAT2-4KR, four C-terminal lysines (K) at position 518, 527, 551, and 571were replaced by arginine (R). It had been suggested that ubiquitylation of these C-terminal lysine residues mediates the interaction of the transporter with the endocytic machinery in a PKC-dependent manner (Gonzalez-Gonzalez et al., 2008) which may influence the availability of EAAT2 protein at synaptic sites.

The images obtained from the dorsal striatum of WT and HET (**Figure 4C**) illustrate, first of all, a noticeable shift toward lower EAAT2 immunofluorescence (IF) levels in HET, thereby confirming previous studies from non-injected HD mice (Estrada-Sanchez et al., 2009; Tong et al., 2014). **Figure 4D** shows the respective single synapse immunofluorescence (IF) in ROIs containing only one vGluT1-positive spot, i.e., one corticostriatal presynaptic terminal. The EAAT2-positive pixels co-localized with mRuby, i.e., they belonged to a perisynaptic astrocyte process (PAP). The graph of **Figure 4E** and **Table 2** show the results of statistical evaluation of the EAAT2-immunofluorescent clusters within the analyzed ROIs. Both the HET:EAAT2-S506X and the HET:EAAT2-4KR groups differed from the

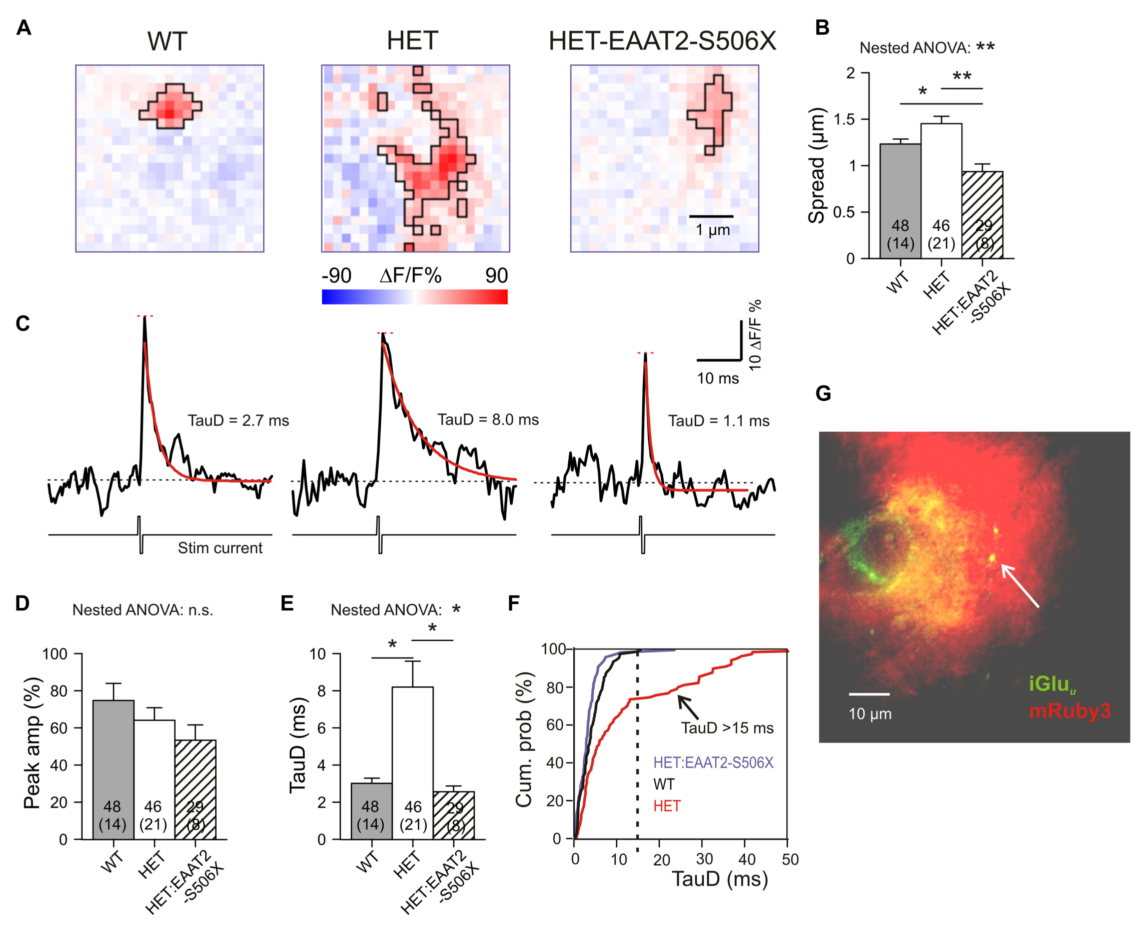

FIGURE 6 | Single synapse glutamate clearance in the striatum after expression of EAAT2-S506X. **(A)** Representative examples from iGlu$_u$ imaging of single corticostriatal synaptic terminals in slices from WT, HET, and treated HET. Bilateral intracranial injections of HET with EAAT2-S506X. The selected images were acquired at the response peak to illustrate the extension of iGlu$_u$ elevation (boxed area). Pink pixels within the black boundaries are pixels where stimulation of the bouton elicited a fluorescence increase (Δ*F*) to values larger than the resting level prior to stimulation (*F*). **(B)** Glutamate spread at the ROI peak of the glutamate elevation (see Section "Materials and Methods" for definition of the parameter "Spread"). **(C)** iGlu$_u$ transients for the examples shown in **(A)**. Recordings before and after electrical stimulation of the given bouton in the presence of TTX. The traces represent the mean fluorescence intensity calculated from all suprathreshold pixels in the ROI. Red curves: Monoexponential functions fitted to the iGluu traces. In black – respective time constants of decay (TauD). **(D,E)** Quantification of results obtained from the pixel with the highest elevation of iGlu$_u$ fluorescence. **(F)** Cumulative probability plot to illustrate the absence of TauD values > 15 ms in WT and in EAAT2-S506X-treated HET. TauD values > 15 ms identify pathological synapses in HET. **(G)** Only synapses in the immediate vicinity of transduced astrocytes were included, as confirmed by the location of the tested iGluu-expressing varicosity on the territory of mRuby-positive astrocytes (arrowhead). *$p < 0.05$, **$p < 0.05$, n.s., not significant.

HET:CTRL group, as their synaptic EAAT2 IF increased to nearly WT:CTRL level.

These results support the idea that expression of C-terminal-modified EAAT2 can increase the availability of native EAAT2 at corticostriatal synapses. Moreover, elimination of four lysines may already be sufficient to rescue more than half of the lost native EAAT2 protein.

Recovery of Astrocytic Glutamate Uptake

To validate the results from corticostriatal synapses in fixed sections and to obtain an estimate for the glutamate uptake capacity of individual astrocytes, a series of imaging experiments was performed in acute striatal slices loaded with the Na^+ indicator SBFI-AM. Glutamate transport was elicited with L-aspartate. It is known that L-glutamate, L-aspartate, and D-aspartate are taken up with similar micromolar affinity (Arkhipova et al., 2019). In the present experiments L-aspartate was chosen for its physiological role as excitatory neurotransmitter (Morland et al., 2013) and its negligible effects at G-protein-coupled glutamate receptors. A major part of the L-aspartate-induced response but not the entire sodium signal was blocked by the high-affinity glutamate transport inhibitor TFB-TBOA (**Figure 5A**). Residual TFB-TBOA insensitive components are common and were attributed to additional effects on other transporters such as the Na, K-ATPase (Rimmele et al., 2017). Therefore only the amplitude of the TFB-TBOA-sensitive component of the Na^+ elevation was used for quantification of the glutamate uptake activity. The first series of experiments compared four animal groups (**Figure 5B**). The traces of the averaged responses (**Figure 5C**) visualize the differences between WT and HET and the similarity of responses obtained from WT:CTRL, HET:EAAT2-S506X, and HET:EAAT2-4KR. Multilevel (nested) ANOVA confirmed a significant recovery of astrocytes transduced with EAAT2-S506X and EAAT2-4KR (**Figure 5D** and **Table 2**).

The present SBFI-loading protocol was adjusted to preferentially label astrocytes (Dvorzhak et al., 2016). This offered an opportunity to determine, in the same view field, the L-aspartate-induced glutamate uptake activity of transduced versus non-transduced astrocytes (**Figures 5E,F**). The difference between individual transduced and not-transduced astrocytes reached significance in HET:EAAT2-S506X (**Figure 5G**).

These results are in line with our quantification of native EAAT2 protein and show that in HET astrocytes not only C-terminal-truncated but also 4KR-edited EAAT2 can alleviate the mHTT-induced depression of glutamate uptake.

Expression of Excitatory Amino Acid Transporter 2-S506X Promotes Glutamate Clearance at Corticostriatal Synapses

A previous publication from our lab (Dvorzhak et al., 2019) addressed the role of EAAT2 in single corticostriatal synapses by using CaMKII-driven expression of the genetically encoded "ultrafast" glutamate indicator $iGlu_u$ (Helassa et al., 2018). According to the previously established criteria, about 40% of corticostriatal synapses (19/46) in HET can be regarded as functionally impaired because glutamate clearance was significantly slower than in WT. But is this deficit due to a failure of astrocytic EAAT2? And if so, could a recovery of synaptic glutamate clearance be achieved by expression of truncated EAAT2? To answer both questions we now examined the effect of the EAAT2-S506X transgene in a set of 29 single corticostriatal synapses from 8 HET with manifest symptoms of hypokinesia. The present results from WT and HET were pooled with the previously characterized non-injected WT and HET synapses. The specimen recordings of **Figure 6A** illustrate our principal finding: Both in WT and in HET:EAAT2-S506X, the area of glutamate elevation is larger in HET. The quantification for the important parameter "Spread"(see section "Materials and Methods" for definition) is given in **Figure 6B**.

Further information on single synapse glutamate clearance was derived from evaluation of time-dependent changes of the $iGlu_u$ signal. The traces of **Figure 6C** represent the mean $iGlu_u$ intensity values ($\Delta F/F$ %) for the ROIs shown in **Figure 5A**. The recordings were taken in the presence of TTX before and after a short biphasic electrical stimulus via a glass pipette in the immediate vicinity of a labeled presynaptic terminal. Traces like these were used to extract two important indicators: "Peak amplitude" (short red horizontal line) and "Time constant of glutamate concentration decay" (TauD, see values next to the red monoexponential fitting curve). Similar traces were constructed from single pixels. The transients derived from the pixel with the highest fluorescence increase reflect the release and clearance of glutamate next to the presynaptic active zone, i.e., the site of vesicle exocytosis. It was found that TauD, but not peak amplitude, were affected by the expression of EAAT2-S506X (**Figures 6D,E** and **Table 2**). In contrast to untreated HET, synapses with prolonged decay (>15 ms) were never encountered in HET:EAAT2-S506X (**Figure 6F**). It should be pointed out that the present single synapse data has exclusively been collected from terminals located on the territory of transduced astrocytes. The arrowhead in **Figure 6G** points to a bright varicosity on the background of the red fluorescent area generated by the dendritic field of one mRuby-expressing astrocyte.

These results (i) verify the contribution of astrocytic EAAT2 to the corticostriatal glutamate clearance and (ii) demonstrate the capacity of corticostriatal synapses to return to normal performance. C-terminal EAAT2 truncation accelerated glutamate uptake and reduced its spread.

Recovery of Motor Performance in Treated Q175 Heterozygote

Starting with an age of 10–12 months Q175 HET exhibit symptoms of hypokinesia. Thus, by the time of testing (14–18 months) mHTT-expressing neurons and astrocytes must have undergone progressive changes for several months. The aim of the following experiments was to quantify the mHTT-induced alterations in the locomotion and to find out to what extent these alterations could still be influenced. To gain a set of easy-to-quantify indicators of hypokinesia, the mice were submitted to two video-recorded tests: (i) the step-over latency test, SOLT (Dvorzhak et al., 2019) and (ii) the open field test, OFT (Menalled et al., 2012; Rothe et al., 2015). The tests were performed immediately before the viral vector injection and 3–6 weeks later, before animal sacrifice. The compared animal groups were WT:CTRL, HET:CTRL and HET:EAAT2-S506X. All animals were carefully matched according to CAG repeat numbers and age.

The behavioral examination provided us with a set of six criteria to classify an animal or animal group as being hypokinetic

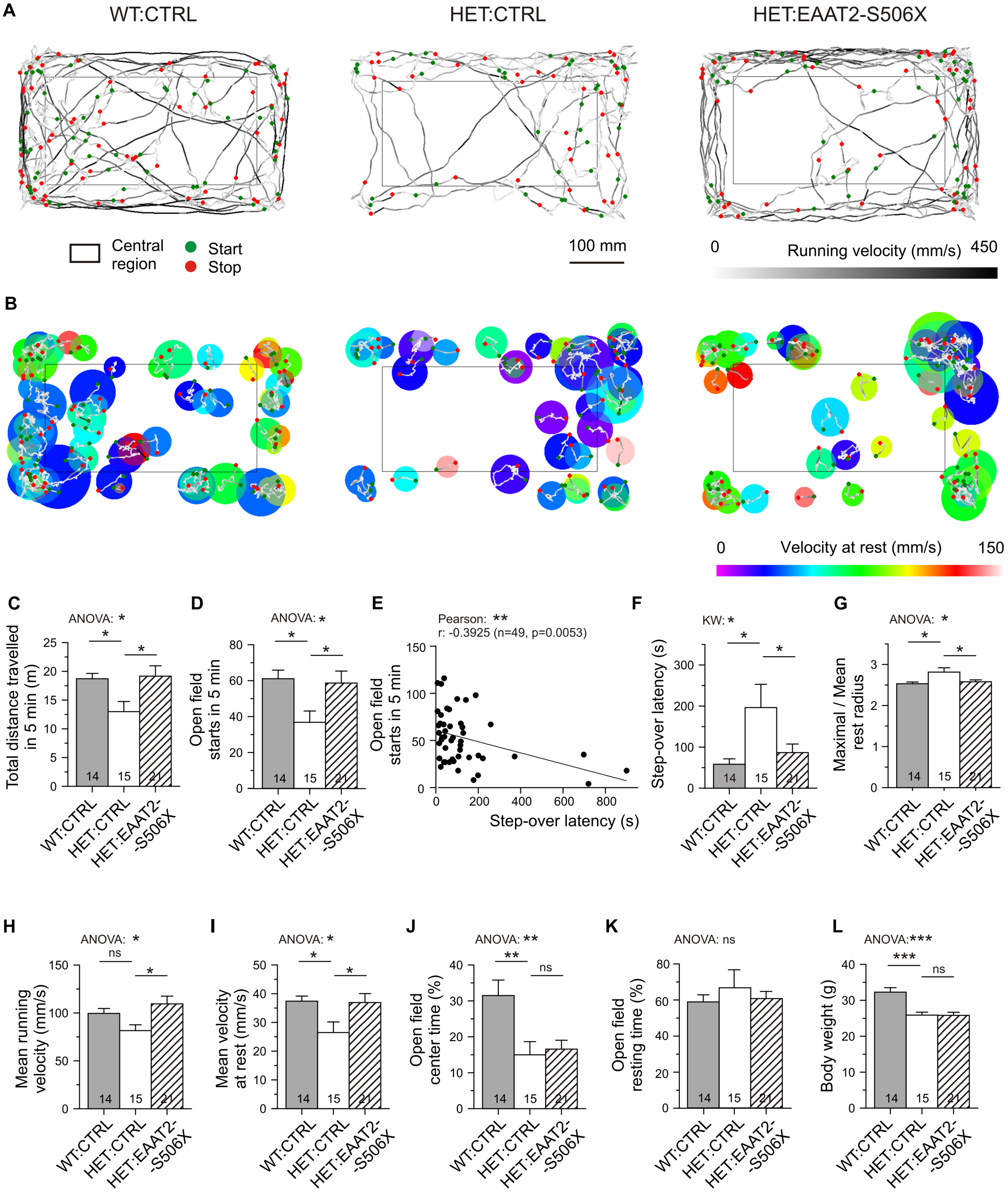

FIGURE 7 | Effects of bilateral EAAT2-S506X expression on the motor performance of Q175 mice. **(A)** Recordings of open field trajectories showing the mean running velocity between starts and stops (green or red circles, respectively). Gray level coding of instantaneous running velocity. **(B)** Motor activity at rest. Color coding of movement velocity at rest. **(C,D,F–K)** Quantification of results from open field testing. **(E,F)** Step-over latency – inverse relationship with number of starts in the open field, and sensitivity of step-over latency to mHTT and treatment. **(L)** Matched age-, CAG-, and body-weight composition of the test groups (only body weight illustrated). $^*p < 0.05$, $^{**}p < 0.01$, $^{***}p < 0.001$.

TABLE 2 | Summary of experiments with functional testing.

mHTT-sensitive functional indicator	**WT-CTRL**				**HET-CTRL**				**HET-EAAT2-S506X**				**Statistics**			***Post hoc* MC HET-CTRL vs. HET-S506X**		
	Mean	***SE***	**N-c/t**	**N-a**	**Mean**	***SE***	**N-c/t**	**N-a**	**Mean**	***SE***	**N-c/t**	**N-a**	**Test**	***F* (DFn, Dfd)**	***P***	**Test**	***P***	**Hedges' G**
#CAG repeats	nd				186.1	1.2		22	185.6	1.7		15				*t*-test	ns	
Body weight at sacrifice	31.28	0.86		21	25.35	0.77		22	26.41	1.08		15	ANOVA	0.29 (2, 55)	<0.0001	Tukey	ns	
OF total distance traveled (m/5 min)	18.72	**0.93**		**14**	**12.99**	**1.77**		**15**	**19.16**	**1.80**		**21**	**ANOVA**	**4.09 (2, 47)**	**0.0230**	**Tukey**	**0.027**	**−0.81**
OF #starts/stops (in 5 min)	**61.07**	**4.78**		**14**	**36.80**	**6.23**		**15**	**58.67**	**6.66**		**21**	**Kruskal–Wallis**	**4.17 (2, 47)**	**0.0216**	**B-K-Y**	**0.040**	**−0.78**
Step-over latency (s)	**56.7**	**10.00**		**18**	**179.1**	**46.6**		**19**	**51.6**	**9.8**		**14**	**Kruskal–Wallis**	**7.37 (2, 47)**	**0.0251**	**B-K-Y**	**0.041**	**0.79**
Maximal/mean rest radius	**2.53**	**0.04**		**14**	**2.81**	**0.11**		**15**	**2.58**	**0.21**		**21**	**ANOVA**	**4.64 (2, 47)**	**0.01**	**Tukey**	**0.038**	**0.75**
Mean running velocity (mm/s)	**99.53**	**5.14**		**14**	**81.57**	**6.04**		**15**	**109.45**	**8.06**		**21**	**ANOVA**	**4.15 (2, 26)**	**0.0220**	**Tukey**	**0.017**	**−0.87**
Mean velocity at rest (mm/s)	**37.39**	**1.78**		**14**	**26.48**	**3.69**		**15**	**36.91**	**3.12**		**21**	**ANOVA**	**3.72 (2, 47)**	**0.0318**	**Tukey**	**0.048**	**−0.70**
Open field center time (%)	**31.48**	**4.32**		**14**	**14.98**	**3.67**		**15**	**16.57**	**2.47**		**21**	**ANOVA**	**6.59 (2, 47)**	**0.0030**	Tukey	ns	
Syn Glu transient spread (μ m)	**1.23**	**0.05**	**48**	**14**	**1.45**	**0.08**	**46**	**21**	**0.94**	**0.08**	**29**	**8**	**Nested ANOVA**	**6.282 (2, 40)**	**0.0042**	**B-K-Y**	**0.0011**	**1.03**
Syn Glu transient(max) TauD (ms)	**3.03**	**0.28**	**48**	**14**	**8.21**	**1.39**	**46**	**21**	**2.57**	**0.31**	**28**	**8**	**Nested ANOVA**	**4.528 (2, 40)**	**0.0169**	**B-K-Y**	**0.012**	**0.76**
Syn Glu transient(max) amp (DF/F%)	**74.85**	**9.21**	**48**	**14**	**64.20**	**6.77**	**46**	**21**	**53.5**	**8.3**	**28**	**8**	**Nested ANOVA**	**0.31 (2, 40)**	**0.4751**	**B-K-Y**	**ns**	**0.24**
Syn EAAT2 IF total (a.u.)*	**5230**	**168.7**	**12/360**	**2**	**3663**	**81.42**	**12/360**	**2**	**4638**	**205.8**	**12/360**	**2**	**Nested ANOVA**	**12.25 (3,4)**	**0.0175**	**Dunnett**	**0.048**	**−1.87**
SPN input resistance (MOhm)	**114**	**10.3**	**18**	**8**	**165**	**17.0**	**14**	**8**	**127**	**13.5**	**8**	**5**	**Nested ANOVA**	**4.05 (2, 37)**	**0.0256**	B-K-Y	0.104	0.64
ITonic(GABA) amp (pA)	**11.33**	**2.37**	**13**	**6**	**2.99**	**1.03**	**14**	**8**	**5.78**	**3.37**	**7**	**5**	**Nested ANOVA**	**6.19 (2, 16)**	**0.0102**	B-K-Y	ns	

**Test includes 4KR group.*

MC, multiple comparison test; BKY, Benjamini, Krieger, Yekutieli test. In bold: Indicators with sensitivity to X-effect.

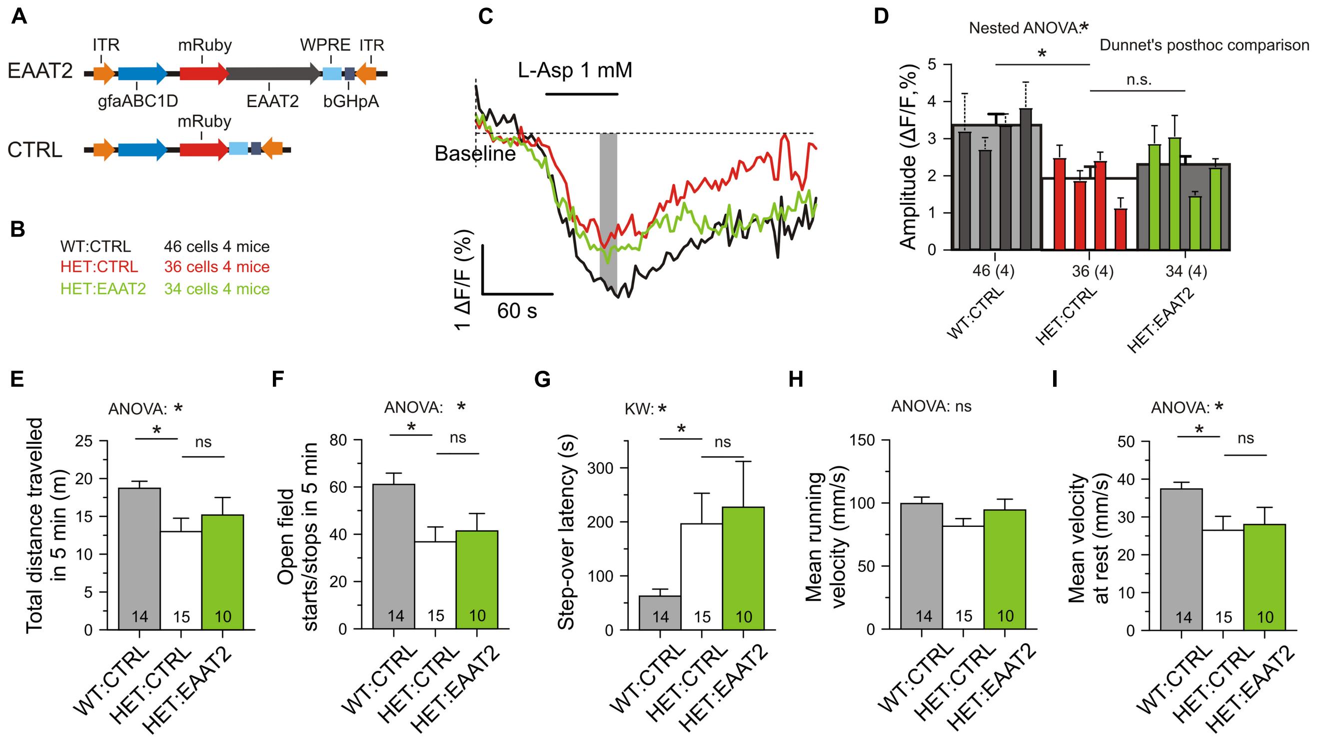

FIGURE 8 | No recovery of astrocytic glutamate uptake and motor performance in mice overexpressing the full-length form of EAAT2. **(A)** Injected vectors. **(B)** Animal groups. The injected animals were matched for age, body-weight and the number of CAG-repeats. The numbers refer to the experiments with SBFI imaging. **(C)** Measurement of single-cell glutamate uptake by sodium imaging with SBFI. Same conditions as in **Figure 5**. Averaged traces from mRuby3+ astrocytes only. **(D)** Quantification of results with two-level ("nested") ANOVA statistics (animal level and cell level) and two-level *post hoc* tests for the differences between the test groups. **(E–I)** Lack of recovery from the signs of hypokinesia. Here as in all other figures: n.s., not significant. $^*p < 0.05$.

or recovered from hypokinesia. Specifically, the step-over latency of SOLT was regarded as a direct measure of the time needed to initiate exploration in the open field. Its usefulness was supported by a larger number of observations from non-injected HD mice (**Supplementary Figure 1**). Step-over latencies longer than 300 ms were almost exclusively found in HET which could contribute to the detection of recovery effects. The other indicators are based on a more complex analysis of the movement trajectories in the open field (**Figures 7A,B**, see **Supplementary Table 2** for definitions of the analyzed parameters). Five out of 6 movement parameters extracted from OFT were sensitive to the C-terminal-modified EAAT2. The most commonly used OFT indicator "total distance traveled in 5 min" was found to be decreased in HET:CTRL and recovered in HET:EAAT2-S506X if compared to WT:CTRL (**Figures 7A,C**).

The incidence of starts from rest is possibly the most reliable indicator of depressed movement initiation (**Figures 7A,D**). It is inversely correlated with the step-over latency (**Figure 7E**). After treatment with EAAT2-S506X both parameters exhibited changes toward WT:CTRL levels (**Figures 7D,F**). Also noteworthy is the treatment-related reduction of the maximal to mean radius of the resting area, i.e., the extension of the resting area until a new movement starts (**Figures 7B,G**). One could further expect an mHTT-related alteration in the velocity of body displacement, but it is not known whether this would equally apply to rest and running. It turned out, that EAAT2-S506X affects movement velocity both during the resting and running phases. Moreover, the direction of the changes treatment were similar and showed recovery with EAAT2-S506X (**Figures 7H,I**).

Other aspects of open field behavior were unchanged by viral treatment, such as the relative time spent in the open field center, or the open field resting time (**Figures 7J,K**) which suggests that these indicators might not be related to the site of injection, the dorsal striatum, or not be representative of exploratory motor activity. The typical reduction in the body weight remained as well (**Figure 7L**).

Together, these experiments present another strong argument in support of the hypothesis that molecular uncoupling of EAAT2 from its intraastrocytic interaction partners can alleviate mHTT-induced symptoms even at advanced stages of the disease. The results also underscore the relevance of striatal astrocytes for the initiation and speed of exploratory movements.

Over-Expression of Full-Length *Slc1a2* Is Not Sufficient to Alleviate the Symptoms of Hypokinesia

Finally we wanted to clarify the performance of mice with a full-length EAAT2 transgene (**Figures 8A,B**). SBFI imaging was again performed in transduced astrocytes, but a recovery of glutamate uptake was not observed (**Figures 8C,D**). Moreover, comparison of the L-aspartate-induced Na transients in HET:CTRL, HET:EAAT2-S506X, and HET:EAAT2 showed that EAAT2-S506X-treated mice outperformed (Kruskal–Wallis test: P = 0.0004) not only with respect to HET:CTRL (Dunn's test: P = 0.0004) but also with respect to HET:EAAT2 (Dunn's test: P = 0.0052). The respective mean, SE and N of $\Delta F/F$ (%) were for HET:CTRL: 2.01 ± 0.18 (N = 36), HET-EAAT2: S506X: 3.28 ± 0.23 (N = 23), HET:EAAT2: 2.31 ± 0.23 (N = 34). Locomotion did not recover either (**Figures 8E–I**). The comparison of HET:EAAT2 with HET:EAAT2-S506X-treated mice showed that the latter outperformed (ANOVA $p < 0.05$) with regard to the number of open field starts/stops in 5 min and the mean running velocity (mm/s). The respective mean, SE and N were for HET:CTRL: 36.80 ± 6.23 and 81.57 ± 6.04 (N = 15), HET:EAAT2-S506X: 58.67 ± 6.66 and 109.45 ± 8.06 (N = 21), HET:EAAT2: 41.40 ± 7.38 and 94.45 ± 8.57 (N = 10).

We concluded that over-expression of full-length EAAT2 is not sufficient to rescue astrocytic glutamate uptake in the striatum and it does not ease the symptoms of hypokinesia.

Supplemental Experiments

A series of supplemental experiments addressed the efficacy of EAAT2-S506X treatment with systemically applied vectors (**Supplementary Figure 2**) and the influence on neuronal excitability (**Supplementary Figure 3**). In both cases the effects of S506X remained below the significance level required with nested ANOVA.

DISCUSSION

The results underscore the importance of C-terminal-dependent EAAT2 molecular interactions and demonstrate that mHTT-related deficits can be reversed by the expression of a C-terminal-modified EAAT2 transgene. The latter conclusion is based on tests for changes in synaptic glutamate clearance, astrocytic glutamate uptake and self-induced locomotion.

What Could Be the Cause of Failing Glutamate Uptake and a Molecular Basis of Partial Recovery?

In principle, insufficient glutamate uptake could be due to changes in the relative abundance of functional EAAT2 isoforms (Goursaud et al., 2011) or aberrant RNA splicing (Lin et al., 1998; Scott et al., 2011). At least 3 EAAT2 variants are known to differ in their C-terminal sequence: EAAT2a, EAAT2b, and EAAT2c [GLT-1a, GLT-1b and GLT1c in rodents, see Vandenberg and Ryan (2013) for further information]. In the rat brain, EAAT2a is ∼15-fold more abundant than EAAT2b (Holmseth et al., 2009). Both are found at glutamatergic synapses (Al Awabdh et al., 2016), but only EAAT2b is required for the regulated as opposed to constitutive glutamate transport (Underhill et al., 2015). The C-terminus of EAAT2b but not EAAT2a contains a sequence predicted to interact with PDZ-containing proteins, including PICK1 (Wheatley et al., 1992; Bassan et al., 2008), PSD95 (Gonzalez-Gonzalez et al., 2009), or DLG1 (Underhill et al., 2015). By interaction with these proteins, EAAT2 can increase its internalization and/or lateral mobility in the astrocyte membrane due to activation of CamKII (Underhill et al., 2015) or high concentration of glutamate (Al Awabdh et al., 2016). It was shown that experimental immobilization of EAAT2 prolongs the postsynaptic synaptic currents (Murphy-Royal et al., 2015). Given that the duration of the glutamate transport cycle [∼12 ms at Schaffer collateral synapses (Bergles and Jahr, 1998)] is relatively long in comparison with the glutamate receptor binding, it was hypothesized that lateral movement of the substrate-transporter complex and a rapid membrane turnover to replenish fresh unbound transporter molecules are requirements for effective glutamate buffering at synaptic sites. To ensure the high abundance of transporter molecules around a glutamate-releasing terminal (Lehre and Danbolt, 1998) the turnover of the transporter from the cytoplasm into the membrane should also be high. However, how the degradation/replenishment of EAAT2 protein at a tripartite synapse actually works is not yet clear.

The present experiments in symptomatic Q175 HET are, to the best of our knowledge, the first attempt to characterize an HD phenotype in the EAAT2 interactome by using immunoprecipitation of mYFP-tagged native and C-terminal-truncated EAAT2 as "bait." The focus was on alterations produced by mHTT, on one side, and changes due to C-terminal truncation of EAAT2, on the other side. It became quite obvious that the presence of mHTT produced major changes in the abundance of full-length EAAT2 binding partners, while expression of EAAT2-S506X resulted in a partial or even full return to the interaction pattern seen in WT.

The changes in HET included the disappearance of normally existing, potentially necessary interactors, such as dystrophin or PDE10a, and the appearance of new, potentially pathological interactors, such as the proteins encoded by *Tln1*, *Rab2b*, *Cacnb3*, or *UBA2*. Dystrophin is quite plentiful in astrocytes, especially at the endfeet, and it has been shown that dystrophin-glycoprotein complexes provide a link between laminin and the cytoskeleton (Sato et al., 2018) thereby contributing to the stabilization of aquaporin4 and Kir4.1 in particular subregions of the astrocyte plasma membrane (Enger et al., 2012). The function of dystrophin at glutamatergic corticostriatal synapses has not yet been explored, but there is evidence for a role of a dystrophin-associated protein complex in the pathogenesis of parkinsonian symptoms (Spuler et al., 2010). That PDE10a belongs to the astrocytic interactor proteins of EAAT2 is new information, but it has been reported that loss of PDE10a could be an important early biomarker of human HD (Ahmad et al., 2014; Russell et al., 2014) and has been considered as a potential target for molecular intervention (Beaumont et al., 2016). While our results confirmed the mHTT-related loss of PDE10a, we found no evidence for C-terminal-related recovery which points to other sites of interaction.

Of particular interest are the up-regulated proteins and their sensitivity to treatment with EAAT2-S506X. Talin1 links integrins to the actin filaments of the cytoskeleton and thereby contributes to the first steps of local cell adhesion (Campbell and Ginsberg, 2004). Its role in astrocytes and/or HD is unknown but its plasma titer is reported to increase during active phases of multiple sclerosis (Muto et al., 2017). Iqsec3 belongs to the group of guanine exchange factors (GEFs) and is implicated in synapse assembly. An up-regulation of Iqsec3 was implicated in the formation of inhibitory synapses (Kim et al., 2020) which could be part of a compensatory response in HET.

Concerning Uba2, it is known that UBA2 and SAE1 form a heterodimer that functions as a SUMO-activating enzyme. Sumoylation – the covalent attachment of SUMO1 to lysine residues – is a posttranslational modification process with relevance to HD (Steffan et al., 2004). Interestingly, non-sumoylated EAAT2 resides in the plasma membrane while the product of SUMO fusion with EAAT2 tends to form aggregates in the cytoplasm (Foran et al., 2011). When comparing the UBA2 levels precipitated by EAAT2-S506X vs. EAAT2 in HET, it was apparent that the loss of C-terminal interaction motives largely prevented the interaction between EAAT2 and UBA2. In cultured astrocytes, a proteolytically released C-terminal fragment of EAAT2 modified by SUMO1 was also found in the nucleus, with inhibitory effects on EAAT2 transcription (Gibb et al., 2007; Foran et al., 2011). The relevance of this EAAT2-derived signaling mechanism was demonstrated *in vivo,* in a mutant SOD1 mouse model of amyotrophic lateral sclerosis (ALS), where knock-in of a modified *Slc1a2* isoform with a defective caspase-3 cleavage site prolonged the life span of mice afflicted by the disease (Rosenblum et al., 2017).

It is interesting that the present evaluation of native EAAT2 protein at glutamatergic synapses and glutamate uptake in striatal astrocytes rendered almost equal effects of EAAT2-4KR and EAAT2-S5096X. This result underlines the critical role of C-terminal lysine-mediated interactions such as sumoylation and ubiquitination in the regulation of glutamate uptake. It should also be noted that there is a basal constitutive internalization of the transporter, with a critical role of the lysines 497, 517, 526, 550, 558, 570, and 573 NCBI Reference Sequence: XP_030104754.1 at the EAAT2 C-terminal (Gonzalez-Gonzalez et al., 2008; Martinez-Villarreal et al., 2012). Here we mutated only the lysine residues with the most prominent effect on transporter internalization also considering their shifted position in the human EAAT2 sequence, i.e., 518, 527, 551, and 571.

In the context of previous reports on the constitutive internalization of EAAT2 and the toxic effects of sumoylated C-terminal EAAT2 cleavage products, it is tempting to propose that an astrocyte expressing *mHTT* presents with largely altered conditions for both transcriptional control and protein sorting, which perhaps explains why in Q175 HET a mere stimulation of full-length EAAT2 failed to eliminate the deficits in the glutamate uptake and motor performance of HET:EAAT2. Of course, much more work is needed to fully unravel the molecular determinants of EAAT2 function in the striatum and other regions of the brain.

Which Cellular Markers Report Failure or Rescue of Glutamate Clearance?

In the past glutamate uptake has mostly been quantified on the basis of tritium-labeled striatal tissue or synaptosomal preparations (see Section "Introduction"). In comparison with the measurement of tissue glutamate uptake, SBFI imaging of individual fluorescence-tagged astrocytes offers the advantage that the uptake activity can directly be compared in transduced *vs.* non-transduced astrocytes. In this way the results should be less affected by other mHTT-induced alterations, such as changes in the size and density of astroglia in the striatum. Our present analysis provides the still missing proof that the deficits in locomotion and synaptic glutamate clearance were in fact associated with: (i) signals mediated via the EAAT2-C-terminal, as opposed to other EAAT2 domains and (ii) striatal astrocytes as opposed to other cell types/regions in the mouse brain.

Unfortunately, the subcellular resolution of glutamate uptake with sodium imaging is not very high, even in the case of focal glutamate uncaging (Dvorzhak et al., 2016). This limits the use of SBFI imaging for the estimation of the glutamate clearance at the sites where it matters – the tripartite synapse. Previous attempts to reveal mHTT-related clearance deficits with glutamate sensors (Parsons et al., 2016; Parievsky et al., 2017) also failed, most likely due to methodical limitations (slow glutamate sensors, non-selective general tissue depolarization, low temporal and spatial resolution of synaptic responses). Considering, however, the importance of the corticostriatal pathway for the initiation of self-induced movements (Plotkin and Surmeier, 2015) it was found worthwhile to establish a new approach for the evaluation of the glutamate transients at individual glutamatergic synapses in the dorsal striatum (Dvorzhak and Grantyn, 2020). The most telling indicators of clearance deficiency were the time constant of decay and the spread of the stimulus-induced glutamate elevation as reported by the ultrafast glutamate sensor iGlu$_u$ (Helassa et al., 2018; Dvorzhak et al., 2019). It was already known that the duration of corticostriatal EPSCs increased in HD mice (Dvorzhak et al., 2019) and, respectively, decreased after the exposure to pharmacological blockers of glutamate transport or modulators of NF-κB-dependent transcription (Lee et al., 2008; Ghosh et al., 2016). A faster decay of the glutamate elevation at corticostriatal terminals located on S506X-expressing astrocytes can therefore be regarded as the currently most convincing argument in support of the astrocytic contribution to the glutamate clearance in mice expressing a mutant form of huntingtin.

Is Region- and Cell-Type-Restricted Expression of Artificial Excitatory Amino Acid Transporter 2 Variants a Useful Approach to Study Disease-Related Pathology?

Huntington's disease is a severe inherited neurological disorder with diverse clinical symptoms and variable onset. With a respective gene test it can be diagnosed much before the onset of motor or other symptoms. Great efforts are therefore being made to reduce the expression of *mHTT* inside and outside the central nervous system before the disease actually starts (Mrzljak and Munoz-Sanjuan, 2015; Tabrizi et al., 2019). *mHTT*-lowering therapies have reached an advanced stage of preclinical testing or even entered the phase of first clinical trials (Mullard, 2019). In animal models of HD, the most effective approaches include the use of self-inactivating KamiCas9 system for editing the huntingtin gene (Merienne et al., 2017), injection of *mHTT* transcription-targeting viral vectors (Zeitler et al., 2019) and application of siRNAs, shRNAs, or miRNAs for the reduction of *mHTT* mRNA and protein level (see Kaemmerer and Grondin, 2019 for review).

It is obvious that gene therapy is becoming more problematic at symptomatic stages of the disease. In HD, as well as other neurodegenerative disorders, late-stage pathology may include numerous compensatory mechanisms which would make it increasingly difficult to implement a causal therapy. But substantial therapeutic benefits may still be possible, notably if basic research can reveal a (virtual) bypass in the signal flow connecting the elements of molecular intervention and motor outcome. In the present experiments with mHTT-expressing Q175 mice, a robust motor response was induced by local (striatum), cell-selective (astrocytes) and site-directed (EAAT2 C-terminus) transgene expression. Such result is to some extent surprising because most evidence-based models describe the initiation of voluntary movements as the result of a multi-level parallel and distributed information processing in a large number of brain structures [see for instance (Morita, 2014)]. That a particular cell population can effectively control a set of motor acts has mostly been implicated in "lower" vertebrates or invertebrates. However, reports on specific links between motor performance and specific transgene expression are already accumulating [see, for instance, Nagai et al. (2019); Percie du et al. (2020)] and may help to identify new signaling pathways.

It is interesting and important that not all symptoms of HD were sensitive to the expression of modified EAAT2. There was, for instance, no change in the body weight or in the open field center time. This might be regarded as one more argument in support of the idea that the modification of EAAT2 in striatal astrocytes preferentially affects the performance of the synapses.

The present results have promise with regard to small molecule therapy of neurological conditions with hypokinesia, including HD, Parkinson's disease, stroke and toxin-induced brain damage. These disorders may share similar alterations in the regulation of synaptic glutamate transport. We therefore consider it highly interesting that the interruption of C-terminal-dependent regulation of EAAT2 renders beneficial effects at both the cellular and behavioral level. Blocking pathological signals might be a good strategy where causal therapy is difficult to achieve.

DATA AVAILABILITY STATEMENT

The data presented in the study are deposited in the PRIDE repository, accession number PXD029194.

ETHICS STATEMENT

The animal study was reviewed and approved by Berlin Office of Health Protection and Technical Safety (G0218/17).

AUTHOR CONTRIBUTIONS

SH prepared and injected the vectors, validated the transgene expression, and contributed to the mass spectrometry, Western blotting, sodium imaging, and behavioral experiments. AD performed the single synapse imaging and behavioral data analysis and contributed to the sodium imaging experiments. MK and RG accomplished the proteomics analysis. SR-N performed patch-clamp recordings and astrocyte imaging. SA performed immunostaining and confocal microscopy. All authors listed have made a substantial, direct, and intellectual contribution to the work, and approved it for publication.

FUNDING

This work was supported by CHDI (A-12467), the German Research Foundation, under Germany's Excellence Strategy (Exc 2049 – 390688087) and intramural Charité Research Funds to RG.

ACKNOWLEDGMENTS

Thanks are due to Arnd Baumann and Christoph Fahlke, Forschungszentrum Jülich for the EYFP EAAT2 S506X plasmid, Francisco Zafra, Universidad Autónoma de Madrid, for important information on the 4KR-edited EAAT2 isoform, K. Török, St. George's, University of London, and N. Helassa, University of Liverpool, for the iGlu$_u$ plasmid. Gudrun Ahnert-Hilger, Charité – Universitätsmedizin Berlin and Hannes Schmidt, Eberhard Karls Universität Tübingen, contributed numerous helpful suggestions. D. Betances and A. Schönherr provided excellent technical assistance.

SUPPLEMENTARY MATERIAL

The Supplementary Material for this article can be found online at: https://www.frontiersin.org/articles/10.3389/fncel.2021.792652/full#supplementary-material

REFERENCES

Ahmad, R., Bourgeois, S., Postnov, A., Schmidt, M. E., Bormans, G., Van Laere, K., et al. (2014). PET imaging shows loss of striatal PDE10A in patients with Huntington disease. *Neurology* 82, 279–281. doi: 10.1212/WNL.0000000000000037

Al Awabdh, S., Gupta-Agarwal, S., Sheehan, D. F., Muir, J., Norkett, R., Twelvetrees, A. E., et al. (2016). Neuronal activity mediated regulation of glutamate transporter GLT-1 surface diffusion in rat astrocytes in dissociated and slice cultures. *Glia* 64, 1252–1264. doi: 10.1002/glia.22997

Arkhipova, V., Trinco, G., Ettema, T. W., Jensen, S., Slotboom, D. J., and Guskov, A. (2019). Binding and transport of D-aspartate by the glutamate transporter homolog Glt(Tk). *Elife* 8:e45286. doi: 10.7554/eLife.45286

Bassan, M., Liu, H., Madsen, K. L., Armsen, W., Zhou, J., Desilva, T., et al. (2008). Interaction between the glutamate transporter GLT1b and the synaptic PDZ domain protein PICK1. *Eur. J. Neurosci.* 27, 66–82. doi: 10.1111/j.1460-9568.2007.05986.x

Beart, P. M., and O'Shea, R. D. (2007). Transporters for L-glutamate: an update on their molecular pharmacology and pathological involvement. *Br. J. Pharmacol.* 150, 5–17. doi: 10.1038/sj.bjp.0706949

Beaumont, V., Zhong, S., Lin, H., Xu, W., Bradaia, A., Steidl, E., et al. (2016). Phosphodiesterase 10A inhibition improves cortico-basal ganglia function in Huntington's disease models. *Neuron* 92, 1220–1237. doi: 10.1016/j.neuron.2016.10.064

Berardelli, A., Noth, J., Thompson, P. D., Bollen, E. L., Curra, A., Deuschl, G., et al. (1999). Pathophysiology of chorea and bradykinesia in Huntington's disease. *Mov. Disord.* 14, 398–403. doi: 10.1002/1531-8257(199905)14:3<398::aid-mds1003>3.0.co;2-f

Bergles, D. E., and Jahr, C. E. (1998). Glial contribution to glutamate uptake at Schaffer collateral- commissural synapses in the hippocampus. *J. Neurosci.* 18, 7709–7716. doi: 10.1523/JNEUROSCI.18-19-07709.1998

Bradford, J., Shin, J. Y., Roberts, M., Wang, C. E., Li, X. J., and Li, S. (2009). Expression of mutant huntingtin in mouse brain astrocytes causes age-dependent neurological symptoms. *Proc. Natl. Acad. Sci. U.S.A.* 106, 22480–22485. doi: 10.1073/pnas.0911503106

Burgold, J., Schulz-Trieglaff, E. K., Voelkl, K., Gutierrez-Angel, S., Bader, J. M., Hosp, F., et al. (2019). Cortical circuit alterations precede motor impairments in Huntington's disease mice. *Sci. Rep.* 9:6634. doi: 10.1038/s41598-019-43024-w

Campbell, I. D., and Ginsberg, M. H. (2004). The talin-tail interaction places integrin activation on FERM ground. *Trends Biochem. Sci.* 29, 429–435. doi: 10.1016/j.tibs.2004.06.005

Carrillo-Reid, L., Day, M., Xie, Z., Melendez, A. E., Kondapalli, J., Plotkin, J. L., et al. (2019). Mutant huntingtin enhances activation of dendritic Kv4 K(+) channels in striatal spiny projection neurons. *Elife* 8:40818. doi: 10.7554/eLife.40818

Chai, H., Diaz-Castro, B., Shigetomi, E., Monte, E., Octeau, J. C., Yu, X., et al. (2017). Neural circuit-specialized astrocytes: transcriptomic, proteomic, morphological, and functional evidence. *Neuron* 95, 531–549. doi: 10.1016/j.neuron.2017.06.029

Chan, K. Y., Jang, M. J., Yoo, B. B., Greenbaum, A., Ravi, N., Wu, W. L., et al. (2017). Engineered AAVs for efficient noninvasive gene delivery to the central and peripheral nervous systems. *Nat. Neurosci.* 20, 1172–1179. doi: 10.1038/nn.4593

Danbolt, N. C. (2001). Glutamate uptake. *Prog. Neurobiol.* 65, 1–105.

Deng, Y. P., Wong, T., Bricker-Anthony, C., Deng, B., and Reiner, A. (2013). Loss of corticostriatal and thalamostriatal synaptic terminals precedes striatal projection neuron pathology in heterozygous Q140 Huntington's disease mice. *Neurobiol. Dis.* 60, 89–107. doi: 10.1016/j.nbd.2013.08.009

Dvorzhak, A., and Grantyn, R. (2020). Single synapse indicators of glutamate release and uptake in acute brain slices from normal and Huntington mice. *J. Vis. Exp.* doi: 10.3791/60113

Dvorzhak, A., Helassa, N., Torok, K., Schmitz, D., and Grantyn, R. (2019). Single synapse indicators of impaired glutamate clearance derived from fast iGluu imaging of cortical afferents in the striatum of normal and Huntington (Q175) mice. *J. Neurosci.* 39, 3970–3982. doi: 10.1523/JNEUROSCI.2865-18.2019

Dvorzhak, A., Vagner, T., and Grantyn, R. (2016). Functional indicators of glutamate transport in single striatal astrocytes and the influence of Kir4.1 in normal and Huntington mice. *J. Neurosci.* 16, 4959–4975. doi: 10.1523/JNEUROSCI.0316-16.2016

Enger, R., Gundersen, G. A., Haj-Yasein, N. N., Eilert-Olsen, M., Thoren, A. E., Vindedal, G. F., et al. (2012). Molecular scaffolds underpinning macroglial polarization: an analysis of retinal Muller cells and brain astrocytes in mouse. *Glia* 60, 2018–2026. doi: 10.1002/glia.22416

Estrada-Sanchez, A. M., Montiel, T., Segovia, J., and Massieu, L. (2009). Glutamate toxicity in the striatum of the R6/2 Huntington's disease transgenic mice is age-dependent and correlates with decreased levels of glutamate transporters. *Neurobiol. Dis.* 34, 78–86. doi: 10.1016/j.nbd.2008.12.017

Faideau, M., Kim, J., Cormier, K., Gilmore, R., Welch, M., Auregan, G., et al. (2010). In vivo expression of polyglutamine-expanded huntingtin by mouse striatal astrocytes impairs glutamate transport: a correlation with Huntington's disease subjects. *Hum. Mol. Genet.* 19, 3053–3067. doi: 10.1093/hmg/ddq212

Foran, E., Bogush, A., Goffredo, M., Roncaglia, P., Gustincich, S., Pasinelli, P., et al. (2011). Motor neuron impairment mediated by a sumoylated fragment of the glial glutamate transporter EAAT2. *Glia* 59, 1719–1731. doi: 10.1002/glia.21218

Ghosh, M., Lane, M., Krizman, E., Sattler, R., Rothstein, J. D., and Robinson, M. B. (2016). The transcription factor Pax6 contributes to the induction of GLT-1 expression in astrocytes through an interaction with a distal enhancer element. *J. Neurochem.* 136, 262–275. doi: 10.1111/jnc.13406

Gibb, S. L., Boston-Howes, W., Lavina, Z. S., Gustincich, S., Brown, R. H. Jr., Pasinelli, P., et al. (2007). A caspase-3-cleaved fragment of the glial glutamate transporter EAAT2 is sumoylated and targeted to promyelocytic leukemia nuclear bodies in mutant SOD1-linked amyotrophic lateral sclerosis. *J. Biol. Chem.* 282, 32480–32490. doi: 10.1074/jbc.M704314200

Gonzalez-Gonzalez, I. M., Garcia-Tardon, N., Gimenez, C., and Zafra, F. (2008). PKC-dependent endocytosis of the GLT1 glutamate transporter depends on ubiquitylation of lysines located in a C-terminal cluster. *Glia* 56, 963–974. doi: 10.1002/glia.20670

Gonzalez-Gonzalez, I. M., Garcia-Tardon, N., Gimenez, C., and Zafra, F. (2009). Splice variants of the glutamate transporter GLT1 form hetero-oligomers that interact with PSD-95 and NMDA receptors. *J. Neurochem.* 110, 264–274. doi: 10.1111/j.1471-4159.2009.06125.x

Goursaud, S., Focant, M. C., Berger, J. V., Nizet, Y., Maloteaux, J. M., and Hermans, E. (2011). The VPAC2 agonist peptide histidine isoleucine (PHI) up-regulates glutamate transport in the corpus callosum of a rat model of amyotrophic lateral sclerosis (hSOD1G93A) by inhibiting caspase-3 mediated inactivation of GLT-1a. *FASEB J.* 25, 3674–3686. doi: 10.1096/fj.11-182337

Hart, E. P., Marinus, J., Burgunder, J. M., Bentivoglio, A. R., Craufurd, D., Reilmann, R., et al. (2013). Better global and cognitive functioning in choreatic versus hypokinetic-rigid Huntington's disease. *Mov. Disord.* 28, 1142–1145. doi: 10.1002/mds.25422

Helassa, N., Durst, C. D., Coates, C., Kerruth, S., Arif, U., Schulze, C., et al. (2018). Ultrafast glutamate sensors resolve high-frequency release at Schaffer collateral synapses. *Proc. Natl. Acad. Sci. U.S.A.* 115, 5594–5599. doi: 10.1073/pnas.1720648115

Holmseth, S., Scott, H. A., Real, K., Lehre, K. P., Leergaard, T. B., Bjaalie, J. G., et al. (2009). The concentrations and distributions of three C-terminal variants of the GLT1 (EAAT2; slc1a2) glutamate transporter protein in rat brain tissue suggest differential regulation. *Neuroscience* 162, 1055–1071. doi: 10.1016/j.neuroscience.2009.03.048

Horton, M. C., Nopoulos, P., Nance, M., Landwehrmyer, G. B., Barker, R. A., Squitieri, F., et al. (2019). Assessment of the performance of a modified motor scale as applied to juvenile onset Huntington's disease. *J. Huntingtons. Dis.* 8, 181–193. doi: 10.3233/JHD-180306

Kaemmerer, W. F., and Grondin, R. C. (2019). The effects of huntingtin-lowering: what do we know so far? *Degener. Neurol. Neuromuscul. Dis.* 9, 3–17. doi: 10.2147/DNND.S163808

Kalandadze, A., Wu, Y., and Robinson, M. B. (2002). Protein kinase C activation decreases cell surface expression of the GLT-1 subtype of glutamate transporter. Requirement of a carboxyl-terminal domain and partial dependence on serine 486. *J. Biol. Chem.* 277, 45741–45750. doi: 10.1074/jbc.M203771200

Kim, S., Kim, H., Park, D., Kim, J., Hong, J., Kim, J. S., et al. (2020). Loss of IQSEC3 disrupts GABAergic synapse maintenance and decreases somatostatin expression in the hippocampus. *Cell Rep.* 30, 1995–2005. doi: 10.1016/j.celrep.2020.01.053

Kirschner, M. A., Copeland, N. G., Gilbert, D. J., Jenkins, N. A., and Amara, S. G. (1994). Mouse excitatory amino acid transporter EAAT2: isolation, characterization, and proximity to neuroexcitability loci on mouse chromosome 2. *Genomics* 24, 218–224. doi: 10.1006/geno.1994.1609

Lee, S. G., Su, Z. Z., Emdad, L., Gupta, P., Sarkar, D., Borjabad, A., et al. (2008). Mechanism of ceftriaxone induction of excitatory amino acid transporter-2 expression and glutamate uptake in primary human astrocytes. *J. Biol. Chem.* 283, 13116–13123. doi: 10.1074/jbc.M707697200

Lehre, K. P., and Danbolt, N. C. (1998). The number of glutamate transporter subtype molecules at glutamatergic synapses: chemical and stereological quantification in young adult rat brain. *J. Neurosci.* 18, 8751–8757. doi: 10.1523/JNEUROSCI.18-21-08751.1998

Leinenweber, A., Machtens, J. P., Begemann, B., and Fahlke, C. (2011). Regulation of glial glutamate transporters by C-terminal domains. *J. Biol. Chem.* 286, 1927–1937. doi: 10.1074/jbc.M110.153486

Lin, C. L., Bristol, L. A., Jin, L., Dykes-Hoberg, M., Crawford, T., Clawson, L., et al. (1998). Aberrant RNA processing in a neurodegenerative disease: the cause for absent EAAT2, a glutamate transporter, in amyotrophic lateral sclerosis. *Neuron* 20, 589–602. doi: 10.1016/s0896-6273(00)80997-6

Martinez-Villarreal, J., Garcia, T. N., Ibanez, I., Gimenez, C., and Zafra, F. (2012). Cell surface turnover of the glutamate transporter GLT-1 is mediated by ubiquitination/deubiquitination. *Glia* 60, 1356–1365. doi: 10.1002/glia.22354

Menalled, L. B., Kudwa, A. E., Miller, S., Fitzpatrick, J., Watson-Johnson, J., Keating, N., et al. (2012). Comprehensive behavioral and molecular characterization of a new knock-in mouse model of Huntington's disease: zQ175. *PLoS One* 7:e49838. doi: 10.1371/journal.pone.0049838

Merienne, N., Vachey, G., de Longprez, L., Meunier, C., Zimmer, V., Perriard, G., et al. (2017). The self-inactivating KamiCAS9 system for the editing of cns disease genes. *Cell Rep.* 20, 2980–2991. doi: 10.1016/j.celrep.2017.08.075

Meunier, C., Merienne, N., Jolle, C., Deglon, N., and Pellerin, L. (2016). Astrocytes are key but indirect contributors to the development of the symptomatology and pathophysiology of Huntington's disease. *Glia* 64, 1841–1856. doi: 10.1002/glia.23022

Miller, B. R., Dorner, J. L., Bunner, K. D., Gaither, T. W., Klein, E. L., Barton, S. J., et al. (2012). Up-regulation of GLT1 reverses the deficit in cortically evoked striatal ascorbate efflux in the R6/2 mouse model of Huntington's disease. *J. Neurochem.* 121, 629–638. doi: 10.1111/j.1471-4159.2012.07691.x

Morita, K. (2014). Differential cortical activation of the striatal direct and indirect pathway cells: reconciling the anatomical and optogenetic results by using a computational method. *J. Neurophysiol.* 112, 120–146. doi: 10.1152/jn.00625.2013

Morland, C., Nordengen, K., Larsson, M., Prolo, L. M., Farzampour, Z., Reimer, R. J., et al. (2013). Vesicular uptake and exocytosis of L-aspartate is independent of sialin. *FASEB J.* 27, 1264–1274. doi: 10.1096/fj.12-206300

Mrzljak, L., and Munoz-Sanjuan, I. (2015). Therapeutic strategies for huntington's disease. *Curr. Top. Behav. Neurosci.* 22, 161–201.

Mullard, A. (2019). Pioneering antisense drug heads into pivotal trials for Huntington disease. *Nat. Rev. Drug. Discov.* 18, 161–163. doi: 10.1038/d41573-019-00018-7

Murphy-Royal, C., Dupuis, J. P., Varela, J. A., Panatier, A., Pinson, B., Baufreton, J., et al. (2015). Surface diffusion of astrocytic glutamate transporters shapes synaptic transmission. *Nat. Neurosci.* 18, 219–226. doi: 10.1038/nn.3901

Muto, M., Mori, M., Liu, J., Uzawa, A., Uchida, T., Masuda, H., et al. (2017). Serum soluble Talin-1 levels are elevated in patients with multiple sclerosis, reflecting its disease activity. *J. Neuroimmunol.* 305, 131–134. doi: 10.1016/j.jneuroim.2017.02.008

Nagai, J., Rajbhandari, A. K., Gangwani, M. R., Hachisuka, A., Coppola, G., Masmanidis, S. C., et al. (2019). Hyperactivity with disrupted attention by activation of an astrocyte synaptogenic cue. *Cell* 177, 1280–1292. doi: 10.1016/j.cell.2019.03.019

Parievsky, A., Moore, C., Kamdjou, T., Cepeda, C., Meshul, C. K., and Levine, M. S. (2017). Differential electrophysiological and morphological alterations of thalamostriatal and corticostriatal projections in the R6/2 mouse model of Huntington's disease. *Neurobiol. Dis.* 108, 29–44. doi: 10.1016/j.nbd.2017.07.020

Parsons, M. P., Vanni, M. P., Woodard, C. L., Kang, R., Murphy, T. H., and Raymond, L. A. (2016). Real-time imaging of glutamate clearance reveals normal striatal uptake in Huntington disease mouse models. *Nat. Commun.* 7:11251. doi: 10.1038/ncomms11251

Percie du, S. N., Ahluwalia, A., Alam, S., Avey, M. T., Baker, M., Browne, W. J., et al. (2020). Reporting animal research: explanation and elaboration for the ARRIVE guidelines 2.0. *PLoS Biol.* 18:e3000411. doi: 10.1371/journal.pbio.3000411

Piniella, D., Martinez-Blanco, E., Ibanez, I., Bartolome-Martin, D., Porlan, E., Diez-Guerra, J., et al. (2018). Identification of novel regulatory partners of the glutamate transporter GLT-1. *Glia* 66, 2737–2755. doi: 10.1002/glia.23524

Plotkin, J. L., and Surmeier, D. J. (2015). Corticostriatal synaptic adaptations in Huntington's disease. *Curr. Opin. Neurobiol.* 33C, 53–62. doi: 10.1016/j.conb.2015.01.020

Plotkin, J. L., Day, M., Peterson, J. D., Xie, Z., Kress, G. J., Rafalovich, I., et al. (2014). Impaired TrkB receptor signaling underlies corticostriatal dysfunction in Huntington's disease. *Neuron* 83, 178–188. doi: 10.1016/j.neuron.2014.05.032

Reiner, A., and Deng, Y. P. (2018). Disrupted striatal neuron inputs and outputs in Huntington's disease. *CNS Neurosci. Ther.* 24, 250–280. doi: 10.1111/cns.12844

Rimmele, T. S., Rocher, A. B., Wellbourne-Wood, J., and Chatton, J. Y. (2017). Control of glutamate transport by extracellular potassium: basis for a negative feedback on synaptic transmission. *Cereb. Cortex* 27, 3272–3283. doi: 10.1093/cercor/bhx078

Rosenblatt, A., Abbott, M. H., Gourley, L. M., Troncoso, J. C., Margolis, R. L., Brandt, J., et al. (2003). Predictors of neuropathological severity in 100 patients with Huntington's disease. *Ann. Neurol.* 54, 488–493. doi: 10.1002/ana.10691

Rosenblum, L. T., Shamamandri-Markandaiah, S., Ghosh, B., Foran, E., Lepore, A. C., Pasinelli, P., et al. (2017). Mutation of the caspase-3 cleavage site in the astroglial glutamate transporter EAAT2 delays disease progression and extends lifespan in the SOD1-G93A mouse model of ALS. *Exp. Neurol.* 292, 145–153. doi: 10.1016/j.expneurol.2017.03.014

Rothe, T., Deliano, M., Wojtowicz, A. M., Dvorzhak, A., Harnack, D., Paul, S., et al. (2015). Pathological gamma oscillations, impaired dopamine release, synapse loss and reduced dynamic range of unitary glutamatergic synaptic transmission in the striatum of hypokinetic Q175 Huntington mice. *Neuroscience* 311, 519–538. doi: 10.1016/j.neuroscience.2015.10.039

Russell, D. S., Barret, O., Jennings, D. L., Friedman, J. H., Tamagnan, G. D., Thomae, D., et al. (2014). The phosphodiesterase 10 positron emission tomography tracer, [18F]MNI-659, as a novel biomarker for early Huntington disease. *JAMA Neurol.* 71, 1520–1528. doi: 10.1001/jamaneurol.2014.1954

Sato, J., Horibe, S., Kawauchi, S., Sasaki, N., Hirata, K. I., and Rikitake, Y. (2018). Involvement of aquaporin-4 in laminin-enhanced process formation of mouse astrocytes in 2D culture: roles of dystroglycan and alpha-syntrophin in aquaporin-4 expression. *J. Neurochem.* 147, 495–513. doi: 10.1111/jnc.14548

Scott, H. A., Gebhardt, F. M., Mitrovic, A. D., Vandenberg, R. J., and Dodd, P. R. (2011). Glutamate transporter variants reduce glutamate uptake in Alzheimer's disease. *Neurobiol. Aging* 32:553.e1–11. doi: 10.1016/j.neurobiolaging.2010.03.008

Sharma, K., Schmitt, S., Bergner, C. G., Tyanova, S., Kannaiyan, N., Manrique-Hoyos, N., et al. (2015). Cell type- and brain region-resolved mouse brain proteome. *Nat. Neurosci.* 18, 1819–1831. doi: 10.1038/nn.4160

Shin, J. Y., Fang, Z. H., Yu, Z. X., Wang, C. E., Li, S. H., and Li, X. J. (2005). Expression of mutant huntingtin in glial cells contributes to neuronal excitotoxicity. *J. Cell Biol.* 171, 1001–1012. doi: 10.1083/jcb.200508072

Spuler, S., Krug, H., Klein, C., Medialdea, I. C., Jakob, W., Ebersbach, G., et al. (2010). Myopathy causing camptocormia in idiopathic Parkinson's disease: a multidisciplinary approach. *Mov. Disord.* 25, 552–559. doi: 10.1002/mds.22913

Steffan, J. S., Agrawal, N., Pallos, J., Rockabrand, E., Trotman, L. C., Slepko, N., et al. (2004). SUMO modification of huntingtin and Huntington's disease pathology. *Science* 304, 100–104. doi: 10.1126/science.1092194

Tabrizi, S. J., Ghosh, R., and Leavitt, B. R. (2019). Huntingtin lowering strategies for disease modification in Huntington's disease. *Neuron* 101, 801–819.

Tabrizi, S. J., Scahill, R. I., Owen, G., Durr, A., Leavitt, B. R., Roos, R. A., et al. (2013). Predictors of phenotypic progression and disease onset in premanifest and early-stage Huntington's disease in the TRACK-HD study: analysis of 36-month observational data. *Lancet Neurol.* 12, 637–649. doi: 10.1016/S1474-4422(13)70088-7

Tong, X., Ao, Y., Faas, G. C., Nwaobi, S. E., Xu, J., Haustein, M. D., et al. (2014). Astrocyte Kir4.1 ion channel deficits contribute to neuronal dysfunction in Huntington's disease model mice. *Nat. Neurosci.* 17, 694–703. doi: 10.1038/nn.3691

Underhill, S. M., Wheeler, D. S., and Amara, S. G. (2015). Differential regulation of two isoforms of the glial glutamate transporter EAAT2 by DLG1 and CaMKII. *J. Neurosci.* 35, 5260–5270. doi: 10.1523/JNEUROSCI.4365-14.2015

Vandenberg, R. J., and Ryan, R. M. (2013). Mechanisms of glutamate transport. *Physiol. Rev.* 93, 1621–1657.

Veldman, M. B., and Yang, X. W. (2018). Molecular insights into cortico-striatal miscommunications in Huntington's disease. *Curr. Opin. Neurobiol.* 48, 79–89. doi: 10.1016/j.conb.2017.10.019

Vonsattel, J. P., and DiFiglia, M. (1998). Huntington disease. *J. Neuropathol. Exp. Neurol.* 57, 369–384.

Wanker, E. E., Ast, A., Schindler, F., Trepte, P., and Schnoegl, S. (2019). The pathobiology of perturbed mutant huntingtin protein-protein interactions in Huntington's disease. *J. Neurochem.* 151, 507–519. doi: 10.1111/jnc.14853

Wheatley, S. C., Suburo, A. M., Horn, D. A., Vucicevic, V., Terenghi, G., Polak, J. M., et al. (1992). Redistribution of secretory granule components precedes that of synaptic vesicle proteins during differentiation of a neuronal cell line in serum-free medium. *Neuroscience* 51, 575–582. doi: 10.1016/0306-4522(92)90297-f

Zeitler, B., Froelich, S., Marlen, K., Shivak, D. A., Yu, Q., Li, D., et al. (2019). Allele-selective transcriptional repression of mutant HTT for the treatment of Huntington's disease. *Nat. Med.* 25, 1131–1142. doi: 10.1038/s41591-019-0478-3

Conflict of Interest: The authors declare that the research was conducted in the absence of any commercial or financial relationships that could be construed as a potential conflict of interest.

frontiers
in Cellular Neuroscience

ORIGINAL RESEARCH
published: 04 March 2022
doi: 10.3389/fncel.2022.831061

Activation of Glutamate Transport Increases Arteriole Diameter *in vivo*: Implications for Neurovascular Coupling

Joshua G. Jackson[1,2*†], Elizabeth Krizman[1,2], Hajime Takano[1,3], Meredith Lee[1], Grace H. Choi[4], Mary E. Putt[4] and Michael B. Robinson[1,5*]

[1] Children's Hospital of Philadelphia, Philadelphia, PA, United States, [2] Department of Pediatrics, University of Pennsylvania, Philadelphia, PA, United States, [3] Department of Neurology, University of Pennsylvania, Philadelphia, PA, United States, [4] Department of Biostatistics, Epidemiology & Informatics, University of Pennsylvania, Philadelphia, PA, United States, [5] Department of Systems Pharmacology and Translational Therapeutics, University of Pennsylvania, Philadelphia, PA, United States

Edited by:
Arturo Ortega,
Centro de Investigación y de Estudios Avanzados del Instituto Politécnico Nacional, Mexico

Reviewed by:
Emmanuel Hermans,
Catholic University of Louvain, Belgium
Yun Zhou,
University of Oslo, Norway

***Correspondence:**
Joshua G. Jackson
Jgj33@drexel.edu
Michael B. Robinson
robinson@pennmedicine.upenn.edu

†Present address:
Joshua G. Jackson,
Department of Pharmacology and Physiology,
Drexel University College of Medicine,
Philadelphia, PA, United States

Specialty section:
This article was submitted to Cellular Neurophysiology, a section of the journal Frontiers in Cellular Neuroscience

Received: *07 December 2021*
Accepted: *24 January 2022*
Published: *04 March 2022*

Citation:
Jackson JG, Krizman E, Takano H, Lee M, Choi GH, Putt ME and Robinson MB (2022) Activation of Glutamate Transport Increases Arteriole Diameter in vivo: Implications for Neurovascular Coupling. Front. Cell. Neurosci. 16:831061. doi: 10.3389/fncel.2022.831061

In order to meet the energetic demands of cell-to-cell signaling, increases in local neuronal signaling are matched by a coordinated increase in local blood flow, termed neurovascular coupling. Multiple different signals from neurons, astrocytes, and pericytes contribute to this control of blood flow. Previously, several groups demonstrated that inhibition/ablation of glutamate transporters attenuates the neurovascular response. However, it was not determined if glutamate transporter activation was sufficient to increase blood flow. Here, we used multiphoton imaging to monitor the diameter of fluorescently labeled cortical arterioles in anesthetized C57/B6J mice. We delivered vehicle, glutamate transporter substrates, or a combination of a glutamate transporter substrate with various pharmacologic agents via a glass micropipette while simultaneously visualizing changes in arteriole diameter. We developed a novel image analysis method to automate the measurement of arteriole diameter in these time-lapse analyses. Using this workflow, we first conducted pilot experiments in which we focally applied L-glutamate, D-aspartate, or L-*threo*-hydroxyaspartate (L-THA) and measured arteriole responses as proof of concept. We subsequently applied the selective glutamate transport substrate L-THA (applied at concentrations that do not activate glutamate receptors). We found that L-THA evoked a significantly larger dilation than that observed with focal saline application. This response was blocked by co-application of the potent glutamate transport inhibitor, L-(2S,3S)-3-[3-[4-(trifluoromethyl)-benzoylamino]benzyloxy]-aspartate (TFB-TBOA). Conversely, we were unable to demonstrate a reduction of this effect through co-application of a cocktail of glutamate and GABA receptor antagonists. These studies provide the first direct evidence that activation of glutamate transport is sufficient to increase arteriole diameter. We explored potential downstream mechanisms mediating this transporter-mediated dilation by using a Ca^{2+} chelator or inhibitors of reversed-mode Na^+/Ca^{2+} exchange, nitric oxide synthetase, or cyclo-oxygenase. The estimated effects and confidence intervals suggested some form of inhibition for a number of these inhibitors. Limitations to our study design prevented definitive conclusions with respect to these downstream inhibitors; these limitations are discussed along with possible next steps.

Understanding the mechanisms that control blood flow are important because changes in blood flow/energy supply are implicated in several neurodegenerative disorders and are used as a surrogate measure of neuronal activity in widely used techniques such as functional magnetic resonance imaging (fMRI).

Keywords: glutamate transport, arteriole diameter, neurovascular coupling, astrocyte, *in vivo* microscopy

INTRODUCTION

The adult human brain represents about 2% of total body weight, but consumes up to 20% of the basal metabolic rate (for reviews, see Shulman et al., 2004; Hertz et al., 2007; Harris et al., 2012; Stobart and Anderson, 2013; Weber and Barros, 2015). Compared to other organs, the brain has relatively low levels of stored glucose in the form of glycogen (Obel et al., 2012) and instead depends on local delivery of energy substrates by a dense network of blood vessels (Bohn et al., 2016). Acute decreases in and/or a loss of blood flow, such as those observed with stroke or a heart attack, are associated with rapid brain damage (Hinzman et al., 2014; Jackman and Iadecola, 2015), and chronic decreases in blood flow have been observed in individuals with cognitive decline and dementia (Leeuwis et al., 2017, 2018).

The brain matches increases in local metabolic demand caused by neuronal activity with corresponding increases in local blood flow, in a process termed neurovascular coupling (NVC). This process supports the energetic costs of cellular signaling, including costs associated with vesicular transmitter packaging/release and membrane repolarization after activation of ligand-/voltage-gated ion channels (Howarth et al., 2012). Neurovascular coupling provides the signal for functional/BOLD magnetic resonance imaging (fMRI) studies. It also underlies some versions of 2-deoxyglucose-based positron emission tomography (PET) imaging, and near-infrared spectroscopy (Raichle and Mintun, 2006; Hillman, 2014).

Release of neurotransmitters, particularly glutamate, stimulates increases in Ca^{2+} in astrocytes and results in the production/release of various vasoactive molecules on to the vasculature to drive changes in vessel diameter (Porter and McCarthy, 1996; Zonta et al., 2003; Filosa et al., 2004; Mishra et al., 2016). Uncaging of Ca^{2+} from astrocyte endfeet is sufficient to evoke vessel dilation (Takano et al., 2006), and inhibition of metabotropic glutamate receptor 5 (mGluR5) reduces neurovascular coupling evoked by odor (Petzold et al., 2008) and whisker stimulation (Wang et al., 2006) *in vivo*. The role of mGluR5 activation in this response is, however, complicated by the observation that most mGluR5 is expressed by neurons in the cortex in the adult nervous system (Sun et al., 2013; Zhang et al., 2014). Interestingly many of these studies also implicated an additional pathway, glutamate uptake, in mediating NVC (Gurden et al., 2006; Petzold et al., 2008; Schummers et al., 2008). Using genetic approaches to reduce expression of astrocytic glutamate transporters, three different groups implicated glutamate uptake in the regulation of NVC (Voutsinos-Porche et al., 2003; Herard et al., 2005; Martin et al., 2012). Three additional studies have also demonstrated that acute inhibition of glutamate uptake with threo-ß-benzyloxyaspartate (TBOA) attenuates stimulus-evoked changes in the intrinsic optical signal (a measure of blood O_2) or stimulus-induced increases in blood flow in olfactory bulb or visual cortex (Gurden et al., 2006; Petzold et al., 2008; Schummers et al., 2008). Together, these studies suggested that glutamate transport is required for neuronal activity-dependent increases in blood flow, but it has not been determined if activation of glutamate transport is sufficient to increase blood flow.

In this study, we developed an approach pairing multiphoton imaging of arteriole diameter with focal application of glutamate transporter substrates and pharmacological inhibitors in the cortex of mice. We provide direct evidence that activation of glutamate transport is sufficient to cause an increase in arteriole diameter. We show that this effect is blocked by co-application of a selective, pan inhibitor of glutamate transporters, but there was little evidence of inhibition by a cocktail of glutamate and GABA receptor antagonists. We explored the effects of a number of pharmacologic inhibitors of some of the downstream signals that have been implicated in neurovascular coupling. While a clear effect of transporter substrates on arteriole diameter is observed, limitations to the study design prevent us from making firm conclusions as to the ultimate downstream mediators. We discuss these limitations and provide a roadmap for potential next steps.

MATERIALS AND METHODS

Materials

Reagent	Dose/Concentration (if applicable)	Company	Catalog Number
C57BL/6J mice		Jackson Laboratories	000664
Head Plate		Narishige	CP-1
VetBond		3M	006245
Dental Acrylic		Lang Dental Mfg. Co. Inc.	1334
Trephine drill bit		Fine Science Tools	18004-27
Borosilicate Glass Capillaries	Used to make glass pipettes	Kwik-Fil	18150F-4
Isofluorane	3–4% induction, 1-2% maintenance	Piramal	66794-017-10
Alpha Chloralose	5mg/ml in 20% PEG. Inject 50 ug/g mouse weight	Sigma	23120
PEG; Polyethylene glycol	20% solution in saline	Fluka	81300

(Continued)

(Continued)

Reagent	Dose/Concentration (if applicable)	Company	Catalog Number
Fluorescein Dextran, 70,000 MW, Anionic	5% stock solution in saline. Inject 65 μl in tail vein.	Invitrogen	D1823
Rhodamine Dextran, 10,000 MW, Anionic	5% stock solution in saline. Dilute to 0.5% with drug/vehicle for picospritz.	Invitrogen	D1824
AlexaFluor 633 hydrazide	1mg/ml stock solution in saline. Inject 25 μl in tail vein.	Invitrogen	A30634
L-Glutamic acid	100 μM and 1mM in ACSF. Equimolar equivalent of NaOH. pH = 7.4	Sigma	G1251
D-Aspartic acid	100 μM and 1 mM in ACSF. Equimolar equivalent of NaOH. pH = 7.4	Sigma	219096
L-THA; L-(-)-threo-3-Hydroxyaspartic acid	100 μM and 1 mM in ACSF Equimolar equivalent of NaOH. pH = 7.4	Tocris	0183
[1.2pt] TFB-TBOA; (3S)-3-[[3-[[4-(Trifluoromethyl) benzoyl]amino]phenyl] methoxy]-L-aspartic acid	1 μM in ACSF Equimolar equivalent of NaOH, pH = 7.4	Tocris	2532
KB-R7943; 2-[2-[4-(4-Nitrobenzyloxy)phenyl]ethyl] isothiourea mesylate	15 μM in 0.1% DMSO in ACSF	Tocris	1244
[1.2pt] YM-244769; N-[(3-Aminophenyl)methyl]-6-[4-[(3-fluorophenyl)methoxy] phenoxy]-3-pyridinecarboxamide dihydrochloride	1 μM in 0.1% DMSO in ACSF	Tocris	4544
DNQX; 6,7-Dinitroquinoxaline-2,3-dione	10 μM in ACSF	Tocris	2312
D-APV; D-(-)-2-Amino-5-phosphonopentanoic acid	50 μM in ACSF	Tocris	0106
MCPG; (RS)-α-Methyl-4-carboxyphenylglycine disodium salt	1 mM in ACSF	Tocris	3696
R-Baclofen; (R)-4-Amino-3-(4-chlorophenyl)butanoic acid	100 μM in ACSF	Tocris	0796
BAPTA; 1,2-Bis(2-aminophenoxy)ethane-N,N,N′,N′-tetraacetic acid tetrakis(acetoxymethyl ester)	200 μM in ACSF	Tocris	2787
NPA; N5-[Imino(propylamino)methyl]-L-ornithine hydrochloride	2 μM in ACSF	Tocris	1200
Indomethacin; 1-(4-Chlorobenzoyl)-5 -methoxy-2-methyl-1H-indole	10 μM in 0.1% DMSO in ACSF	Tocris	1708
Dimethyl sulfoxide (DMSO)		Sigma	34869

Source of Mice and Preparation for Imaging

This study was reviewed and approved by the Institutional Animal Care and Use Committee at The Children's Hospital of Philadelphia prior to performing these procedures and imaging. Adult (6–12 weeks old) male and female C57BL/6J mice were initially purchased from an outside vendor and used to establish a breeding colony that was maintained at the Children's Hospital of Philadelphia. Replacement breeders were periodically purchased from the same vendor to prevent genetic drift. If acquired from an outside vendor, the mice acclimated to the animal facility for at least 24 h prior to the procedure. Mice were housed in cages of two to five in 12-h light/dark cycles and given access to food *ad libitum*.

Mice were anesthetized in an induction chamber by inhalation of 3–4% isoflurane. Once the mouse was anesthetized as evidenced by lack of spontaneous movement or vocalization and lack of response to a tail or paw pinch, the mouse was placed on a heated pad and the head was stabilized in a stereotaxic frame (Kopf Instruments). The mouse was kept under 1–2% isofluorane anesthesia throughout the surgical procedure. Alexafluor633 hydrazide (Invitrogen, 25 μl of 1mg/ml in saline) was injected via the lateral tail vein to allow selective labeling of the arteries (Shen et al., 2012). This was done prior to surgery to allow sufficient time for the dye to label the vascular smooth muscle cells, but clear from the vessel lumen. One to two drops of sterile eye drops were applied to each eye prior to surgery to protect from dehydration. The fur on the mouse's head was removed with scissors and the skin was cleaned with a 70% alcohol wipe. Using surgical scissors an incision was made along the midline. The skull surface was scraped with a scalpel so the VetBond used in the next step could adhere efficiently. A head plate with a 5 mm diameter observation hole was glued (using VetBond) to the skull. The plate was further sealed to the skull with dental acrylic. The acrylic was allowed to set for 20 min prior to drilling. A small craniotomy over the somatosensory cortex (2.4 mm in diameter) was made 1mm posterior to bregma and 3.5 mm lateral from midline over on the right hemisphere (Sato et al., 2007) with a trephining bit using a high-speed surgical drill (Foredom) taking care to avoid penetrating the dura. The circular flap of bone was removed to expose the dura, which was then dissected off the surface of the brain using a pair of fine tip (Dumont #5.5) forceps and a surgical needle (30G) bent to form a hook-like cutting tool. The surface of the cortex was kept moist with sterile artificial cerebrospinal fluid (ACSF; 125 mM NaCl, 5 mM KCl, 10 mM glycine, 10 mM HEPES, 3.1 mM $CaCl_2$, 1.2 mM $MgCl_2$, 10 mM glucose, pH 7.4, sterile filtered). Extreme care was taken to ensure that the cortical surface was undamaged. The surface was sealed with low-melt agarose (1% in sterile ACSF w/v). A rectangular piece of #1 coverglass was positioned on top of the agarose and secured with a small drop of acrylic dental cement at the edges. A small gap, oriented perpendicular to the micropipette, was left uncovered at the edge of the craniotomy to allow pipette placement. To visualize the vasculature, Fluorescein Dextran (70K MW, Invitrogen, 65 μl of 5% solution in saline w/v) was injected into the tail vein.

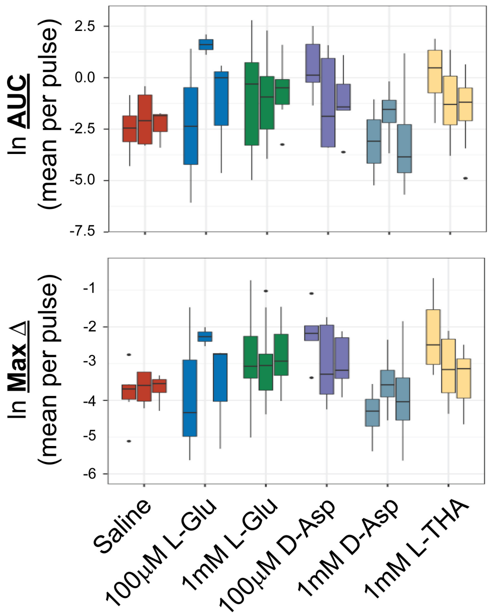

FIGURE 1 | Effects of saline or glutamate transporter substrates on arteriole diameter. Saline, L-glutamate, D-aspartate, or L-THA were picospritzed near cortical arterioles. The area of the largest dilation and the maximum change were measured as described in the text. The original data were the mean values for each animal. The median is indicated by the horizontal line and the interquartile range (25th to 75th percentile) by the box. The whiskers are 1.5 times the interquartile range, added or subtracted to the percentiles, and drawn back to the nearest point. Values outside of the whiskers are outliers (dots). The data for saline are from 6 animals (3 male,3 female), the data for 100 μM L-Glu are from 3 animals (1 male, 2 females), the data for 1 mM L-Glu are from 12 animals (12 males), the data for 100 μM D-Asp are from 5 animals (3 males, 2 females), the data for 1 mM D-Asp are from 4 animals (4 males), the data for 1 mM L-THA are from 11 animals (7 males, 4 females).

Others have loaded BAPTA-AM or Ca^{2+} dyes to the cortex which are subsequently dispersed through the astrocytic syncytium (Nimmerjahn et al., 2004). For one experimental group, the Ca^{2+} chelator/indicator, BAPTA-AM (20 μM) was applied to the cortical surface for 20 min followed by a rinse with sterile ACSF and sealing with low-melt agarose as described above. Then Fluorescein Dextran was injected as described above. Next, the mouse was transitioned from isoflurane to alpha chloralose anesthesia (50 μg/g, intraperitoneal) followed by a slow elimination of isoflurane.

2-Photon Imaging

Following installation of the cranial window, the entire stereotactic base (SR-9AM, Narishige) with the mouse mounted by a head plate (CP1, Narishige) was placed on the microscope stage (MP200, Thorlabs). Glass micropipettes (borosilicate Kwik-Fil, World Precision Instruments) were prepared on a Flaming-Brown pipette puller (Sutter). Resistance of each pipette (∼10 MΩ) was verified prior to use to prevent leakage of dye/drug into the cortex prior to pressure ejection. Glass micropipettes were filled with vehicle (saline or saline with 0.1% DMSO both containing 0.5% Rhodamine Dextran; Invitrogen) or vehicle with pharmacologic agents. The pipette was attached to a pressure transduction system (Picospritzer III, Parker Hannifin) and was roughly positioned over a field containing a descending arteriole using a micromanipulator (ROE-200, Sutter Instruments) while visualized using a 4x objective under epi-illumination. The objective was then switched to a water immersion 16x lens (LWD, NA = 0.8, Nikon) attached to a Thorlabs Bergamo multiphoton microscope equipped with a femtosecond laser (MaiTaiDeepSee, Spectra Physics), and images were captured with ThorImage software (Thorlabs). An area containing 1-4 arterioles was identified based on the Alexafluor633 hydrazide and the pipette was visualized with rhodamine such that the distance between both was kept relatively consistent at approximately 40 μm. We utilized an episodic imaging framework with each epoch consisting of a 5-sec baseline period followed by a 50 ms (5psi) pressure pulse and a 2-min acquisition period (10–20Hz sampling frequency). Based on the pilot experiments and previous reports in the literature, we anticipated relatively small effect sizes and possible variability in the responses, therefore we recorded a total of 3 pulses from each field with a 5-min recovery period between each pulse. The pulse delay (relative to acquisition start) was controlled using ThorImage software and a Master8 pulse stimulator (AMPI). To further control for pipette leaks, a sham imaging epoch was performed prior to each experiment, where the pipette was positioned close to the vessel, but no pressure injection was initiated. Injection (or leak) were verified by increases in red fluorescence intensity (0.5% Rhodamine Dextran) at the tip of the pipette. In several cases, the effects of a particular agent or vehicle were examined in more than one field, but no more than 2 fields were included in the analysis. At the end of the imaging session, the mouse was euthanized by cervical dislocation while still under anesthesia.

Image Analyses

Initially, images were analyzed in a semi-automated manner using a series of custom macros in ImageJ/FIJI. Briefly, a user-defined line was placed perpendicular to the long-axis of the arteriole and the profile of the vessel (full-width, half max) calculated for all time-points in the image series. Multiple parameters including max change in vessel diameter, area-under the curve, and vessel duration were extracted from the xt profile. These programs were used to analyze the initial observations of L-glutamate, D-aspartate, and L-THA-evoked changes in vessel diameter.

To standardize the analyses, we subsequently created a fully automated, multi-step workflow to analyze the arteriole images. First, ImageJ/FIJI was used to de-interleave the two channels and standardize all the time-series images (videos). One channel captured Fluorescein Dextran which was used to measure arteriole diameter, and in the other channel Rhodamine Dextran and AlexaFluor 633 fluorescence were used to test for pipette leaks during the initial sham imaging epoch, identify the pulse frame, confirm pressure ejection, and measure the distance between the pipette and the vessel. The videos were standardized according to the following parameters: Scale change to width 544 pixels, height 336 pixels, depth 1400 images, Interpolation Bilinear, Average process; Converted to Gray scale;

and saved as 8-bit tiff files. Next, we analyzed the Fluorescein Dextran videos of the arterioles using custom Matlab code. Zonta and colleagues previously drew several lines across each vessel to measure changes in diameter over time (Zonta et al., 2003). We used a similar strategy and the first Matlab program, BloodV10, automatically drew up to 8 lines perpendicular to the centerline of the arteriole of interest. When the program identified more than one useable arteriole, one arteriole was randomly chosen and kymographs from the resulting time-series images were generated. Lines that did not cross the arteriole were eliminated. Artifacts caused by movements during imaging were detected by calculating an image feature related to the focus of the image at each timepoint, e.g., edge sharpness. The focus feature was normalized to baseline and if it exceeded three standard deviations above or below baseline recording, the data at the time point were excluded from subsequent analysis. The second Matlab program, KymoHT6, applied a spatial mean filter and binarized the kymographs using two Gaussian fit to image intensity histogram to yield the width of the arteriole as a function of time. The width data were averaged every second and normalized to baseline (3 s before the pulse). The MATLAB programs created for this analysis are freely available on GitHub[1].

The data from all kymographs for each line were exported and using the area-under-the-curve analysis function in Graphpad PRISM 9.0, the number of peaks, the total area under each individual peak (AUC), as well as data about each individual peak including the maximum change, the time of this maximum change, and the times of the beginning and end of each peak were calculated for each line profile. Baseline was set at zero and only dilations were quantified. Analyses of these results included some exploratory data visualization as well as data cleaning and transformation. These steps were performed reproducibly using Python code (version 3.8) in Jupyter notebooks.[2] To visualize the diameter of the blood vessel over time for each pulse, the data for that pulse, including up to 8 line profiles, were isolated using a unique pulse identifier and plotted. To identify the peak with the largest area, the original data were transposed so that the individual line profiles were put in rows, and the peak data were put in columns. From there, the maximum percent area could be identified. Data cleaning to unambiguously identify column names was required. The data for the peak with the largest percent area for each line profile were saved in new data file.

The numbers of animals used in preliminary studies are presented in the legend to **Figure 1**. For the rest of the studies, a total of 99 animals (48 males, 51 females) were initially used with 93 (94%) yielding usable data. The number of animals per experimental group ranged from 3 (receptor antagonists) to 12 (100 μM L-THA alone) (see figure legends for specific numbers). Data were excluded based on the following criteria: BloodV10 was unable to draw lines across the vessel, KymoHT6 could not analyze at least 5 kymographs/lines for an individual pulse, no positive peaks were identified, gaps in recordings were greater than 20 s, fewer than 60 s of data out of 120 s, or maximum change was greater than 30%. The final analytic dataset included a total of 3055 lines.

Statistical Analyses

Initially, to explore the distribution of the area of the largest arteriole dilation (AUC) and maximum change in diameter variables, as well as broad trends across groups, we created boxplots using data pooled across fields and animals. The boxplots indicated AUC and maximum change, were strongly right-skewed [positive]. To fit the statistical models, the data were log-transformed (Ln) to achieve approximate normality of the independent variable. We fit a mixed effects model using either AUC or maximum change as the dependent variable with a random intercept term, allowing for correlations between repeated measurements on the same animal and indicating individual animals as the independent unit of analysis. Pharmacologic agent, field, pulse and the interaction between pulse and pharmacologic agent were included as fixed independent variables. A single model was fit to the entire dataset in order to use both the same negative controls (saline alone or saline plus DMSO) and positive intervention (L-THA alone) throughout. The interaction term potentially allowed the effects of a pharmacologic agent to vary by pulse; because an omnibus likelihood ratio test indicated that interaction term was highly significant ($p < 0.001$ for both AUC and Max Change), this term was retained in the final model. Using the fitted model, we constructed contrasts of interest and then exponentiated to determine ratios of the mean outcome for pairs of groups. For agents dissolved in saline, the contrasts were formed based on a direct comparison with saline, or L-THA in saline. For agents dissolved in Saline/DMSO, we first estimated the effect of the agent alone, or agent in combination with L-THA, by simply subtracting the mean of the Saline/DMSO control. The effect of the agent in combination with L-THA versus L-THA was estimated using a difference of difference approach, i.e., we took the difference of the agent plus L-THA in Saline/DMSO versus the Saline/DMSO control and then subtracted the difference between L-THA in Saline versus Saline alone. In this way we compared effects of the agent with L-THA versus L-THA alone after removing effects of Saline and DMSO, noting that no direct effect of L-THA in Saline with DMSO was measured. Using data from each pulse, differences were created on the natural log scale and then exponentiated to obtain a ratio. Effects are reported both for individual pulses, as well as by averaging across pulses. Hypothesis tests were based on Wald tests using a small-sample Satterthwaite correction to the degrees of freedom (Luke, 2017) and were two-sided without adjustment for multiple comparisons. Because the number of animals, and thus the statistical power to detect a specific effect, differed across interventions, ranking the efficacy of the interventions based on p-values would be misleading (Putt, 2021). Notably p-values lack context without an *a priori* power calculation based on assumptions about effect size and standard deviation. We thus report 95% confidence intervals (CIs) in order to assess and compare possible effect sizes. With high probability, these 95% CIs cover the unknown effect size under the hypothetical

---

[1] www.github.com/takano2050/BloodVesselAnalysis

[2] https://github.com/leemc-data-ed/blood-vessel-diameter

scenario that an infinite number of animals could be sampled and analyzed; the width of the CI reflects the precision of the estimate, a function of both the variability in the outcome and the number of animals. Unlike p-values, no *a priori* assumptions about effect sizes, standard deviations or sample size are needed to accurately interpret a 95% CI. Using forest plots, we report both the mean of the three pulses to summarize possible effects, as well as means for the individual pulses. Specifically, we report contrasts between the pharmacologic agents and the appropriate control, exponentiated to yield relative effects (ratios of the intervention to the appropriate control). For L-THA alone and L-THA with TFB-TBOA, the model for AUC was repeated separately for the male and female animals to assess the possibility of effects related to biological sex. Analyses were carried out in R version 4.0.5 (2021-03-31) R Core Team (2021). Using packages lme4 and lmerTest for the mixed effects models, and ggplot2 for graphics.

RESULTS

Several groups have demonstrated that pharmacologic inhibition or genetic deletion of glutamate transporters attenuates, or completely blocks, the increase in energy delivery or blood flow that is observed following neuronal activation (Voutsinos-Porche et al., 2003; Gurden et al., 2006; Petzold et al., 2008; Schummers et al., 2008). These studies imply that glutamate transport contributes to the coupling of neuronal activity to increased blood flow. The goal of the present study was to determine if activation of glutamate transport causes an increase in arteriole diameter *in vivo*. The overall model and the general approach is schematically summarized in **Figure 2**. In the mammalian brain, the bulk of glutamate transport is mediated by two Na^+-dependent glutamate transporters, called GLT-1 and GLAST (or EAAT2 and EAAT1, respectively) that are enriched in astrocytes (Rothstein et al., 1994; Danbolt et al., 2016).

To determine if activation of glutamate transport is sufficient to cause an increase in arteriole diameter, a small cranial window was made over the primary somatosensory "barrel" cortex in adult mice (**Figure 3**). Arterioles were differentiated from other blood vessels by injecting AlexaFluor 633 hydrazide (red), a dye that binds to elastin in vascular smooth muscle cells (Shen et al., 2012; Hill et al., 2015), via the lateral tail vein. Fluorescein-dextran (green; 70 kDa) was also injected into the tail vein and used to visualize arteriole diameter before and after a brief pulse of vehicle containing rhodamine-dextran with or without pharmacologic agents. Every application was confirmed by the appearance of extracellular rhodamine fluorescence (see **Figure 3**). This was repeated two more times at 5 min intervals. In an effort to reduce variability, we imaged arterioles of similar size; the median diameter was 16.6 μm (Interquartile range = 12.5–21.4, $n = 185$). We also tried to position the pipette at a similar distance to each arteriole. The median distance was 38.0 μm (Interquartile range = 29.9–50.3, $n = 185$).

We first tested the effects of several different transporter substrates, including L-Glu (100 μM or 1 mM), D-Asp (100 μM, or 1 mM), and L-THA (1 mM). These compounds are substrates for the Na^+-dependent glutamate transporters, but they also activate glutamate receptors (Arriza et al., 1994; Erreger et al., 2007). After all experiments were complete, we used an automated image analysis method to analyze these data (Methods: Image Analysis). In brief, the program drew up to 8 lines across the blood vessel, filtered images not in the plane/focus, calculated the average diameter from the 3 s of baseline data obtained prior to pressure application, and then generated kymographs of changes in blood vessel diameter over time for each of the lines. These kymographs were converted into two-dimensional graphs of arteriole diameter (normalized to baseline) as a function of time.

The analyses of the effects of L-Glu (100 μM or 1 mM), D-Asp (100 μM, or 1 mM), and L-THA (1 mM) are from relatively few animals and were done as pilot experiments. Therefore, the data were explored visually with no formal statistical inference. These data are included to explain the development of the methods. The boxplots suggest some trends toward larger peaks (AUC) after application of Glu, D-Asp, or 1 mM L-THA compared to saline (**Figure 1**). Similarly, there are some trends for larger effects on the maximum change observed after application of these substrates, however, as the analyses were likely underpowered to detect relevant biological effects, no statistical comparisons were made. Based on these observations, we focused our subsequent analyses on the effects of lower concentrations of L-THA (100 μM). At this concentration, L-THA does not activate ionotropic glutamate receptors (Erreger et al., 2007).

To test the hypothesis that L-THA causes an increase in arteriole diameter in excess of that observed after application of saline, we identified the largest dilation, as defined by the peak with the largest area (AUC), and measured the maximum change in diameter, time to the maximum change in diameter, and the duration of this peak. We report changes in arteriole diameter both in terms of max change and largest AUC as the area provides an integration of arteriole dilation over time whereas the max change allows one to directly calculate the size of the effect on arteriole diameter as these provide somewhat different information. The experiments with 100 μM L-THA and vehicle were inter-mixed with studies of the effects of various pharmacologic inhibitors. Across **Figures 4**, **5–8**, the saline and L-THA groups represent identical animals and are repeated for purposes of comparison. The boxplots (**Figure 4A**) suggest a substantial response to L-THA at each pulse, both for AUC and Max Change. As indicated in the methods, the overall statistical model provided evidence of different effects for at least some of the pharmacologic agents by pulse. Therefore, we have compared the data for each treatment at each individual pulse. **Tables 1–4** and the forest plots in **Figures 4**, **5–8** thus show the overall effect of each agent, summarized across the pulses, as well as the effect for each pulse. The forest plot (**Figure 4B**) present the model-based estimates of the mean difference, after exponentiating, to give a ratio of the effect of L-THA over that observed for saline. The top row shows the combination of the three pulses with individual pulses in the lower rows. The error bars show 95% CIs. Note that when a 95% CI for the ratio includes a value of 1.0, the null hypothesis of no effect cannot be ruled out at the 0.05 level, i.e., $p > 0.05$. When the effects of the three pulses are combined, the mean area of the largest dilation, area under

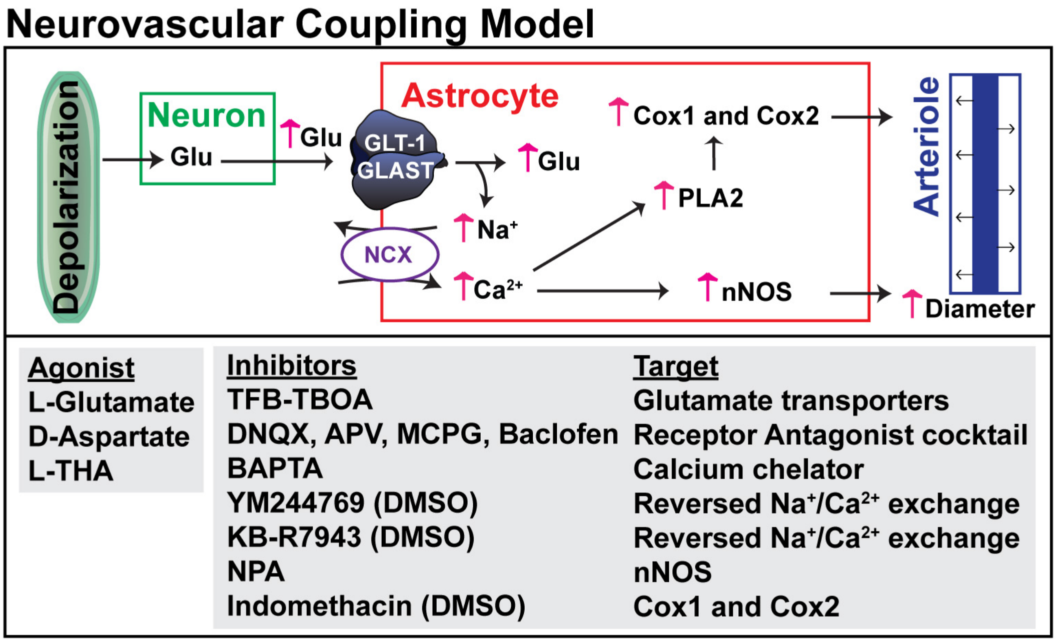

FIGURE 2 | Hypothesized mechanism for glutamate transport-dependent vasodilation. After neuronal depolarization, most of the glutamate released into the extracellular space is cleared by the astrocytic glutamate transporters, GLT-1 and GLAST. Several groups have shown that the simultaneous influx of Na^+ that drives glutamate uptake can trigger reversed operation of the Na^+/Ca^{2+} exchangers and increase in cytosolic Ca^{2+}. This Ca^{2+} can activate nitric oxide synthetase (NOS), phospholipase 2 (which generates arachidonic acid and can activate cyclooxygenase, Cox1 and Cox2), or other Ca^{2+}-activated processes. These pathways have been linked to vasodilation in several studies (for references, see results). The pharmacologic agents used to test each of these targets is also included.

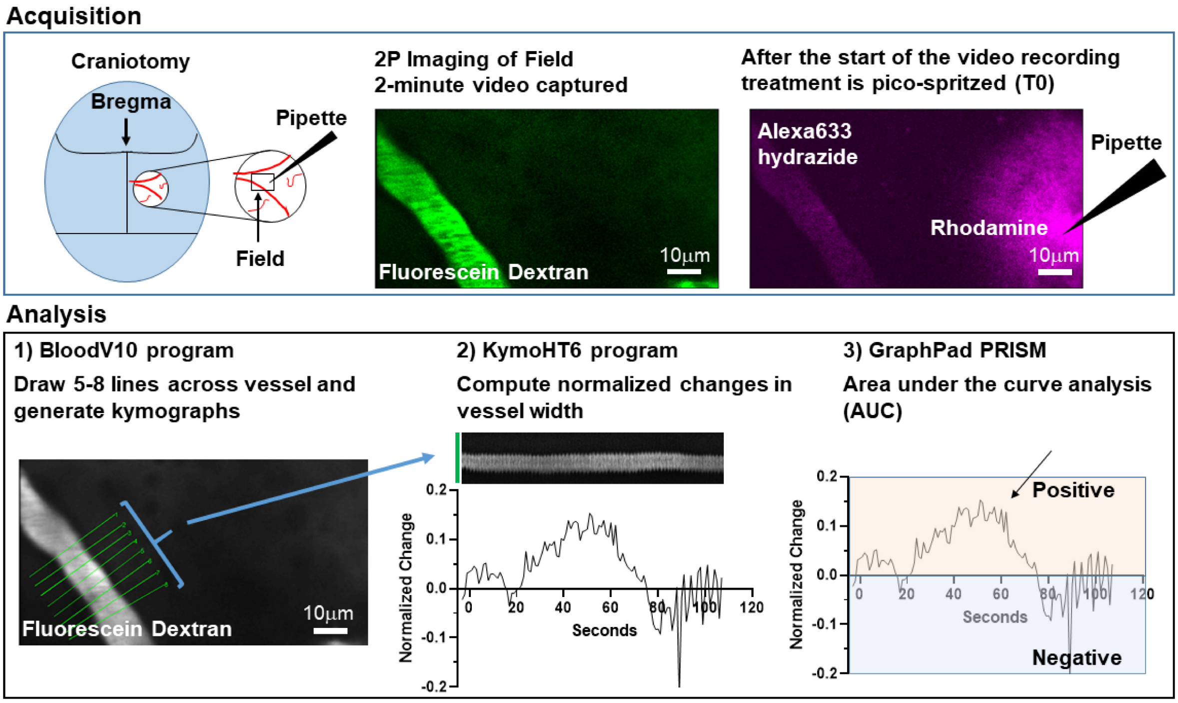

FIGURE 3 | Schematic model of methods used to analyze changes in arteriole diameter.

the curve (AUC), caused by L-THA was 5.7-fold larger than that observed after saline (95% CI, 1.7–19, p = 0.006, **Figure 4B** and **Table 1**). Similarly, the maximum change in arteriole diameter was 2.4-fold larger than that observed with saline (95% CI, 1.3–4.5, p = 0.005, **Figure 4B** and **Table 3**). The mean L-THA-induced increase in blood vessel diameter was 5.8%. As blood flow should correlate to the fourth power of radius (Poiseuille's equation) (Petzold et al., 2008), this change in arteriole diameter represents an ∼25% increase in blood flow and is similar to that elicited by sensory stimulation (whisker stimulation or odorants) (Petzold et al., 2008; Masamoto et al., 2015; Tran and Gordon, 2015). The median time to peak observed after 100 μM L-THA was 44.60 s (interquartile range = 26.0–67.5, n = 283) and the median duration of these peaks was 18.2 s (interquartile range = 6.1–41.1, n = 283). These data show that pulse application of L-THA causes a substantial increase in arteriole diameter and that this effect cannot be attributed the mechanical force of pressure application. Although we tested the effects of two different concentrations of L-Glu, D-Asp, and L-THA, it is not possible to test for concentration-dependence of these effects with so few concentrations.

As we observed considerable variability in responses to L-THA (and other agents) both within and between animals, we examined several possible sources that might modulate these results. First, we tested for overall sex differences in the responsiveness of arterioles to L-THA. Since the study was not designed to test hypotheses regarding different responses to L-THA for males and females, we refit the model used in the main analysis separately for the two biological sexes. For saline, the study included 3 females and 3 males; for L-THA, there were 5 females and 7 males, and for L-THA+ TFB-TBOA there were 2 females and 3 males. Averaged across pulses, the mean AUC after THA was 5.8-fold larger than in saline in females (95% CI 0.95–35.5, p = 0.056) and 12.9-fold larger in males (95% CI 1.7–97.6, p = 0.015). The maximum increase in diameter observed after L-THA was 2.25-fold larger than in saline for females (95% CI 0.93–5.45, p = 0.071), and 3.20 fold larger in males (95% CI 1.20–8.52, p = 0.021). Thus, the response to L-THA was substantial for both sexes. It is also possible that there is uncontrolled anatomic variability. The spread of L-THA is likely to be restricted due to the focal application and by the robust clearance mediated by Na^+-dependent glutamate transporters (Garthwaite, 1985; Herman and Jahr, 2007). **Figure 9** shows the L-THA-induced changes in diameter that were observed at individual locations (8) along the same arteriole. We depict these responses across multiple animals and with each individual L-THA application (pulse, typically 3). This illustrates three sources of variability, between-animal, between pulses within animals, and across lines within animals. For example, animals examined on 031618-2 and 092617-3 showed a substantially stronger response than, for example, 020618-1. Formal statistical methods for discerning latent classes of responders and non-responders to L-THA would require substantially larger sample sizes than used here. As indicated above, the statistical model detected variability in the response by pulse, noted previously in the boxplots and evident here as well in some animals, e.g., 051517-1. Moreover, there was considerable variability in the functional form of the response across the lines. For example, 031618-2 and 051517-1 shows little variation across lines for the individual pulses while 022018-1 tends to increase with higher values for line 6–8 compared to 1–3.

We next tested whether the L-THA-evoked increases in vessel diameter could be blocked by inhibiting glutamate transporters. We focally applied (2S,3S)-3-[3-[4-(trifluoromethyl)-benzoylamino]benzyloxy]-aspartate (TFB-TBOA) and TFB-TBOA in combination with L-THA (**Figure 4**) at descending arterioles. TFB-TBOA is a pan-inhibitor of the Glu transporters with IC_{50} values of ∼20 nM for the glial Glu transporters, 300 nM for EAAC1, and no interactions with Glu receptors at concentrations up to 100 μM (Shimamoto et al., 2004). Expressed as a ratio compared to saline, the dilations observed after application of TFB-TBOA trended toward increases in AUC (2.7-fold 95%, CI 0.6–12.6, p = 0.20, **Table 1**) and in Max Change (1.8-fold 95% CI 0.8–3.9, p = 0.12) (see **Figure 4B**, **Table 3**). When combined with L-THA, levels were near those of saline, i.e., for AUC (1.2-fold, 95% CI 0.3–4.9, p = 0.84) and Max Change (1.2-fold, 95% CI 0.6–2.4, p = 0.65) (**Tables 1**, **3**). Compared to L-THA alone, the effects observed after TFB-TBOA with L-THA tended to be lower for AUC (0.20-fold, 95% CI 0.06-0.72, p = 0.014) and Max Change (0.48-fold, 95% CI 0.26–0.91, p = 0.024) (see forest plots, **Figure 4C**). These results indicate that the effects of L-THA are blocked by TFB-TBOA. We also examined possible sex differences in this group. Averaged across pulses, the mean AUC after L-THA with TFB-TBOA was 0.27-fold that of L-THA in females (95% CI 0.04–1.87, p = 0.18) and 0.13-fold that of L-THA in males (95% CI 0.02–0.98, p = 0.048). Averaged across pulses, the maximum change after L-THA with TFB-TBOA was 0.53-fold of L-THA alone in females (95% CI 0.20–1.39, p = 0.19) and 0.41-fold of L-THA in males (95% CI 0.15–1.07, p = 0.068). Thus, within the precision of our study design, the data suggest TFB-TBOA substantially blocks the effects of L-THA in both sexes.

We tested the effects of a cocktail of iGluR antagonists, including DNQX (10 μM), D-APV (50 μM), MCPG (1 mM), and baclofen (100 μM). An identical strategy (and concentrations) was employed by Petzold et al. to demonstrate a TBOA and dihydrokainate-sensitive (i.e., glutamate transport-dependent) component to olfaction-evoked neurovascular coupling (Petzold et al., 2008). These receptor antagonists were also dissolved in saline. Although the sample sizes are small and the confidence intervals wide, this combination of receptor antagonists appeared to have minimal effect on arteriole diameter (AUC or Max Change, **Figure 5**) when expressed as a ratio of that observed with saline (1.3 or 0.9, respectively, **Tables 1**, **3**). When applied in combination with L-THA, peaks were nearly as big as those observed after THA alone (Area 4.3 versus 5.7, and max change 1.7 versus 2.4). As can been seen in the forest plots (**Figure 5B**), this cocktail of receptor antagonists trended toward a small decrease.

To determine if the effects of L-THA were dependent upon increases in astrocytic Ca^{2+}, we tested if the effects of L-THA could be blocked by application of a Ca^{2+} chelator. As others have done, we relied on the observation that cortical surface loading of various acetyl-methyl ester indicators (e.g., Oregon-green BAPTA; OGB) and chelators (e.g., BAPTA-AM)

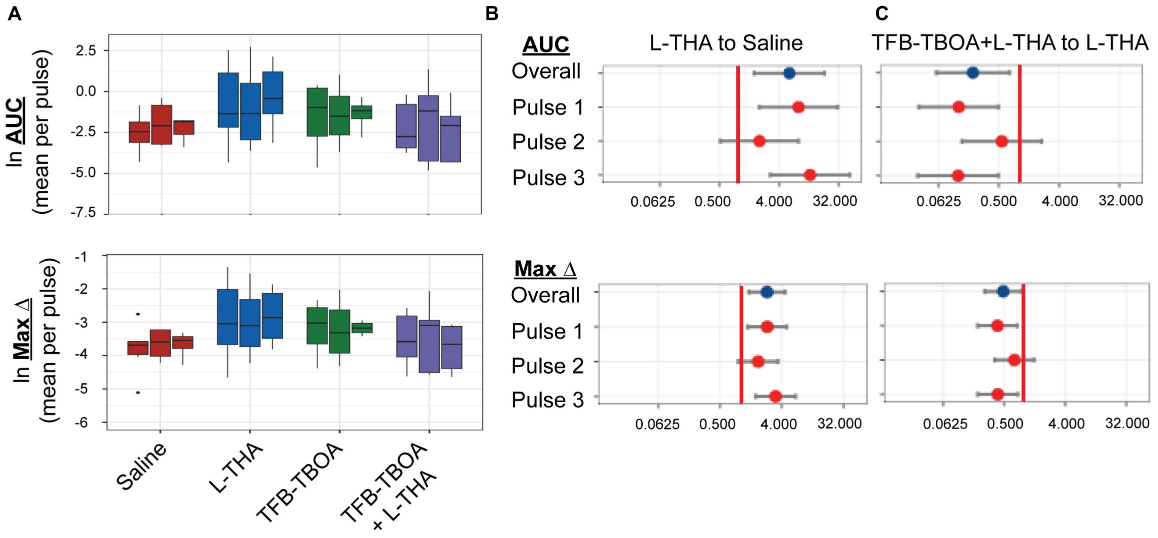

FIGURE 4 | Effects of saline, L-THA, TFB-TBOA, and TFB-TBOA with L-THA on arteriole diameter. Saline, L-THA (100 μM), TFB-TBOA (2 μM), or a combination of TFB-TBOA with L-THA were picospritzed near cortical arterioles. **(A)** Natural log (ln)-transformed raw data are presented as boxplots, using the mean of repeated measures from each animal. Raw values are from dilations (positive values), however, as data are ln-transformed, values > 1 are positive while values between 0 and 1 will appear on this scale as negative values **(B,C)** forest plots are included to visualize the results of the model and show the mean differences expressed as ratios of the effect observed with L-THA over that observed with saline **(B)** or TFB-TBOA with L-THA over that observed with L-THA **(C)**. The redline is at 1 and represents no difference. The data for saline are from 6 animals (3 males, 3 females) and are the same data as that presented in **Figures 1**, **5–9**, the data for L-THA are from 12 animals (7 males, 5 females) and are also the same as those presented in **Figures 5–9**. The data for TFB-TBOA are from 4 animals (2 males, 2 females) and the data for TFB-TBOA with L-THA are from 5 animals (3 males, 2 females).

favor distribution of dye throughout the astrocytic syncytium (Nimmerjahn et al., 2004; Navarrete et al., 2012). We applied BAPTA-AM (20 μM) to the cortical surface for 20 min prior to sealing the cranial window and moving the animal to the microscope. We did not observe overall group differences between the effects of L-THA alone and L-THA after application of BAPTA, but there is a trend toward a decrease after the first pulse (see **Figure 6**). It is conceivable that BAPTA is cleared after longer times.

Na^+-dependent glutamate uptake causes a rapid increase in intracellular Na^+ and astrocytic depolarization (Bergles and Jahr, 1997; Langer et al., 2017). The Na^+/Ca^{2+} exchangers (NCX) exchange 3 Na^+ ions for 1 Ca^{2+} ion (Minelli et al., 2007; Pappalardo et al., 2014) in either direction depending on membrane potential and the ionic gradients of Na^+ and Ca^{2+}. The reversal potential of the NCX isoforms is close to the astrocytic resting membrane potential (Kirischuk et al., 1997; Reyes et al., 2012), thus the exchangers frequently operate in the so-called "reverse-mode" (Ca^{2+} in /Na^+ out) (Blaustein et al., 2002). These transporters have turnover numbers of 2000-5000/sec giving them almost channel-like kinetic properties (Blaustein and Lederer, 1999). Na^+-dependent Glu uptake couples to increases in intracellular Ca^{2+} through this reversed operation in cell lines (Magi et al., 2013), cultured astrocytes (Reyes and Parpura, 2008; Rojas et al., 2013; Parpura et al., 2016), and in processes in organotypic cultures of rat hippocampus (Jackson and Robinson, 2015). Here, we tested the effects of two structurally dissimilar inhibitors of the reversed-mode of these exchangers, YM244769 and KB-R7943, on arteriole diameter alone and the presence of L-THA. These drugs were dissolved in DMSO and then saline to final concentration of 0.1% DMSO. Unexpectedly, compared to Saline, DMSO may have caused a small increase in AUC (Ratio of 1.89, 95% CI 0.43–8.3) and Max Change (Ratio of 1.57, 95% CI 0.75–3.27) (**Tables 1**, **3**), and we have no direct information about effects of L-THA alone in the presence of DMSO relative to saline. The effects of YM244769 and KB-R7943 alone are reported relative to saline with DMSO and then normalized to saline alone. The effects of YM244769 and KB-R7943 in combination with L-THA are reported relative to Saline with DMSO, and then normalized to the effect of L-THA alone compared to Saline **Figure 7**, see **Tables 1–4**). Our results are inconclusive, however, the findings, particularly for pulses 1 and 3, suggest that this mechanism should not be ruled out.

Several groups have demonstrated that pharmacological inhibition or genetic deletion of neuronal nitric oxide synthetase (nNOS) blocks the neurovascular response (Faraci and Breese, 1993; Yang et al., 2003; Kitaura et al., 2007; Toda et al., 2009). Although the levels of nNOS are higher in subsets of neurons, both mRNA and protein for the various nNOS isoforms are found in astrocytes (Kugler and Drenckhahn, 1996; Togashi et al., 1997; Zhang et al., 2014; Munoz et al., 2015). Based on these observations, we tested the effects of the selective inhibitor of nNOS inhibitor, Nω-propyl-L-arginine (L-NPA) (2 μM), which was dissolved in saline (Zhang et al., 1997). The effects of NPA alone or in combination with L-THA are presented in **Figure 8** (**Tables 1–4** for summary data). Compared to saline, the peaks observed after NPA trended toward being larger (AUC 3.9-fold, 95% CI 0.91–16.9, $p = 0.07$, Maximum change 2.4-fold, 95% CI

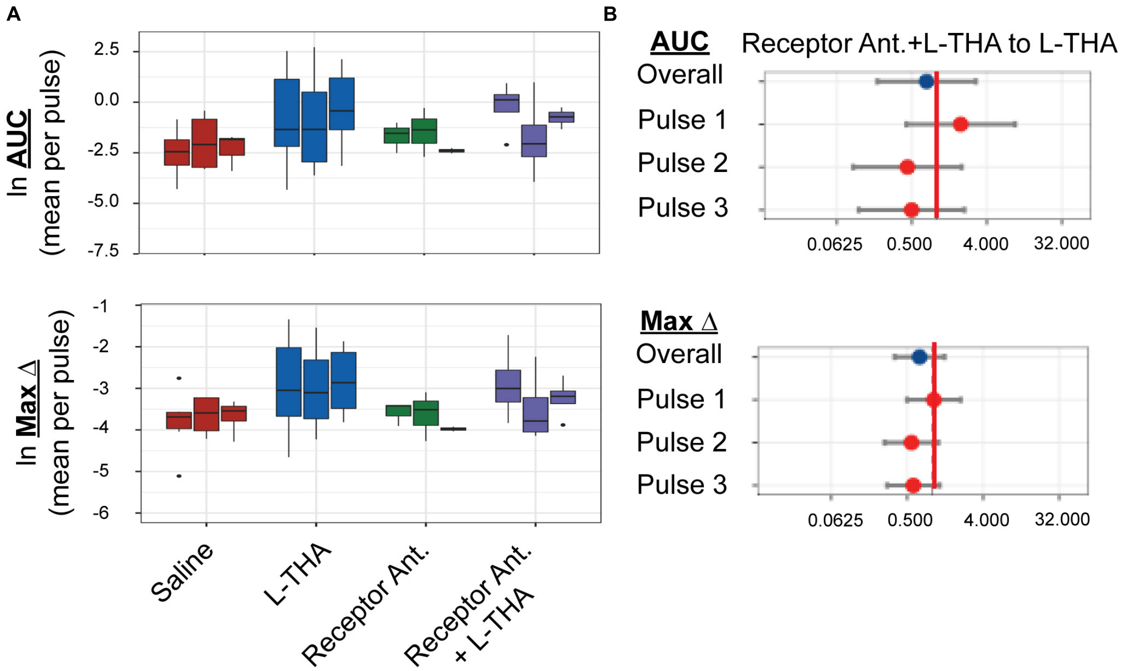

FIGURE 5 | Effects of saline, L-THA, receptor antagonists, and receptor antagonists with L-THA on arteriole diameter. Saline, L-THA (100 μM), receptor antagonist cocktail [DNQX (10 μM)/D-APV (50 μM)/MCPG (1 mM)/R-Baclofen (100 μM)], or a combination of receptor antagonist cocktail with L-THA were picospritzed near cortical arterioles. **(A)** Data are presented as boxplots. **(B)** Forest plots are also included to show the mean differences expressed as ratios of the effect of Receptor Antagonists with L-THA over that observed with L-THA. The redline is at 1 and represents no difference. The data for saline and L-THA are described in **Figure 4** legend, the data for receptor antagonists are from 3 animals (1 male, 2 females) and the data for receptor antagonists with L-THA are from 4 animals (1 male, 3 females).

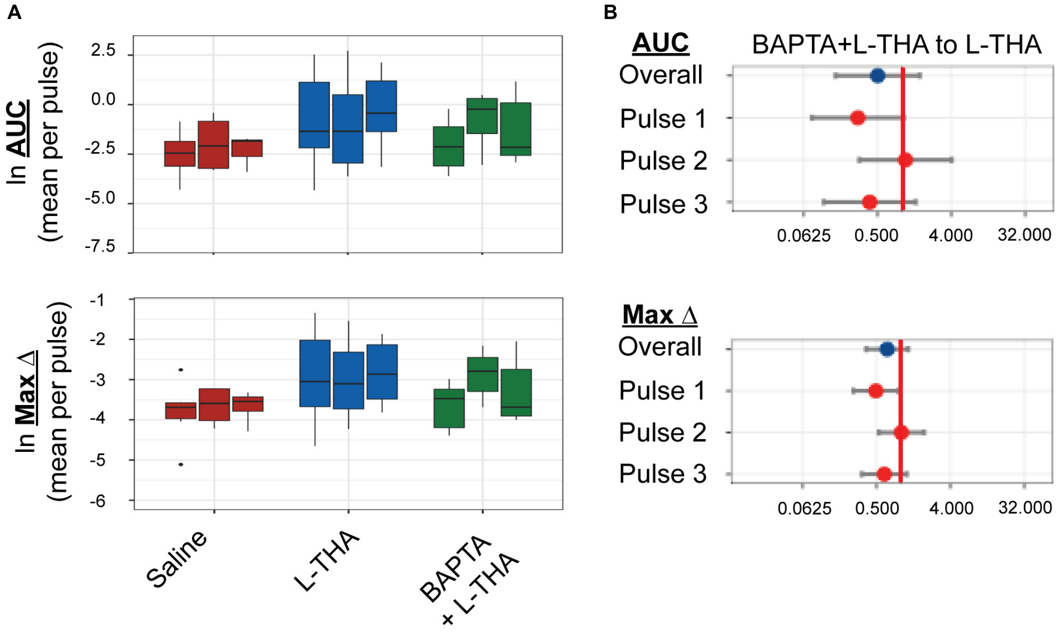

FIGURE 6 | Effects of saline, L-THA, or L-THA with BAPTA pretreatment on arteriole diameter. Saline, L-THA (100 μM), or L-THA after pre-treatment with BAPTA (see methods) were picospritzed near cortical arterioles. **(A)** Data are presented as boxplots. **(B)** Forest plots are also included to show the mean differences expressed as ratios of the effect of BAPTA with L-THA over that observed with L-THA. The redline is at 1 and represents no difference. The data for saline and L-THA are described in **Figure 4** legend, the data for BAPTA with L-THA are from 6 animals (2 males, 4 females).

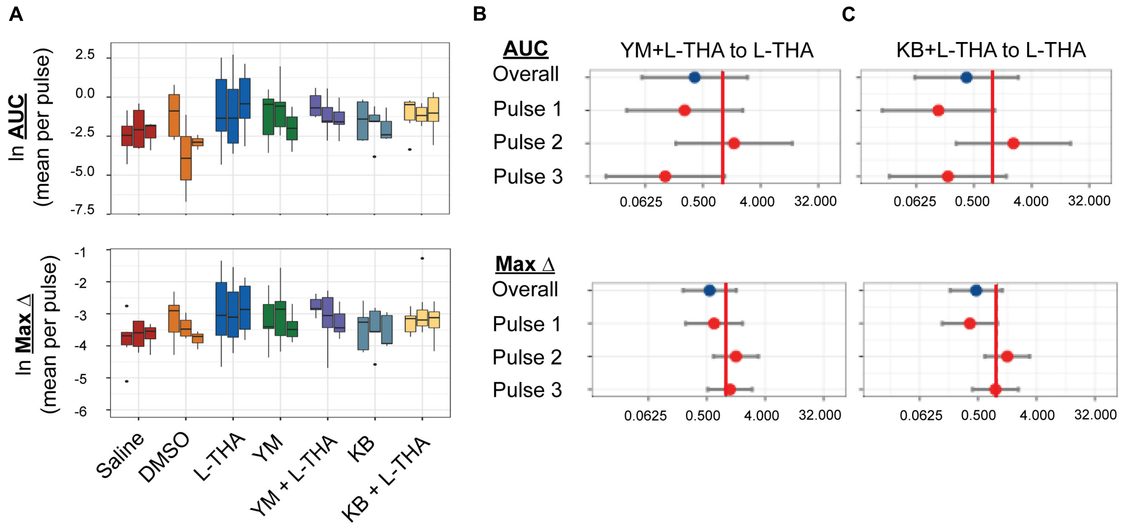

FIGURE 7 | Effects of saline, L-THA, YM-244769, KB-R7943, and YM or KB with L-THA on arteriole diameter. Saline, L-THA (100 μM), YM-244769 (1 μM), KB-R7943 (15 μM), or a combination of YM or KB with L-THA were picospritzed near cortical arterioles. **(A)** Data are presented as boxplots. Forest plots are also included to show the mean differences expressed as ratios of the effect observed with YM with L-THA **(B)** or KB with L-THA **(C)** over that observed with L-THA. The redline is at 1 and represents no difference. The data for saline and L-THA are described in **Figure 4** legend, the data for YM are from 6 animals (3 males, 3 females), the data for YM with L-THA are from 6 animals (2 males, 4 females), the data from KB are from 5 animals (1 male, 4 females) and the data for KB with L-THA are from 7 animals (5 males, 2 females).

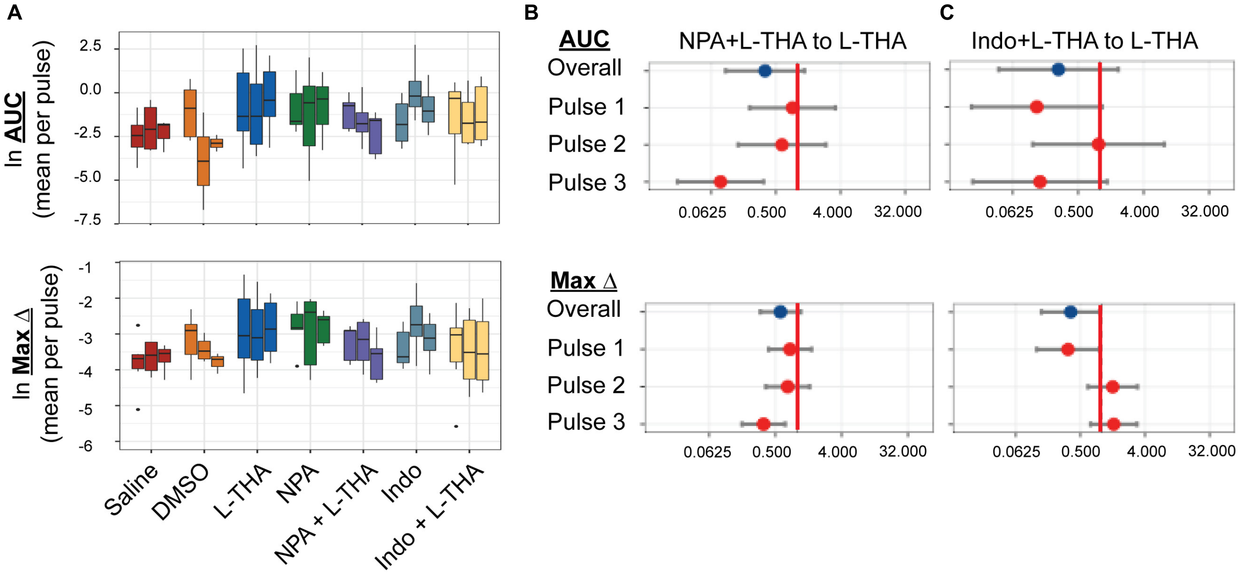

FIGURE 8 | Effects of saline, L-THA, L-NPA, Indomethacin, and L-NPA or Indomethacin with L-THA on arteriole diameter. Saline, L-THA (100 μM), L-NPA (2 μM), Indomethacin (10 μM), or a combination of NPA or Indomethacin with L-THA were picospritzed near cortical arterioles. **(A)** Data are presented as boxplots. Forest plots are also included to show the mean differences expressed as ratios of the effect observed with NPA with L-THA **(B)** or Indomethacin with L-THA **(C)** over that observed with L-THA. The redline is at 1 and represents no difference. The data for saline and L-THA are described in **Figure 4** legend, the data for NPA are from 5 animals (4 males, 1 female), the data for NPA with L-THA are from 5 animals (3 males, 2 females), the data from Indomethacin are from 8 animals (3 males, 5 females) and the data for Indomethacin with L-THA are from 6 animals (3 males, 3 females).

1.2–5.0, $p = 0.02$). When combined with L-THA, the effects were similar to those of Saline, i.e., for AUC (2.0-fold, 95% CI 0.5–8.7, $p = 0.33$) and for Max Change (1.4-fold 95% CI 0.7–3.0, $p = 0.33$; see forest plots, **Figure 8B**).

The mRNA and protein for the enzymes that generate archidonic acid (phospholipase A2, PLA2) and the metabolite PGE2 (cyclooxygenase, Cox1,2) have been identified in astrocytes (Takano et al., 2006; Gordon et al., 2008; Shi et al., 2008;

TABLE 1 | Combined pulses – Area under the curve[1].

Contrast	**Difference (natural log scale)**			**Ratio**		
	Mean[2]	**SE[3]**	***P*-value[4]**	**Estimate[5]**	**95% CI[6]**	
					Lower	**Upper**
DMSO to Saline	0.636	0.745	0.396	1.889	0.429	8.320
L-THA to Saline	1.741	0.617	0.006	5.706	1.670	19.490
TFB-TBOA to Saline	0.998	0.771	0.200	2.713	0.583	12.616
TFB-TBOA + L-THA to Saline	0.151	0.730	0.836	1.163	0.272	4.979
TFB-TBOA + L-THA to L-THA	−1.590	0.633	0.014	0.204	0.058	0.721
Receptor Ant. to Saline	0.251	0.857	0.771	1.285	0.233	7.090
Receptor Ant. + L-THA to Saline	1.456	0.775	0.064	4.288	0.916	20.080
Receptor Ant. + L-THA to L-THA	−0.286	0.685	0.678	0.751	0.192	2.940
BAPTA to Saline	1.054	0.696	0.134	2.868	0.716	11.480
BAPTA to L-THA	−0.688	0.594	0.251	0.503	0.154	1.640
YM to DMSO	0.446	0.731	0.544	1.562	0.364	6.690
YM + L-THA to DMSO	0.750	0.730	0.308	2.116	0.494	9.060
YM + L-THA-D to L-THA-Saline	−0.992	0.956	0.303	0.371	0.055	2.490
KB to DMSO	0.049	0.756	0.949	1.050	0.233	4.740
KB + L-THA to DMSO	0.781	0.705	0.272	2.184	0.536	8.890
KB + L-THA-D to L-THA-Saline	−0.961	0.937	0.309	0.383	0.059	2.470
NPA to Saline	1.367	0.734	0.066	3.923	0.909	16.930
NPA + L-THA to Saline	0.699	0.733	0.343	2.012	0.467	8.670
NPA + L-THA to L-THA	−1.042	0.637	0.106	0.353	0.099	1.250
Indo to DMSO	1.038	0.686	0.134	2.824	0.720	11.080
Indo + L-THA to DMSO	0.422	0.726	0.563	1.525	0.359	6.480
Indo + L-THA-D to L-THA-Saline	−1.320	0.953	0.170	0.267	0.040	1.780

[1] Results based on a mixed effects model using the natural log of AUC as the outcome and including all experimental conditions; [2] Difference of means (natural log scale), equivalently ln(Ratio); [3] Standard error; [4] P-value for Wald test; [5] Exponentiated Difference of Means; [6] 95% confidence interval.

Zhang et al., 2014). Inhibition of these enzymes blocks the vasodilation induced by uncaging Ca^{2+} in astrocytes and/or attenuates stimulus-evoked increases in blood flow (Takano et al., 2006; Gordon et al., 2008; Shi et al., 2008). To determine if prostaglandin E2 (PGE$_2$) is involved in the effects of L-THA, we tested the effects of inhibition of both cytochrome oxidase 1 and 2 (Cox1 & 2) with the pan-Cox inhibitor indomethacin (10 μM), which was also dissolved in DMSO and then saline (Mulligan and MacVicar, 2004). While the sizes of peaks observed after application of indomethacin trend toward being smaller than those observed after L-THA alone (**Figure 8C** and **Tables 1–4**), we did not examine the effects of L-THA in the presence of 0.1% DMSO.

DISCUSSION

The regulation of neurovascular coupling is complex, with multiple cell types participating depending on context and localization, including excitatory and inhibitory neurons, pericytes, astrocytes, vascular smooth muscle cells, and endothelia (Iadecola and Nedergaard, 2007; Koehler et al., 2009; Attwell et al., 2010; Hamilton et al., 2010; Petzold and Murthy, 2011; Filosa and Iddings, 2013; Gurden, 2013; Stobart and Anderson, 2013; Hillman, 2014; Howarth, 2014; Filosa et al., 2015; Hill et al., 2015; Tran and Gordon, 2015; Mishra et al., 2016; Uhlirova et al., 2016; Mateo et al., 2017). Moreover, there is evidence of cross-talk between these cells and the various signals that modulate the responses.

Several studies have implicated a role for glutamate transporters in the neurovascular response. Genetic or pharmacologic inhibition of glutamate transport reduces neural activity-induced increases in blood flow or energy delivery. For example, antisense knockdown of GLAST reduces whisker stimulation-induced 2-deoxyglucose accumulation in barrel cortex of rats (Cholet et al., 2001), and genetic deletion of either GLT-1 or GLAST reduces whisker-stimulation-induced accumulation of 2-deoxyglucose in young (10 days of age) mice (Voutsinos-Porche et al., 2003). A similar effect of GLT-1 knockout was observed with visual stimulation in the superior colliculus (Herard et al., 2005). Odor-induced increases in intrinsic optical signals in rats (Gurden et al., 2006) or blood flow in mice (Petzold et al., 2008) are attenuated by pharmacologically blocking glutamate uptake with DL-*threo*-ß-benzyloxyaspartic acid (TBOA). Similarly, TBOA blocks visual stimulus-induced increases in intrinsic hemodynamic signal in ferret visual cortex (Schummers et al., 2008). Together these studies strongly suggest that glutamate transport contributes to neuronal activity-dependent increases in blood flow. All of these experiments used inhibition/ablation of glutamate uptake

TABLE 2 | Individual pulses – Area under the curve[1].

Contrast	Pulse	Difference (natural log scale)			Ratio		
		Mean[2]	**SE[3]**	***P*-value[4]**	**Estimate[5]**	**95% CI[6]**	
						Lower	**Upper**
DMSO to Saline	1	1.632	0.809	0.046	5.116	1.030	25.400
	2	−0.382	0.831	0.647	0.682	0.132	3.540
	3	0.658	0.858	0.445	1.931	0.354	10.550
L-THA to Saline	1	2.062	0.691	0.003	7.860	2.003	30.836
	2	0.698	0.691	0.314	2.009	0.512	7.885
	3	2.465	0.702	0.001	11.763	2.934	47.154
TFB-TBOA to Saline	1	1.401	0.844	0.100	4.059	0.761	21.650
	2	0.316	0.846	0.710	1.371	0.256	7.335
	3	1.278	0.852	0.137	3.588	0.662	19.438
TFB-TBOA + L-THA to Saline	1	−0.016	0.803	0.984	0.984	0.200	4.833
	2	0.106	0.805	0.895	1.112	0.226	5.484
	3	0.364	0.815	0.656	1.440	0.286	7.238
TFB-TBOA + L-THA to L-THA	1	−2.078	0.693	0.003	0.125	0.032	0.495
	2	−0.591	0.693	0.395	0.554	0.140	2.188
	3	−2.101	0.705	0.004	0.122	0.030	0.494
Receptor Ant. to Saline	1	1.123	0.933	0.231	3.073	0.484	19.510
	2	0.392	0.935	0.676	1.480	0.232	9.440
	3	−0.762	0.995	0.445	0.467	0.065	3.340
Receptor Ant. + L-THA to Saline	1	2.722	0.862	0.002	15.209	2.759	83.830
	2	−0.118	0.862	0.892	0.889	0.161	4.910
	3	1.763	0.844	0.039	5.831	1.093	31.100
Receptor Ant. + L-THA to L-THA	1	0.660	0.760	0.387	1.935	0.429	8.720
	2	−0.816	0.759	0.285	0.442	0.098	1.990
	3	−0.702	0.738	0.344	0.496	0.115	2.140
BAPTA to Saline	1	0.816	0.768	0.290	2.262	0.494	10.360
	2	0.793	0.774	0.308	2.210	0.477	10.240
	3	1.552	0.771	0.047	4.720	1.024	21.760
BAPTA to L-THA	1	−1.245	0.651	0.059	0.288	0.079	1.050
	2	0.095	0.657	0.885	1.100	0.299	4.040
	3	−0.913	0.653	0.165	0.401	0.110	1.470
YM to DMSO	1	0.064	0.797	0.937	1.066	0.220	5.170
	2	1.348	0.803	0.096	3.848	0.783	18.910
	3	−0.074	0.825	0.929	0.929	0.181	4.760
YM + L-THA to DMSO	1	0.711	0.799	0.376	2.035	0.417	9.930
	2	1.126	0.803	0.164	3.083	0.628	15.140
	3	0.412	0.821	0.617	1.510	0.297	7.670
YM + L-THA-D to L-THA-Saline	1	−1.351	1.057	0.203	0.259	0.032	2.100
	2	0.428	1.059	0.687	1.534	0.188	12.510
	3	−2.053	1.080	0.060	0.128	0.015	1.090
KB to DMSO	1	−0.065	0.804	0.936	0.937	0.190	4.630
	2	0.454	0.828	0.584	1.575	0.305	8.140
	3	−0.243	0.849	0.775	0.784	0.146	4.210
KB + L-THA to DMSO	1	0.086	0.753	0.909	1.090	0.244	4.860
	2	1.426	0.778	0.070	4.162	0.890	19.470
	3	0.831	0.802	0.302	2.295	0.469	11.220
KB + L-THA-D to L-THA-Saline	1	−1.976	1.022	0.056	0.139	0.018	1.050
	2	0.728	1.041	0.486	2.071	0.264	16.270
	3	−1.634	1.066	0.128	0.195	0.024	1.610
NPA to Saline	1	1.741	0.811	0.034	5.704	1.145	28.427
	2	0.754	0.819	0.359	2.125	0.419	10.762

(Continued)

TABLE 2 | (Continued)

Contrast	Pulse	Difference (natural log scale)			Ratio		
		Mean[2]	SE[3]	*P*-value[4]	Estimate[5]	95% CI[6]	
						Lower	Upper
	3	1.606	0.820	0.053	4.981	0.982	25.273
NPA + L-THA to Saline	1	1.904	0.805	0.020	6.714	1.362	33.091
	2	0.201	0.822	0.807	1.223	0.240	6.227
	3	−0.007	0.811	0.993	0.993	0.199	4.949
NPA + L-THA to L-THA	1	−0.158	0.695	0.821	0.854	0.215	3.389
	2	−0.497	0.713	0.487	0.608	0.148	2.497
	3	−2.472	0.699	0.001	0.084	0.021	0.338
Indo to DMSO	1	−0.216	0.733	0.769	0.806	0.188	3.450
	2	2.262	0.757	0.003	9.600	2.141	43.050
	3	1.068	0.779	0.173	2.910	0.623	13.600
Indo + L-THA to DMSO	1	0.054	0.785	0.945	1.056	0.222	5.010
	2	0.559	0.819	0.496	1.749	0.346	8.850
	3	0.652	0.796	0.414	1.919	0.396	9.300
Indo + L-THA-D to L-THA-Saline	1	−2.007	1.046	0.057	0.134	0.017	1.070
	2	−0.046	1.054	0.965	0.955	0.118	7.710
	3	−1.906	1.078	0.080	0.149	0.018	1.260

[1] Results based on a mixed effects model using the natural log of AUC as the outcome and including all experimental conditions; [2] Difference of means (natural log scale), equivalently ln(Ratio); [3] Standard error; [4] P-value for Wald test; [5] Exponentiated Difference of Means; [6] 95% confidence interval.

TABLE 3 | Combined pulses – Max change[1].

Contrast	Difference (natural log scale)			Ratio		
	Mean[2]	SE[3]	*P*-value[4]	Estimate[5]	95% CI[6]	
					Lower	Upper
DMSO to Saline	0.450	0.369	0.226	1.568	0.753	3.268
L-THA to Saline	0.892	0.306	0.005	2.439	1.328	4.481
TFB-TBOA to Saline	0.593	0.385	0.127	1.810	0.841	3.895
TFB-TBOA + L-THA to Saline	0.164	0.363	0.653	1.178	0.571	2.428
TFB-TBOA + L-THA to L-THA	−0.728	0.316	0.024	0.483	0.257	0.907
Receptor Ant. to Saline	−0.085	0.426	0.842	0.918	0.393	2.140
Receptor Ant. + L-THA to Saline	0.538	0.386	0.167	1.713	0.794	3.690
Receptor Ant. + L-THA v L-THA	−0.353	0.342	0.305	0.702	0.355	1.390
BAPTA to Saline	0.499	0.347	0.154	1.647	0.826	3.280
BAPTA to L-THA	−0.393	0.297	0.190	0.675	0.374	1.220
YM to DMSO	0.154	0.363	0.674	1.166	0.565	2.400
YM + L-THA to DMSO	0.301	0.363	0.409	1.352	0.656	2.790
YM + L-THA-D to L-THA-Saline	−0.590	0.475	0.217	0.554	0.215	1.430
KB to DMSO	−0.185	0.377	0.625	0.831	0.392	1.760
KB + L-THA to DMSO	0.130	0.351	0.711	1.139	0.566	2.290
KB + L-THA-D to L-THA-Saline	−0.761	0.465	0.106	0.467	0.185	1.180
NPA to Saline	0.893	0.365	0.017	2.442	1.181	5.050
NPA + L-THA to Saline	0.359	0.364	0.328	1.432	0.693	2.960
NPA + L-THA to L-THA	−0.533	0.318	0.098	0.587	0.312	1.110
Indo to DMSO	0.234	0.341	0.496	1.263	0.640	2.494
Indo + L-THA to DMSO	−0.111	0.362	0.759	0.895	0.435	1.839
Indo + L-THA-D to L-THA-Saline	−1.003	0.474	0.037	0.367	0.143	0.942

[1] Results based on a mixed effects model using the natural log of Max change as the outcome and including all experimental conditions; [2] Difference of means (natural log scale), equivalently ln(Ratio); [3] Standard error; [4] P-value for Wald test; [5] Exponentiated Difference of Means; [6] 95% confidence interval.

TABLE 4 | Individual pulses – Max change[1].

Contrast	Pulse	Difference (natural log scale)			Ratio		
		Mean[2]	SE[3]	*P*-value[4]	Estimate[5]	95% CI[6]	
						Lower	Upper
DMSO to Saline	1	0.647	0.392	0.102	1.909	0.878	4.150
	2	0.346	0.402	0.391	1.413	0.637	3.130
	3	0.357	0.412	0.388	1.430	0.632	3.230
L-THA to Saline	1	0.899	0.332	0.008	2.457	1.274	4.740
	2	0.594	0.335	0.079	1.810	0.933	3.514
	3	1.182	0.338	0.001	3.261	1.669	6.372
TFB-TBOA to Saline	1	0.664	0.411	0.109	1.944	0.860	4.391
	2	0.344	0.414	0.408	1.410	0.621	3.204
	3	0.772	0.416	0.066	2.164	0.949	4.935
TFB-TBOA + L-THA to Saline	1	−0.024	0.389	0.950	0.976	0.451	2.113
	2	0.247	0.393	0.530	1.280	0.588	2.790
	3	0.268	0.396	0.499	1.308	0.597	2.867
TFB-TBOA + L-THA to L-THA	1	−0.923	0.339	0.008	0.397	0.203	0.778
	2	−0.346	0.339	0.309	0.707	0.361	1.386
	3	−0.914	0.344	0.009	0.401	0.203	0.793
Receptor Ant. to Saline	1	0.209	0.453	0.645	1.233	0.502	3.030
	2	0.012	0.456	0.980	1.012	0.409	2.500
	3	−0.477	0.479	0.321	0.620	0.240	1.600
Receptor Ant. + L-THA to Saline	1	0.937	0.417	0.027	2.553	1.116	5.840
	2	0.019	0.420	0.964	1.019	0.443	2.340
	3	0.658	0.412	0.114	1.931	0.852	4.380
Receptor Ant. + L-THA to L-THA	1	0.038	0.371	0.918	1.039	0.498	2.170
	2	−0.575	0.370	0.124	0.563	0.270	1.170
	3	−0.524	0.362	0.152	0.592	0.288	1.220
BAPTA to Saline	1	0.187	0.372	0.616	1.206	0.576	2.521
	2	0.601	0.377	0.114	1.825	0.864	3.853
	3	0.708	0.375	0.062	2.030	0.965	4.271
BAPTA to L-THA	1	−0.712	0.318	0.028	0.491	0.261	0.923
	2	0.008	0.321	0.980	1.008	0.534	1.904
	3	−0.474	0.319	0.141	0.623	0.330	1.173
YM to DMSO	1	0.104	0.389	0.790	1.109	0.513	2.400
	2	0.227	0.391	0.563	1.254	0.578	2.720
	3	0.131	0.399	0.744	1.140	0.517	2.510
YM + L-THA to DMSO	1	0.465	0.390	0.235	1.593	0.735	3.450
	2	0.212	0.390	0.589	1.236	0.570	2.680
	3	0.227	0.398	0.570	1.255	0.570	2.760
YM + L-THA-D to L-THA-Saline	1	−0.434	0.512	0.399	0.648	0.235	1.790
	2	−0.382	0.514	0.459	0.682	0.246	1.890
	3	−0.955	0.522	0.070	0.385	0.137	1.080
KB to DMSO	1	−0.233	0.395	0.557	0.792	0.361	1.737
	2	−0.248	0.404	0.541	0.780	0.350	1.739
	3	−0.074	0.412	0.857	0.928	0.410	2.101
KB + L-THA to DMSO	1	−0.088	0.369	0.813	0.916	0.440	1.907
	2	0.182	0.378	0.632	1.199	0.566	2.539
	3	0.297	0.388	0.445	1.346	0.625	2.901
KB + L-THA-D to L-THA-Saline	1	−0.987	0.496	0.049	0.373	0.139	0.998
	2	−0.412	0.505	0.417	0.662	0.243	1.803
	3	−0.885	0.514	0.088	0.413	0.149	1.144
NPA to Saline	1	0.905	0.392	0.023	2.472	1.135	5.381
	2	0.786	0.398	0.051	2.195	0.997	4.832

(Continued)

TABLE 4 | (Continued)

Contrast	Pulse	Difference (natural log scale)			Ratio		
		Mean[2]	SE[3]	*P*-value[4]	Estimate[5]	95% CI[6]	
						Lower	Upper
	3	0.987	0.398	0.015	2.683	1.219	5.903
NPA + L-THA to Saline	1	0.668	0.390	0.090	1.950	0.900	4.228
	2	0.289	0.399	0.471	1.335	0.605	2.945
	3	0.120	0.394	0.761	1.128	0.516	2.465
NPA + L-THA to L-THA	1	−0.231	0.340	0.498	0.794	0.405	1.557
	2	−0.305	0.347	0.381	0.737	0.371	1.466
	3	−1.062	0.341	0.002	0.346	0.176	0.681
Indo to DMSO	1	−0.136	0.359	0.707	0.873	0.428	1.783
	2	0.456	0.368	0.218	1.578	0.761	3.273
	3	0.381	0.377	0.314	1.463	0.694	3.086
Indo + L-THA to DMSO	1	−0.193	0.384	0.617	0.825	0.385	1.769
	2	−0.227	0.388	0.560	0.797	0.370	1.720
	3	0.085	0.397	0.830	1.089	0.496	2.391
Indo + L-THA-D to L-THA-Saline	1	−1.092	0.508	0.034	0.336	0.123	0.918
	2	−0.820	0.512	0.112	0.440	0.160	1.216
	3	−1.097	0.521	0.038	0.334	0.119	0.938

[1]Results based on a mixed effects model using the natural log of Max change as the outcome and including all experimental conditions; [2]Difference of means (natural log scale), equivalently ln(Ratio); [3]Standard error; [4]P-value for Wald test; [5]Exponentiated Difference of Means; [6]95% confidence interval.

to infer a role for glutamate transport in the neurovascular response, however, none tested for a direct effect of glutamate transport activation.

The goal of the present study was to address this gap and to test a model by which glutamate uptake might contribute to neurovascular coupling (schematized in **Figure 2**). We used a non-endogenous glutamate transporter substrate (L-THA) to determine if direct activation of glutamate transport is sufficient to cause an increase in arteriole diameter. We show that focal application of L-THA causes increases in arteriole diameter (maximum change and AUC) that are larger than those observed after focal application of saline. We also show that this effect is abolished by co-application of the pan-inhibitor of Na^+-dependent glutamate transporters (TFB-TBOA). This observation is consistent with the notion that direct activation of glutamate transport is sufficient to cause an increase in arteriole diameter. Substrate inhibitors of these transporters can also stimulate the release of glutamate through hetero-exchange (Bridges et al., 1999; Danbolt, 2001). Therefore, it is also possible that L-THA may be causing an increase in extracellular glutamate/aspartate which could in turn cause an increase in arteriole diameter by activating glutamate receptors. We think this is less likely for two reasons. First, there is little evidence that the effects of L-THA were altered by co-application of inhibitors of the major glutamate receptors (DNQX, AP5, MCPG). Second, as indicated above, TBOA attenuates activity induced increases in blood flow (Gurden et al., 2006; Petzold et al., 2008; Schummers et al., 2008). These investigators were concerned that TBOA might be increasing extracellular glutamate and that glutamate might be causing vasoconstriction by activating glutamate receptors. They tested either the same cocktail of receptor antagonists that were used in the present study (Petzold et al., 2008) or slightly different receptor antagonists (Schummers et al., 2008). Based on these observations, we propose that a direct effect of glutamate transport activation on arteriole diameter is the simplest explanation of these data. Petzold and colleagues came to the same conclusion, but wondered how glutamate activation might trigger an increase in arteriole diameter (for review, see Petzold and Murthy, 2011).

One possible explanation for glutamate receptors and transporters both triggering dilations is convergence upon a common signaling pathway. Petzold et al. suggested that both pathways might converge upon increases in intracellular Ca^{2+}, although through an unknown mechanism (Petzold and Murthy, 2011). Several different studies have examined the potential contributions of changes in astrocytic Ca^{2+} to changes in arteriole diameter, and the results are somewhat varied (for discussions, see Biesecker and Srienc, 2015; Khakh and McCarthy, 2015; Munoz et al., 2015; Bazargani and Attwell, 2016; Lia et al., 2021). Takano and colleagues photo-uncaged Ca^{2+} in astrocyte endfeet and found that this causes an increase in blood flow *in vivo* (Takano et al., 2006). Others have linked increases in astrocytic Ca^{2+} to vasodilation, to vasoconstriction, and finally to bi-directional control vessel diameter (Zonta et al., 2003; Winship et al., 2007; Girouard et al., 2010; Gordon et al., 2011; Nizar et al., 2013; Institoris et al., 2015; Otsu et al., 2015; Biesecker et al., 2016; Lind et al., 2018). Ca^{2+} signaling is complex with multiple pathways/sources that can cause increases in cytoplasmic levels of Ca^2. In a cell with processes, it is also possible to stimulate local increases in Ca^{2+} that do not necessarily propagate throughout the cell; this has been clearly documented in astrocyte

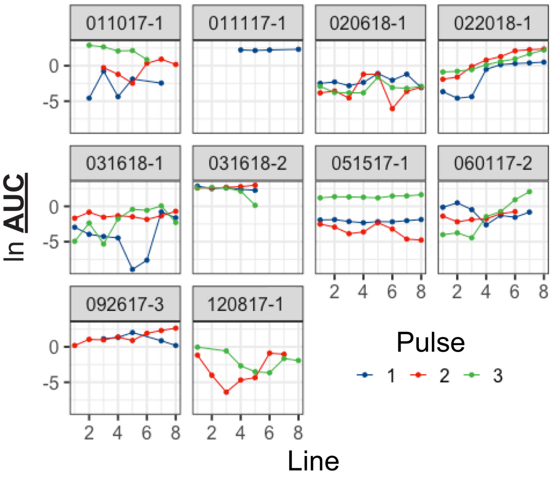

FIGURE 9 | Visual exploration of responders and non-responders. Arteriole responses (ln-transformed AUC) are plotted for each individual arteriole in response to 100 μM L-THA. The responses at each individual arteriole segment (lines) are represented as points. Each graph represents data obtained from an individual animal and the effects of different pulses are shown in different colors. Note two animals are not presented. On the Ln scale, the mean response is –0.55 (95% CI –1.25 to 0.15).

processes (O'Donnell et al., 2016; Robinson and Jackson, 2016; Agarwal et al., 2017 for reviews, see Khakh and McCarthy, 2015; Bazargani and Attwell, 2016; Lia et al., 2021). While the contributions of Ca^{2+} to the control of neurovascular coupling have been considered controversial, it seems likely that contributions are a matter of source, magnitude, and location of the change in Ca^{2+} that governs the direction of the effect on arteriole diameter.

The levels of the glutamate transporters are very high in the nervous system and GLT-1 has been estimated at 1% of brain protein (Danbolt, 2001). Both GLT-1 and GLAST display some heterogeneity in their distribution on the astrocyte membrane; they are enriched on endfeet facing the neuropil and with lower expression on the luminal side facing the blood vessel (Chaudhry et al., 1995; Lehre et al., 1995; Langer et al., 2017). The transport of glutamate by GLT-1, GLAST, and the other members of this family is accompanied by the simultaneous movement of 3Na^{+} ions and one H^{+}, resulting in local depolarization and the accumulation of Na^{+} in the astrocytes (Wadiche et al., 1995; Zerangue and Kavanaugh, 1996). Over two decades ago, several groups demonstrated that glutamate uptake causes fairly robust depolarization of astrocytes; this was demonstrated using physiologic recording in the astrocyte cell body (Bergles and Jahr, 1997; Diamond et al., 1998). In a more recent study, Langer and colleagues used a Na^{+} indicator and fluorescent imaging to demonstrate that neuronal activity or a transporter substrate (D-aspartate) cause a rapid increase Na^{+} in astrocytic endfeet; these Na^{+} signals can travel at speeds of up to 120 μm/sec (Langer et al., 2017). The Na^{+}/Ca^{2+} exchangers are bi-directional transporters and can move these ions in either direction based on the membrane potential (Blaustein and Lederer, 1999; Blaustein et al., 2002). The resting potential of an astrocyte is not far from this reversal potential. Several studies have demonstrated the glutamate transport is linked to either increases in Ca^{2+} or downstream effects of glutamate transport activation using agents that selectively block the reversed operation of these Na^{+}/Ca^{2+} exchangers in cell culture systems (Reyes and Parpura, 2008; Magi et al., 2013; Rojas et al., 2013; Balderas et al., 2014; Parpura et al., 2016; Rose et al., 2020). It has been suggested that these exchangers might contribute to regenerative Ca^{2+} in astrocyte processes (Brazhe et al., 2018). Schummers and colleagues demonstrated the inhibition of glutamate transport with TBOA blocks stimulus induced increases Ca *in vivo* (Schummers et al., 2008). We found that TFB-TBOA or YM244769 (an inhibitor of reversed Na^{+}/Ca^{2+} exchanger) reduce basil Ca^{2+} in astrocyte processes in an organotypic slice (Jackson and Robinson, 2015). A recent study also identified a Ca^{2+} signal in radial astrocytes that was blocked by either inhibiting glutamate uptake or these Na^{+}/ Ca^{2+} exchangers in the developing xenopus (Benfey et al., 2021). Together these studies strongly suggest that glutamate transport and reversed Na^{+}/Ca^{2+} exchange are coupled to increased increases in Ca^{2+} in astrocytes, but these effects have not been linked to glutamate transport-induced increases in arteriole diameter. In future studies, it will be important to examine the direct effects of glutamate transport activation on Ca^{2+} in astrocyte processes. If our model is correct, one would predict that glutamate transport-induced changes in astrocyte Ca^{2+} would follow kinetics that are consistent with changes in arteriole diameter. Although not trivial, these studies can be performed by selectively expressing genetically encoded Ca^{2+} indicators in astrocytes and testing the effects of inhibitors of various sources of Ca^{2+} including the Na^{+}/Ca^{2+} exchangers.

In the model, we also show two different Ca^{2+} activated processes that have been previously linked to increases arteriole diameter, nitric oxide synthase and signaling through phospholipase A2 and activation of cyclooxygenase. While we cannot rule-out the contributions of either of these potential pathways to transport-induced increases in arteriole diameter. Petzold and colleagues linked cyclo-oxygenase to mGluR-dependent dilations and provide evidence that transport-dependent dilations are independent of cyclo-oxygenase (Petzold et al., 2008). The signals downstream of glutamate transport will need further investigation.

Why couple glutamate transport to local blood flow control? Astrocytes play an important role in maintaining excitatory neurotransmission via the clearance of synaptically released glutamate. Glutamate is almost entirely cleared into astrocytes via GLAST and GLT-1 (Rothstein et al., 1994; Tanaka et al., 1997; Robinson, 1999; Danbolt, 2001). The glutamate transporters couple the movement of glutamate with the co-transport of 3Na^{+} and a H^{+} and the counter transport of a K^{+} ion (Zerangue and Kavanaugh, 1996). This is in turn coupled to activation of the Na^{+}/ K^{+} ATPase and hydrolysis of ATP. Thus, glutamate transport consumes energy (Attwell and Laughlin, 2001). Glutamate uptake causes activation of the Glut1 subtype of glucose transporter in astrocytes (Loaiza et al., 2003; Porras et al., 2008) and increases in glycolysis and lactate release (Voutsinos-Porche et al., 2003). Coupling of glutamate transport to changes in local blood flow would potentially provide astrocytic access to energetic substrates necessary to maintain glutamate uptake and to support the other metabolic costs of glutamate recycling.

Like many other cells in the nervous system, astrocytes are heterogeneous (for reviews, see Farmer and Murai, 2017; Khakh and Deneen, 2019; Kohler et al., 2021). Therefore, it is possible that glutamate transport may not be coupled to changes in arteriole diameter in all brain areas, but the fact that genetic deletion or inhibition of glutamate transport attenuates activity-dependent increases in blood flow or energy delivery in different areas of the cortex, olfactory bulb, visual cortex, and sensory cortex suggests that this may be a widespread phenomenon. Although there is astrocyte heterogeneity, the levels of GLT-1 do not vary much across the forebrain (Danbolt, 2001) and are not different in at least two populations of cortical astrocytes (Miller et al., 2019).

During the analysis of changes in arteriole diameter in response to L-THA (and other substrates), we encountered some variability to the responses both in terms of overall vessel responsiveness and local responsiveness. When we explored the data visually, it is apparent that there are animals that are responders and non-responders (**Figure 9**), although we did not try to make any statistical inferences. Differences in the responsiveness of individual vessel segments in response to the same stimulus is also apparent (**Figure 9**). Most of our results for the inhibitors were not statistically conclusive, and it is possible that there was indeed no effect. However, in most cases we were intrigued by trends toward inhibition in at least two of the three pulses. It is possible that we were underpowered to detect biologically relevant effects. When designing a study of this type, the statistical power for a given sample size depends on the ratio of the change in AUC to the standard deviation of the outcome. Larger changes in AUC might be effected by optimizing concentrations of drugs, but these experiments would be time consuming. The standard deviation reflects two variance components: the between-animal variability and the within-animal variability. For example, for AUC (ln scale), the total variance in our models had an estimated value of 5.75 with a between-animal component of 1.24 and a within-animal variance of 4.51. Increasing sample sizes beyond 5-6 animals per group is probably not realistic given the logistical cost of doing this experiment. However, if the variance could be reduced, one could obtain better precision. In addition to neurovascular coupling, blood flow is maintained by a process termed "cerebral autoregulation." This is essentially a pressure-dependent phenomenon. When blood pressure increases, vessel diameter decreases, and the opposite occurs when blood pressure decreases (for recent reviews/discussions see Filosa et al., 2015; Kim et al., 2015, 2016; Rosenegger et al., 2015). We did not control for blood pressure in this study and changes in blood pressure could increase between pulse and between animal variability. Another way to reduce variability would be to more closely target the anatomy so that the pipette was consistently in the region of an astrocyte that projects an endfoot to the area of the arteriole being imaged. While the specialized endfoot processes of astrocytes are estimated to cover 99.7% of the abluminal surface of the arteriole surface (Simard and Nedergaard, 2004; Mathiisen et al., 2010), the structural relationship of any one astrocyte to a specific segment of arteriole is likely to be highly restricted. Previous anatomic studies using confocal microscopy demonstrated diversity in the extent to which astrocytes contact vascular elements, with a single astrocyte contacting several vascular sites via many endfeet or a single vascular site receiving endfoot contact from several astrocytes (Kacem et al., 1998). Finally, as mentioned in the previous paragraph, there is clear evidence for astrocyte heterogeneity, it is possible that this heterogeneity also contributes to the variability observed in the current studies.

In conclusion, our study provided a physiologically intact system with normal blood pressure and blood flow. We wanted to adapt a method that could be used to monitor arteriole diameter and to acutely modulate glutamate transporters *in vivo*. Here, we employed two-photon *in vivo* microscopy along with acute labeling of the vasculature (arterioles) using fluorescent dyes to monitor the diameter of arterioles *in vivo*. Using an acute, partial cranial window and local application of transporter substrates and inhibitors, we were able to demonstrate that glutamate transport alone is sufficient to evoke arteriole dilation in the cortex of live mice. We created image-analysis methods, implemented in freely available code, and established a workflow to analyze the two-photon time-lapse micrographs in an automated objective manner. This workflow will greatly simplify future analyses of blood vessel diameter and contribute to a mechanistic dissection of various downstream signals (NCX activation, mitochondrial) or parallel pathways controlling NVC.

DATA AVAILABILITY STATEMENT

The raw data supporting the conclusions of this article will be made available by the authors, without undue reservation.

ETHICS STATEMENT

The animal study was reviewed and approved by Institutional Animal Care and Use Committee at the Children's Hospital of Philadelphia.

AUTHOR CONTRIBUTIONS

JJ designed and conducted the experiments, contributed to the data analysis, and the preparation of the manuscript. EK contributed to the data analysis, and preparation of figures and the manuscript. HT contributed to the experimental design, made BloodV10 & KymoHT6, and contributed to preparation of the manuscript. ML contributed to the data analysis, wrote the Python script, and contributed to the preparation of the manuscript. GC wrote the code for statistical comparisons. MP oversaw and conducted statistical analyses and wrote several sections of the manuscript. MR contributed to conceptualization of the study, to data analyses and interpretation, and to preparation of the manuscript. All authors reviewed and approved the final version of the manuscript.

FUNDING

This work was supported by the National Institutes of Neurologic Disease and Stroke of the NIH (R01 NS106693). The institutional Intellectual and Developmental Disabilities Research Center funded by the Eunice Kennedy Shriver National Institutes of Child Health and Human Development (P50 HD105354) provided support for the imaging conducted in these studies (Neuroimaging and Neurocircuitry Core) and for statistical analyses (Biostatistics and Data Science Core). JJ was supported by WW Smith Charitable Trust during the writing phase.

ACKNOWLEDGMENTS

We would like to thank Douglas Coulter for consultative expertise and for the use of the microscopes. We would also like to thank Isabella Song for her help with analyzing the kymographs.

REFERENCES

Agarwal, A., Wu, P. H., Hughes, E. G., Fukaya, M., Tischfield, M. A., Langseth, A. J., et al. (2017). Transient opening of the mitochondrial permeability transition pore induces microdomain calcium transients in astrocyte processes. *Neuron* 93, 587–605 e587. doi: 10.1016/j.neuron.2016.12.034

Arriza, J. L., Fairman, W. A., Wadiche, J. I., Murdoch, G. H., Kavanaugh, M. P., and Amara, S. G. (1994). Functional comparisons of three glutamate transporter subtypes cloned from human motor cortex. *J. Neurosci.* 14, 5559–5569. doi: 10.1523/JNEUROSCI.14-09-05559.1994

Attwell, D., and Laughlin, S. B. (2001). An energy budget for signaling in the grey matter of the brain. *J. Cereb. Blood Flow Metab.* 21, 1133–1145. doi: 10.1097/00004647-200110000-00001

Attwell, D., Buchan, A. M., Charpak, S., Lauritzen, M., Macvicar, B. A., and Newman, E. A. (2010). Glial and neuronal control of brain blood flow. *Nature* 468, 232–243. doi: 10.1038/nature09613

Balderas, A., Guillem, A. M., Martinez-Lozada, Z., Hernandez-Kelly, L. C., Aguilera, J., and Ortega, A. (2014). GLAST/EAAT1 regulation in cultured *Bergmann glia* cells: role of the NO/cGMP signaling pathway. *Neurochem. Int.* 73, 139–145. doi: 10.1016/j.neuint.2013.10.011

Bazargani, N., and Attwell, D. (2016). Astrocyte calcium signaling: the third wave. *Nat. Neurosci.* 19, 182–189. doi: 10.1038/nn.4201

Benfey, N. J., Li, V. J., Schohl, A., and Ruthazer, E. S. (2021). Sodium-calcium exchanger mediates sensory-evoked glial calcium transients in the developing retinotectal system. *Cell Rep.* 37:109791. doi: 10.1016/j.celrep.2021.109791

Bergles, D. E., and Jahr, C. E. (1997). Synaptic activation of glutamate transporters in hippocampal astrocytes. *Neuron* 19, 1297–1308. doi: 10.1016/s0896-6273(00)80420-1

Biesecker, K. R., and Srienc, A. I. (2015). The functional role of astrocyte calcium signaling in cortical blood flow regulation. *J. Neurosci.* 35, 868–870. doi: 10.1523/JNEUROSCI.4422-14.2015

Biesecker, K. R., Srienc, A. I., Shimoda, A. M., Agarwal, A., Bergles, D. E., Kofuji, P., et al. (2016). Glial cell calcium signaling mediates capillary regulation of blood flow in the retina. *J. Neurosci.* 36, 9435–9445. doi: 10.1523/JNEUROSCI.1782-16.2016

Blaustein, M. P., and Lederer, W. J. (1999). Sodium/calcium exchange: its physiological implications. *Physiol. Rev.* 79, 763–854. doi: 10.1152/physrev.1999.79.3.763

Blaustein, M. P., Juhaszova, M., Golovina, V. A., Church, P. J., and Stanley, E. F. (2002). Na/Ca exchanger and PMCA localization in neurons and astrocytes: functional implications. *Ann. N. Y. Acad. Sci.* 976, 356–366. doi: 10.1111/j.1749-6632.2002.tb04762.x

Bohn, K. A., Adkins, C. E., Mittapalli, R. K., Terrell-Hall, T. B., Mohammad, A. S., Shah, N., et al. (2016). Semi-automated rapid quantification of brain vessel density utilizing fluorescent microscopy. *J. Neurosci. Methods* 270, 124–131. doi: 10.1016/j.jneumeth.2016.06.012

Brazhe, A. R., Verisokin, A. Y., Verveyko, D. V., and Postnov, D. E. (2018). Sodium-calcium exchanger can account for regenerative Ca(2+) entry in thin astrocyte processes. *Front. Cell Neurosci.* 12:250. doi: 10.3389/fncel.2018.00250

Bridges, R. J., Kavanaugh, M. P., and Chamberlin, A. R. (1999). A pharmacological review of competitive inhibitors and substrates of high-affinity, sodium-dependent glutamate transport in the central nervous system. *Curr. Pharm. Des.* 5, 363–379.

Chaudhry, F. A., Lehre, K. P., Campagne, M. V. L., Ottersen, O. P., Danbolt, N. C., and Storm-Mathisen, J. (1995). Glutamate transporters in glial plasma membranes: highly differentiated localizations revealed by quantitative ultrastructural immunocytochemistry. *Neuron* 15, 711–720. doi: 10.1016/0896-6273(95)90158-2

Cholet, N., Pellerin, L., Welker, E., Lacombe, P., Seylaz, J., Magistretti, P., et al. (2001). Local injection of antisense oligonucleotides targeted to the glial glutamate transporter GLAST decreases the metabolic response to somatosensory activation. *J. Cereb. Blood Flow Metab.* 21, 404–412. doi: 10.1097/00004647-200104000-00009

Danbolt, N. C. (2001). Glutamate uptake. *Prog. Neurobiol.* 65, 1–105.

Danbolt, N. C., Furness, D. N., and Zhou, Y. (2016). Neuronal vs glial glutamate uptake: resolving the conundrum. *Neurochem. Int.* 98, 29–45. doi: 10.1016/j.neuint.2016.05.009

Diamond, J. S., Bergles, D. E., and Jahr, C. E. (1998). Glutamate release monitored with astrocyte transporter currents during LTP. *Neuron* 21, 425–433. doi: 10.1016/s0896-6273(00)80551-6

Erreger, K., Geballe, M. T., Kristensen, A., Chen, P. E., Hansen, K. B., Lee, C. J., et al. (2007). Subunit-specific agonist activity at NR2A-, NR2B-, NR2C-, and NR2D-containing N-methyl-D-aspartate glutamate receptors. *Mol. Pharmacol.* 72, 907–920. doi: 10.1124/mol.107.037333

Faraci, F. M., and Breese, K. R. (1993). Nitric oxide mediates vasodilatation in response to activation of N-methyl-D-aspartate receptors in brain. *Circ. Res.* 72, 476–480. doi: 10.1161/01.res.72.2.476

Farmer, W. T., and Murai, K. (2017). Resolving astrocyte heterogeneity in the CNS. *Front. Cell Neurosci.* 11:300. doi: 10.3389/fncel.2017.00300

Filosa, J. A., and Iddings, J. A. (2013). Astrocyte regulation of cerebral vascular tone. *Am. J. Physiol. Heart Circ. Physiol.* 305, H609–H619. doi: 10.1152/ajpheart.00359.2013

Filosa, J. A., Bonev, A. D., and Nelson, M. T. (2004). Calcium dynamics in cortical astrocytes and arterioles during neurovascular coupling. *Circ. Res.* 95, e73–e81. doi: 10.1161/01.RES.0000148636.60732.2e

Filosa, J. A., Morrison, H. W., Iddings, J. A., Du, W., and Kim, K. J. (2015). Beyond neurovascular coupling, role of astrocytes in the regulation of vascular tone. *Neuroscience* 323, 96–109. doi: 10.1016/j.neuroscience.2015.03.064

Garthwaite, J. (1985). Cellular uptake disguises action of L-glutamate on N-methyl-D-aspartate receptors. *Br. J. Pharmacol.* 85, 297–307. doi: 10.1111/j.1476-5381.1985.tb08860.x

Girouard, H., Bonev, A. D., Hannah, R. M., Meredith, A., Aldrich, R. W., and Nelson, M. T. (2010). Astrocytic endfoot Ca2+ and BK channels determine both arteriolar dilation and constriction. *Proc. Natl. Acad. Sci. U.S.A.* 107, 3811–3816. doi: 10.1073/pnas.0914722107

Gordon, G. R., Choi, H. B., Rungta, R. L., Ellis-Davies, G. C., and Macvicar, B. A. (2008). Brain metabolism dictates the polarity of astrocyte control over arterioles. *Nature* 456, 745–749. doi: 10.1038/nature07525

Gordon, G. R., Howarth, C., and Macvicar, B. A. (2011). Bidirectional control of arteriole diameter by astrocytes. *Exp. Physiol.* 96, 393–399. doi: 10.1113/expphysiol.2010.053132

Gurden, H. (2013). Astrocytes: can they be the missing stars linking neuronal activity to neurofunctional imaging signals? *Front. Cell Neurosci.* 7:21. doi: 10.3389/fncel.2013.00021

Gurden, H., Uchida, N., and Mainen, Z. F. (2006). Sensory-evoked intrinsic optical signals in the olfactory bulb are coupled to glutamate release and uptake. *Neuron* 52, 335–345. doi: 10.1016/j.neuron.2006.07.022

Hamilton, N. B., Attwell, D., and Hall, C. N. (2010). Pericyte-mediated regulation of capillary diameter: a component of neurovascular coupling in health and disease. *Front. Neuroenerget.* 2:5. doi: 10.3389/fnene.2010.00005

Harris, J. J., Jolivet, R., and Attwell, D. (2012). Synaptic energy use and supply. *Neuron* 75, 762–777. doi: 10.1016/j.neuron.2012.08.019

Herard, A. S., Dubois, A., Escartin, C., Tanaka, K., Delzescaux, T., Hantraye, P., et al. (2005). Decreased metabolic response to visual stimulation in the superior colliculus of mice lacking the glial glutamate transporter GLT-1. *Eur. J. Neurosci.* 22, 1807–1811. doi: 10.1111/j.1460-9568.2005.04346.x

Herman, M. A., and Jahr, C. E. (2007). Extracellular glutamate concentration in hippocampal slice. *J. Neurosci.* 27, 9736–9741. doi: 10.1523/JNEUROSCI.3009-07.2007

Hertz, L., Peng, L., and Dienel, G. A. (2007). Energy metabolism in astrocytes: high rate of oxidative metabolism and spatiotemporal dependence on glycolysis/glycogenolysis. *J. Cereb. Blood Flow Metab.* 27, 219–249. doi: 10.1038/sj.jcbfm.9600343

Hill, R. A., Tong, L., Yuan, P., Murikinati, S., Gupta, S., and Grutzendler, J. (2015). Regional blood flow in the normal and ischemic brain is controlled by arteriolar smooth muscle cell contractility and not by capillary pericytes. *Neuron* 87, 95–110. doi: 10.1016/j.neuron.2015.06.001

Hillman, E. M. (2014). Coupling mechanism and significance of the BOLD signal: a status report. *Annu. Rev. Neurosci.* 37, 161–181. doi: 10.1146/annurev-neuro-071013-014111

Hinzman, J. M., Andaluz, N., Shutter, L. A., Okonkwo, D. O., Pahl, C., Strong, A. J., et al. (2014). Inverse neurovascular coupling to cortical spreading depolarizations in severe brain trauma. *Brain* 137, 2960–2972. doi: 10.1093/brain/awu241

Howarth, C. (2014). The contribution of astrocytes to the regulation of cerebral blood flow. *Front. Neurosci.* 8:103. doi: 10.3389/fnins.2014.00103

Howarth, C., Gleeson, P., and Attwell, D. (2012). Updated energy budgets for neural computation in the neocortex and cerebellum. *J. Cereb. Blood Flow Metab.* 32, 1222–1232. doi: 10.1038/jcbfm.2012.35

Iadecola, C., and Nedergaard, M. (2007). Glial regulation of the cerebral microvasculature. *Nat. Neurosci.* 10, 1369–1376. doi: 10.1038/nn2003

Institoris, A., Rosenegger, D. G., and Gordon, G. R. (2015). Arteriole dilation to synaptic activation that is sub-threshold to astrocyte endfoot Ca2+ transients. *J. Cereb. Blood Flow Metab.* 35, 1411–1415. doi: 10.1038/jcbfm.2015.141

Jackman, K., and Iadecola, C. (2015). Neurovascular regulation in the ischemic brain. *Antioxid. Redox. Signal.* 22, 149–160. doi: 10.1089/ars.2013.5669

Jackson, J. G., and Robinson, M. B. (2015). Reciprocal regulation of mitochondrial dynamics and calcium signaling in astrocyte processes. *J. Neurosci.* 35, 15199–15213. doi: 10.1523/JNEUROSCI.2049-15.2015

Kacem, K., Lacombe, P., Seylaz, J., and Bonvento, G. (1998). Structural organization of the perivascular astrocyte endfeet and their relationship with the endothelial glucose transporter: a confocal microscopy study. *Glia* 23, 1–10. doi: 10.1002/(sici)1098-1136(199805)23:1<1::aid-glia1>3.0.co;2-b

Khakh, B. S., and Deneen, B. (2019). The emerging nature of astrocyte diversity. *Annu. Rev. Neurosci.* 42, 187–207. doi: 10.1146/annurev-neuro-070918-050443

Khakh, B. S., and McCarthy, K. D. (2015). Astrocyte calcium signaling: from observations to functions and the challenges therein. *Cold Spring Harb. Perspect. Biol.* 7:a020404. doi: 10.1101/cshperspect.a020404

Kim, K. J., Iddings, J. A., Stern, J. E., Blanco, V. M., Croom, D., Kirov, S. A., et al. (2015). Astrocyte contributions to flow/pressure-evoked parenchymal arteriole vasoconstriction. *J. Neurosci.* 35, 8245–8257. doi: 10.1523/JNEUROSCI.4486-14.2015

Kim, K. J., Ramiro Diaz, J., Iddings, J. A., and Filosa, J. A. (2016). Vasculo-neuronal coupling: retrograde vascular communication to brain neurons. *J. Neurosci.* 36, 12624–12639. doi: 10.1523/JNEUROSCI.1300-16.2016

Kitaura, H., Uozumi, N., Tohmi, M., Yamazaki, M., Sakimura, K., Kudoh, M., et al. (2007). Roles of nitric oxide as a vasodilator in neurovascular coupling of mouse somatosensory cortex. *Neurosci. Res.* 59, 160–171. doi: 10.1016/j.neures.2007.06.1469

Kirischuk, S., Kettenmann, H., and Verkhratsky, A. (1997). Na^{+}/Ca2^{+} exchanger modulates kainate-triggered Ca2^{+} signaling in Bergmann glial cells *in situ*. *FASEB J.* 11, 566–572. doi: 10.1096/fasebj.11.7.9212080

Koehler, R. C., Roman, R. J., and Harder, D. R. (2009). Astrocytes and the regulation of cerebral blood flow. *Trends Neurosci.* 32, 160–169.

Kohler, S., Winkler, U., and Hirrlinger, J. (2021). Heterogeneity of astrocytes in grey and white matter. *Neurochem. Res.* 46, 3–14. doi: 10.1007/s11064-019-02926-x

Kugler, P., and Drenckhahn, D. (1996). Astrocytes and Bergmann glia as an important site of nitric oxide synthase I. *Glia* 16, 165–173. doi: 10.1002/(SICI)1098-1136(199602)16:2<165::AID-GLIA8>3.0.CO;2-2

Langer, J., Gerkau, N. J., Derouiche, A., Kleinhans, C., Moshrefi-Ravasdjani, B., Fredrich, M., et al. (2017). Rapid sodium signaling couples glutamate uptake to breakdown of ATP in perivascular astrocyte endfeet. *Glia* 65, 293–308. doi: 10.1002/glia.23092

Leeuwis, A. E., Benedictus, M. R., Kuijer, J. P. A., Binnewijzend, M. A. A., Hooghiemstra, A. M., Verfaillie, S. C. J., et al. (2017). Lower cerebral blood flow is associated with impairment in multiple cognitive domains in Alzheimer's disease. *Alzheimers Dement.* 13, 531–540. doi: 10.1016/j.jalz.2016.08.013

Leeuwis, A. E., Smith, L. A., Melbourne, A., Hughes, A. D., Richards, M., Prins, N. D., et al. (2018). Cerebral blood flow and cognitive functioning in a community-based, multi-ethnic cohort: the sabre study. *Front. Aging Neurosci.* 10:279. doi: 10.3389/fnagi.2018.00279

Lehre, K. P., Levy, L. M., Ottersen, O. P., Storm-Mathisen, J., and Danbolt, N. C. (1995). Differential expression of two glial glutamate transporters in the rat brain: quantitative and immunocytochemical observations. *J. Neurosci.* 15, 1835–1853. doi: 10.1523/JNEUROSCI.15-03-01835.1995

Lia, A., Henriques, V. J., Zonta, M., Chiavegato, A., Carmignoto, G., Gomez-Gonzalo, M., et al. (2021). Calcium signals in astrocyte microdomains, a decade of great advances. *Front. Cell Neurosci.* 15:673433. doi: 10.3389/fncel.2021.673433

Lind, B. L., Jessen, S. B., Lonstrup, M., Josephine, C., Bonvento, G., and Lauritzen, M. (2018). Fast Ca(2+) responses in astrocyte end-feet and neurovascular coupling in mice. *Glia* 66, 348–358. doi: 10.1002/glia.23246

Loaiza, A., Porras, O. H., and Barros, L. F. (2003). Glutamate triggers rapid glucose transport stimulation in astrocytes as evidenced by real-time confocal microscopy. *J. Neurosci.* 23, 7337–7342. doi: 10.1523/JNEUROSCI.23-19-07337.2003

Luke, S. G. (2017). Evaluating significance in linear mixed-effects models in R. *Behav. Res. Methods* 49, 1494–1502. doi: 10.3758/s13428-016-0809-y

Magi, S., Arcangeli, S., Castaldo, P., Nasti, A. A., Berrino, L., Piegari, E., et al. (2013). Glutamate-induced ATP synthesis: relationship between plasma membrane Na+/Ca2+ exchanger and excitatory amino acid transporters in brain and heart cell models. *Mol. Pharmacol.* 84, 603–614. doi: 10.1124/mol.113.087775

Martin, C., Houitte, D., Guillermier, M., Petit, F., Bonvento, G., and Gurden, H. (2012). Alteration of sensory-evoked metabolic and oscillatory activities in the olfactory bulb of GLAST-deficient mice. *Front. Neural Circuits* 6:1. doi: 10.3389/fncir.2012.00001

Masamoto, K., Unekawa, M., Watanabe, T., Toriumi, H., Takuwa, H., Kawaguchi, H., et al. (2015). Unveiling astrocytic control of cerebral blood flow with optogenetics. *Sci. Rep.* 5:11455. doi: 10.1038/srep11455

Mateo, C., Knutsen, P. M., Tsai, P. S., Shih, A. Y., and Kleinfeld, D. (2017). Entrainment of arteriole vasomotor fluctuations by neural activity is a basis of blood-oxygenation-level-dependent "resting-state" connectivity. *Neuron* 96, 936–948.e933. doi: 10.1016/j.neuron.2017.10.012

Mathiisen, T. M., Lehre, K. P., Danbolt, N. C., and Ottersen, O. P. (2010). The perivascular astroglial sheath provides a complete covering of the brain microvessels: an electron microscopic 3D reconstruction. *Glia* 58, 1094–1103. doi: 10.1002/glia.20990

Miller, S. J., Philips, T., Kim, N., Dastgheyb, R., Chen, Z., Hsieh, Y. C., et al. (2019). Molecularly defined cortical astroglia subpopulation modulates neurons via secretion of Norrin. *Nat. Neurosci.* 22, 741–752. doi: 10.1038/s41593-019-0366-7

Minelli, A., Castaldo, P., Gobbi, P., Salucci, S., Magi, S., and Amoroso, S. (2007). Cellular and subcellular localization of Na+-Ca2+ exchanger protein isoforms, NCX1, NCX2, and NCX3 in cerebral cortex and hippocampus of adult rat. *Cell Calcium* 41, 221–234. doi: 10.1016/j.ceca.2006.06.004

Mishra, A., Reynolds, J. P., Chen, Y., Gourine, A. V., Rusakov, D. A., and Attwell, D. (2016). Astrocytes mediate neurovascular signaling to capillary pericytes but not to arterioles. *Nat. Neurosci.* 19, 1619–1627.

Mulligan, S. J., and MacVicar, B. A. (2004). Calcium transients in astrocyte endfeet cause cerebrovascular constrictions. *Nature* 431, 195–199. doi: 10.1038/nature02827

Munoz, M. F., Puebla, M., and Figueroa, X. F. (2015). Control of the neurovascular coupling by nitric oxide-dependent regulation of astrocytic Ca(2+) signaling. *Front. Cell Neurosci.* 9:59. doi: 10.3389/fncel.2015.00059

Navarrete, M., Perea, G., Fernandez De Sevilla, D., Gomez-Gonzalo, M., Nunez, A., Martin, E. D., et al. (2012). Astrocytes mediate in vivo cholinergic-induced synaptic plasticity. *PLoS Biol.* 10:e1001259. doi: 10.1371/journal.pbio.1001259

Nimmerjahn, A., Kirchhoff, F., Kerr, J. N., and Helmchen, F. (2004). Sulforhodamine 101 as a specific marker of astroglia in the neocortex in vivo. *Nat. Methods* 1, 31–37. doi: 10.1038/nmeth706

Nizar, K., Uhlirova, H., Tian, P., Saisan, P. A., Cheng, Q., Reznichenko, L., et al. (2013). In vivo stimulus-induced vasodilation occurs without IP3 receptor activation and may precede astrocytic calcium increase. *J. Neurosci.* 33, 8411–8422. doi: 10.1523/JNEUROSCI.3285-12.2013

Obel, L. F., Muller, M. S., Walls, A. B., Sickmann, H. M., Bak, L. K., Waagepetersen, H. S., et al. (2012). Brain glycogen-new perspectives on its metabolic function and regulation at the subcellular level. *Front. Neuroenerget.* 4:3. doi: 10.3389/fnene.2012.00003

O'Donnell, J. C., Jackson, J. G., and Robinson, M. B. (2016). Transient oxygen/glucose deprivation causes a delayed loss of mitochondria and increases spontaneous calcium signaling in astrocytic processes. *J. Neurosci.* 36, 7109–7127. doi: 10.1523/JNEUROSCI.4518-15.2016

Otsu, Y., Couchman, K., Lyons, D. G., Collot, M., Agarwal, A., Mallet, J. M., et al. (2015). Calcium dynamics in astrocyte processes during neurovascular coupling. *Nat. Neurosci.* 18, 210–218. doi: 10.1038/nn.3906

Pappalardo, L. W., Samad, O. A., Black, J. A., and Waxman, S. G. (2014). Voltage-gated sodium channel Nav 1.5 contributes to astrogliosis in an in vitro model of glial injury via reverse Na+ /Ca2+ exchange. *Glia* 62, 1162–1175. doi: 10.1002/glia.22671

Parpura, V., Sekler, I., and Fern, R. (2016). Plasmalemmal and mitochondrial Na(+) -Ca(2+) exchange in neuroglia. *Glia* 64, 1646–1654. doi: 10.1002/glia.22975

Petzold, G. C., Albeanu, D. F., Sato, T. F., and Murthy, V. N. (2008). Coupling of neural activity to blood flow in olfactory glomeruli is mediated by astrocytic pathways. *Neuron* 58, 897–910. doi: 10.1016/j.neuron.2008.04.029

Petzold, G. C., and Murthy, V. N. (2011). Role of astrocytes in neurovascular coupling. *Neuron* 71, 782–797. doi: 10.1016/j.neuron.2011.08.009

Porras, O. H., Ruminot, I., Loaiza, A., and Barros, L. F. (2008). Na(+)-Ca(2+) cosignaling in the stimulation of the glucose transporter GLUT1 in cultured astrocytes. *Glia* 56, 59–68. doi: 10.1002/glia.20589

Porter, J. T., and McCarthy, K. D. (1996). Hippocampal astrocytes in situ respond to glutamate released from synaptic terminals. *J. Neurosci.* 16, 5073–5081. doi: 10.1523/JNEUROSCI.16-16-05073.1996

Putt, M. E. (2021). Assessing risk factors with information beyond P value thresholds: statistical significance does not equal clinical importance. *Cancer* 127, 1180–1185. doi: 10.1002/cncr.33369

R Core Team (2021). *R: A Language and Environment for Statistical Computing.* Vienna: R Foundation for Statistical Computing.

Raichle, M. E., and Mintun, M. A. (2006). Brain work and brain imaging. *Annu. Rev. Neurosci.* 29, 449–476. doi: 10.1146/annurev.neuro.29.051605.112819

Reyes, R. C., and Parpura, V. (2008). Mitochondria modulate Ca2+-dependent glutamate release from rat cortical astrocytes. *J. Neurosci.* 28, 9682–9691. doi: 10.1523/JNEUROSCI.3484-08.2008

Reyes, R. C., Verkhratsky, A., and Parpura, V. (2012). Plasmalemmal Na^+/Ca^{2+} exchanger modulates Ca^{2+}-dependent exocytotic release of glutamate from rat cortical astrocytes. *ASN Neuro.* 4:e00075. doi: 10.1042/AN20110059

Robinson, M. B. (1999). The family of sodium-dependent glutamate transporters: a focus on the GLT-1/EAAT2 subtype. *Neurochem. Int.* 33, 479–491. doi: 10.1016/s0197-0186(98)00055-2

Robinson, M. B., and Jackson, J. G. (2016). Astroglial glutamate transporters coordinate excitatory signaling and brain energetics. *Neurochem. Int.* 98, 56–71. doi: 10.1016/j.neuint.2016.03.014

Rojas, H., Colina, C., Ramos, M., Benaim, G., Jaffe, E., Caputo, C., et al. (2013). Sodium-calcium exchanger modulates the L-glutamate Ca(i) (2+) signalling in type-1 cerebellar astrocytes. *Adv. Exp. Med. Biol.* 961, 267–274. doi: 10.1007/978-1-4614-4756-6_22

Rose, C. R., Ziemens, D., and Verkhratsky, A. (2020). On the special role of NCX in astrocytes: translating Na(+)-transients into intracellular Ca(2+) signals. *Cell Calcium* 86:102154. doi: 10.1016/j.ceca.2019.102154

Rosenegger, D. G., Tran, C. H., Wamsteeker Cusulin, J. I., and Gordon, G. R. (2015). Tonic local brain blood flow control by astrocytes independent of phasic neurovascular coupling. *J. Neurosci.* 35, 13463–13474. doi: 10.1523/JNEUROSCI.1780-15.2015

Rothstein, J. D., Martin, L., Levey, A. I., Dykes-Hoberg, M., Jin, L., Wu, D., et al. (1994). Localization of neuronal and glial glutamate transporters. *Neuron* 13, 713–725. doi: 10.1016/0896-6273(94)90038-8

Sato, T. R., Gray, N. W., Mainen, Z. F., and Svoboda, K. (2007). The functional microarchitecture of the mouse barrel cortex. *PLoS Biol.* 5:e189. doi: 10.1371/journal.pbio.0050189

Schummers, J., Yu, H., and Sur, M. (2008). Tuned responses of astrocytes and their influence on hemodynamic signals in the visual cortex. *Science* 320, 1638–1643. doi: 10.1126/science.1156120

Shen, Z., Lu, Z., Chhatbar, P. Y., O'herron, P., and Kara, P. (2012). An artery-specific fluorescent dye for studying neurovascular coupling. *Nat. Methods* 9, 273–276. doi: 10.1038/nmeth.1857

Shi, Y., Liu, X., Gebremedhin, D., Falck, J. R., Harder, D. R., and Koehler, R. C. (2008). Interaction of mechanisms involving epoxyeicosatrienoic acids, adenosine receptors, and metabotropic glutamate receptors in neurovascular coupling in rat whisker barrel cortex. *J. Cereb. Blood Flow Metab.* 28, 111–125. doi: 10.1038/sj.jcbfm.9600511

Shimamoto, K., Sakai, R., Takaoka, K., Yumoto, N., Nakajima, T., Amara, S. G., et al. (2004). Characterization of novel L-threo-beta-benzyloxyaspartate derivatives, potent blockers of the glutamate transporters. *Mol. Pharmacol.* 65, 1008–1015. doi: 10.1124/mol.65.4.1008

Shulman, R. G., Rothman, D. L., Behar, K. L., and Hyder, F. (2004). Energetic basis of brain activity: implications for neuroimaging. *Trends Neurosci.* 27, 489–495. doi: 10.1016/j.tins.2004.06.005

Simard, M., and Nedergaard, M. (2004). The neurobiology of glia in the context of water and ion homeostasis. *Neuroscience* 129, 877–896. doi: 10.1016/j.neuroscience.2004.09.053

Stobart, J. L., and Anderson, C. M. (2013). Multifunctional role of astrocytes as gatekeepers of neuronal energy supply. *Front. Cell Neurosci.* 7:38. doi: 10.3389/fncel.2013.00038

Sun, W., Mcconnell, E., Pare, J. F., Xu, Q., Chen, M., Peng, W., et al. (2013). Glutamate-dependent neuroglial calcium signaling differs between young and adult brain. *Science* 339, 197–200. doi: 10.1126/science.1226740

Takano, T., Tian, G. F., Peng, W., Lou, N., Libionka, W., Han, X., et al. (2006). Astrocyte-mediated control of cerebral blood flow. *Nat. Neurosci.* 9, 260–267. doi: 10.1038/nn1623

Tanaka, K., Watase, K., Manabe, T., Yamada, K., Watanabe, M., Takahashi, K., et al. (1997). Epilepsy and exacerbation of brain injury in mice lacking the glutamate transporter GLT-1. *Science* 276, 1699–1702. doi: 10.1126/science.276.5319.1699

Toda, N., Ayajiki, K., and Okamura, T. (2009). Cerebral blood flow regulation by nitric oxide: recent advances. *Pharmacol. Rev.* 61, 62–97. doi: 10.1124/pr.108.000547

Togashi, H., Sasaki, M., Frohman, E., Taira, E., Ratan, R. R., Dawson, T. M., et al. (1997). Neuronal (type I) nitric oxide synthase regulates nuclear factor kappaB activity and immunologic (type II) nitric oxide synthase expression. *Proc. Natl. Acad. Sci. U.S.A.* 94, 2676–2680. doi: 10.1073/pnas.94.6.2676

Tran, C. H., and Gordon, G. R. (2015). Acute two-photon imaging of the neurovascular unit in the cortex of active mice. *Front. Cell Neurosci.* 9:11. doi: 10.3389/fncel.2015.00011

Uhlirova, H., Kilic, K., Tian, P., Thunemann, M., Desjardins, M., Saisan, P. A., et al. (2016). Cell type specificity of neurovascular coupling in cerebral cortex. *Elife* 5:e14315. doi: 10.7554/eLife.14315

Voutsinos-Porche, B., Bonvento, G., Tanaka, K., Steiner, P., Welker, E., Chatton, J. Y., et al. (2003). Glial glutamate transporters mediate a functional metabolic crosstalk between neurons and astrocytes in the mouse developing cortex. *Neuron* 37, 275–286. doi: 10.1016/s0896-6273(02)01170-4

Wadiche, J. I., Arriza, J. L., Amara, S. G., and Kavanaugh, M. P. (1995). Kinetics of a human glutamate transporter. *Neuron* 14, 1019–1027. doi: 10.1016/0896-6273(95)90340-2

Wang, X., Lou, N., Xu, Q., Tian, G. F., Peng, W. G., Han, X., et al. (2006). Astrocytic Ca2+ signaling evoked by sensory stimulation in vivo. *Nat. Neurosci.* 9, 816–823. doi: 10.1038/nn1703

Weber, B., and Barros, L. F. (2015). The astrocyte: powerhouse and recycling center. *Cold Spring Harb. Perspect. Biol.* 7:a020396. doi: 10.1101/cshperspect.a020396

Winship, I. R., Plaa, N., and Murphy, T. H. (2007). Rapid astrocyte calcium signals correlate with neuronal activity and onset of the hemodynamic response in vivo. *J. Neurosci.* 27, 6268–6272. doi: 10.1523/JNEUROSCI.4801-06.2007

Yang, G., Zhang, Y., Ross, M. E., and Iadecola, C. (2003). Attenuation of activity-induced increases in cerebellar blood flow in mice lacking neuronal nitric oxide synthase. *Am. J. Physiol. Heart Circ. Physiol.* 285, H298–H304. doi: 10.1152/ajpheart.00043.2003

Zerangue, N., and Kavanaugh, M. P. (1996). Flux coupling in a neuronal glutamate transporter. *Nature* 383, 634–637. doi: 10.1038/383634a0

Zhang, H. Q., Fast, W., Marletta, M. A., Martasek, P., and Silverman, R. B. (1997). Potent and selective inhibition of neuronal nitric oxide synthase by N omega-propyl-L-arginine. *J. Med. Chem.* 40, 3869–3870. doi: 10.1021/jm970550g

Zhang, Y., Chen, K., Sloan, S. A., Bennett, M. L., Scholze, A. R., O'keeffe, S., et al. (2014). An RNA-sequencing transcriptome and splicing database of glia, neurons, and vascular cells of the cerebral cortex. *J. Neurosci.* 34, 11929–11947. doi: 10.1523/JNEUROSCI.1860-14.2014

Zonta, M., Angulo, M. C., Gobbo, S., Rosengarten, B., Hossmann, K. A., Pozzan, T., et al. (2003). Neuron-to-astrocyte signaling is central to the dynamic control of brain microcirculation. *Nat. Neurosci.* 6, 43–50. doi: 10.1038/nn980

Conflict of Interest: The authors declare that the research was conducted in the absence of any commercial or financial relationships that could be construed as a potential conflict of interest.

frontiers | Frontiers in Cellular Neuroscience

BRIEF RESEARCH REPORT
published: 09 May 2022
doi: 10.3389/fncel.2022.821036

The Cystine/Glutamate Antiporter, System x_c^-, Contributes to Cortical Infarction After Moderate but Not Severe Focal Cerebral Ischemia in Mice

Yan He† **and Sandra J. Hewett***

Program in Neuroscience, Department of Biology, Syracuse University, Syracuse, NY, United States

OPEN ACCESS

Edited by:
Lisa Mapelli,
University of Pavia, Italy

Reviewed by:
Nikolaus Plesnila,
LMU Munich University Hospital, Germany
Jan Lewerenz,
University of Ulm, Germany

***Correspondence:**
Sandra J. Hewett
shewett@syr.edu

†Present address:
Yan He,
Research and Development Department, Akoya Biosciences, Marlborough, MA, United States

Specialty section:
This article was submitted to Cellular Neurophysiology, a section of the journal Frontiers in Cellular Neuroscience

Received: *23 November 2021*
Accepted: *04 April 2022*
Published: *09 May 2022*

Citation:
He Y and Hewett SJ (2022) The Cystine/Glutamate Antiporter, System x_c^-, Contributes to Cortical Infarction After Moderate but Not Severe Focal Cerebral Ischemia in Mice. Front. Cell. Neurosci. 16:821036. doi: 10.3389/fncel.2022.821036

Understanding the mechanisms underlying ischemic brain injury is of importance to the goal of devising novel therapeutics for protection and/or recovery. Previous work in our laboratory and in others has shown that activation of cystine/glutamate antiporter, system x_c^- (Sx_c^-), facilitates neuronal injury in several *in vitro* models of energy deprivation. However, studies on the contribution of this antiporter to ischemic brain damage *in vivo* are more limited. Since embolic or thrombotic transient or permanent occlusion of a cerebral blood vessel eventually leads to brain infarction in most stroke cases, we evaluated the contribution of Sx_c^- to cerebral ischemic damage by comparing brain infarction between mice naturally null for SLC7a11 (SLC7a11$^{sut/sut}$ mice) – the gene the encodes for the substrate specific light chain for system x_c^- – with their wild type (SLC7a11$^{+/+}$) littermates following photothrombotic ischemic stroke of the middle cerebral artery (PTI) and permanent middle cerebral artery occlusion (pMCAo) rendered by cauterization. In the PTI model, we found a time-dependent reduction in cerebral blood flow that reached 50% from baseline in both genotypes 47–48 h post-illumination. Despite this, a remarkable reduction in incidence and total infarct volume of SLC7a11$^{sut/sut}$ mice was revealed 48 h following PTI as compared to SLC7a11$^{+/+}$ mice. No difference in injury markers and/or infarct volume was measured between genotypes when occlusion of the MCA was permanent, however. Present data demonstrate a model-dependent differential role for Sx_c^- in focal cerebral ischemic damage, further highlighting that ischemic severity activates heterogeneous biochemical events that lead to damage engendered by stroke.

Keywords: mouse, cystine/glutamate exchanger, photothrombosis, system x_c^-, permanent ischemia, transient ischemia

INTRODUCTION

It is well established that neuronal cell death in the acute phase of cerebral ischemia is caused by extracellular accumulation of the excitatory amino acid glutamate and consequent over-stimulation of postsynaptic glutamate receptors (Meldrum et al., 1985; Choi, 1988; Benveniste, 1991; Lipton and Rosenberg, 1994; Dirnagl et al., 1999). Surrounding this ischemic core is a region of reduced blood flow (10–50%) known as the penumbra. Evidence from both animal and human studies indicates that injury in this area continues to progress for hours and perhaps days following disruption of blood flow to the core (Heiss et al., 1992; Garcia et al., 1993; Du et al., 1996; Marchal et al., 1996; Baird et al., 1997; Schwamm et al., 1998). The mechanisms contributing to progression of injury in the penumbra are incompletely understood, although studies suggest that this may ensue from hypoxic spreading depression-like depolarizations that promote ongoing excitotoxicity (Somjen, 2001; Pietrobon and Moskowitz, 2014). Using a mixed cortical cell culture system, we previously found that astrocytic system x_c^- (Sx_c^-)—a cystine/glutamate antiporter that exports Glu when importing cystine—contributed to glutamate-mediated excitotoxic neuronal death under simulated ischemic penumbral conditions (Fogal et al., 2007; 2010; 2012). Others demonstrated that pharmacological block of Sx_c^- reduced oxygen-glucose deprivation-induced neuronal currents (i.e., anoxic depolarizations) and cell death in slice and slice cultures, respectively (Soria et al., 2014), as well as in cortical cells (Hsieh et al., 2017). *In vivo*, a rapid increase in Sx_c^- activity in rat brain after focal experimental cerebral ischemia induced by transient middle cerebral artery occlusion (tMCAo) was found (Soria et al., 2014) along with increased xCT protein levels localized to microglia/macrophages, neurons and astrocytes (Domercq et al., 2016; Hsieh et al., 2017). All together, these data support the idea that Sx_c^- may play a deleterious role in brain damage that follows cerebral ischemia. Thus, in this study we determined the contribution of Sx_c^- to neocortical infarction engendered by moderate or permanent focal ischemia, by comparing brain damage of mice wild type (*Slc7a11*$^{+/+}$) or null (*Slc7a11*$^{sut/sut}$) for Sx_c^- following photothrombotic ischemia (PTI) or permanent middle cerebral artery occlusion (pMCAo), respectively.

MATERIALS AND METHODS

Animals and Animal Husbandry

This study was conducted in accordance with the National Institute of Health guidelines for the use and care of experimental animals as approved by the Institutional Animal Care and Use Committee. We utilized male mice on the C3H/HeSnJ background that have a naturally occurring deletion mutation in *Slc7a11*, the gene that encodes for the substrate-specific light-chain for Sx_c^- (xCT) (Chintala et al., 2005). Experimental littermate mice—wild-type ($Slc7a11^{+/+}$) or lacking system x_c^- ($Slc7a11^{sut/sut}$)—were derived from F1 heterozygous ($Slc7a11^{+/sut}$) breeding units created by crossing $Slc7a11^{sut/sut}$ C3H/HeSnJ male mice [Jackson Laboratories (JAX) Stock #001310] with $Slc7a11^{+/+}$ C3H/HeSnJ female mice (JAX, Stock #000661). Mice were only used up to the F3 generation.

At weaning, genotyping was performed *via* PCR analysis of tail genomic DNA samples as described (Sears et al., 2019), after which mice were housed three to five per cage such that at least one mouse of each genotype was represented (pseudo-randomized design). Genotype was reconfirmed *via* PCR upon sacrifice. Mice were maintained in a controlled temperature environment operating on a 12 h light/dark cycle with standard mouse chow and water provided *ad libitum*. These breeding and housing strategies were utilized to control for environmental differences, genetic background influences, and genetic drift (Wolfer and Lipp, 2000; Wolfer et al., 2002).

Ischemic Stroke Models

On each of the 5 days prior to a study, mice (23–30 g; 9–14 weeks) were physically held so that they would become accustomed to being touched. On the surgical day, mice were brought into the procedure room, weighed, and allowed to acclimatize for at least 1 h. Investigator was blind to mouse's genotype at time of experimentation (i.e., surgery) and during all subsequent analyses. All mice were sacrificed 48 h after the induction of cerebral ischemia as described below. **Supplementary Figure 1** provides a diagrammatic schematic depicting the timeline of each protocol. In both models, ischemic damage is largely restricted to the neocortex.

Photothrombosis-Induced Ischemia

Cerebral ischemic damage was induced *via* photothrombosis *via* laser irradiation of the photosensitive compound Rose bengal (Boquillon et al., 1992; Ding et al., 2009). Mice, fully anesthetized with avertin (0.4 g/kg), were placed in a stereotaxic frame using tooth and ear bars. Using aseptic technique, the skull was exposed by making a 1.5–2 cm incision above the sagittal suture. A 5.5 mm × 5.0 mm rectangle metal sheet with a 1.5 mm diameter hole in the middle was gently attached to the right frontal-parietal area with glue (3M Vetbond®). Freshly made Rose bengal (Abcam, Cambridge, United Kingdom) was then injected retro-orbitally (0.03 g/kg in saline) using a 28-gauge, 1/2 inch, 0.5 ml insulin needle and syringe. Three minutes after injection, the frame containing the mouse was mounted on an upright microscope platform and the exposed but otherwise intact skull was illuminated through the 1.5 mm diameter hole for 2 min using a 10x objective with a green light of bandwidth 540–580 nm by means of an X-cite 120Q light source to activate the dye to induce a thrombus. A heating pad was used to maintain mouse's body temperature (36.5–37°C) during and following the procedure. Mortality with this procedure is very low with only one mouse of each genotype lost during surgery.

Ischemic damage was determined 48 h after surgery. Mice were perfused with cold PBS followed by 4% (v/v) paraformaldehyde (PFA). After perfusion, brains were removed and post-fixed in 4% PFA/PBS for 12 h and then placed in 20% (w/v) sucrose for an additional 12–24 h (4°C). Tissue was then embedded in Tissue Tec OCT and solidified in liquid nitrogen. Brain sections (20 μm) cut serially through the rostro-caudal extent of each brain (−2.0 to −3.6 relative to bregma) (Microm HM-550 cryostat, Thermo Fisher Scientific) were stained with 0.5% thionin as described in detail (Claycomb et al., 2011). Images were acquired by a DP73 digital color camera (Digital Video Camera Co.) mounted on an Olympus IX50 inverted microscope controlled by CellSens Standard software (Olympus, Center Valley, PA). Infarct area (A) was directly measured using the free hand tool of ImageJ by tracing the area of the ipsilateral cortex that lacked thionin stain. The lesion area, identified by absence of thionin staining, was quantified using NIH Image J at four levels spanning from −2.0 to −3.6 from bregma by two individuals blind to genotype. Area measurements were converted to volume using Cavalieri's principle: $V = Ai \times D + Aii \times D + Aiii \times D + Aiv$ with V = total infarct volume (mm^3) and Ai = mean infarct area of each section derived from two measurements and D represents the distance between 2 sections (Shih et al., 2003).

Laser Speckle Contrast Analysis was used to measure microvascular cerebral blood flow in the right MCA territory where the Rose Bengal was activated [PSI HR real time laser speckle perfusion imager; Pericam (Las Vegas, NV)] in a separate cohort of mice (see **Supplementary Figure 2** for representative video). Briefly, after making the incision and exposing the skull, mouse was moved to the imager to access the baseline of blood flow for 30 sec per manufacturer's instruction. Then a 5.5 mm × 5.0 mm rectangle metal sheet with a 1.5 mm diameter hole in the middle was gently attached to the right frontal-parietal area with glue (3M Vetbond®), followed by the retro-orbital injection and laser activation of Rose Bengal as described above. After the activation, the metal sheet was gently removed, and mouse was immediately moved to the imager to access the real time blood flow for 30 sec (time zero). The incision was sealed lightly by glue, after which the mouse was put back into their cage containing a heating-pad and allowed to recover. Mice were re-anesthetized, the incision gently re-opened and additional blood flow measurements taken over the same region at 4–6, 24, and 47–48 h post-illumination. Data at each time point was normalized to baseline for each mouse and expressed as mean percentage ± S.D.

Permanent Middle Cerebral Artery Occlusion

Permanent cerebral cortical ischemia was induced in avertin-anesthetized male mice by ligating the right common carotid artery (CCA) and cauterizing the right middle cerebral artery (MCA) distal to the striatal branch as described in Piao et al. (2009) and Cui et al. (2015). The mouse's body temperature was maintained at 36.5–37°C during the surgery and during recovery *via* heat pad. With respect to mortality, we lost one $Slc7a11^{+/+}$ and two $Slc7a11^{sut/sut}$ mice 1 day after surgery. Those surviving were sacrificed 48hr later and brains directly sectioned into 1 mm coronal sections. The 4th, 6th, 8th, and 10th sections were stained with 2% 2,3,5-triphenyl-tetrazolium chloride (TTC; Sigma-Aldrich, St. Louis, MO) for 30 min at 37°C in the dark. Slices were then carefully transferred into 10% formalin for 24 h. Images (300 dpi) were captured by scanning (Epson Perfection 3170). The non-injury areas of both contralateral and ipsilateral hemispheres—denoted by red staining—were measured using NIH ImageJ for all sections by two experimenters blind to the genotype of the mice and infarct area and volume determined. Infarct area (A) was determined by subtracting the non-injured ipsilateral area from the area of the contralateral hemisphere. Total infarct volume (mm3) was calculated using the following equation: $V = Ai \times 2 + Ai \times 2 + Aii \times 2 + Aiii \text{ x } 2 + Aiv$ with V = total infarct volume and Ai = infarct area of each section with 2 representing the distance between slices (i.e., 2 mm) (Shih et al., 2003).

To measure spectrin breakdown products, shown previously to correlate nicely with final infarct volume (Davoli et al., 2002), contralateral and ipsilateral sides of the 5th, 7th, and 9th sections were separately pooled and homogenized in RIPA buffer containing: 0.5% Sodium deoxycholate, 25 mM Tris, 150 mM NaCl, 0.1% SDS, 1% Triton X-100, 5 mM iodoacetamide, 5 mM EDTA, 5 mM EGTA, and 1 X Complete Protease Inhibitor (Roche). Cellular debris was removed by centrifugation (12,000 g; 20 min; 4°C). Supernatants were collected and 15 μg (BCA assay; Pierce; Rockford, IL) of protein was separated by 10% SDS-PAGE under reducing conditions, followed by electrophoretic transfer to PVDF membrane (Bio-Rad; Hercules, CA). Membranes were blocked (Odyssey® blocking buffer; at 25°C for 1 h) and then probed (4°, overnight) with an anti-α Fodrin monoclonal antibody (AA6, 100 ng/ml; Enzo) and a mouse monoclonal antibody directed against β-actin to correct for protein loading (650 ng/ml; Sigma). Species-specific secondary antibodies labeled with spectrally distinct IRDye® fluorescent dyes (LI-COR Biosciences; Lincoln, NE) were used to detect primary antibodies (1 h at 25°C). Results were recorded on LI-COR ODYSSEY® Fc Imaging system (LI-COR Biosciences) and protein levels quantified using Image Studio 3.1 (LI-COR Biosciences; Lincoln, NE). Results were obtained by normalizing fodrin protein levels to their respective β-actin levels and expressed as mean fold change over the corresponding contralateral hemisphere (set to 1).

Statistical Analysis

All statistical analyses and graphics were compiled using GraphPad Prism (Version 6.0.3, GraphPad Software, Inc. or higher; Graphpad Software, Inc., La Jolla, CA). Cerebral blood flow (CBF) were analyzed using a mixed effects model with the Geisser-Greenhouse correction for normality followed by Šídák's multiple comparisons test. αII-spectrin breakdown products (SBDPs) where analyzed using two-way ANOVA of log transformed data [$y = \log(y)$] followed by Šídák's multiple comparisons test. Infarct volumes were analyzed *via* two-tailed Mann Whitney U-test. Exact or adjusted p-values are included in text, in a table and/or described in figure legends as appropriate.

RESULTS

Anatomical damage due to PTI was greatly reduced in mice lacking Sx_c^- with overall infarct volume being significantly smaller (two-tailed Mann Whitney U-test; $p = 0.0007$) in $SLC7a11^{sut/sut}$ as compared to $SLC7a11^{+/+}$ littermate controls (**Figures 1A,C,D**). This change was driven mostly by a reduction in the overall incidence of damage evidenced by the fact that 92% of $SLC7a11^{+/+}$ mice (12/13) had quantifiable cortical infarction as compared to just 25% (4/16) of $SLC7a11^{sut/sut}$ mice (**Figure 1A**; Fishers exact test, $p = 0.005$). Differing amounts of occlusion could not account for the dissimilarity in PTI-mediated damage as similar decreases in rCBF starting

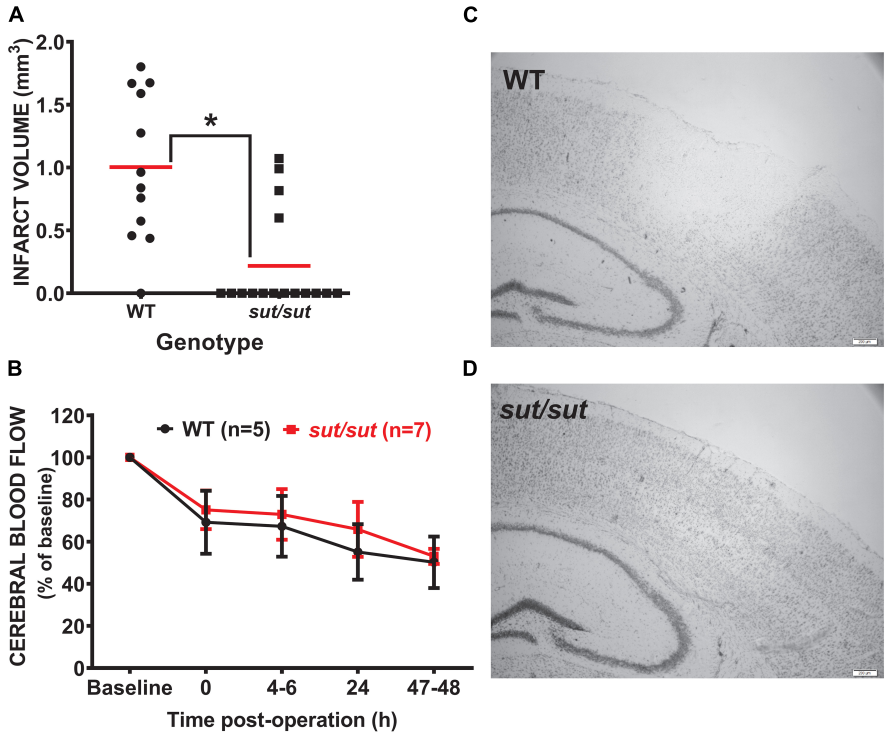

FIGURE 1 | Comparison of infarct incidence and size between WT and Sx_c^- null mice following photothrombotic-induced ischemia. **(A)** Forty-eight h after PTI, brains of sut/sut (n = 16) mice and their WT (n = 13) littermates were removed. Coronal sections (20 μm) were cut along the rostral-caudal axis (−2.0 to −3.6 relative to bregma) and stained with thionin, with areas lacking thionin staining represent ischemic damage. Infarct volume was determined as described in Methods. Each data point (black dot: WT; black square: sut/sut) represents total infarct volume in mm^3 from an individual mouse, whereas the horizontal red line represents the mean **(B)** Depicts rCBF as determined *via* laser speckle contrast imaging represented as mean fold change ± *SD* from baseline (set to 100) taken immediately prior to illumination and at intervals following illumination as described in methods. **(C)** Representative thionin staining of brain tissue of Slc7a11$^{+/+}$ (WT) and **(D)** Slc7a11$^{sut/sut}$ (sut/sut) mice. A significant difference in infarct volume (*p = 0.0007) was determined by two-tailed Mann Whitney U-test. Infarct incidence −defined as the number of mice with any size infarct divided by the total number of mice—also differed significantly between genotypes as assessed by Fisher's exact test (p = 0.005).

at ≈25–30% (69.2 ± 14.9 vs. 75.1 ± 9.1 of baseline levels for SLC7a11$^{+/+}$ vs. SLC7a11$^{sut/sut}$, respectively) measured directly after laser illumination progressing to ≈50% reduction of pre-illumination levels (50.2 ± 12.2 vs. 53.0 ± 3.6 for SLC7a11$^{+/+}$ vs. SLC7a11$^{sut/sut,}$ respectively) by the time of sacrifice occurred irrespective of the mouse's genotype (**Figure 1B**). Mixed effect model analysis shows a significant effect of time ($p < 0.0001$) with *post hoc* analyses revealing a significant reduction from baseline in SLC7a11$^{+/+}$ mice occurring at 24 and 48 h, respectively. In contrast, significant changes from baseline occurred at all-time points post-illumination in SLC7a11$^{sut/sut}$ mice. Pertinently, no significant between genotype differences was found at any time post-illumination (**Table 1**).

In contrast to what we found with PTI, a well demarcated infarct was visible 48 hr following pMCAo in all mice regardless of genotype (**Figure 2A**). Analysis of infarct volume showed no significant difference in infarct size between SLC7a11$^{+/+}$ and SLC7a11$^{sut/sut}$ mice (two tailed Mann Whitney U-test, $p > 0.999$) (**Figure 2B**). The levels of αII spectrin breakdown products, measured as an additional index of ischemic injury, also did not differ between genotypes (**Figures 2C,D**; two-way ANOVA; $p = 0.925$).

DISCUSSION

Occlusion of a major blood vessel, most notably the middle cerebral artery (Olsen et al., 1985), leads to cerebral ischemia in the vast majority of stroke cases. The pace of brain circuitry loss in humans from a typical large vessel occlusion is estimated to be a staggering 120 million neurons and 830 billion synapses per hour (Saver, 2006). Given that > 750,000 persons in the US will have a stroke this year, it is imperative that more therapies be made available, which necessitates our need to understand more fully

TABLE 1 | Statistical analysis of rCBF following PTI (**Figure 1B**).

Blood flow	**SLC7a11$^{+/+}$**	**SLC7a11$^{sut/sut}$**	**+/+ vs. sut/sut**
Post-illumination time (h)	***P*-value (change from baseline)**	***p*-value (change from baseline)**	***p*-value (between group difference)**
0	0.096	0.004	0.956
4–6	0.069	0.023	0.970
24	0.016	0.005	0.666
47–48	0.008	<0.0001	0.994

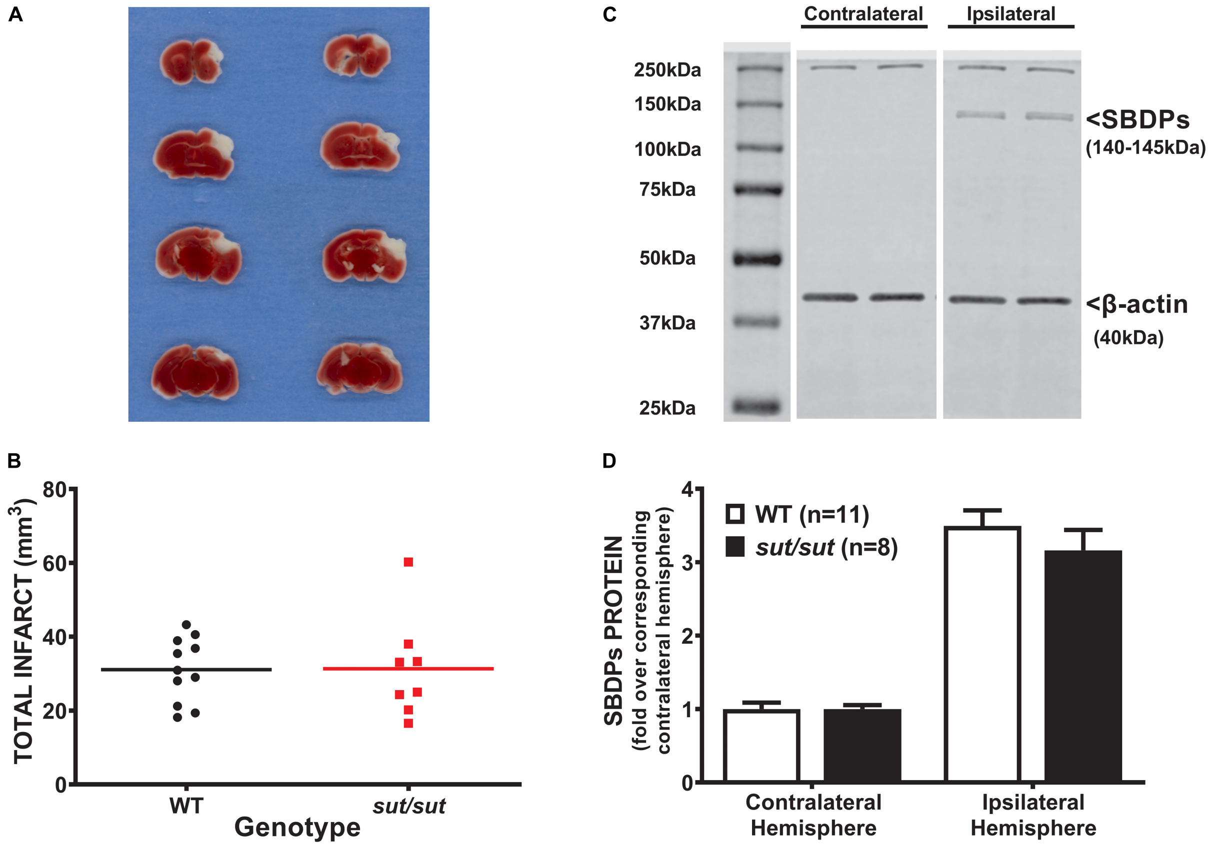

FIGURE 2 | Comparison of pMCAo-induced brain damage between system x_c^- null (*sut/sut*) mice and their wild type (WT) littermates. Forty-eight hr after pMCAo, brains were harvested from *sut/sut* (n = 8) mice and their WT (n = 11) littermates and cut in 1mm sections along the rostral-caudal axis. Sections 4, 6, 8, and 10 were used to quantify infarct volume, while the 5th, 7th and, 9th sections were used for immunoblot analysis of SBDPs, each as described in methods. **(A)** Representative TTC staining of coronal brain sections from WT (left panel) and *sut/sut* littermates (right panel). Lack of TTC staining delineates infarct. **(B)** Each data point (black dot: WT; red square: *sut/sut*) represents total infarct volume in mm^3 from an individual mouse, whereas the horizontal line represents the mean of all mice. **(C)** Representative blot of SBDPs **(D)** SBDPs protein levels, normalized to their corresponding β-actin, are expressed as mean fold change + SEM over the corresponding contralateral hemisphere (set to 1).

the mechanisms underlying ischemic brain damage. Previous PET imaging studies demonstrated increased Sx_c^- activity in rat brain *in vivo* following transient focal ischemia produced *via* intraluminal occlusion of MCA followed by reperfusion (Soria et al., 2014; Domercq et al., 2016). The models chosen in this study to assess the role of Sx_c^- to ischemic damage directly mimic different clinical conditions. Photosensitization of intravascular Rose Bengal by laser illumination (Watson et al., 1985; Pevsner et al., 2001) at the territory of the MCA induces platelet aggregation, vascular thrombosis and, as we demonstrated herein, incomplete blood flow reduction, while pMCAo *via* direct electrocoagulation mimics severe ischemic stroke without vessel recanalization (Sommer, 2017). Present data demonstrate that activity of Sx_c^- promotes cortical infarction after moderate (PTI) but not severe (pMCAo) focal cerebral ischemia in mice.

The mouse utilized in this study was first identified by its subtle gray coat pigmentation that sequencing and subsequent experimentation revealed resulted from a large deletion mutation in Exon 12 of the *Slc7a11* gene (Chintala et al., 2005), which encodes the substrate specific light chain (xCT) for the cystine/glutamate exchanger, system x_c^-. Importantly, we and others (Swank et al., 1996) have found that on a non-agouti background the reduction in pigmentation arising from the sut mutation becomes nearly imperceptible when the mice are adults making homozygotes difficult to distinguish from wild-type littermate controls; hence our ability to remain blind to genotype during experimentation. Additionally, despite the identification of an alternative transcript *via* 3'RACE, northern blot analysis reveals no xCT mRNA in brain of $Slc7a11^{sut/sut}$ mice (Chintala et al., 2005). This is likely due to the fact that loss of the 3'UTR *via* this deletion leads to absence of polyadenylation, which is necessary for mRNA stability and translation (Muhlemann and Jensen, 2012; Lykke-Andersen and Bennett, 2014). Additionally, no xCT protein in brain was found *via* Western Blot analysis (McCullagh and Featherstone, 2014).

We initially considered that changes in clotting —either initial aggregation or more pronounced lysis—might explain the results in the PTI model given a reduction in collagen-mediated platelet aggregation *ex vivo* has been reported in $SLC7a11^{sut/sut}$ mice (Swank et al., 1996). However, our data showing a sustained reduction in CBF over the 48 hr period suggests this is not the case. This may not be too surprising given the complexity of factors/mechanisms known to facilitate platelet aggregation *in vivo* (Rumbaut and Thiagarajan, 2010). Given this, we conclude that the neocortical tissue of mice is remarkably less vulnerable to death when Sx_c^- function is absent under conditions where blood flow is moderately disrupted (**Figure 1**).

Our PTI results are somewhat in keeping with those of Hsieh and colleagues, who demonstrated a reduction in infarct volume in genetically manipulated mice lacking Sx_c^- ($xCT^{-/-}$) when subjected to cerebral ischemia followed by reperfusion (Hsieh et al., 2017). Both of these findings might seem surprising given the importance of Sx_c^- to the production of GSH, at least, *in vitro*, where growth of xCT-deficient cells is dependent on the addition of a reducing agent (Bannai and Tateishi, 1986; Chintala et al., 2005; Shih et al., 2006; Jackman et al., 2010). However, $xCT^{-/-}$ and $Slc7a11^{sut/sut}$ mice have normal brain GSH levels (De Bundel et al., 2011; Sears et al., 2019), at least under basal conditions, suggesting that other cyste(i)ne transporter systems compensate for loss *in vivo* (Sosnoski et al., 2020). We cannot discount that there might be GSH dysregulation following ischemic stress. However, if so, the impact would appear minimal as evidenced by a reduction in damage following PTI and a lack of injury enhancement after pMCAo.

Interestingly, following tMCAo, $xCT^{-/-}$ mice had appreciably less extracellular glutamate levels in the ischemic cortex at early (2–5 hr) and late time points (1–3 days), indicating a role for Sx_c^- as a source of extracellular glutamate post-ischemia (Hsieh et al., 2017). Relevant to this, we demonstrated increased astrocytic system x_c^- levels and activity contributes to enhanced extracellular Glu levels, which precipitates excitotoxic neuronal cell death in an *in vitro* model of the ischemic penumbra (Fogal et al., 2007; Jackman et al., 2010). Together, these results help explain the intriguing observation made by Obrenovitch that neither vesicle exocytosis or reversed Glu uptake could account for all the cerebral ischemic extracellular Glu levels measured *in vivo* (Obrenovitch, 1996). Together, these results extend the current, perhaps oversimplified, concept of excitotoxicity that has heretofore dominated current thinking to include Sx_c^-. Given the lack of specificity of the commercial antibodies directed against xCT (Van Liefferinge et al., 2016), we did not explore its cell-type expression following ischemia in our models. However, others have demonstrated increased immunofluorescence for xCT in microglia/macrophages at 3 and 7 days post-ischemia and in astrocytes up to 28 days post-ischemia (Domercq et al., 2016) while Hsieh and colleagues report a post-ischemic increase in expression in both astrocytes and neurons (Hsieh et al., 2017).

Despite the evidence demonstrating the contribution of Sx_c^- to ischemic damage when blood flow is moderately (this study) or transiently (Hsieh et al., 2017) reduced, a very different picture emerged when the MCA was permanently occluded. Finding no difference in infarct volume or other markers of injury (**Figure 2**), we can only conclude that other biochemical mechanisms clearly predominate when blood flow disruption is severe. This is perhaps not surprising as many potential therapeutics have been described in the literature that show potential promise in transient but not permanent ischemia models and the idea has been put forth that salvageable tissue exits only in the ischemic penumbra (for review see Moskowitz et al., 2010).

Studies in genetically modified mice are useful for potential target identification. However, in the interest of therapeutic development, it is important to note that in keeping with the observations described above, pharmacological inhibition of Sx_c^- reduced ischemia-induced inflammation (Domercq et al., 2016) and infarct volume (Hsieh et al., 2017) subsequent to transient ischemia in rats, but not following permanent ischemia in mouse (our unpublished observations). While it is clear that additional studies are needed to determine the relevance of our and other findings to human stroke, it is intriguing to speculate that should strategies to mitigate Sx_c^- activity ever be employed in a clinical setting, it may only be beneficial to patients whose vessel recanalizes leading to revascularization or in patients with penumbra where blood flow is mildly to moderately interrupted (10–50% of baseline).

DATA AVAILABILITY STATEMENT

The raw data supporting the conclusions of this article will be made available by the authors, without undue reservation.

ETHICS STATEMENT

The animal study was reviewed and approved by the Syracuse University's Institutional Animal Care and Use Committee.

AUTHOR CONTRIBUTIONS

YH and SH: conceptualization, methodology, funding acquisition, writing of original draft, reviewing and editing, and statistical analysis. YH: investigation. SH: resources and supervision. Both authors contributed to the article and approved the submitted version.

FUNDING

This work was supported by grant NINDS/NIH 5R21NS096676 to SH and AHA Postdoctoral Fellowship to YH.

ACKNOWLEDGMENTS

We would like to thank Drs. Shinghua Ding and Li-Ru Zhao for their help in training. YH to perform PTI and pMCAo, respectively.

SUPPLEMENTARY MATERIAL

The Supplementary Material for this article can be found online at: https://www.frontiersin.org/articles/10.3389/fncel.2022.821036/full#supplementary-material

REFERENCES

Baird, A. E., Benfield, A., Schlaug, G., Siewert, B., Lovblad, K. O., Edelman, R. R., et al. (1997). Enlargement of human cerebral ischemic lesion volumes measured by diffusion-weighted magnetic resonance imaging. *Ann. Neurol.* 41, 581–589. doi: 10.1002/ana.410410506

Bannai, S., and Tateishi, N. (1986). Role of membrane transport in metabolism and function of glutathione in mammals. *J. Membr. Biol.* 89, 1–8. doi: 10.1007/BF01870891

Benveniste, H. (1991). The excitotoxin hypothesis in relation to cerebral ischemia. *Cerebrovasc. Brain Metab. Rev.* 3, 213–245.

Boquillon, M., Boquillon, J. P., and Bralet, J. (1992). Photochemically induced, graded cerebral infarction in the mouse by laser irradiation evolution of brain edema. *J. Pharmacol. Toxicol. Methods* 27, 1–6. doi: 10.1016/1056-8719(92)90013-q

Chintala, S., Li, W., Lamoreux, M. L., Ito, S., Wakamatsu, K., Sviderskaya, E. V., et al. (2005). Slc7a11 gene controls production of pheomelanin pigment and proliferation of cultured cells. *Proc. Natl. Acad. Sci. U S A* 102, 10964–10969. doi: 10.1073/pnas.0502856102

Choi, D. W. (1988). Glutamate neurotoxicity and diseases of the nervous system. *Neuron* 1, 623–634. doi: 10.1016/0896-6273(88)90162-6

Claycomb, R. J., Hewett, S. J., and Hewett, J. A. (2011). Prophylactic, prandial rofecoxib treatment lacks efficacy against acute PTZ-induced seizure generation and kindling acquisition. *Epilepsia* 52, 273–283. doi: 10.1111/j.1528-1167.2010.02889.x

Cui, L., Duchamp, N. S., Boston, D. J., Ren, X., Zhang, X., Hu, H., et al. (2015). NF-kappaB is involved in brain repair by stem cell factor and granulocyte-colony stimulating factor in chronic stroke. *Exp. Neurol.* 263, 17–27. doi: 10.1016/j.expneurol.2014.08.026

Davoli, M. A., Fourtounis, J., Tam, J., Xanthoudakis, S., Nicholson, D., Robertson, G. S., et al. (2002). Immunohistochemical and biochemical assessment of caspase-3 activation and DNA fragmentation following transient focal ischemia in the rat. *Neuroscience* 115, 125–136. doi: 10.1016/s0306-4522(02)00376-7

De Bundel, D., Schallier, A., Loyens, E., Fernando, R., Miyashita, H., Van Liefferinge, J., et al. (2011). Loss of system $x_c{}^-$ does not induce oxidative stress but decreases extracellular glutamate in hippocampus and influences spatial working memory and limbic seizure susceptibility. *J. Neurosci.* 31, 5792–5803. doi: 10.1523/jneurosci.5465-10.2011

Ding, S., Wang, T., Cui, W., and Haydon, P. G. (2009). Photothrombosis ischemia stimulates a sustained astrocytic Ca2+ signaling in vivo. *Glia* 57, 767–776. doi: 10.1002/glia.20804

Dirnagl, U., Iadecola, C., and Moskowitz, M. A. (1999). Pathobiology of ischaemic stroke: an integrated view. *Trends Neurosci.* 22, 391–397. doi: 10.1016/s0166-2236(99)01401-0

Domercq, M., Szczupak, B., Gejo, J., Gomez-Vallejo, V., Padro, D., Gona, K. B., et al. (2016). PET Imaging with [(18)F]FSPG Evidences the Role of System xc(-) on Brain Inflammation Following Cerebral Ischemia in Rats. *Theranostics* 6, 1753–1767. doi: 10.7150/thno.15616

Du, C., Hu, R., Csernansky, C. A., Hsu, C. Y., and Choi, D. W. (1996). Very delayed infarction after mild focal cerebral ischemia: a role for apoptosis? *J. Cereb. Blood Flow Metab.* 16, 195–201. doi: 10.1097/00004647-199603000-00003

Fogal, B., Li, J., Lobner, D., McCullough, L. D., and Hewett, S. J. (2007). System x(c)- activity and astrocytes are necessary for interleukin-1beta-mediated hypoxic neuronal injury. *J. Neurosci.* 27, 10094–10105. doi: 10.1523/JNEUROSCI.2459-07.2007

Garcia, J. H., Yoshida, Y., Chen, H., Li, Y., Zhang, Z. G., Lian, J., et al. (1993). Progression from ischemic injury to infarct following middle cerebral artery occlusion in the rat. *Am. J. Pathol.* 142, 623–635.

Heiss, W. D., Huber, M., Fink, G. R., Herholz, K., Pietrzyk, U., Wagner, R., et al. (1992). Progressive derangement of periinfarct viable tissue in ischemic stroke. *J. Cereb. Blood Flow Metab.* 12, 193–203. doi: 10.1038/jcbfm.1992.29

Hsieh, C. H., Lin, Y. J., Chen, W. L., Huang, Y. C., Chang, C. W., Cheng, F. C., et al. (2017). HIF-1alpha triggers long-lasting glutamate excitotoxicity via system xc(-) in cerebral ischaemia-reperfusion. *J. Pathol.* 241, 337–349. doi: 10.1002/path.4838

Jackman, N. A., Melchior, S. E., Hewett, J. A., and Hewett, S. J. (2012). Non-cell autonomous influence of the astrocyte system xc- on hypoglycaemic neuronal cell death. *ASN Neuro.* 4:e00074. doi: 10.1042/AN20110030

Jackman, N. A., Uliasz, T. F., Hewett, J. A., and Hewett, S. J. (2010). Regulation of system x(c)(-)activity and expression in astrocytes by interleukin-1beta: implications for hypoxic neuronal injury. *Glia* 58, 1806–1815. doi: 10.1002/glia.21050

Lipton, S. A., and Rosenberg, P. A. (1994). Excitatory amino acids as a final common pathway for neurologic disorders [see comments]. *N. Engl. J. Med.* 330, 613–622. doi: 10.1056/nejm199403033300907

Lykke-Andersen, J., and Bennett, E. J. (2014). Protecting the proteome: eukaryotic cotranslational quality control pathways. *J. Cell Biol.* 204, 467–476. doi: 10.1083/jcb.201311103

Marchal, G., Beaudouin, V., Rioux, P., de la Sayette, V., Le Doze, F., Viader, F., et al. (1996). Prolonged persistence of substantial volumes of potentially viable brain tissue after stroke: a correlative PET-CT study with voxel-based data analysis. *Stroke* 27, 599–606. doi: 10.1161/01.str.27.4.599

McCullagh, E. A., and Featherstone, D. E. (2014). Behavioral characterization of system xc- mutant mice. *Behav. Brain Res.* 265, 1–11. doi: 10.1016/j.bbr.2014.02.010

Meldrum, B., Evans, M., Griffiths, T., and Simon, R. (1985). Ischaemic brain damage: the role of excitatory activity and of calcium entry. *Br. J. Anaesth.* 57, 44–46. doi: 10.1093/bja/57.1.44

Moskowitz, M. A., Lo, E. H., and Iadecola, C. (2010). The science of stroke: mechanisms in search of treatments. *Neuron* 67, 181–198. doi: 10.1016/j.neuron.2010.07.002

Muhlemann, O., and Jensen, T. H. (2012). mRNP quality control goes regulatory. *Trends Genet.* 28, 70–77. doi: 10.1016/j.tig.2011.11.001

Obrenovitch, T. P. (1996). Origins of glutamate release in ischaemia. *Acta Neurochir. Suppl.* 66, 50–55. doi: 10.1007/978-3-7091-9465-2_9

Olsen, T. S., Skriver, E. B., and Herning, M. (1985). Cause of cerebral infarction in the carotid territory. Its relation to the size and the location of the infarct and to the underlying vascular lesion. *Stroke* 16, 459–466. doi: 10.1161/01.str.16.3.459

Pevsner, P. H., Eichenbaum, J. W., Miller, D. C., Pivawer, G., Eichenbaum, K. D., Stern, A., et al. (2001). A photothrombotic model of small early ischemic infarcts in the rat brain with histologic and MRI correlation. *J. Pharmacol. Toxicol. Methods* 45, 227–233. doi: 10.1016/s1056-8719(01)00153-8

Piao, C. S., Gonzalez-Toledo, M. E., Xue, Y. Q., Duan, W. M., Terao, S., Granger, D. N., et al. (2009). The role of stem cell factor and granulocyte-colony stimulating factor in brain repair during chronic stroke. *J. Cereb. Blood Flow Metab.* 29, 759–770. doi: 10.1038/jcbfm.2008.168

Pietrobon, D., and Moskowitz, M. A. (2014). Chaos and commotion in the wake of cortical spreading depression and spreading depolarizations. *Nat. Rev. Neurosci.* 15, 379–393. doi: 10.1038/nrn3770

Rumbaut, R. E., and Thiagarajan, P. (2010). *Platelet-Vessel Wall Interactions in Hemostasis and Thrombosis*. San Rafael (CA): Morgan & Claypool Life Sciences

Saver, J. L. (2006). Time is brain–quantified. *Stroke* 37, 263–266. doi: 10.1161/01.STR.0000196957.55928.ab

Schwamm, L. H., Koroshetz, W. J., Sorensen, A. G., Wang, B., Copen, W. A., Budzik, R., et al. (1998). Time course of lesion development in patients with acute stroke: serial diffusion- and hemodynamic-weighted magnetic resonance imaging. *Stroke* 29, 2268–2276. doi: 10.1161/01.str.29.11.2268

Sears, S. M. S., Hewett, J. A., and Hewett, S. J. (2019). Decreased epileptogenesis in mice lacking the System xc (-) transporter occurs in association with a reduction in AMPA receptor subunit GluA1. *Epilepsia. Open* 4, 133–143. doi: 10.1002/epi4.12307

Shih, A. Y., Erb, H., Sun, X., Toda, S., Kalivas, P. W., and Murphy, T. H. (2006). Cystine/Glutamate Exchange Modulates Glutathione Supply for Neuroprotection from Oxidative Stress and Cell Proliferation. *J. Neurosci.* 26, 10514–10523. doi: 10.1523/jneurosci.3178-06.2006

Shih, A. Y., Johnson, D. A., Wong, G., Kraft, A. D., Jiang, L., Erb, H., et al. (2003). Coordinate regulation of glutathione biosynthesis and release by Nrf2-expressing glia potently protects neurons from oxidative stress. *J. Neurosci.* 23, 3394–3406.

Somjen, G. G. (2001). Mechanisms of spreading depression and hypoxic spreading depression-like depolarization. *Physiol. Rev.* 81, 1065–1096. doi: 10.1152/physrev.2001.81.3.1065

Sommer, C. J. (2017). Ischemic stroke: experimental models and reality. *Acta Neuropathol.* 133, 245–261. doi: 10.1007/s00401-017-1667-0

Soria, F. N., Perez-Samartin, A., Martin, A., Gona, K. B., Llop, J., Szczupak, B., et al. (2014). Extrasynaptic glutamate release through cystine/glutamate antiporter contributes to ischemic damage. *J. Clin. Invest.* 124, 3645–3655. doi: 10.1172/JCI71886

Sosnoski, H. M., Sears, S. M. S., He, Y., Frare, C., and Hewett, S. J. (2020). Sexually dimorphic and brain region-specific transporter adaptations in system x_c^- null mice. *Neurochem. Int*. 141:104888. doi: 10.1016/j.neuint.2020.104888

Swank, R. T., Reddington, M., and Novak, E. K. (1996). Inherited prolonged bleeding time and platelet storage pool deficiency in the subtle gray (sut) mouse. *Lab. Anim. Sci.* 46, 56–60.

Van Liefferinge, J., Bentea, E., Demuyser, T., Albertini, G., Follin-Arbelet, V., Holmseth, S., et al. (2016). Comparative analysis of antibodies to xCT (Slc7a11): forewarned is forearmed. *J. Comp. Neurol.* 524, 1015–1032. doi: 10.1002/cne.23889

Watson, B. D., Dietrich, W. D., Busto, R., Wachtel, M. S., and Ginsberg, M. D. (1985). Induction of reproducible brain infarction by photochemically initiated thrombosis. *Ann. Neurol.* 17, 497–504. doi: 10.1002/ana.410170513

Wolfer, D. P., Crusio, W. E., and Lipp, H. P. (2002). Knockout mice: simple solutions to the problems of genetic background and flanking genes. *Trends Neurosci.* 25, 336–340. doi: 10.1016/s0166-2236(02)02192-6

Wolfer, D. P., and Lipp, H. P. (2000). Dissecting the behaviour of transgenic mice: is it the mutation, the genetic background, or the environment? *Exp. Physiol.* 85, 627–634. doi: 10.1111/j.1469-445x.2000.02095.x

Conflict of Interest: The authors declare that the research was conducted in the absence of any commercial or financial relationships that could be construed as a potential conflict of interest.

frontiers | Frontiers in Cellular Neuroscience

BRIEF RESEARCH REPORT
published: 03 June 2022
doi: 10.3389/fncel.2022.905299

Deletion of the Sodium-Dependent Glutamate Transporter GLT-1 in Maturing Oligodendrocytes Attenuates Myelination of Callosal Axons During a Postnatal Phase of Central Nervous System Development

Elizabeth J. Thomason[1]†, Edna Suárez-Pozos[1]†, Fatemah S. Afshari[1], Paul A. Rosenberg[2], Jeffrey L. Dupree[1] and Babette Fuss[1]*

[1] Department of Anatomy and Neurobiology, Virginia Commonwealth University School of Medicine, Richmond, VA, United States, [2] Department of Neurology and the F.M. Kirby Neurobiology Center, Boston Children's Hospital, Boston, MA, United States

Edited by:
Sandra Hewett,
Syracuse University, United States

Reviewed by:
Stephen Crocker,
University of Connecticut Health Center, United States
Michael B. Robinson,
Children's Hospital of Philadelphia Research Institute, United States

***Correspondence:**
Babette Fuss
babette.fuss@vcuhealth.org

†These authors have contributed equally to this work and share first authorship

Specialty section:
This article was submitted to Cellular Neurophysiology, a section of the journal Frontiers in Cellular Neuroscience

***Received:** 26 March 2022*
***Accepted:** 16 May 2022*
***Published:** 03 June 2022*

Citation:
Thomason EJ, Suárez-Pozos E, Afshari FS, Rosenberg PA, Dupree JL and Fuss B (2022) Deletion of the Sodium-Dependent Glutamate Transporter GLT-1 in Maturing Oligodendrocytes Attenuates Myelination of Callosal Axons During a Postnatal Phase of Central Nervous System Development. Front. Cell. Neurosci. 16:905299. doi: 10.3389/fncel.2022.905299

The sodium-dependent glutamate transporter GLT-1 (EAAT2, SLC1A2) has been well-described as an important regulator of extracellular glutamate homeostasis in the central nervous system (CNS), a function that is performed mainly through its presence on astrocytes. There is, however, increasing evidence for the expression of GLT-1 in CNS cells other than astrocytes and in functional roles that are mediated by mechanisms downstream of glutamate uptake. In this context, GLT-1 expression has been reported for both neurons and oligodendrocytes (OLGs), and neuronal presynaptic presence of GLT-1 has been implicated in the regulation of glutamate uptake, gene expression, and mitochondrial function. Much less is currently known about the functional roles of GLT-1 expressed by OLGs. The data presented here provide first evidence that GLT-1 expressed by maturing OLGs contributes to the modulation of developmental myelination in the CNS. More specifically, using inducible and conditional knockout mice in which GLT-1 was deleted in maturing OLGs during a peak period of myelination (between 2 and 4 weeks of age) revealed hypomyelinated characteristics in the corpus callosum of preferentially male mice. These characteristics included reduced percentages of smaller diameter myelinated axons and reduced myelin thickness. Interestingly, this myelination phenotype was not found to be associated with major changes in myelin gene expression. Taken together, the data presented here demonstrate that GLT-1 expressed by maturing OLGs is involved in the modulation of the morphological aspects associated with CNS myelination in at least the corpus callosum and during a developmental window that appears of particular vulnerability in males compared to females.

Keywords: glutamate transport, oligodendrocyte, myelination, development, conditional and inducible knockout

INTRODUCTION

The sodium-dependent glutamate transporter GLT-1 (EAAT2, SLC1A2) has been well-characterized for its role in regulating extracellular glutamate homeostasis in the central nervous system (CNS), a function that is performed mainly through its presence on astrocytes (Rothstein et al., 1996; Tanaka et al., 1997; Danbolt, 2001; Petr et al., 2015; Rose et al., 2018). In general, glutamate uptake by sodium-dependent glutamate transporters is driven by co-transport of sodium ions and protons, as well as counter-transport of potassium ions (Rose et al., 2018). The complexity of this transport mechanism allows active transport of glutamate into the cell against a steep concentration gradient. At the same time, it enables functional consequences that are beyond the regulation of glutamate homeostasis and have in astrocytes been shown to include alterations in brain energetics and intracellular signaling (Chen et al., 2006; Martinez-Lozada et al., 2011; Maria Lopez-Colome et al., 2012; Flores-Mendez et al., 2013; Robinson and Jackson, 2016; Robinson et al., 2020). Such multifaceted roles of sodium-dependent glutamate transporters are further broadened by their expression in CNS cells other than astrocytes. In the case of GLT-1, its neuronal presence at presynaptic sites has been functionally implicated not only in glutamate uptake but also in the regulation of gene expression and mitochondrial function (Petr et al., 2015; Rimmele and Rosenberg, 2016; Laprairie et al., 2019; McNair et al., 2019, 2020; Zhou et al., 2019; Rimmele et al., 2021). GLT-1 expression and GLT-1 mediated glutamate uptake have also been reported for the myelinating cells of the CNS, namely oligodendrocytes (OLGs) (Domercq and Matute, 1999; Regan et al., 2007; Arranz et al., 2008; DeSilva et al., 2009; Kukley et al., 2010; Lee A. et al., 2012; Martinez-Lozada et al., 2014; Suarez-Pozos et al., 2020). However, the extent to which OLG expressed GLT-1 may exert functional outcomes *via* mechanisms downstream of its transporter activation remains largely unknown.

First evidence for potential roles of OLG expressed GLT-1 beyond glutamate uptake were revealed by our previous studies in which activation of sodium-dependent glutamate transporters and particularly GLT-1 was shown to enhance the morphological aspects of OLG maturation (Martinez-Lozada et al., 2014; Spencer et al., 2020; Suarez-Pozos et al., 2020; Thomason et al., 2020). More specifically, glutamate uptake was found to be associated with a reversal of sodium-calcium exchange leading to intracellular calcium transients and alterations in actin cytoskeletal organization (Martinez-Lozada et al., 2014; Spencer et al., 2020; Suarez-Pozos et al., 2020) that likely drive process outgrowth and branching (Martinez-Lozada et al., 2014; Thomason et al., 2020) and, thus, morphological alterations thought to be crucial for effective initiation of CNS myelination (Zuchero et al., 2015; Seixas et al., 2019). Based on these data, OLG expressed GLT-1 emerges as a potential modulator of CNS myelination. In order to better assess such a functional role of GLT-1, we generated inducible and conditional knockout mice in which GLT-1 can be deleted from maturing OLGs during the peak period of myelination. Using this approach, our data shown here revealed hypomyelinated features in the male corpus collosum that were not found associated with significant changes in myelin gene expression. Thus, our findings demonstrate that OLG expressed GLT-1 can modulate developmental CNS myelination, at least in the male corpus callosum, by controlling a morphology regulatory program that functions largely independent from the well-described program directing myelin gene expression.

MATERIALS AND METHODS

Reagents and Antibodies

Unless otherwise stated, all reagents were purchased from Sigma-Aldrich or Thermo Fisher Scientific. Details to antibodies are listed below and PCR primers are shown in **Table 1**.

For flow cytometry, Fc receptors were blocked using anti-CD16/CD32 antibodies (rat IgG2a, 1:50, Thermo Fisher Scientific Cat# 14-0161-86, RRID:AB_467135). The following antibodies were used to determine the percentage of GLT-1-positive maturing OLGs: O4 (phycoerythrin-conjugated, mouse IgM, 10 μl/million cells, R&D Systems Cat# FAB1326P, RRID:AB_664169), isotype control to O4 (phycoerythrin-conjugated, mouse IgM, 10 μl/million cells, R&D Systems Cat# IC015P, RRID:AB_2885000), anti-EAAT2/GLT-1 (rabbit polyclonal, 1:50, Novus Cat# NBP1-20136, RRID:AB_1641916), isotype control to anti-EAAT2/GLT-1 (rabbit IgG polyclonal, 1:50, Novus Cat# NBP2-24891, RRID: AB_2811130), and Alexa 633-conjugated anti-rabbit secondary antibodies (goat anti-rabbit IgG, Molecular Probes Cat# A-21071, RRID:AB_141419).

For immunocytochemistry, anti-APC (CC-1; mouse IgG$_{2b}$, 1:100, Millipore Cat# OP80, RRID:AB_2057371) antibodies in combination with goat anti-mouse IgG$_{2b}$, AlexaFluor 568 conjugated secondary antibodies (1:00, Thermo Fisher Scientific Cat# A-21144, RRID:AB_2535780). YFP was detected using anti-GFP antibodies (rabbit polyclonal IgG, 1:100, Millipore Cat# AB3080, RRID:AB_91337) in combination with Alexa 488-conjugated secondary antibodies (1:500, goat

TABLE 1 | List of primer sequences used for RT-qPCR analysis.

	Forward primer (5’–3’)	Reverse primer (5′–3’)
Mouse genes		
Mbp	GTGACACCTCGTACACCCCCTCCA	GCTAAATCTGCTGAGGGACAGGCCT
Plp1	CCACACTAGTTTCCCTGCTCACCT	GGTGCCTCGGCCCATGAGTT
Mog	ATCTGCTACAACTGGCTGCAC	GGGAAATCCCCAAGGACCTGC
Mouse reference genes		
Ppia	GGAGACGAACCTGTAGGACG	GATGCTCTTTCCTCCTGTGC
Pgk1	ATGCAAAGACTGGCCAAGCTAC	AGCCACAGCCTCAGCATATTTC
Rpl13a	GCGCCTCAAGGTGTTGGATG	CGCCCCAGGTAAGCAAACTTTC

Mbp, myelin basic protein; Mog, myelin oligodendrocyte glycoprotein; Pgk1, phosphoglycerate kinase 1; Plp1, proteolipid protein; Ppia, peptidylprolyl isomerase A (cyclophilin A); Rpl13a, ribosomal protein L13a.

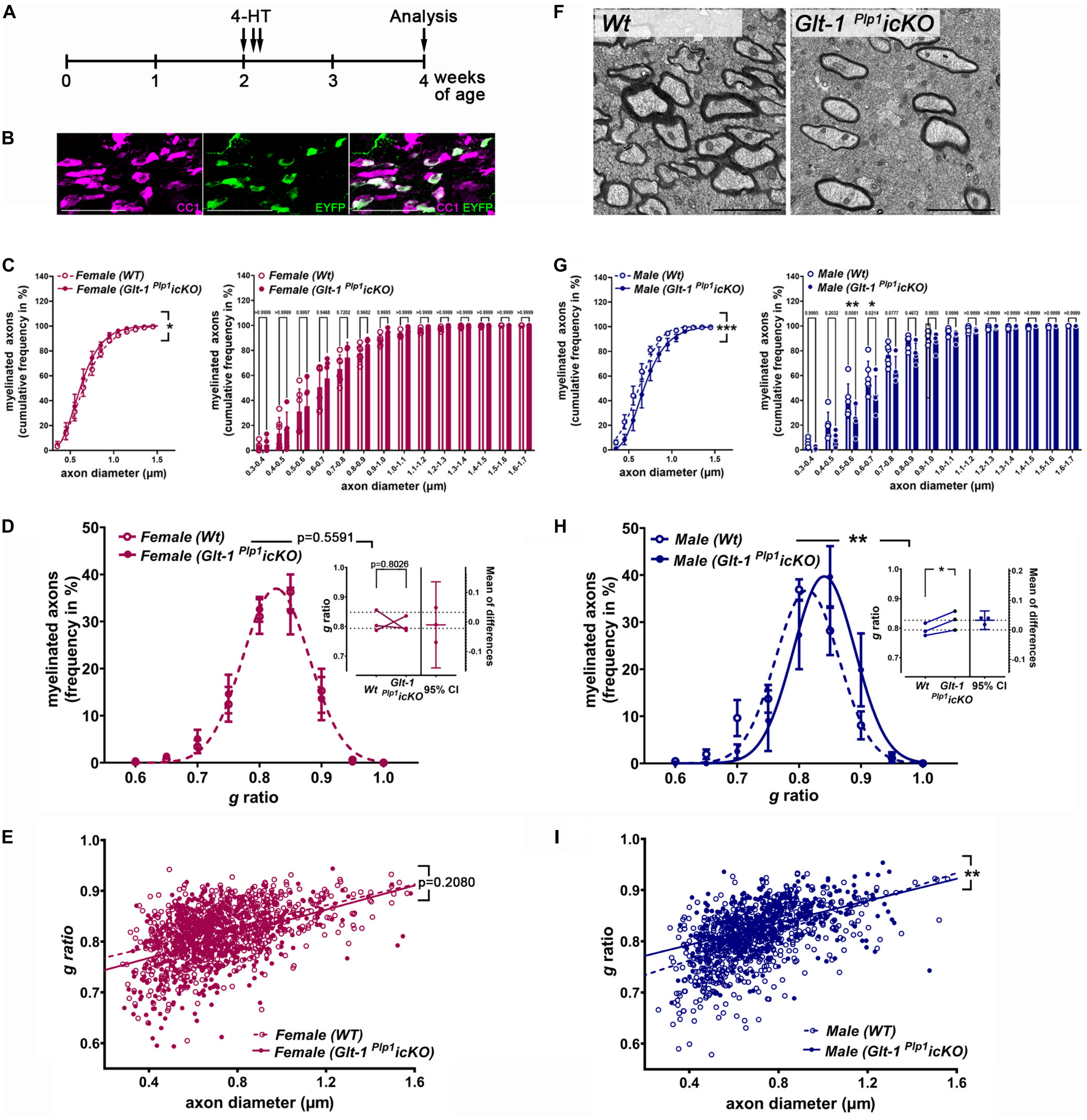

FIGURE 1 | Conditional deletion of *Glt-1* from maturing OLGs attenuates CNS myelination in the corpus callosum of male mice. **(A)** Scheme depicting the timing of intraperitoneal injections of 4-hydroxytamoxifen (4-HT; P14,16,17) in *Glt-1* ^{Plp1}*icKO* and *Wt* (*Plp1*^{CreERT}-negative littermate) mice and the developmental time-point of analysis (4 weeks of age). **(B)** Representative confocal image of the corpus callosum (midline); CC1 marks maturing OLGs (Fuss et al., 2000; Bin et al., 2016) and EYFP, derived from the ROSA reporter, marks cells in which Cre-mediated recombination has occurred successfully (Srinivas et al., 2001). Sale Bar: 50 μm. **(C,G)** Line (left) and bar (right) graphs depicting the cumulative frequency distribution of myelinated fibers in the corpus callosum of *Wt* (open circles) and *Glt-1* ^{Plp1}*icKO* (filled circles) female **(C)** and male **(G)** mice based on axon diameter; for the line graphs, the Gompertz growth curve was used as non-linear regression model (least squares regression) and extra sum-of-squares *F*-test was used to determine significant differences between regression curves; for the bar graphs, two-way ANOVA and Šidák multiple-comparisons test were used [$p = 0.0307$ (female) and $p < 0.0001$ (male) for overall difference between genotypes]. **(D,H)** Line graphs depicting the frequency distribution of myelinated fibers in the corpus callosum of *Wt* (open circles) and *Glt-1* ^{Plp1}*icKO* (filled circles) female **(D)** and male **(H)** mice based on *g*-ratio. Gaussian distribution was used as non-linear regression model (least squares regression); extra sum-of-squares *F*-test was used to determine significant differences between regression curves. The insets depict mean *g*-ratios per animal pairs of individual litters; paired *t*-test (between individual animals from the same litter; data are shown for 3 litter pairs) was used to determine significance. **(E,I)** Scatter plots depicting g-ratios vs. axon diameter for the corpus callosum of *Wt* (open circles) and *Glt-1*^{Plp1}*icKO* (filled circles) female **(E)** and male **(I)** mice. The lines represent linear regression fits to pooled data from all animals for each genotype; an *F*-test was used to determine significant differences between the slopes of the regression curves. **(F)** Representative electron microscopic images of the corpus callosum of *Glt-1* ^{Plp1}*icKO* and *Wt* (*Plp1*^{CreERT}-negative littermate) male mice injected with 4-HT. Scale bar: 2 μm. female *Glt-1* ^{Plp1}*icKO* ($n = 5$), female *Wt* ($n = 6$), male *Glt-1* ^{Plp1}*icKO* ($n = 4$), male *Wt* ($n = 6$). $^{*}p \leq 0.05$, $^{**}p \leq 0.01$, $^{***}p \leq 0.001$.

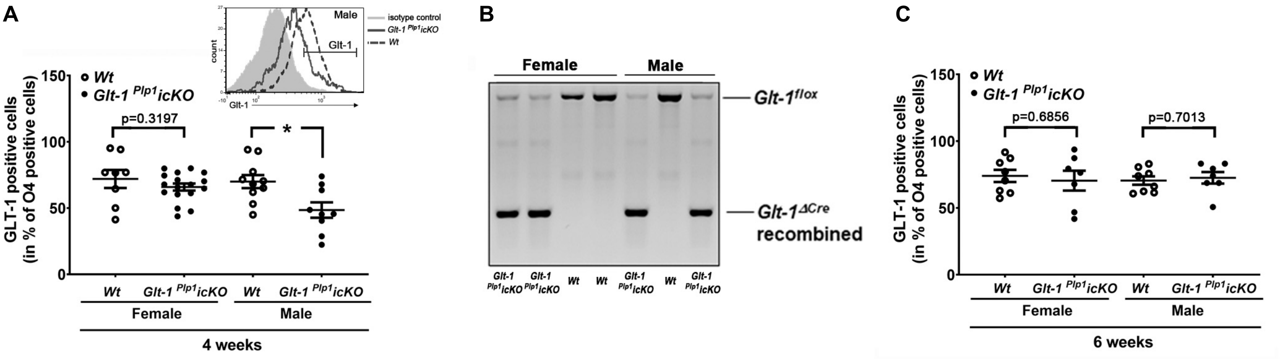

FIGURE 2 | The percentage of GLT-1-positive maturing (O4-positive) OLGs is transiently reduced in male *Glt-1* ^{Plp1}*icKO* brains at 4 weeks of age. **(A,C)** Graphs depicting the percentage of maturing (O4-positive) OLGs with surface expression of GLT-1, as determined by flow cytometry, at 4 **(A)** and 6 **(C)** weeks of age. *Glt-1* ^{Plp1}*icKO* and *Wt* (*Plp1*^{CreERT}-negative littermate) mice were treated as depicted in **Figure 1A** and analyzed at 4 and 6 weeks of age. Dots represent individual samples (animals), horizontal lines indicate means, error bars are depicted as SEM. *$p \leq 0.05$, multiple comparisons, two-way ANOVA with *post-hoc* Tukey's test; there is no significant interaction; individual *p*-values are depicted for $p > 0.05$. The inset in panel **(A)** depicts a representative histogram displaying relative fluorescence intensity (x-axis) vs. event number (y-axis) gated for O4 positivity; overlaid histogram subtraction (GLT-1 histogram—IgG isotype control histogram) was used to determine the percentage of GLT-1-positive maturing (O4-positive) OLGs. **(B)** Representative genomic PCR results for brain tissue taken from *Glt-1* ^{Plp1}*icKO* and *Wt* (*Plp1*^{CreERT}-negative littermate) female and male mice.

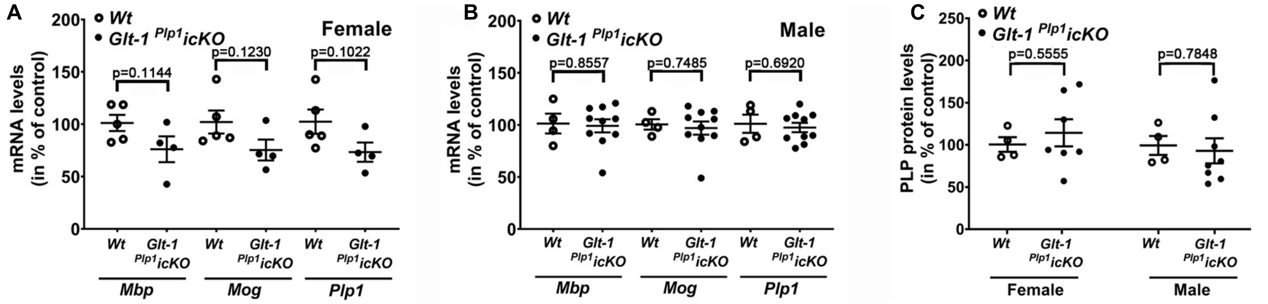

FIGURE 3 | Conditional deletion of *Glt-1* from maturing OLGs does not significantly affect myelin gene expression in the corpus callosum of female and male mice. **(A,B)** Graphs depicting mRNA levels for the myelin genes genes *myelin basic protein (Mbp)*, *myelin oligodendrocyte glycoprotein (Mog)*, and *proteolipid protein (Plp1)* in female **(A)** and male **(B)** corpus callosum as determined by reverse transcriptase quantitative polymerase chain reaction (RT-qPCR). **(C)** Graph depicting PLP protein levels as determined by Western blot analysis. *Glt-1* ^{Plp1}*icKO* and *Wt* (*Plp1*^{CreERT}-negative littermate) mice were treated as depicted in **Figure 1A** and analyzed at 4 weeks of age. Dots represent individual samples (animals), horizontal lines indicate means, error bars are depicted as SEM; individual *p*-values are depicted for $p > 0.05$, unpaired *t*-test (two-tailed).

anti-rabbit IgG, Thermo Fisher Scientific Cat# A-11008, RRID:AB_143165).

Animals

Glt-1^{flox} (*Slc1a2*$^{TM1.1Pros}$; MGI: 5752263) mice were generated as previously described (Petr et al., 2015) and crossbred to *Plp1*^{CreERT} (RRID:IMSR_JAX:005975) driver (Doerflinger et al., 2003) and *ROSA-EYFP* [*Gt(ROSA)26Sor*$^{TM1(EYFP)Cos}$; RRID:IMSR_JAX:006148] reporter (Srinivas et al., 2001) mice to obtain *Glt-1*$^{flox/flox}$:*Plp1*$^{CreERT\pm}$:*ROSA-EYFP* mice, here referred to as *Glt-1*^{Plp1}*icKO* mice; animals were kept heterozygous for *Plp1*^{CreERT} and on a C57BL/6J background. *Plp1*^{CreERT}-negative littermates were used as controls and are referred to as *Wt*. Recombination was induced by intraperitoneal injection of 4-hydroxy-tamoxifen (4-HT; 1 mg; Sigma Aldrich Cat# H7904) at P14, P16, and P17, followed by analysis at 4 weeks of age; both *Glt-1* ^{plp1}*icKO* and *Wt* mice were treated with 4-HT. Genotypes for all animals were confirmed by genomic PCR using tail tissue; in the flow cytometry and RT-qPCR experiments 4-HT-induced recombination was confirmed by genomic PCR using spinal cord and brain tissue, respectively. Mice were housed in humidity- and temperature-controlled spaces, on a normal 12/12 h light/dark cycle, with free access to standard chow and water. All animal studies were approved by the Institutional Animal Care and Use Committees at Virginia Commonwealth University (IACUC #AM10229).

Confocal and Electron Microscopy

For confocal imaging, 40 μm cryostat sections were prepared and immunstained in principle as previously described (Dupree et al., 1999; Benusa et al., 2017). Briefly, male and female *Glt-1* ^{plp1}*icKO* and control mice were anesthetized and transcardially perfused with 4% paraformaldehyde in 0.1 M Millonig's phosphate buffer

(Karlsson and Schultz, 1965), and brains were removed, post-fixed for 24 h in perfusion fixative, cryoprotected by immersion in 30% sucrose in PBS for 48 h, and then embedded and frozen in Tissue-Tek O.C.T. compound (Sakura Finetek Cat# 4583). Serial coronal sections were prepared using a Leica CM 1850 cryostat and stored at -80°C. Tissue sections were permeabilized for 10 min in ice-cold acetone and blocked for 1 h at room temperature using PBS containing 1% Triton X-100 and 5% cold water fish skin gelatin (Electron Microscopy Science cat# 25560). Primary antibodies were diluted in blocking solution, and sections were incubated for 48 h at 4°C followed by incubation with secondary antibodies for 90 min at room temperature. Nuclei were counterstained using Hoechst 33342 and sections were mounted using Vectashield Antifade Mounting Medium (Vector Laboratories Cat# H-1000-10). Images were collected using a Zeiss LSM 710 confocal laser scanning microscope located within VCU's Microcopy Shared Resource. Confocal z-stacks, each spanning an optical distance of 15 μm, were collected at 1 μm intervals using a 40x oil-immersion objective with a numerical aperture of 1.3 and the following settings: a pinhole size of one Airy unit, a dimension of 1248×1248 pixels and 4 times line averaging. For image acquisition and the generation of maximum intensity projections ZEN imaging software (Carl Zeiss Microscopy, LLC, Thornwood, NY, United States; RRID:SCR_013672) was used. For electron microscopy, brain tissue was prepared as previously described (Dupree et al., 1998; Marcus et al., 2006; Forrest et al., 2009; Waggener et al., 2013). In brief, male and female *Glt-1* ^{plp1}*icKO* and control mice were deeply anesthetized, transcardially perfused and post-fixed for 2 weeks. Brains were harvested and 60 μm sagittal sections were prepared on a Leica VT1000S Vibratome. Sections were processed for standard EM analysis as previously described (Dupree et al., 1998). Ultrathin sections were imaged using a Jeol JEM-1400Plus equipped with a Gatan CCD camera and located within VCU's Microcopy Shared Resource; to ensure comparable area representation within the corpus callosum, the following structures were used as landmarks: fornix, longitudinal lines, hippocampus, and cortex. 10–20 images obtained at 5000x magnification representing a minimum of 100 axons with diameters > 0.3 μm were assessed per animal (Mason et al., 2001); axon diameter, myelin thickness and *g*-ratio were determined manually using Fiji-ImageJ (Schindelin et al., 2012).

Flow Cytometry

Male and female *Glt-1* ^{plp1}*icKO* and control mice were euthanized using intraperitoneal injection of an overdose of tribromomethanol (2–3 times 250 mg/Kg, Sigma Aldrich Cat# T48401) and brains were removed and coarsely chopped with microdissecting scissors. Single cell suspensions were prepared by enzymatic digestion at 37°C/CO$_2$ for 30 min (1 ml per brain, StemPro Accutase, Thermo Fisher Scientific Cat# A1110501) followed by enzyme inactivation [addition of 2 ml 10% fetal bovine serum (FBS) in Hank's Balanced Salt Solution (HBSS)], physical dissociation *via* trituration and filtration using 100 μm cell strainers. To purify cells from myelin debris, cells were resuspended in 40% Percoll (GE Healthcare Cat# 17-0891-02) in HBSS and centrifuged at 650 × *g* without brake for 25 min at room temperature. The myelin top layer was aspirated and cells were resuspended in Dulbecco's Modified Eagle's Medium (DMEM)/10% FBS also used as immuno-labeling buffer. 10^6 cells per sample were used for immuno-labeling and analysis. Briefly, Fc receptors were blocked using CD16/CD32 antibodies (15 min on ice) followed by incubation with primary antibodies (or isotype control; 30 min on ice), fluorescently labeled secondary antibodies (30 min on ice), and 7-AAD Viability Staining Solution (5 μl/million cells, Thermo Fisher Scientific Cat# 00-6993-50). Cells were resuspended in flow cytometry buffer [0.1% bovine serum albumin (BSA) in phosphate buffered saline (PBS) containing 2 mM ethylenediaminetetraacetic acid (EDTA)] and run on an LSRFortessa-X20 flow cytometer (BD Biosciences). Settings were carefully determined empirically and exactly reproduced in each experiment. Gates were demarcated to count phycoerythrin and Alexa 633 double positive (7-AAD-negative) cells up to 10,000 events. FACSDIVA software (BD Biosciences, RRID:SCR_001456) was used for acquisition, and data were analyzed using FCS Express Flow Cytometry software (*DeNovo* Software, RRID:SCR_016431).

RNA Isolation and RT-qPCR

RNA was purified from dissected corpus callosum tissue using a Qiagen RNeasy Micro kit (Qiagen Cat# 74004). RNA quality and concentrations were determined on a 2100 Bioanalyzer (Agilent) using an RNA 6000 Pico kits (Agilent Cat# 5067), and samples with an RNA integrity number above 7 were used for further analysis. cDNA synthesis was performed using a Sensiscript reverse transcription kit (Qiagen Cat# 205213) according to the manufacturer's guidelines. RNA samples were normalized to the same approximate concentration, and the same amount of RNA was used for all conditions of an individual independent RT-qPCR experiment.

For all RT-qPCR experiments the Minimum Information for Publication of Quantitative Real-Time PCR *E*xperiments (MIQE) guidelines were followed (Bustin et al., 2009). Briefly, RT-qPCR primers (**Table 1**) were designed and *in silico* tested for specificity using the National Center for Biotechnology Information's basic local alignment search tool (Primer-BLAST) (Ye et al., 2012). All primers were designed to amplify all known splice variants, and for all primer pairs melting curves were used to ensure specificity. cDNA reactions without reverse transcriptase were performed for all samples to ensure no-reverse-transcriptase quantitation cycle (C_q) numbers of at least five cycles below the lowest C_q for any of the experimental samples. RT-qPCR reactions with three technical replicates per sample were performed on a CFX96 real-time PCR detection system (Bio-Rad) using the iTaq Universal SYBR Green Supermix (Bio-Rad Cat# 1725121). PCR conditions were set to 95°C for 3 min followed by 40 cycles of 95°C for 15 s, 58°C for 30 s, and 95°C for 10 s. Relative expression levels were determined using the $\Delta\Delta$CT method relative to the geometric mean of the three reference genes (Livak and Schmittgen, 2001).

Western Blot Analysis

For Western blot analysis, dissected mouse corpus callosum samples were homogenized in lysis buffer [10 μL per mg tissue;

phosphate-buffered saline (PBS), 2 mM EDTA] containing 1x Halt protease and phosphatase inhibitor cocktail (Thermo Fisher Scientific Cat# 78430). Protein concentrations were determined using a BCA protein assay kit (Pierce/Thermo Fisher Scientific Cat# 23225). Equal amounts of denatured protein samples (60 μg) were separated by electrophoresis through 4–20% gradient sodium dodecyl sulfate (SDS)-polyacrylamide gels (Bio-Rad Cat# 4561094) and electroblotted onto Immobilon-P polyvinylidene difluoride (PVDF) membranes (MilliporeSigma Cat# IPVH00010). For normalization, membranes were incubated with a Revert 700 Total Protein Stain (LI-COR Biosciences Cat# 926-11011) and imaged on an Odyssey infrared imaging system. Subsequently, membranes were incubated in blocking buffer (LI-COR Biosciences Cat# 927-70001) for 1 h at room temperature followed by incubation with anti-proteolipid protein (PLP) rat hybridoma supernatants [clone AA3 (Yamamura et al., 1991); kindly provided by Dr. Wendy Macklin, University of Colorado] for 48 h at 4°C. Bound primary antibodies were detected using IRDye 680RD-conjugated secondary antibodies (LI-COR Biosciences Cat# 926-68076, RRID:AB_10956590). For quantification, membranes were imaged using an Odyssey infrared imaging system and analyzed using Image Studio (LI-COR Biosciences software, RRID:SCR_015795) and Empiria Studio software packages (LI-COR Biosciences software Cat# 9141-500E).

Statistical Analysis

GraphPad Prism (GraphPad Software Inc., RRID:SCR_002798) was used for all statistical analyses. Prior sample size calculations were not performed. Data were assessed for normality using the Shapiro-Wilk normality test prior to analysis. Data compared with a set control value lacking variability were analyzed using the one-sample *t*-test (Skokal and Rohlf, 1995; Dalgaard, 2008). Data with two groups were analyzed by unpaired *t*-test (two-tailed), in case of pairs of *Glt-1* ^{plp1}*icKO* and control mice per litter a nested *t*-test was used, and comparisons with two parameters were analyzed for significance using two-way ANOVA with Tukey *post-hoc* testing. Frequency distributions were analyzed using Gompertz growth curves as a non-linear regression model, followed by an *F*-test to determine statistical significance.

RESULTS

In order to investigate developmental myelination upon deletion of *Glt-1* in maturing OLGs, *Glt-1* ^{Plp1}*icKO* and *Wt* (*Plp1*^{CreERT}-negative littermate) mice were treated with 4-HT at postnatal days 14, 16, and 17, and myelination of the corpus callosum was investigated at 4 weeks of age (**Figure 1A**). The above-described timing was chosen since it coincides with the reported developmental expression of *Glt-1* in OLGs (Regan et al., 2007; DeSilva et al., 2009) and a period of active myelination in the corpus callosum (Caley and Maxwell, 1968; Foran and Peterson, 1992; Leone et al., 2003). In addition, while *PLP*^{CreERT}-driven recombination has been reported to occur in cells other than OLGs (Kang et al., 2010), it has been established to be largely restricted to OLG lineage cells when induced around postnatal day 16 and beyond (Michalski et al., 2011). Consistently, when using the strategy outlined in **Figure 1A** and assessing successful recombination *via* EYFP expression derived from the ROSA-EYFP reporter, more than 95% of EYFP positive cells were also found to be positive for CC1, a marker for maturing OLGs (Fuss et al., 2000; Bin et al., 2016; **Figure 1B**). Few (less than 5%) EYFP positive cells were observed to be CC1-negative; based on previously published data, these cells likely represent OLG progenitor cells (Guo et al., 2009). At 4 weeks of age, recombination could be detected in approximately 50% of CC1 positive maturing OLGs, an effect level that is consistent with previously published studies demonstrating clear functional consequences (Traka et al., 2010; Koenning et al., 2012; Jeffries et al., 2016). Importantly, the inducible *Plp1*^{CreERT} system has been used successfully by us (Forrest et al., 2009) and others (Doerflinger et al., 2003; Kang et al., 2010; Michalski et al., 2011) with no evidence of Cre-mediated toxicity.

Assessing myelination of the corpus callous at 4 weeks of age by ultrastructural analysis, revealed a slight shift toward smaller diameter axons in female *Glt-1* ^{Plp1}*icKO* mice (**Figure 1C**). However, pairwise comparisons per 0.1 μm axon diameter bins revealed no differences, suggesting a slight increase of myelination over a larger range of smaller diameter axons. In contrast to females, a significant shift toward larger diameter myelinated axons was observed in male *Glt-1* ^{Plp1}*icKO* mice (**Figures 1F,G**). Notably, this effect appears largely due to a decrease in myelination of axons within a narrow range of diameter, namely between 0.5 and 0.7 μm (bar graph in **Figure 1G**). No change in myelin thickness, as assessed by calculating *g*-ratios, was noted in female *Glt-1* ^{Plp1}*icKO* mice (**Figure 1D**). In contrast, in male *Glt-1* ^{Plp1}*icKO* mice an increase in *g*-ratios, reflecting thinner myelin sheaths, was noted (**Figures 1G,H**). In particular, despite variances between animals from different litters, the increase in *g*-ratio seen in male *Glt-1* ^{Plp1}*icKO* mice appears consistent when evaluating pairs of *Wt* and *Glt-1* ^{Plp1}*icKO* mice within individual litters (see inset in **Figure 1H**). Notably, these alterations in myelination were not found accompanied by obvious signs of widespread cell death or axonal pathology (**Figure 1F**). Furthermore, plotting *g*-ratios vs. axon diameter, revealed that the differences in *g*-ratios between *Glt-1* ^{Plp1}*icKO* and *Wt* (*Plp1*^{CreERT}-negative littermate) male mice is most prominently seen for smaller diameter myelinated axons (**Figure 1I**). Thus, the increase in *g*-ratio (and reduction in myelin thickness) in the corpus callosum of *Glt-1* ^{Plp1}*icKO* male mice does not reflect an indirect effect due to the observed shift toward larger diameter myelinated axons; instead, it largely represents an additional characteristic of the hypomyelination phenotype that is seen in the male *Glt-1* ^{Plp1}*icKO* corpus callosum at 4 weeks of age and that appears to be particularly relevant to smaller diameter axons.

In light of the rather unexpected differences in myelination phenotype seen between males and females (**Figure 1**), flow cytometry was performed to assess the presence of GLT-1 on maturing OLGs. O4 antibodies were used to mark OLG lineage cells that are in the process of differentiation (Bansal et al., 1989). As shown in **Figure 2A**, at 4 weeks of age, a significant reduction in the percentage of GLT-1 positive maturing OLGs was observed for male but not female *Glt-1* ^{Plp1}*icKO* brains. Based on genomic PCR analysis, no significant differences in recombination efficiency were noted between male and female brain tissues (**Figure 2B**). Interestingly, it has been reported that there is a higher turnover of OLGs in female brains compared to male brains (Cerghet et al., 2006, 2009), suggesting that in female brains GLT-1 deficient OLGs may have been replaced by newly differentiated OLG progenitor cells that had remained unaffected by the initial 4-HT injections at postnatal days 14, 16, and 17. Indeed, when assessing maturing OLGs at 6 weeks of age, there was no difference in the percentage of GLT-1 positive maturing OLGs in the brains of both male and female *Glt-1* ^{Plp1}*icKO* mice (**Figure 2C**). Thus, in *Glt-1* ^{Plp1}*icKO* mice, recombination induced by postnatal 4-HT injections leads to a transient reduction in GLT-1 positive maturing OLGs in male brains that is functionally associated with an attenuation of CNS myelination characterized by decreases in myelination and myelin thickness of predominantly smaller diameter axons. In this context, the slight shift toward smaller diameter myelinated axons seen in the corpus callosum of female *Glt 1* ^{Plp1}*icKO* mice (**Figure 1C**) may be a reflection of a compensatory mechanism in response to a shorter period (compared to males) of reduced percentages of GLT-1 positive maturing OLGs in female brains.

In our previous studies, using cultures of differentiating OLGs, the effects of GLT-1 activation on OLG maturation were selective for morphological aspects and largely unrelated to a regulation of myelin gene expression (Martinez-Lozada et al., 2014; Thomason et al., 2020). Consistent with these *in vitro* findings, no differences in myelin gene expression or proteolipid protein (PLP) levels were noted in the corpus callosum between *Glt-1* ^{Plp1}*icKO* mice and *Wt* (*Plp1*^{CreERT}-negative littermate) mice (**Figure 3**). Thus, taken together, our data demonstrate that postnatal loss of GLT-1 in maturing OLGs attenuates myelination in primarily male mice without significantly affecting myelin gene expression.

DISCUSSION

The data presented in this study identified the sodium-dependent glutamate transporter GLT-1 (EAAT2, SLC1A2) as a novel modulator of developmental CNS myelination. More specifically, our data revealed that deletion of GLT-1 in maturing OLGs during a peak period of developmental myelination attenuates CNS myelination in the corpus callosum of primarily male mice as evidenced by a decreased percentage of smaller diameter myelinated axons and thinner myelin sheaths. These alterations in myelination were not found associated with major changes in myelin gene expression, thus suggesting that mechanisms downstream of GLT-1 activation in maturing OLGs are primarily involved in regulating the morphological aspects of OLG maturation and their association with the initiation of CNS myelination and the thickening of CNS myelin sheaths.

Based on our previous studies (Martinez-Lozada et al., 2014; Spencer et al., 2020; Suarez-Pozos et al., 2020; Thomason et al., 2020), the downstream mechanisms mediating GLT-1's modulatory effects on CNS myelination are, at least in part, mediated by intracellular calcium transients. In this context, it is notable that calcium transients have been observed in actively myelinating internodes, whereby neuronal activity dependent and independent mechanisms have been described (Micu et al., 2016; Baraban et al., 2018; Krasnow et al., 2018; Battefeld et al., 2019). In addition, localized calcium signals at points of contact between individual OLG processes and axons have been implicated in the initiation of myelination of preferentially electrically active axons by mechanisms that involve non-synaptic vesicular release of glutamate and locally restricted translation of the myelin protein MBP (Wake et al., 2011, 2015). Thus, GLT-1 expressed by maturing OLGs may represent one of the glutamate responsive transmembrane proteins sensing non-synaptic glutamate release by electrically active axons and triggering modulatory changes in CNS myelination. Such modulation of myelination is to be seen as an adaptive mechanism, also referred to as myelin plasticity, that fine-tunes developmental myelination by addition of new myelin and modifications to pre-existing myelin sheaths (Liu et al., 2012; Makinodan et al., 2012; Hill et al., 2018; Hughes et al., 2018; Bacmeister et al., 2020), and by complementing a so-called intrinsic process of myelination, which is thought to occur independently of axonal signals (Lee S. et al., 2012; Bechler et al., 2015, 2018; Mayoral et al., 2018). The concept of adaptive myelination from the initial stages of myelination onward and regulated by the properties of individual axons is further supported by *in vivo* imaging studies done in the developing zebrafish (Hines et al., 2015; Mensch et al., 2015; Koudelka et al., 2016; Nelson et al., 2020). Importantly, the extent and timing of CNS myelination, and thus their modulation by electrical activity, contributes significantly to neuronal circuitry function and its behavioral outputs (Forbes and Gallo, 2017; Bonnefil et al., 2019; Suminaite et al., 2019; Liu et al., 2020; Moore et al., 2020; Pan et al., 2020; Steadman et al., 2020; Xin and Chan, 2020; Fletcher et al., 2021). Notably, in addition to the above signaling downstream of activation of GLT-1, there is the potential of a role of GLT-1 imported glutamate in regulating metabolism. In this context, lipid and protein synthesis during active myelination have been well-established to impose high energetic costs (Harris and Attwell, 2012; Rosko et al., 2019; Tepavcevic, 2021), and an increasing number of studies point toward a high demand of oxidative phosphorylation/mitochondrial metabolism in actively myelinating cells during development. Independent of the exact molecular mechanism, the functional role of GLT-1 in modulating CNS myelination, as described here, coincides with a developmental time window of particular vulnerability for adaptive white matter alterations associated with adult behavioral and cognitive dysfunctions (Kikusui et al., 2007; Liu et al., 2012; Makinodan et al., 2012). In addition, *EAAT2*/*Glt-1* polymorphisms and mutations have been associated with cognitive defects in schizophrenia (Spangaro et al., 2014, 2018; Fiorentino et al., 2015; Mazza et al., 2019) and an increased risk for autism (Autism Genome Project Consortium, Szatmari et al., 2007; Xu et al., 2008), respectively. These findings raise the intriguing possibility that GLT-1 function in maturing OLGs may critically contribute to behaviors regulated by adaptive myelination and that GLT-1 dysfunction in maturing OLGs may represent a critical component of the pathophysiology and behavioral symptoms in certain neuropsychiatric disorders.

DATA AVAILABILITY STATEMENT

The raw data supporting the conclusions of this article will be made available by the authors, without undue reservation.

ETHICS STATEMENT

All animal studies were approved by the Institutional Animal Care and Use Committees at Virginia Commonwealth University (IACUC #AM10229).

AUTHOR CONTRIBUTIONS

ET, ES-P, JD, and BF were directly involved in the design of the study, the analysis of data, and the preparation of the manuscript. FA performed experiments, acquired data, and contributed to method optimization. PR provided study materials and contributed critical revisions to the manuscript. All authors gave consent for publication.

FUNDING

This work was supported, in part, by the following grants: R21NS090901 (BF), R01NS045883 (BF), P30HD018655 (PR), R01NS066019 (PR), and R01EY027881 (PR). Services in support of microscopy and flow cytometry were supported, in part, by funding from NIH-NCI Cancer Center Support Grant P30CA016059.

ACKNOWLEDGMENTS

The authors would like to extend their thanks to Dr. Brian Popko (Northwestern University) for providing *Plp1*^{CreERT} driver mice and Dr. Wendy Macklin (University of Colorado) for providing the AA3 hybridoma cell line. In addition, the authors thank VCU's microscopy and flow cytometry shared resource staff for their help and advice.

REFERENCES

Arranz, A. M., Hussein, A., Alix, J. J., Perez-Cerda, F., Allcock, N., Matute, C., et al. (2008). Functional glutamate transport in rodent optic nerve axons and glia. *Glia* 56, 1353–1367. doi: 10.1002/glia.20703

Autism Genome Project Consortium, Szatmari, P., Paterson, A. D., Zwaigenbaum, L., Roberts, W., Brian, J., et al. (2007). Mapping autism risk loci using genetic linkage and chromosomal rearrangements. *Nat. Genet.* 39, 319–328. doi: 10.1038/ng1985

Bacmeister, C. M., Barr, H. J., McClain, C. R., Thornton, M. A., Nettles, D., Welle, C. G., et al. (2020). Motor learning promotes remyelination via new and surviving oligodendrocytes. *Nat. Neurosci.* 23, 819–831. doi: 10.1038/s41593-020-0637-3

Bansal, R., Warrington, A. E., Gard, A. L., Ranscht, B., and Pfeiffer, S. E. (1989). Multiple and novel specificities of monoclonal antibodies O1, O4, and R-mAb used in the analysis of oligodendrocyte development. *J. Neurosci. Res.* 24, 548–557. doi: 10.1002/jnr.490240413

Baraban, M., Koudelka, S., and Lyons, D. A. (2018). Ca (2+) activity signatures of myelin sheath formation and growth in vivo. *Nat. Neurosci.* 21, 19–23. doi: 10.1038/s41593-017-0040-x

Battefeld, A., Popovic, M. A., de Vries, S. I., and Kole, M. H. P. (2019). High-Frequency Microdomain Ca(2+) Transients and Waves during Early Myelin Internode Remodeling. *Cell Rep.* 26, 182–191.e5. doi: 10.1016/j.celrep.2018.12.039

Bechler, M. E., Byrne, L., and Ffrench-Constant, C. (2015). CNS Myelin Sheath Lengths Are an Intrinsic Property of Oligodendrocytes. *Curr. Biol.* 25, 2411–2416. doi: 10.1016/j.cub.2015.07.056

Bechler, M. E., Swire, M., and Ffrench-Constant, C. (2018). Intrinsic and adaptive myelination-A sequential mechanism for smart wiring in the brain. *Dev. Neurobiol.* 78, 68–79. doi: 10.1002/dneu.22518

Benusa, S. D., George, N. M., Sword, B. A., DeVries, G. H., and Dupree, J. L. (2017). Acute neuroinflammation induces AIS structural plasticity in a NOX2-dependent manner. *J. Neuroinflammation* 14:116. doi: 10.1186/s12974-017-0889-3

Bin, J. M., Harris, S. N., and Kennedy, T. E. (2016). The oligodendrocyte-specific antibody 'CC1' binds Quaking 7. *J. Neurochem.* 139, 181–186. doi: 10.1111/jnc.13745

Bonnefil, V., Dietz, K., Amatruda, M., Wentling, M., Aubry, A. V., Dupree, J. L., et al. (2019). Region-specific myelin differences define behavioral consequences of chronic social defeat stress in mice. *Elife* 8:e40855. doi: 10.7554/eLife.40855

Bustin, S. A., Benes, V., Garson, J. A., Hellemans, J., Huggett, J., Kubista, M., et al. (2009). The MIQE guidelines: minimum information for publication of quantitative real-time PCR experiments. *Clin. Chem.* 55, 611–622. doi: 10.1373/clinchem.2008.112797

Caley, D. W., and Maxwell, D. S. (1968). An electron microscopic study of neurons during postnatal development of the rat cerebral cortex. *J. Comp. Neurol.* 133, 17–44. doi: 10.1002/cne.901330103

Cerghet, M., Skoff, R. P., Bessert, D., Zhang, Z., Mullins, C., and Ghandour, M. S. (2006). Proliferation and death of oligodendrocytes and myelin proteins are differentially regulated in male and female rodents. *J. Neurosci.* 26, 1439–1447. doi: 10.1523/JNEUROSCI.2219-05.2006

Cerghet, M., Skoff, R. P., Swamydas, M., and Bessert, D. (2009). Sexual dimorphism in the white matter of rodents. *J. Neurol. Sci.* 286, 76–80. doi: 10.1016/j.jns.2009.06.039

Chen, C. J., Ou, Y. C., Lin, S. Y., Liao, S. L., Huang, Y. S., and Chiang, A. N. (2006). L-glutamate activates RhoA GTPase leading to suppression of astrocyte stellation. *Eur. J. Neurosci.* 23, 1977–1987. doi: 10.1111/j.1460-9568.2006.04728.x

Dalgaard, P. (2008). *Introductory Statistics with R*. New York: Springer.

Danbolt, N. C. (2001). Glutamate uptake. *Prog. Neurobiol.* 65, 1–105. doi: 10.1016/s0301-0082(00)00067-8

DeSilva, T. M., Kabakov, A. Y., Goldhoff, P. E., Volpe, J. J., and Rosenberg, P. A. (2009). Regulation of glutamate transport in developing rat oligodendrocytes. *J. Neurosci.* 29, 7898–7908. doi: 10.1523/JNEUROSCI.6129-08.2009

Doerflinger, N. H., Macklin, W. B., and Popko, B. (2003). Inducible site-specific recombination in myelinating cells. *Genesis* 35, 63–72. doi: 10.1002/gene.10154

Domercq, M., and Matute, C. (1999). Expression of glutamate transporters in the adult bovine corpus callosum. *Brain Res. Mol. Brain Res.* 67, 296–302. doi: 10.1016/s0169-328x(99)00072-8

Dupree, J. L., Coetzee, T., Suzuki, K., and Popko, B. (1998). Myelin abnormalities in mice deficient in galactocerebroside and sulfatide. *J. Neurocytol.* 27, 649–659. doi: 10.1023/a:1006908013972

Dupree, J. L., Girault, J. A., and Popko, B. (1999). Axo-glial interactions regulate the localization of axonal paranodal proteins. *J. Cell Biol.* 147, 1145–1152. doi: 10.1083/jcb.147.6.1145

Fiorentino, A., Sharp, S. I., and McQuillin, A. (2015). Association of rare variation in the glutamate receptor gene SLC1A2 with susceptibility to bipolar disorder and schizophrenia. *Eur. J. Hum. Genet.* 23, 1200–1206. doi: 10.1038/ejhg.2014.261

Fletcher, J. L., Makowiecki, K., Cullen, C. L., and Young, K. M. (2021). Oligodendrogenesis and myelination regulate cortical development, plasticity and circuit function. *Semin. Cell Dev. Biol.* 118, 14–23. doi: 10.1016/j.semcdb.2021.03.017

Flores-Mendez, M. A., Martinez-Lozada, Z., Monroy, H. C., Hernandez-Kelly, L. C., Barrera, I., and Ortega, A. (2013). Glutamate-dependent translational control in cultured Bergmann glia cells: eIF2alpha phosphorylation. *Neurochem. Res.* 38, 1324–1332. doi: 10.1007/s11064-013-1024-1

Foran, D. R., and Peterson, A. C. (1992). Myelin acquisition in the central nervous system of the mouse revealed by an MBP-Lac Z transgene. *J. Neurosci.* 12, 4890–4897. doi: 10.1523/JNEUROSCI.12-12-04890.1992

Forbes, T. A., and Gallo, V. (2017). All Wrapped Up: environmental Effects on Myelination. *Trends Neurosci.* 40, 572–587. doi: 10.1016/j.tins.2017.06.009

Forrest, A. D., Beggs, H. E., Reichardt, L. F., Dupree, J. L., Colello, R. J., and Fuss, B. (2009). Focal adhesion kinase (FAK): a regulator of CNS myelination. *J. Neurosci. Res.* 87, 3456–3464. doi: 10.1002/jnr.22022

Fuss, B., Mallon, B., Phan, T., Ohlemeyer, C., Kirchhoff, F., Nishiyama, A., et al. (2000). Purification and analysis of in vivo-differentiated oligodendrocytes expressing the green fluorescent protein. *Dev. Biol.* 218, 259–274. doi: 10.1006/dbio.1999.9574

Guo, F., Ma, J., McCauley, E., Bannerman, P., and Pleasure, D. (2009). Early postnatal proteolipid promoter-expressing progenitors produce multilineage cells in vivo. *J. Neurosci.* 29, 7256–7270. doi: 10.1523/JNEUROSCI.5653-08.2009

Harris, J. J., and Attwell, D. (2012). The energetics of CNS white matter. *J. Neurosci.* 32, 356–371. doi: 10.1523/JNEUROSCI.3430-11.2012

Hill, R. A., Li, A. M., and Grutzendler, J. (2018). Lifelong cortical myelin plasticity and age-related degeneration in the live mammalian brain. *Nat. Neurosci.* 21, 683–695. doi: 10.1038/s41593-018-0120-6

Hines, J. H., Ravanelli, A. M., Schwindt, R., Scott, E. K., and Appel, B. (2015). Neuronal activity biases axon selection for myelination in vivo. *Nat. Neurosci.* 18, 683–689. doi: 10.1038/nn.3992

Hughes, E. G., Orthmann-Murphy, J. L., Langseth, A. J., and Bergles, D. E. (2018). Myelin remodeling through experience-dependent oligodendrogenesis in the adult somatosensory cortex. *Nat. Neurosci.* 21, 696–706. doi: 10.1038/s41593-018-0121-5

Jeffries, M. A., Urbanek, K., Torres, L., Wendell, S. G., Rubio, M. E., and Fyffe-Maricich, S. L. (2016). ERK1/2 Activation in Preexisting Oligodendrocytes of Adult Mice Drives New Myelin Synthesis and Enhanced CNS Function. *J. Neurosci.* 36, 9186–9200. doi: 10.1523/JNEUROSCI.1444-16.2016

Kang, S. H., Fukaya, M., Yang, J. K., Rothstein, J. D., and Bergles, D. E. (2010). NG2+ CNS glial progenitors remain committed to the oligodendrocyte lineage in postnatal life and following neurodegeneration. *Neuron* 68, 668–681. doi: 10.1016/j.neuron.2010.09.009

Karlsson, U., and Schultz, R. L. (1965). Fixation of the Central Nervous System from Electron Microscopy by Aldehyde Perfusion. I. Preservation with Aldehyde Perfusates Versus Direct Perfusion with Osmium Tetroxide with Special Reference to Membranes and the Extracellular Space. *J. Ultrastruct. Res.* 12, 160–186. doi: 10.1016/s0022-5320(65)80014-4

Kikusui, T., Kiyokawa, Y., and Mori, Y. (2007). Deprivation of mother-pup interaction by early weaning alters myelin formation in male, but not female ICR mice. *Brain Res.* 1133, 115–122. doi: 10.1016/j.brainres.2006.11.031

Koenning, M., Jackson, S., Hay, C. M., Faux, C., Kilpatrick, T. J., Willingham, M., et al. (2012). Myelin gene regulatory factor is required for maintenance of myelin and mature oligodendrocyte identity in the adult CNS. *J. Neurosci.* 32, 12528–12542. doi: 10.1523/JNEUROSCI.1069-12.2012

Koudelka, S., Voas, M. G., Almeida, R. G., Baraban, M., Soetaert, J., Meyer, M. P., et al. (2016). Individual Neuronal Subtypes Exhibit Diversity in CNS Myelination Mediated by Synaptic Vesicle Release. *Curr. Biol.* 26, 1447–1455. doi: 10.1016/j.cub.2016.03.070

Krasnow, A. M., Ford, M. C., Valdivia, L. E., Wilson, S. W., and Attwell, D. (2018). Regulation of developing myelin sheath elongation by oligodendrocyte calcium transients in vivo. *Nat. Neurosci.* 21, 24–28. doi: 10.1038/s41593-017-0031-y

Kukley, M., Nishiyama, A., and Dietrich, D. (2010). The fate of synaptic input to NG2 glial cells: neurons specifically downregulate transmitter release onto differentiating oligodendroglial cells. *J. Neurosci.* 30, 8320–8331. doi: 10.1523/JNEUROSCI.0854-10.2010

Laprairie, R. B., Petr, G. T., Sun, Y., Fischer, K. D., Denovan-Wright, E. M., and Rosenberg, P. A. (2019). Huntington's disease pattern of transcriptional dysregulation in the absence of mutant huntingtin is produced by knockout of neuronal GLT-1. *Neurochem. Int.* 123, 85–94. doi: 10.1016/j.neuint.2018.04.015

Lee, A., Anderson, A. R., Beasley, S. J., Barnett, N. L., Poronnik, P., and Pow, D. V. (2012). A new splice variant of the glutamate-aspartate transporter: cloning and immunolocalization of GLAST1c in rat, pig and human brains. *J. Chem. Neuroanat.* 43, 52–63. doi: 10.1016/j.jchemneu.2011.10.005

Lee, S., Leach, M. K., Redmond, S. A., Chong, S. Y., Mellon, S. H., Tuck, S. J., et al. (2012). A culture system to study oligodendrocyte myelination processes using engineered nanofibers. *Nat. Methods* 9, 917–922. doi: 10.1038/nmeth.2105

Leone, D. P., Genoud, S., Atanasoski, S., Grausenburger, R., Berger, P., Metzger, D., et al. (2003). Tamoxifen-inducible glia-specific Cre mice for somatic mutagenesis in oligodendrocytes and Schwann cells. *Mol. Cell Neurosci.* 22, 430–440. doi: 10.1016/s1044-7431(03)00029-0

Liu, J., Dietz, K., DeLoyht, J. M., Pedre, X., Kelkar, D., Kaur, J., et al. (2012). Impaired adult myelination in the prefrontal cortex of socially isolated mice. *Nat. Neurosci.* 15, 1621–1623. doi: 10.1038/nn.3263

Liu, J., Likhtik, E., Shereen, A. D., Dennis-Tiwary, T. A., and Casaccia, P. (2020). White Matter Plasticity in Anxiety: disruption of Neural Network Synchronization During Threat-Safety Discrimination. *Front. Cell Neurosci.* 14:587053. doi: 10.3389/fncel.2020.587053

Livak, K. J., and Schmittgen, T. D. (2001). Analysis of relative gene expression data using real-time quantitative PCR and the 2(-Delta Delta C(T)) Method. *Methods* 25, 402–408. doi: 10.1006/meth.2001.1262

Makinodan, M., Rosen, K. M., Ito, S., and Corfas, G. (2012). A critical period for social experience-dependent oligodendrocyte maturation and myelination. *Science* 337, 1357–1360. doi: 10.1126/science.1220845

Marcus, J., Honigbaum, S., Shroff, S., Honke, K., Rosenbluth, J., and Dupree, J. L. (2006). Sulfatide is essential for the maintenance of CNS myelin and axon structure. *Glia* 53, 372–381. doi: 10.1002/glia.20292

Maria Lopez-Colome, A., Martinez-Lozada, Z., Guillem, A. M., Lopez, E., and Ortega, A. (2012). Glutamate transporter-dependent mTOR phosphorylation in Muller glia cells. *ASN Neuro* 4:e00095. doi: 10.1042/AN20120022

Martinez-Lozada, Z., Hernandez-Kelly, L. C., Aguilera, J., Lopez-Bayghen, E., and Ortega, A. (2011). Signaling through EAAT-1/GLAST in cultured Bergmann glia cells. *Neurochem* 59, 871–879. doi: 10.1016/j.neuint.2011.07.015

Martinez-Lozada, Z., Waggener, C. T., Kim, K., Zou, S., Knapp, P. E., Hayashi, Y., et al. (2014). Activation of sodium-dependent glutamate transporters regulates the morphological aspects of oligodendrocyte maturation via signaling through calcium/calmodulin-dependent kinase IIbeta's actin-binding/-stabilizing domain. *Glia* 62, 1543–1558. doi: 10.1002/glia.22699

Mason, J. L., Langaman, C., Morell, P., Suzuki, K., and Matsushima, G. K. (2001). Episodic demyelination and subsequent remyelination within the murine central nervous system: changes in axonal calibre. *Neuropathol. Appl. Neurobiol.* 27, 50–58. doi: 10.1046/j.0305-1846.2001.00301.x

Mayoral, S. R., Etxeberria, A., Shen, Y. A., and Chan, J. R. (2018). Initiation of CNS Myelination in the Optic Nerve Is Dependent on Axon Caliber. *Cell Rep.* 25, 544-550.e3. doi: 10.1016/j.celrep.2018.09.052

Mazza, E., Spangaro, M., Poletti, S., Cavallaro, R., and Benedetti, F. (2019). Genetic variability of glutamate reuptake: effect on white matter integrity and working memory in schizophrenia. *Schizophr. Res.* 208, 457–459. doi: 10.1016/j.schres.2019.03.004

McNair, L. F., Andersen, J. V., Aldana, B. I., Hohnholt, M. C., Nissen, J. D., Sun, Y., et al. (2019). Deletion of Neuronal GLT-1 in Mice Reveals Its Role in Synaptic Glutamate Homeostasis and Mitochondrial Function. *J. Neurosci.* 39, 4847–4863. doi: 10.1523/JNEUROSCI.0894-18.2019

McNair, L. F., Andersen, J. V., Nissen, J. D., Sun, Y., Fischer, K. D., Hodgson, N. W., et al. (2020). Conditional Knockout of GLT-1 in Neurons Leads to Alterations in Aspartate Homeostasis and Synaptic Mitochondrial Metabolism in Striatum and Hippocampus. *Neurochem. Res.* 45, 1420–1437. doi: 10.1007/s11064-020-03000-7

Mensch, S., Baraban, M., Almeida, R., Czopka, T., Ausborn, J., El Manira, A., et al. (2015). Synaptic vesicle release regulates myelin sheath number of individual oligodendrocytes in vivo. *Nat. Neurosci.* 18, 628–630. doi: 10.1038/nn.3991

Michalski, J. P., Anderson, C., Beauvais, A., De Repentigny, Y., and Kothary, R. (2011). The proteolipid protein promoter drives expression outside of the oligodendrocyte lineage during embryonic and early postnatal development. *PLoS One* 6:e19772. doi: 10.1371/journal.pone.0019772

Micu, I., Plemel, J. R., Lachance, C., Proft, J., Jansen, A. J., Cummins, K., et al. (2016). The molecular physiology of the axo-myelinic synapse. *Exp. Neurol.* 276, 41–50. doi: 10.1016/j.expneurol.2015.10.006

Moore, S., Meschkat, M., Ruhwedel, T., Trevisiol, A., Tzvetanova, I. D., Battefeld, A., et al. (2020). A role of oligodendrocytes in information processing. *Nat. Commun.* 11:5497. doi: 10.1038/s41467-020-19152-7

Nelson, H. N., Treichel, A. J., Eggum, E. N., Martell, M. R., Kaiser, A. J., Trudel, A. G., et al. (2020). Individual neuronal subtypes control initial myelin sheath growth and stabilization. *Neural Dev.* 15:12. doi: 10.1186/s13064-020-00149-3

Pan, S., Mayoral, S. R., Choi, H. S., Chan, J. R., and Kheirbek, M. A. (2020). Preservation of a remote fear memory requires new myelin formation. *Nat. Neurosci.* 23, 487–499. doi: 10.1038/s41593-019-0582-1

Petr, G. T., Sun, Y., Frederick, N. M., Zhou, Y., Dhamne, S. C., Hameed, M. Q., et al. (2015). Conditional deletion of the glutamate transporter GLT-1 reveals that astrocytic GLT-1 protects against fatal epilepsy while neuronal GLT-1 contributes significantly to glutamate uptake into synaptosomes. *J. Neurosci.* 35, 5187–5201. doi: 10.1523/JNEUROSCI.4255-14.2015

Regan, M. R., Huang, Y. H., Kim, Y. S., Dykes-Hoberg, M. I., Jin, L., Watkins, A. M., et al. (2007). Variations in promoter activity reveal a differential expression and physiology of glutamate transporters by glia in the developing and mature CNS. *J. Neurosci.* 27, 6607–6619. doi: 10.1523/JNEUROSCI.0790-07.2007

Rimmele, T. S., and Rosenberg, P. A. (2016). GLT-1: the elusive presynaptic glutamate transporter. *Neurochem. Int.* 98, 19–28. doi: 10.1016/j.neuint.2016.04.010

Rimmele, T. S., Li, S., Andersen, J. V., Westi, E. W., Rotenberg, A., Wang, J., et al. (2021). Neuronal Loss of the Glutamate Transporter GLT-1 Promotes Excitotoxic Injury in the Hippocampus. *Front. Cell Neurosci.* 15:788262. doi: 10.3389/fncel.2021.788262

Robinson, M. B., and Jackson, J. G. (2016). Astroglial glutamate transporters coordinate excitatory signaling and brain energetics. *Neurochem. Int.* 98, 56–71. doi: 10.1016/j.neuint.2016.03.014

Robinson, M. B., Lee, M. L., and DaSilva, S. (2020). Glutamate Transporters and Mitochondria: signaling, Co-compartmentalization, Functional Coupling, and Future Directions. *Neurochem. Res.* 45, 526–540. doi: 10.1007/s11064-020-02974-8

Rose, C. R., Ziemens, D., Untiet, V., and Fahlke, C. (2018). Molecular and cellular physiology of sodium-dependent glutamate transporters. *Brain Res. Bull.* 136, 3–16. doi: 10.1016/j.brainresbull.2016.12.013

Rosko, L., Smith, V. N., Yamazaki, R., and Huang, J. K. (2019). Oligodendrocyte Bioenergetics in Health and Disease. *Neuroscientist* 25, 334–343. doi: 10.1177/1073858418793077

Rothstein, J. D., Dykes-Hoberg, M., Pardo, C. A., Bristol, L. A., Jin, L., Kuncl, R. W., et al. (1996). Knockout of glutamate transporters reveals a major role for astroglial transport in excitotoxicity and clearance of glutamate. *Neuron* 16, 675–686. doi: 10.1016/s0896-6273(00)80086-0

Schindelin, J., Arganda-Carreras, I., Frise, E., Kaynig, V., Longair, M., Pietzsch, T., et al. (2012). Fiji: an open-source platform for biological-image analysis. *Nat. Methods* 9, 676–682. doi: 10.1038/nmeth.2019

Seixas, A. I., Azevedo, M. M., Paes de Faria, J., Fernandes, D., Mendes Pinto, I., and Relvas, J. B. (2019). Evolvability of the actin cytoskeleton in oligodendrocytes during central nervous system development and aging. *Cell Mol. Life Sci.* 76, 1–11. doi: 10.1007/s00018-018-2915-8

Skokal, R. R., and Rohlf, F. J. (1995). *Biometry: The Principle and Practice in Biological Research*. New York: W. H. Freeman and Company.

Spangaro, M., Bosia, M., Bechi, M., Buonocore, M., Cocchi, F., Guglielmino, C., et al. (2018). Neurobiology of cognitive remediation in schizophrenia: effects of EAAT2 polymorphism. *Schizophr. Res.* 202, 106–110. doi: 10.1016/j.schres.2018.06.059

Spangaro, M., Bosia, M., Zanoletti, A., Bechi, M., Mariachiara, B., Pirovano, A., et al. (2014). Exploring effects of EAAT polymorphisms on cognitive functions in schizophrenia. *Pharmacogenomics* 15, 925–932. doi: 10.2217/pgs.14.42

Spencer, S. A., Suarez-Pozos, E., Escalante, M., Myo, Y. P., and Fuss, B. (2020). Sodium-Calcium Exchangers of the SLC8 Family in Oligodendrocytes: functional Properties in Health and Disease. *Neurochem. Res.* 45, 1287–1297. doi: 10.1007/s11064-019-02949-4

Srinivas, S., Watanabe, T., Lin, C. S., William, C. M., Tanabe, Y., Jessell, T. M., et al. (2001). Cre reporter strains produced by targeted insertion of EYFP and ECFP into the ROSA26 locus. *BMC Dev. Biol.* 1:4. doi: 10.1186/1471-213x-1-4

Steadman, P. E., Xia, F., Ahmed, M., Mocle, A. J., Penning, A. R. A., Geraghty, A. C., et al. (2020). Disruption of Oligodendrogenesis Impairs Memory Consolidation in Adult Mice. *Neuron* 105, 150–164.e6. doi: 10.1016/j.neuron.2019.10.013

Suarez-Pozos, E., Thomason, E. J., and Fuss, B. (2020). Glutamate Transporters: expression and Function in Oligodendrocytes. *Neurochem. Res.* 45, 551–560. doi: 10.1007/s11064-018-02708-x

Suminaite, D., Lyons, D. A., and Livesey, M. R. (2019). Myelinated axon physiology and regulation of neural circuit function. *Glia* 67, 2050–2062. doi: 10.1002/glia.23665

Tanaka, K., Watase, K., Manabe, T., Yamada, K., Watanabe, M., Takahashi, K., et al. (1997). Epilepsy and exacerbation of brain injury in mice lacking the glutamate transporter GLT-1. *Science* 276, 1699–1702. doi: 10.1126/science.276.5319.1699

Tepavcevic, V. (2021). Oligodendroglial Energy Metabolism and (re)Myelination. *Life* 11, 238. doi: 10.3390/life11030238

Thomason, E. J., Escalante, M., Osterhout, D. J., and Fuss, B. (2020). The oligodendrocyte growth cone and its actin cytoskeleton: a fundamental element for progenitor cell migration and CNS myelination. *Glia* 68, 1329–1346. doi: 10.1002/glia.23735

Traka, M., Arasi, K., Avila, R. L., Podojil, J. R., Christakos, A., Miller, S. D., et al. (2010). A genetic mouse model of adult-onset, pervasive central nervous system demyelination with robust remyelination. *Brain* 133, 3017–3029. doi: 10.1093/brain/awq247

Waggener, C. T., Dupree, J. L., Elgersma, Y., and Fuss, B. (2013). CaMKIIbeta regulates oligodendrocyte maturation and CNS myelination. *J. Neurosci.* 33, 10453–10458. doi: 10.1523/JNEUROSCI.5875-12.2013

Wake, H., Lee, P. R., and Fields, R. D. (2011). Control of local protein synthesis and initial events in myelination by action potentials. *Science* 333, 1647–1651. doi: 10.1126/science.1206998

Wake, H., Ortiz, F. C., Woo, D. H., Lee, P. R., Angulo, M. C., and Fields, R. D. (2015). Nonsynaptic junctions on myelinating glia promote preferential myelination of electrically active axons. *Nat. Commun.* 6:7844. doi: 10.1038/ncomms8844

Xin, W., and Chan, J. R. (2020). Myelin plasticity: sculpting circuits in learning and memory. *Nat. Rev. Neurosci.* 21, 682–694. doi: 10.1038/s41583-020-00379-8

Xu, S., Han, J. C., Morales, A., Menzie, C. M., Williams, K., and Fan, Y. S. (2008). Characterization of 11p14-p12 deletion in WAGR syndrome by array CGH for identifying genes contributing to mental retardation and autism. *Cytogenet. Genome Res.* 122, 181–187. doi: 10.1159/000172086

Yamamura, T., Konola, J. T., Wekerle, H., and Lees, M. B. (1991). Monoclonal antibodies against myelin proteolipid protein: identification and characterization of two major determinants. *J. Neurochem.* 57, 1671–1680. doi: 10.1111/j.1471-4159.1991.tb06367.x

Ye, J., Coulouris, G., Zaretskaya, I., Cutcutache, I., Rozen, S., and Madden, T. L. (2012). Primer-BLAST: a tool to design target-specific primers for polymerase chain reaction. *BMC Bioinform.* 13:134. doi: 10.1186/1471-2105-13-134

Zhou, Y., Hassel, B., Eid, T., and Danbolt, N. C. (2019). Axon-terminals expressing EAAT2 (GLT-1; Slc1a2) are common in the forebrain and not limited to the hippocampus. *Neurochem. Int.* 123, 101–113. doi: 10.1016/j.neuint.2018.03.006

Zuchero, J. B., Fu, M. M., Sloan, S. A., Ibrahim, A., Olson, A., Zaremba, A., et al. (2015). CNS myelin wrapping is driven by actin disassembly. *Dev. Cell* 34, 152–167. doi: 10.1016/j.devcel.2015.06.011

Conflict of Interest: BF was a consultant for Gryphon Bio, Inc.

The remaining authors declare that the research was conducted in the absence of any commercial or financial relationships that could be construed as a potential conflict of interest.